UNIVERSITY OF SOUTHAMPTON

SCHOOL OF ENGINEERING SCIENCES

MATERIALS RESEARCH GROUP

EFFECT OF MICROSTRUCTURE VARIATION ON TURBINE DISC FATIGUE LIVES

By Hon Tong Pang

Thesis submitted for the degree of Doctor of Philosophy

May 2003

UNIVERSITY OF SOUTHAMPTON

ABSTRACT

FACULTY OF ENGINEERING AND APPLIED SCIENCES

MATERIALS RESEARCH GROUP

Doctor of Philosophy

EFFECT OF MICROSTRUCTURE VARIATION ON TURBINE DISC FATIGUE LIVES

By Hon Tong Pang

This project was initiated to further develop the understanding of high temperature fatigue and creep-fatigue behaviour, both in the crack initiation/short crack growth and long crack growth regimes. It comprises in part a continuation of a post-doctoral project investigating microstructural effects on the creep-fatigue behaviour of U720Li. It builds upon the work already done in the post-doctoral project and further investigates the creep-fatigue behaviour of RR1000, a turbine disc superalloy recently developed by Rolls-Royce.

Short crack and long crack tests at room and elevated temperatures were carried out on U720Li and its large grain (U720Li-LG) and large precipitate (U720Li-LP) variant as well as on the RR1000 material to complement the elevated temperature long crack data already obtained in the post-doctoral project. In the room temperature short crack tests, U720Li-LP exhibits the longest overall fatigue lifetime, followed by lower lifetime in RR1000, U720Li-LG and U720Li. The results of the room temperature long crack tests indicate approximately similar crack growth resistance of RR1000, U720Li and U720Li-LG while U720Li-LP shows lower crack growth resistance. Elevated temperature tests generally indicate better fatigue crack initiation and growth resistance in U720Li-LG and RR1000 compared to U720Li and U720Li-LP. Crack initiation and growth mechanisms under different testing conditions were identified and the complex interactions between microstructure and fatigue crack initiation and growth were examined through detailed testing and analysis. The difference in the trends of fatigue resistance of the materials under different testing conditions was attributed to the different effects of microstructure and/or alloy chemistry on fatigue mechanisms in the various fatigue crack initiation and growth regimes.

Overall, larger grains and larger size and higher volume fraction of coherent γ' precipitates were identified to be microstructural characteristics necessary for improved fatigue performance of turbine discs. Large grains have been shown to be beneficial under most of the different test conditions conducted in the current study. In terms of the size and volume fraction of coherent γ' precipitates, generally higher crack growth resistance was noted for larger size and higher volume fraction of coherent γ' precipitates in the elevated temperature long crack tests conducted in air. Although turbine disc fatigue life has been known to be dominated by crack initiation and short crack growth at elevated temperatures, higher crack growth resistance in elevated temperature long crack tests in air which has been shown to correlate to improved high temperature short crack growth resistance will give increased confidence in the overall fatigue performance of the turbine disc alloy. Porosity control is also important as porosity was noted to be the predominant crack initiation mechanism at both room temperature and at 650°C.

TABLE OF CONTENTS

ACKNOWLEDGEMENT

I would like to express my sincere gratitude to my project supervisor Dr. Philippa Reed for her continuous guidance and support. Thanks also go to Dr. Marco Starink and Dr. Ian Sinclair for their various input and discussions during the PhD.

I would also like to particularly thank Dr. Nick Hide, Dr. Thomas Connolley and Dr. Mark Joyce for showing me the various tricks and tips in research and mechanical testing. I wish to thank also the technical and support staff, Dave Beckett, Eric Bonner, Eric Roszkowiak, Sheila Clearly, Sue Walker, Gwyneth Skiller and Gill Rood for their kind assistance throughout.

For their financial support and materials supply I would also like to acknowledge Rolls-Royce and DERA/QinetiQ Farnborough. Particular thanks are owed to Dr. Mike Henderson (now at ALSTOM Power) and Mr. Ian Wilcock for their valuable technical input. Financial support from the Overseas Research Students Awards Scheme, administered by the Committee of Vice-Chancellors and Principals of the Universities of United Kingdom, are also gratefully acknowledged.

My thanks also go to colleagues and office mates for their enthusiasms, and the endless supply of coffee (and sometimes alcohol) and humour/light entertainment.

Finally, special thanks to my parents and family for their continuous and unconditional support.

SYMBOLS

E	elastic modulus
G	shear modulus
G_m	shear modulus of matrix
H_v	Vickers hardness
K	stress intensity factor
K_{max}	maximum value of stress intensity factor
K_{min}	minimum value of stress intensity factor
ΔK	stress intensity factor range
ΔK_{th}	threshold stress intensity factor range
N	number of fatigue cycles
N_f	number of cycles to specimen fracture = fatigue life
P	load
R	load ratio
T	temperature
V_f	volume fraction
a	crack depth
b	bend specimen breadth
c	half surface crack length (short crack)
d	notch depth
s	span
w	bend specimen width

ε	strain
$\Delta\varepsilon$	strain range
η	backscattered electron coefficient
σ	applied stress
σ_{cy}	cyclic yield stress
σ_{min}	minimum applied stress
σ_{max}	maximum applied stress
σ_y	yield stress
$\Delta\sigma$	applied stress range
ν	Poisson's ratio

ABBREVIATIONS

APB	Antiphase Boundary
BEI	Backscattered Electron Imaging
CT	Compact Tension
EBSD	Electron Back-scatter Diffraction
EDM	Electrostatic Discharge Machining
EDX	Energy-dispersive X-ray Spectroscopy
FCC	Face Centred Cubic
FCP	Fatigue Crack Propagation
FE	Finite Element
HCF	High Cycle Fatigue
HCP	Hexagonal Close Packed
LCF	Low Cycle Fatigue
LEFM	Linear Elastic Fracture Mechanics
PM	Powder Metallurgy
SEI	Secondary Electron Imaging
SEM	Scanning Electron Microscope
SENB	Single Edge Notch Bend
SFE	Stacking Fault Energy
TEM	Transmission Electron Microscope

1. Introduction

In modern gas turbine engines, operating efficiencies need to be continuously improved due to economic and environmental considerations. Higher operating efficiencies give increased thrust-to-weight ratios which are more economically favourable. Thermodynamically, engine efficiency improvement can be achieved by operating the engine at higher temperatures. In addition to the high operating temperatures, turbine discs are also subjected to severe loads during service. The highest stresses are experienced in the bore of the disc, in the temperature range between 200°C to 300°C. Stresses in the rim region are much lower, but at higher temperatures, currently approaching or projected to approach 725°C. Under these conditions, fatigue (repeated start-up and shut-down cycles) and creep (prolonged application of loads at high temperatures) are of major importance in determining the life of components.

To assess the safe component life, various approaches have been developed. All these approaches involve characterisation of fatigue and creep-fatigue behaviour in standard test pieces in the laboratory under conditions similar to those found in service, and an accurate non-destructive test to determine the smallest flaw in the component. While these approaches will predict the behaviour of long fatigue cracks, less is known of crack initiation and short crack growth behaviour in turbine disc alloys. Crack initiation and short crack growth life is equally as important as the lifetime during propagation of an initiated crack to failure. It is estimated that at elevated operating temperatures and stresses, a majority of the total life is spent in the crack initiation and short crack growth regime.

This project was initiated to further develop the understanding of high temperature fatigue and creep-fatigue behaviour, both in the crack initiation/short crack growth and long crack growth regime. The project comprises in part a continuation of a post-doctoral project investigating microstructural effects on the creep-fatigue behaviour of U720Li, i.e. it builds upon the work already done in the post-doctoral project and further investigates the creep-fatigue behaviour of RR1000, a turbine disc superalloy recently developed by Rolls-Royce. The original post-doctoral project was funded by DERA (DERA Agreement No. SMC/4U1605) and materials for testing were supplied by DERA/Rolls-Royce.

In the post-doctoral project, the effects of varying Cr level, grain size and coherent γ' size on fatigue crack propagation have been studied at high temperatures and low frequencies. Similar to the post-doctoral project, temperature and hold time effects on crack growth in RR1000 have been studied in vacuum at 650°C and 725°C. Air tests conducted at QinetiQ (formerly DERA) Farnborough were used for comparison and the effects of environment on crack growth behaviour were examined. As RR1000 has very similar strengthening mechanisms to U720Li and its variants, the data from this project were compared to those obtained in the post-doctoral project

and the effects of microstructure on fatigue crack propagation behaviour under different conditions were further determined.

Short crack and long crack tests at room temperature have been carried out on U720Li and its large grain (U720Li-LG) and large precipitate (U720Li-LP) variant as well as on the RR1000 material. To complement the elevated temperature long crack data obtained in the post-doctoral project, high temperature short crack tests have also been carried out on these materials to establish fatigue crack initiation and early crack propagation behaviour under conditions similar to those in service. The complex interactions between microstructure and fatigue crack initiation and growth were examined through this detailed combined test matrix and subsequent analysis.

The aims of the research presented in this thesis, concentrating on U720Li and its variants as well as on RR1000, are:

- To study fatigue crack initiation and growth mechanisms in different fatigue regimes.
- To establish the effects of microstructure on various mechanisms of fatigue crack initiation and fatigue crack growth.
- To identify optimal microstructural parameters for improved fatigue performance of the service component.

2. Literature review

Superalloys are metallic materials based on iron, nickel or cobalt developed for high temperature, high stress applications. They are usually characterised by long-term strength at elevated temperature, fatigue resistance, creep resistance and resistance to high temperature corrosion and erosion. Their applications are usually in the hot sections of gas power turbines in aircraft and in land-based power generation facilities.

Nickel-base superalloys currently used for turbine disc applications include Waspaloy, Udimet 720 (U720), Udimet 720Li (U720Li) and RR1000. Waspaloy was developed and used extensively for turbine disc applications during the 1970's. The U720 and U720Li alloys which have been developed much more recently represent a newer generation of superalloys for turbine disc applications. RR1000 is the latest superalloy developed by Roll-Royce for turbine disc applications and much work is still being carried out to quantify its high temperature properties for safe commercial applications.

2.1. Composition and physical metallurgy

Nickel-base superalloys have an austenitic face-centre cubic (FCC) phase, commonly known as the gamma (γ) phase. It also contains nickel-rich $Ni_3(Ti,Al)$ precipitates, generally referred to as gamma-prime (γ') precipitate [1]. Depending on the alloying elements present, various other precipitates may also be formed in the alloy. The γ' precipitates are the main strengthening precipitates in this alloy system, particularly at high temperatures.

Chromium (Cr) forms the main alloying addition in many nickel-base superalloys and is added to the alloy for improved high temperature properties, i.e. increased resistance to corrosion and oxidation due to formation of an adherent and non-porous, and hence protective Cr_2O_3 oxide layer. Increased Cr levels may limit intergranular oxygen diffusion ahead of the crack tip due to enhanced formation of protective Cr_2O_3, thus reducing high temperature oxidation-assisted fatigue cracking [2]. Depending on the alloy system, the Cr content for optimum oxidation resistance was found to be in the range of 15 wt % to 30 wt % [1]. However, increased Cr levels have been associated with lower volume fractions of γ' in nickel-base superalloys as Cr preferentially forms the γ phase with Ni, hence reducing the amount of Ni available to form the γ' phase. Overly high chromium contents in nickel-base superalloys have also been associated with an increased propensity to formation of the deleterious σ phase.

Aluminium (Al) and titanium (Ti), which are the major constituents of the γ' phase, are the next most important alloying elements. The volume fraction of γ' present is directly related to the amount of Al and Ti present in the alloy [1,3,4,5]. Niobium (Nb) can to some extent substitute Al and

Ti in the formation of γ', but when the Nb content is high enough (>4 wt %), it can form a separate hardening phase, Ni_3Nb, as in the case of Inconel 718.

Cobalt (Co) is also added to nickel-base superalloys as it reduces the solubility of Al and Ti in the γ matrix, hence favouring formation of the γ' phase, maintaining strength of the alloy at high temperatures [1]. The presence of cobalt also reduces creep deformation by lowering stacking fault energy (SFE) between partial dislocations, thus hindering dislocation cross-slip and climb. The presence of 15 wt % cobalt has been indicated to generate a minimum SFE which promotes planar slip and potentially improves fatigue crack propagation (FCP) resistance [3].

At higher temperatures, diffusion and dislocation cross-slip are important in determining material strength. Atoms which diffuse slowly such as molybdenum (Mo) and tungsten (W) are useful as solid-solution additions and can help reduce creep deformation. Mo, W and tantalum (Ta) also dissolve to a certain extent in the γ' phase and thereby affect the parameters of this phase which determine its strengthening characteristics, e.g. the γ' solvus temperature and the matrix/precipitate lattice mismatch [1]. In addition, these elements also form complex carbides with each other and with other elements, such as chromium and iron [1]. Refractory elements, i.e. Mo, W and particularly Ta at optimum concentrations have been indicated to be necessary for oxidation resistance [6].

Addition of Ta has been shown to increase the tensile strength but segregates to form very stable tantalum carbide (MC carbide). The Ta concentration can be controlled to allow the MC carbide to breakdown and promote formation of grain boundary carbides [3]. Addition of Ta has also been associated with enhanced oxidation resistance [6,7] and contribution to γ' strengthening (increased hardness of the γ' phase) [4,7].

Addition of trace elements (boron and carbon) was found to give significantly lower creep rates [8]. Addition of these elements significantly reduces dislocation mobility by cluster pinning of the dislocations. This impedance to dislocation motion gives rise to an anomalously high activation energy for creep. Addition of boron and zirconium in Waspaloy was also found to be important where environmental and/or creep interactions were present. Under these conditions, removal of boron and zirconium drastically increased crack growth rates [9].

Small additions of magnesium (Mg) have been associated with improved creep and fatigue properties in IN718 and Waspaloy [10,11]. Mg addition also increases tensile strength, and high temperature tensile and creep ductilities [11].

The presence of carbon significantly lowers the solidus temperature of nickel, hence gives better control of liquid metal properties. Carbon can also help remove any detrimental elements such as sulphur and oxygen from the melt.

2.2. Microstructure

The high strength of nickel-base superalloys arises from solid solution strengthening (due to Fe, Cr, Al, Ti, Mo and Co) [1,12] and precipitation hardening of the γ matrix by various phases.

2.2.1. Strengthening precipitates

$Ni_3(Al,Ti)$ precipitates, i.e. the γ' phase, gives the main form of strengthening in nickel-base superalloys. The γ' phase has an ordered FCC crystal structure (type $L1_2$) which is coherent with the FCC γ matrix [4,13]. The γ' phase can have a range of composition depending especially on the Al and Ti contents in the alloy. The γ' phase is also a reasonably ductile phase, this is useful since it will not cause embrittlement when formed along grain boundaries in the alloy [1].

Primary γ' precipitates, which are incoherent with the γ matrix, are present at grain boundaries and their size and volume fraction are controlled during the solution treatment stage (for powder metallurgy routes usually employed in the manufacture of turbine discs). Within the grains, there are finer secondary and tertiary γ' precipitates which are coherent with the γ matrix. The main difference between secondary and tertiary γ' precipitates is in the size and shape, where secondary γ' are larger and usually cuboidal in shape (due to larger lattice mismatch) [13], and tertiary γ' are finer and spherical in shape.

2.2.2. Carbides

Primary carbides are generally of the form MC, where M is Ti, Nb, Ta, Hf, Th or Zr. MC carbides have a B1 (NaCl) crystal structure. They are generally very stable and form during solidification of the material [1,4]. Primary carbides are difficult to dissolve in the solid phase and they play an important part in restricting grain growth during the solution treatment stage. Lower carbides which can be dissolved by solution treatment in the range 1050°C to 1200°C have the general formula M_6C, $M_{23}C_6$ or M_7C_3 where M denotes the metallic constituent. M_7C_3 carbides are only observed in certain alloys, such as Nimonic 80A and are rarely seen in other alloys [1].

During heat treatment or service, primary carbides may react with the γ matrix to form lower carbides. Lower carbides are formed from primary carbides according to the following equations:

$$MC + \gamma \rightarrow M_6C + \gamma' \qquad \text{Equation 2-1}$$

$$MC + \gamma \rightarrow M_{23}C_6 + \gamma' \qquad \text{Equation 2-2}$$

Carbides in commercial alloys can form both at grain boundaries and within grains. In nickel-base superalloys, the effects of coherent γ' precipitates within the grains dominate over the effect of any carbides in these region and hence only intergranular carbides are important to the mechanical properties [1].

Carbides are generally harder and more brittle than the alloy matrix, hence their distribution along the grain boundaries is important. When carbide is present as a continuous film along the grain boundaries it tends to delineate grain boundaries, giving a continuous fracture path and is therefore detrimental to the alloy. During creep deformation, a continuous film of carbide also restricts grain boundary sliding, leading to stress build-up and early fracture. On the other hand if there are no grain boundary carbides present, excessive grain boundary sliding and growth of voids along grain boundaries occur during high temperature deformation. An optimum amount and distribution of carbide is therefore necessary to limit grain boundary movement for best high temperature performance [1].

Although blocky MC and M_6C carbides may be formed in the alloy, the beneficial effect of carbon has been attributed primarily to the intergranular $M_{23}C_6$ carbides which are formed during heat treatment giving improved high temperature strength by inhibiting grain boundary sliding. The increase in strength is however, offset by a concomitant reduction in fracture ductility [14].

2.2.3. Other phases

Ni_3Nb, generally designated as the γ" phase, is a less frequently occurring hardening phase. It forms the major strengthening constituent in Inconel 718, distinguishing this alloy from other nickel-base superalloys which are usually strengthened by γ' precipitates. The γ" phase has an ordered body-centred-tetragonal crystal structure (type DO_{22}) and is coherent with the γ matrix [15]. It usually forms as discs in the γ matrix [1].

The δ phase is also found in some nickel-base superalloys and gives additional strengthening when present in an optimum condition [16]. It is the stable orthorhombic form of Ni_3Nb and forms at grain boundaries, at primary carbides or inside grains during ageing treatments or after prolonged thermal exposure [17].

Other intermetallic phases, such as the Laves phase and σ phase, can also form within the complex alloy systems of nickel-base superalloys. Precipitation of the σ phase has been found to be deleterious to the strength and ductility of the alloy [18], as well as giving poorer creep and fatigue resistance [3,19]. The formation of these intermetallic phases is generally avoided for two reasons. Firstly these intermetallic phases themselves are brittle and hard, hence liable to fracture. When formed as needles, large platelets or continuous intergranular film, these phases facilitate propagation of cracks through the matrix. The hard σ phase, especially in a plate-like or needle

morphology at grain boundaries, also offer ideal sites for crack initiation [19]. Secondly the formation of these phases is also not desired as they remove useful strengthening elements from the matrix [1]. Topologically-closed-packed phases such as the σ phase are rich in refractory elements such as Cr, Co, Mo and W. Precipitation of these phases will result in solute depletion in the surrounding γ matrix leading to localised compositional weakening. The susceptibility to environmental attack may likewise be increased if formation of the protective Cr_2O_3 scale is inhibited through chromium depletion [19].

Numerous other phases are also present in nickel-base superalloys; these include nitrides, borides, sulphides and phosphides.

2.2.4. Microstructure and processing routes

Turbine discs may be produced by one of two manufacturing processes, i.e. either by a cast and wrought route or through powder metallurgy (PM) techniques. In the cast and wrought process, melting is usually carried out in vacuum followed by pouring into moulds and various final forging processes. However, increased difficulties in forgeability and machineability due to increases in alloy strength, as well as problems associated with shrinkage and grain size control have been reported. Powder metallurgy techniques were used to overcome some of the problems encountered during manufacture using the cast and wrought technique. Highly alloyed atomised powder particles can be compacted and sintered usually through hot extrusion or hot isostatic pressing allowing formation of these high strength alloys with minimal segregation. Although powder metallurgy fabricated alloys are usually associated with improved properties, the drawback is usually the high cost associated with the manufacturing process.

A range of heat treatment processes is employed to produce optimal microstructures in nickel-base superalloys for good high temperature properties. The heat treatment usually involves a solution treatment followed by one or more ageing treatments [20]. By varying the heat treatment parameters, it is possible to produce a variety of grain size and γ' size and distribution in the alloys. Fine grain, coarse grain or a bimodal "necklace" microstructure through controlled recrystallisation are possible with different heat treatment parameters.

Solution treatment is carried out to dissolve the precipitate phases, principally the γ' phase and carbides, prior to their controlled precipitation during subsequent heat treatment stages [1]. Solution treatment is usually carried out at temperatures below the γ' solvus temperature, typically in the range from 1040°C to 1230°C, depending on alloy composition and the required grain size [20]. At the γ' solvus temperature of the alloy, the γ' phase is completely dissolved in the γ matrix. Complete dissolution of the γ' phase would minimise serrated grain boundary morphology and increase the amount of γ'-forming elements available for γ' precipitation during subsequent ageing

treatment [21]. Performing the solution treatment at temperatures below the γ' solvus retains some γ' (primary γ' precipitates) at grain boundaries to prevent migration of grain boundaries and hence allows control of the grain size. Carbides at or near grain boundaries also act to restrict grain growth during solution treatment [22]. Higher solution treatment temperatures bring more γ' into solution and will give larger grains and lower volume fractions of primary γ' precipitates. The grain size is controlled more by the solution temperature than by the time of treatment [1,23]. A higher amount of γ'-forming elements in the solution with higher solution temperatures implies greater formation of secondary and tertiary γ' precipitates, usually manifesting itself as subsequent increase in hardness [23].

On cooling from solution temperature, nucleation of the γ' phase occurs uniformly throughout the γ matrix [3,13]. Secondary and tertiary γ' precipitates are formed during cooling from solution temperature [23,24,25]. Although tertiary γ' precipitates are generally believed to also form during ageing or during cooling from ageing temperature [26], no concrete experimental evidence could be found in the literature to validate this statement. Formation of secondary and tertiary γ' precipitates during cooling from solution temperature can be understood in the following way [23]. Early on during cooling from solution temperature, nucleation of secondary γ' precipitates occurs in the supersaturated γ matrix. As temperature decreases further, growth of secondary γ' precipitates occurs with partitioning of solutes into surrounding matrix. Eventually, diffusion rates of the solutes decrease and the γ' precipitates cannot grow fast enough to keep supersaturation of the matrix low. Eventually, at a critical undercooling, the driving force is sufficient to allow nucleation of tertiary γ' precipitates to occur.

Nucleation and growth kinetics of γ' precipitates strongly depend on the cooling rate from solution temperature [25], hence the cooling rate from solution temperature can be manipulated to change the frequency of nucleation as well as the distribution of precipitates in the matrix [27]. During cooling from solution temperature, the size and volume fraction of secondary γ' precipitates formed were noted to decrease with higher cooling rates [24,25], while the size of tertiary γ' precipitates formed appear to be relatively insensitive to the cooling rate [23]. Higher cooling rates result in more undercooling and subsequently more supersaturation build-up, leading to larger numbers of small secondary γ' nuclei with small interparticle spacing [4,24,25]. Since growth of γ' precipitates is essentially a diffusion-controlled process, growth of secondary γ' precipitates is suppressed during fast cooling due to rapid temperature drop and limited time for diffusion, i.e. higher cooling rates result in larger numbers of small secondary γ' precipitates with small interparticle spacing, and vice versa for slower cooling rates [25]. The volume fraction of secondary γ' precipitates decreases with increasing cooling rates as fast cooling suppresses growth of secondary γ' precipitates [24]. When nucleation of tertiary γ' precipitates is expected, the temperature is likely to be relatively low

to allow intensive solute diffusion, and growth of tertiary γ' precipitates is restricted [25]. The size of tertiary γ' precipitates is therefore relatively insensitive to the cooling rate.

Ageing treatments are carried out below the γ' solvus temperature to allow precipitation and growth of the γ' hardening phase. Strengthening of solution-treated and as-quenched materials due to subsequent ageing occurred regardless of the cooling rate from solution temperature [24,25]. Higher cooling rates from solution temperature result in more ageing strengthening than a lower cooling rate, as faster cooling results in lower volume fraction of secondary γ' precipitates and retains a higher amount of γ'-forming elements in solution for precipitation of tertiary γ' during ageing [25]. It was noted that ageing treatment does not cause secondary γ' precipitates to grow significantly, and the main microstructural activity during ageing is the continuous growth of very fine tertiary γ' precipitates nucleated during cooling from solution temperature [23,25]. The full equilibrium volume fraction of γ' is formed very early in the ageing treatment and any subsequent change in the γ' precipitates during ageing treatment or during service involves only precipitate coarsening [1,13].

For many modern turbine disc alloys, double ageing treatments are usually carried out as they are believed to give a duplex γ' distribution to provide a combination of high strength and good creep resistance [28,29]. Duplex γ' distribution has been indicated to arise during cooling from solution temperature anyway for U720Li [23,25]. High ageing temperatures produce high creep extensions before fracture, and lower ageing temperatures reduce creep rate, combining the two, i.e. a two stage ageing treatment, gives better creep characteristics than are obtained by a simple precipitation treatment [1].

Typical heat treatment routes employed by Rolls-Royce for U720 and U720Li are [30]:

U720: 4h 1105°C→oil quench→24h 650°C→air cool→16h 760°C→air cool

U720Li: 4h 1105°C→oil quench→24h 650°C→air cool→16h 760°C→air cool

Ageing treatment of 24h at 650°C→air cool→16h at 760°C→air cool denotes the standard "yo-yo" heat treatment profile employed by Rolls-Royce after the solution treatment stage [30].

2.2.5. Stability of nickel-base alloys

During service and prolonged high temperature exposure, coarsening of γ' precipitates was found to occur in some nickel-base superalloys, including Udimet 500 [31], Nimonic 115 [31] and IN100 [4]. Under LCF testing conditions at elevated temperatures, coarsening of γ' was also observed in Waspaloy [22], Rene 80 [28], Rene 77 [18] and Nimonic 90 [28]. During LCF testing, coarsening of γ' was found to be more pronounced at higher temperatures and lower test frequencies [28]. The dislocations generated during LCF testing may play an important accelerating role in the

coarsening of γ' precipitates. Dislocations can be seen to connect γ' precipitates, presumably providing rapid diffusion paths for solute elements leading to coarsening [18]. In IN718 where the primary strengthening precipitates are the γ'' precipitates, coarsening of γ'' was also noted after prolonged thermal exposure at 650°C [32].

Precipitation of the topologically-closed-packed σ phase was also noted after prolonged exposure at elevated temperatures [4,31,19] or during LCF testing [18]. The quantity of σ phase precipitated increases with increase in temperature seen by the component [19,31]. It is generally accepted that σ phase nucleates at grain boundaries. The σ phase forms first as small discrete particles and grows into platelets [4,31].

Carbide precipitation was also noted during high temperature LCF testing in Waspaloy [18,22,28] and Nimonic 90 [18]. Carbide precipitation was noted to occur at grain boundaries, twin boundaries and slip bands [22]. The precipitation may be strain induced, as evidenced by precipitation on slip bands. It is well known that dislocations can significantly reduce the activation energy for precipitation [28].

2.3. Deformation behaviour

During deformation in nickel-base superalloys, dislocations may in principle bypass precipitates by three processes, i.e. precipitate cutting, Orowan looping/bowing between precipitates, or by glide and climb around precipitates [33]. The first two processes are typically athermal. Dislocation glide and climb around precipitates is dependent on diffusion, and hence will generally dominate over athermal mechanisms at high temperatures and relatively low applied stresses.

In the precipitate shearing process, build-up of dislocation density within the planar deformation band (known as slip band) occurs initially. In the process, the dislocation density becomes high enough that the effective stress is sufficient for a dislocation to penetrate a precipitate (e.g. coherent γ' precipitates). When this happens the next dislocation is pulled through by the antiphase boundary (APB) energy that is created by the cutting of ordered γ' precipitates. The final precipitate offset is two Burgers vectors and the reduced cross-section of the precipitate in the slip plane makes it easier for the next dislocation pair to go through the precipitate at a lower stress level, leading to softening in a preferential slip direction and hence concentration of slip in that particular slip direction [22,34].

When dislocations bypass precipitates by Orowan bowing mechanism, dislocation loops are left around the precipitates. Formation of loops around precipitates increases the internal resistance to succeeding dislocations in the same slip plane owing to a decrease in the effective spacing between precipitates [35]. This forces dislocations to move out to adjacent planes in the same slip system when the strain amplitude is small or to cross-slip on to other systems when the strain amplitude is

large, with both processes leading to a more homogeneous distribution of dislocations in the matrix, and an increased rate of work hardening [34,36].

2.3.1. Planarity of slip in nickel-base alloys

In nickel-base superalloys, slip occurs heterogeneously, i.e. dislocation motion is concentrated in well-defined planar bands. This is due to their low SFE and the formation of APBs on shearing of ordered γ' precipitates [37,38]. Low SFE promotes dissociation of screw dislocations into partial dislocations separated by a low energy stacking fault. The mixed screw and edge character of the partial dislocations means that they are no longer able to cross-slip. The pairing of dislocations favoured by minimising the APB caused on shearing of ordered γ' precipitates and the low SFE makes cross-slip difficult and encourages planar deformation in nickel-base superalloys.

The homogeneity of slip in the material can be characterised by the density of the slip bands or the average spacing of the slip bands [36,39]. Wider spaced but more intense slip bands indicate greater strain localisation, i.e. more heterogeneous slip behaviour. Higher density of less intense slip bands implies a more homogeneous slip. Homogeneity of slip is promoted by high temperatures and high loading frequencies. Increased heterogeneity of slip is also promoted in vacuum as there is less gas absorption and oxide formation, hence giving rise to more reversible slip [40]. In addition, homogeneity of slip is also affected by the microstructure of the materials, i.e. the grain size and the size and volume fraction of γ' precipitates and this is further discussed in section 2.13.2.

2.3.2. Effects of slip behaviour on mechanical and fatigue properties

Strain localisation or heterogeneous slip does not appear to have any significant effect on yield strength but generally has a deleterious effect on the toughness [41,42,43]. The influence of slip characteristics on fatigue and creep-fatigue behaviour varies in different fatigue regimes. In the fatigue crack initiation and short crack growth regime, the effects of slip behaviour are of major importance. Where environmental interactions are important during crack growth, the effects of slip behaviour on crack growth are extremely complex. These effects are reviewed in detail in the relevant sections of the literature review. Overall the effects of slip deformation on fatigue and creep-fatigue behaviour are complex and in some respect unclear, and much investigation is still being carried out.

In general, the impingement of intense slip bands associated with heterogeneous deformation may act as stress concentrators across grain boundaries, leading to premature intergranular failure [41,44], or premature transgranular failure in coarser slip bands [41]. Dislocations pile up at grain boundaries at isolated points, and the large associated tensions across the grain boundaries open intergranular cracks that propagate without absorbing much energy [34,44]. A more homogeneous deformation would reduce the localised stress concentration and minimise the chances of intergranular cracking due to relaxation of the stress generated between a grain boundary and an impinging slip band [32].

Impingement of slip bands can also cause decohesion of the matrix/carbide interface, leading to intergranular cracking [36].

In fatigue crack growth experiments, strain localisation in slip bands may also enhance extrinsic shielding mechanisms, such as roughness-induced closure, crack branching and crack deflection [41]. In addition, heterogeneous slip increases the reversibility of slip, which reduces the extent of fatigue damage, thereby increasing the FCP resistance [41,45,46].

2.4. Fatigue

Fatigue of materials refers to failure of material due to repeated load cycling or fluctuating stresses. Under these circumstances, it is possible that failure occurs at stress levels much lower than the tensile or yield stress for a static load. In engineering, this form of failure constitutes a majority of all the failures in structural and mechanical systems, final failure sometimes occurring very suddenly and without warning. It is of great concern to be able to quantify fatigue, and various approaches to safe-life prediction have been developed over the years.

The overall fatigue life of a component is characterised by three distinct regimes, i.e. the crack initiation period, where small cracks form at some point of high stress concentration, followed by subsequent short and long crack growth, where the crack advances incrementally with every stress cycle, and finally followed by final fracture after the flaw has reached a critical size. The relative time spent in each regime depends on various factors, primarily on the material, initial defect size, loading conditions and environment.

Cracks will initiate at the most favourable sites, usually at points of high stress concentrations, i.e. at defects or discontinuities in the components, and in smooth components, microcracks can initiate at the surface, e.g. at persistent slip bands. This is followed by rapid growth in the early stages of the short crack under local stress/strain conditions which caused the initiation, until some type of microstructural barrier is encountered [47]. The short crack growth may then undergo acceleration and/or deceleration due to various intrinsic and extrinsic factors. As the crack length increases, the crack will propagate more steadily as the crack tip process zone also increases and starts to sample a larger volume of material, i.e. the crack grows under conditions nearer to the material's average properties. At this point, crack growth behaviour will approximate to what is known as the long crack growth behaviour.

2.4.1. Characterisation of fatigue behaviour

Various fracture mechanics approaches have been developed over the years to characterise fatigue crack growth with loading conditions, the most widely used being the Linear Elastic Fracture Mechanics (LEFM) approach. In this approach, local stresses ahead and near the crack tip are

correlated to the far-field applied stress and the flaw length. For example, consider a sharp, through thickness crack of length 2a in a thin elastic plate as shown in Figure 2-1.

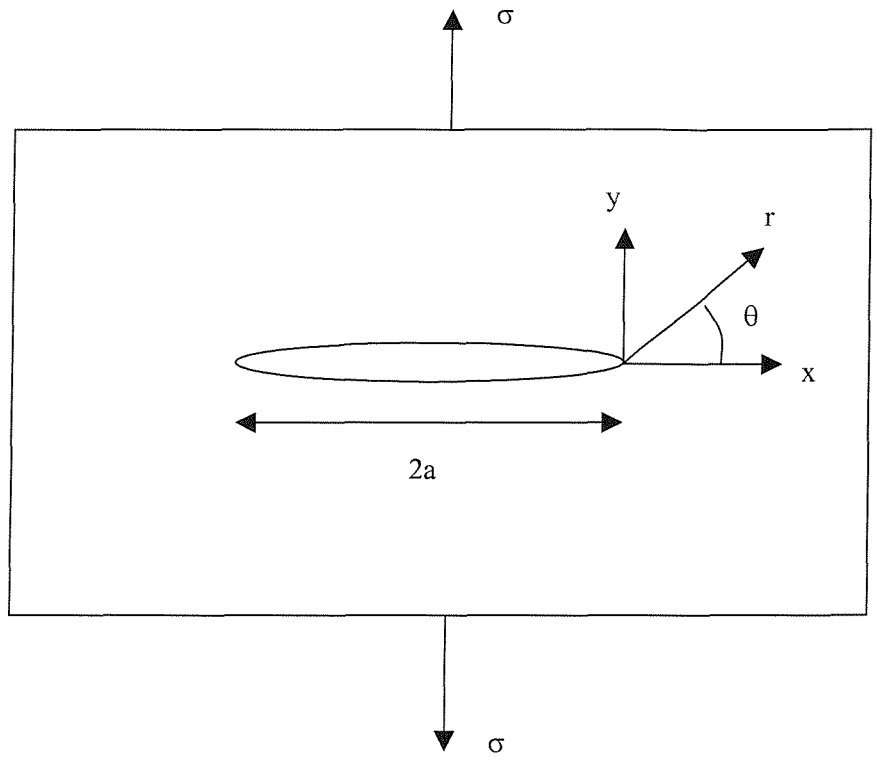

Figure 2-1: Sharp crack length 2a in a thin elastic plate, with a nominal applied stress σ.

The local stresses at co-ordinates (r,θ) close to the crack tip are given, to a first approximation, by [48]:

$$\sigma_{xx} = \sigma\left(\frac{a}{2r}\right)^{1/2}\left[\cos\frac{\theta}{2}\left(1-\sin\frac{\theta}{2}\sin\frac{3\theta}{2}\right)\right] \qquad \text{Equation 2-3}$$

$$\sigma_{yy} = \sigma\left(\frac{a}{2r}\right)^{1/2}\left[\cos\frac{\theta}{2}\left(1+\sin\frac{\theta}{2}\sin\frac{3\theta}{2}\right)\right] \qquad \text{Equation 2-4}$$

$$\sigma_{xy} = \sigma\left(\frac{a}{2r}\right)^{1/2}\left[\sin\frac{\theta}{2}\cos\frac{\theta}{2}\cos\frac{3\theta}{2}\right] \qquad \text{Equation 2-5}$$

Note that the stresses tend to infinity as r tends to zero. In reality this does not occur due to plastic yielding.

The term stress intensity factor, denoted K, was introduced to describe the elastic stress field near the crack tip. The general form of equation relating K to the load and flaw size is given by:

$$K = \sigma_f \sqrt{\pi a}\, f\left(\frac{a}{W}\right)$$ Equation 2-6

where σ_f is the far-field applied stress, a is the flaw size and f(a/W) is the compliance function to accommodate different component geometry and shape. K is very useful as it describes the local crack tip stress state (and strains). If two cracks of different geometry have similar value of K, in theory the stress fields around the two flaws are identical. The use of K is convenient as it can be easily calculated from specimen dimensions and external loading conditions.

Instead of the stress range $\Delta\sigma$, the stress intensity factor range ΔK was adopted widely to characterise fatigue crack growth as it describes the range of crack tip stress field. Plots of the crack growth rate per cycle, da/dN vs. ΔK (on logarithmic scale) generally show a sigmoidal relationship divided into three distinct regimes, as shown in Figure 2-2.

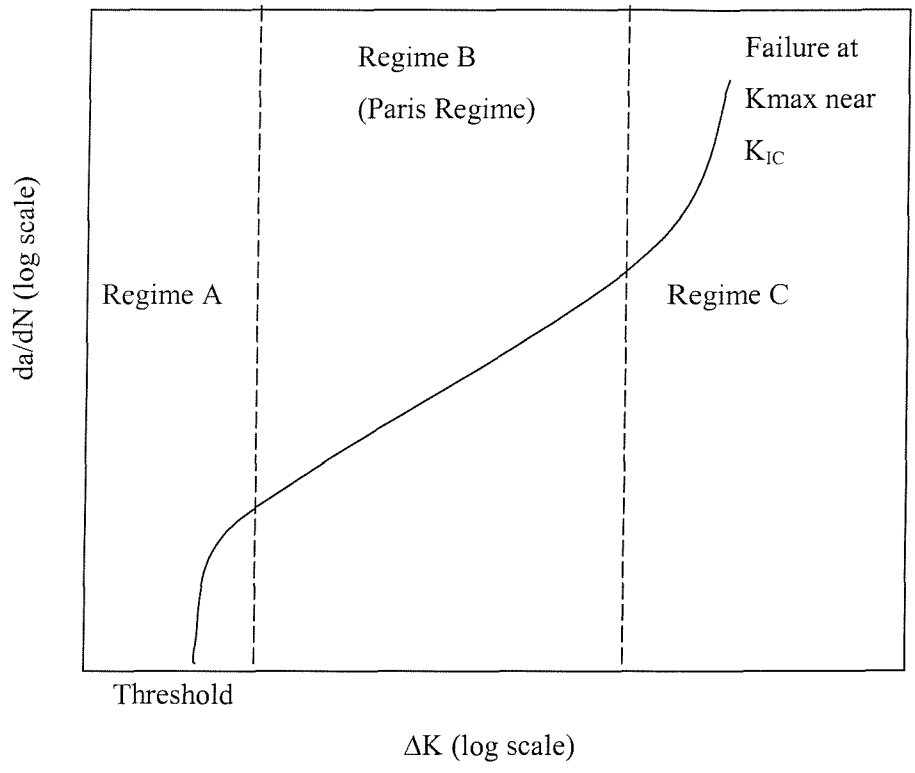

Figure 2-2: Typical da/dN vs. ΔK curve.

Regime A describes the low ΔK region where non-continuum behaviour is observed. Below the threshold stress intensity factor range ΔK_{th}, crack growth is arrested or imperceptible. A large influence of microstructure, environment and mean stress on crack growth is generally observed in this region. Regime B denotes the region of stable crack growth which can generally be described by the Paris Equation:

$$\frac{da}{dN} = C\Delta K^m$$ Equation 2-7

where C and m are constants. Regime C is the region of high ΔK where the crack growth accelerates rapidly to final failure.

The ΔK however does not consider plastic behaviour, and when significant amount of plastic deformation is taking place, alternative parameters such as the J-integral would have to be employed to characterise fatigue crack growth under these conditions. When plastic deformation is occurring at the crack tip, the use of ΔK is still valid provided there is sufficient material around the plastic zone which is behaving elastically to provide true constraint. Other factors, such as microstructural effects, crack deflection and crack closure can also alter the effective value of ΔK relative to the global ΔK calculated from the crack geometry and loading. These effects are discussed in subsequent sections of the literature review.

There are also some uncertainties in extending linear elastic concepts to high temperature crack growth where plastic flow near the crack tip could be extensive [49]. In addition, there could also be superimposed non-linear effects at these high temperatures such as time-dependent creep effects and environmental effects, which could alter the characteristics of the crack tip.

2.5. Initiation and short crack growth behaviour

Fatigue crack initiation and short crack growth are important as a majority of turbine disc fatigue life is spent in this fatigue regime during service [50,51,52,53]. High component stresses result in relatively small extent of fatigue crack propagation prior to fast fracture, limiting a large proportion of the usable fatigue life to the short crack growth regime [54,55]. The influence of microstructure and environment on fatigue crack initiation and short crack growth has been shown to play a dominant role, especially on cracks which are of a size comparable to the scale of characteristic microstructural features [51,56]. Different authors have different definitions of the length which corresponds to a short crack, but in general this corresponds to the length at which non-continuum mechanics are operating. The definition of short cracks, according to Suresh [48], is as follows:

a) microstructurally short crack where the crack size is comparable to the scale of characteristic microstructural dimension such as the grain size for monolithic materials.

b) mechanically short crack i.e. small fatigue cracks in smooth specimens where the near-tip plasticity is comparable to the crack size, or cracks which are engulfed by the plastic strain field of a notch.

c) physically short crack where the flaws are significantly larger than the characteristic microstructural dimension and the scale of local plasticity, but are merely physically small with length typically smaller than a millimetre or two.

d) chemically short cracks which are nominally amenable to linear elastic fracture mechanics analyses, but exhibit apparent anomalies in propagation rates when below a certain crack size as a consequence of the dependence of environmental stress corrosion fatigue effects on crack dimensions.

The first definition represents a limitation as to the relevance of continuum mechanics, while the second represents a limitation on current LEFM descriptions of the crack driving force [57].

2.5.1. Crack initiation in nickel-base superalloys

Naturally initiated cracks will form at the least resistant point in the microstructure, i.e. at defects or in slip bands in favourably oriented groups of grains [58]. The number of cycles required to initiate a crack will decrease as the amplitude of the cyclic load is raised. The number of cracks that appear will also increase with the amplitude of the cyclic load [53,59].

A variety of crack initiation mechanisms is possible in nickel-base superalloys. The mechanisms of crack initiation in nickel-base superalloys will depend strongly on various factors including microstructure, environment and temperature. At room temperature, it is possible for fatigue cracks to initiate from slip bands [18,22,47,55,56,60,61,62,63,64,65,66], twin boundaries [50,56,62,65], grain boundaries [59,65,67,68], at carbides [60,69,70], due to cracking of inclusions/precipitates [28,47,51,65,71,72] or at defects [69,70,71]. At elevated temperatures, crack initiation has been observed to occur from slip bands [22,50,55,60,63,73], grain boundaries [29,68], twin boundaries [63,64], at inclusions [64,70,74,75] or at defects [69].

The predominant mechanism of crack initiation in nickel-base superalloys, especially at room temperature, is extensive stage I cracking along persistent slip bands [47,56,60,63,76]. Cracks initiate at approximately 45° (some noted an angle between 30° to 60°) to the principal or maximum stress axis, i.e. in the direction of maximum shear stress. All observations suggest that slip band crack initiation is promoted by heterogeneous slip. Slip band crack initiation has been noted to be more extensive in microstructures with coarse grain and fine coherent γ' precipitates, both of which give rise to heterogeneous slip [22,61,69]. Alloys with fine grain and coarse coherent γ' precipitates showed little tendency for stage I cracking. Slip band cracks formed more frequently in coarse grains in the microstructure [63,65,69,77,78]. The greater slip band lengths in coarse grains promote easier crack initiation in planar slip bands. Longer slip band lengths will accumulate a larger amount of irreversible slip, resulting in more dislocation damage accrual [63]. Larger surface grains also have the least constraint, allowing slip to occur more easily [77]. Fine grains are known to inhibit crack

initiation by promoting more homogeneous deformation through slip dispersal at grain boundaries, thereby reducing the stress concentration effect of planar slip offsets [65]. A pair of large neighbouring grains adjoined by a grain boundary with low relative misorientation may also effectively act as an extra large grain which favours slip band crack initiation [62].

Crack initiation resistance was also noted to be higher with coarse coherent γ' microstructures compared to fine coherent γ' microstructures [78]. In the fine coherent γ' material, crack initiation was noted to occur along intense slip bands generated by heterogeneous planar slip owing to shearing of fine γ' by dislocations. Intrusions or extrusions resulting from the intense slip bands become sites for crack initiation. In the coarse coherent γ' material however, slip becomes wavy due to Orowan looping around γ' by dislocations and formation of intense slip bands is retarded; as a result fatigue crack initiation resistance is increased.

Crack initiation at grain boundaries and annealing twin boundaries was also observed [18,50,59,63,65]. In nickel-base superalloys, annealing twins are known to act as efficient dislocation barriers. Slip bands impinging on these twins and on oxidised grain boundaries may cause local decohesion as a result of the high stresses at the ends of the slip bands, causing cracks to initiate [18,50,63,65].

Fatigue cracks initiating from inclusions or precipitates usually arise due to the difference in thermal expansion or the difference in strength between inclusions/precipitates and matrix [59,60,65]. When there is significant difference in the thermal expansion between the inclusions/precipitates and the matrix, local tensile stresses may form in the matrix during the cooling process and separation of the interface between the inclusions/precipitates and the matrix may occur and eventually lead to crack initiation [60]. Crack initiation at inclusions appears to be favoured by inclusions of large size, as the volume of material that is subjected to the stress concentration increases with inclusion size [59]. Cracks may initiate at inclusions either by inclusion cracking or by inclusion-matrix interface decohesion, depending on the relative strengths of the inclusion and the inclusion-matrix interface [59]. Impingement of slip bands on inclusions may also cause crack initiation [77].

In a crack initiation and short crack growth study on U720Li at room temperature by Goto and Knowles [51], cracking of TiN particles was found to occur at extremely early stages of cycling. The cracked particles were responsible for subsequent fatigue crack initiation. Measurement of crack orientation in the TiN particles indicated that they cracked nearly perpendicular to the loading direction, i.e. the TiN particles were fractured by the principal tensile stress. Cracking of the particles is governed by the localised strain around the particle, where cracking will occur when the localised strain exceeds a critical value. The early cracking of the particles indicates that localised strain due to cycling stabilises rapidly and no cracked TiN particles are observed at the later stages when cycling stabilisation is achieved.

Crack initiation at carbides may occur due to oxidation at elevated temperatures [70,74,79,80], due to carbide cracking [60], or due to impingement of slip bands which causes decohesion at the carbide/matrix interface [70]. Carbides also have lower ductility compared to the matrix, hence they may be prone to cracking [79].

Crack initiation from porosity was generally noted to be significant only at room temperature. Davidson and Chan [81] have noted crack initiation from porosity in Astroloy tested at 20°C, and one of the slip directions was always within 40° of the surface normal, indicating mode III crack opening was likely. In another short crack study at room temperature by Davidson and Hudak [61] in Astroloy, small cracks were found to initiate from small voids which are pores not closed during sintering. Accelerated initiation of microcracks at pores was also noted, and this was attributed to stress concentrations near the pore which resulted in localised slip even though the nominal stress remained elastic [82,83]. Higher porosity volume fraction was also noted to reduce the number of cycles to initiate a crack [82]. The sensitivity to crack nucleation is also affected by the shape of the pore. More angular pores have been suggested to promote higher stress concentrations and stress intensity factors than a rounded pore [83]. At elevated temperatures, porosity was found to have little effect on the crack initiation process. In a LCF study by Choe et al [73] on Astroloy at 650°C and 725°C, it was noted that pre-existing pores did not affect crack initiation.

2.5.2. Short crack growth

Short crack growth is the regime of crack growth bridging the crack initiation process and the long crack growth process. Non-continuum mechanics are at work during short crack growth, hence the application of LEFM to characterise small crack growth may be inappropriate.

The general characteristics of short crack growth include:

i) Short cracks exhibit anomalously high, irregular growth rates when compared to larger cracks at the same ΔK [51,57,59,60,61,84,85,86,87,88].

ii) Short cracks can also grow below the ΔK_{th} found for long crack.[47,57,59,60,84,85,86,87,88].

iii) Considerable fluctuations and scatter are seen in short crack growth data [47].

The application of the conventional method of life prediction, i.e. using integration of the da/dN vs. ΔK relationship with an initial flaw size and a critical flaw size may lead to non-conservative estimates of component life, if the characteristics of short crack growth are not taken into account [84].

The anomalous short crack growth behaviour is attributed to the invalidity of using ΔK to characterise short crack growth due to the non-continuum behaviour of the cracks [52,59,84], due to

microstructural effects [52,59], and due to absence of crack closure [59]. Accelerated chemical attack due to relative ease of access to the short crack tips has also been cited to cause anomalous short crack growth behaviour [59]. The ΔK is unable to correctly describe the magnitude of crack tip stress-strain field for the case of short cracks [84]. The driving force for short crack growth is noted to be significantly higher than that described by ΔK and LEFM predictions [84]. Results show that the growth rates of small cracks correlate well with long crack LEFM data when an appropriate elastic-plastic driving force parameter was used [76]. The usual description of the stress field ahead of a crack as a function of K is based on the assumptions of continuum mechanics and small-scale yielding [87]. Microstructurally small crack growth, however, violates these two assumptions, since it is associated with small crack dimensions and a relatively large plastic zone size (PZS). To use the elastic stress intensity factor K, the PZS should be small compared to the intensified stress field, i.e. the PZS should be small, typically much less than the crack length [52]. Validity of the continuum assumption of LEFM is thought to hold when the plastic zone size to crack length ratio (r_p/a) is less than 0.02 [57]. This is not satisfied in short crack situations as the crack length is initially even smaller or equivalent to the grain size, hence invalidating the use of LEFM [59,89].

The high values of applied stress at which short crack studies are normally performed also result in extensive monotonic plasticity and hence growth at an effectively high value of R [38,86]. Also, at the surface, plane stress condition prevails and the material flow resistance is reduced compared to the bulk, resulting in plastic zone sizes that are large compared with those in the interior which will be under plane strain condition [87]. The loss of crack closure has also been associated with the anomalous high mean growth rates of small cracks [38,59,88]. Crack closure is the term used to describe load transfer in the wake of a growing crack, due to contact between the crack faces. Crack closure could arise due to surface roughness, oxide debris or plasticity ahead or the crack tip. Very often more than one of these mechanisms are in operation during the event of crack closure. All these mechanisms cause contact of the crack surfaces at a stress intensity greater than the applied minimum stress intensity, hence the crack tip experiences an effective ΔK that is less than the applied ΔK, i.e. a lower crack tip driving force. At short crack lengths where the 'wake' beyond the crack tip is limited, a small closure contribution is experienced [5,60]. Also, the greater plastic strain experienced at the crack tip of the short crack (as the crack is in plane stress state) results in greater crack opening displacements at the same nominal ΔK compared to a through-thickness long crack (which is in plane strain state), resulting in the loss of closure [38,88].

The fluctuations and scatter observed in short crack growth data are associated with interactions between the crack tip and microstructural features [59]. When the crack tip encounters a microstructural barrier, deceleration of the crack growth may occur, and may even lead to total arrest of the crack propagation [55,77,80,90]. Furthermore the crack path may also be altered when overcoming the microstructural barrier. The concentration of deformation into intense slip bands

means that cracks can propagate in a crystallographic manner across grains. As the crack grows, microstructural barriers are encountered. Temporary crack arrest and deflections can occur at grain boundaries [55,63,65,72,75], annealing twins [55,63,65], inclusions [51,72] and intersecting slip systems [60,65]. Each individual crack might show a different behaviour since it is affected by different local microstructures [47].

Deceleration in crack growth rates and deflection of short crack paths at grain boundaries have been highlighted in the majority of studies conducted [38,47,56,58,59,63,64,65,81,88,90,91,92]. The effectiveness of grain boundaries as crack growth barriers is shown in a study which compares the short crack growth behaviour in single crystal and polycrystalline U720 [88]. Due to the absence of grain boundaries, short crack growth rates of single crystal U720 are found to be well above the short crack growth rates of polycrystalline U720. The grain boundary blocking effect usually occurs over several grains, but the first one or two boundaries were noted to be most effective in reducing crack growth rates [56,91]. Crack growth deceleration or arrest may occur as grain boundaries are acting as hard barriers [38,65], or due to crystallographic misorientation between two neighbouring grains [65,90,92,87]. The change in operating slip systems necessary as a crack crosses a grain boundary results in grain boundaries being barriers for crack growth. The actual deceleration of a small crack is thought to start once its plastic zone, not its tip, reaches a grain boundary [56,87,90]. The retardation of crack growth continues until its plastic deformation has passed the grain boundary into the next grain. The stress intensity along the slip band in the adjacent grain must be sufficiently high such that dislocation sources can be unlocked and plastic slip initiates in the next grain to enable crack propagation to proceed [56]. Large deflections in the crack path may occur at grain boundaries, depending on the relative orientations of adjacent grains [62]. It is generally believed that larger misorientation between two grains will give more pronounced deceleration in crack growth rates at grain boundaries [57,59,90]. The lower the angle of misorientation at a grain boundary, the easier slip can traverse the grain boundary [62]. Two grains separated by a low angle grain boundary were observed to respond to the fatigue crack as one equivalent large grain, i.e. there was no crack growth deceleration at the respective grain boundary [62]. For situations in which small cracks clearly prefer to grow in Mode II, they either arrest, retard, or grow at slower average rates, when forced to shift to Mode I upon entering a new, less favourably oriented grain [57].

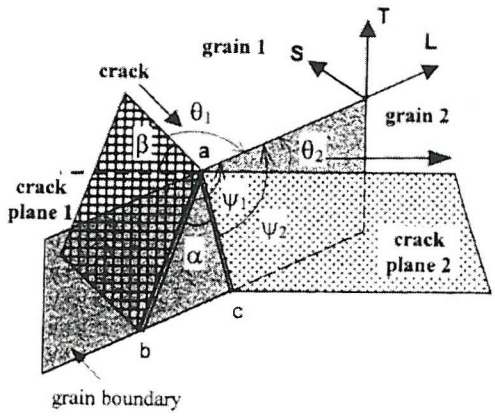

Figure 2-3: A crystallographic model for crack retardation at a grain boundary. θ and ψ angles are the crack angles with L axis on the sample surface and the grain boundary plane [92].

In studies conducted on Al-Li alloys, the path of short crack across grain boundaries was found to be mainly controlled by the twist angle of crack-plane deflection at the grain boundary plane (between the two favoured slip planes across the grain boundary), rather than by the grain boundary misorientation [92]. Because of crack-plane twist, for a crack to grow across a grain boundary, the area **abc** covered by the twist angle has to be fractured (see Figure 2-3), which results in significant resistance to crack growth. Therefore a crack usually grows across a grain boundary on the slip plane in the neighbouring grain that has the smallest twist angle with the crack plane (among the four possible slip planes). A grain boundary with a large twist component could cause a short crack to arrest or branch, i.e. due to the twist angle being large, a new/branched crack which has a smaller twist angle may be formed at the grain boundary [92].

Non-parallel sets of slip bands or orientation changes at the boundaries of annealing twins may also cause retardation in short crack growth [38,60,65]. These orientation changes within grains provide soft barriers to crack growth [65].

Temporary crack arrests at inclusions/precipitates have also been observed. Goto and Knowles [51] have noted a sudden drop in short crack growth rates when the crack tip ran into primary γ' precipitates. At this point the crack frequently stopped growing for a period of time, followed by subsequent recovery of crack growth rates. The crack growth path suggests that a fatigue crack tends to go round the γ' precipitates after being halted at the γ matrix-primary γ' interface.

At the shortest crack lengths, the crack may well be experiencing an essentially single crystal environment [93]. The small crack tip deformation will be maximised when the crack is within a single grain since little constraint is provided from surrounding grains, leading to fast growth rates [60,87,91]. The crystallographic crack growth rates in a single crystal material should provide an upper bound for the highest short crack growth rates observed in the polycrystalline form of the

material [88]. The upper bound short crack growth rates can generally be correlated to crack propagation directly across the centre of a grain along slip bands with minimum influence of grain boundaries [88]. The intermediate growth rates were attributed to perturbations of the crack path as a result of propagation between non-parallel sets of slip bands or due to orientation changes at the boundaries of annealing twins [38,65]. Overall crystallographic microcracks appear to grow much faster than small cracks which grow non-crystallographically [57,92].

Below certain crack lengths, short cracks grow in a very crystallographic manner, indicative of stage I crack propagation. In most cases the straight segments of crystallographic cracks on specimen surfaces were very nearly parallel to {111} planes [59,90]. Crack growth along the {100} cleavage plane has also been noted [94]. When the crack has reached a critical length, crack propagation proceeds through a stage II mechanism, which leads to a flatter fracture surface [51,56,62,65,79,90]. Stage I crack growth, as defined by Suresh [48], corresponds to cracks where the crack and the zone of plastic deformation surrounding the crack tip are confined to within a few grain diameters, and crack growth occurs predominantly by single shear, in the direction of the primary slip system. This single slip system mechanism gives rise to a zig-zag crack path and a predominantly faceted fracture surface. At higher stress intensity values, the plastic zone of the crack encompasses many grains. The crack growth process in this case involves simultaneous or alternating flow along two slip systems. This duplex slip mechanism results in a planar (mode I) crack path normal to the far-field tensile axis, i.e. stage II crack growth.

Zig-zagging of the crack path during stage I crack growth indicates that mode I and mode II influences are important [62]. The mode I component tends to both orientate and drive crack paths perpendicular to the tensile axis due to crack opening. However, the grains are randomly oriented and crack growth occurs along available slip planes. The attempt to satisfy both these conditions results in a zig-zag path. The mode II component assists in driving the crack at 45° to the tensile axis. At a given ΔK, short crack paths (where the fracture surface was predominantly facetted) through surface grains were observed to be less tortuous on average compared to short crack paths through subsurface grains [62]. The complexities in crack paths through subsurface grains were necessary in order to link the path of a fatigue crack from grain to grain. The face of a surface grain at the top surface of the specimen does not experience this constraint and therefore the paths through surface grains are less constrained than crack paths through subsurface grains.

In general, a surface initiated crack will assume a semi-circular shape. The crack tip tends to bulge out between strong arrest points causing the driving force to reduce at the bulge and increase at the arrest points either side of the bulge [62]. As a consequence, the short crack front become approximately semi-circular [62]. The average value of the ratio of crack depth to half surface crack length (a/c) was found to be approximately 1 in a majority of studies [59,61,65,87,91,95]. Slight variations

in the a/c ratio do not appear to have a strong effect on ΔK values calculated using empirical equations [59]. When the a/c ratio of the short cracks was varied between 1 and 1.2, the corresponding change in ΔK values computed from empirical equations was less than 5% [59].

2.5.3. Convergence with long crack behaviour

As the short crack increases in size and more grains are encountered, deformation within the plastic zone is constrained by the need to maintain compatibility between randomly oriented grains, and the small crack growth rates will be expected to gradually merge with long crack growth data [87]. Convergence of short and long crack behaviour is generally assumed to occur when the short crack begins to sample the material as a continuum [60], i.e. when the constraints are sufficient to compel the microcrack to grow like a large crack, i.e. at a slower, "average" rate. The general indication of convergence of short and long crack behaviour is the transition from stage I structure-sensitive crack growth to stage II structure-insensitive crack growth [38,47,56]. Many studies have noted convergence of short and long crack data when the crack length has spanned as many as eight to ten microstructural elements [56,57,60,65]. Other researchers have noted convergence of short and long crack data when the crack tip plastic zone size exceeds the grain size of the materials [5,38,57,87,88,96]. These two are essentially similar conditions as the crack tip plastic zone size often exceeds the grain size when the crack has grown across approximately 8-10 grains [65] at the stress levels typically used in these studies. Only one particular study [86] indicated convergence of short and long crack data when the crack length is approximately 20 grain diameters.

However it was found that convergence of short and long crack data when the crack tip plastic zone size exceeds the microstructural element size appeared to be valid only at room temperature under conditions of heterogeneous deformation [63]. Breakdown of this observation at higher temperatures may be related to changes in crack growth mode (through the availability of multiple slip systems and the enhanced dislocation mobility).

2.6. Threshold and near-threshold crack growth

Threshold or near-threshold crack growth is essentially the early portion of long crack growth regime, where under certain circumstances, e.g. low ΔK, the crack is unable to propagate or propagates very slowly. Crack propagation occurs in a very crystallographic manner in this crack growth regime, giving rise to a facetted fracture surface. In this regime, microstructure, temperature and environment have been shown to have significant effects on crack propagation behaviour.

Non-continuum failure processes are at work in the near-threshold crack growth regime. However, as the crack length is much larger than both the microstructural element size and the crack tip plastic zone size, stress intensity solutions can be applied to characterise crack growth in this

regime. In many ways, the near-threshold crack growth regime and the short crack growth regime are similar. In both cases, the crack tip plastic zone is confined to a single grain causing the crack to propagate in stage I crack growth mode. However, in the near-threshold crack growth regime, the crack samples the material's average properties due to its larger crack dimensions, whereas in the short crack growth regime the crack samples only the material local to the crack.

A transition from structure-sensitive near-threshold crack growth to structure-insensitive long crack growth is found to occur when the crack tip plastic zone size exceeds the grain size of the materials [37,69,97,98]. Beyond the transition, a much flatter fracture surface is observed [98]. The transition was observed to be independent of R-ratio and the change from an air to vacuum environment [98]. Some studies have also noted a discontinuity in the crack growth rates da/dN vs. ΔK plot to correspond to the transition [97,98].

2.7. Long crack growth behaviour

Long crack growth corresponds to crack growth where the flaw size is large compared to the scale of plasticity or microstructural elements. Continuum mechanics are at work in this crack growth regime and the crack growth behaviour can be described by the Paris equation (Equation 2-7).

The fatigue crack growth process is a complicated function of a number of variables, including stress intensity, load ratio, temperature, frequency, hold time and environment. In general, the crack growth process can be grouped into two categories, i.e. cycle-dependent crack growth and time-dependent crack growth. Generally, cycle-dependent behaviour is favoured by low temperatures, high cycling frequencies and inert environment, whereas time-dependent behaviour is prevalent at high temperatures, low cycling frequencies, and detrimental environments [99,100].

In the cycle-dependent regime, the crack growth rate per cycle, da/dN, is controlled by the characteristics of the loading cycle, i.e. ΔK and the load ratio. Temperature has little effect on the crack propagation process except as they affect the yield strength and modulus of the material. Other factors, e.g. frequency, hold-time and environment, which are essentially time-dependent parameters will also have little effect on cycle-dependent crack growth processes. Crack propagation in the cycle-dependent regime is characterised by a transgranular crack path with evidence of striations in many cases.

Creep and environmental effects are the main processes giving rise to time-dependent behaviour in fatigue of superalloys. Creep is defined as the time-dependent deformation of a material under an applied load at elevated temperatures. It is an inherent characteristic of the material and occurs even in absence of any environmental effects. Contribution of creep to overall deformation increases with temperature until it dominates material behaviour. Environmental effects include oxidation and corrosion, which are time-dependent due to the kinetics of the chemical reactions

involved. The thermally activated processes of environmental degradation and creep produce a temperature and time-dependent crack growth. In the time-dependent regime, crack growth is characterised by an intergranular crack path [101].

At some intermediate temperatures and frequencies, cycle-dependent and time-dependent components contribute to crack growth, i.e. the cycle-dependent and time-dependent regimes are not mutually exclusive. This regime is known as the mixed cycle and time-dependent crack growth regime, where creep-fatigue-environmental interactions may be taking place. Crack propagation in this regime is characterised by mixed transgranular and intergranular crack growth.

It is possible to separate the various effects on fatigue crack growth by testing under different conditions. Testing in air and in high vacuum will enable the effects of environment to be separated from those of fatigue and/or creep-fatigue as vacuum suppresses oxidation which takes place in the air environment. When testing in vacuum, any time-dependent behaviour present is principally due to creep alone. The interactions of creep and fatigue can be further assessed by testing using high frequencies in vacuum, which will reveal the pure fatigue crack growth behaviour, or by imposition of hold times at maximum load in vacuum to quantify the creep-fatigue interactions. The growth of cracks under service conditions is usually due to a combination of fatigue, creep and environmental effects. The complex interaction of all these effects is not usually a straightforward summation of the individual effects, and this makes the characterisation of fatigue crack growth even more complicated under these conditions [99]. Depending on the load, creep and environmental effects can augment one another thus accelerating crack growth or oppose each other thereby retarding crack growth and sometimes even contributing to crack arrest [99].

Creep is an inelastic deformation, hence the standard LEFM parameter ΔK used to characterise fatigue becomes invalid. Attempts to characterise creep-fatigue are based on partitioning crack growth rates into fatigue and creep components, or by partitioning crack growth driving forces into elastic and inelastic components. Various attempts have been made to characterise crack growth in the mixed cycle and time-dependent regime, the most simplistic being the summation of the individual effects of fatigue and creep component of the crack growth [100,102,103], i.e.

$$\frac{da}{dN} = \left(\frac{da}{dN}\right)_c + \left(\frac{da}{dN}\right)_f \qquad \text{Equation 2-8}$$

where $(da/dN)_c$ and $(da/dN)_f$ are the crack growth rates due to the creep and fatigue components respectively. Good correlation between calculated and experimental results was found only in a limited number of studies [100]. Apparently this approach only works if there is no interaction between creep and fatigue crack growth, giving a total crack growth rate equal to the sum of the

individual fatigue and creep components of the crack growth. When creep-fatigue interactions occur at the crack tip, acceleration of crack growth due to creep crack growth or retardation of crack growth due to stress relief from creep deformation may occur. Environmental effects, if any are present, are also not considered in this simple approach. Linear superposition would generally underestimate crack growth rates in the mixed crack growth mode regime as creep and environment effects tend to accelerate crack growth. The applicability of this simple cumulative damage concept at lower R-ratios where crack closure effects might be important is also questionable [100].

A more sophisticated approach initially proposed by Saxena and used by Gayda et al [9] and other researchers [104] with higher degree of success is the time integration method. The general form of the equation is:

$$da/dN = (da/dN)_f + \int (da/dt)dt \qquad \text{Equation 2-9}$$

where the term $(da/dN)_f$ is the crack growth rates due to "pure" fatigue unaffected by creep or environment effects. This can be obtained experimentally by testing at high frequencies in vacuum. The integral term corresponds to any time-dependent contribution to crack growth, and to calculate this portion of the equation, data from sustained load tests under conditions similar to the creep-fatigue tests are required. Effects of waveform used in the creep-fatigue tests are taken into account when calculating the integral term. This method has been used by Gayda et al [9] and Byrne et al [104] to account for the effects of dwell time during creep-fatigue cycling in their tests, and good correlation was found in regions where environmental effects are not significant [9]. In the time integration scheme, any effects of environment are clearly not taken into account except as they affect creep crack growth. Any interactive effects between the air environment and fatigue loading are also not considered.

2.8. Effect of R-ratio

The load ratio is defined as the ratio of minimum stress to maximum stress in a fatigue cycle, i.e.

$$R = \frac{\sigma_{min}}{\sigma_{max}} \qquad \text{Equation 2-10}$$

2.8.1. Near-threshold and long crack growth

When compared on a ΔK basis, crack growth rates at a given temperature generally increases with increasing R-ratio [101,105,106]. At a given temperature, the crack growth out curves on the da/dN vs. ΔK plot are shifted to the left and up, i.e. lower ΔK_{th} and higher crack growth rates are seen with increasing R-ratio [37,85,88,97,106,107,108,109,110].

Near-threshold crack growth has been shown to be sensitive to R-ratio. The R-ratio effect is more pronounced in coarse grain material, while in fine grain material, ΔK_{th} and near-threshold crack growth rates appear to be rather independent of R-ratio [109,110]. The observed R-ratio effect is largely attributed to crack closure, specifically surface roughness-induced crack closure [37,88,109], and at elevated temperatures, oxide-induced crack closure may also be important [109]. At low R-ratio, the highly facetted crack profile in the near-threshold crack growth regime causes contact of the crack faces to occur easily, i.e. surface roughness-induced crack closure. During crack closure, contact of the crack faces occurs at a stress intensity level above the applied K_{min}, hence the crack tip does not experience the full range of applied stress intensities. This reduces the crack growth driving force at a given ΔK, and a higher applied ΔK value is required to give a similar crack growth driving force as in a closure-free situation, leading to higher apparent threshold ΔK values. A high R-ratio keeps the crack open due to higher mean loads. This reduces or eliminates crack closure effects, giving rise to a reduction in ΔK_{th}. With larger grain sizes, the facets formed during near-threshold crack growth at low temperature on the fracture surface are expected to be larger. This will increase the extent of roughness-induced crack closure in the material, giving rise to a higher dependence of ΔK_{th} value on R-ratio. The R-ratio effect is minimal in fine grain material as the corresponding smaller facets on the fracture surface only give rise to a small closure contribution [109].

When the crack growth data are plotted against an effective stress intensity factor range, ΔK_{eff}, instead of ΔK, most of the results obtained at different R-ratio fit together within a small scatter and a common intrinsic threshold can be observed in a majority of studies [85]. The effective stress intensity factor range, ΔK_{eff} is defined as

$$\Delta K_{eff} = K_{max} - K_{closure} \qquad \text{Equation 2-11}$$

where K_{max} is the maximum applied stress intensity factor and $K_{closure}$ is the stress intensity factor below which crack face contact will occur.

Under long crack time-dependent conditions, high R-ratio usually produces higher degree of creep damage [107] or increased oxidation damage [111] due to higher mean loads, leading to higher crack growth rates. Crack growth due to creep and oxidation damage mechanisms become more dominant at higher R-ratio due to the higher mean loads, whereas fatigue is favoured by large load amplitude variations [100,102,107].

2.9. Effect of temperature

With an increase in temperature, there is an increased tendency for homogeneous slip and an increased degree of creep and environmental interactions. Prolonged high testing temperatures may also cause changes in the microstructure, e.g. coarsening of the strengthening precipitates.

2.9.1. Deformation behaviour

At higher temperatures, dislocation motion, i.e. dislocation cross-slip and climb are enhanced [112,113]. More slip systems are also activated at higher temperatures. Both these factors produce a more homogeneous slip due to the reduced tendency for precipitate shearing [5]. Cyclic loading at room temperature produced very intense planar slip bands, i.e. very heterogeneous slip behaviour compared to deformation at higher temperatures [114,115]. The enhanced dislocation motion at high temperatures will give a drop in the yield stress of the material [5,113]. The increase in crack tip opening displacement (CTOD) with a decrease in strength and modulus at higher temperatures is expected to increase crack growth rates [105,116].

Changes in slip mode also affect the crack path and the extent of crack blunting, crack branching, fracture surface roughness, and hence the extent of surface roughness-induced crack closure [112]. Strain localisation has been cited to inhibit crack tip blunting and promote crack growth [117]. Crack tip blunting at high temperature has been cited to give a reduction in crack growth rates [101]. Nucleation of secondary cracks was noted to be assisted by the concentration of slip close to the crack tip during heterogeneous deformation at room temperature [94], i.e. crack branching phenomena is enhanced with heterogeneous slip. Formation of secondary cracks decreases the ΔK at the crack tip and thus lowers crack growth rates [94]. An increase in temperature leading to more homogeneous slip also gives rise to a flatter and less facetted fracture surface. This reduces the degree of surface roughness-induced closure and the extrinsic resistance to crack growth, leading to higher crack growth rates [60]. In summary, more homogeneous slip at higher temperatures may give rise to more extensive crack tip blunting, which improves crack growth resistance, but at the same time may reduce the crack tip branching and crack closure contribution to crack growth resistance.

2.9.2. Initiation and short crack growth

The crack initiation period may be lengthened or shortened with an increase in temperature [70,78]. Homogenisation of slip with an increase in temperature may suppress slip band cracking [78], but with further rise in temperature, oxidation is enhanced and this may significantly reduce crack initiation resistance [70]. Short crack growth rates were noted to be faster at elevated temperatures than at room temperature [60]. This acceleration is usually accompanied by a change in slip character from highly faceted growth to a more homogeneous growth, giving a flatter fracture surface [60,61].

In a short crack growth study on Waspaloy by Stephens et al [55,63], the fatigue life was noted to decrease when temperature was raised from 25°C to 500°C. Short crack growth rates were faster and less scattered at 500°C than at 25°C. As the temperature is increased, microstructural effects on crack growth decreased, resulting in a reduced microstructural short crack effect, i.e. the extent of discontinuous crack growth rates decreased with an increase in temperature [63]. With an increase in temperature, a change in slip character and a reduction in barrier efficiency was noted. A transition from heterogeneous to homogeneous deformation will occur as thermally activated cross-slip and climb becomes easier. At 500°C, the additional active slip systems present in adjacent grains increases the likelihood for favourable aligned slip systems in more than one grain. This reduces the effectiveness of grain and twin boundaries as barriers to crack growth. Instead of these barriers providing resistance to crack growth, the favourably aligned slip systems covering more than one grain reduce crack growth processes associated with discontinuous crack growth rates observed at 25°C, as well as giving higher growth rates due to more homogenised slip [63]. At 700°C, the classical short crack effect in Waspaloy was minimal, and typically did not extend beyond the first grain [63].

2.9.3. Near-threshold crack growth

An increase in temperature was shown to give lower ΔK_{th} [5,97,109,110]. However this trend appear to be observed only in the coarse grain material in studies comparing the threshold crack growth behaviour of fine and coarse grain materials [109,110]. At higher temperatures, the fracture surface will be flatter although it may still exhibit some crystallographic features [109,110,115]. This reduces surface roughness-induced crack closure, giving rise to lower ΔK_{th} [5,109,110]. For the fine grain material, there is little change in the fracture surface roughness with increase in temperature [109,110], hence a similar ΔK_{th} was observed at room and elevated temperature. Conflicting results have also been noted where ΔK_{th} increases with increasing temperatures [101,118]. The increase in ΔK_{th} with increasing temperature is attributed to oxide-induced crack closure effects, as oxidation rate increases with temperature hence producing thicker oxide layers. Overall, it appears that an increase in temperature will initially reduce ΔK_{th} due to a change to a flatter fracture surface topology. With further increase in temperature, oxidation starts to become significant and may give rise to oxide-induced crack closure, causing an increase in ΔK_{th}.

2.9.4. Long crack growth

When testing in air, an increase in temperature will generally lead to an increase in crack growth rates [79,94,104,109,111,119,120,121,122]. Smaller effects of temperature on crack growth rates were noted in vacuum tests compared to testing in air [101,105].

In the cycle-dependent crack growth regime, the increase in crack growth rates with temperature was found to be minimal [47,107,116]. In most cases, the variation in crack growth rates can be

rationalised in terms of changes in yield strength and modulus of the material with temperature. A change in slip character might also be responsible for the higher crack growth rates. An increase in temperature giving a more homogeneous slip would enable strain accommodation and hence reduce the localised stress concentrations, but at the same time the reduced degree of slip heterogeneity may lead to more irreversible slip and greater damage accumulation, which may be detrimental to crack growth resistance.

In the time-dependent crack growth regime, an increase in temperature will lead to a more pronounced increase in crack growth rates. In addition to changing slip deformation characteristics, changes in temperature also change the degree of time-dependent phenomena, i.e. creep and environmental degradation. The degree of creep and environment damage increases with temperature as both processes are thermally activated [99,101,123]. As temperature is increased, a transition from transgranular crack growth indicative of cycle-dependent crack growth to a mixed transgranular and intergranular crack growth or a predominantly intergranular crack growth will occur, indicating increasing contribution of creep and/or environmental damage to the crack growth process [22,79,112,123,124].

In tests involving hold times at maximum load, some studies [101,104] have noted that the crack growth rates increase with an initial increase in temperature, but with further increase in temperature, a decrease in crack growth rates was observed. This was attributed to crack tip blunting at the elevated temperature, or due to coarsening of shearable precipitates [104] leading to a more homogeneous slip process. As mentioned previously this will reduce the localised stress concentration and minimise the chance of intergranular cracking due to relaxation of the stresses generated between a grain boundary and an impinging slip band. This may also increase the intergranular crack tip resistance to environmental damage.

2.10. Frequency and waveform effects

The fatigue crack tip damage ranges from purely cycle-dependent at high frequency loadings to fully time-dependent at very low frequency loadings. The link between crack tip damage mode and loading frequency has been suggested to be controlled by the loading frequency-associated slip line density and the related degree of homogeneity of plastic deformation generated in the crack tip plastic zone region [125].

2.10.1. Deformation behaviour

High frequency loadings will lead to a more homogeneous slip behaviour [126], as evident from the high slip line density produced in the crack tip region [125,127,128,129]. This was shown in a study investigating the effects of frequency on crack growth rates conducted by Ghonem and Zheng [127]. Slip line density was noted to increase proportionally with the loading frequency. In the same study by Ghonem and Zheng [127], it was also noted that prior application of high frequency loading

results in reduction of subsequent low frequency crack growth rates. This was attributed to crack tip conditioning through the increase in slip line density during the high frequency part of the loading, i.e. a more homogeneous deformation at the crack tip, leading to lower crack growth rates in subsequent low frequency cycling. The slip line density in areas of low frequency loading, while lower than that in areas of high frequency loading, was found to be higher than the slip line density corresponding to continuous low frequency loading. The higher slip line density due to prior application of high frequency loading in the low frequency areas was noted to give increased crack growth resistance to environmental degradation compared to the material which was only subjected to continuous low frequency loading. A change from 'ductile' to 'brittle' striations with decreasing frequency has also been noted, and this may be due to the lower strain rates resulting in more localised slip, thereby inhibiting crack tip blunting and promoting crack growth [117].

2.10.2. Long crack growth

In the cycle-dependent crack growth regime, i.e. at sufficiently high loading frequencies, crack growth rates are largely independent of frequency. A transgranular crack propagation is usually observed under such circumstances. Cycle-dependent crack growth rates at high temperature correspond closely to crack growth rates observed at room temperature as well as those seen in vacuum, indicating the lack of time-dependent component in the crack growth process [105,111].

Below a certain frequency, known as the transitional frequency, the component of time-dependent contribution to the overall crack growth process starts to gain significance, causing the onset of the mixed cycle and time-dependent regime and the time-dependent regime. In this regime there is a general trend for crack growth rates at a given ΔK to increase with a decrease in loading frequency at high temperatures [50,100,101,102,105,112,126,129,130,131,132,133]. The accelerated crack growth rates are usually accompanied by a transition from transgranular crack propagation to a mixed transgranular/intergranular crack propagation or a predominantly intergranular crack propagation, indicating the onset of time-dependent crack growth [101,102,112,111,130,133].

At lower frequencies, the higher crack growth rates observed have been attributed to a higher contribution of creep to crack growth [117], or a greater extent of environmental damage contributing to crack growth [9,111], or a combination of the two [112,116,132]. This is reinforced by the intergranular crack propagation mode observed at low frequencies. At low loading frequencies, the conditions approximate closer to that of a sustained load test, hence the contribution of creep damage per loading cycle is increased. Under these conditions, the crack growth rates are inversely proportional to the frequency and are sensitive to any dwell times imposed at maximum or minimum load. The increased environmental damage may be explained on the basis that embrittling species diffuse to crack tips from within the material [112]. Lower cyclic frequencies would allow more time for diffusion to occur so that greater concentrations of embrittling species

would then be present at crack tips to promote cracking [9,112]. High loading frequencies suppress intergranular crack growth possibly by interrupting the oxygen diffusion process [129]. At lower frequencies, the cracks also tend to be more open due to an enhanced development of oxides inside the crack [112,134]. This could give oxygen from the environment an easier access to the crack tip.

The effects of cyclic frequency on crack growth rates are noted to be less pronounced at lower temperatures [112,117,132]. Generally, frequency effects are only observed at elevated temperatures and not at room temperature [101,105]. The influence of frequency is also stronger in air compared to in an inert environment (helium or vacuum) [9,101,105,112].

The observed frequency effects may also be rationalised in terms of the slip behaviour associated with the loading frequencies. In the cycle-dependent crack growth regime, i.e. at frequencies higher than the transitional frequency, the increased slip line density was assumed to lead to strain accommodation as well as stress relief along strained grain boundaries in the crack tip region [127,129]. Crack propagation is predominantly transgranular in this case. The loading frequency required to produce this type of cycle-dependent response is lower when the magnitude of applied ΔK is increased, as increasing ΔK tends to lead to an increased degree of slip homogeneity. As loading frequency is lowered, the degree of slip homogeneity in the crack tip zone was found to decrease, thus resulting in grain boundary stress concentration and a relative increase in the intergranular oxygen diffusion. Under these conditions, crack tip damage is due to a combination of oxidation and cycle-dependent components [127,129].

The influence of frequency on crack growth rates can be most clearly demonstrated using a frequency mechanism map. The map is obtained by plotting the crack growth rates obtained at a particular ΔK against the loading frequency. To illustrate the typical features noted in a majority of studies, an example of the frequency mechanism map is taken from the study investigating the effects of frequency by Winstone et al [102].

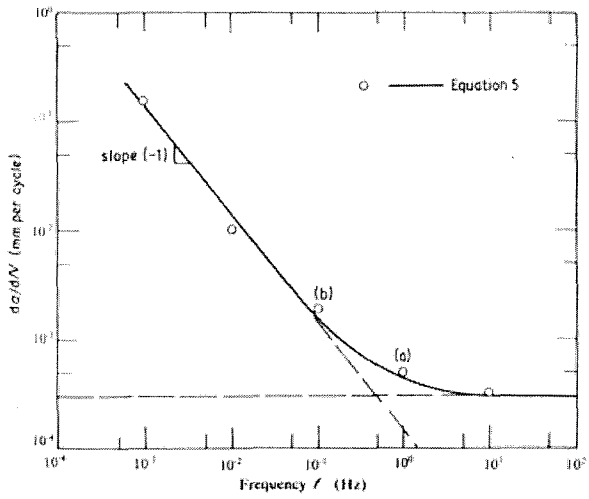

Figure 2-4: Frequency mechanism map after Winstone et al [102] for alloy AP1 at 700°C, $\Delta K = 20$ MPa$\sqrt{m}$ and R = 0.7.

In the cycle-dependent crack growth regime where fatigue processes dominate, frequency independence of crack growth is observed, i.e. a horizontal line on the frequency map [101,102,111]. Below a certain frequency, the slope of the da/dN vs. frequency plot approaches a value of –1, which corresponds to a fully time-dependent behaviour. This is consistent when the da/dN is converted to å, i.e. the crack growth velocity through the following equation:

$$\frac{da}{dN} = \frac{1}{3600}\left(\frac{\text{å}}{f}\right) \qquad \text{Equation 2-12}$$

where da/dN is in mm/cycle, f in Hz and å in mmh^{-1}. When time-dependent processes control crack growth, å will be expected to be constant and a slope of –1 is obtained [111]. Between these two extremes, there exists a regime of mixed cycle and time-dependent behaviour [101,102]. Creep-fatigue interactions are generally observed to occur over about two decades of frequencies [100,102,111].

A similar frequency mechanism map has also been plotted by Tong and Byrne [130] for their tests on U720Li at 650°C, but the slope of the da/dN vs. frequency in the time-dependent regime was noted to be –0.38 rather than –1. This may be due to the lower R-ratio used in their study, which may give rise to significant crack closure in addition to pure creep-fatigue interaction.

2.10.3. Waveform effects

The effects of waveform and loading rate have also been investigated in fatigue studies involving frequency. The loading rate was generally noted to be the controlling factor in the case of waveform effects on crack growth rates. This has been noted by many researchers, although some have reported little or no effect of loading rate. At temperatures where frequency effects are

associated more with corrosion/oxidation processes, loading rate has been cited to have a larger effect than unloading rate [99]. Under such conditions, the waveform effect will be sensitive to the combined frequency of the loading and unloading cycle segments in relation to the material transition frequency [105].

The effects of waveform on fatigue crack growth process have been studied by Clavel and Pineau [126] using square and triangular waveforms at 550°C in IN718. The cyclic waveforms were chosen to differentiate the effect of loading and unloading rate as well as the effect of hold time at maximum and minimum load.

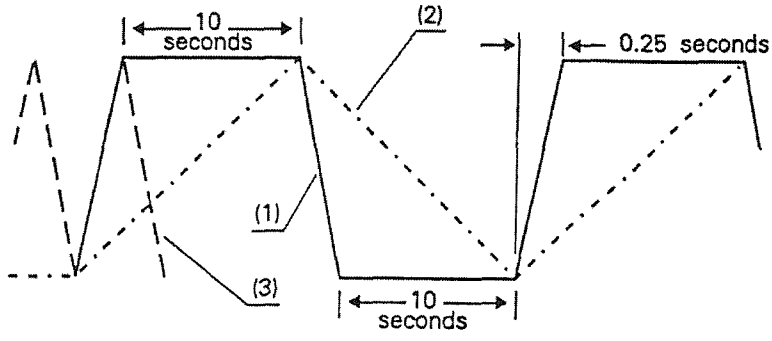

Figure 2-5: Cyclic waveforms used by Clavel and Pineau.

Waveform 3 corresponds to a frequency of 2Hz, whereas waveform 2 leads to a frequency of 0.05Hz. Waveform 1 has the same loading and unloading rate as waveform 3 but superposes a 10 seconds hold time at maximum and minimum load, and its cyclic duration is the same as that of waveform 2. Their results show that the crack growth rates of waveform 2 with a slow loading rate are higher than those of the other two waveforms. The square wave (waveform 1) of the same loading rate as the 2Hz triangular wave (waveform 3) was noted to give marginally higher crack growth rates, i.e. the hold time of 10 seconds at both maximum and minimum load has only minimal effects on the crack growth rates. The results of this study suggest that the effects of waveform are governed by the loading and unloading rate rather than by the frequency.

The loading rate has also been noted to be the controlling factor in waveform effects on crack growth by Ashbaugh as reviewed by Ghonem et al [105]. Ashbaugh has conducted a series of test on CT specimens of IN718 at 649°C using triangular waveforms and R=0.1. In addition to the symmetric waveform with frequency covering the range from 0.01 to 10Hz, asymmetric waveforms were also used in which the rise and fall times had different values corresponding to the baseline frequency of the symmetric waveform tests. For various combinations of rising and falling frequencies from 0.01Hz to 1Hz, crack growth rates are essentially equivalent to those obtained using symmetric waveform where the frequency was that of the rising portion of the

asymmetric wave. This observation implies that the fatigue damage occurs almost exclusively during the rising load portion of the fatigue cycle.

In a study by Lynch et al [112], tests using different waveforms (triangular, skewed triangular and trapezoidal) on Waspaloy at 700°C showed that the strain rate during loading (i.e. rise time) controlled the transgranular striation spacing and appearance; unloading rate was found to have no effect. There is also a lack of hold time effect on striation spacing and appearance. This again suggests that the crack growth process is governed by the loading rate, and the hold time during square waveform cycling has only minimal effect on crack growth rates.

On the other hand, Tong and Byrne [129] have noticed no significant difference between triangular and trapezoidal waveform of the same overall frequency in their tests on U720Li at 650°C. With the same overall frequency, the trapezoidal waveform has a higher loading rate, hence would be expected to show lower crack growth rates according to the trends observed by Clavel and Pineau [126]. Similar crack growth rates of 1-1-1-1 and 30-1-1-1 cycles in air and vacuum were also noted in U720Li at 700°C [107], which suggests that damage during the loading part is not significant for loading rates below certain levels in this alloy.

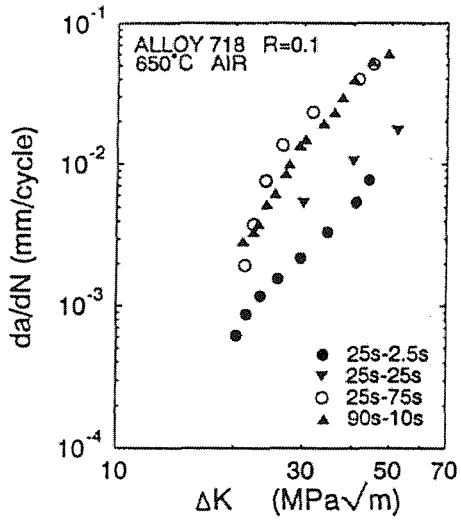

Figure 2-6: Crack growth behaviour for different frequencies with different loading and unloading rate [105].

Conflicting results have also been obtained by Ghonem and Zheng [105], where the overall cycling period, rather than loading rate, was found to govern crack growth rates. In their investigation using IN718 at 650°C, the cyclic durations of the triangular waves included 27.5s (25s-2.5s), 50s (25s-25s), 100s (25s-75s) and 100s (90s-10s), which are denoted as case A B, C and D respectively, and the numbers in parentheses denote the times of the rising and falling portion of the wave. The results of da/dN vs. ΔK are shown in Figure 2-6. It can be seen from the plot that

the crack growth rate for case C is identical to that of case D, indicating that, for the same cycling period, varying the ratio of the loading and unloading portions of the cycle does not affect the crack growth behaviour. Furthermore, cases A, B and C, which have different frequencies but identical loading times, did not result in similar crack growth behaviour and an increase in the total cycle duration yields an increase in crack growth rates.

It appears that the effects of waveform on crack growth is dependent on the crack growth regime, i.e. cycle-dependent or time-dependent, due to the degree of slip homogeneity associated with loading rate and overall frequency. Where tests are conducted at low overall frequencies, environmental effects may be significant, i.e. the time-dependent contribution to crack growth may mask any effects of waveform on the cycle-dependent crack growth process.

2.11. Effect of environment

Oxidation and corrosion are the main effects which the environment can have on the growth of fatigue cracks. Environmental effects are thermally activated and time-dependent, hence an increase in temperature will lead to more rapid environmental degradation of the material [99,135]. When testing in air, crack growth rates are generally found to be higher than when the same material is tested in vacuum or inert environment. This is due to the presence of oxygen in air which oxidises the material near the crack tip as well as giving grain boundary embrittlement thus weakening the material.

In oxidising environments, oxide formation at crack tips and diffusion of oxygen ahead of cracks occur preferentially along grain boundaries due to these being a less oxidation-resistant region in the microstructure and faster diffusion of oxygen occurring along the boundaries than within grains [21,112]. Crack growth can then be promoted by brittle cracking of thick oxide films [116] or along grain boundaries contaminated with oxygen atoms [9,22,113,124,136], or through strain localisation in intergranular zones weakened by depletion of alloying elements due to their preferential oxidation [9,70,73,137]. Intergranular cracking involving these processes is promoted by a more inhomogeneous slip mode. Oxygen diffusion along grain boundaries has also been cited to promote a reduction in grain boundary ductility, inhibition of planar slip and an acceleration of cavity formation [101].

Oxide layers were found to be rich in Al and Ti which are required in the formation of γ' precipitates, and this give rise to a depletion of γ' precipitates along the fatigue cracks [70,137]. Choe et al [73] has noted Cr denuded zones adjacent to the grain boundaries with imposition of prolonged hold times in Astroloy at 650°C and 725°C, which gives a high, localised crack growth rate. Formation of non-protective oxides which flake off the surface also promotes more rapid oxidation through fretting [134]. Fresh material is exposed when the oxide debris flakes off and there is also a

possibility that any adherent and protective Cr_2O_3 oxide layer is damaged by this oxide debris, further increasing the degree of oxidation.

Matrix oxidation was also noted in many studies [47,130,137]. However the depth of matrix oxidation is not as significant as the depth of penetration of oxidation along grain boundaries [136]. Matrix oxidation also causes depletion of oxide forming elements (Al, Ti, Cr), and hence the dissolution of γ' under the oxidised surface [136]. Contrary to grain boundary oxidation which is accelerated by mechanical loading, observations suggest that no interaction exists between matrix oxidation and mechanical loading [136]. The matrix oxidation was found to have a minimal effect on crack growth rates in most studies. In one particular LCF study in air, matrix oxidation was found to enhance the crack initiation period at low stress amplitudes compared to testing in vacuum, with the actual life to crack initiation directly linked to the number of cycles required to break the matrix oxide scale in the most critical areas [137].

Ghonem et al [128] reviewed a crack tip oxidation mechanism which is divided into two main categories, i.e. in terms of short and long-range oxygen diffusion processes. In the short-range diffusion, oxygen forms an oxide layer at the crack tip with a depth that depends on many operating and materials parameters. The formation of this layer, under the restricted concave crack tip geometry, results in high stresses that could easily be transmitted to the substrate. There is also a possibility of the formation of wedge-shaped intrusions along the crack front, and the rupture of these wedges at the grain boundaries would result in accelerated intergranular crack growth.

In the long-range diffusion, oxygen penetrates the crack tip material along rapid diffusion paths, such as slip planes and grain boundaries. The internal oxidation process taking place along these paths could occur in the form of internal oxide sites, cavity formations and/or solute segregation. It is also possible for oxygen to take part in chemical reactions releasing known embrittlement agents onto grain boundaries. These processes, in particular along grain boundaries, result in inhibition of sliding and migration of these boundaries and thus reduce their ability to relieve local stress build-up during deformation. The oxidation mechanisms associated with short and long-range diffusion are not completely separated, and experimental observations indicate that, for alloy 718 at intermediate temperature range and low loading frequencies, short-range oxygen diffusion contributes primarily to the occurrence of an intergranular fracture mode.

The partial pressure of oxygen, PO_2, is also a significant parameter in relation to the oxidation mechanism [128]. The presence of oxygen at different partial pressures will control the preferential formation of one given species of oxide that may either shield or contribute to the crack tip damage process through passivation or enhancement of the oxidation process respective. Andrieu [138], using Auger spectrometer analysis, found that at the start of the oxidation process, when atmospheric oxygen partial pressure is available for the crack tip material, the first oxides to

form will consist of selective oxides of FeO and NiO and their spinels. These porous oxides, which cannot serve as an oxygen diffusion barrier, permit continuous oxidation reaction at the base grain boundary material. As the thickness of these oxides increases, thus leading to a decrease in the oxygen partial pressure at the oxide/metal interface, the reaction kinetics required for the formation of a denser Cr_2O_3 sublayer is attained. This dense layer, which is thermodynamically stable at high temperature, is considered protective in the sense that it limits oxygen diffusion to the grain boundary material, thus resulting in a decrease in the oxidation reaction as time elapses. When the build-up of the Cr_2O_3 layer is fully completed no further oxidation of the base material would take place and a condition of oxidation passivation is said to occur. No further oxidation takes place until the chromia layer is fractured, thus exposing fresh metal to the repetition of the oxidation cycle [127].

Evidence of the importance of oxygen partial pressure PO_2 on crack growth was provided by Andrieu et al [139]. The authors noted a transitional oxygen partial pressure on crack growth rates at approximately 10^{-2} mbar. At PO_2 below 10^{-2} mbar, crack growth rates were independent of PO_2, and crack growth was controlled by mechanical parameters. Selective oxidation of chromium was identified and transgranular crack growth was noted. At PO_2 above approximate 10^{-2} mbar, crack growth rates were noted to increase with PO_2. Crack growth was fully controlled by oxidation kinetics which corresponds to nickel-oxide scale growth and intergranular crack growth was noted. At high PO_2 and low frequencies, crack growth rates reach a saturation regime and become independent of the PO_2, where crack growth rates are significantly higher and intergranular crack growth was noted.

Although oxidation has been viewed as detrimental to crack growth resistance thus far, nevertheless oxidation can also contribute to reduce crack growth rates [140]. Oxidation can result in blunting of cracks and prevent resharpening, and can produce oxide-induced crack closure, thereby decreasing crack growth driving force and lowering crack growth rates [112,141]. Increased ΔK_{th} for crack growth in air has also been associated with oxide-induced crack closure.

2.11.1. Deformation behaviour

In an oxidising environment, the nature of slip damage is important with respect to the diffusion of oxidising species to grain boundaries along intense slip band. Microstructures producing a more intense slip behaviour have been inferred to produce an easier path for diffusion of oxidising species [113].

The effects of frequency on the extent of environmental damage discussed previously may be linked by considering the possible effects of slip homogeneity on the environmental interactions. One of the effects of slip behaviour on environmental interactions is the concept of oxidation shielding nodes. The basis of the oxidation shielding concept assumes that the slip line density is

the rate controlling element of the chromium oxide build up taking place at the slip line/grain boundary intersection nodes within the crack tip region. The increase of slip line density (due to more homogeneous slip at higher loading frequencies) along a grain boundary path in this region signifies the occurrence of two effects i) the decrease of stress concentration owing to the increased possibility of slip line matching and consequently the decrease of dislocation pile-up along this path; and ii) the increase of chromium concentration along this path owing to the increased transport of this element from the matrix via slip bands. The availability of higher chromium concentration and the higher stress levels at the slip line/grain boundary intersection due to dislocation pile-ups (compared to areas free of slip line/grain boundary intersection) provide the intersection regions with the kinetics required for Cr_2O_3 to build up at a rate faster than that in the grain boundary regions which are free of such intersections. If one views the Cr_2O_3 at the intersection points to act as oxidation shielding nodes, higher slip line density in the crack tip zone would give higher grain boundary resistance in this zone to environmental degradation during intergranular cracking, leading to lower crack growth rates [125,127].

Another governing factor influencing the intergranular oxygen diffusion process is the grain boundary diffusivity parameter, D_g, which depends on the stress and strain states along the affected grain boundary paths [128]. During high frequency loading, high slip line density would limit the stress built-up along affected grain boundaries owing to the high percentage of slip line matching across these boundaries. In this case, the grain boundary oxygen diffusivity, being a stress-dependent parameter, is assumed to show only a minimal variation [32,125]. In addition, the increase in slip line density generally leads to an increase in lateral volume diffusion across affected grain boundaries (higher oxidation shielding contribution). These two combined effects result in limited or no acceleration of intergranular oxygen diffusion rate, and hence a lower oxygen penetration depth. Under this condition, the influence of crack tip oxidation is minimal and crack tip damage becomes generally dominated by cycle-dependent effects. During low loading frequency cycling however, low slip line density promotes stress concentration along grain boundaries in the crack tip region resulting in an increase in the magnitude of D_g [125,132]. Furthermore, a decrease in slip line density would limit the grain boundary lateral volume diffusion process (giving a lower oxidation shielding contribution). Hence an expected increase in grain boundary diffusivity and associated increase in the oxygen intergranular depth of diffusion could result in an increase in the crack tip damage due to environmental effects.

Both the concept relating environment interactions and slip behaviour (oxygen diffusivity parameter concept and the concept of oxidation shielding node) suggests that a reduced sensitivity to environmental damage will be observed for testing conditions or microstructures which give rise to a more homogeneous slip behaviour. Ghonem and Zheng [127] in a study investigating the effects of frequency on crack growth rates using sequential high frequency and low frequency loadings

has found that increased slip line density in the crack tip region through prior application of high frequency loading has lowered the influence of environment during subsequent low frequency crack growth through this modified region. The researchers have attributed this observation to oxidation shielding nodes giving rise to improved resistance to environmental attack. In a more definitive study to investigate the oxidation shielding node concept conducted by Zheng et al [125], prestrained specimens (containing a higher slip line density) and as-received (undeformed material with limited slip lines) were used. If the shielding mechanism is operative, then two outcomes would be expected from the tests, i.e. i) the thickness of the oxide layer formed, and consequently the depth of oxygen penetration in the case of the prestrained material should be smaller than that formed in the case of the as-received material, and ii) the chromium content in the crack tip region of the prestrained material would be higher than that in corresponding as-received material. Both these observations were noted from the results of the analysis, supporting the occurrence of the oxidation shielding mechanism.

2.11.2. Initiation and short crack growth

Longer crack initiation periods and lower short crack growth rates were noted when testing in vacuum compared to testing in an air environment, especially at elevated temperatures [36,134]. This is due to oxygen in the air environment, where penetration of oxygen along persistent slip bands was cited to enhance stage I crack initiation and stage II crack growth, and penetration of oxygen along grain boundaries was linked to accelerated intergranular cracking in a variety of nickel-base superalloys, including Rene 80, MAR-M-200, IN738 and IN718 [36]. In a LCF study by Reger and Remy [134] on IN100 at 1000°C, life spent in crack initiation was observed to be in the range of 10-30% in air, but in vacuum this fraction increases with increasing fatigue life and is about 60-80% of the total life.

2.11.3. Near-threshold crack growth

The effect of environment on near-threshold crack growth is far from clear. In a study investigating the effects of environment on near-threshold crack growth in IN718 at 20°C and 538°C, Yuen et al [97] has reported higher ΔK_{th} in air compared to in helium. The higher ΔK_{th} reported in air compared to in helium at room and elevated temperature was attributed to accumulation of oxide in the crack which enhances crack closure through oxide fretting mechanism. At room temperature, oxidation in nickel-base superalloys is expected to be negligible but in this study significant oxide thickness was found on the crack face in tests at room temperature.

Contradicting results, i.e. higher ΔK_{th} was observed in vacuum compared to in air were found by King [98] and by Loo and Reed [142]. In the work by King [98] on Nimonic AP1 at room temperature, the higher ΔK_{th} observed in vacuum compared to in air was attributed to crack face rewelding in

vacuum at room temperature. The welded joints would have an effect of reducing the effective ΔK seen by the crack tip even more than the simple crack closure occurring in air, because the crack cannot open again until the welded junctions have been torn apart. In air, rewelding did not occur due the protective Cr_2O_3 layer formed when testing in air. This layer does not crack easily and is able to reform quickly. In the study by Loo and Reed [142] on U720 at room temperature under vacuum conditions, stage I crack growth was found to be greatly enhanced and the fracture surface was noted to be much rougher compared to testing in air conditions. This is due to the increased reversibility of slip under vacuum conditions. Although the fracture surface is much rougher, the higher ΔK_{th} observed in vacuum were however not a result of higher surface roughness-induced crack closure as there is limited evidence of fretting debris or rewelding of the crack in the crack wake. The greater reversibility of slip in vacuum implies that the crack faces are less likely to undergo an irreversible mode II displacement relative to each other, thereby inhibiting or limiting the extent of surface roughness-induced crack closure. The higher ΔK_{th} under vacuum conditions was attributed to extrinsic shielding due to crack branching and the formation of secondary cracks during facetted crack growth. The highly complex crack shape resulted in the crack tip being shielded from experiencing the full range of the applied ΔK.

2.11.4. Long crack growth

In the time-dependent regime, testing in an air environment has been associated with higher crack growth rates compared to testing in vacuum or an inert environment [19,21,94,113,116,123,130,134,122,140,141]. Testing in air resulted in oxidation-dominated intergranular fracture in many studies [21,113]. The effect of air as an oxidising environment was more marked in lower frequency and/or longer hold time tests [113,117,134], or at higher temperatures [113,123,124].

It has also been noted that the m-values, i.e. the slope of the da/dN vs. ΔK plot remained almost constant under various temperatures and imposed dwell time for tests carried out in an air environment [113,124]. Oxidation embrittlement along grain boundaries which dominates crack growth under the various test conditions could explain the similar m-values observed.

In the long crack growth regime, the effect of environment on crack growth rates is generally more marked in fine grain microstructures [124,135]. This is due to the higher amount of grain boundaries in the fine grain microstructure, which increases the influence of environment on the crack growth process. The intergranular crack growth process usually associated with environment interactions in fine grain microstructure is usually suppressed when the material is tested in vacuum, further supporting that environmental attack is predominant in air tests for fine grain microstructures.

2.12. Hold time effects

2.12.1. Long crack growth

In the cycle-dependent crack growth regime, hold time does not have any significant effect on crack growth rates. In the time-dependent regime where creep and environmental degradation is significant, hold time markedly affects crack growth rates.

In the time-dependent regime, testing in air with imposition of hold time at maximum load has generally been associated with higher crack growth rates [2,10,11,99,101,105,124,141,143]. Hold time of 1 minute at minimum load in air has also been found to increase crack growth rates in IN718 at 650°C and R=0.05, with exception for one test at R=0.5 where crack growth retardation and arrest occurred [99,106]. Hold time at minimum load in vacuum was found to have no effect on crack growth rates [106].

The hold time effect is also observed when testing in vacuum or an inert environment [116,122], but the effect is not as marked compared to observations noted during testing in air [99,105,135]. Hold time effect is also more pronounced at higher test temperatures [101,117,131,135], as time-dependent contributions to crack growth are enhanced. Longer applied dwell generally causes a more severe increase in crack growth rates [108], to the extent that the crack growth rates approximate close to those obtained in static load tests [99,144]. In some studies [112,131], long hold times, particularly at higher temperatures (≥700°C) have been associated with crack growth retardations.

The hold time effects observed are due to creep contribution to crack growth [116] and/or crack growth contribution from environmental interactions [34,69,73,112,141]. In nickel-base superalloys, increase in crack growth rates with imposition of dwell in air is usually attributed largely to environmental interactions, as many researchers have found limited or no evidence associated with creep damage near the crack tip (e.g. cavitation, void formation) [129]. It appears that the rapid environmental effects have swamped the slower creep damage in tests incorporating dwell in air [113]. Environmental interactions as described in the previous section, e.g. grain boundary oxidation, are found to be enhanced by the presence of tensile dwell [69], or an increase in the cycle period [141]. Oxide layers were also found to be thicker after dwell cycling compared to continuous cycling, probably because there is easier access of oxygen to the crack tip when the crack is held open at maximum load [112,117].

Many researchers have also found no effect of dwell, or decreasing crack growth rates with imposition of dwell [132], to the extent that complete crack arrest occurred [103,106]. In general, these observations were attributed to creep deformation during hold time, or due to formation of a protective oxide layer with imposition of dwell, prohibiting further attack of oxygen at grain boundaries.

Creep deformation can cause crack tip blunting [73,94,106,145], or stress relaxation [99,103], or a combination of the two [99,112], leading to reduced crack growth driving force. This happens particularly when the stress intensity during hold time is less than the threshold stress intensity for creep crack growth, K_{thc} during dwell cycling, where creep deformation can still occur, contributing to crack tip blunting or relaxation of stresses at the crack tip, but not to crack growth. Crack tip blunting and stress relaxation may suppress environmental effects, in addition creep can also cause reduction in environment sensitivity in several ways; it could shift the maximum of the triaxial stresses away form the crack tip thereby increasing the diffusion distance for oxygen to cause embrittlement. In addition, deformation may provide alternate diffusion paths for oxygen thereby dispersing it away from grain boundaries where it is most damaging [99].

In a fatigue crack growth study by Sadananda and Shahinian [103], it was noted that crack growth behaviour depends on the initial ΔK and the duration of hold time at peak load. At initial ΔK lower than the threshold stress intensity for creep crack growth, crack growth rates decreased with increase in hold time, to the extent that complete crack arrest can occur at prolonged hold times. They have attributed this to stress relaxation due to creep. The decrease in stress intensity due to stress relaxation might be larger than the increase in stress intensity due to increase in crack length, giving rise to crack arrest. For longer hold times, a larger degree of creep relaxation is experienced. For initial ΔK higher than the threshold stress intensity for creep crack growth, crack growth rates increased with increase in hold times. At intermediate loads, crack growth rates initially decrease then increase. This is attributed to creep relaxation initially slowing down the crack growth but the crack growth rates were large enough to overcome this, causing an eventual rise in crack growth rates. Their results also imply an increased threshold for fatigue crack growth with imposition of dwell, possibly due to stress relaxation during hold which could effectively decrease the stress intensity at the crack tip.

At low ΔK, increases in surface roughness-induced crack closure and crack branching (due to increased intergranular cracking at longer cycle periods) could also decrease crack growth driving force, leading to lower crack growth rates [112]. This effect may again be small in comparison to the detrimental environmental attack giving accelerated crack growth. It was noted by Lynch et al that at 700°C, crack growth rates are lower and ΔK_{th} values are higher for cycling with 60s hold time than for continuous cycling in Waspaloy [112] and IN718 [132]. For long hold times at low ΔK, they have attributed the observations to reduced crack growth driving force not only by fracture surface roughness-induced crack closure and intergranular crack branching/deflection but also by an additional contribution from oxide-induced crack closure.

2.13. Role of microstructure

The characteristics of the microstructure are of utmost significance in the quest to achieve superior performance of a material. With understanding of the effects of microstructure on the various properties required for high performance, a material can be tailored, by alteration to the microstructure through appropriate processing routes, to have a good balance between high strength and good creep and fatigue resistance. The effects of microstructure on fatigue crack growth resistance are dependent on the crack growth regime. As will be shown later, the microstructure can have a different effect on each of the different regimes of crack growth, i.e. crack initiation and short crack growth, near-threshold crack growth, and long crack growth. In the long crack growth regime, there are also slight differences in the effects of microstructure on crack growth in the different crack growth regimes, i.e. the cycle-dependent regime, time-dependent regime or a combination of the two.

2.13.1. Strength

Higher alloy strength can be achieved by altering grain size and by attaining a more effective γ' dispersion [21,78]. Finer grain size was noted to give higher strength [21,27,51] as expected from the Hall-Petch relation. For a given grain size, higher γ' volume fraction [3,21,27] and finer γ' precipitates [21,26] also raises the alloy strength. As mentioned in section 2.2.4, finer γ' precipitates are a consequent of fast cooling rates during cooling from solution temperature, hence higher cooling rates are also linked to higher strength for a given grain size [23,24,25,27].

Higher strength alloys generally possess longer fatigue lives at low strain ranges of interest in disc applications, due to the increased resistance to crack initiation [69,145]. In the cycle-dependent crack growth regime where the crack propagates in a transgranular manner, an increase in strength has generally been associated with improved crack growth resistance [21,146]. During service, the crack usually propagates in the time-dependent crack growth regime where environment and creep effects are significant, and an increase in alloy strength is usually accompanied by poorer fatigue crack propagation resistance [10,69,129,145]. Initially it was unclear whether the poorer crack growth resistance is due to the higher strength, or the fine grain size of the material. However a number of studies carried out has established that the poorer crack growth resistance is due to the fine grain, and not the high strength of the material [21,146]. Fine grain microstructures are more susceptible to environmental damage due to the greater amount of grain boundaries. The accelerated crack growth in air of fine grain microstructures compared to coarse grain microstructures was suppressed in vacuum, where both microstructures show approximately similar crack growth resistance [9].

Ductility improvement by means of softening heat treatments has been associated with increased crack growth resistance [10], or a reduced sensitivity to environmental degradation [99]. One reason for

this is that higher ductility which is usually associated with lower yield strength results in more crack tip blunting owing to plastic deformation ahead of the crack tip [35], giving lower crack growth driving force.

2.13.2. Deformation behaviour

Precipitate shearing is promoted by fine γ' precipitates, while precipitate looping is favoured by large γ' precipitates [21,22,45]. Although a lower volume fraction of γ' precipitates has been cited to promote precipitate shearing by Antolovich and Jayaraman [18,28], the opposite is believed to be true. For a given γ' precipitate size, a higher volume fraction of γ' precipitates means that the precipitates are closer together, i.e. there is increased difficulty for bowing of dislocations between the precipitates and the dislocation may shear the γ' precipitates instead [5]. Precipitate shearing was also cited to be favoured by low APB and low γ' misfit, while Orowan looping was cited to be favoured by high APB and γ' misfit [18].

In terms of the homogeneity of slip, more homogeneous slip deformation is generally observed for microstructures with finer grain due to slip dispersal [45,65,78]. The slip bands were noted to be longer [147] and typically spaced further apart [148] for microstructures with larger grains.

Contradictory effects of precipitate size on slip behaviour are widely reported in the literature, where larger precipitates have been associated with both a higher degree of heterogeneous slip as well as a higher degree of homogeneous slip. The contradicting results appear to stem from the difference in the precipitate-dislocation interactions. In studies where larger precipitates were associated with more heterogeneous slip behaviour, the precipitate sizes were noted to be relatively fine such that precipitate cutting is prevalent for all precipitate sizes. In studies where larger precipitates were associated with more homogeneous slip behaviour, the fine precipitates were noted to be cut by dislocations, leading to highly planar slip, while larger precipitates were looped by dislocations, giving a more homogenous slip behaviour [43].

For relatively fine precipitate sizes where the precipitates are cut by dislocations, materials with larger shearable precipitates have been indicated to show more heterogeneous deformation [44]. In a study on Alloy 718 where all the precipitates were noted to be sheared by dislocations, slip bands were noted to be thinner in width and more widely spaced for larger γ" precipitates [147]. In studies involving Al-Li alloys containing shearable δ' precipitates, a higher degree of heterogeneous slip was also noted for materials containing larger shearable precipitates [43,66,149]. Conflicting results were reported where increasing γ' precipitate sizes were associated with more homogenous slip when the precipitates are still being cut by dislocations [39]. The slip band spacing was noted to decrease with increasing γ' precipitate size in Nimonic PE16 with γ' precipitate sizes ranging from 12.5nm to 30nm where the γ' precipitates were noted to be sheared by dislocations [39].

Although shearing of precipitates has been indicated to be promoted by finer γ' precipitates and intuitively finer γ' sizes are also expected to lead to higher degree of heterogeneous slip, the discussion above indicates that slip heterogeneity is promoted by *larger shearable* γ' precipitates. This has been considered to be due to shearing of larger shearable γ' precipitates giving a higher degree of slip band softening and hence a higher number of dislocations in the slip band. Softening occurs due to precipitate shearing by dislocations and the strength of the slip band is regained from hardening due to the pile-up of dislocations at grain boundaries/unshearable precipitates. In materials with larger shearable γ' precipitates this leads to greater concentration of slip in the particular slip band and a more heterogeneous slip behaviour in the material [44].

In studies where larger γ' precipitates were associated with more homogenous slip [21,22,32,45,78,150], materials with fine γ' precipitates were indeed noted to show precipitate shearing by dislocations giving highly planar slip, while the materials with larger γ' precipitates were noted to show precipitate looping leading to wavy slip and a homogenous slip behaviour. Many authors have also noted shearing of precipitates by dislocations leading to formation of planar slip bands in large grain/fine γ' precipitate microstructures, and precipitate looping leading to wavy slip for fine grain/large γ' precipitate microstructures [14,22,34,45]. When the coherent γ' precipitates are bowed by dislocations, increasing precipitate size and therefore spacing would also lead to reduction in the stresses required to bow the precipitates compared to precipitate shearing, giving a more homogeneous slip behaviour.

Higher volume fraction of shearable precipitates is also believed to increase the heterogeneity of slip [44] as higher volume fraction of γ' precipitates promotes precipitate shearing, hence a more heterogeneous deformation may be expected [5].

2.13.3. Initiation and short crack growth

Slip band crack initiation, which is the predominant crack initiation mechanism in nickel-base superalloys, is promoted by the planar slip behaviour of the material, hence microstructures giving a more homogeneous slip will result in improved resistance to crack initiation. Enhanced crack initiation resistance was noted for microstructures with finer grain size [38,65,86] and/or larger coherent γ' [78,133]. In the short crack growth regime, grain boundaries have been shown to be important as crack growth barriers which markedly reduced short crack growth rates. Finer grain size [54,65,72,86] or necklace microstructures [86] which have a higher amount of grain boundaries have been noted to give improved short crack growth resistance. The retained work in the unrecrystallised grains in the necklace microstructure may have an additional effect of reducing crack growth rates by restricting the development of localised planar slip [86]. In addition, at small crack lengths the crack propagates through a stage I crack growth mode, which is promoted by a more planar slip. Finer grain and/or coarse γ' microstructures have shown less tendency towards

strong stage I crack growth [78], instead exhibiting a mixed stage I/stage II crack growth. This may also improve the short crack growth resistance.

2.13.4. Near-threshold crack growth

At a given R-ratio, coarse grain microstructures generally show higher ΔK_{th} and lower growth rates in the near-threshold crack growth regime compared to fine grain microstructures [5,65,86,96,110]. This is due to surface roughness-induced crack closure being more extensive in coarse grain microstructures, giving reduced crack growth driving force and lower crack growth rates [65,101]. Larger grains can also result in higher ΔK_{th} due to intrinsic toughening effects, i.e. through less fatigue damage accumulation due to more reversible slip [65]. However the contribution to improved ΔK_{th} from this effect is expected to be small [65].

Finer γ' precipitate size and higher volume fraction of shearable precipitates have also been associated with lower crack growth rates and higher ΔK_{th} in the near-threshold crack growth regime [5]. This was attributed to easily shearable precipitates giving a rougher fracture surface, leading to higher roughness-induced crack closure, more tortuous and longer actual crack path as well as possible reduction in local ΔK due to deviation from the maximum tensile stress.

2.13.5. Cycle-dependent long crack growth

In the cycle-dependent long crack growth regime where environment and creep effects are insignificant, a coarse grain [22, 45,133,151] and/or fine coherent γ' [5,22,45] microstructure has generally been associated with improved crack growth resistance. However, some studies have also noted no apparent improvement in crack growth rates with larger grain sizes [113].

At a given temperature, microstructures with coarse grains and fine coherent γ' precipitates have generally been associated with increased tendency to cyclic softening compared to microstructures with fine grains and coarse coherent γ' precipitates [22]. The stress ranges associated with the cyclic softening for the coarse grain/fine γ' microstructure would give rise to lower crack growth driving force for a given applied strain range [22]. The fine grain/coarse γ' microstructure does not cyclically soften [22] or shows a lesser degree of cyclic softening, hence the driving force for crack growth should consequently be higher than for the coarse grain/fine γ' microstructure.

The more extensive crystallographic crack growth in the coarse grain/fine γ' microstructure also gives rise to a longer effective crack path, i.e. numerous deviations from the nominal crack plane. This in addition may cause a reduction in the crack growth driving force as a result of roughness-induced crack closure and/or due to crack tip shielding giving rise to reduction in the local ΔK. In addition, the crystallographic surface can also introduce a mechanical locking effect near the crack tip which would reduce the effective crack growth driving force. The fracture

surface of the fine grain/coarse γ' microstructure is expected to be less tortuous than for coarse grain/fine γ' microstructure, contributing to more rapid crack growth [22].

Due to increased planarity of slip, larger grains and finer coherent γ' sizes also promote greater reversibility of slip [65,151]. This leads to greater slip reversal during the unloading cycle and reduces fatigue damage accumulation, giving rise to lower crack growth rates. Large grains offer less constraint to slip and longer slip paths and are therefore able to accommodate more slip damage than finer grains before additional slip planes become operative. Thus, coarser grains are expected to show a lower slip band density, but with slip being more persistent within the active slip bands. In contrast, a fine grain size promotes more homogeneous slip because of the small slip length.

The effect of coherent γ' sizes on cycle-dependent crack growth rates is not apparent. The effect of coherent γ' size on cycle-dependent crack growth also appear to be strongly dependent on temperature. At room temperature, finer coherent γ' sizes have been associated with lower crack growth rates [45,121]. At elevated temperatures (600°C-650°C), coarser coherent γ' sizes were noted to either have no effect on crack growth resistance [113,133], or gave improved crack growth resistance [121], or gave decreased crack growth resistance [21].

In a study by Morley and Martin [121], crack growth rates were lower in alloy AP1 with fine coherent γ' precipitates at room temperature. In the study, the improved crack growth resistance was attributed to increased reversibility of slip with the heterogeneous deformation behaviour of fine coherent γ' precipitates.

Where crack growth rates are lower with coarser coherent γ' at elevated temperatures, the improved crack growth resistance was attributed to a change in the crack growth behaviour. At 600°C, Morley and Martin [121] have noted that the crack is mainly confined to the γ matrix, and the coherent γ' precipitates were rarely cut by the crack. The yield stress of the γ' phase is known to increase with temperature to reach a peak at 700°C (due to increased dislocation tangling processes), while the flow stress of the γ matrix will fall with increasing temperature (due to increased dislocation mobility). This leads to fatigue crack growth at elevated temperatures taking place mainly in the γ matrix. A crack in the γ matrix will follow a more convoluted path in the coarse γ' precipitate microstructure compared to the fine γ' precipitate microstructure, i.e. a longer actual crack path. The speed of crack tip advance in both microstructures may be similar, but a more convoluted path of the coarse γ' precipitate microstructure will give lower crack growth rates.

Conflicting results were found by Gayda and Miner in their study [21], which reported improved crack growth resistance with decreasing coherent γ' sizes when crack propagation was transgranular. In their study three grain sizes were used, i.e. 5μm, 20μm and 50μm, and the

coherent γ' sizes were systematically varied by ageing at different temperature and time to give three different coherent γ' size distributions of 0.03μm, 0.25μm and 0.60μm in each of the grain sizes. In the microstructure with larger grain sizes where the crack propagated in a transgranular manner, crack growth rates tend to decrease with decreasing γ' size. A marked decrease in crack growth rates was also noted as the solution temperature, and hence the volume fraction of fine ageing γ' is increased.

In the study by Morley and Martin [121], the crack growth appeared to be through decohesion of the γ-γ' interface as suggested by the crack being mainly confined to the γ matrix. This is contrary to the general observations and that in the study of Gayda and Miner [21] where crack growth were noted to be transgranular in the cycle-dependent regime. The difference in the crack growth mechanism may explain the difference in the effects of coherent γ' size on crack growth resistance. In the case of Gayda and Miner, the effect of varying coherent γ' sizes appears to be similar to the general trends observed at room temperature. The increased reversibility of slip argument giving rise to reduced crack growth rates also appears to be applicable to the results of Gayda and Miner. Hence when transgranular crack propagation is predominant at elevated temperatures, a decrease in the coherent γ' size is expected to lead to improved crack growth resistance, similar to observations at room temperature.

In studies where variation in the coherent γ' precipitate size did not show any effect on the crack growth resistance [78,113,133], it is possible that the γ' size was not varied significantly, hence the effects of varying the coherent γ' size are not revealed. It has been cited that there may be a critical γ' size below which improvement in fatigue resistance will be noted. This size is related to the onset of planar slip, which occurs only for very small γ' sizes in alloys with large γ-γ' misfit [78]. The coherent γ' size in the alloy is clearly important as it influences the deformation behaviour of the material, and hence would also influence the crack growth behaviour.

2.13.6. Time-dependent long crack growth

In this regime, microstructures with larger grains and necklace microstructures have been found to give better crack growth resistance compared to fine grain microstructures [21,69,101,113,123,135,128,146]. This is generally associated with the improved oxidation-assisted crack growth resistance of large grain microstructures as there are less grain boundaries for diffusion of oxygen. This reduces the embrittlement of grain boundaries due to oxidation. The improvement exhibited by the coarse grain microstructures may also be due to the improved creep properties of coarse grain microstructures compared to fine grain microstructures. A decrease in grain size generally promote a transition of crack propagation mode from transgranular to intergranular, which is associated more with environmental interactions as the intergranular crack growth did not occur in vacuum conditions in most of the studies [21,69,146].

In the time-dependent crack growth regime, creep and environmental effects are significant, hence microstructural properties giving improved resistance to creep and/or environmental effects, e.g. larger grains and serrated grain boundaries would be expected to give improved crack growth resistance [113,133]. In addition, the factors giving rise to improved crack growth resistance, e.g. crack tip shielding for coarser grain sizes in the cycle-dependent regime may also be operating in this regime [113], but their effect may be small in comparison to the rapid environmental and creep interactions.

It has also been suggested by Gayda et al [9,146] that smaller grain sizes lead to a larger amount of grain boundary area, hence giving an effective dilution of the alloy strengthening elements, e.g. B and Zr at grain boundaries. Both elements are thought to enhance grain boundary properties. Therefore, in addition to poorer oxidation resistance due to larger grain boundary area (more oxygen diffusion paths), fine grain microstructures are also weakened by low concentrations of alloy strengthening elements at grain boundaries.

Serrated/wavy grain boundaries which improve creep crack growth resistance [133] were also noted to improve creep-fatigue crack growth resistance [123,135]. Serrated grain boundaries were found to have no effect on crack growth resistance when crack propagation is transgranular, i.e. under cycle-dependent conditions [45,133]. The improvement in crack growth resistance due to serrated grain boundaries in the time-dependent regime is usually accompanied by modification of crack propagation modes which are predominantly intergranular for materials with smooth grain boundaries to mixed intergranular-transgranular for materials with serrated grain boundaries [123,135].

In terms of the effect of coherent γ' size, coarser coherent γ' precipitates were noted to either have a minimal effect on crack growth resistance [21], or that they gave slight improvement in crack growth resistance [32,113]. Coarser coherent γ' size is expected to give better time-dependent crack growth resistance as it gives rise to a more homogeneous deformation, which could contribute to improved grain boundary oxidation resistance and a reduced propensity for intergranular crack propagation due to lower localised stress concentrations.

2.13.7. Summary of the role of microstructure

In summary, fatigue crack initiation and short crack growth resistance is enhanced by finer grain size and coarser coherent γ' precipitates giving rise to less planar slip, while long crack growth resistance is greater with larger grain size. An improvement in fatigue crack initiation and short crack growth resistance therefore only appears to be achievable at the expense of long crack growth resistance, and vice versa [22,54,151].

Where the crack is most likely to initiate, i.e. in the bore region of the turbine disc where stresses are highest (although at lower temperatures of about 300°C), a fine grain microstructure is

required. In the rim region where the highest temperatures (in the region of 650°C) are experienced, there is a requirement for maximum resistance both to fatigue crack propagation and to creep, and a larger grain size is desired [146].

In any case, the microstructure must be optimised for the total spectrum of properties desired in service, giving a good balance between crack initiation and short crack growth resistance in addition to long crack growth resistance [151]. This can be achieved by a necklace microstructure, which reportedly gives a good compromise between short crack and long crack growth resistance in many studies [65,86]. The coarse grains give rise to improved resistance to environmental and creep interactions in addition to increased extrinsic toughening from crack closure effects, while grain boundaries in fine grain regions act as efficient crack growth barriers [65].

2.14. Summary of literature review

RR1000 is a nickel-base superalloy for turbine disc applications which is very similar to Waspaloy, Udimet 720 and Udimet 720Li. It has the typical strengthening mechanisms as other nickel-base superalloys, i.e. a γ matrix strengthened by coherent and incoherent γ' precipitates.

The general relationship of creep-fatigue-environment interactions and the microstructure of the superalloys have been investigated by many workers over the years. Various models and mechanisms have been proposed to account for their observations and experimental results. However much work is still needed to develop a more complete understanding of the underlying principles governing high temperature creep-fatigue-environmental interactions.

Generally, larger grains have been associated with improved long crack growth resistance, but are less resistant to short crack growth. The coherent and incoherent γ' distribution also affects crack growth resistance during long and short crack growth. The complex interaction between creep-fatigue-environment makes the actual effects of varying microstructural parameters difficult to establish, and the reasons for the observed crack growth behaviour remain somewhat unclear.

It is therefore the aim of this project to gain further understanding of the complex interactions affecting crack growth in the creep-fatigue-environment domain. This project further investigates the creep-fatigue behaviour of RR1000, a nickel-base superalloy recently developed for turbine disc applications, as well as establishing the effects of microstructure on short crack growth resistance of U720Li and RR1000. The results of this project will be pooled with that already obtained by previous researchers, and it is hoped that further understanding of the effects of microstructure on fatigue crack initiation and growth resistance will be obtained.

3. Experimental Methods

3.1. Materials

The materials used in this project were powder metallurgy turbine disc materials RR1000, Udimet 720Li (U720Li) and microstructural variants of U720Li, i.e. U720Li-LG (large grain variant) and U720Li-LP (large intragranular coherent γ' precipitate variant). Microstructural variants of U720Li were produced by increasing the solution temperature (to increase grain size) and by slowing the cooling rate from the solution temperature (to increase the coherent γ' precipitate size). The heat treatment routes to produce RR1000, U720Li, U720Li-LG and U720Li-LP are as follows:

RR1000: 4h 1120°C→ fan air cool →24h 650°C→air cool→16h 760°C→air cool

U720Li: 4h 1105°C→oil quench→24h 650°C→air cool→16h 760°C→air cool

U720Li-LG: 4h 1135°C→ air cool →24h 650°C→air cool→16h 760°C→air cool

U720Li-LP: 4h 1105°C→ insulated air cool →24h 650°C→air cool→16h 760°C→air cool

The approximate compositions of RR1000 [3] as well as the composition of U720Li as defined by chemical analysis conducted by Rolls-Royce plc, Derby are given in Table 3-1.

Element	RR1000	U720Li
Cr	14.35-15.15	15.92
Co	14.0-19.0	14.57
Ti	3.45-4.15	5.18
Mo	4.25-5.25	2.98
Al	2.85-3.15	2.44
W	-	1.35
Fe	0.0-1.0	0.08
Zr	0.05-0.07	0.042
B	0.01-0.025	0.016
C	0.012-0.033	0.023
Ta	1.35-2.15	-
Hf	0.5-1.0	-

Table 3-1: Chemical compositions of RR1000 and U720Li.

All materials were supplied by DERA as SENB specimens with a 60° starter notch based upon BS6835. Specimens were taken from the disc with their long axes tangential to the disc circumference. U720Li, U720Li-LG and U720Li-LP SENB specimens have 12.5mm x 12.5mm square section. RR1000 SENB specimens have a 12.0mm x 12.0mm square section labelled RR1000 MO1547 POS 1-POS 10 (10 specimens) or a 12.5mm x 12.5mm square section labelled RR1000 MO1751 POS 201-POS 210 (10 specimens). Typical specimen geometries are shown in Figure 3-1. Additional U720Li specimens were supplied by DERA as 6mm x 15mm cross-section and 12.5mm x 12.5mm cross-section plain bend bar specimens.

3.2. Microstructural characterisation

Microstructural characterisation work was carried out on RR1000 and U720Li and its variants to reveal grain size and primary γ' size. Further microstructural characterisation work was also carried out on RR1000 to measure the coherent γ' precipitate sizes.

3.2.1. Grain size and primary γ' size characterisation

Sectioned specimens were mounted on bakelite using a mounting press. Mounted specimens were ground first on 600 grit paper until planar, followed by grinding on 1200 grit for about 3 minutes. Polishing was then carried out with 6 μm diamond paste on Struers DP-PAN polishing cloth lubricated with Metadi followed by a 1 μm diamond polishing on Struers DP-NAP polishing cloth.

Etching was initially carried out on RR1000 using Fry's reagent which is a γ' etch. The etch consists of 500ml of concentrated HCl and 100g of CuCl mixed in 500ml of H_2O. Typical etching times for RR1000 were about 4 to 7 seconds. However, although this etch reveals the primary γ' precipitates relatively well, it was found that Fry's reagent gave poor grain boundary resolution of the RR1000 material.

Further etching of RR1000 was carried out through electrolytic etching using 10% orthophosphoric acid in H_2O. This etch also preferentially removes the γ' on the surface. Stainless steel wires were used as electrodes and a voltage of about 2 volts was employed. The specimen was made anodic by attaching the electrode to one corner of the specimen and the cathode was moved at a close distance (about 1mm) from the specimen surface covering the entire surface. Typical etching times for RR1000 were about 3-4 seconds. This etch gave a much better resolution of grain boundaries in RR1000 compared to Fry's reagent. To maintain consistency, U720Li, U720Li-LG and U720Li-LP specimens were also etched using 10% orthophosphoric acid in H_2O for grain size and primary γ' size quantification. Typical etching times for U720Li and its variants were about 3-4 seconds which is similar to the etching times of RR1000.

Grain size and primary γ' size and volume fraction information was obtained from the microstructure which has been etched with orthophosphoric acid. The microstructure of the etched specimens was captured using a digital camera mounted on an Olympus stereomicroscope with XCAP imaging software. The image of the etched microstructure in the as-captured form had poor contrast which is unsuitable for automatic image analysis. To overcome the poor contrast, a binary image of the grain structure and the primary γ' was produced manually by carefully tracing over several enlarged micrographs. The binary images were then scanned and saved into the computer for further analysis.

To measure grain and precipitate size and distribution, an automatic image analysis software Carl Zeiss KS300 (by Carl Zeiss Vision) was used. Parameters such as perimeter, area and feret diameters (X-direction, Y-direction, minimum, maximum) of the grain and primary γ' binary images were measured. Incomplete objects at the edge of the binary were removed using the image analysis software. The number of objects analysed for the grain size was no less than 250 in each case and no less than 500 objects were analysed for the primary γ'.

The circularity, which gives an insight into the degree of homogeneity of the grains and primary γ', and the volume fraction of primary γ' were calculated from the data obtained by automatic image analysis. A statistical analysis of the data was also carried out. Circularity is defined by the following equation:

$$Circularity = \frac{4\pi(Area)}{(Perimeter)^2} \qquad \text{Equation 3-1}$$

The equation assigns a circularity value of 1 for a circle, and this value will decrease as the object varies to a less circular shape, e.g. an ellipse.

3.2.2. Coherent γ' size quantification

To characterise the coherent secondary and tertiary γ' sizes in RR1000, a carbon extraction replica method was used. The method involves an initial γ' etch (10% orthophosphoric etch) to remove the coherent γ' precipitates on the specimen surface, followed by carbon coating and a second etch to remove the carbon coat (electrolytic etching in 20% perchloric acid in ethyl alcohol) from the specimen surface. The outlines of the coherent γ' precipitates will be copied onto the carbon layer during carbon coating, hence observations of these carbon replicas will yield information on the coherent γ' precipitate sizes. The carbon replicas were observed in a TEM at low magnification (50000x) and high magnification (200000x). Images obtained from the TEM observations were then binarised in a similar manner as for the grain size and primary γ' precipitate size

characterisation. Subsequent automatic image analysis was carried out on the binarised images to obtain coherent γ' size information.

3.2.3. Hardness testing

Hardness testing was carried out to get an estimate of the yield stress of RR1000. The tests were done on specimens mounted on bakelite and polished to a 1 μm finish. An average of eight measurements was taken, using a load of 30kg.

3.3. Short crack testing

3.3.1. Test matrix

Short crack tests at room and elevated temperature in air were proposed to investigate the short crack behaviour of RR1000, U720Li, U720Li-LG and U720Li-LP. The elevated temperature chosen was 650°C as this is a realistic service temperature.

The test matrix for short crack testing is as follows:

Material	Environment	Temperature (°C)	Frequency (Hz)	R-ratio
RR1000 U720Li U720Li-LG U720Li-LP	Air	20 650	20 0.25 (1-1-1-1)	0.1

Table 3-2: Summary of short crack test matrix.

3.3.2. Specimen geometry

For room temperature short crack testing, the U720Li-LG, U720Li-LP and RR1000 specimens were initially SENB specimens of the same geometry as shown in Figure 3-1 but were subsequently machined to obtain plain bend bars. The U720Li specimens used for room temperature short crack testing were the 6mm x 15mm cross-section plain bend bars.

The dimensions of the room temperature short crack specimens after machining and subsequent specimen preparation are given in the following table.

Material	Specimen no.	Test no.	Breadth, b (mm)	Width, w (mm)
U720Li	#1	11S	15.16	6.71
U720Li	#2	10S	15.17	6.71
U720Li-LG	XA08316	7S	12.48	9.29
U720Li-LG	XA08320	4S	12.50	9.28
U720Li-LP	PPT9	9S	12.50	9.22
U720Li-LP	PPT10	6S	12.31	9.27
RR1000	MO1751 POS 201	3S	12.59	8.52
RR1000	MO1547 POS 7	8S	11.99	8.67

Table 3-3: Room temperature short crack test specimen dimensions.

The high temperature short crack tests were carried out on notched specimens to assess crack initiation and early crack growth behaviour at 650°C. The notch geometry was used to ensure sufficiently high stresses were achieved in a bend loading geometry. This allowed sufficient local stresses/strains to be developed in the notch root to give reasonable lifetimes for the tests. Figure 3-3 shows the design of the notch geometry, which has an elastic stress concentration factor of approximately 2.

Due to limitations in servohydraulic machine availability and the amount of time required to obtain replicas in the tests, stress levels were chosen to give lifetimes of approximately 10000 cycles for each test. In the absence of any detailed materials model to predict the strain ranges produced in the materials on loading, the far-field stresses were chosen to give nominal stresses of 750-850 MPa across the uncracked ligament. Similar high temperature short crack tests carried out using a similar notch geometry on IN718 have shown these stresses to give lifetimes of approximately 10000 cycles at 650°C [152]. These stresses correspond to total strain ranges of the order of 0.3-0.4 in IN718. In the IN718 study, strain-life curves and suitable materials models were available to estimate the stresses required to give the desired lifetimes. The strain range required to produce the desired lifetime was noted from the strain-life curve, and the materials model was used to calculate the required stresses to achieve notch root strain levels to give these desired lifetimes.

The U720Li-LG, U720Li-LP and RR1000 specimens were initially standard SENB specimens with a standard 60° notch, and a U-notch was subsequently machined into the specimens using EDM. The U720Li material was a new batch of material supplied as 12.5mm x 12.5mm cross-section plain bend bars by DERA, and a U-notch was subsequently machined into the

specimens using EDM. For RR1000, U-notch specimens were obtained by machining RR1000 MO1751 SENB specimens.

3.3.3. Experimental methods

3.3.3.1. Room temperature short crack testing

Tests were carried out on an Instron 8802 servohydraulic testing machine (±10kN capacity) and an Instron 8502 servohydraulic testing machine (±100kN capacity). All room temperature tests were conducted on plain bend bar specimens in 3-point bend under load control. When using the Instron 8802 servohydraulic machine, the loading span was varied to give the desired stress levels due to the maximum load limitation, whereas for testing on the Instron 8502 the span was kept constant at 30mm and the desired stress levels were achieved by varying the loads. An illustration of the short crack test set-up is shown in Figure 3-2.

Stress levels of 95% σ_y were used in all the tests, except for Test 3S where a stress level of 83% σ_y was used. The yield stresses of the materials were estimated using the yield stress of U720 supplied by Loo-Morrey [142] and the relative hardness values of U720 and other materials [30]. All tests were conducted using a load ratio of 0.1 and a 20Hz sinusoidal cycling waveform.

The top surfaces of the test specimens were ground and polished to 1 μm finish. The edge of the specimens was also rounded and eventually polished to 1 μm at the same time to prevent cracks initiating and propagating from the edge. Tests were done on both as-polished specimens and specimens etched with Fry's reagent. Tests on etched specimens reveal the crack path relative to grain boundaries and primary γ', whereas the as-polished specimens enable easier detection of initiation events and also serve as a check to see if etching has any effect on crack initiation and fatigue lifetimes.

Crack initiation and growth were monitored using the acetate replica technique. Acetate was softened using acetone as solvent before being put onto the specimen surface to get a replica. The replica was held until it was firmly stuck on the specimen surface and typically left for about 3-5 minutes to dry before being taken off. Care was taken to ensure no bubbles were trapped when taking replicas as this might cause loss of important surface and crack details. A replica of the surface was taken every 10000 cycles until a crack was first observed, and subsequent replicas were taken at 5000 cycle intervals.

3.3.3.2. High temperature short crack testing

High temperature short crack testing was carried out on an Instron 8501 (capacity ±50kN) servohydraulic testing machine equipped with an ESH high temperature vacuum chamber. High temperature heating was provided by four high-power quartz lamps controlled using an Eurotherm

815 thermal controller. The temperature was monitored with a Type "R" (Platinum/Platinum-Rhodium) thermocouple spot-welded to the specimen close to the notch. In all the tests the maximum temperature variation was within ±2°C. The specimen was placed in the middle of the hot-zone to ensure uniform temperature distribution throughout the specimen.

The notch root of the specimens used for high temperature short crack testing were polished using dental felt on a pillar drill. The specimens were initially subjected to a 15 μm diamond grinding to remove machining marks followed by a 6 μm polish and a 1 μm fine polish. Appropriate diamond paste and lubricant were used in each polishing stage. The change in notch geometry due to the polishing process was minimal, approximately 0.1mm to 0.2mm at most. A check on the stress concentration charts indicated that these minimal changes in the geometry caused little change in the stress concentration factors of the notches (approximately ±0.1 maximum). All specimens were subsequently etched using Fry's reagent prior to testing to reveal the microstructure.

All tests were conducted at 650°C using a 1-1-1-1 waveform in air. Tests were conducted in 3-point bend under load control using an R-ratio of 0.1. A span of 25mm and ceramic rollers were used in all the tests. Nominal stresses of 750-850 MPa were applied across the uncracked ligament during runout tests to establish lifetimes. Replication tests were carried out at 840MPa in light of runout test results.

During replication tests, a replica of the notch root was taken every 500 or 1000 cycles. The specimens were cycled for the required number of cycles at test temperature, then the test was stopped and the specimen was allowed to cool slowly to room temperature, which took approximately two to three hours. During the cooling down period the specimen was held on the machine with a small load, typically between 0.8kN and 1.0kN. During the replication process, the specimen was held at mean load used during the test and replicas of the notch root were taken using replicas which had been rounded to fit the notch better. After the required replicas were obtained, the specimen was again held on the machine with a small load and reheated to test temperature at a rate of 20°C/min (approximately 30 minutes to reach test temperature of 650°C). The whole setup was then allowed to sit for 10 minutes for temperature controls, etc to stabilise. The test was then resumed for another 500/1000 cycles and the replication process repeated.

3.3.3.3. Short crack analysis

During post-test analysis, acetate replicas were examined using an Olympus stereomicroscope. The images obtained on the stereomicroscope can be captured and stored in the computer using a digital camera mounted on the microscope. Characterisation of the crack field on the top surface of the short crack test specimens and crack length measurements were carried out through the replica analysis.

A characterisation of the crack field was carried out by examining the replicas at fixed intervals and counting the number of cracks on the top surface of the short crack test specimens. The examination interval was arbitrarily chosen to be approximately every 20% of the total life depending on the replication intervals during the tests, i.e. 5 readings of the number of cracks on the top surface of the short crack test specimens were recorded for every test.

Crack length measurement was carried out to characterise short crack growth rates. The measurements were taken only from larger cracks which were greater than 50 μm in length when the specimens failed as smaller cracks usually showed slow or arrested crack growth. Images of the cracks were captured during analysis of the replicas and crack length measurements were then made from the images. Cracks were traced from their longest length back to the initiation site. The longest crack was printed out and the crack lengths of shorter cracks (from replicas earlier in the tests) were marked on the printout. The half surface crack lengths in both directions from the crack initiation point, c_1 and c_2, and the total crack length c_{tot} (as illustrated in Figure 3-4) were measured. This measured crack length was then converted to the actual crack length according to the measurement of the graticule at the appropriate magnification. Crack growth rates of the surface crack in both directions (dc_1/dN and dc_2/dN) as well as the average growth rate ($d(c_{tot}/2)/dN$) were calculated from the crack length measurements.

Short crack growth rates were plotted against crack length as well as against ΔK. Stress intensity factor K values were calculated from the half surface crack length using the empirical formula of Scott and Thorpe [89]. Both the surface and depth stress intensity factors were calculated. The formulation for the surface stress intensity is given in the following equation:

$$K_I = \left[\left[M_{f(0)}\left(1-0.3\frac{a}{t}\right)\left(1-\left(\frac{a}{t}\right)^{12}\right)\right]+\left[0.394\cdot E(k)\cdot\left(\frac{a}{t}\right)^{12}\cdot\sqrt{\frac{a}{c}}\right]\right]\frac{\sigma_b}{E(k)}\sqrt{\pi a}$$

Equation 3-2

where

$$M_{f(0)} = \left[1.21-0.1\left(\frac{a}{c}\right)+0.1\left(\frac{a}{c}\right)^4\right]\sqrt{\frac{a}{c}}$$

Equation 3-3

$$E(k) = \left[1+1.47\left(\frac{a}{c}\right)^{1.64}\right]^{0.5}$$

Equation 3-4

The depth stress intensity factor is calculated using the following equation:

$$K_I = M_{f(\pi/2)}\left[1-1.36\left(\frac{a}{t}\right)\left(\frac{a}{c}\right)^{0.1}\right]\frac{\sigma_b}{E(k)}\sqrt{\pi a} \qquad \text{Equation 3-5}$$

where E(k) is given by the same equation as used for the surface stress intensity factor and

$$M_{f(\pi/2)} = 1.13 - 0.07\left(\frac{a}{c}\right)^{0.5} \qquad \text{Equation 3-6}$$

All K calculations were done by assuming a crack depth to half surface crack length ratio (a/c) of 1. The validity of this assumption is discussed later in the results section.

3.3.4. Short crack fractography

The fracture surface was examined using a Wild M420 macroscope, a Jeol JSM-T300 SEM operating at an accelerating voltage of 20kV and a Jeol JSM-6500 FEGSEM operating at an accelerating voltage of 10kV. The overall fracture surface was captured with the Wild macroscope, while details of crack initiation and growth mechanisms on the fracture surface were carefully observed in the SEM. The room temperature short crack fracture test surfaces were examined in the Jeol JSM-T300 SEM while the elevated temperature short crack test fracture surfaces were examined in the Jeol JSM-6500 FEGSEM.

3.4. Long crack testing

3.4.1. Test matrix

To investigate the effects of temperature and dwell time on the creep-fatigue crack growth behaviour of RR1000, high temperature long crack tests in vacuum on RR1000 were carried out at 650°C and 725°C using a 1-1-1-1 and 1-20-1-1 loading cycle. High temperature vacuum long crack tests on U720Li, U720Li-LG and U720Li-LP have been carried out previously at similar temperatures using similar loading cycles [30]. The temperatures chosen, i.e. 650°C and 725°C, are respectively the operating temperature of current turbine disc alloys and a proposed extreme service condition temperature. The 1-x-1-1 loading cycle was used to investigate dwell time effects. The 1-x-1-1 loading cycle consists of a ramp up time of 1 second, then a dwell at maximum load for x seconds, followed by a ramp down time of 1 second and a dwell at minimum load of 1 second, where x is 1 second or 20 seconds. A dwell time of 20 seconds has been shown to be sufficient to demonstrate the effects of dwell [30]. Results of elevated temperature long crack tests in air from QinetiQ/DERA are also available for the test materials, allowing a full examination of the effects of alloy type, microstructural variables, temperature, environment and dwell on fatigue crack initiation and growth behaviour to be ascertained.

Long crack tests at room temperature were also carried out on all the test materials. These tests were done at an R-ratio of 0.1 and using a 20Hz sinusoidal cycling similar to room temperature short crack testing conditions.

Material	Environment	Temperature (°C)	Dwell (s)	R-ratio
RR1000 U720Li [30] U720Li-LG [30] U720Li-LP [30]	Vacuum	650 & 725	1 & 20	0.1
RR1000 U720Li U720Li-LG U720Li-LP	Air (QinetiQ/DERA)	650 & 725	1 & 20	0.1
RR1000 U720Li U720Li-LG U720Li-LP	Air	20	20Hz sinusoidal	0.1

Table 3-4: Summary of long crack test matrix.

3.4.2. Specimen geometry

The specimens used in the long crack tests are as shown in Figure 3-1. The U720Li and variants specimens are 12.5mm x 12.5mm square section SENB specimens with a 60° starter notch. For RR1000, SENB specimens with 12.0mm x 12.0mm square section labelled RR1000 MO1547 were used.

3.4.3. Experimental methods

Room temperature long crack tests were carried out on an Instron 8802 servohydraulic testing machine (±10kN capacity) while high temperature long crack tests were carried out on an Instron 8501 (capacity ±50kN) servohydraulic testing machine equipped with an ESH high temperature vacuum chamber.

Tests were conducted in 3-point bend under load control. A span of 20mm and ceramic rollers were used in all the tests. Specimens may develop a lop-sided crack if there is any unevenness in loading. This was minimised by checking that the specimen was loaded up evenly from front to back with a flashlight, as well as assessing the roller movement when the specimen was loaded with a small load, typically about 0.05 kN to 0.1 kN. The latter procedure was a very effective check for this problem. For an evenly loaded specimen the roller would rotate about the middle of the contact line between the roller and specimen, while for an unevenly loaded specimen the roller

tended to rotate at a point nearer to the front or the back of the contact line between the roller and specimen.

Crack lengths were monitored using a 2-point potential drop method as per ASTM 647 calibrated for the notch type used. P.D. detection wires were spot-welded at opposite ends of the notch, one on each side, and current supply bolts were attached to both ends of the specimens. An illustration of the long crack test set-up is shown in Figure 3-5. The current supplied was chosen to give an initial start P.D. of about 2 volts at the beginning of the pre-cracking. The P.D. was monitored continuously with a chart recorder. The P.D. calibration for the notch type used was previously carried out in the post-doctoral project [30].

The room temperature long crack tests were carried out using an R-ratio of 0.1 and a 20Hz sinusoidal cycling waveform. Pre-cracking was started at an approximate ΔK of 20 MPa$\sqrt{m}$ for approximately 0.5mm of crack growth and eventually load shedding by 10% of initial load after the crack had grown through four monotonic plastic zone sizes. Load shedding (in 10% decrements after growth through four monotonic plastic zone sizes) was continued until the crack growth rate reached the order of 10^{-12} m/cycle. This was followed by growth out at constant load, i.e. increasing ΔK as the crack grows. The loads for growth out were calculated to give an initial ΔK of approximately 14 MPa$\sqrt{m}$ at the start of the growth out. Testing was usually stopped at an a/W of ~0.75, typically corresponding to a ΔK level of 40~60 MPa$\sqrt{m}$ depending on the loads used. The specimen was then broken open by applying a heavy load (~5kN) to the specimen such that the remainder of the specimen failed in a monotonic manner.

For high temperature long crack tests, vacuum levels of the order of $1x10^{-5}$ mbar were achieved at test temperatures between 650°C and 725°C. The vacuum level initially deteriorated as the temperature was switched on due to outgassing, but improved after a period of time. Vacuum tests were started only when vacuum levels had improved to at least $1x10^{-4}$ mbar. High temperature heating was provided by four high-power quartz lamps controlled using an Eurotherm 815 thermal controller. The temperature was monitored with a Type "R" (Platinum/Platinum-Rhodium) thermocouple spot-welded to the specimen close to the notch. In all the tests the maximum variation of temperature was within ±2°C. The specimen was placed in the middle of the hot-zone to ensure uniform temperature distribution throughout the specimen.

Specimens were pre-cracked at room temperature using a 20Hz triangular wave at an R-ratio of 0.1 to ensure subsequent crack growth during high temperature testing began from a microscopically sharp crack away from any machining effects of the notch. Pre-cracks were started at a ΔK of 20 MPa$\sqrt{m}$ for approximately 0.5mm of crack growth and eventually load shedding in steps of 10% reduction in load after the crack had grown through four monotonic

plastic zone sizes. The pre-cracking was carried on down to a ΔK of 14.6 MPa$\sqrt{m}$ and a typical a/W of 0.35. High temperature tests were carried out at an R-ratio of 0.1 using a trapezoidal waveform with a standard 1-1-1-1 cycle (0.25 Hz) or a 1-20-1-1 dwell cycle (0.0435 Hz). Tests were carried out under constant applied load (i.e. increasing ΔK as the crack grows) starting with an initial ΔK of ~15MPa$\sqrt{m}$. High temperature testing was stopped at an a/W of ~0.65, typically corresponding to a ΔK level of 30-60 MPa$\sqrt{m}$ depending on the loads used. This was achieved by setting the event detection on the servohydraulic machine to stop the test after the P.D. corresponding to a/W of 0.65 has been reached. At this point the machine control reset itself and the specimen was left at the mean load used in the test. The specimen was then fatigued open at room temperature using loads similar to the high temperature test but with a 20Hz triangular wave as in the pre-cracking of the specimen.

Occasionally, during the high temperature tests, the loads had to be increased due to slow crack growth or to overcome transient effects of growth from the notch or due to initial oxidation when the specimen was heated and outgassing occurred. The load was increased to give a 10% increase in the ΔK at this point during the tests. During analysis of the test data, care was taken to ensure that the transients associated with this load increase, if any are present, are not included in the growth out curve.

After testing the actual crack lengths corresponding to the notch, pre-crack and final fracture were measured using an Olympus microscope. For the room temperature tests the actual crack lengths corresponding to the notch, threshold region and final fracture points were measured. This was done with the graticule on one of the eyepieces of the microscope. From the chart recorder, a P.D. against time trace was obtained. The P.D. and time information was subsequently converted to corresponding crack length and cycle information. The loads, the crack length information from optical measurement and the crack length and cycle information from the chart trace were fed into a spreadsheet to calculate relevant parameters including the crack growth rates da/dN and ΔK. Crack growth rates da/dN were calculated using the secant method. These parameters were then used to plot the da/dN vs. ΔK curve as well as the crack growth curve. In the spreadsheet, a linear correction factor was used to correlate the crack lengths obtained from the P.D. measurements and the actual crack lengths observed on the fracture surface. This was to correct changes in the P.D. measurements due to the difference in temperature during calibration and testing, as well as to correct possible electrical closure effects during the tests.

3.4.4. Long crack fractography

Post-test fractographic work included examination of the fracture surfaces using a Wild M420 macroscope and detailed fractographic work carried out on a SEM and a FEGSEM. The Wild M420 macroscope was used to obtain a photograph of the overall fracture surface. A Jeol

JSM-T300 SEM operating at an accelerating voltage of 20kV was used to obtain micrographs of the pre-crack and fatigue fracture surfaces of the elevated temperature long crack tests. With the introduction of a new Jeol JSM-6500 FEGSEM in the department during the course of the PhD. fractographic work on room temperature long crack tests was carried out on the FEGSEM operating at an accelerating voltage of 10kV. Micrographs of the fatigue fracture surfaces were taken at low, medium and high ΔK levels.

The fracture surfaces were also sectioned longitudinally (along the crack growth direction) to enable the crack propagation path to be observed with respect to the microstructure. Specimens were prepared by removing the bulk of the specimen from the fracture surface region and subsequent sectioning of the fracture surface longitudinally using EDM. A sketch of the cut-up sequence is shown in Figure 3-6. The sectioned fracture surface was then coated with silica reinforced lacomit varnish to protect the fracture surface and mounted on epoxy cold mounting resin. Grinding and polishing using standard metallographic techniques to 1 μm finish was carried out and subsequently the polished surface was etched with Fry's reagent. The etched surface was temporarily coated with lacomit to protect the etched surface whilst the epoxy was removed. All the lacomit was then removed and the fracture surface was subsequently examined in the SEM with a 10° tilt to enable both the fracture surface and sub-surface microstructure to be observed.

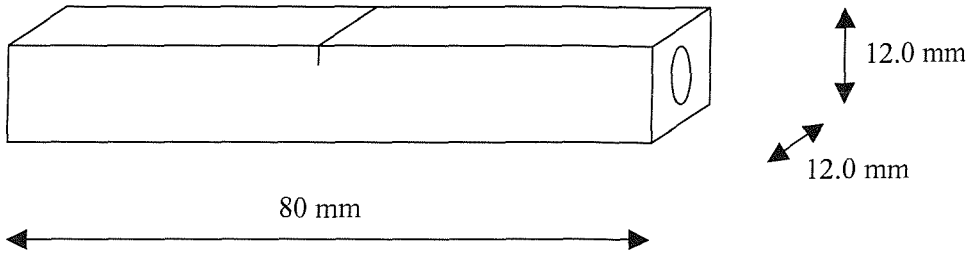

Figure 3-1a: Specimen dimensions of RR1000 labelled
RR1000 MO1547 POS 1- POS 10.

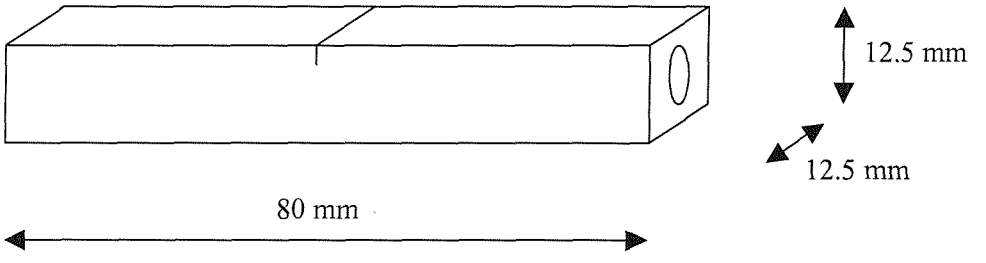

Figure 3-1b: Specimen dimensions of U720Li, U720Li-LG, U720Li-LP; and RR1000 labelled
RR1000 MO1751 POS 201- POS 210.

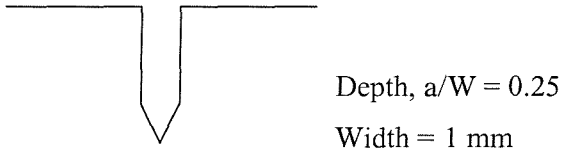

Figure 3-1c: Notch geometry.

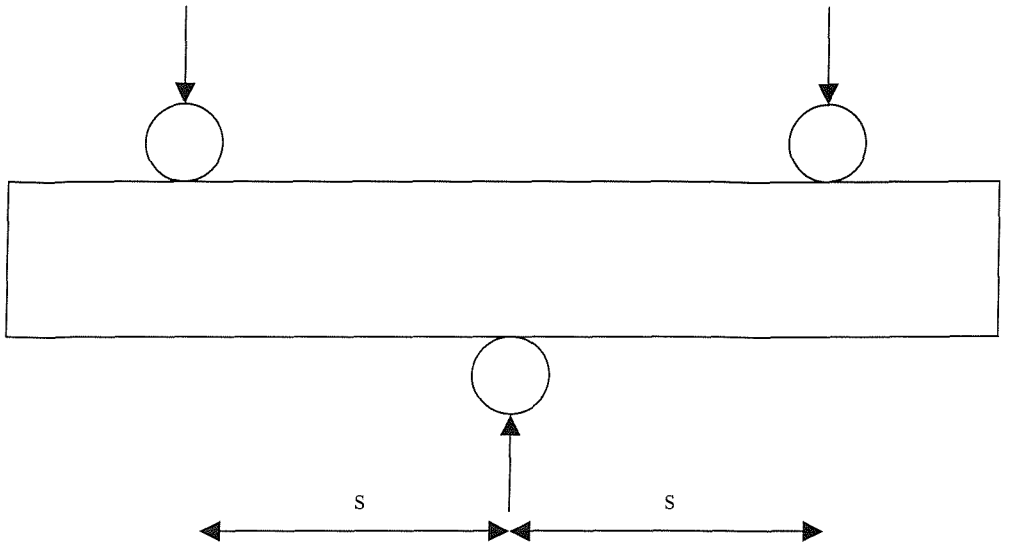

Figure 3-2: Room temperature short crack test setup.

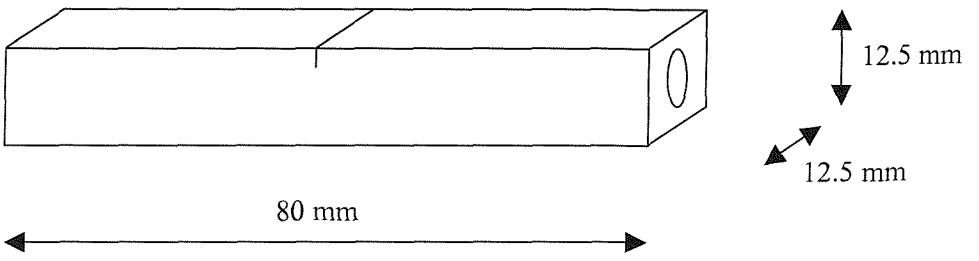

Figure 3-3a: Specimen geometry for high temperature short crack testing.

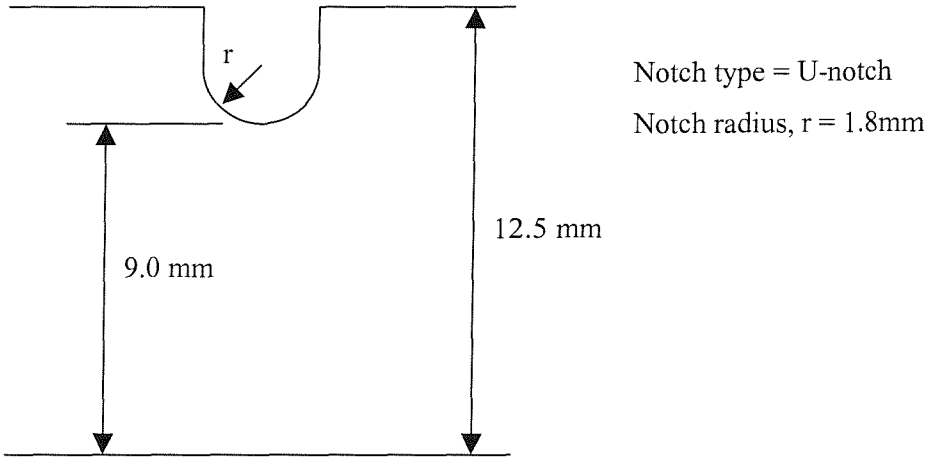

Figure 3-3b: Notch geometry for high temperature short crack testing.

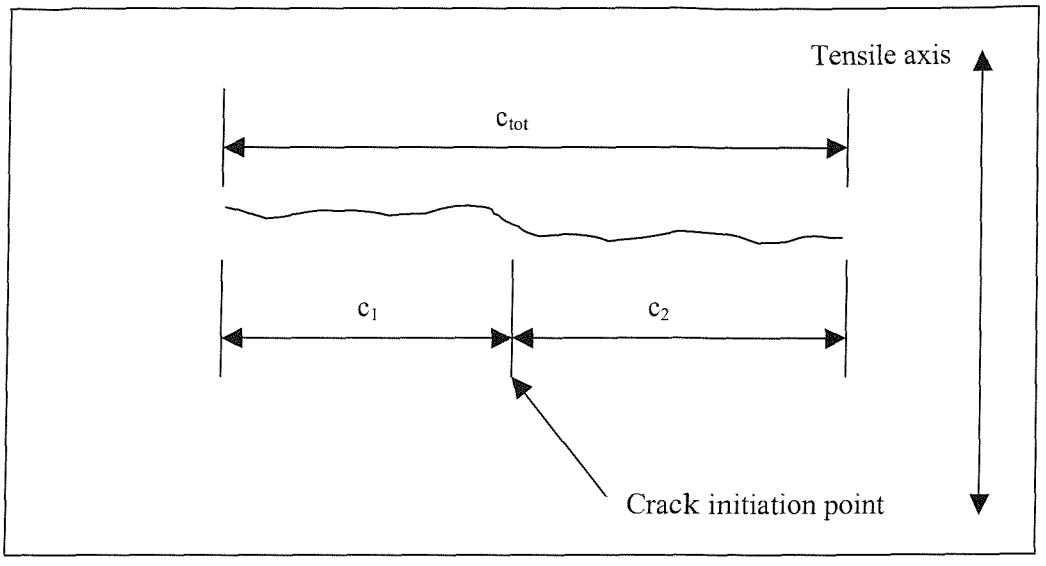

Figure 3-4: Short crack length measurement.

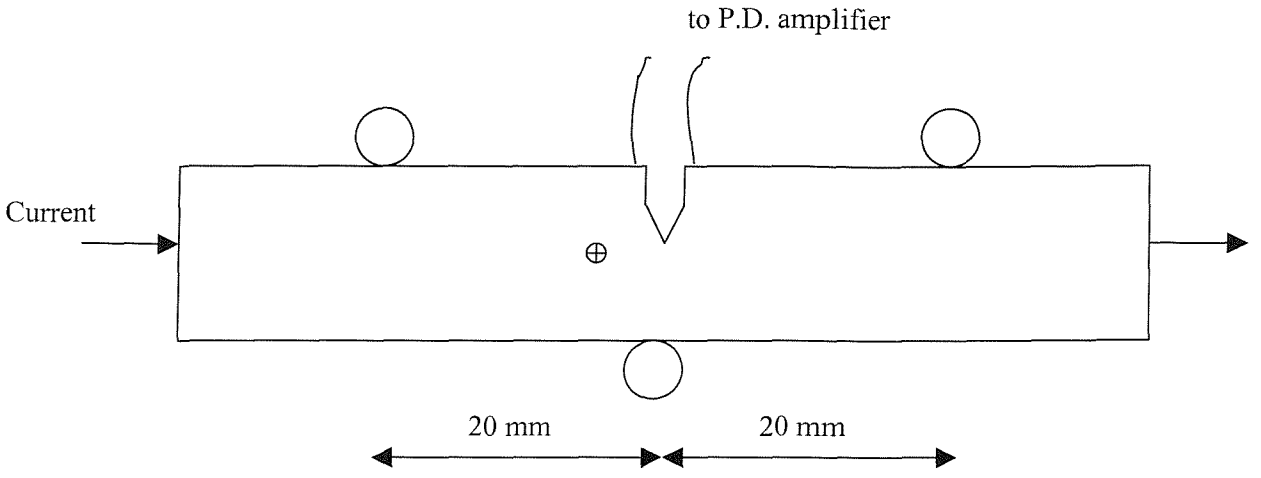

⊕ Thermocouple location

Figure 3-5a: High temperature long crack test setup.

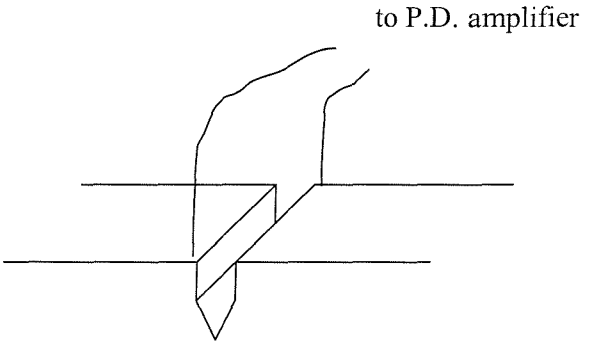

Figure 3-5b: P.D. wires positions at notch.

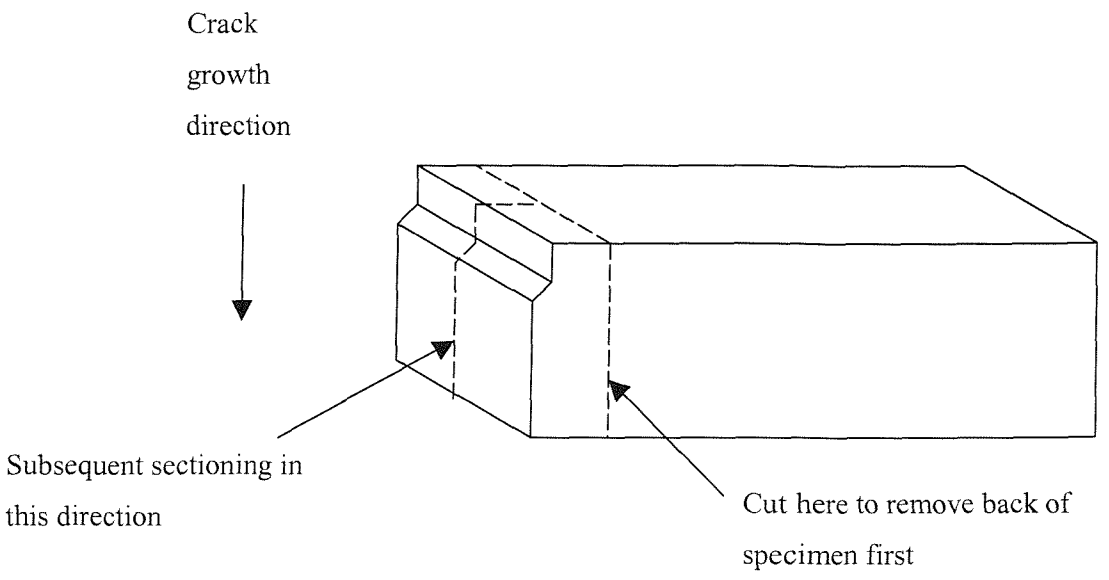

Figure 3-6: Cutting sequence for sectioned fracture surface observations.

4. Results

4.1. Microstructural characterisation

The microstructures of the test materials etched electrolytically with 10% orthophosphoric acid in H_2O are shown in Figure 4-1. Other than for U720Li-LP, the matrix grain boundaries are reasonably visible in all the materials, together with primary γ' precipitates which can be seen clearly. The primary γ' precipitates reside mainly at grain boundaries and grain boundary triple points, and are also occasionally observed within the grains.

Figure 4-2 shows the microstructures of RR1000 and U720Li and variants [30] revealed using Fry's etch. Primary γ' precipitates can be clearly observed in all the materials but matrix grain boundaries are only visible in U720Li and U720Li-LG. As both orthophosphoric acid etch and Fry's etch were unable to satisfactorily reveal the matrix grain boundary of U720Li-LP, further etching of U720Li-LP has been carried out using 10% bromine in ethanol [30]. The U720Li-LP microstructure revealed using 10% bromine in ethanol etch is shown in Figure 4-3 where the outlines of the grain boundaries and primary γ' precipitates are reasonably visible.

The microstructures of RR1000, U720Li, U720Li-LG and U720Li-LP have also been obtained using backscattered electron imaging on a SEM on unetched polished samples. The microstructures are shown in Figure 4-4. The γ matrix in U720Li, U720Li-LG and U720Li-LP appears much brighter than the primary γ' precipitates, while in RR1000 the primary γ' precipitates appear much brighter than the γ matrix. In the RR1000 material, bright spots can also be seen throughout the material, while in U720Li and its variants these spots were not observed.

Energy-dispersive X-ray (EDX) analysis was also carried out on RR1000 and U720Li to ascertain the elements present in each of the γ and γ' phases in the materials. The EDX analysis results on the γ and γ' phases of RR1000 and U720Li are shown in Figure 4-5 and Figure 4-6 respectively. For a given material, the elements present in the γ and γ' phases appear to be similar, only differences in the quantity of elements present as denoted by the height of the peaks were noted. In both RR1000 and U720Li, the γ matrix appears to have higher Cr and Co contents compared to the γ' phase which are generally richer in Al and Ti. For a given phase (γ or γ'), the elements present in each phase in both RR1000 and U720Li were noted to be similar, and only minor differences in the relative amounts of elements present were noted. The peaks of the γ phase of both RR1000 and U720Li appear to be similar, while for the γ' phase, U720Li appears to show slightly higher Ti content and lower Cr and Co contents compared to RR1000.

4.1.1. Grain size and primary γ' size characterisation

The microstructural characterisation results of RR1000 and U720Li and variants obtained using Carl Zeiss KS300 automatic image analysis software on the orthophosphoric acid etched microstructures are given in Table 4-1. Note that the grain size information of U720Li-LP were results from the post-doctoral project [30] obtained from image analysis on the microstructure etched with 10% bromine in ethanol as the etching process using both Fry's reagent and orthophosphoric acid did not produce a reasonable grain resolution in U720Li-LP for a comprehensive analysis. The grain size distribution and primary γ' size distribution of both batches of RR1000 are shown in Figure 4-7 and a comparison of the grain and primary γ' precipitate size distribution of all test materials is given in Figure 4-8.

	RR1000 MO1547	RR1000 MO1751	U720Li	U720Li-LG	U720Li-LP
Grains					
Range (μm)	2.3-16.0	2.6-15.6	2.1-13.1	4.8-41.3	1.9-21.3 [30]
Average (μm)	7.4	7.1	6.4	15.4	10.1 [30]
Size standard deviation	2.8	2.5	1.8	6.5	3.4 [30]
Average relative circularity	0.66	0.66	0.65	0.66	0.63 [30]
Primary γ' precipitates					
Range (μm)	0.4-6.3	0.5-6.3	0.5-6.9	0.9-7.6	0.7-6.5
Average (μm)	1.75	1.80	1.99	2.52	2.12
Size standard deviation	0.9	0.9	0.9	0.9	0.9
Average relative circularity	0.70	0.67	0.70	0.72	0.67
V_f (%)	8.7	11.8	18.9	8.6	18.3

Table 4-1: Grain and primary γ' characteristics of test materials obtained using automatic image analysis.

From Table 4-1 and Figure 4-7a, it can be seen that both batches of RR1000 material have approximately similar grain size distribution and characteristics. A similar picture emerges when comparing the primary γ' characteristics of both batches of RR1000 material, bar the difference in

the primary γ' volume fraction in both batches. RR1000 MO1751 appears to have slightly higher primary γ' volume fraction, i.e. 11.8% c.f. 8.7% for RR1000 MO1547.

Both batches of RR1000 and U720Li were observed to have a similar grain size distribution, while for U720Li-LP and U720Li-LG larger grain sizes were observed. In terms of primary γ' precipitate sizes, both batches of RR1000, U720Li and U720Li-LP have approximately similar primary γ' sizes and distribution. The primary γ' precipitates in U720Li-LG are slightly larger compared to the other materials. The equi-axed nature of the grains and the primary γ' precipitates can be inferred from the circularity index values shown in Table 4-1. Other than the large grain size range and large standard deviation of the grain size observed in U720Li-LG, low standard deviation of the grain size and primary γ' size measurement was noted which is indicative of the relatively uniform microstructures of the test materials.

4.1.2. Primary γ' precipitate line intercept counting

Another analysis of the microstructural characteristics was carried out by counting the number of primary γ' precipitates that will be encountered on a straight line in the microstructures. Primary γ' precipitates may act as crack growth barriers or discontinuities in the microstructure during crack propagation, hence this analysis should provide some useful insight into the number of primary γ' precipitates encountered by the cracks in the fatigue tests.

The analysis was carried out by drawing random straight lines on the microstructure captured at a magnification of 500x and the number of primary γ' precipitates encountered was recorded at every 50 μm interval for a straight line with widths of zero, 5 μm and 10 μm. The number of precipitates encountered is counted for the different sampling line widths to allow for possible minor deflections in the crack path which may cause changes in the number of precipitates encountered. It should be noted that the experimental crack lengths were measured as straight projected cracks perpendicular to the applied stress (Figure 3-4) and no account of minor crack path deviations was made in the crack length assessment. The analysis was carried out on two images from each microstructure, and on each image ten lines were used for the analysis, i.e. the data obtained is averaged over 20 lines. This should be sufficient to remove any sampling effect which may be present due to inhomogeneity in the microstructures.

The results of this analysis are shown in Figure 4-9 for individual microstructures. The results indicate increasing number of precipitates encountered with increasing sampling line width as expected. The slope of the plots in Figure 4-9 gives the number of precipitates encountered per unit sampling length in number of precipitates per μm. The slope of the plots was calculated for all the sampling line widths used in the analysis for all the microstructures and is plotted against the sampling line width in Figure 4-10 for comparison. The analysis shows that the highest number of

precipitates was encountered in U720Li and U720Li-LP. The number of precipitates encountered in U720Li-LP was marginally lower than that of U720Li. The lowest number of precipitates was encountered in U720Li-LG. The number of precipitates encountered in RR1000 is between that of U720Li/U720Li-LP and U720Li-LG. RR1000 MO1751 appears to encounter a higher number of precipitates compared to RR1000 MO1547.

4.1.3. RR1000 coherent γ' size characterisation

Carbon extraction replicas have been used to investigate the sizes of coherent γ' precipitates in RR1000 MO1547 and RR1000 MO1751. TEM images from the replicas are shown in Figure 4-12 and Figure 4-13. Figure 4-12a and Figure 4-13a taken at low magnification (50000x) shows irregular shaped secondary γ' as well as fine tertiary γ' precipitates, while Figure 4-12b and Figure 4-13b taken at higher magnification (200000x) shows typically spherical tertiary γ'. The high magnification view was taken to show tertiary γ' at greater resolution with a high number of these precipitates present for a representative quantitative analysis, while the low magnification view was taken to ensure a high number of secondary γ' precipitates was present. Corresponding TEM images from carbon extraction replicas of other materials studied during the post-doctoral project [30] are shown in Figure 4-14 for comparison.

Comparing both batches of RR1000 in Figure 4-12 and Figure 4-13, it is observed that both batches of RR1000 have approximately similar secondary and tertiary γ' sizes. When comparing the RR1000 and U720Li, it can be seen that RR1000 has larger secondary and tertiary γ' precipitates compared to U720Li. U720Li-LG has larger secondary γ' compared to RR1000 but approximately similar tertiary γ' sizes to RR1000. U720Li-LP has both larger secondary and tertiary γ' precipitates compared to RR1000.

A summary of the coherent γ' size results of RR1000 is given in Table 4-2. Results of coherent γ' sizes for U720Li, U720Li-LG and U720Li-LP [30] are also included in the table for comparison. The similarity in the coherent γ' sizes in both batches of RR1000 is observed from the results. The results also indicate that RR1000 has an average secondary γ' precipitate size between that of U720Li (~100nm) and that of U720Li-LG and U720Li-LP (~190nm-250nm). The tertiary coherent γ' precipitate sizes of U720Li, U720Li-LG and RR1000 were very similar, in the range of 16nm to 21nm. Only the tertiary γ' precipitate sizes of U720Li-LP were distinctly coarser compared to that of RR1000, with an average size of 27nm.

Material	Secondary γ' (nm)		Tertiary γ' (nm)	
	Average	Range	Average	Range
RR1000 MO1547	140	40-200	18	6-30
RR1000 MO1751	146	60-195	21	15-30
U720Li	102	51-150	16	1-45
U720Li-LG	190	81-300	17	6-30
U720Li-LP	254	151-400	27	6-55

Table 4-2: Summary of coherent γ' sizes.

The secondary and tertiary γ' precipitate size distribution is shown in Figure 4-11a and Figure 4-11b. The secondary γ' precipitate sizes are obtained by taking information only from the low magnification views (higher number of precipitates for representative quantitative analysis), and likewise only the high magnification views are used to obtain the tertiary γ' precipitate sizes (to give higher accuracy).

4.1.4. Thermo-calc predictions of phases

Predictions have been made using Thermo-calc [1] to calculate the equilibrium γ-γ'-σ phase distribution in U720Li and RR1000. The predicted γ-γ'-σ phase distribution for the alloys are shown in Figure 4-15. From these plots, the equilibrium γ-γ' phase distribution of U720Li and RR1000 beyond about 900°C appear to be very similar. Note that these predictions also highlight the increased propensity to formation of the detrimental σ-phase in RR1000 compared to U720Li.

As γ' precipitate distributions are important to material properties during high temperature service, the expected equilibrium volume fraction of γ' present in the alloys has been estimated during the post-doctoral project [30] and is shown in Table 4-3. The quantity of equilibrium γ' present at the solution temperature should correspond to the quantity of primary γ' precipitates.

[1] Thermo-calc predictions carried out by D. Hunt, Department of Materials Science and Metallurgy, University of Cambridge.

Material	Solution temp (°C)	V_f γ' from micrographs (%)	V_f γ' from Thermo-calc (%)	ΔV_f (%)
U720Li	1105	18.9	15.4	+3.5
U720Li-LG	1135	8.6	7.92	+0.7
U720Li-LP	1105	18.3	15.4	+2.9
RR1000 MO1547	1120	8.7	12.5	-3.8
RR1000 MO1751	1120	11.8	12.5	-0.7

Table 4-3: Comparison between observed and predicted γ' at solution temperature.

Equilibrium predictions have also been made at 250°C, because the volume fraction of γ' expected is close to its maximum value as this temperature in cooling is reached. This enables an approximation of the total volume fraction of γ' that will be present at room temperature to be made and the volume fraction of residual (and thus coherent) γ' can then be calculated (by subtracting the volume fraction of primary γ' precipitate observed from micrographs from the total predicted volume fraction of γ'). This is useful in interpreting the material properties of the alloy (e.g. hardness and high temperature behaviour) as well as the possible slip character of the material. The predicted volume fractions of γ' at 250°C and the estimates of the volume fractions of coherent γ' are shown in Table 4-4.

Material	Total γ' predicted at 250°C (%)	Primary γ' V_f from micrographs (%)	Remaining coherent γ' (%)
U720Li	48.3	18.9	29.4
U720Li-LG	48.3	8.6	39.7
U720Li-LP	48.3	18.3	30.0
RR1000 MO1547	49.2	8.7	40.5
RR1000 MO1751	49.2	11.8	37.4

Table 4-4: Predictions of coherent γ' present at 250°C.

From Table 4-4, RR1000 was shown to have a higher estimated volume fraction of coherent γ' present compared to U720Li and U720Li-LP. The U720Li-LG has an approximately similar or slightly higher estimated volume fraction of coherent γ' compared to both the RR1000 batch of materials.

4.1.5. Hardness testing

Room temperature hardness tests on RR1000 revealed a hardness value of 457 Hv(30) for RR1000 MO1547 and 452 Hv(30) for RR1000 MO1751. A comparison of the hardness values of RR1000 and other test materials [30] is given in Table 4-5 and Figure 4-16.

From Table 4-5, the hardness of RR1000 MO1547 is comparable to the hardness of U720Li but slightly greater than that of U720Li-LG and significantly greater than that of U720Li-LP. RR1000 MO1751 has a hardness value between that of U720Li and U720Li-LG.

Material	RR1000 MO1547	RR1000 MO1751	U720Li	U720Li-LG	U720Li-LP
Hardness (Hv 30)	457±4.8	452±2.7	458±2.9	445±1.2	427±2.5

Table 4-5: Comparison of room temperature hardness values of different alloys.

4.2. Room temperature short crack tests

4.2.1. General results

A summary of the short crack test results is given in Table 4-6. Overall it is noted that there are greater number of cracks in the as-polished specimens compared to the etched specimens, although this may be due to cracks being less easily observed in the etched specimens. As-polished specimens also appear to possess a slightly shorter lifetimes compared to etched specimens.

Test	Stress level (% σ_y)	Stress level (MPa)	Material	Specimen treatment	Total number of cracks	Lifetime (cycles)
11S	95	1155	U720Li	Polished	35	105467
10S	95	1155	U720Li	Etched	15	128476
7S	95	1123	U720Li-LG	Polished	41	170486
4S	95	1123	U720Li-LG	Etched	19	175867
9S	95	1077	U720Li-LP	Polished	10	217861
6S	95	1077	U720Li-LP	Etched	8	248570
3S	83	1004	RR1000 MO1751	Etched	1	321924
8S	95	1146	RR1000 MO1547	Etched	1	192077

Table 4-6: Summary of short crack test results.

Generally, U720Li and U720Li-LG are observed to have more cracks compared to U720Li-LP and RR1000. In terms of fatigue lifetime, U720Li-LP shows the longest life, followed by RR1000, U720Li-LG and U720Li. RR1000 in test 3S shows a much longer lifetime compared to all other tests due to the lower stress level (83% σ_y) used in the test.

Although the dimensions of U720Li specimens used (Table 3-3) are very different from the dimensions of other specimens used in the tests, the approximate ΔK near the end of the tests before the final failure of the specimens are very similar (see Figure 4-18a and Figure 4-19). Hence in this respect a lifetime comparison can still be made for U720Li and other materials.

4.2.2. Fatigue crack initiation

Fatigue crack initiation was divided into two distinct types, i.e. due to porosity or defects on the surface where during examination of the replicas the crack was observed to emanate from a pore or a defect on the surface, and due to slip band cracking or subsurface defects where the crack was noted to appear on the surface without any evidence of surface pore or defect causing the crack

initiation. A summary of the number of cracks due to the two types of fatigue crack initiation is given in Table 4-7.

Crack initiation appears to be largely dominated by porosity in U720Li and U720Li-LG, while in U720Li-LP there is more of a balance between the number of cracks due to porosity/defects on the surface and those due to slip band cracking/subsurface defects. Far fewer cracks are initiated in the RR1000 alloy. From the two tests conducted on RR1000, only one crack initiated and grew to give final failure in each of the specimens.

Material	Specimen treatment	Number of cracks		
		Pores/ defects	Slip band/ subsurface defects	Total
U720Li	Polished	20	15	35
U720Li	Etched	13	2	15
U720Li-LG	Polished	35	6	41
U720Li-LG	Etched	15	4	19
U720Li-LP	Polished	5	5	10
U720Li-LP	Etched	5	3	8
RR1000 MO1751	Etched	1	-	1
RR1000 MO1547	Etched	1	-	1

Table 4-7: Fatigue crack initiation information; number of cracks.

Further fatigue crack initiation information on the number of cycles to the first observed crack and the approximate crack length when the crack is first observed is given in Table 4-8. The number of cycles to first observed crack is taken to the nearest 10000 cycles (when a replica is taken for investigation). Cracks generally initiate much earlier in U720Li and U720Li-LG compared to U720Li-LP and RR1000, which may suggest a less damage tolerant and/or lower crack initiation resistant microstructure of U720Li and U720Li-LG. U720Li-LP also appears to have increased resistance to crack initiation in the presence of surface porosity/defects. Initiation of fatigue cracks due to surface porosity/defects in U720Li-LP is first observed at 70000-80000 cycles, while in U720Li and U720Li-LG it is first observed at 10000-20000 cycles. For the RR1000 material, the number of cycles to crack initiation is higher in test 3S as expected, i.e. a lower stress level gives a longer crack initiation period.

Material	Specimen treatment	No. of cycle to first observed crack		Approximate largest crack length when crack first observed (μm)	
		Pores/ defects	Slip band/ subsurface defects	Pores/ defects	Slip band/ subsurface defects
U720Li	Polished	10000	10000	33.0	64.5
U720Li	Etched	10000	40000	6.65	3.69
U720Li-LG	Polished	10000	10000	21.4	14.0
U720Li-LG	Etched	20000	10000	45.3	8.79
U720Li-LP	Polished	80000	10000	11.1	20.0
U720Li-LP	Etched	70000	50000	31.5	4.48
RR1000 MO1751	Etched	90000	-	54.0	-
RR1000 MO1547	Etched	60000	-	13.5	-

Table 4-8: Fatigue crack initiation information; first observed crack.

An assessment of the crack field was also carried out on the replicas at an interval of approximately every 20% of the total life to investigate the evolution of the crack field during the course of the short crack tests. The assessment was carried out only for U720Li, U720Li-LG and U720Li-LP tests as RR1000 only has one crack for both tests carried out. The result of this assessment is shown Table 4-9 for etched tests and Table 4-10 for as-polished tests. The results are plotted in Figure 4-17a in terms of lifetime and in Figure 4-17b in terms of the fraction of life.

U720Li (10S)		U720Li-LG (4S)		U720Li-LP (6S)	
Cycles	No. of cracks	Cycles	No. of cracks	Cycles	No. of cracks
20000	1	20000	0	40000	0
40000	2	40000	1	80000	2
60000	2	60000	5	120000	3
80000	6	80000	14	160000	6
100000	11	100000	18	200000	6
125000	14	125000	19	245000	8
		150000	19		

Table 4-9: Crack field characterisation; etched tests.

U720Li (11S)		U720Li-LG (7S)		U720Li-LP (9S)	
Cycles	No. of cracks	Cycles	No. of cracks	Cycles	No. of cracks
20000	9	20000	1	40000	2
40000	19	40000	7	80000	3
60000	28	60000	14	120000	6
80000	29	80000	20	160000	7
105000	29	100000	28	200000	9
		120000	33	215000	10
		140000	34		
		165000	41		

Table 4-10: Crack field characterisation; as-polished tests.

From Figure 4-17a, large numbers of cracks were noted to initiate early in the as-polished U720Li test. However the U720Li etched test shows significantly slower rate of crack initiation compared to the as-polished U720Li test. Both the as-polished and etched tests of U720Li-LG show slower crack initiation compared to the as-polished U720Li test while the U720Li-LP tests show the slowest rate of crack initiation. Overall, cracks were noted to initiate relatively uniformly throughout the life in all the materials. A similar picture can be seen in Figure 4-17b.

4.2.3. Short crack growth

The short crack growth rates vs. ΔK plots for each material are shown in Figure 4-18a to Figure 4-18d. Only larger cracks (primary crack and secondary cracks >50 μm at failure) were analysed as most of the smaller cracks (<50 μm at failure) in the tests show small or negligible crack growth rates or were arrested throughout the tests. The plots show the typical scatter of short crack growth, where temporary crack arrests due to obstacles (precipitates, grain boundaries) are common. From these plots, it can be seen that etching has not significantly affected the short crack growth rates, whilst giving the benefit of revealing the crack path relative to the microstructure.

When calculating the ΔK values using the empirical formula of Scott and Thorpe [89], it was assumed that the crack depth is equivalent to half the surface crack length, i.e. an a/c ratio of 1. This assumption was made for simplicity, but apparently the crack shape (e.g. tear-drop crack in Figure 4-24i) may invalidate this assumption at larger crack lengths. Care also has to be exercised when using the ΔK parameter, especially when comparing the results of this study with others due to the number of cracks on each specimen and the proximity of the cracks to one another. Nevertheless, in the absence of a better alternative, ΔK serves as a good correlating parameter within this study to compare the crack growth behaviour of different materials.

Figure 4-19 gives a comparison of the short crack growth rates for all the materials used in the study. In the short crack growth regime (ΔK approximately <10 MPa$\sqrt{m}$, corresponding to crack lengths approximately 200μm), U720Li-LP and RR1000 (both MO1547 and MO1751) appear to exhibit approximately similar or lower crack growth rates compared to U720Li-LG, while U720Li shows the highest average short crack growth rates among all the materials used in the study. U720Li and U720Li-LG show larger scatter in crack growth rates, possibly due to the higher number of cracks in both the U720Li and U720Li-LG tests.

A useful method to quantify the short crack growth resistance of the materials is by comparing the fastest growing crack, usually the largest crack in the specimen (i.e. one which is most critical to failure) in each of the tests. Figure 4-20 shows that while most of the cracks critical to failure initiate after approximately the same number of cycles, the crack growth is distinctly different. Crack growth of the largest crack in U720Li-LP is again slowest, followed by RR1000 MO1547, U720Li-LG and U720Li.

4.2.4. Effect of primary γ' precipitates

In all the short crack tests, multiple temporary crack arrest events were observed when the crack approached a primary γ' precipitate. The crack continued either by cutting through or propagating around the primary γ' precipitates. The number of cycles of crack arrest corresponding to both events appears to be similar. Figure 4-21a gives an example of temporary crack arrest at the crack tip (indicated by arrows) which involves the crack cutting through a primary γ' precipitate in RR1000 MO1547 (Test 8S). Note the initiation of the fatigue crack from surface porosity. An example of temporary crack arrest involving the crack propagating around a primary γ' precipitate is shown in Figure 4-21b, indicating a crack in U720Li-LP (Test 6S).

An assessment of the effects of primary γ' precipitates on the propagating crack tip on the top surface of the short crack specimens was carried out by observation of the acetate replicas. The assessment was carried out on larger cracks (>50 μm) of the etched tests as primary γ' precipitates cannot be observed on the replicas of the as-polished tests. The number of primary γ' precipitates bypassed either through precipitate cutting or propagating around the precipitate was recorded for individual cracks at 40 μm intervals. The results of the assessment are shown as the average behaviour observed for the larger cracks, i.e. the number of primary γ' precipitates encountered and the occurrence of individual primary γ' precipitate bypassing phenomena is averaged for individual 40 μm crack length intervals.

The effects of primary γ' precipitates on the propagating crack tip in individual test materials are shown in Figure 4-22. It was noted that the occurrence of primary γ' precipitates being cut or propagated around by the advancing crack was equally common, with only marginal differences in

the number of precipitates being cut or propagated around by the advancing crack tips. A comparison of the overall number of crack tip interactions with primary γ' precipitates during crack propagation in the test materials is shown in Figure 4-23. The cracks in U720Li-LP are noted to encounter on average the highest number of primary γ' precipitates. The cracks in RR1000 and U720Li encountered intermediate number of primary γ' precipitates while the cracks in U720Li-LG encountered the lowest number of primary γ' precipitates.

4.2.5. Fractography

The overall fracture surfaces and top surfaces (to show crack growth direction) from the tests are shown in Figure 4-24. Arrows on the top surfaces indicate the approximate locations where the primary crack has initiated and subsequently grew to give failure. The cracks tend to develop a "fan" shape when initiated from the centre of the specimen, and "tear-drop" cracking [40] was observed when cracks initiated nearer to one edge of the specimen. The cracks grow almost perpendicular to the tensile axis in the centre of the specimen, but pronounced shear lips at the specimen surface form once the crack reaches a certain length. The overall fracture surface of the large grain variant also appears generally rougher (Figure 4-24e and Figure 4-24g) compared to other materials. This is expected, as larger grains tend to give a more tortuous crack path (e.g. crack grows along slip bands from one grain orientation to another).

Detailed analysis of crack initiation and short crack growth mechanisms in each test was carried out in a SEM. These analyses were carried out on the primary crack and larger secondary cracks of each test. Other features such as the transition from stage I to stage II crack growth were also investigated. SEM observations at and near the crack initiation site of primary cracks are shown in Figure 4-25 to Figure 4-28.

The observation of crack initiation due to porosity on the surface during replica examination was confirmed by SEM observations of the fracture surfaces. Cracks were also noted to initiate from porosity just below the surface. Examples of crack initiation from porosity just below the surface are shown in Figure 4-25b for the primary crack of test 3S (RR1000) and Figure 4-27b for the primary crack of test 4S (U720Li-LG). The primary crack and larger secondary cracks in all the tests were noted to initiate from surface or subsurface porosity.

Crack initiation due to slip band cracking and subsurface porosity and defects are grouped into one category during replica examination due to the limitations of surface acetate replica observations. Unambiguously determining the actual cause of crack initiation for the cracks in this category will require extensive and detailed fractography in the SEM. Most of the cracks that did not initiate from surface or subsurface porosity remained small and rarely coalesce with the primary crack or other larger cracks, hence they rarely appear on the fracture surface making it difficult to carry out detailed analysis on these cracks in the SEM.

The fracture surface at and near the crack initiation site appears faceted, indicative of stage I crack growth. The fracture surfaces become less faceted as the crack grows, indicating the onset of stage II crack growth mode. Another point to note was that the transition from stage I to stage II crack growth was gradual, usually over a few tens of μm.

Figure 4-25a and Figure 4-25b show the initiation site of the primary crack in RR1000 in test 3S. Note the faint riverlines in Figure 4-25a. The crack has initiated from a pore just below the surface as shown in Figure 4-25b. Figure 4-25c shows the highly crystallographic stage I crack growth near the primary crack initiation site. The transition from stage I to a mixed stage I/stage II crack growth is shown in Figure 4-25d with the crack growing from the top to bottom in the figure. Some degree of crystallographic crack growth is observed at the top of the figure, and nearer to the bottom some relatively flat regions indicative of stage II crack growth were noted. Figure 4-25e and Figure 4-25f shows the crack initiation site of the primary crack in RR1000 in test 8S, again indicating crack initiation from a subsurface pore. Note the highly crystallographic crack growth around the pore in Figure 4-25f.

Further evidence of cracks initiating from porosity is shown in Figure 4-26 to Figure 4-28 in U720Li, U720Li-LG and U720Li-LP. The crack-initiating porosity was noted to be on the surface or just below the surface. They may be clustered (Figure 4-27d) or have odd shapes (Figure 4-26d and Figure 4-28b). An interesting point to note is the primary crack initiation in U720Li-LG in test 4S (Figure 4-27a and Figure 4-27b). The flat region suggests the presence of an extra large grain or two reasonably large grains with low relative misorientation. This would give rise to a highly concentrated slip in a particular direction which may result in slip band cracking. The crack initiation in this case may be due to both the pore which acts as a stress concentrator and the presence of the large grain. Figure 4-27f shows the transition from stage I to mixed stage I/stage II crack growth in U720Li-LG in test 7S with the crack growing from the top to bottom in the figure.

A comparison of the crystallographic crack growth nature near the primary crack initiation site in Figure 4-25 to Figure 4-28 indicates highly crystallographic facets in RR1000 (Test 8S) and U720Li-LG, while in U720Li and U720Li-LP these facets were less crystallographic. The ranking of the degree of crystallographic faceting from strongest to weakest appears to be going from RR1000, U720Li-LG, U720Li-LP to U720Li. This observation is useful to indicate the degree of slip planarity experienced in each material when tested under similar conditions and stress levels.

The crack length at which the observed transition from stage I to stage II occurs on the fracture surface were approximated in each material and shown in Table 4-11. These data are used later during the comparison of long and short crack growth at room temperature.

Material	Approximate Stage I to Stage II transition crack length (μm)
RR1000 MO1547 (8S)	130
U720Li	110
U720Li-LG	100
U720Li-LP	90

Table 4-11: Approximate stage I to stage II transition crack lengths.

4.3. Room temperature long crack tests

The growth out curves of the room temperature long crack tests are shown in Figure 4-29. The approximate ΔK_{th} of the materials are presented in Table 4-12.

Material	ΔK_{th} (MPa$\sqrt{m}$)
RR1000	8.0
U720Li	7.6
U720Li-LG	8.5
U720Li-LP	6.2

Table 4-12: ΔK_{th} values of test materials.

From Figure 4-29, it is observed that in the near-threshold and high ΔK region, RR1000, U720Li and U720Li-LG have very similar crack growth rates. U720Li-LP has significantly higher crack growth rates than other materials in the near-threshold ΔK region. At higher ΔK the crack growth rates of U720Li-LP converge close to the crack growth rates of other materials but are still marginally higher compared to other materials.

Comparing the ΔK_{th} in Figure 4-29 and Table 4-12, RR1000, U720Li and U720Li-LG have ΔK_{th} clustered close to each other with U720Li-LP having a significantly lower ΔK_{th} compared to other materials. U720Li-LG which has larger grains exhibits the highest ΔK_{th} as expected. RR1000 and U720Li which have intermediate grain sizes show ΔK_{th} between that of U720Li-LG and U720Li-LP.

The overall facture surface from the room temperature long crack tests are shown in Figure 4-30. All tests show fairly uniform crack growth from the notch with a region of threshold crack growth distinguishable by the naked eye. Figure 4-31 to Figure 4-34 show the fracture surfaces and sectioned fracture surfaces of the room temperature long crack tests as observed in the SEM. The figures are shown in increasing ΔK under load shedding crack growth and increasing ΔK growth out conditions.

In the near-threshold region numerous crystallographic facets corresponding to stage I crack growth were observed on the fracture surfaces in all the materials. The degree of crystallographic faceting at near-threshold ΔK however was somewhat different in all the materials. The most distinct crystallographic facets were observed in U720Li (Figure 4-32c), followed by those in RR1000 (Figure 4-31c) while U720Li-LG (Figure 4-33a) and U720Li-LP (Figure 4-34a) exhibit lower and approximately similar degree of crystallographic faceting. Although U720Li shows the most crystallographic crack growth at near-threshold ΔK, Figure 4-31a and Figure 4-32a appear to show overall a slightly rougher fracture surface in RR1000 with some distinctly large facets

compared to U720Li. Figure 4-33c and Figure 4-34c indicates that U720Li-LG and U720Li-LP tend to show mostly micro-facets and a low proportion of large facets. The degree of faceting decreased with increasing ΔK in all the materials, and eventually the facets were no longer observed at high ΔK. The fracture surface becomes flatter with increasing ΔK, indicative of stage II crack growth. Evidence of fretting is also observed on the fracture surfaces in the near-threshold crack growth region. The degree of fretting damage appear to be most distinct in RR1000 (Figure 4-31a), followed by those in U720Li-LG (Figure 4-33a) and U720Li-LP (Figure 4-34a) while in U720Li (Figure 4-32a) the degree of fretting damage appear to be minimal with crystallographic facets appearing undamaged.

To shed further light on the near-threshold crack growth behaviour, an assessment of the crack deflection during near-threshold crack growth was also carried out. The influence of crack deflection on the crack tip driving force during near-threshold crack growth could be significant. A profile of the crack path in the near-threshold crack growth region was obtained from the sectioned fracture surface fractographs obtained at low magnification in the SEM, i.e. from Figure 4-31b, Figure 4-32b, Figure 4-33b and Figure 4-34b. The crack profiles at near-threshold ΔK are shown in Figure 4-35. The angle of crack deflection and the deflected crack path length at each deflection was measured from these crack profiles. The ratio of actual crack path length to the projected crack length was plotted in Figure 4-37 as a function of the projected crack length in the crack growth direction. Figure 4-37 shows large scatter in the ratio of actual to projected crack length for all the materials, except for U720Li-LG which appears to consistently have a ratio distinctly close to 1.

The effects of the deflections on the elastic crack tip driving force (k) can be calculated using the solutions provided by Bilby et al [48]. The values of the local stress intensities k_1 and k_2 ahead of the crack tip in Figure 4-36 can be related to the remotely applied K_I and deflection angle α according to the following equations:

$$k_1 = \frac{1}{4}\left(3\cos\frac{\alpha}{2} + \cos\frac{3\alpha}{2}\right)K_I \qquad \text{Equation 4-1}$$

$$k_2 = \frac{1}{4}\left(\sin\frac{\alpha}{2} + \sin\frac{3\alpha}{2}\right)K_I \qquad \text{Equation 4-2}$$

The effects of crack deflection in the near-threshold crack growth region is plotted as a function of effective ΔK where

$$K_{eff} = \sqrt{k_1^{\,2} + k_2^{\,2}} \qquad \text{Equation 4-3}$$

against the projected crack length in the crack growth direction in Figure 4-38. Figure 4-38 again shows large scatter in the ΔK_{eff} for all the materials, except for U720Li-LG which shows lower scatter consistent with the observations in Figure 4-35 and Figure 4-37.

4.4. High temperature short crack tests

4.4.1. General results

Runout and replication tests were initially carried out on U720Li at 650°C using 1-1-1-1 cycling to establish the appropriate load levels to be used to achieve a reasonable lifetime for subsequent replication tests. The runout and replication tests on U720Li were carried out at a maximum stress level (of the uncracked ligament) between 750MPa and 850MPa. In light of these results, it was decided that subsequent replication tests would be carried out using a stress level of 840MPa.

A summary of the elevated temperature short crack test results is shown in Table 4-13. The S-N curve of the data is plotted in Figure 4-39. Comparing the runout and replication tests of U720Li, it was noted that the replication process has slightly reduced the fatigue lifetime of the specimens. The runout test of U720Li at 750MPa shows an anomalously lower lifetime compared to the 800MPa runout test, possibly indicating the intrinsic scatter in lifetimes. Replication tests on U720Li at stress levels between 800MPa to 850MPa indicated decreasing lifetime with increasing applied stress levels as expected. At the same stress level (840MPa), U720Li-LG shows the longest life (66165 cycles), while U720Li-LP (8044 cycles) and U720Li (6909 cycles) have approximately similar lifetimes. The RR1000 alloy shows extremely damage-tolerant behaviour, with both specimens unbroken after 110000 cycles at 800MPa and 80000 cycles at 840MPa. No cracks were found on the RR1000 specimen tested at 800MPa, while for the RR1000 specimen tested at 840MPa one small crack was noted. The crack remained small and showed extremely slow, apparently transgranular, crack growth.

Test	Material	Stress level (MPa)	Test type	Lifetime (cycles)
1HS	U720Li	750	Runout	30424
4HS	U720Li	800	Runout	46086
2HS	U720Li	850	Runout	5754
3HS	U720Li	800	Replica	24494
10HS	U720Li	840	Replica	6909
6HS	U720Li	850	Replica	4709
8HS	U720Li-LG	840	Replica	66165
9HS	U720Li-LP	840	Replica	8044
5HS	RR1000 MO1751	800	Replica	>110000
7HS	RR1000 MO1751	840	Replica	>80000

Table 4-13: Summary of elevated temperature short crack test results.

4.4.2. Fractography

The overall fracture surfaces of the runout and replication tests are shown in Figure 4-40 with the arrows indicating primary crack initiation locations on the fracture surfaces. The fracture surfaces generally showed fairly uniform primary crack initiation and growth from the centre of the specimen with exception of Test 2HS (Figure 4-40c) where the primary crack initiated close to the edge (approximately 1mm from the edge) of the specimen. Note also the heavily oxidised fracture surface of the U720Li runout tests (1HS, 2HS and 4HS). These specimens were left in air at a temperature of 650°C for a few hours after they failed (between inspection intervals), whereas in the replication tests the temperature was switched off almost immediately after failure. This gives a less heavily oxidised fracture surface compared to the runout tests. The overall facture surface of the U720Li-LG replication test also appears to indicate a less oxidised fracture surface compared to fracture surfaces from U720Li and U720Li-LP replication tests.

Fractographic observations of the fracture surfaces are shown in Figure 4-41 to Figure 4-45. Porosity on or just below the surface was noted to be the main crack initiation mechanism in all the materials, and occasionally some cracks were also noted to initiate from subsurface porosity. Examples of primary crack initiation sites are shown throughout Figure 4-41 to Figure 4-45. The primary cracks of the U720Li and U720Li-LP replication tests were noted to initiate from porosity on or just below the surface as shown in Figure 4-42b, Figure 4-42h, Figure 4-42l and Figure 4-44b. For the U720Li-LG replication test, a subsurface pore was noted on the fracture surface near the primary crack initiation site as shown in Figure 4-43b which is believed to have aided crack initiation. The primary crack of the RR1000 840MPa replication test was noted to initiate from surface porosity as shown in Figure 4-45b. Examples of secondary crack initiation are also shown in Figure 4-42e where a secondary crack initiated from a subsurface pore and in Figure 4-42f where a secondary crack initiated from surface porosity. There was no distinct similarity between the crack-initiating pores in the materials as these pores were noted to be of various sizes and shapes.

Another feature that was observed on the notch root of the U720Li-LG specimen during the replication test is the occurrence of grain boundary oxidation leading to formation of cracks as shown in Figure 4-43g and Figure 4-43h. The oxide debris is visible on the surface and grain boundaries can be crudely resolved as darker lines in Figure 4-43g and Figure 4-43h. Oxide debris was also noted on the top surface of the primary crack in U720Li-LG test shown in Figure 4-43i and Figure 4-43j, leading to the conclusion that primary crack initiation is in part due to grain boundary oxidation leading to crack initiation in addition to the effect of the subsurface pore noted in Figure 4-43b. The oxide debris on the top surface of the primary crack of the U720Li-LG replication test was noted very early during the test and is not due to subsequent oxidation of the material after the crack has initiated. Further evidence supporting crack initiation from both the

subsurface pore and grain boundary oxidation on the surface for the U720Li-LG replication test is the appearance of the ligament-like feature between the surface and the subsurface pore where the cracks due to both initiation mechanisms may have coalesced. The occurrence of grain boundary oxidation leading to crack initiation was rarely observed in other materials. Oxide debris due to grain boundary oxidation has been noted in other materials but they usually appear during crack propagation near or around the crack tip after the crack has initiated due to other sources e.g. surface/subsurface porosity.

Immediately after crack initiation from a pore the crack path appears flat, indicative of a transgranular stage II crack growth mechanism. The flat region is obvious from the low magnification images of the primary crack initiation site in Figure 4-41 to Figure 4-44. For the same applied load levels (840MPa) in the tests, the flat region of U720Li-LG (Figure 4-43a) was noted to be distinctly larger than the flat area of U720Li-LP (Figure 4-44a) while U720Li tested at 840MPa (Figure 4-42g) shows the smallest flat area. However, as the primary crack in the U720Li-LG replica test is due to both the subsurface pore and grain boundary oxidation on the surface, some degree of flat transgranular crack growth would have occurred in vacuum for the crack which has initiated from the subsurface pore before it coalesces with the crack initiated on the surface by grain boundary oxidation, i.e. before the subsurface initiated crack breaks into air. There is very limited extent of transgranular crack growth in vacuum for both the U720Li and U720Li-LP replication tests at 840MPa as the pores which had initiated the primary cracks in the tests are on or extremely close to the surface.

In an attempt to quantify the extent of flat transgranular crack growth in *air* undergone by the materials, the dimensions of the crack initiation site features, i.e. the features of the crack-initiating pore and the features of the flat area were approximated from Figure 4-42 to Figure 4-44. The quantities measured are the size of the pore, the distance from the centre of the pore to the surface, and the distance from the centre of the pore to the edge of the flat area. For U720Li and U720Li-LP, the crack length corresponding to transgranular stage II crack growth in air is equal to the distance from the centre of pore to the edge of the flat area subtracted by the distance from the centre of the pore to the surface. When the pore is just below the surface as in the case of U720Li-LP, the distance from the centre of the pore to the surface can be regarded as the point when the crack initiated by the pore has broken the surface, i.e. this is also the distance from the centre of the pore to the point when crack growth in air commences in the depth direction.

In the case of U720Li-LG, the complexity associated with the primary crack initiation from two different mechanisms meant that the estimation of the extent of transgranular stage II crack growth in air is not as straightforward. For reasons that will become clear in section 4.4.4, the subsurface initiated crack is assumed to coalesce with the surface initiated crack when the half surface crack

length (c) of the surface initiated crack reaches approximately 30 μm. Before coalescence, the subsurface initiated crack propagated in a transgranular stage II crack growth mode in vacuum, and in the early stages after coalescence, the coalesced crack propagated in a transgranular stage II crack growth mode in air. The extent of flat transgranular crack growth in vacuum and air can then be estimated using the quantities measured earlier as shown in Figure 4-46. As the surface crack length corresponding to the point when the subsurface pore initiated crack coalesces with the surface initiated crack could only be approximated, the crack lengths corresponding to the transgranular crack growth in vacuum and air are also rough estimations.

The dimensions of the crack initiation site features are shown in Table 4-14. The results indicate that approximately 4-6 grains have to be traversed in air before intergranular crack growth modes are fully established.

Material	Size of pore (μm)	Distance from centre of pore to surface (μm)	Distance from centre of pore to edge of flat area (μm)	Crack length under stage II crack growth in air (μm)	Approximate number of grains traversed in stage II in air
U720Li	10	5	42	37	5.8
U720Li-LG	20	60	122	92	6.0
U720Li-LP	22	12	54	42	4.2

Table 4-14: Characterisation of crack initiation site features.

As crack length increases, the crack eventually adopts an oxidation-assisted intergranular crack growth mode. Fractographic observations of the crack growth at distances approximately 0.1mm and 0.2mm below the notch root are shown in Figure 4-41 to Figure 4-44. Predominantly intergranular crack growth was noted in U720Li (Figure 4-42) and U720Li-LP (Figure 4-44) at 0.1mm and 0.2mm below the notch root surface. In U720Li-LG however, crack growth was noted to be of a mixed transgranular/intergranular nature with increasing dominance of intergranular crack growth with increasing crack lengths. At depths of 0.5mm and 1.0mm below the notch root surface, distinctly flat areas corresponding to transgranular stage II crack growth were still observed on the fracture surface of U720Li-LG. The regions of flat area were noted to decrease in size with increasing crack depth.

The proportion of life spent in the flat transgranular crack growth regime (in vacuum as well as in air) before the onset of oxidation-assisted intergranular crack growth modes can be estimated from Table 4-14 and the short crack length measurements and number of cycles information obtained from acetate replica observations. The result of this estimation is shown in Table 4-15 together

with other relevant results and information from previous analysis. The number of cycles is estimated to the closest 500/1000 cycles when a replica of the top surface is taken for analysis.

Material	U720Li (Test 10HS)	U720Li-LG (Test 8HS)	U720Li-LP (Test 9HS)
Lifetime	6909	66165	8044
Crack length corresponding to flat crack growth area (c), (μm)	47	182	66
Number of cycles taken up in flat transgranular crack growth	2500	60000	3500
% life spent to the end of the flat transgranular crack growth	36.2	90.7	43.5

Table 4-15: Life spent in the flat crack transgranular growth regime in elevated temperature short crack tests.

The results shown in Table 4-15 indicate that approximately 40% of life is spent in the flat transgranular crack growth regime in U720Li and U720Li-LP, and the remainder of the life (~60%) is spent in the oxidation-assisted intergranular crack growth regime. For U720Li-LG however, approximately 90% of life was noted to be spent in the flat crack growth region, implying only a limited degree of mixed transgranular/intergranular crack growth modes beyond the flat area before catastrophic failure occurred.

4.4.3. Fatigue crack initiation

Crack initiation from surface porosity observed on fracture surfaces in the SEM was confirmed by surface replica observations. Crack initiation from subsurface pores was only noted on the surface replicas after these cracks break the surface. There was little or no evidence indicating slip band crack initiation in the tests.

An assessment of the crack field was also carried out for the high temperature short crack tests similar to the crack field characterisation carried out for room temperature tests. The assessment was carried out on replication tests of U720Li, U720Li-LG and U720Li-LP. Examination of the replicas was conducted at an interval of approximately every 20% of the total life to investigate the evolution of the crack field during the course of the short crack tests. For tests with extended lifetimes e.g. U720Li tested at 800MPa and U720Li-LG tested at 840MPa, replicas from the earlier part of the life between 1000 to 5000 cycles was also investigated to compare the number of cracks observed to tests which have lifetimes between 4000-7000 cycles.

The results of this assessment are shown for individual tests in Figure 4-47. The number of cracks was noted to generally increase with increasing number of cycles for individual tests. Occasionally the number of cracks was noted to decrease with cycling. This decrease should not be perceived as crack coalescence events as crack coalescence was rarely observed throughout the replica analysis for all the tests. The unexpected decrease in the number of cracks with cycling is attributed to possible errors associated with the analysis. The rounded nature of the replicas meant that the replicas are examined at 100x magnification in this analysis to enable a larger view of the replica to be obtained and at the same time to reduce errors associated with examining the relative locations on the replicas. This causes smaller cracks to be easily obscured by replica features of the etched microstructure on the surface of the notch root. To reduce this error, crack-like features or small hairline features resembling cracks are assumed to be cracks. This analysis would then provide an upper bound for the number of cracks expected for individual tests. A cubic polynomial trend line was fitted to the results of individual tests to allow trends of the crack field evolution to be demonstrated more clearly.

The results of the analysis for individual tests shown in Figure 4-47 indicates that cracks appeared very early in all the replication tests, i.e. on the first replica taken at 500 or 1000 cycles in all the tests. The crack initiation process appears to be very rapid early in the life before slowing down towards the middle of the life. Towards the end of the life (approximately 80-90% of life) the crack initiation process becomes rapid once again until failure. Note the significantly higher number of cracks for the U720Li-LG test as shown in Figure 4-47d. This is in part due to grain boundary oxidation on the surface leading to crack initiation as detailed in section 4.4.2. A high number of small cracks or crack-like features with oxide debris was noted on the replicas from the U720Li-LG test.

A comparison of the crack field evolution in all tests is given in Figure 4-48a. Detailed comparison of the crack field evolution in all tests from the start of the test to 10000 cycles from Figure 4-48a is shown in Figure 4-48b. Comparing the U720Li replication tests, crack initiation appears to be generally more rapid with increasing stress levels as expected. In terms of the replication tests conducted at 840MPa, U720Li and U720Li-LP appear to show approximately similar crack initiation rates, while U720Li-LG was noted to show much more rapid crack initiation. The rapid crack initiation in U720Li-LG will be in part due to grain boundary oxidation on the surface leading to the appearance of small cracks or crack-like features.

4.4.4. Short crack growth

Replica examination indicates that some of the cracks although initiated relatively early in the replication tests remained arrested until very near the end of the life (approximately 80-90% of life) before showing any sign of appreciable growth. Large numbers of small cracks which initiated towards the end of the life were also noted to grow very rapidly.

A plot of the crack length of the primary crack (most critical to failure) against the number of cycles for the U720Li replication tests at differing stress levels is shown in Figure 4-49a, and a similar plot to compare crack growth in the materials tested at 840MPa is shown in Figure 4-49b. Rapid crack growth is generally observed when the crack length reaches approximately 0.1mm-0.2mm. Figure 4-49a shows faster crack growth in U720Li with higher applied stress as expected. Figure 4-49b shows marginally slower crack growth in U720Li-LP compared to U720Li while U720Li-LG and RR1000 MO1751 show similar behaviour where crack growth was very slow in both materials in line with fatigue lifetime observations.

Crack growth rates are plotted against crack length in Figure 4-50a and Figure 4-50b. Only the primary crack was used for crack growth measurement due to the random crack growth nature of smaller secondary cracks. In Figure 4-50a, two distinct crack arrest points were noted from the 800MPa plot in line with the longer lifetime of the 800MPa test. Growth rates of U720Li at 840MPa appear approximately similar to the 800MPa test. However at 840MPa there are less crack arrest events at small crack lengths (up to 0.1mm) and this has contributed to the reduction in lifetime. At 850MPa crack growth is significantly faster than in the 800MPa and 840MPa tests, and this led to a further reduction in lifetime compared to the 840MPa test. In Figure 4-50b, the growth rates of U720Li at 840MPa are slightly higher than that of U720Li-LP, reflecting the relative fatigue lifetimes of the two materials. The highly scattered and slow surface growth of the cracks observed for U720Li-LG and RR1000 demonstrates the higher crack growth resistance of these two materials.

The scatter in the short crack growth rates of the surface crack observed for the U720Li-LG test may be related to the complex primary crack initiation process mentioned in section 4.4.2. The initially high crack growth rates at short crack lengths are followed by a sudden drastic drop in the crack growth rates when the half surface crack length is approximately 25 μm. This is thought to be the point when the plastic zones of the surface initiated crack and the subsurface pore initiated crack meet, the interaction of both leading to a slow down in the apparent crack growth of the surface crack. The crack growth rates increase slightly at a half surface crack length of approximately 30 μm which is assumed to correspond to the coalescence of the two cracks before marginally decreasing again possibly due to crack growth processes to attain a semi-elliptical crack shape. After the two cracks have fully combined to behave as a single large crack at a half surface crack length of approximately 40 μm, the crack growth rates were noted to be steadily increasing with increasing crack length.

For U720Li tested at 800MPa, two distinct arrest points at approximately 7000 cycles and 15000 cycles were noted on the crack growth rates plot. The sequences of crack propagation at these two arrest points are shown in Figure 4-51 and Figure 4-52. The arrows mark the approximate points

where the crack was arrested. The crack arrest may be due to possible crack bifurcation or due to oxidation near or ahead of the crack tip leading to formation of oxide debris (shown circled in Figure 4-51e and Figure 4-52e) which may act as barriers to crack growth. The oxidation appears to be aided by the stress field ahead of the crack tip. A mirrored image of the top surface of the primary crack on the fracture surface obtained in the SEM is shown in Figure 4-53. Figure 4-53 has been mirrored so that it has the same orientation as the replica images in Figure 4-51 and Figure 4-52. The particle-like features shown in the circles in Figure 4-51e and Figure 4-52e can be seen to be oxide debris on the top surface of the primary crack taken in the SEM.

To correlate short crack growth rates on a ΔK basis, the stresses estimated at the notch root were used in the empirical formula of Scott and Thorpe [89]. The stresses at the notch root were computed using finite element analysis with an ANSYS finite element package. Cyclically stabilised stress-strain curves at 650°C from strain-controlled high temperature LCF tests of the materials conducted at QinetiQ Farnborough were used as the materials model in the finite element analysis. Due to the lack of stress-strain curves from stress-controlled tests, the stress-strain curves from the strain-controlled tests were used. The cyclically stabilised behaviour of the materials in the strain-controlled tests should be analogous to the stabilised behaviour in stress-controlled tests. Cyclically stabilised stress-strain curves were only supplied for U720Li and U720Li-LG by QinetiQ, hence finite element analysis was not carried out for U720Li-LP. The cyclically stabilised stress-strain curves from the 1.2% strain-controlled tests were chosen to be used in the finite element models as the stresses generated at that particular strain level (1.2%) are closest to the stresses experienced in notch root of the short crack test specimens. Where necessary the cyclically stabilised stress-strain curves were also extrapolated to the UTS of the materials to enable notch root stresses higher that those obtained from the strain-controlled tests to be computed by the finite element model. At low stresses where the stress-strain curve is approximately linear, a linear function is fitted to the stress-strain curve. When the stress-strain curve starts to deviate from linearity, a cubic function was used to fit the stress-strain curve up to the extrapolated value of the UTS of the material. The stress-strain curve and the fitted stress-strain data used in the finite element model for U720Li are shown in Figure 4-54 as an illustration.

A non-linear analysis was carried out on a single monotonic loading step of the model with application of cyclically stabilised stress-strain data to take into account the elastic-plastic behaviour of the notched specimens. The single monotonic loading step using cyclically stabilised stress-strain data was believed to give a reasonable approximation of the stress and strain ranges achieved in the notch after cyclic hardening/softening had occurred. The finite element modelling was carried out on one half of the specimen due to symmetry of the specimen. The geometry of the model is shown in Figure 4-55. Symmetric boundary conditions were applied along the left edge of the model which is the axis of symmetry on the actual specimen. The model is meshed

appropriately with four-noded quadrilateral elements and loaded using point contacts to simplify computation.

Examples of the contours of the stresses in the x-direction (i.e. in the tensile axis direction) in the short crack test specimens are shown in Figure 4-56. The results of the finite element model show a strong stress gradient in the depth-wise direction from the notch root which is greater than the stress gradient expected from elastic beam theory for the uncracked ligament. It was thought that this strong stress gradient may invalidate the assumptions made by Scott and Thorpe [89] in the computation of ΔK. The stresses in the depth-wise direction from the finite element results were used to extrapolate the point when the stress is zero in the material, i.e. the neutral axis. It was found that the point of zero stress computed from the finite element results was much closer to the notch than that predicted from elastic beam theory. Elastic beam theory predicts the neutral axis to be at halfway of the actual specimen width, i.e. the width of the uncracked ligament in our case. However, calculation of the ΔK using the specimen width predicted by the finite element results (i.e. twice the distance of the point of zero stress from the notch root predicted by finite element results) and the actual specimen width yielded very similar ΔK values. The computation of the range of ΔK values in this work appear to be insensitive to the specimen width used for calculation and it was decided for subsequent ΔK calculations the actual width of the uncracked ligament could be used.

The crack growth rates of the U720Li and U720Li-LG tests are plotted against ΔK in Figure 4-57. The crack growth rates vs. ΔK curves of the U720Li tests are very similar to the crack growth rates against crack length curves shown in Figure 4-50a. When plotted on a ΔK basis, the crack growth curves of the U720Li tests appear to collapse closer into a single curve with scatter observed at low ΔK characteristic of short crack behaviour. The short crack growth rates of U720Li-LG were also plotted against ΔK in Figure 4-57. The crack growth rates of the U720Li-LG test appear to be random in the low ΔK regime before demonstrating a more uniform trend of increasing crack growth rates beyond a ΔK of approximately 8.0 MPa$\sqrt{m}$, which corresponds roughly to the coalescence of the subsurface pore initiated crack and the surface initiated crack. Beyond a ΔK of 8.0 MPa$\sqrt{m}$, corresponding to a half surface crack length of approximately 40 μm, the coalesced crack is assumed to have attained a semi-elliptical shape and is behaving as a single large crack. The crack growth rates of U720Li-LG after formation of the single primary crack are much lower than the corresponding crack growth rates observed for U720Li tested at the same stress level (Test 10HS) which is consistent with the relatively longer lifetime of U720Li-LG compared to U720Li.

Further comparisons of the fatigue lifetimes based on stress-range or strain-range were also made. The plots of fatigue lifetimes against stress-range, total equivalent strain range and equivalent

plastic strain range are plotted in Figure 4-58. The stress-range and strain-range data were obtained from finite element results and are subject to the accuracy of the stress-strain data used for the finite element models. Both the U720Li and U720Li-LG stress-range and strain-range were obtained using stabilised stress-strain curves from the 1.2% strain-controlled tests hence comparisons of the stress-range and strain-range data of the two materials will be consistent. Figure 4-58a indicates that for the same applied stress level of 840MPa, the notch root stresses in U720Li-LG are much lower than that of U720Li. The comparison of lifetime on a stress-range basis in Figure 4-58a appear to suggest that U720Li and U720Li-LG would show similar lifetimes for a given notch root stress-range. In terms of strain range, Figure 4-58b and Figure 4-58c indicates that for the same applied stress level of 840 MPa, both the equivalent total strain and equivalent plastic strain is much greater for U720Li-LG compared to U720Li. A comparison of the lifetime based on both equivalent total strain-range and equivalent plastic strain-range indicates significantly longer lifetime of U720Li-LG compared to U720Li for the same equivalent total strain-range and equivalent plastic strain-range in the notch root.

4.4.5. Summary

High temperature short crack runout and replication tests using polished U-notch specimens have been carried out at 650°C in air using a 1-1-1-1 cycling waveform on the test materials. Stress levels between 750MPa and 850MPa (in the uncracked ligament) were applied in the tests. Crack initiation was primarily observed to be due to porosity on or near the surface as well as due to grain boundary oxidation. Initial transgranular crack growth across 4-6 grains in air was noted at short crack lengths before oxidation-assisted intergranular crack growth modes were established at larger crack lengths. At 840MPa, U720Li and U720Li-LP show approximately similar fatigue lifetimes while U720Li-LG and RR1000 demonstrate significantly improved fatigue performance. Larger grains were noted to give improved crack growth resistance in U720Li and its variants.

4.5. High temperature long crack tests

4.5.1. RR1000 high temperature vacuum tests

The growth out curves of the RR1000 vacuum tests are shown in Figure 4-59. Two tests were carried out for the 725°C 1-1-1-1 condition as the first test was not extended to a high enough ΔK to allow for a definitive comparison with other test conditions. During the 725°C 1-20-1-1 test, the crack constantly arrested at low ΔK levels, and the applied loads had to be increased three times for crack growth to resume. This resulted in the test being extended to higher ΔK levels compared to other tests. At 650°C, the crack growth rates for the 1-1-1-1 and 1-20-1-1 tests appear very similar at low ΔK, but at higher ΔK the crack growth rates for both tests appear to diverge with the 20 seconds dwell test exhibiting lower crack growth rates with increasing ΔK. At 725°C, the crack growth rates for the 1-1-1-1 condition appear lower compared to the 1-20-1-1 condition in the intermediate ΔK range where the growth out curves of the two conditions overlap (after the crack in the 1-20-1-1 test resumed growing). At higher ΔK the crack growth rates of the 725°C 1-1-1-1 condition appear to converge to the crack growth rates of the 725°C 1-20-1-1 condition, with the 725°C 1-20-1-1 growth rates only marginally higher. Turning to the effects of temperature, it can be seen that in the 1-1-1-1 condition, the crack growth rates of the 725°C tests appear lower than that of the 650°C test. In the 1-20-1-1 condition, it appears there is little or no temperature effect, with both the 650°C and 725°C tests showing very similar crack growth rates.

The overall fracture surfaces of the vacuum tests are shown in Figure 4-60. All tests show fairly uniform crack growth from the notch with formation of shear lips when approaching monotonic failure. Pronounced shear lips were formed in the 725°C 1-20-1-1 test. Compared to other fracture surfaces of RR1000, the fracture surface from the 650°C 1-20-1-1 test appears brown. This is thought to be due to oxidation after the termination of the test as good vacuum levels (in the order of 10^{-5} mbar) were typically recorded throughout the test, similar to all other tests. The specimen in the 650°C 1-20-1-1 test has collapsed under the high loads used nearing the end of the test as the crack grew beyond the critical length, leaving the fracture surface fully exposed. This may have led to an increased ease of oxidation of the fracture surface.

The fracture surfaces including sectioned fracture surface observations from the vacuum tests are shown in Figure 4-61 to Figure 4-64. The fracture surfaces of both the 650°C 1-1-1-1 and 1-20-1-1 tests show flat and featureless surfaces at low ΔK, typical of transgranular stage II crack growth. At higher ΔK, both the 1-1-1-1 and 1-20-1-1 tests still exhibit transgranular crack propagation with marginal increase in the roughness of the fracture surface (comparing Figure 4-61c with Figure 4-61d and Figure 4-62c with Figure 4-62d). Overall the 1-20-1-1 fracture surface appears slightly rougher than the 1-1-1-1 fracture surface, as seen when comparing Figure 4-61c with Figure 4-62c and Figure 4-61d with Figure 4-62d.

In the 725°C 1-1-1-1 condition, the fracture surface at low ΔK shown in Figure 4-63a and Figure 4-63c is flat and featureless, again indicating a transgranular crack propagation mode. At higher ΔK, the crack propagation mode is predominantly transgranular, again with increased roughness of the fracture surface observed (comparing Figure 4-63c and Figure 4-63d). Overall, the 725°C 1-1-1-1 fracture surface appears very similar to the 650°C 1-1-1-1 and 1-20-1-1 fracture surfaces in terms of crack propagation mode, with the distinction being the roughness of the fracture surfaces observed.

In the 725°C 1-20-1-1 condition, it should be noted that higher loads were used, hence the fracture surface images were captured at higher ΔK levels compared to other tests. In this condition, the crack propagation mode at intermediate ΔK appears to be mixed transgranular/intergranular. Roughness of the order of the grain size (indicating intergranular crack growth) and small regions of flat and featureless areas (indicating transgranular crack growth) were noted on the fracture surface in Figure 4-64a. At higher ΔK, an increased degree of intergranularity is shown. Figure 4-64b indicates most areas on the fracture surface to be covered by roughness of the order of the grain size. This transition can also be seen from Figure 4-64c and Figure 4-64d, where at intermediate ΔK the crack profile is of mixed transgranular/intergranular crack propagation, but at higher ΔK a predominantly intergranular crack profile is exhibited.

Occasionally, secondary cracks can also be seen on the fracture surface of the 725°C 1-20-1-1 test at high ΔK (>35 MPa$\sqrt{m}$) but were not found in the 725°C 1-1-1-1 tests. Overall the 725°C 1-20-1-1 test was noted to have a more intergranular appearance compared to the 725°C 1-1-1-1 tests at the same ΔK level.

4.5.2. Effect of thermal exposure during fatigue testing on coherent γ' sizes

The coherent γ' precipitate morphology in nickel-base superalloys has been known to change with prolonged exposure to high temperatures [4,31]. This may lead to changes in slip deformation behaviour, and as such to the crack propagation behaviour [32]. The observed effects of temperature and dwell may be explained by possible changes in the coherent γ' sizes in the material due to prolonged thermal exposure at the test temperature. To this end, carbon extraction replications were carried out on the specimens from Test 2 (725°C 1-20-1-1) and Test 4 (650°C 1-20-1-1) which experienced the longest exposures at the respective test temperatures to quantify the coherent γ' precipitate sizes in the materials. Details of the carbon extraction replica method are given in the experimental section. Figure 4-65 and Figure 4-66 are the low and high magnification images showing the secondary and tertiary coherent γ' precipitates respectively in the specimens. This can be compared with Figure 4-12 which shows the coherent γ' precipitates in as-received RR1000 MO1547 specimen. The results of the analysis are shown in Table 4-16 together with the

as-received RR1000 MO1547 results. A comparison of the secondary and tertiary γ' precipitates size distribution in the specimens is shown in Figure 4-67a and Figure 4-67b.

Material	Secondary γ' (nm)		Tertiary γ' (nm)	
	Average	Range	Average	Range
RR1000 MO1547 (as-received)	140	40-200	18	6-30
RR1000 Test 2 (725°C 1-20-1-1)	123	75-185	32	18-40
RR1000 Test 4 (650°C 1-20-1-1)	165	75-230	23	12-35

Table 4-16: Summary of coherent γ' sizes in tested specimens.

A comparison between Figure 4-12a and Figure 4-65a indicates that the number of tertiary γ' precipitates has significantly decreased after prolonged exposure at 725°C. Contrary to this observation the number of tertiary γ' precipitates appear to be similar or higher than the as-received condition after prolonged exposure at 650°C when comparing Figure 4-12a and Figure 4-66a. The number of secondary γ' precipitates in both cases does not appear to be significantly altered by the prolonged high temperature exposure.

Moving on to a comparison of the precipitate sizes, the secondary γ' precipitates appear to have decreased in size while the tertiary γ' precipitates, although lower in number, appear to have coarsened after exposure at 725°C. This observation is immediately obvious when comparing Figure 4-12 and Figure 4-65. In terms of the as-received RR1000 MO1547 and the specimen from Test 2 (650°C 1-20-1-1), both the secondary and tertiary γ' precipitates appear to have coarsened with elevated temperature exposure, with the coarsening of the secondary γ' precipitates being more marked.

4.5.3. RR1000 high temperature air tests

Elevated temperature tests on RR1000 in air at 650°C and 725°C under similar loading conditions were conducted by DERA/QinetiQ Farnborough. The growth out curves of the RR1000 air tests are shown in Figure 4-68. The m-values of the air tests were noted to be relatively similar.

At both test temperatures (650°C and 725°C), the RR1000 air tests exhibit higher crack growth rates with imposition of dwell. The increase in crack growth rates with imposition of dwell was more marked at 725°C compared to at 650°C. With an increase in test temperature, the crack growth rates of the air tests were also noted to be higher for a given cyclic waveform.

Fractographic analysis and sectioning work on the fracture surfaces of the RR1000 air tests were carried out at Southampton. The fracture surfaces and sectioned fracture surfaces are shown in Figure 4-69 to Figure 4-72. Evidence of secondary cracking was noted under all test conditions. The fracture surface from the 650°C 1-1-1-1 air test in Figure 4-69 appears to show evidence of mixed transgranular/intergranular crack growth at low ΔK with increasing degree of intergranular crack growth at higher ΔK. Relatively flat regions were noted on the fracture surface at low ΔK and the proportion of the flat regions was noted to decrease with increasing ΔK. The fracture surfaces from the 650°C 1-20-1-1 air test and both the 725°C air tests exhibit predominantly intergranular crack growth. The degree of intergranularity and surface roughness was noted to increase with increasing severity of the test conditions.

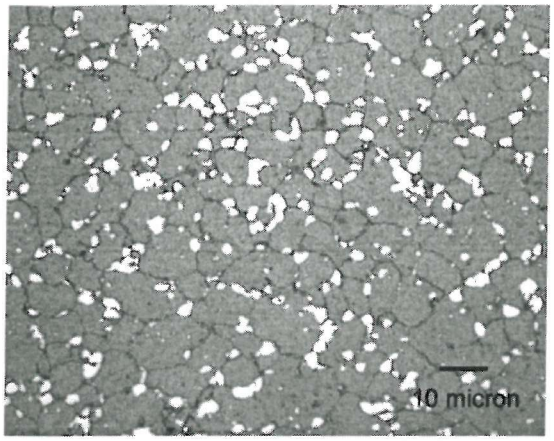

Figure 4-1a: RR1000 MO1547 microstructure (orthophosphoric etch).

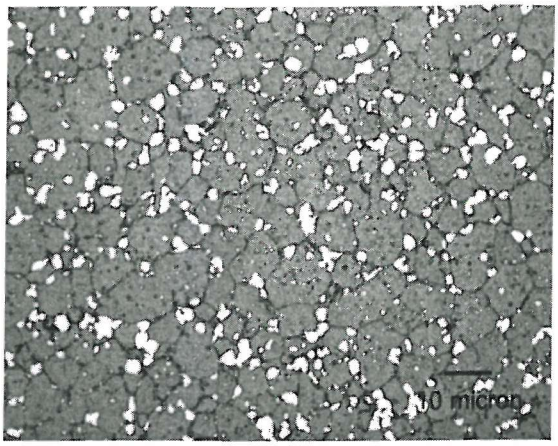

Figure 4-1b: RR1000 MO1751 microstructure (orthophosphoric etch).

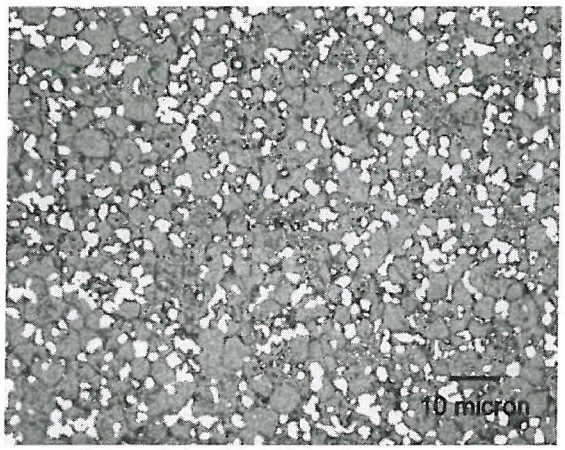

Figure 4-1c: U720Li microstructure (orthophosphoric etch).

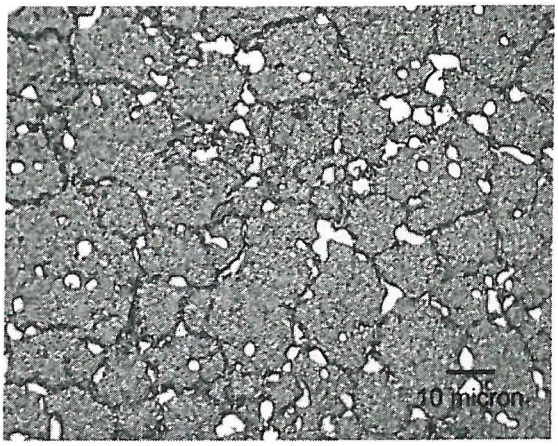

Figure 4-1d: U720Li-LG microstructure (orthophosphoric etch).

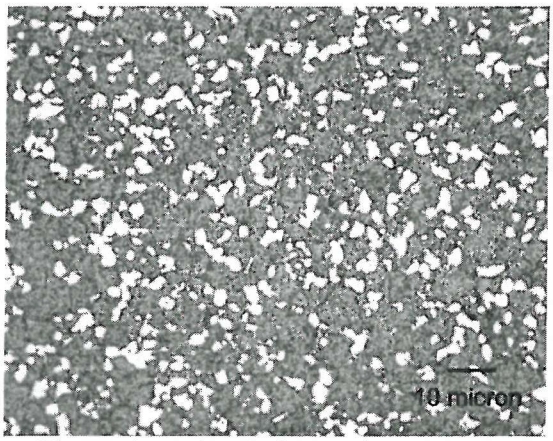

Figure 4-1e: U720Li-LP microstructure (orthophosphoric etch).

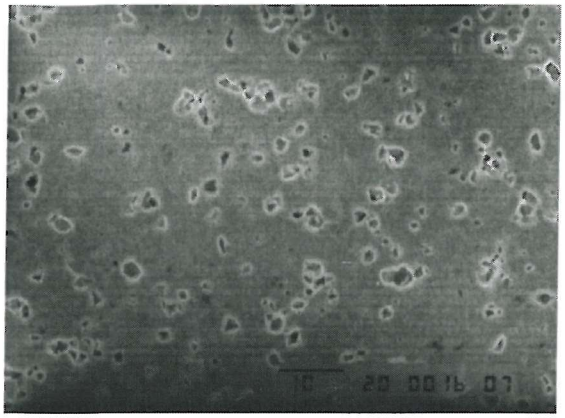

Figure 4-2a: RR1000 MO1547 microstructure (Fry's reagent).

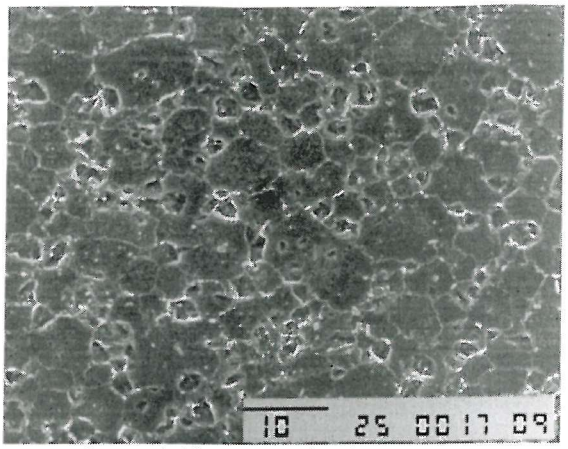

Figure 4-2b: U720Li microstructure (Fry's Reagent) [30].

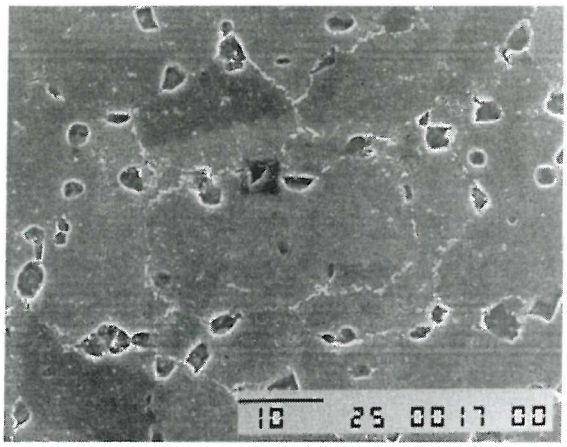

Figure 4-2c: U720Li-LG microstructure (Fry's Reagent) [30].

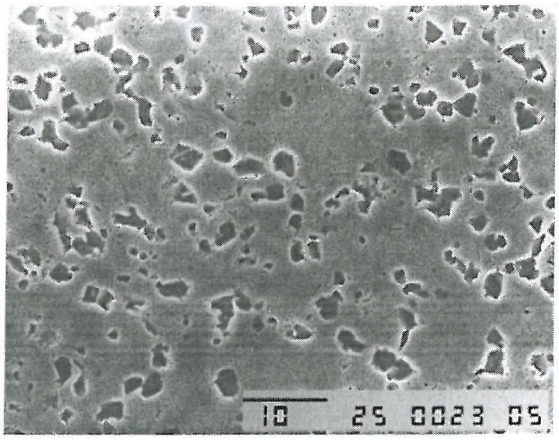

Figure 4-2d: U720Li-LP microstructure (Fry's Reagent) [30].

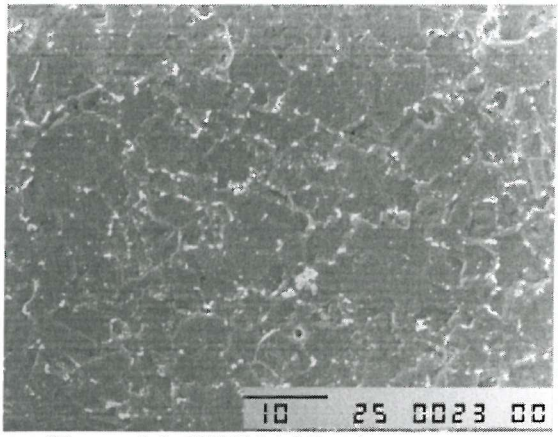

Figure 4-3: U720Li-LP microstructure (10%Br in Ethanol) [30].

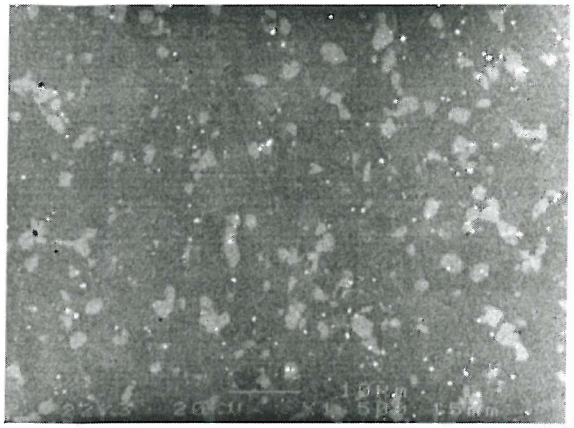

Figure 4-4a: RR1000 MO1547 microstructure (BEI).

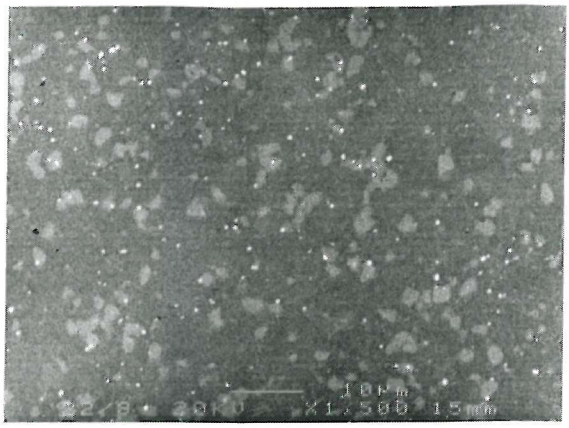

Figure 4-4b: RR1000 MO1751 microstructure (BEI).

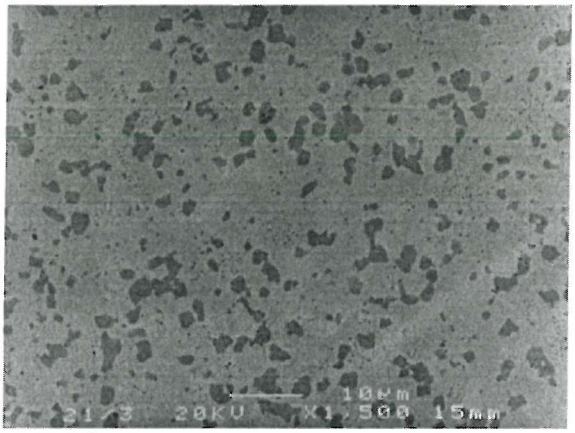

Figure 4-4c: U720Li microstructure (BEI).

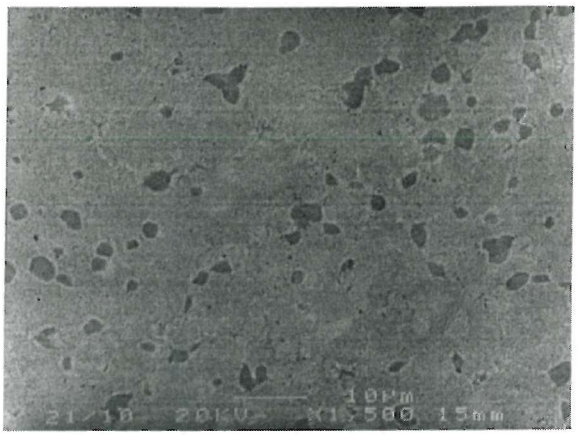

Figure 4-4d: U720Li-LG microstructure (BEI).

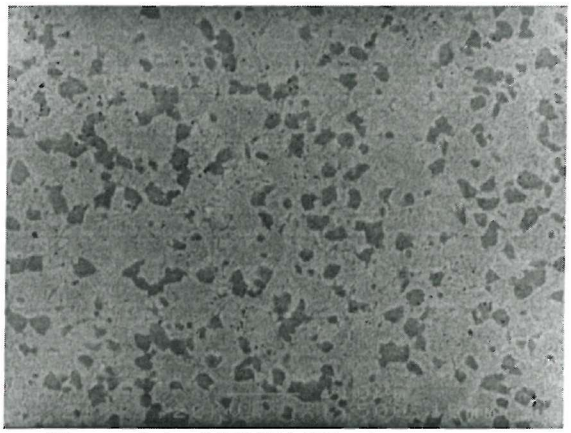

Figure 4-4e: U720Li-LP microstructure (BEI).

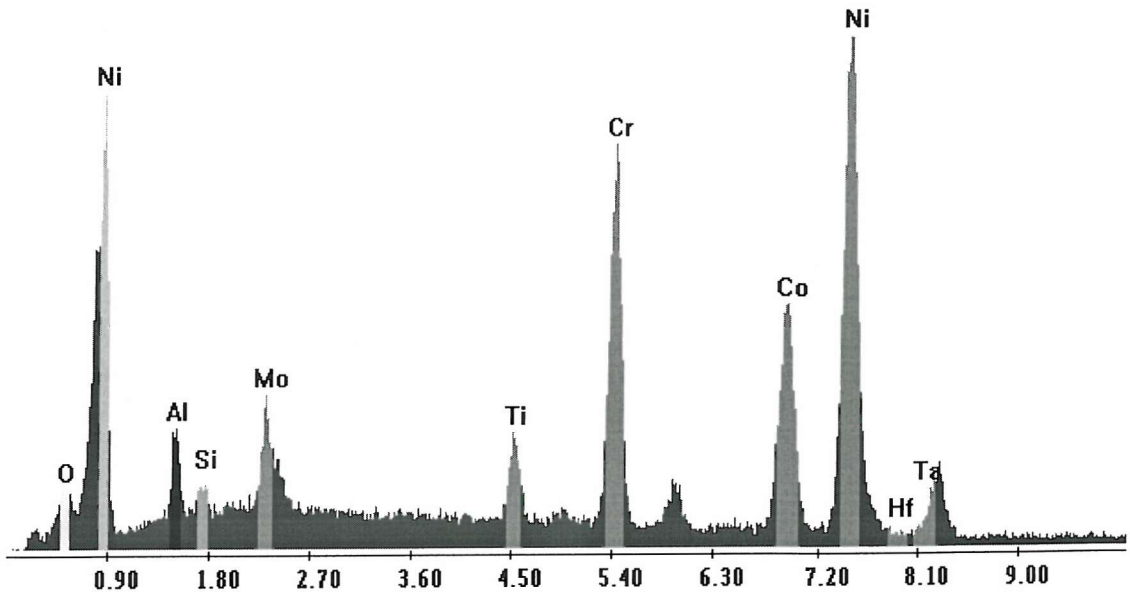

Figure 4-5a: RR1000 γ phase EDX analysis.

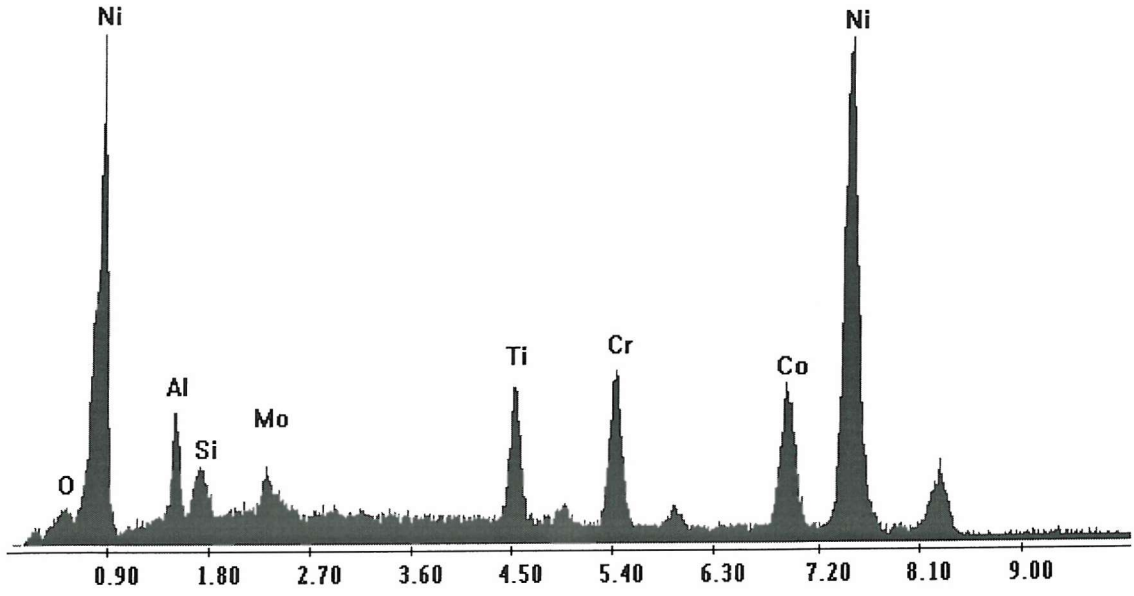

Figure 4-5b: RR1000 γ' phase EDX analysis.

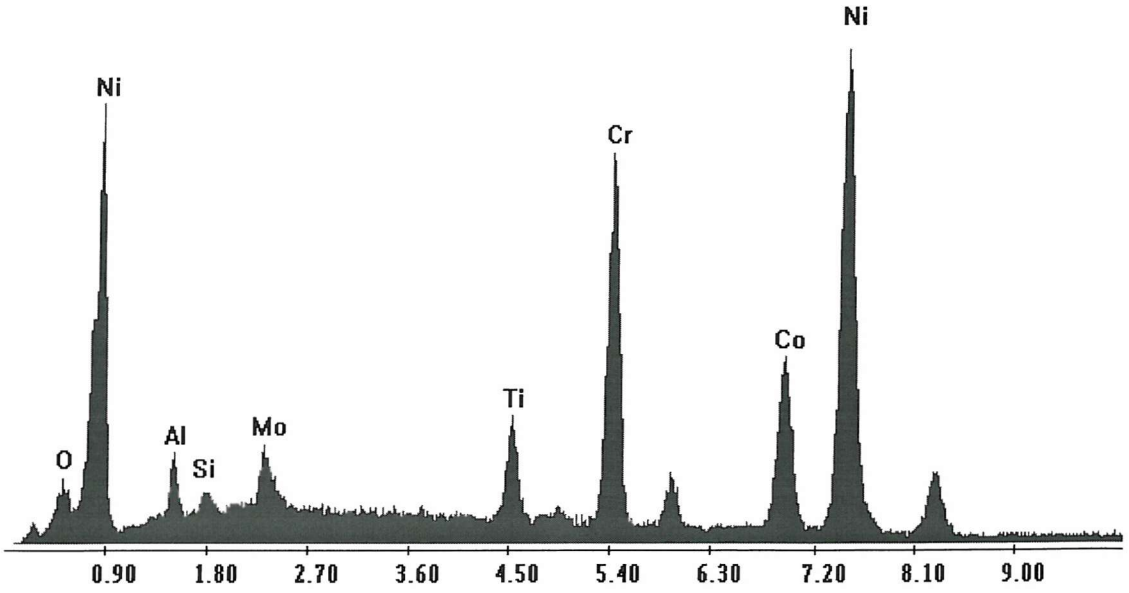

Figure 4-6a: U720Li γ phase EDX analysis.

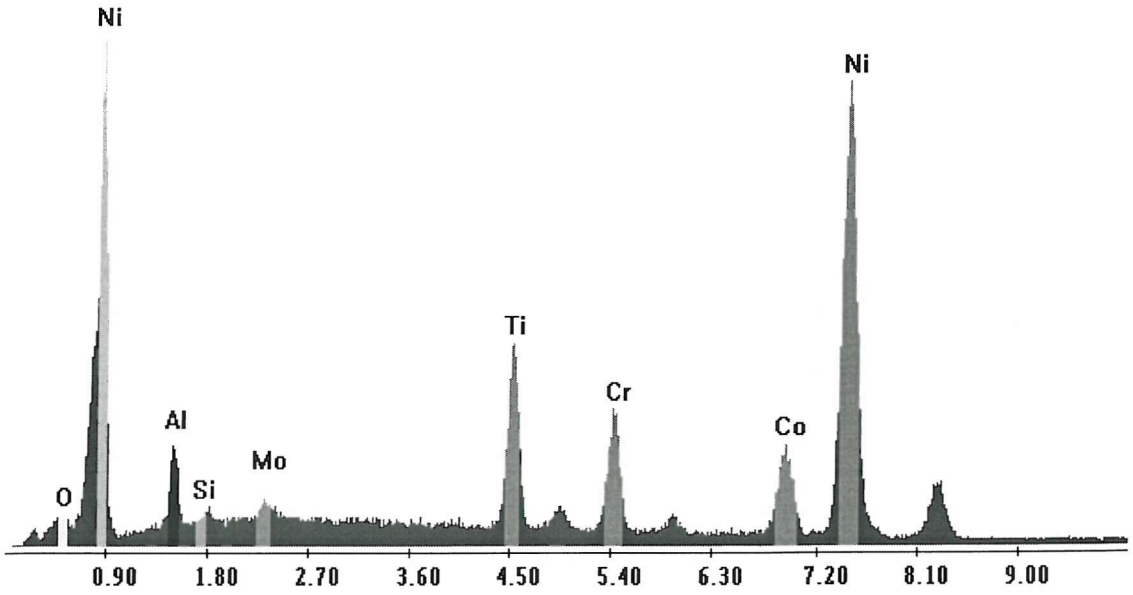

Figure 4-6b: U720Li γ' phase EDX analysis.

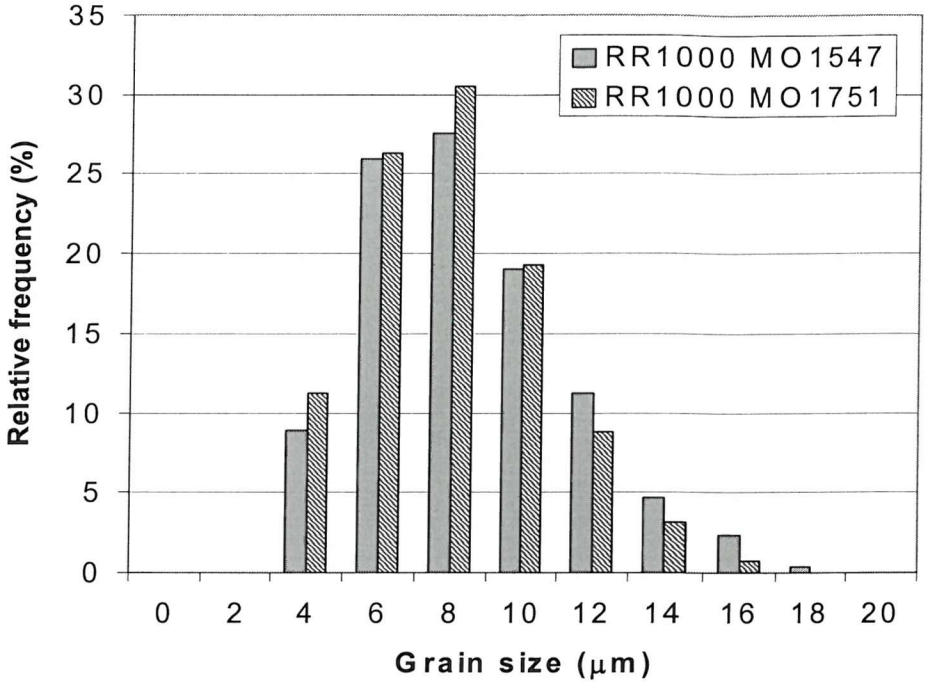

Figure 4-7a: Relative frequency of grain sizes (orthophosphoric etch).

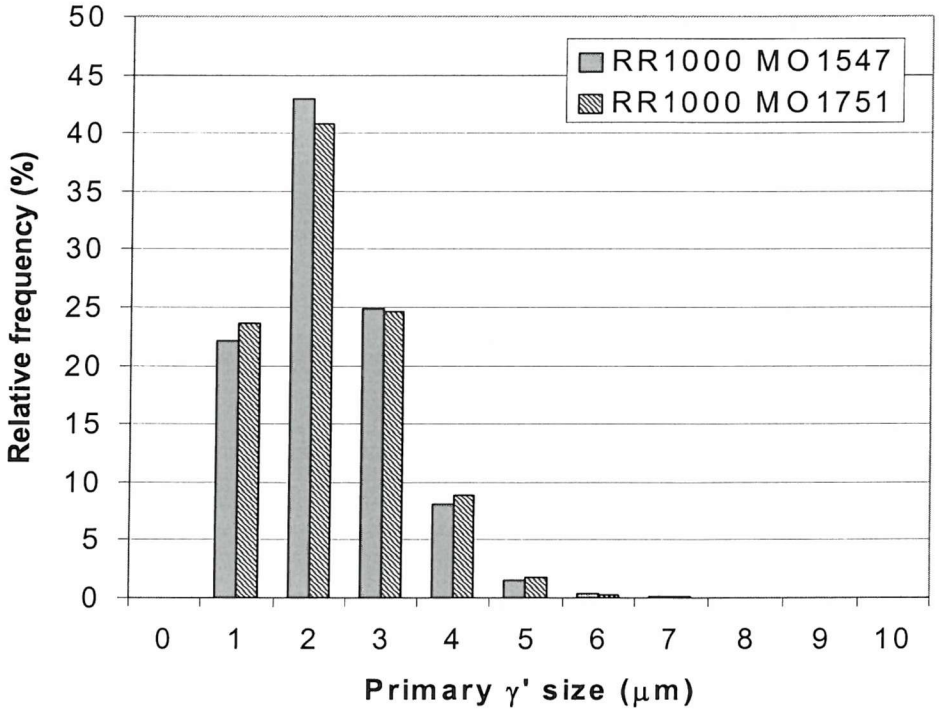

Figure 4-7b: Relative frequency of primary γ' sizes (orthophosphoric etch).

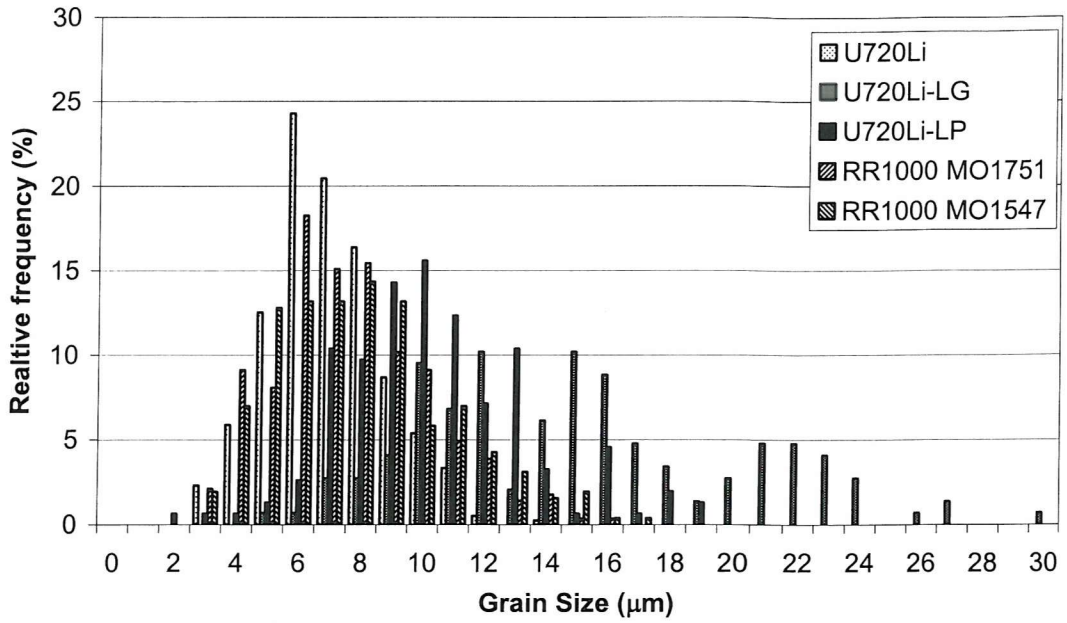

Figure 4-8a: Comparison of grain sizes in different material.

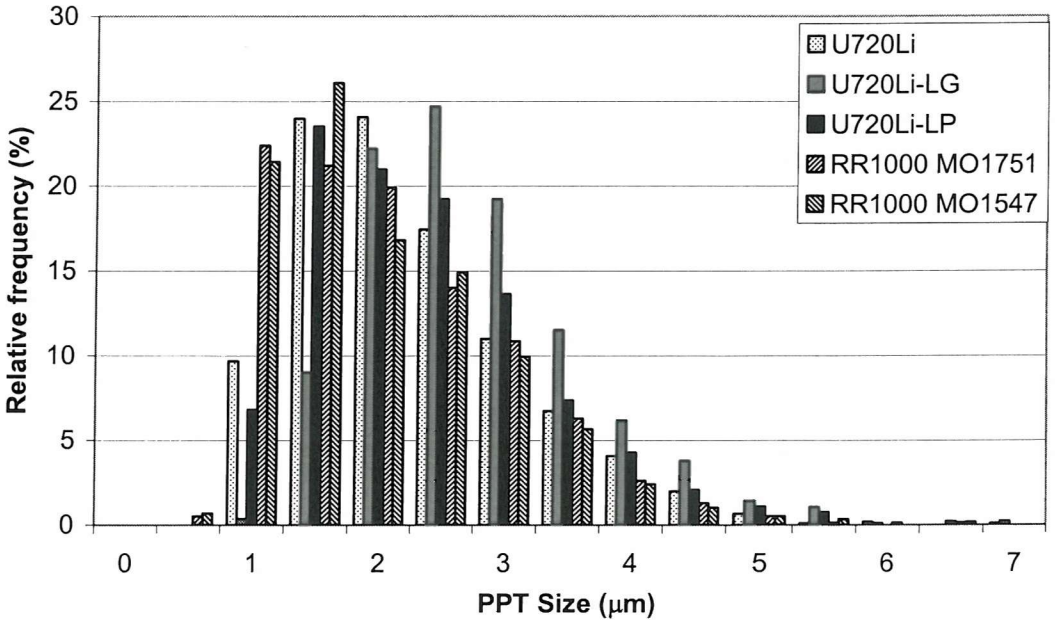

Figure 4-8b: Comparison of primary γ' sizes in different material.

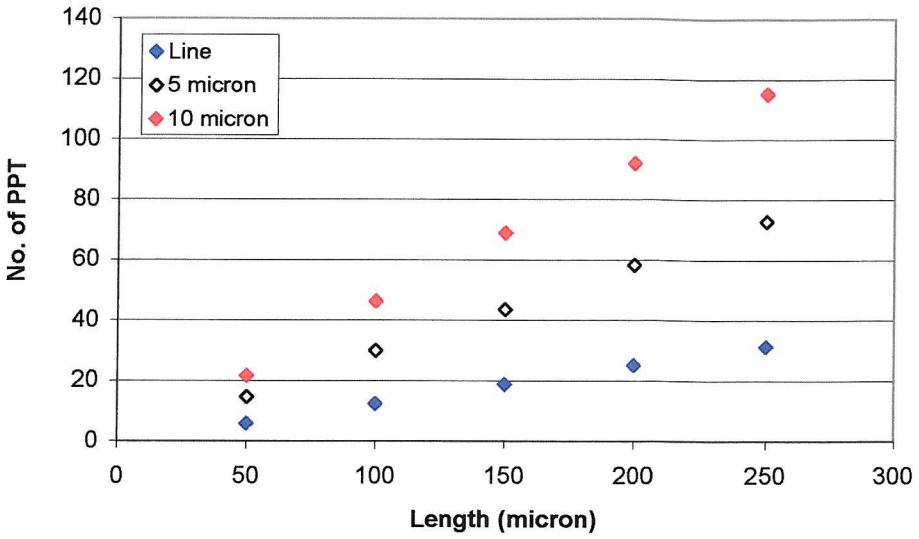

Figure 4-9a: Primary γ' line intercept counting; U720Li.

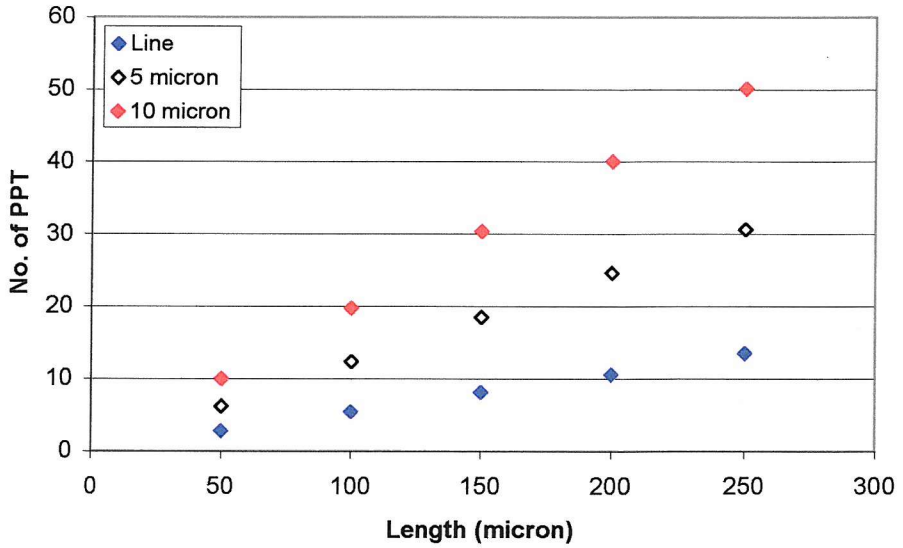

Figure 4-9b: Primary γ' line intercept counting; U720Li-LG.

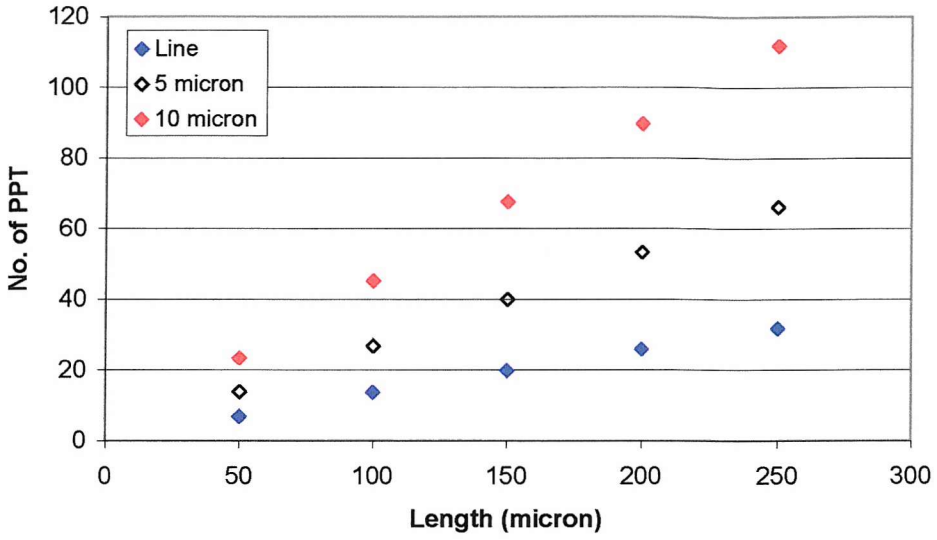

Figure 4-9c: Primary γ' line intercept counting; U720Li-LP.

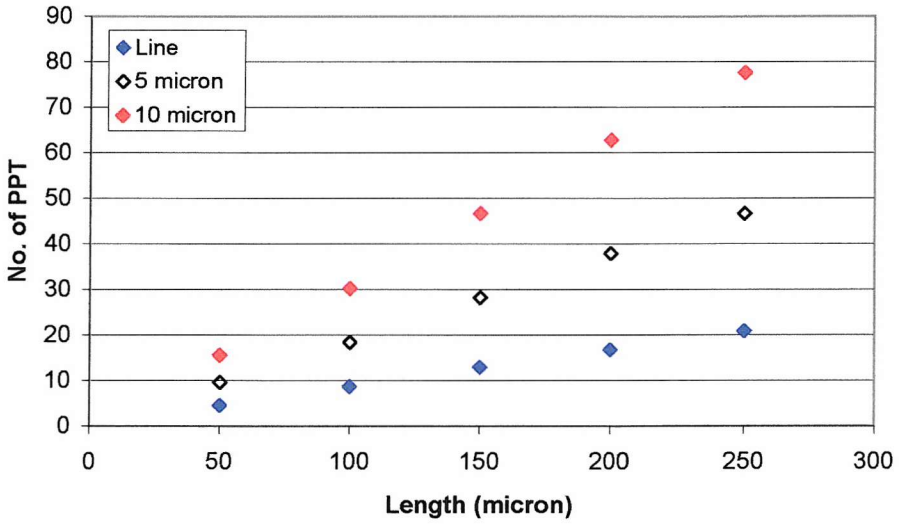

Figure 4-9d: Primary γ' line intercept counting; RR1000 MO1547.

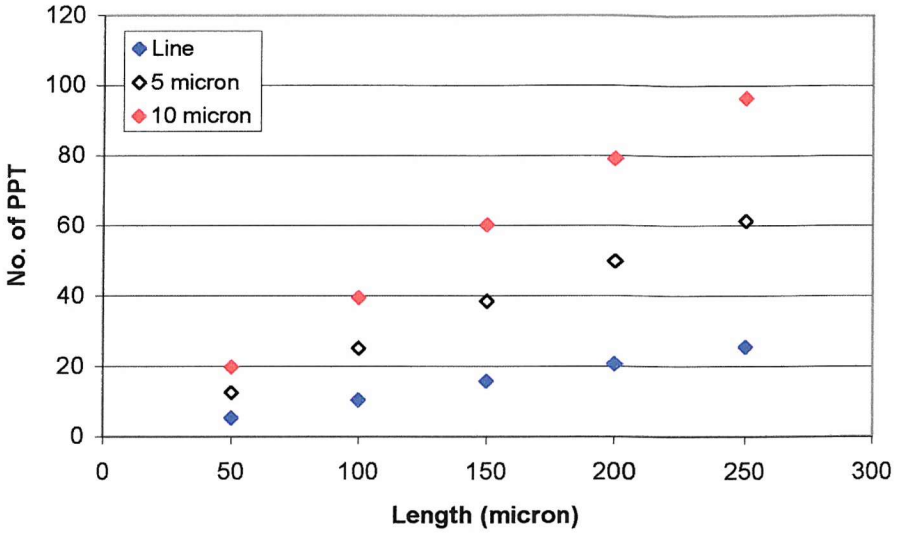

Figure 4-9e: Primary γ' line intercept counting; RR1000 MO1751.

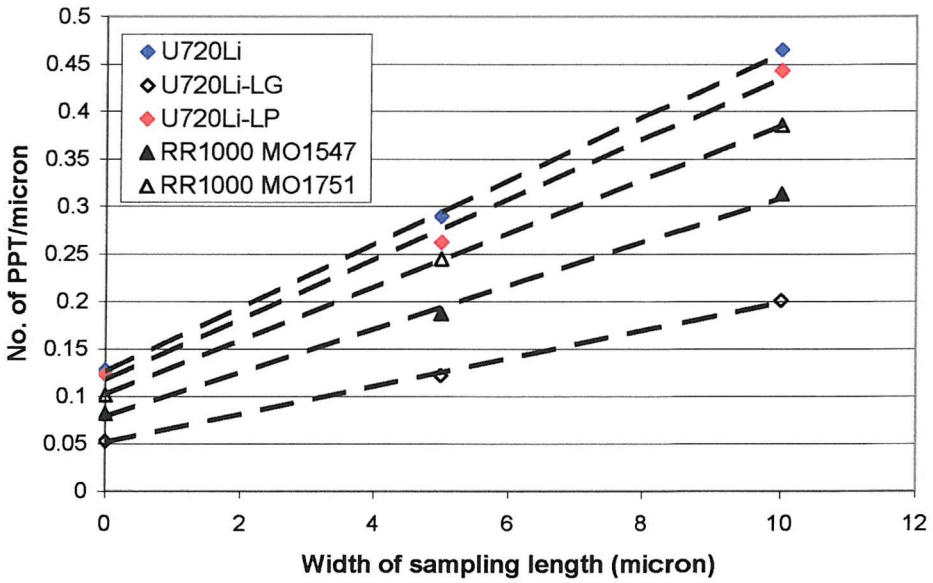

Figure 4-10: Number of precipitates expected per unit sampling length vs. width of sampling length.

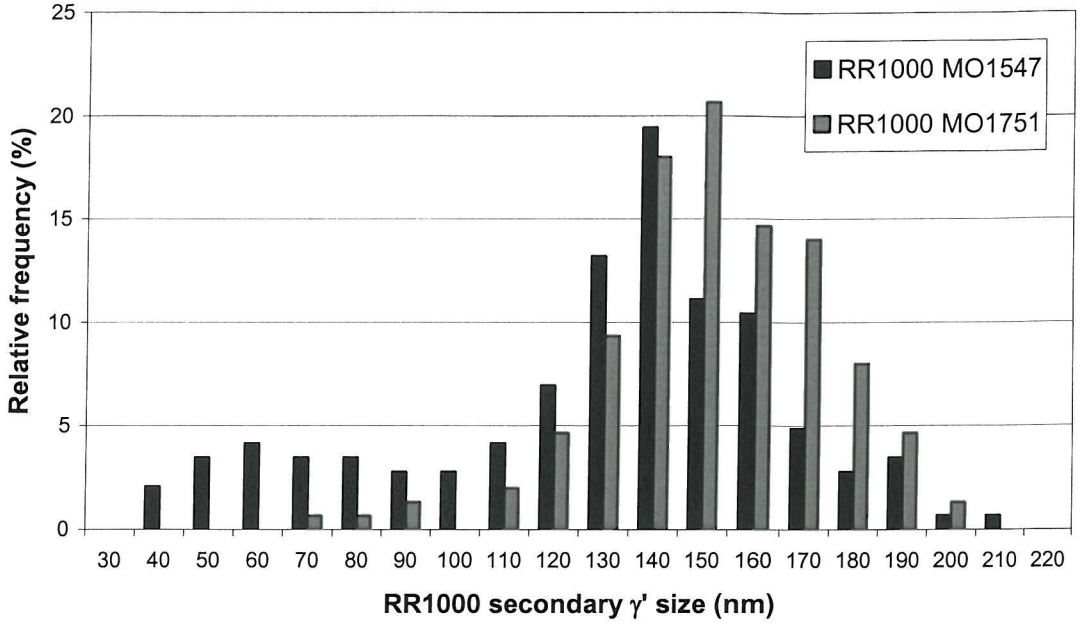

Figure 4-11a: Secondary γ' precipitate size distribution in RR1000 obtained from low magnification (x50000) images.

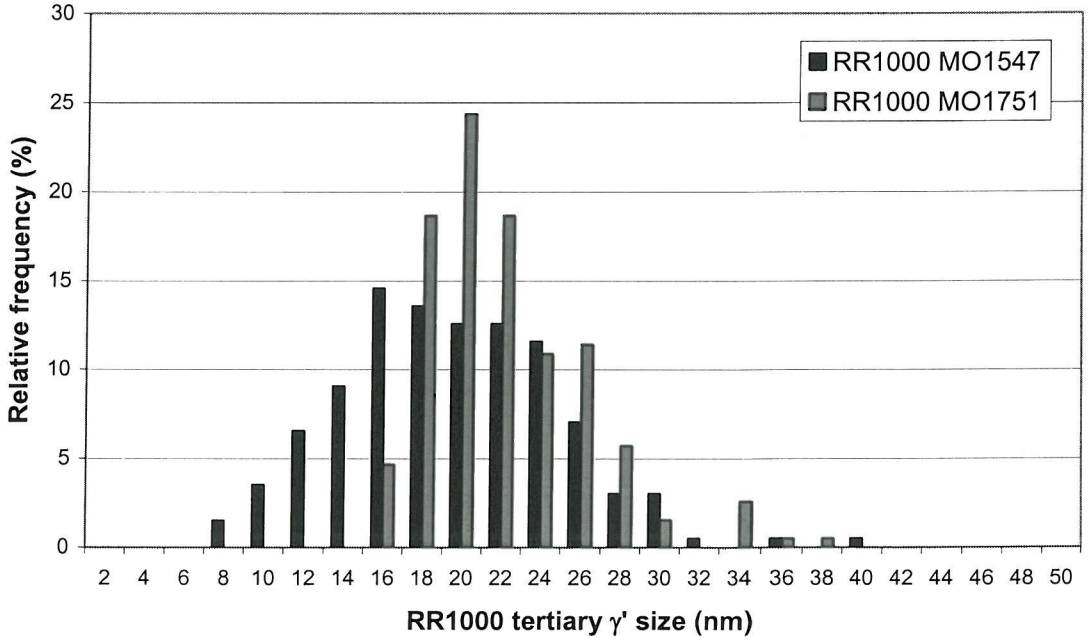

Figure 4-11b: Tertiary γ' precipitate size distribution in RR1000 obtained from high magnification (x200000) images.

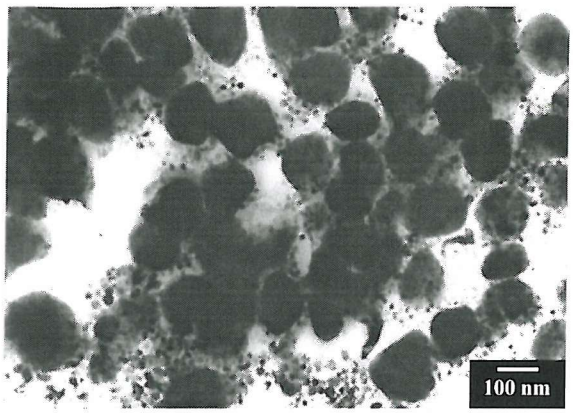

Figure 4-12a: RR1000 MO1547
(low mag x50000).

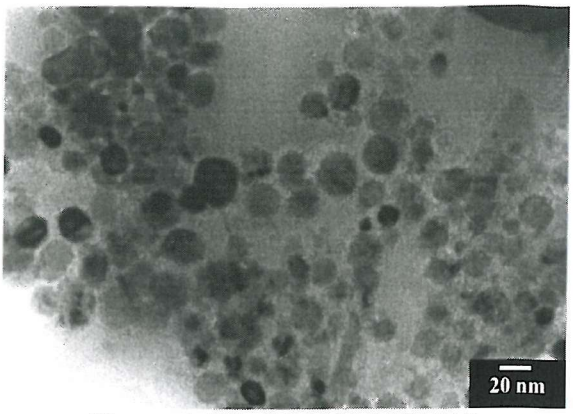

Figure 4-12b: RR1000 MO1547
(high mag x200000).

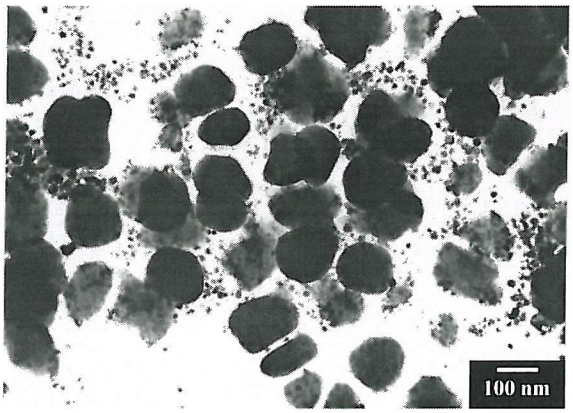

Figure 4-13a: RR1000 MO1751
(low mag x50000).

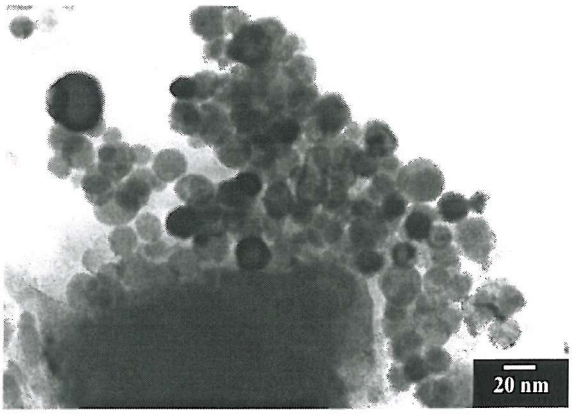

Figure 4-13b: RR1000 MO1751
(high mag x200000).

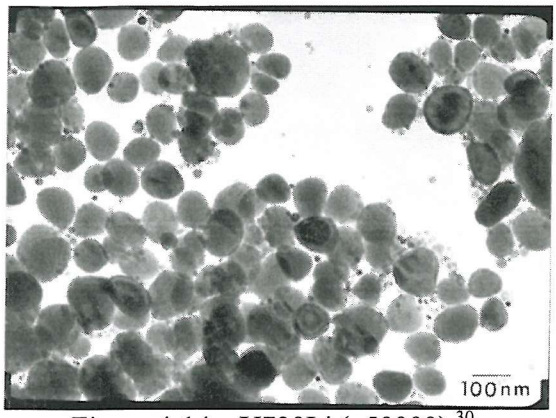

Figure 4-14a: U720Li (x50000) [30].

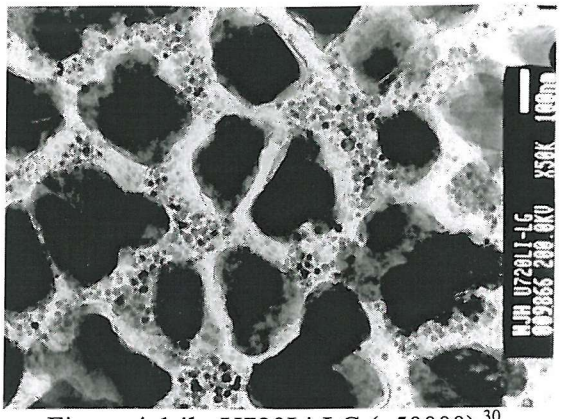

Figure 4-14b: U720Li-LG (x50000) [30].

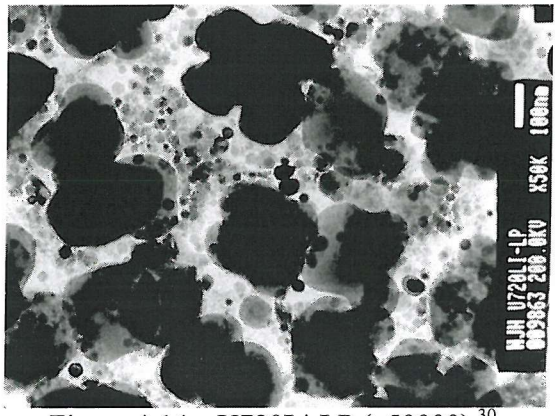

Figure 4-14c: U720Li-LP (x50000) [30].

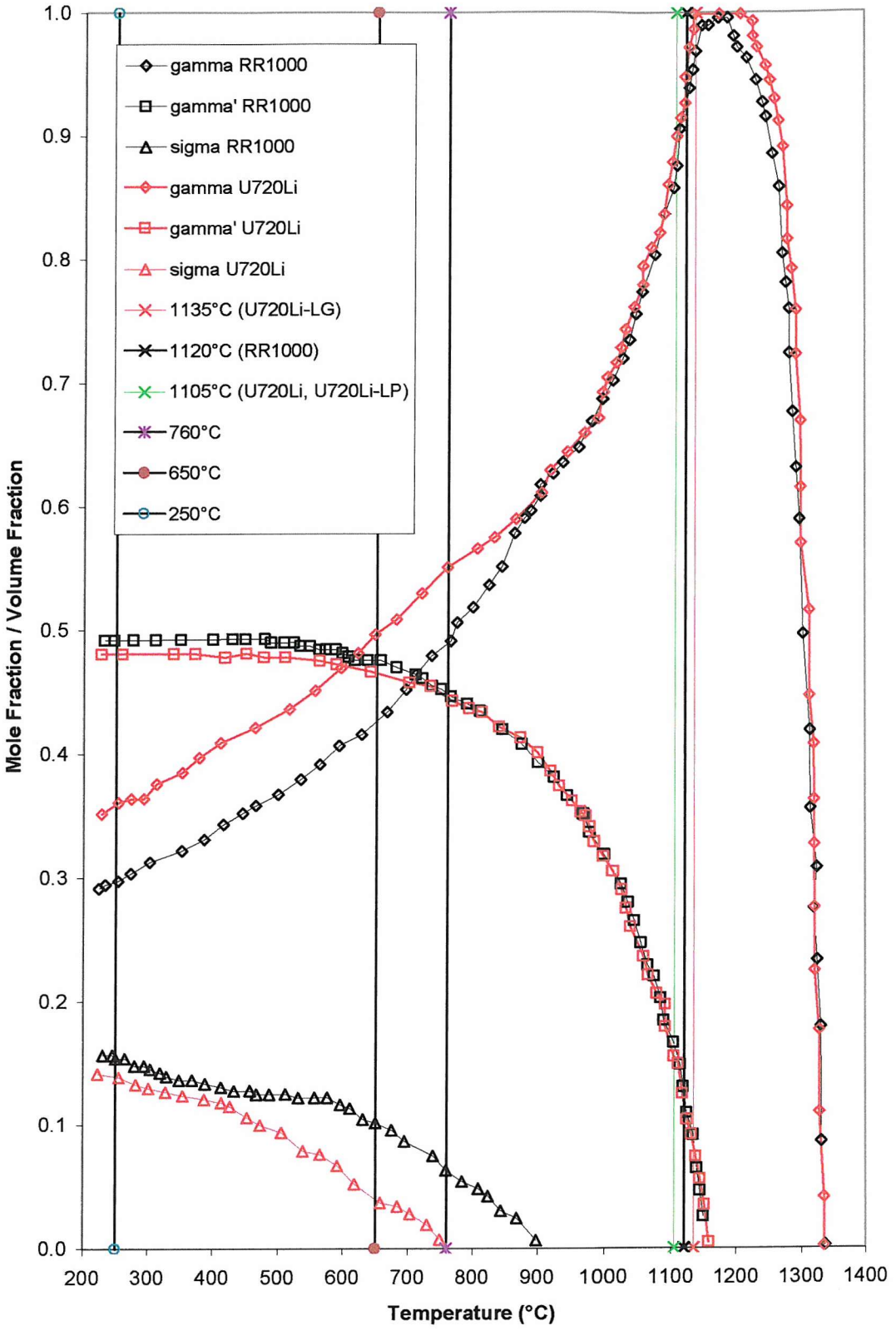

Figure 4-15: Thermo-calc prediction of phase distribution for U720Li and RR1000.

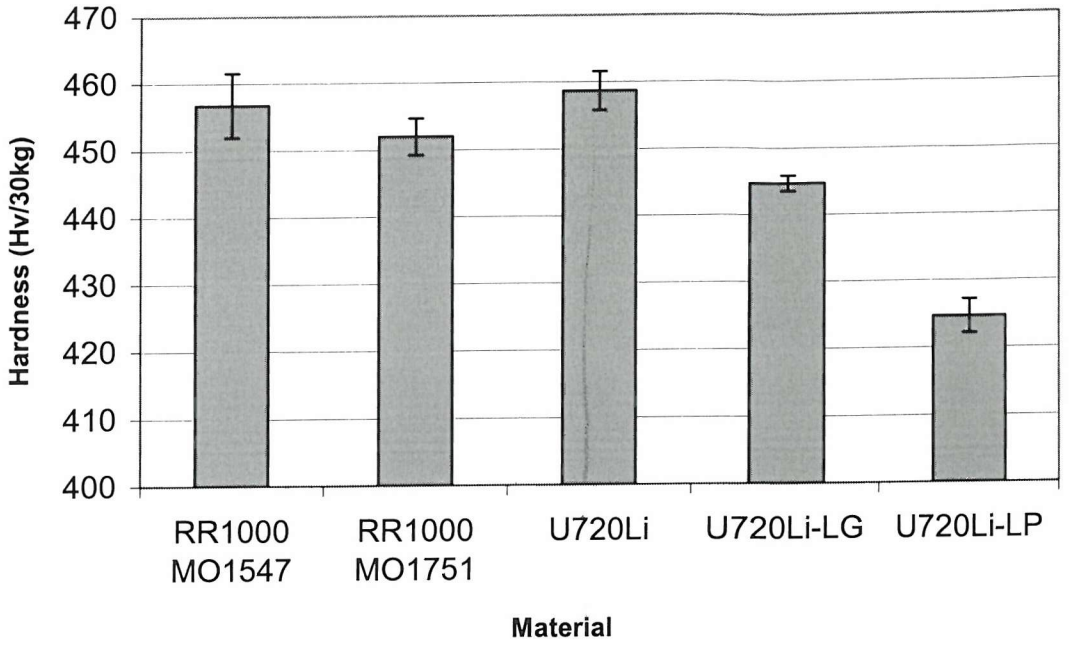

Figure 4-16: Comparison of hardness values of different alloys.

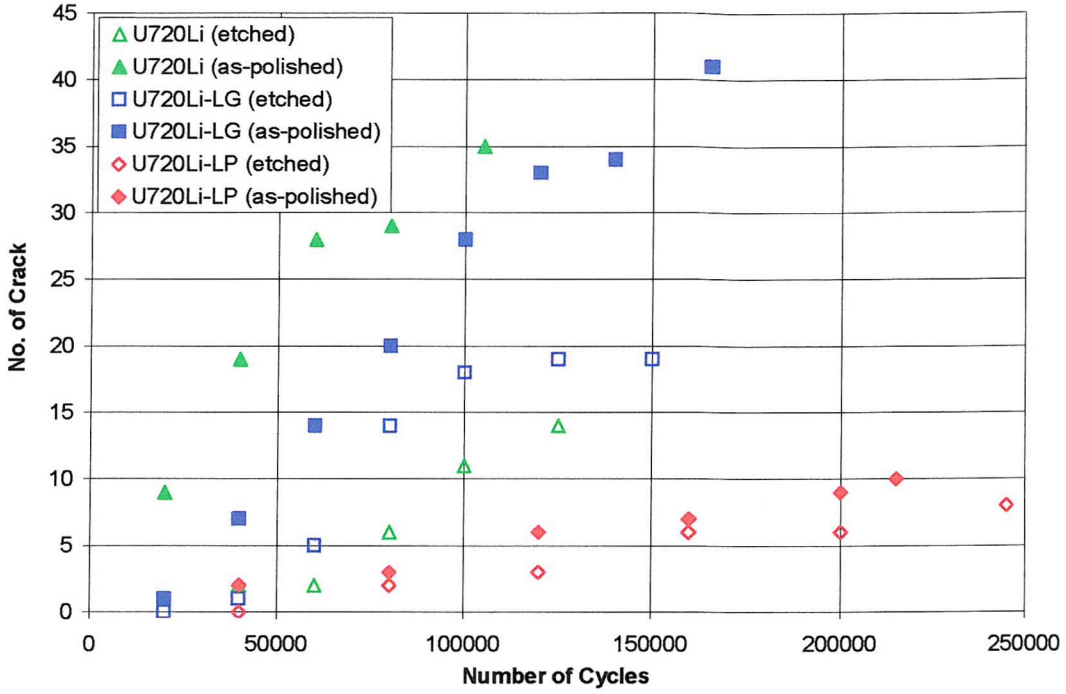

Figure 4-17a: Crack field characterisation; fatigue lifetime.

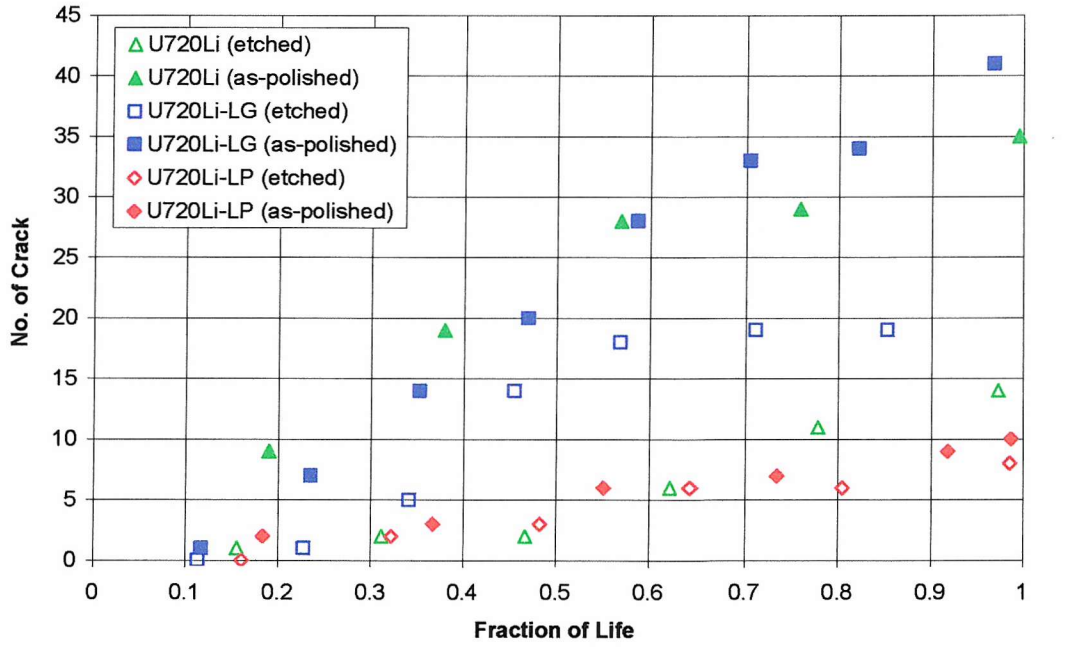

Figure 4-17b: Crack field characterisation; fraction of life.

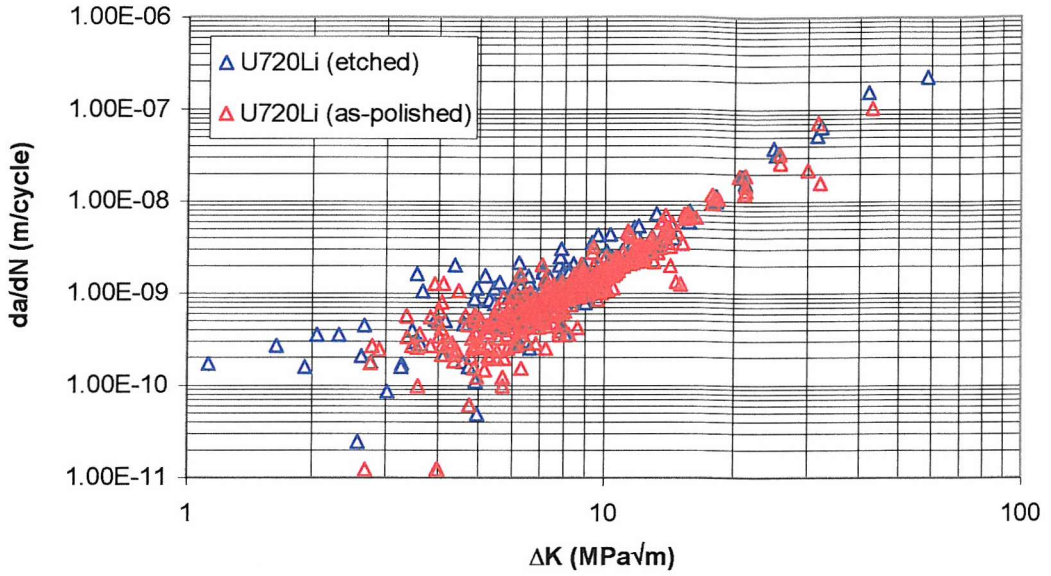

Figure 4-18a: U720Li short crack growth rate.

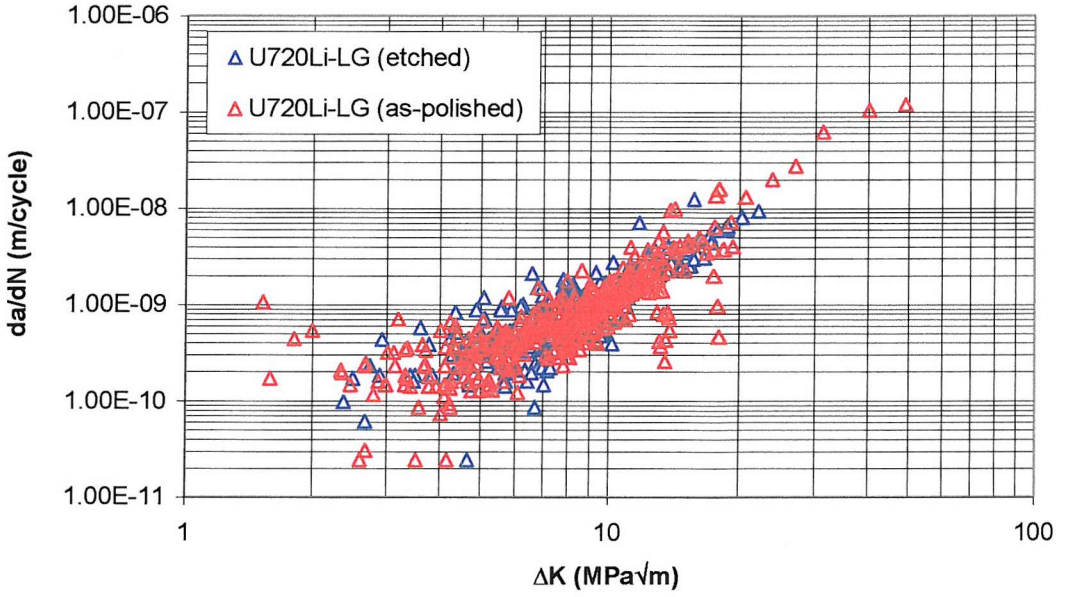

Figure 4-18b: U720Li-LG short crack growth rate.

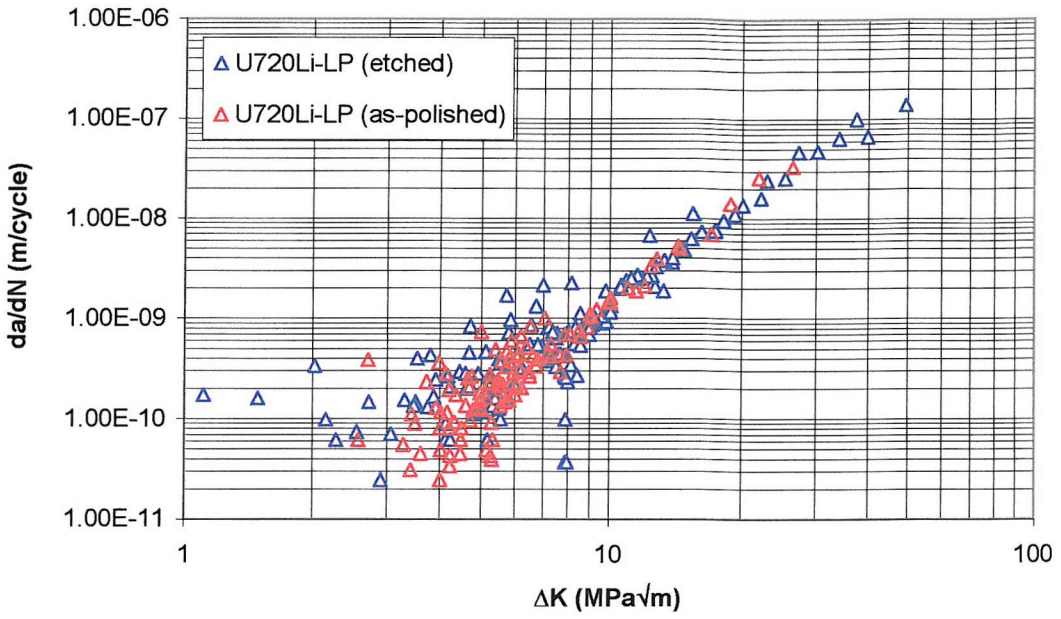

Figure 4-18c: U720Li-LP short crack growth rate.

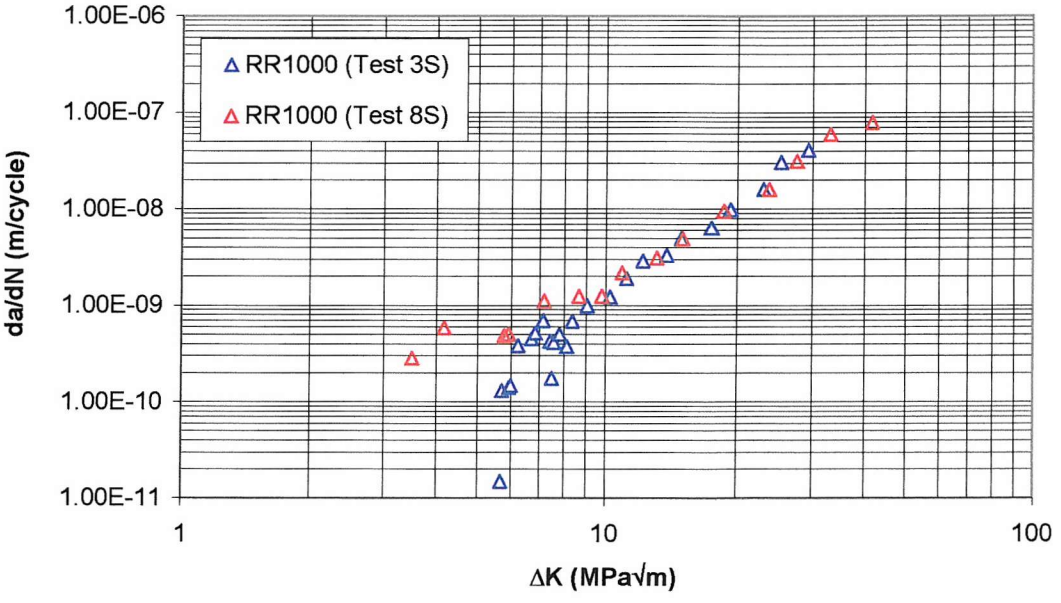

Figure 4-18d: RR1000 short crack growth rate.

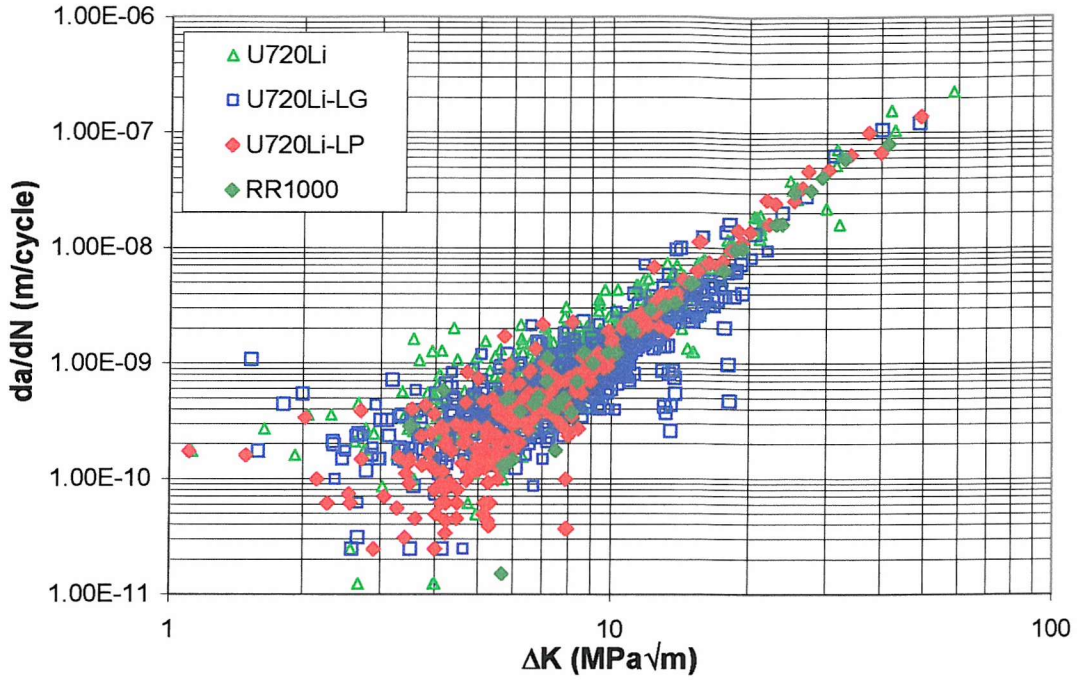

Figure 4-19: Overall short rate growth rates for materials under investigation.

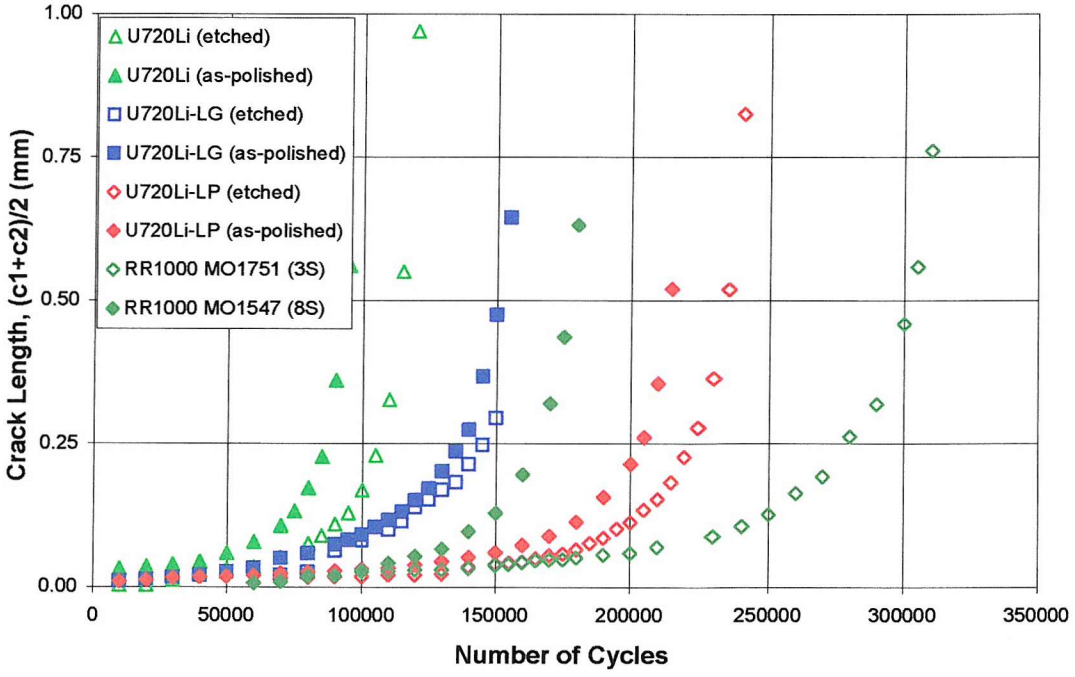

Figure 4-20: Crack growth of fastest growing crack in each test.

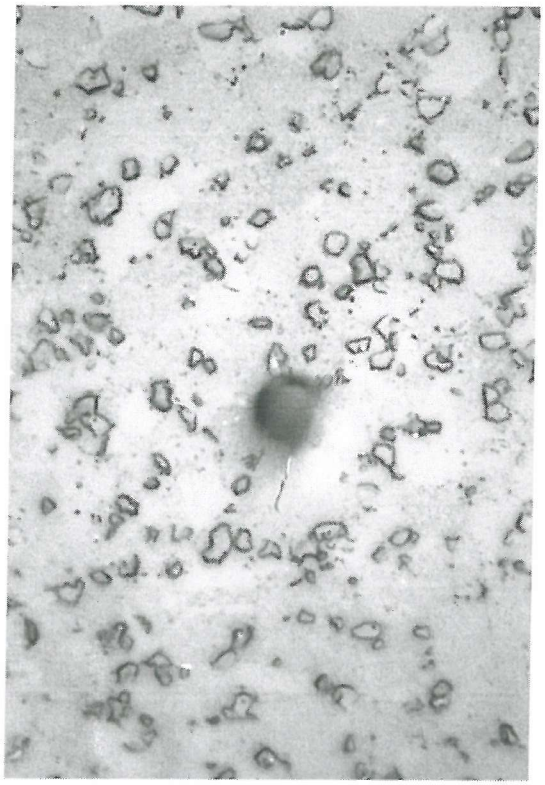

70000 cycles

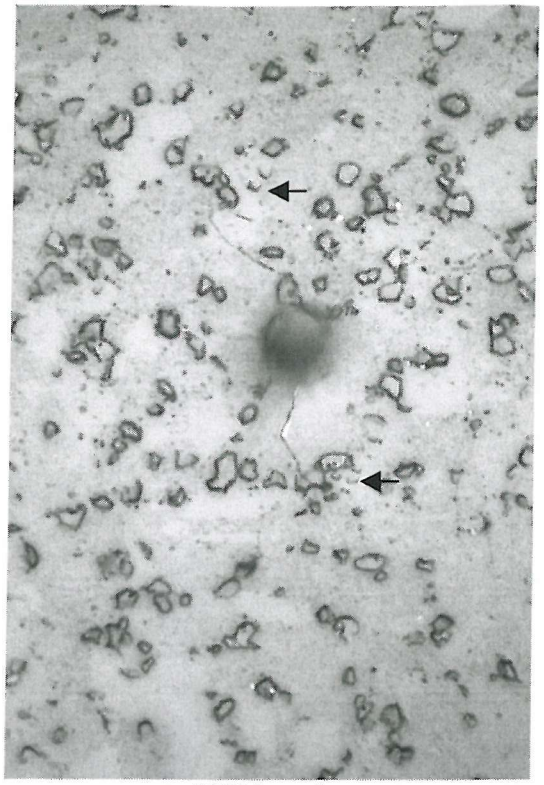

80000 cycles

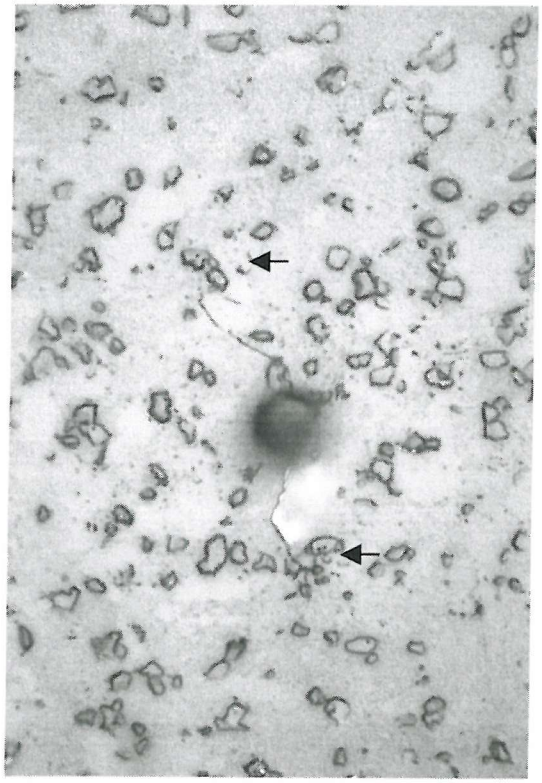

90000 cycles

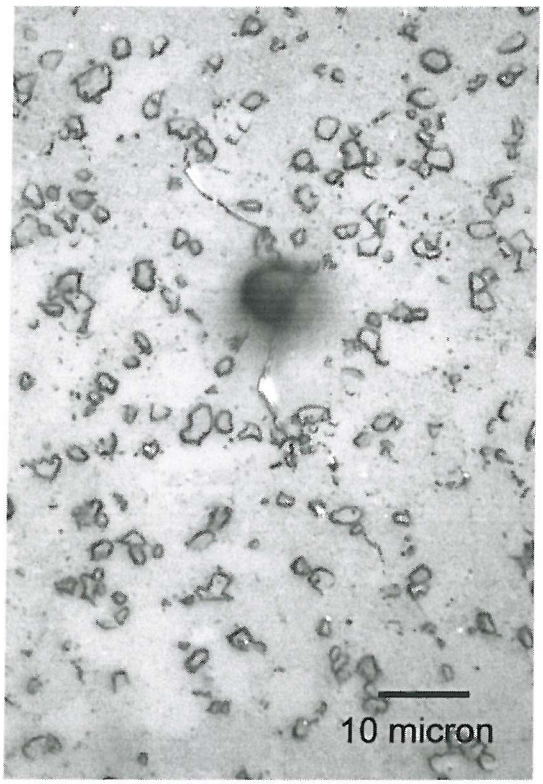

100000 cycles

Figure 4-21a: Crack initiation in RR1000 MO1547; Test 8S.

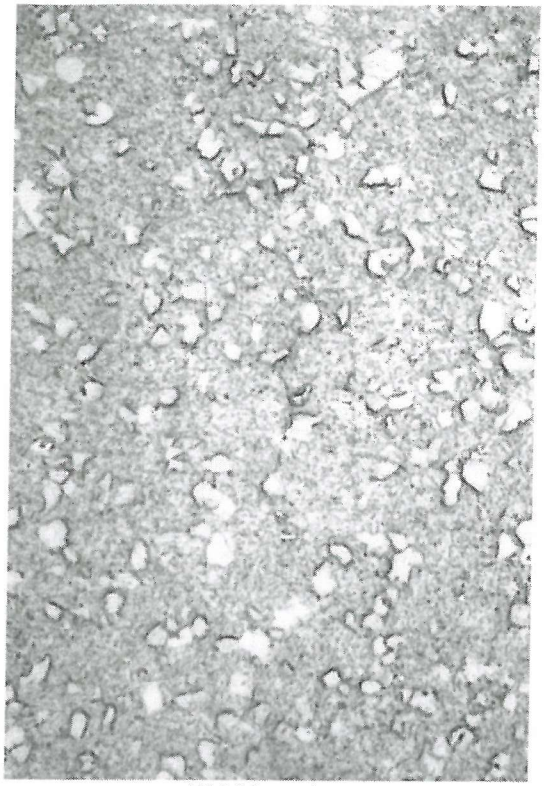

70000 cycles

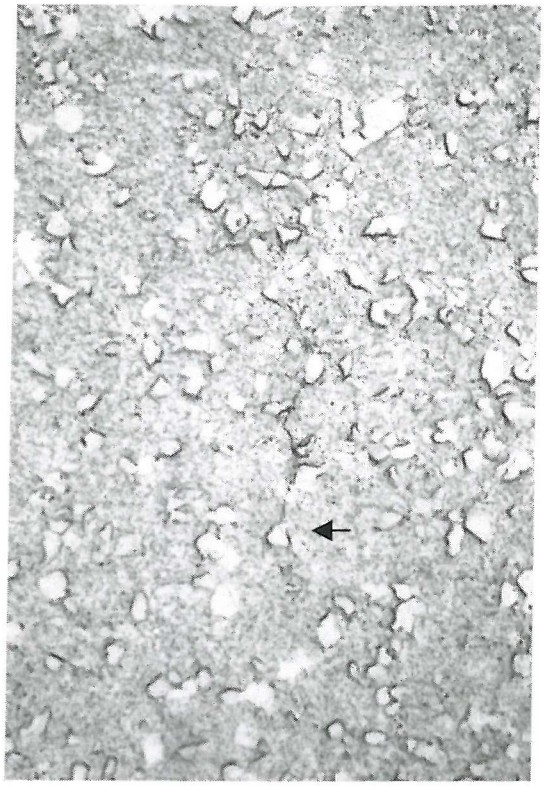

80000 cycles

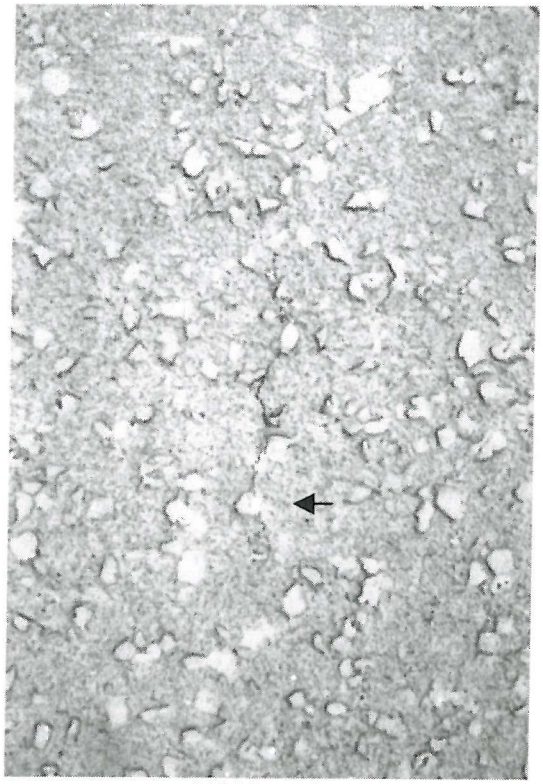

90000 cycles

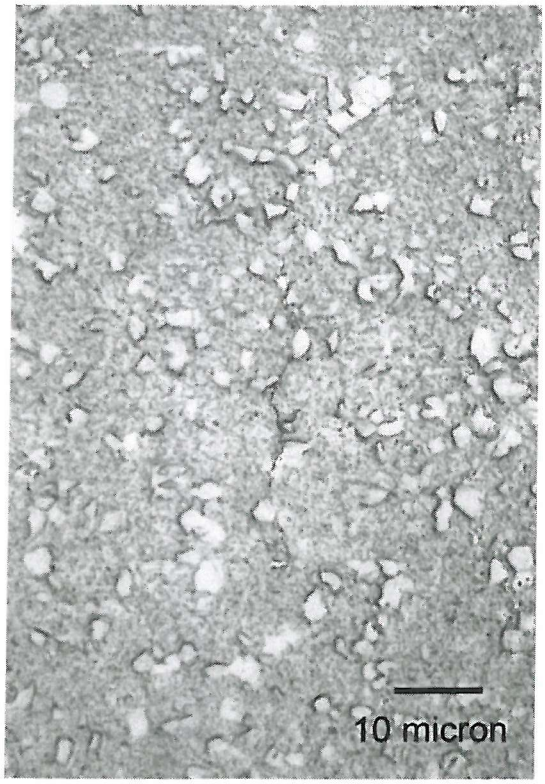

100000 cycles

Figure 4-21b: Crack initiation in U720Li-LP; Test 6S.

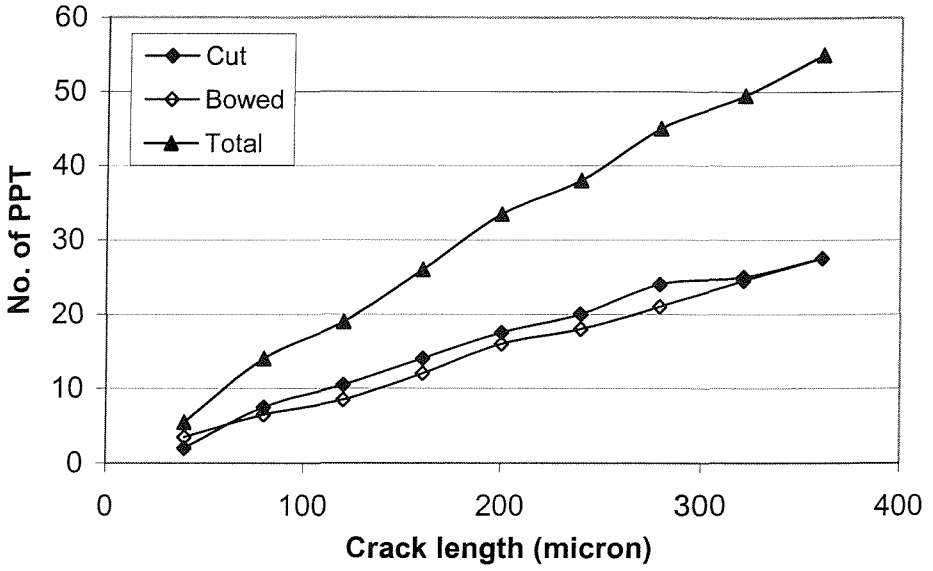

Figure 4-22a: Effects of primary γ' precipitates in U720Li (Test 10S).

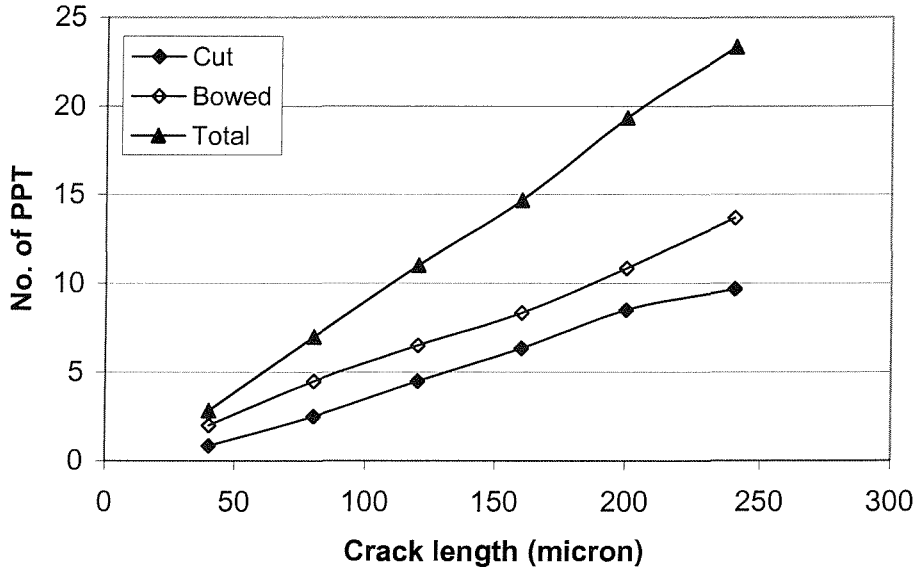

Figure 4-22b: Effects of primary γ' precipitates in U720Li-LG (Test 4S).

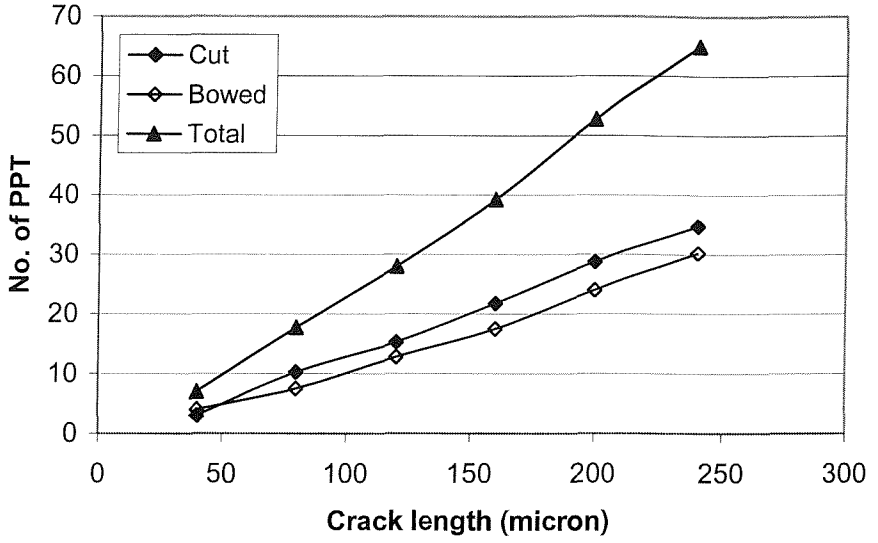

Figure 4-22c: Effects of primary γ' precipitates in U720Li-LP (Test 6S).

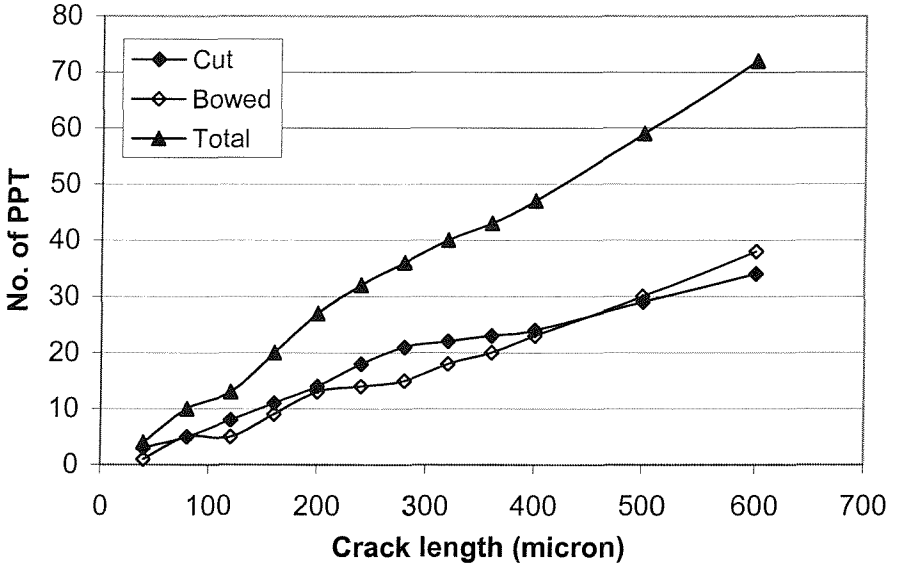

Figure 4-22d: Effects of primary γ' precipitates in RR1000 MO1547 (Test 8S).

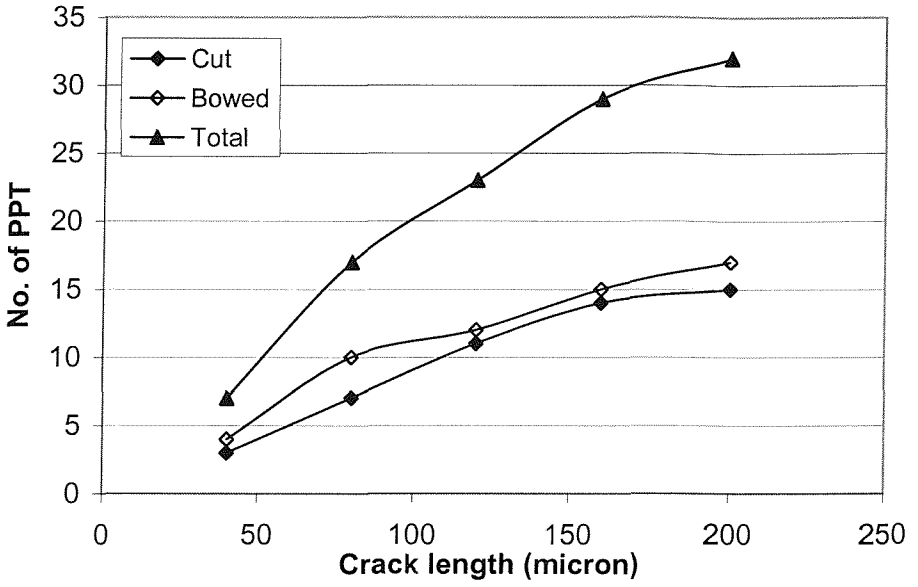

Figure 4-22e: Effects of primary γ' precipitates in RR1000 MO1751 (Test 3S).

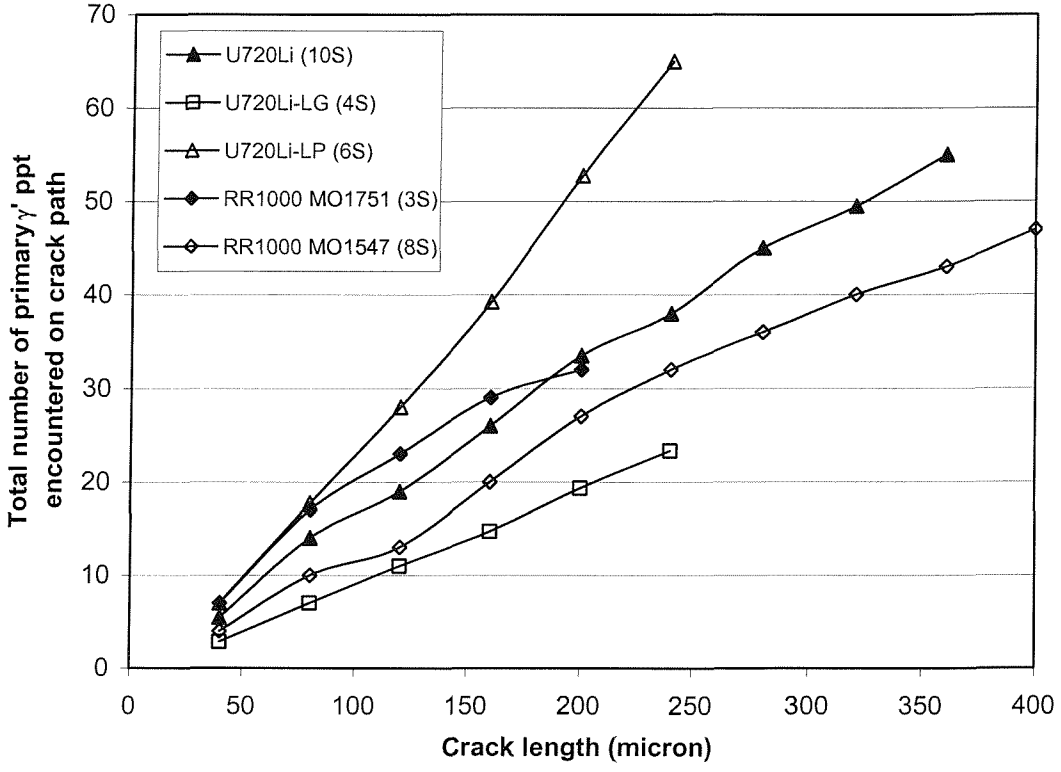

Figure 4-23: Comparison of the effects primary γ' precipitates in the test materials.

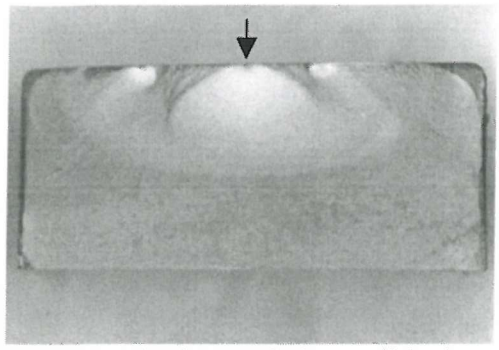

Figure 4-24a: U720Li as-polished (Test 11S); overall fracture surface.

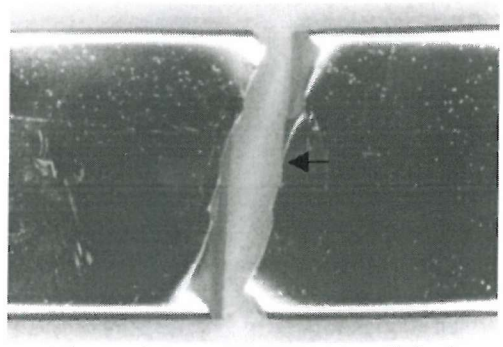

Figure 4-24b: U720Li as-polished (Test 11S); top surface.

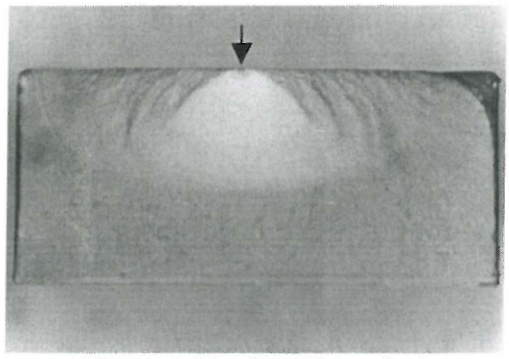

Figure 4-24c: U720Li etched (Test 10S); overall fracture surface.

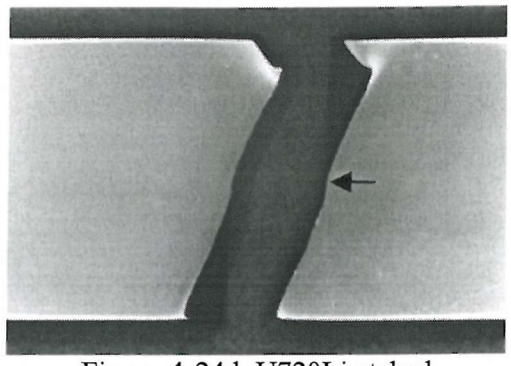

Figure 4-24d: U720Li etched (Test 10S); top surface.

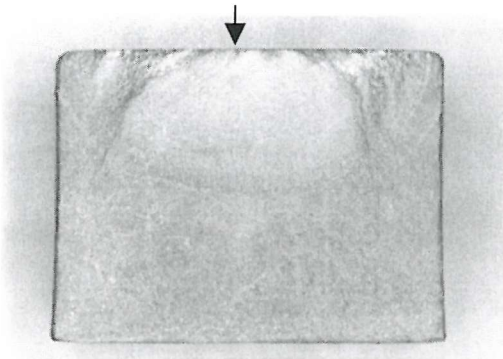

Figure 4-24e: U720Li-LG as-polished (Test 7S); overall fracture surface.

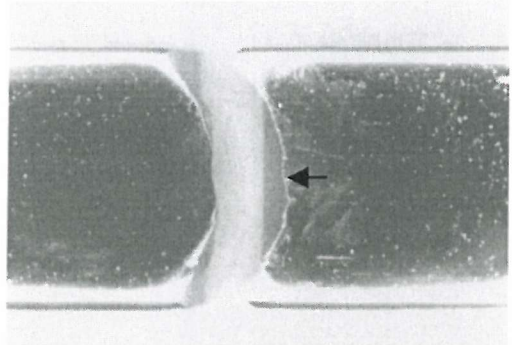

Figure 4-24f: U720Li-LG as-polished (Test 7S); top surface.

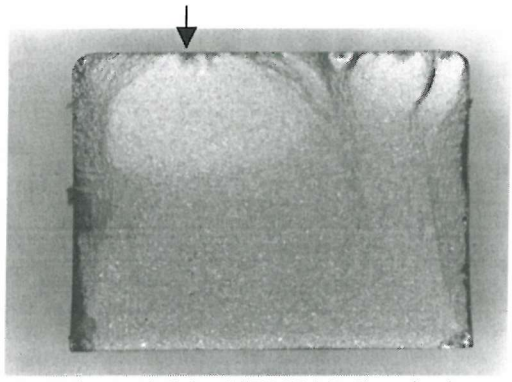

Figure 4-24g: U720Li-LG etched (Test 4S); overall fracture surface.

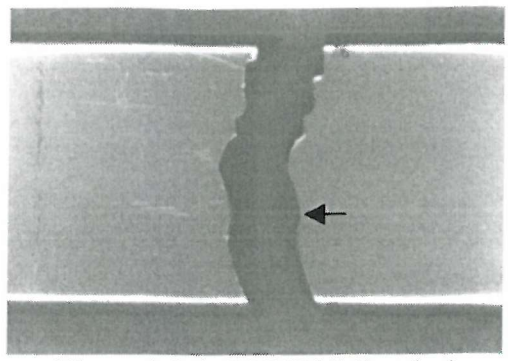

Figure 4-24h: U720Li-LG etched (Test 4S); top surface.

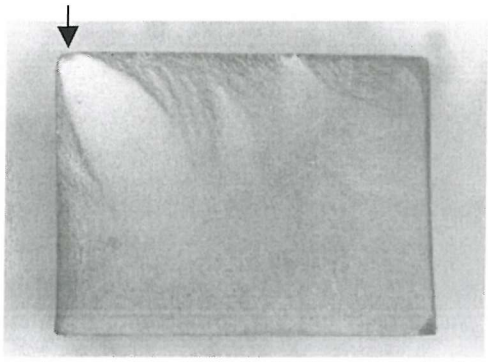

Figure 4-24i: U720Li-LP as-polished (Test 9S); overall fracture surface.

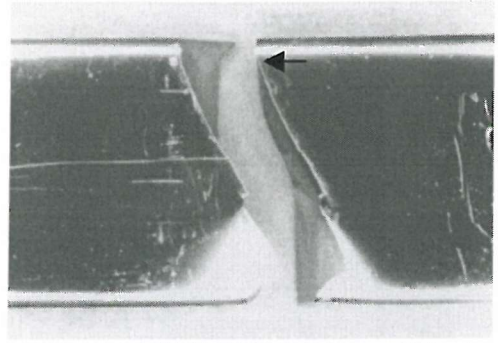

Figure 4-24j: U720Li-LP as-polished (Test 9S); top surface.

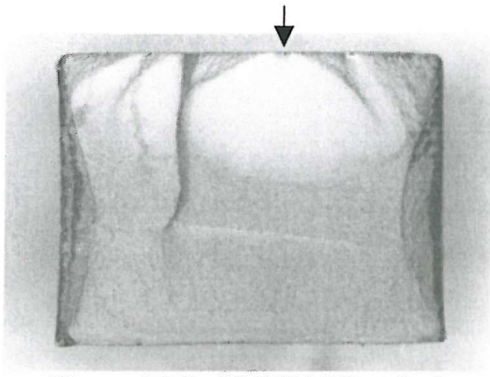

Figure 4-24k: U720Li-LP etched (Test 6S); overall fracture surface.

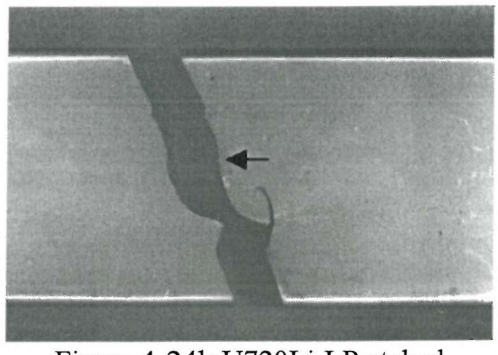

Figure 4-24l: U720Li-LP etched (Test 6S); top surface.

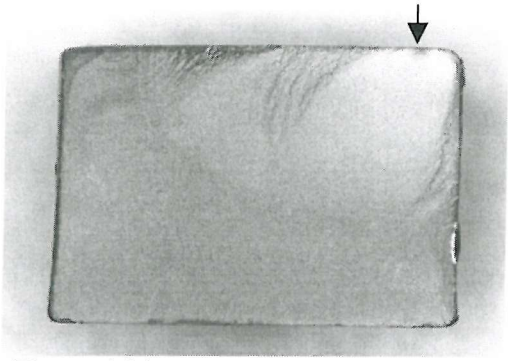

Figure 4-24m: RR1000 MO1751 etched (Test 3S); overall fracture surface.

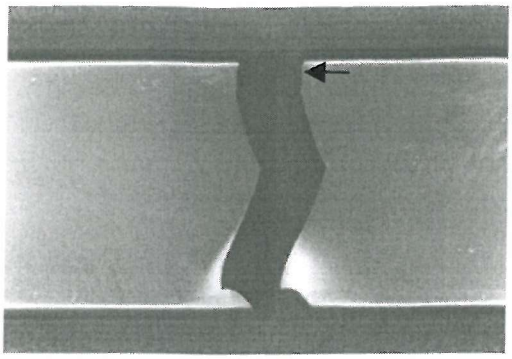

Figure 4-24n: RR1000 MO1751 etched (Test 3S); top surface.

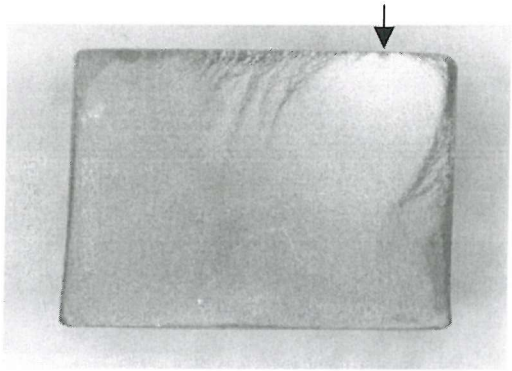

Figure 4-24o: RR1000 MO1547 etched (Test 8S); overall fracture surface.

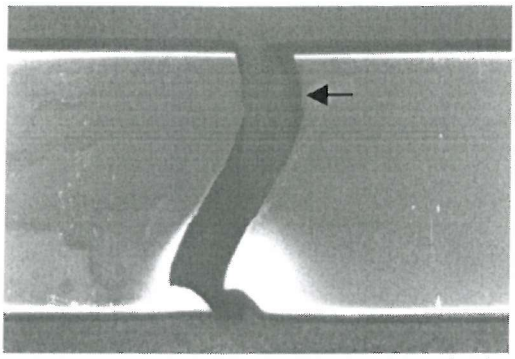

Figure 4-24p: RR1000 MO1547 etched (Test 8S); top surface.

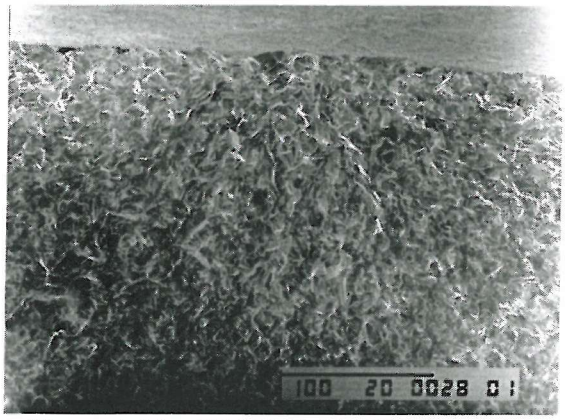

Figure 4-25a: RR1000 MO1751 (Test 3S); primary crack initiation site (low mag).

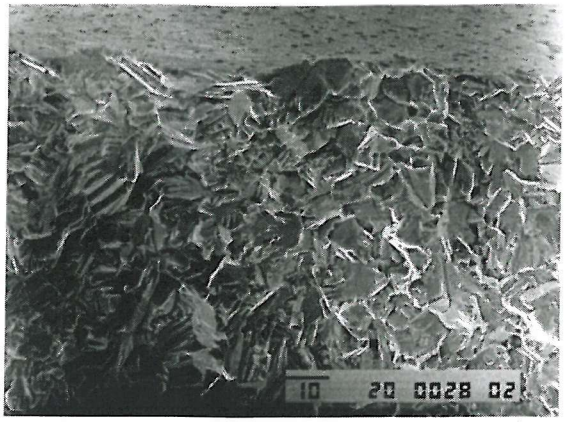

Figure 4-25b: RR1000 MO1751 (Test 3S); primary crack initiation site (high mag).

Figure 4-25c: RR1000 MO1751 (Test 3S); stage I crack growth (approx. 0.12mm below surface).

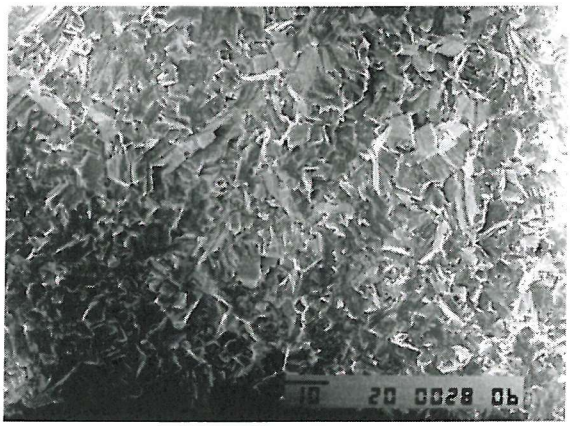

Figure 4-25d: RR1000 MO1751 (Test 3S); stage I to stage II transition (approx. 0.25mm below surface).

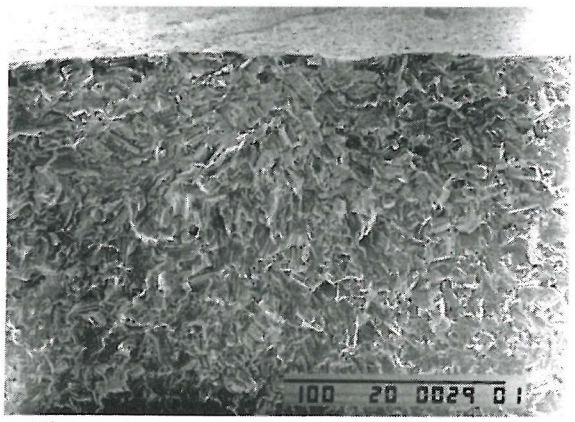

Figure 4-25e: RR1000 MO1547 (Test 8S); primary crack initiation site (low mag).

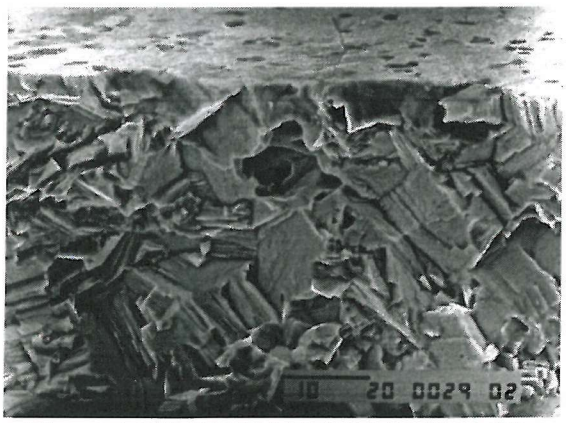

Figure 4-25f: RR1000 MO1547 (Test 8S); primary crack initiation site (high mag).

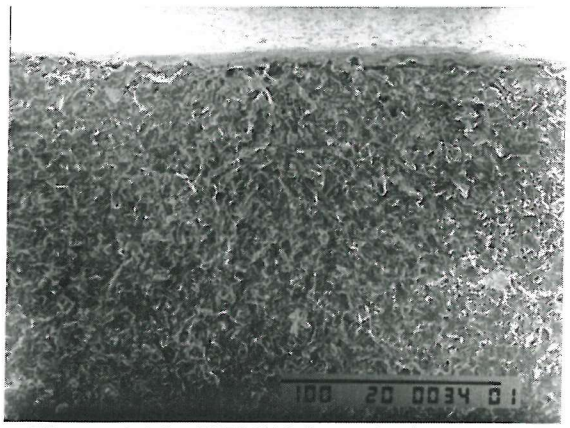

Figure 4-26a: U720Li (Test 10S); primary crack initiation site (low mag).

Figure 4-26b: U720Li (Test 10S); primary crack initiation site (high mag).

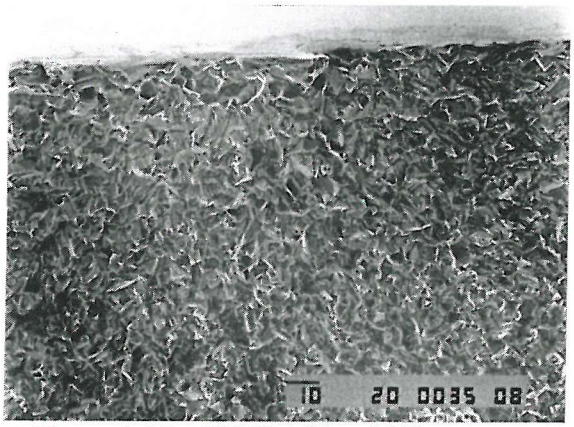

Figure 4-26c: U720Li (Test 11S); primary crack initiation site (low mag).

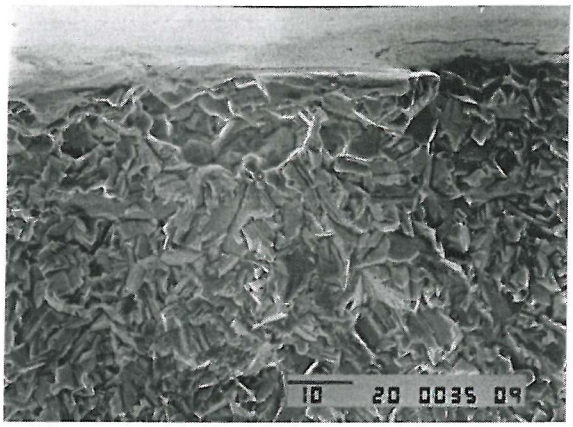

Figure 4-26d: U720Li (Test 11S); primary crack initiation site (high mag).

Figure 4-27a: U720Li-LG (Test 4S); primary crack initiation site (low mag).

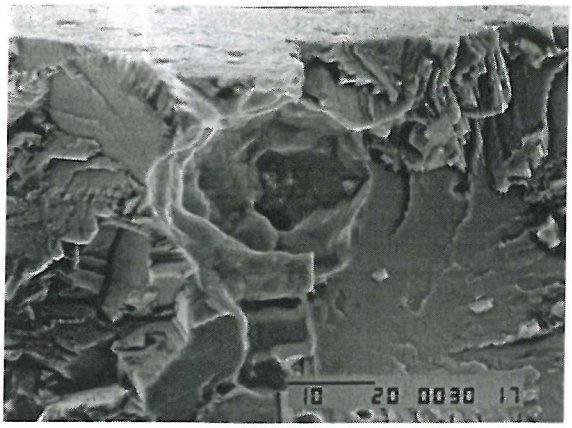

Figure 4-27b: U720Li-LG (Test 4S); primary crack initiation site (high mag).

Figure 4-27c: U720Li-LG (Test 7S); primary crack initiation site (low mag).

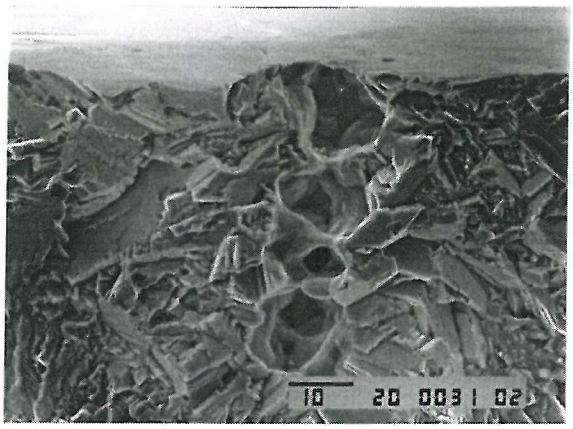

Figure 4-27d: U720Li-LG (Test 7S); primary crack initiation site (low mag).

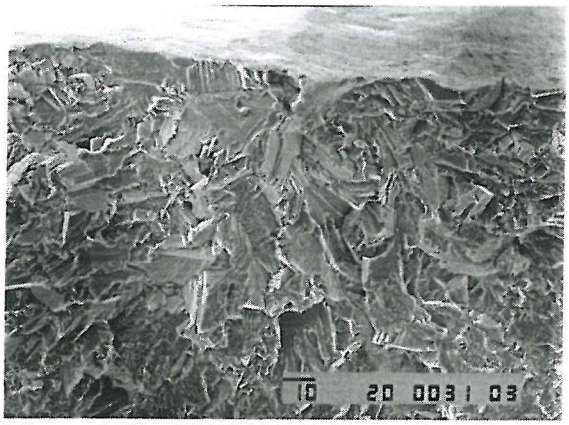

Figure 4-27e: U720Li-LG (Test 7S); initiation site at one of the secondary cracks.

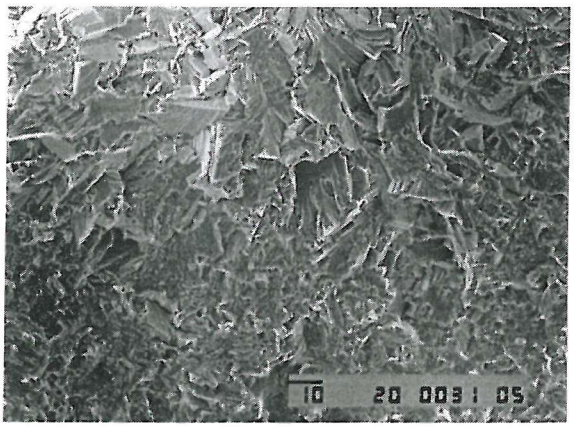

Figure 4-27f: U720Li-LG (Test 7S); Stage I to Stage II transition (approx. 0.10mm below surface).

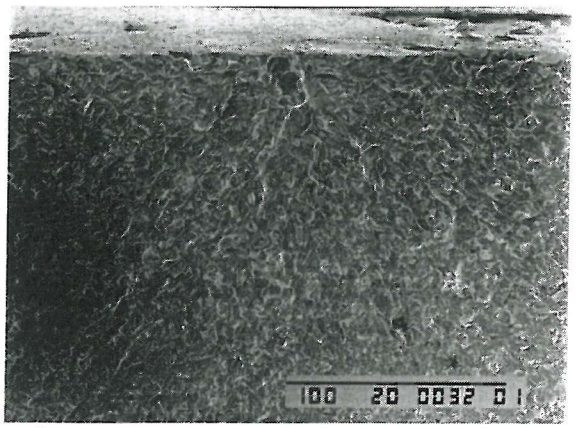

Figure 4-28a: U720Li-LP (Test 6S); primary crack initiation site (low mag).

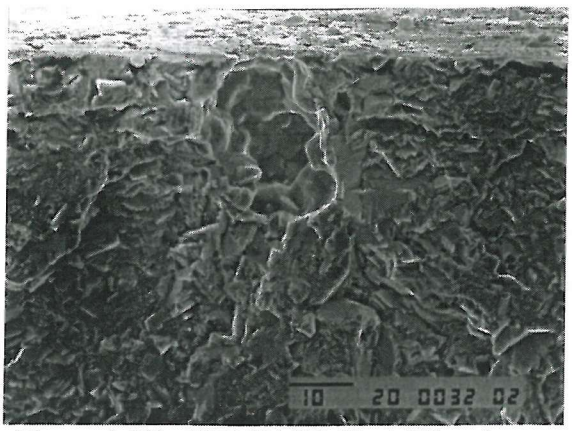

Figure 4-28b: U720Li-LP (Test 6S); primary crack initiation site (high mag).

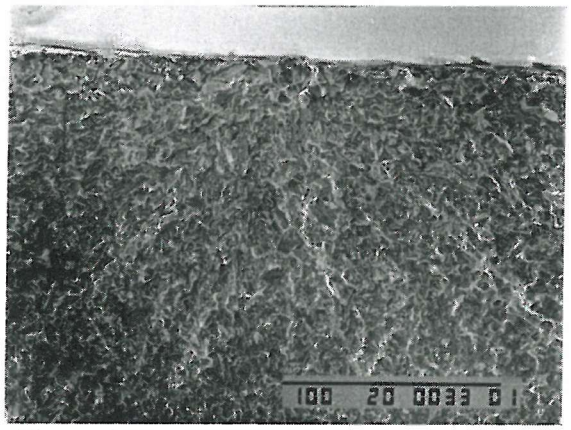

Figure 4-28c: U720Li-LP (Test 9S); primary crack initiation site (low mag).

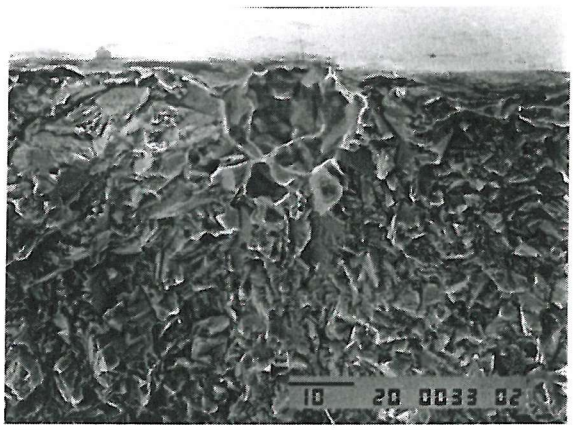

Figure 4-28d: U720Li-LP (Test 9S); primary crack initiation site (high mag).

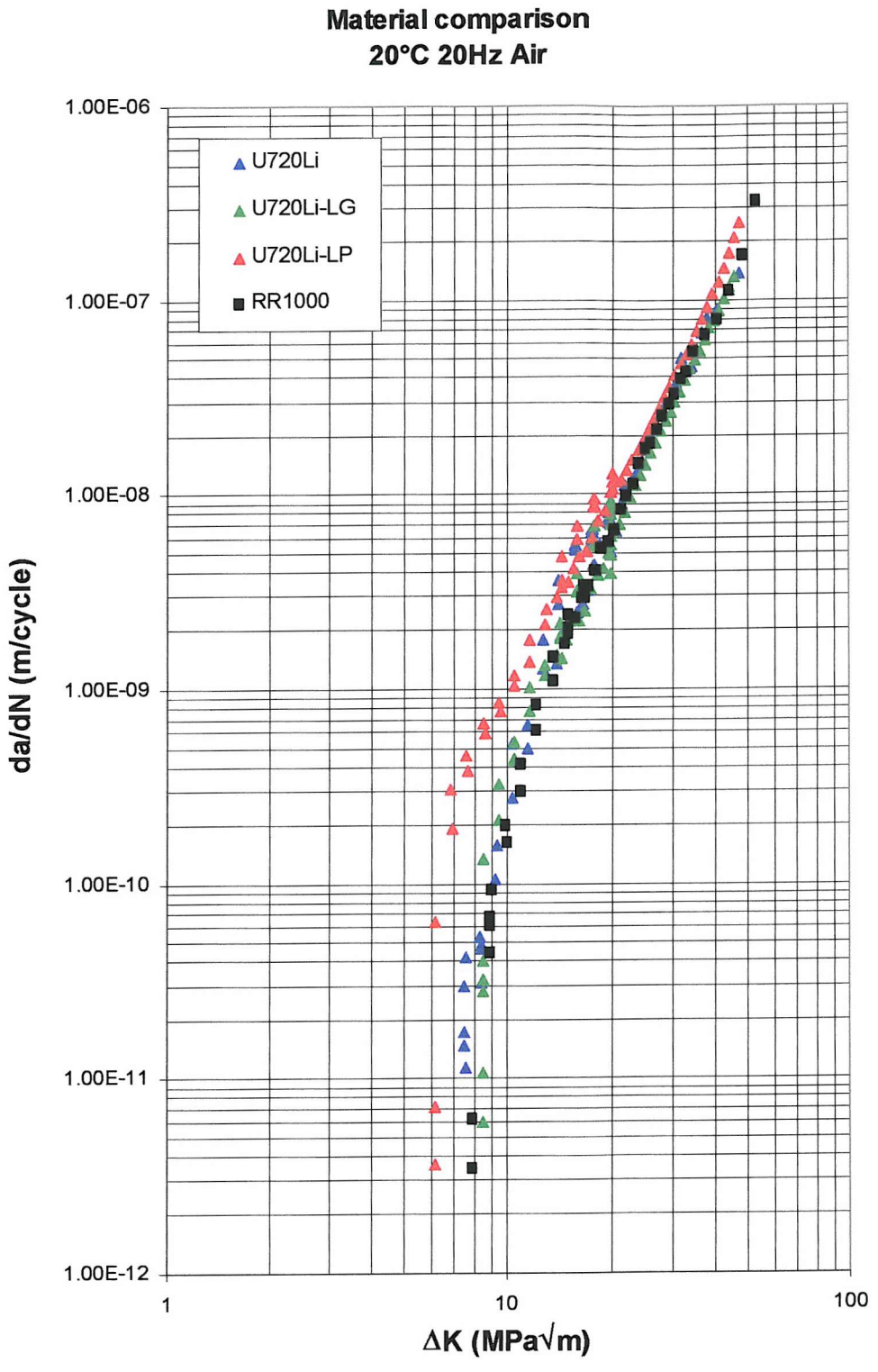

Figure 4-29: Growth out curves of room temperature long crack tests.

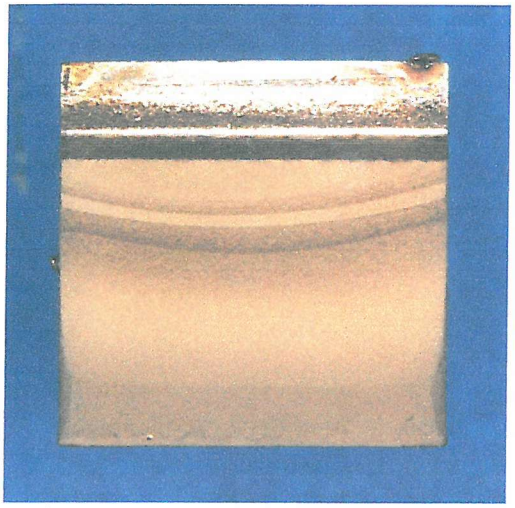

Figure 4-30a: RR1000 (Test 2T); overall fracture surface.

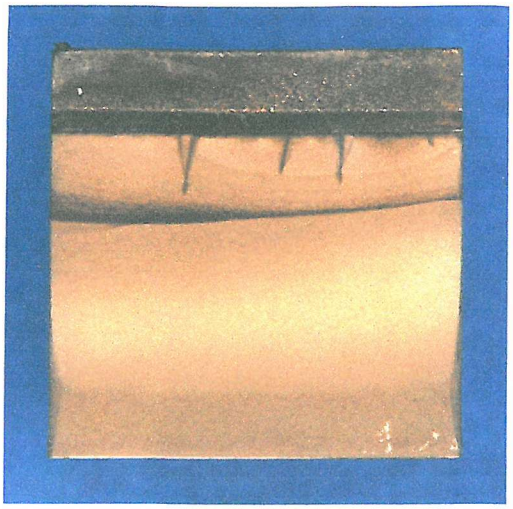

Figure 4-30b: U720Li (Test 1T); overall fracture surface.

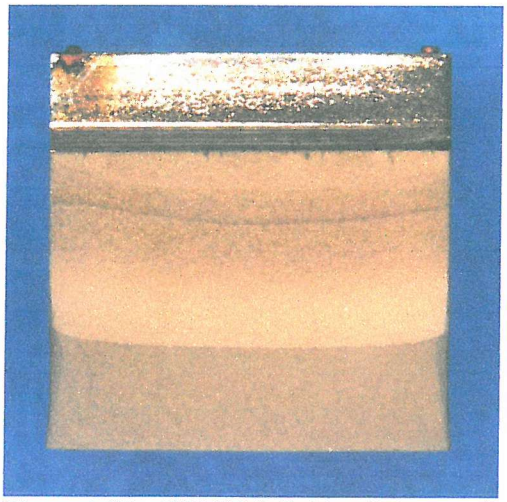

Figure 4-30c: U720Li-LG (Test 3T); overall fracture surface.

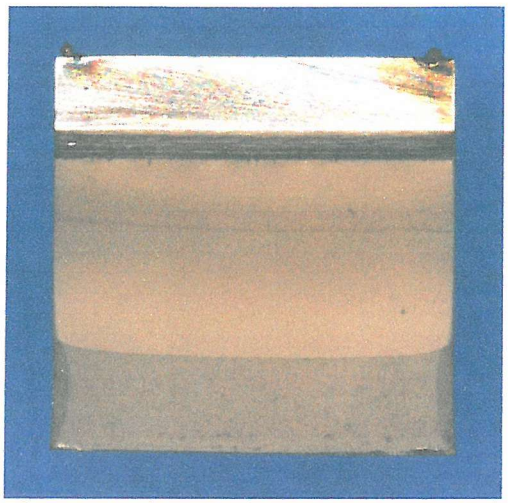

Figure 4-30d: U720Li-LP (Test 4T); overall fracture surface.

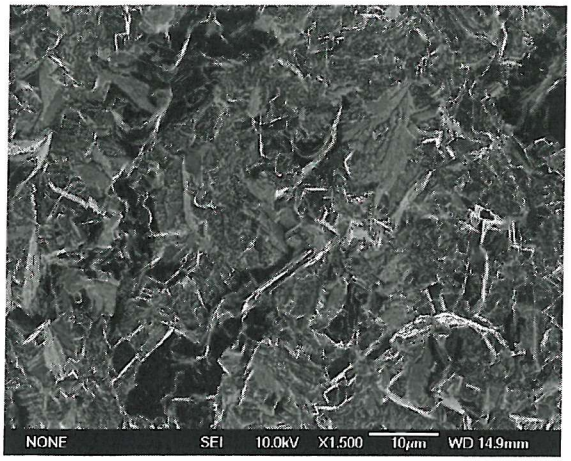

Figure 4-31a: RR1000 (Test 2T) Load Shedding; Low Mag ($\Delta K \approx 8.1$ MPa$\sqrt{m}$).

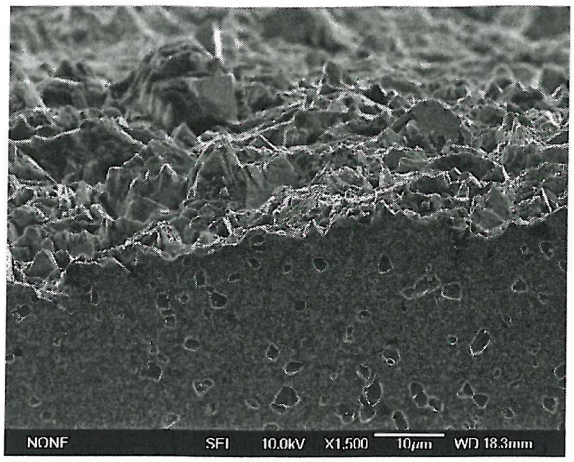

Figure 4-31b: RR1000 (Test 2T) Load Shedding; Low Mag ($\Delta K \approx 8.0$ MPa$\sqrt{m}$).

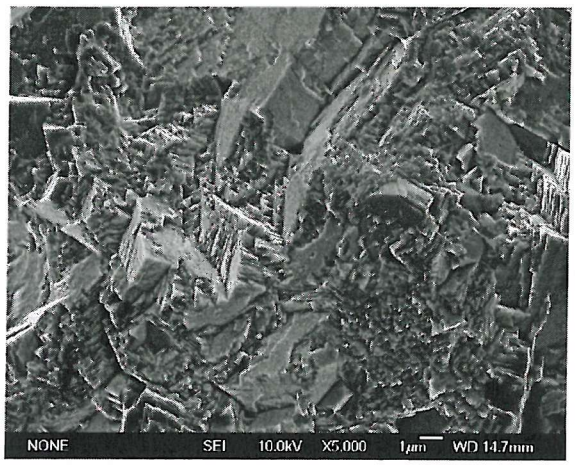

Figure 4-31c: RR1000 (Test 2T) Load Shedding; ($\Delta K \approx 8.1$ MPa$\sqrt{m}$).

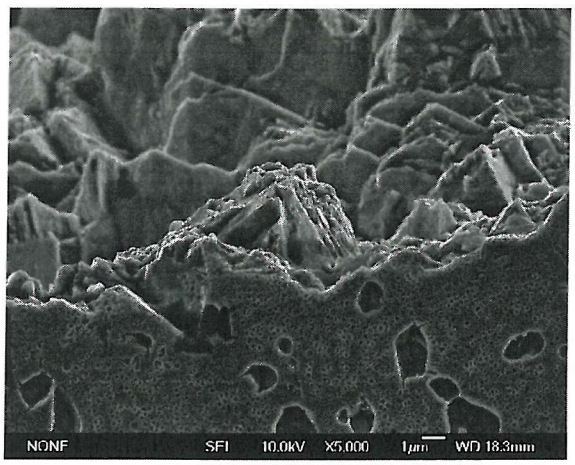

Figure 4-31d: RR1000 (Test 2T) Load Shedding; ($\Delta K \approx 8.0$ MPa$\sqrt{m}$).

Figure 4-31e: RR1000 (Test 2T) Load Shedding; ($\Delta K \approx 13.7$ MPa$\sqrt{m}$).

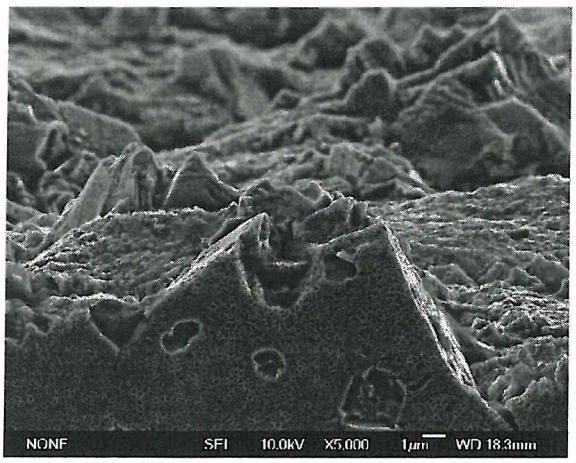

Figure 4-31f: RR1000 (Test 2T) Load Shedding; ($\Delta K \approx 13.6$ MPa$\sqrt{m}$).

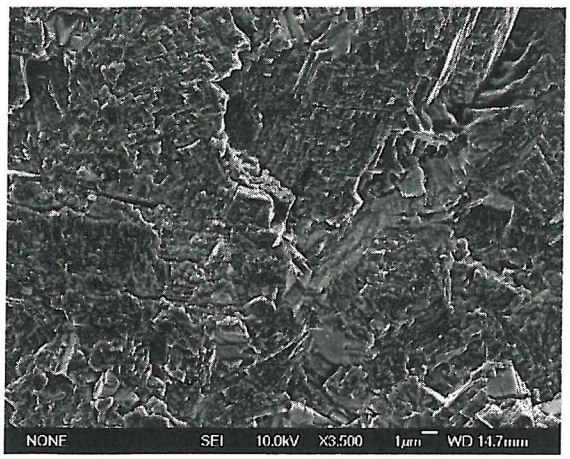

Figure 4-31g: RR1000 (Test 2T) Growth Out; ($\Delta K \approx 18.7$ MPa$\sqrt{m}$).

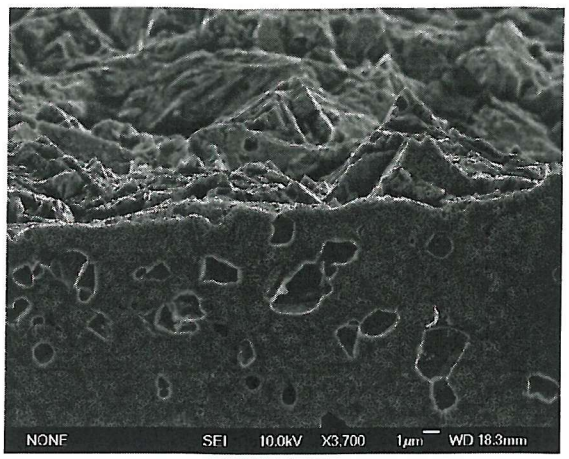

Figure 4-31h: RR1000 (Test 2T) Growth Out; ($\Delta K \approx 18.7$ MPa$\sqrt{m}$).

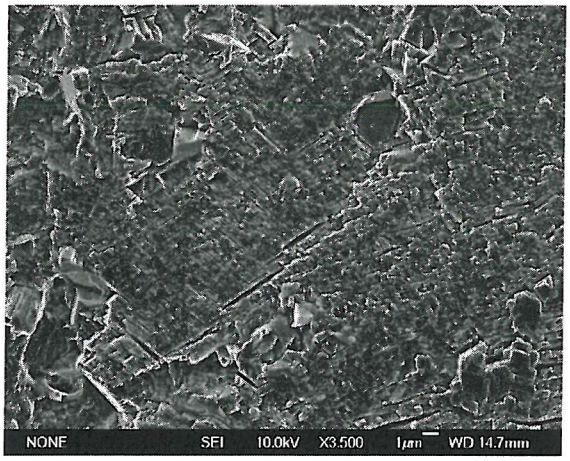

Figure 4-31i: RR1000 (Test 2T) Growth Out; ($\Delta K \approx 23.2$ MPa$\sqrt{m}$).

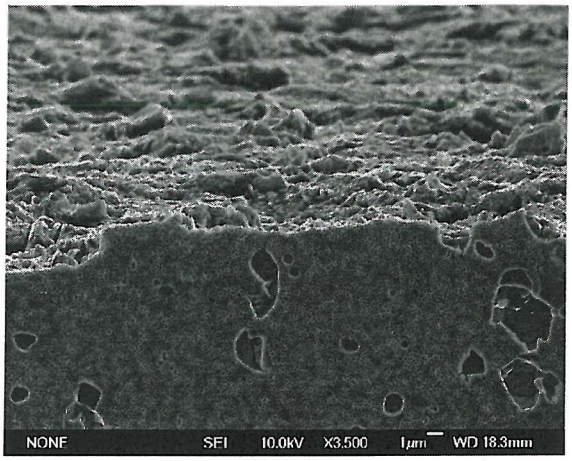

Figure 4-31j: RR1000 (Test 2T) Growth Out; ($\Delta K \approx 24.5$ MPa$\sqrt{m}$).

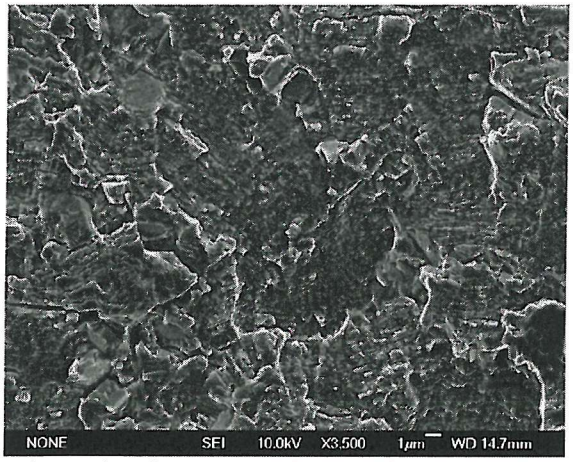

Figure 4-31k: RR1000 (Test 2T) Growth Out; ($\Delta K \approx 37.2$ MPa$\sqrt{m}$).

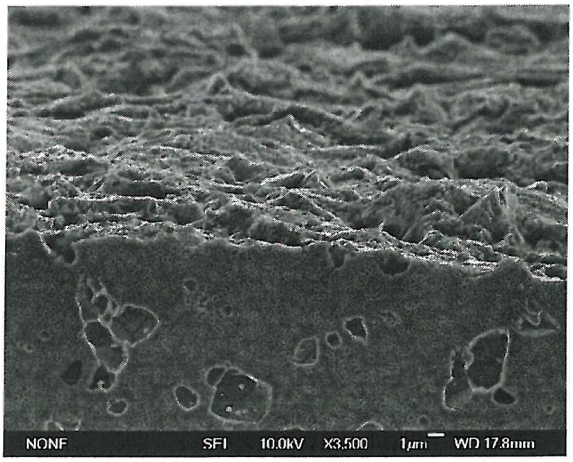

Figure 4-31l: RR1000 (Test 2T) Growth Out; ($\Delta K \approx 34.2$ MPa$\sqrt{m}$).

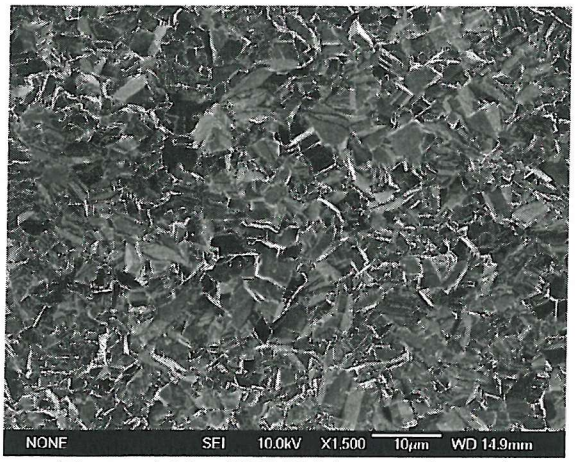

Figure 4-32a: U720Li (Test 1T) Load Shedding; Low Mag ($\Delta K \approx 7.5$ MPa$\sqrt{m}$).

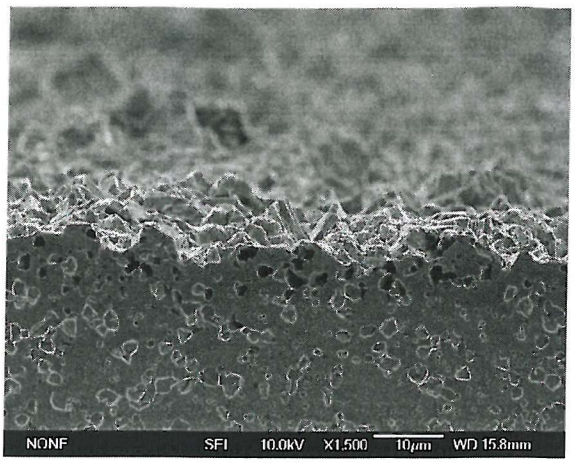

Figure 4-32b: U720Li (Test 1T) Load Shedding; Low Mag ($\Delta K \approx 7.5$ MPa$\sqrt{m}$).

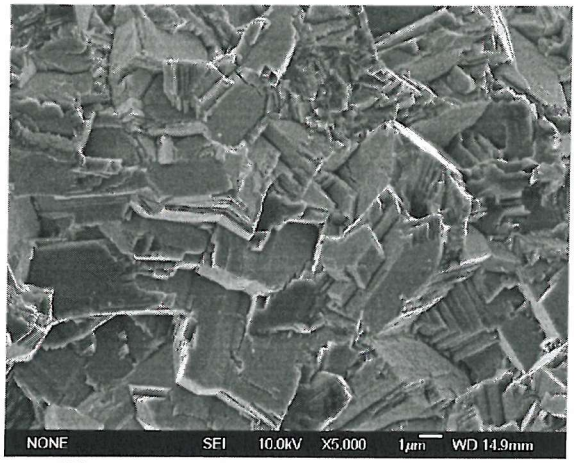

Figure 4-32c: U720Li (Test 1T) Load Shedding; ($\Delta K \approx 7.5$ MPa$\sqrt{m}$).

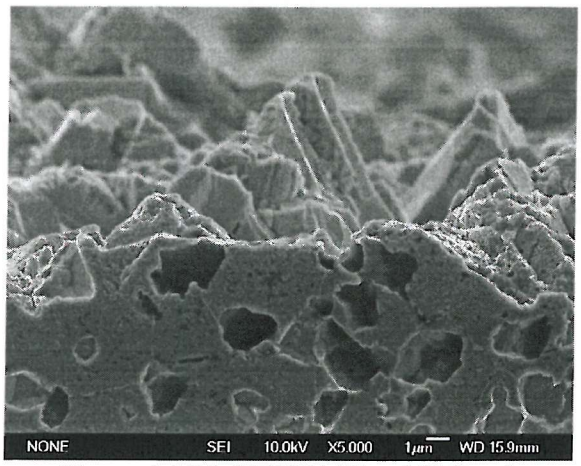

Figure 4-32d: U720Li (Test 1T) Load Shedding; ($\Delta K \approx 7.5$ MPa$\sqrt{m}$).

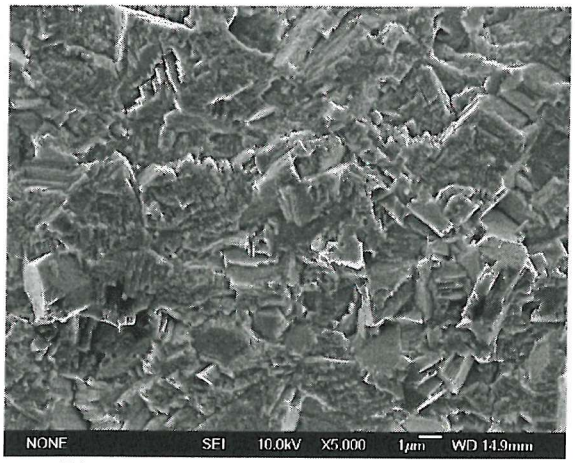

Figure 4-32e: U720Li (Test 1T) Load Shedding; ($\Delta K \approx 10.3$ MPa$\sqrt{m}$).

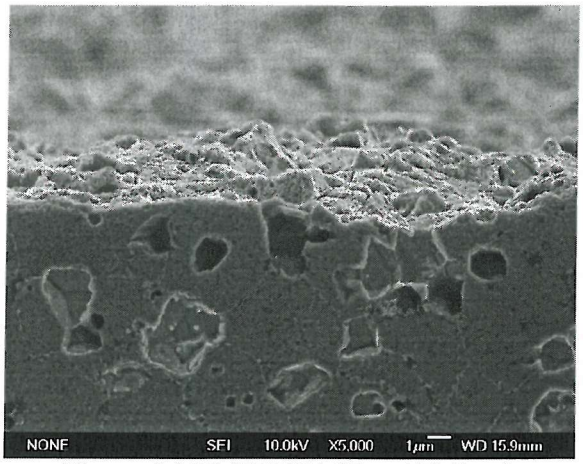

Figure 4-32f: U720Li (Test 1T) Load Shedding; ($\Delta K \approx 11.5$ MPa$\sqrt{m}$).

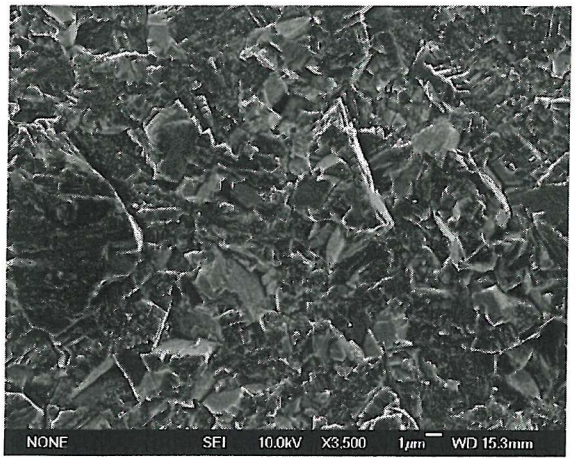

Figure 4-32g: U720Li (Test 1T) Growth Out; ($\Delta K \approx 17.5$ MPa$\sqrt{m}$).

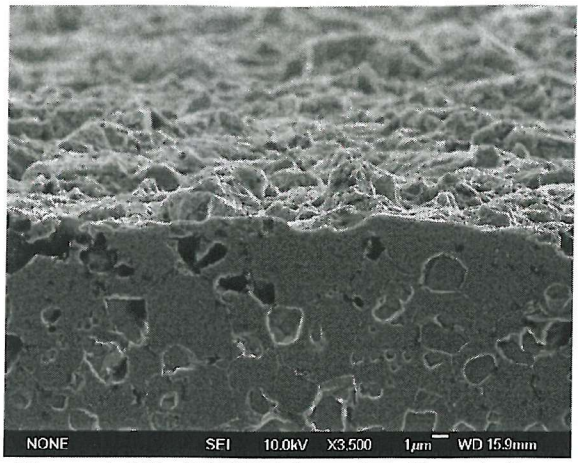

Figure 4-32h: U720Li (Test 1T) Growth Out; ($\Delta K \approx 17.7$ MPa$\sqrt{m}$).

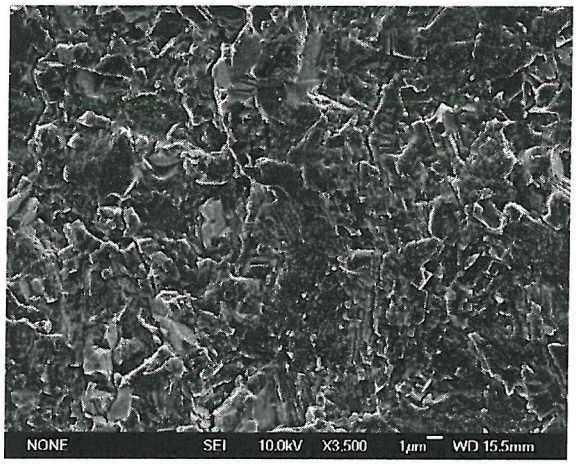

Figure 4-32i: U720Li (Test 1T) Growth Out; ($\Delta K \approx 25.1$ MPa$\sqrt{m}$).

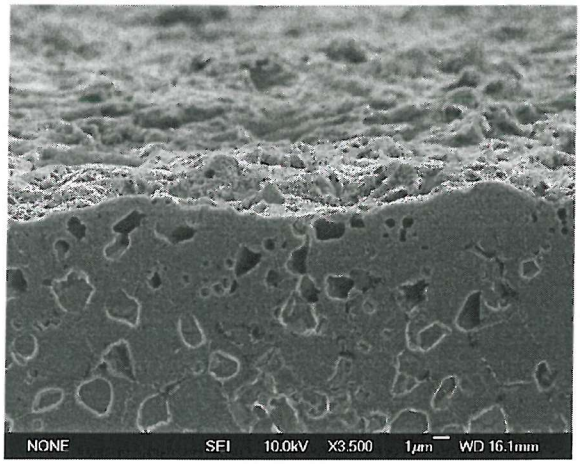

Figure 4-32j: U720Li (Test 1T) Growth Out; ($\Delta K \approx 22.8$ MPa$\sqrt{m}$).

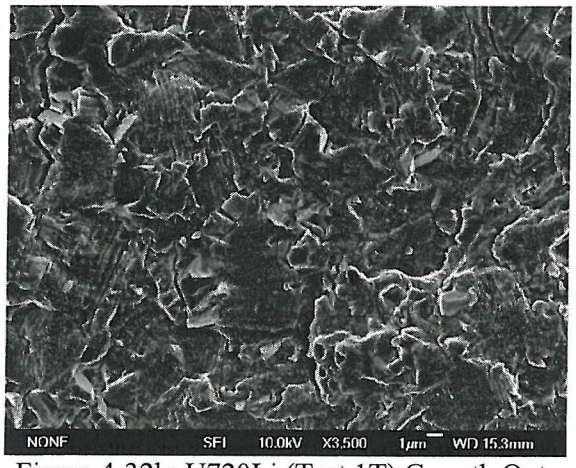

Figure 4-32k: U720Li (Test 1T) Growth Out; ($\Delta K \approx 32.2$ MPa$\sqrt{m}$).

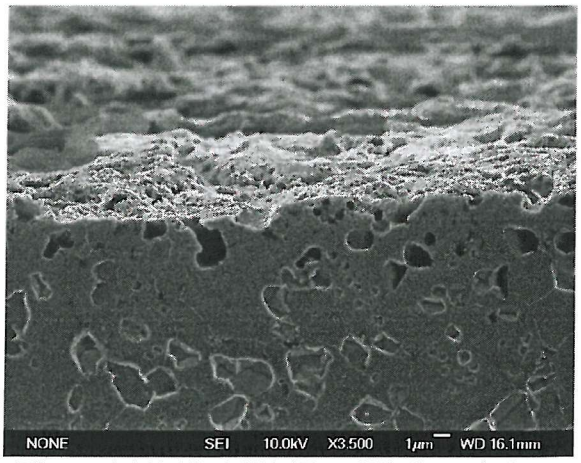

Figure 4-32l: U720Li (Test 1T) Growth Out; ($\Delta K \approx 29.8$ MPa$\sqrt{m}$).

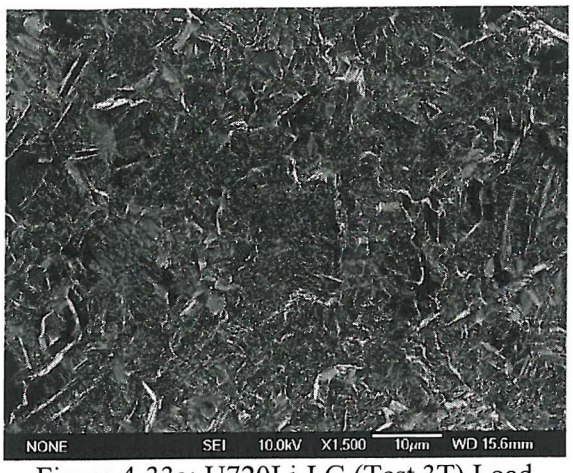

Figure 4-33a: U720Li-LG (Test 3T) Load Shedding; Low Mag ($\Delta K \approx 8.5$ MPa$\sqrt{m}$).

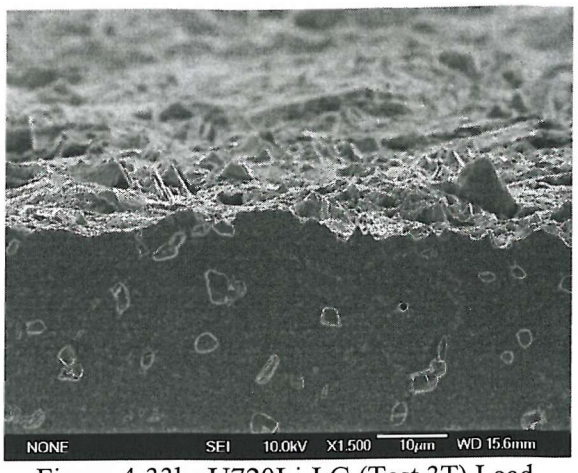

Figure 4-33b: U720Li-LG (Test 3T) Load Shedding; Low Mag ($\Delta K \approx 8.5$ MPa$\sqrt{m}$).

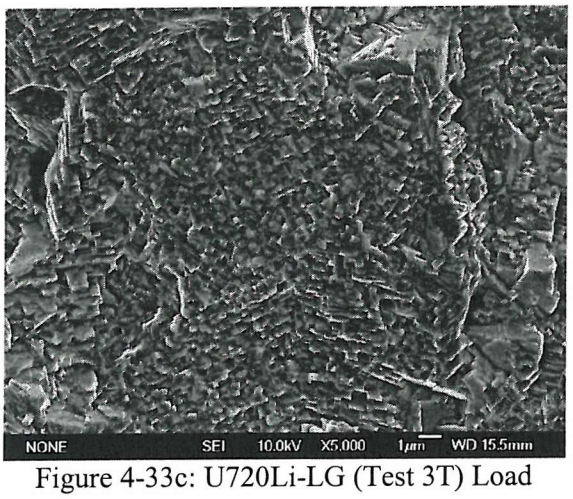

Figure 4-33c: U720Li-LG (Test 3T) Load Shedding; ($\Delta K \approx 8.5$ MPa$\sqrt{m}$).

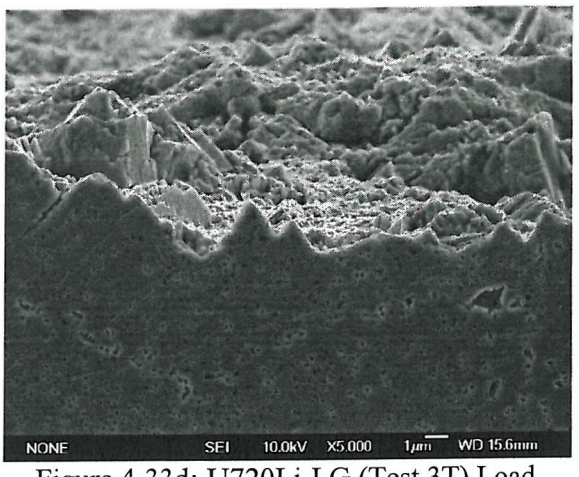

Figure 4-33d: U720Li-LG (Test 3T) Load Shedding; ($\Delta K \approx 8.5$ MPa$\sqrt{m}$).

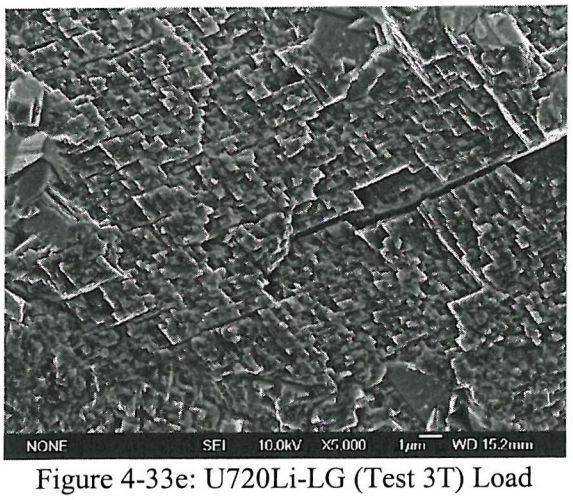

Figure 4-33e: U720Li-LG (Test 3T) Load Shedding; ($\Delta K \approx 14.4$ MPa$\sqrt{m}$).

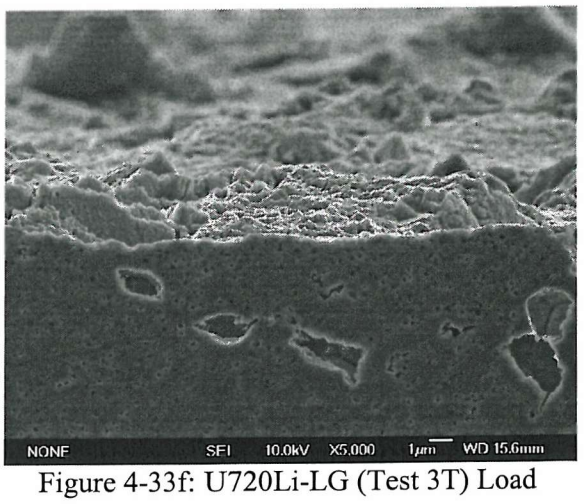

Figure 4-33f: U720Li-LG (Test 3T) Load Shedding; ($\Delta K \approx 16.0$ MPa$\sqrt{m}$).

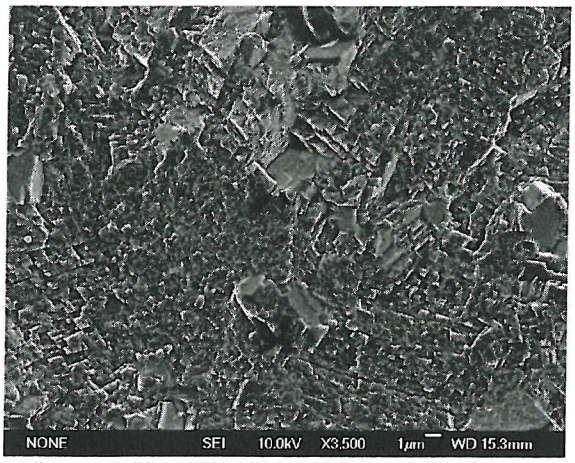

Figure 4-33g: U720Li-LG (Test 3T) Growth Out; ($\Delta K \approx 17.0$ MPa$\sqrt{m}$).

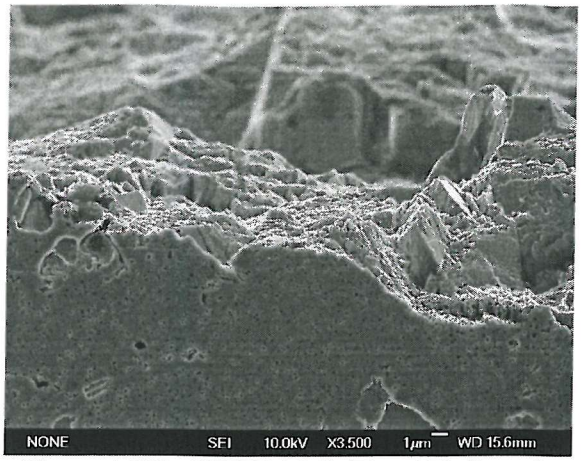

Figure 4-33h: U720Li-LG (Test 3T) Growth Out; ($\Delta K \approx 17.8$ MPa$\sqrt{m}$).

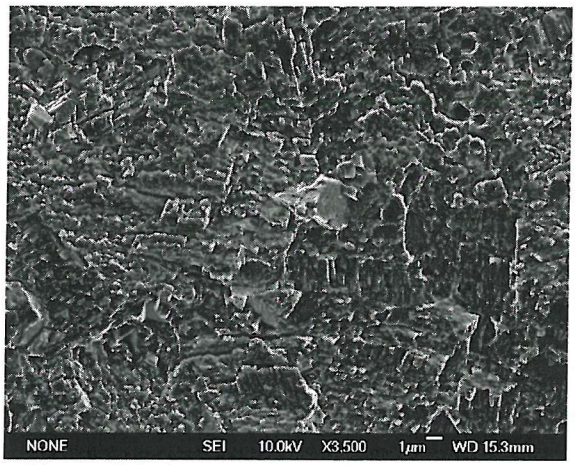

Figure 4-33i: U720Li-LG (Test 3T) Growth Out; ($\Delta K \approx 22.5$ MPa$\sqrt{m}$).

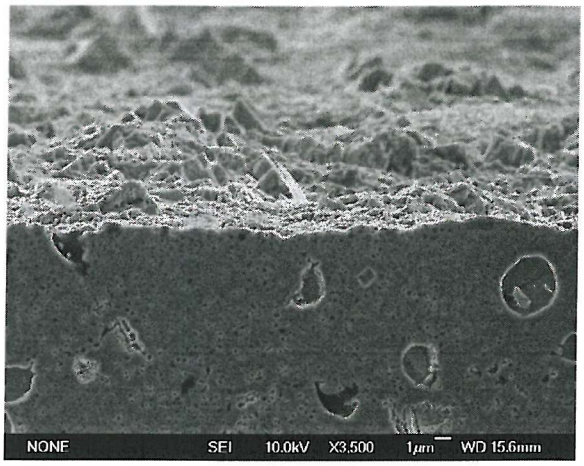

Figure 4-33j: U720Li-LG (Test 3T) Growth Out; ($\Delta K \approx 23.2$ MPa$\sqrt{m}$).

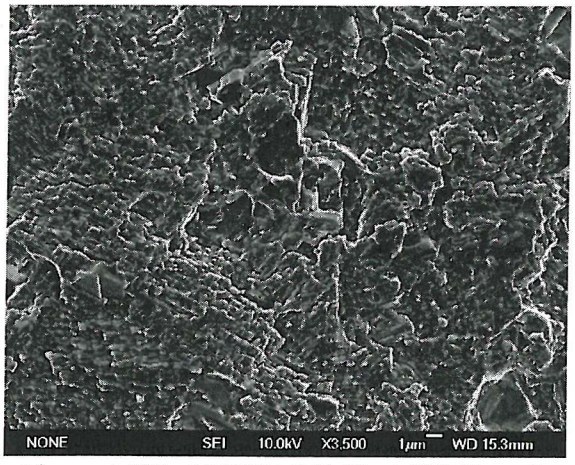

Figure 4-33k: U720Li-LG (Test 3T) Growth Out; ($\Delta K \approx 30.5$ MPa$\sqrt{m}$).

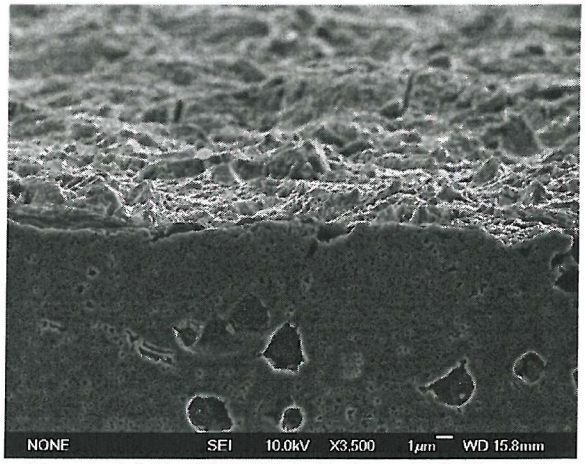

Figure 4-33l: U720Li-LG (Test 3T) Growth Out; ($\Delta K \approx 32.8$ MPa$\sqrt{m}$).

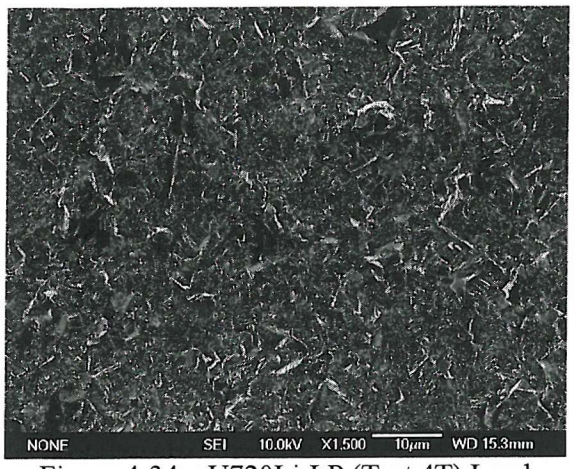

Figure 4-34a: U720Li-LP (Test 4T) Load Shedding; Low Mag ($\Delta K \approx 6.2$ MPa$\sqrt{m}$).

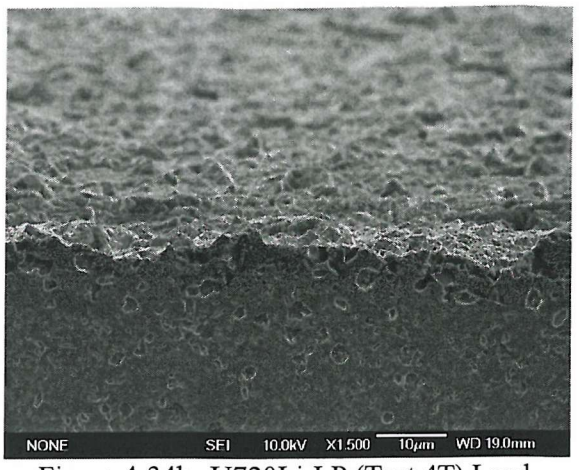

Figure 4-34b: U720Li-LP (Test 4T) Load Shedding; Low Mag ($\Delta K \approx 6.2$ MPa$\sqrt{m}$).

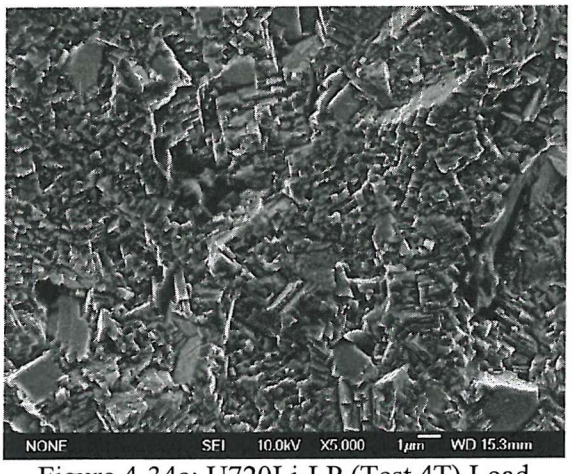

Figure 4-34c: U720Li-LP (Test 4T) Load Shedding; ($\Delta K \approx 6.2$ MPa$\sqrt{m}$).

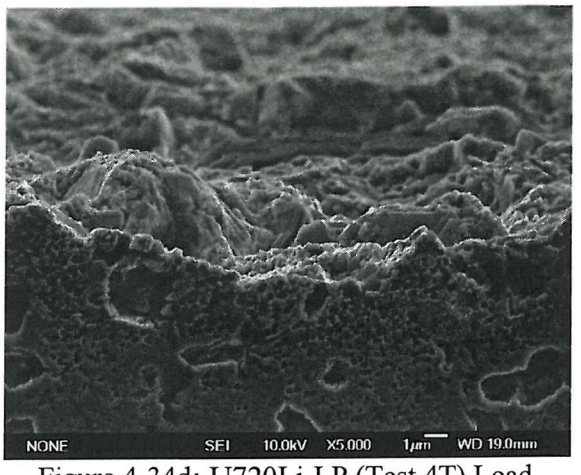

Figure 4-34d: U720Li-LP (Test 4T) Load Shedding; ($\Delta K \approx 6.2$ MPa$\sqrt{m}$).

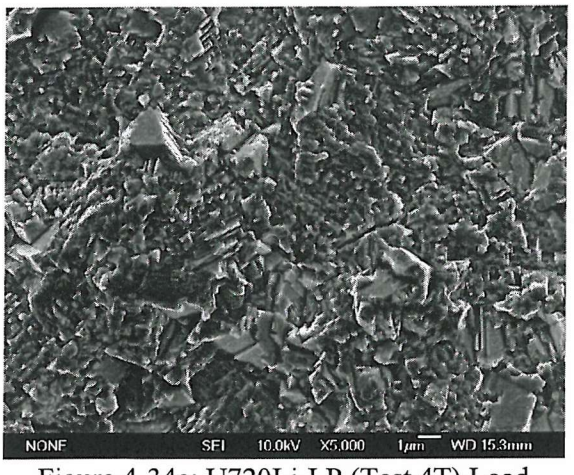

Figure 4-34e: U720Li-LP (Test 4T) Load Shedding; ($\Delta K \approx 14.5$ MPa$\sqrt{m}$).

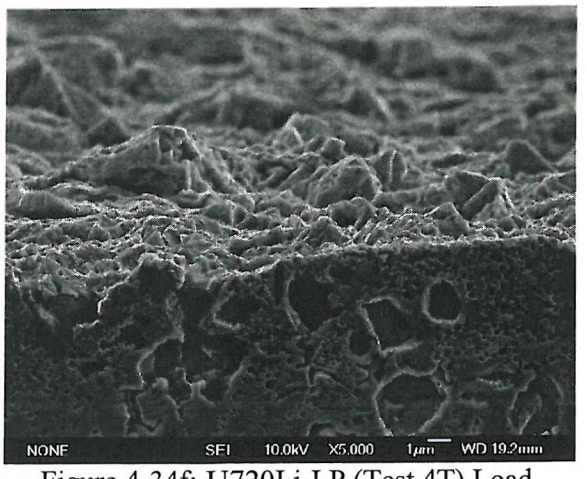

Figure 4-34f: U720Li-LP (Test 4T) Load Shedding; ($\Delta K \approx 13.0$ MPa$\sqrt{m}$).

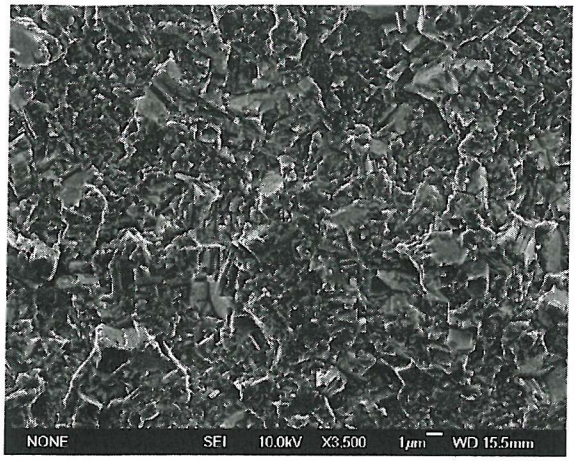

Figure 4-34g: U720Li-LP (Test 4T) Growth Out; ($\Delta K \approx 18.2$ MPa$\sqrt{m}$).

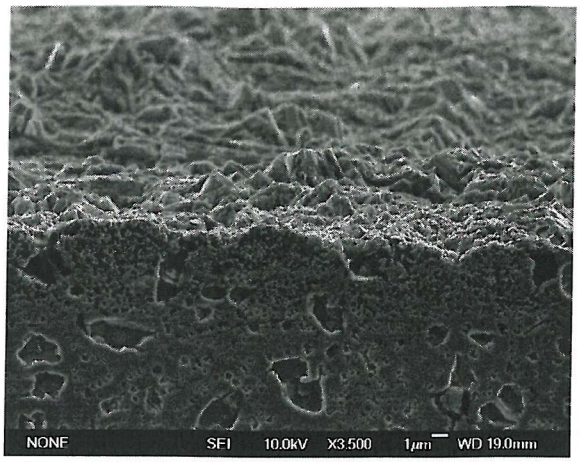

Figure 4-34h: U720Li-LP (Test 4T) Growth Out; ($\Delta K \approx 16.9$ MPa$\sqrt{m}$).

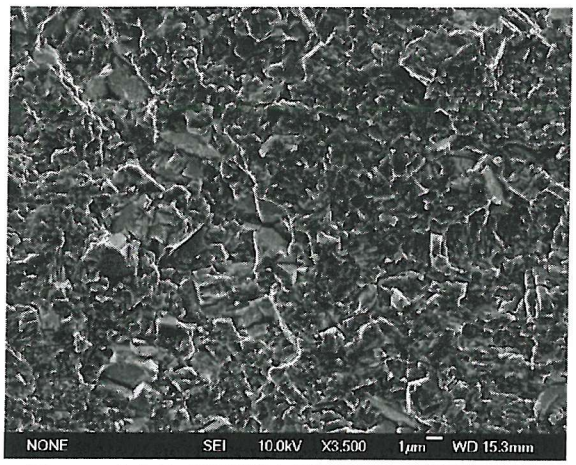

Figure 4-34i: U720Li-LP (Test 4T) Growth Out; ($\Delta K \approx 24.4$ MPa$\sqrt{m}$).

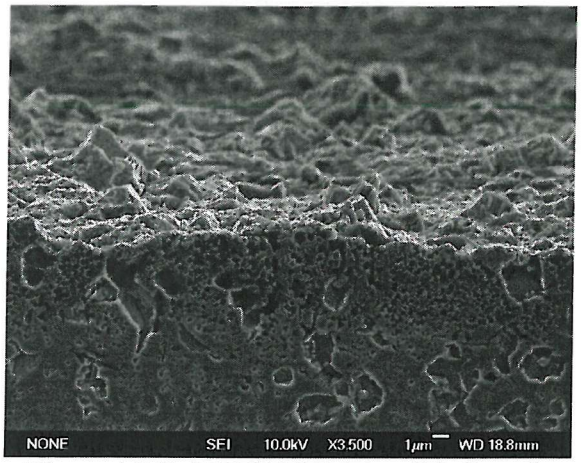

Figure 4-34j: U720Li-LP (Test 4T) Growth Out; ($\Delta K \approx 22.1$ MPa$\sqrt{m}$).

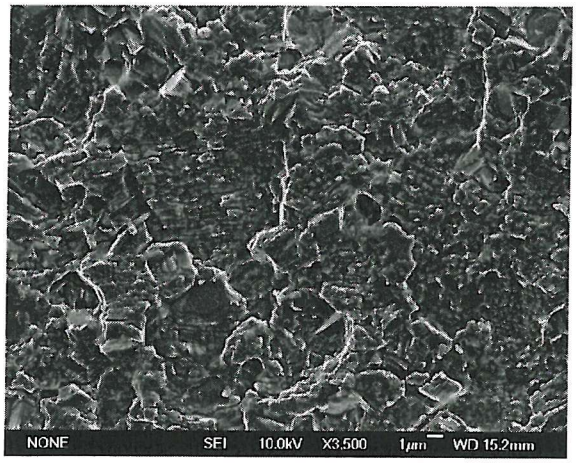

Figure 4-34k: U720Li-LP (Test 4T) Growth Out; ($\Delta K \approx 37.9$ MPa$\sqrt{m}$).

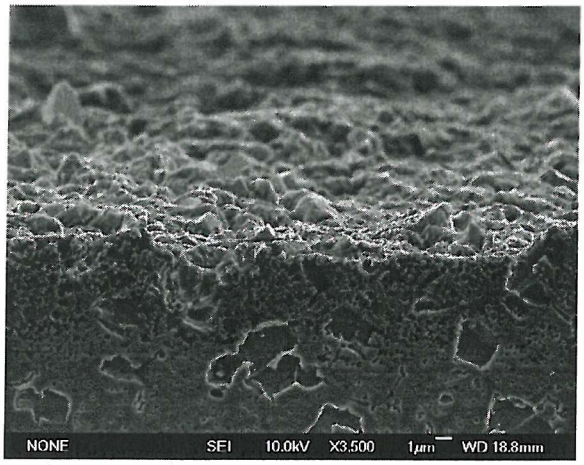

Figure 4-34l: U720Li-LP (Test 4T) Growth Out; ($\Delta K \approx 30.3$ MPa$\sqrt{m}$).

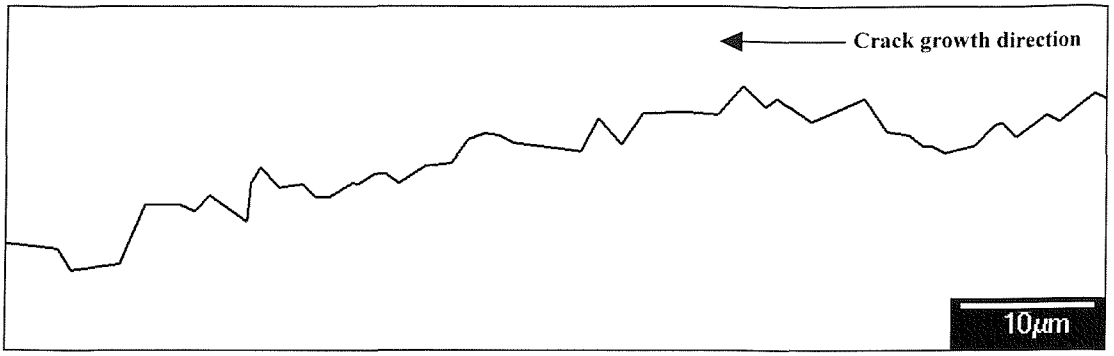

Figure 4-35a: Crack profile at near-threshold ΔK in RR1000.

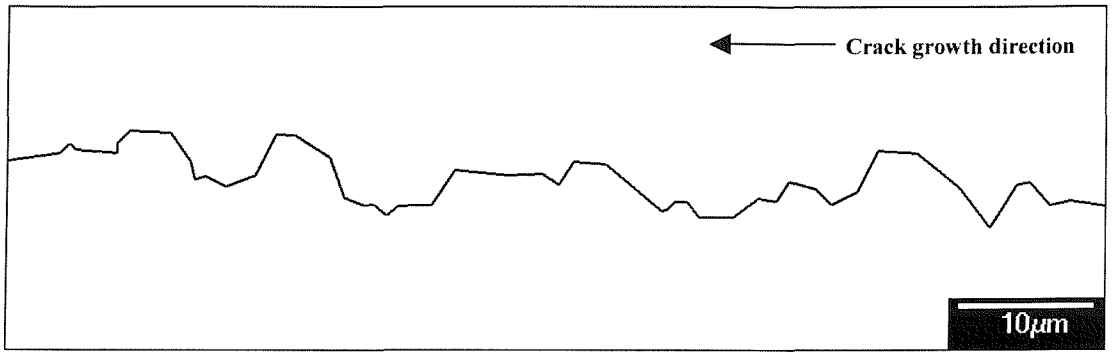

Figure 4-35b: Crack profile at near-threshold ΔK in U720Li.

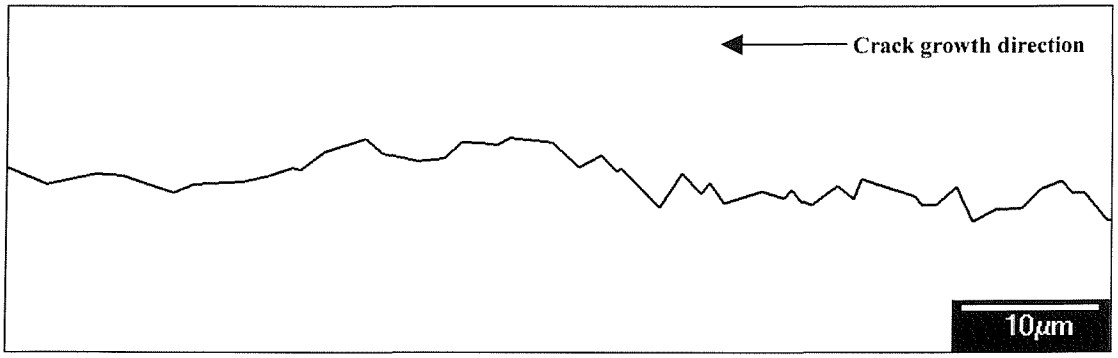

Figure 4-35c: Crack profile at near-threshold ΔK in U720Li-LG.

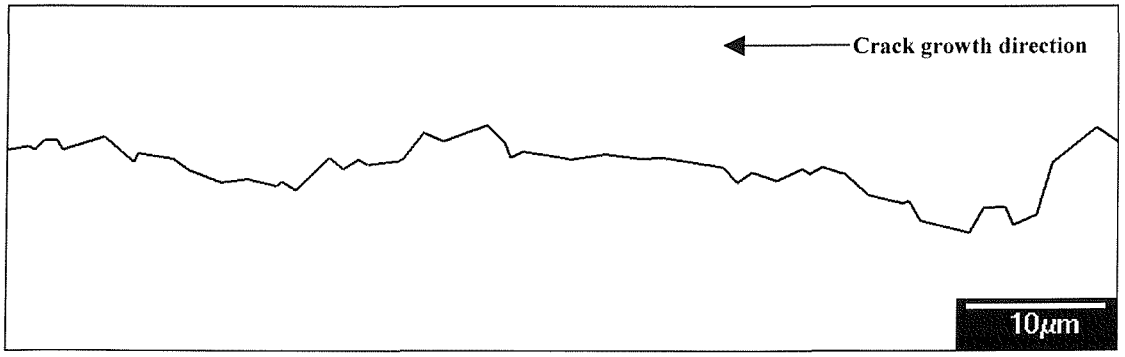

Figure 4-35d: Crack profile at near-threshold ΔK in U720Li-LP.

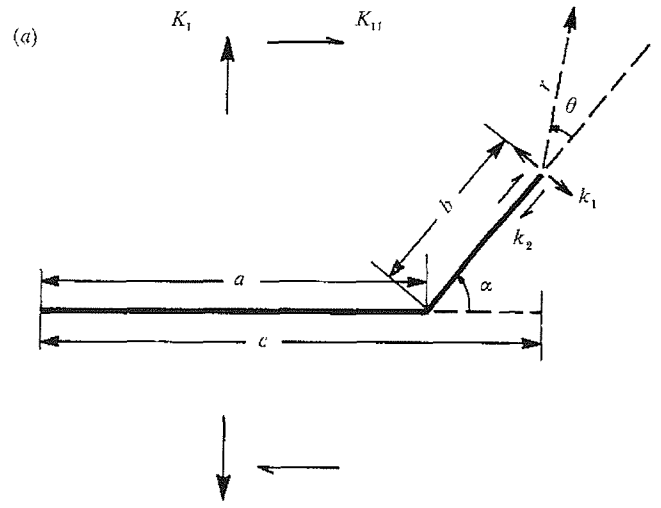

Figure 4-36: Schematic representation of a deflected crack geometry

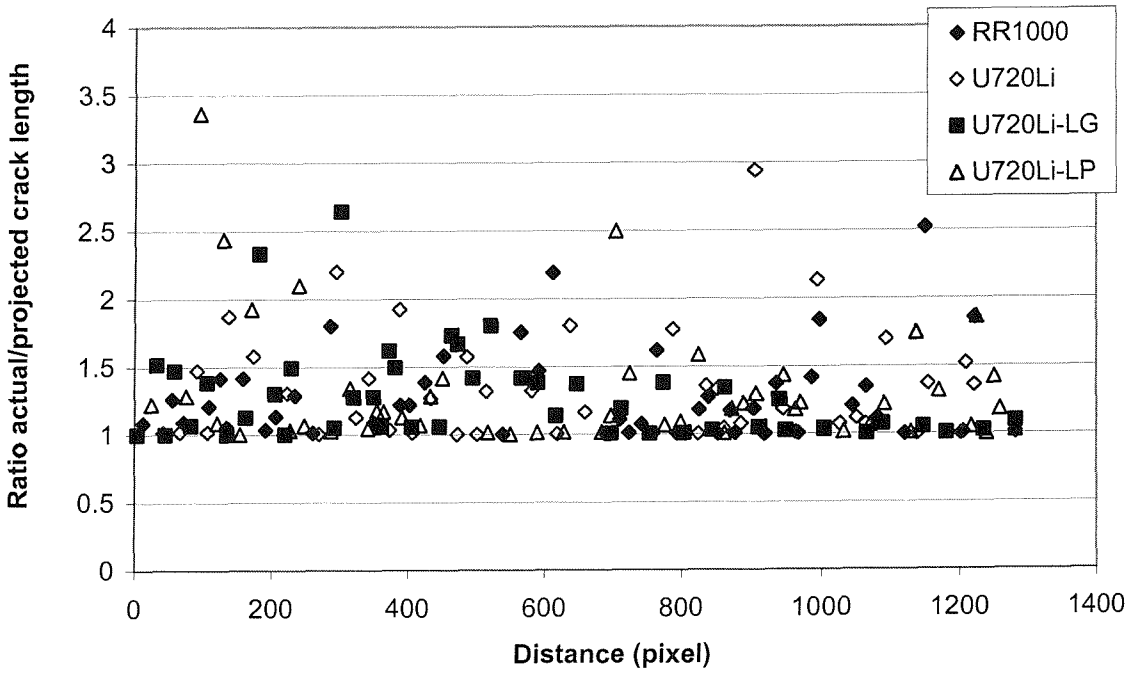

Figure 4-37: Actual/projected crack length.

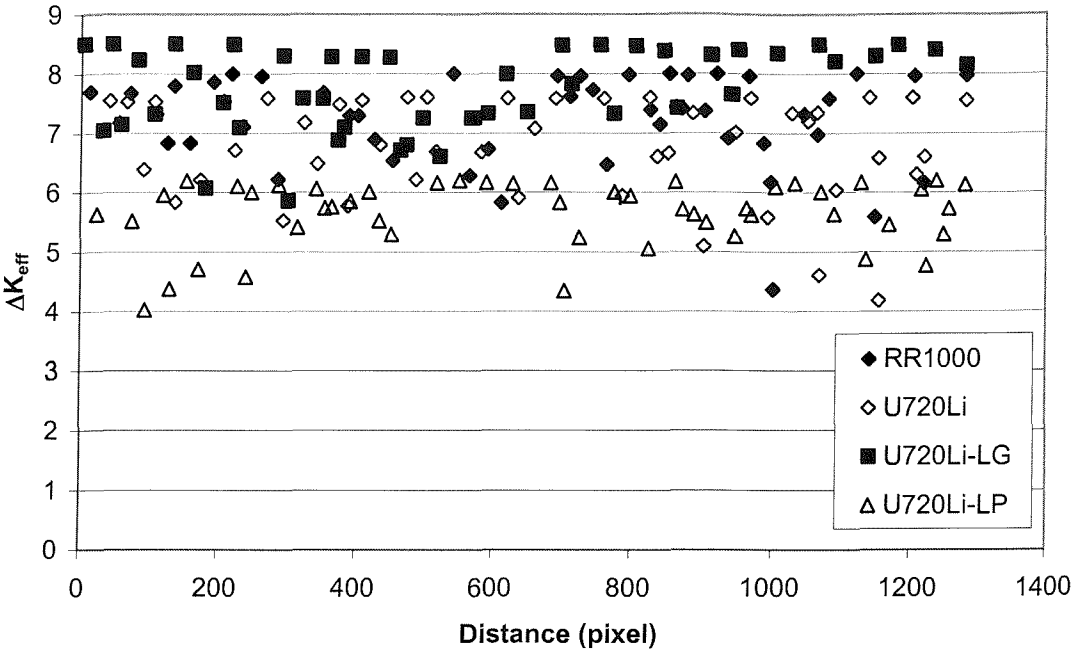

Figure 4-38: Local ΔK_{eff} variation due to crack deflection.

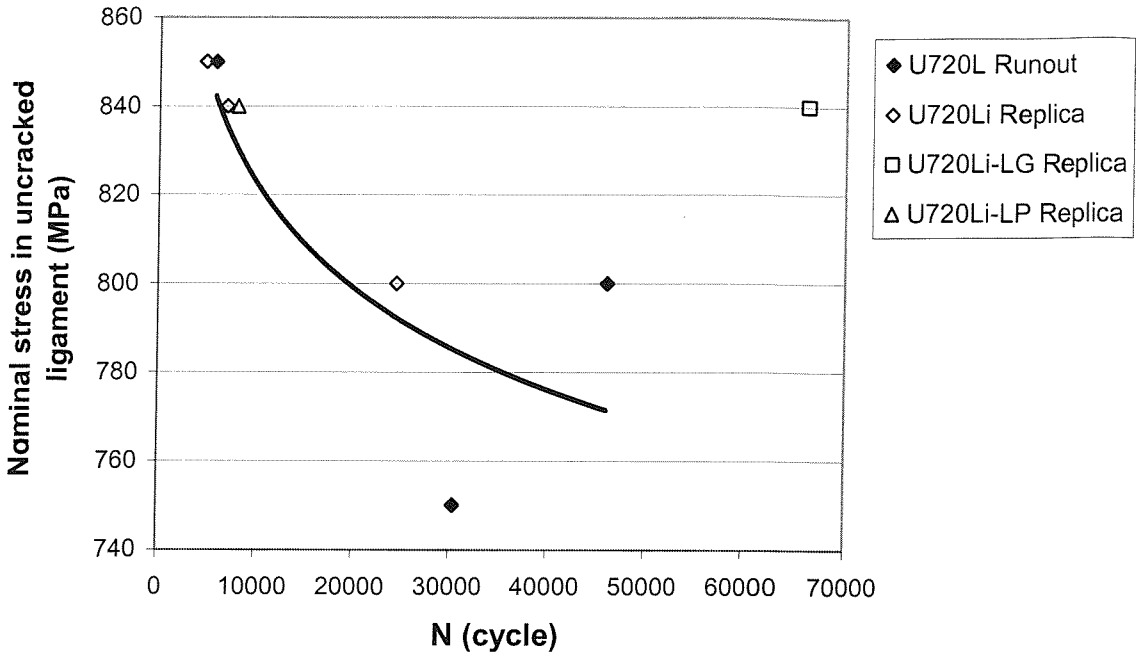

Figure 4-39: S-N curve from runout and replication test results.

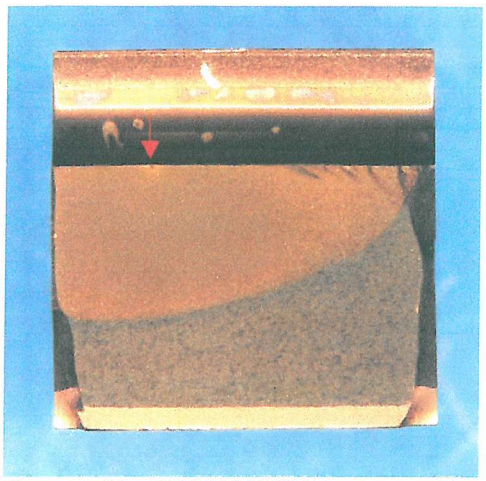

Figure 4-40a: U720Li 750MPa runout (Test 1HS); overall fracture surface.

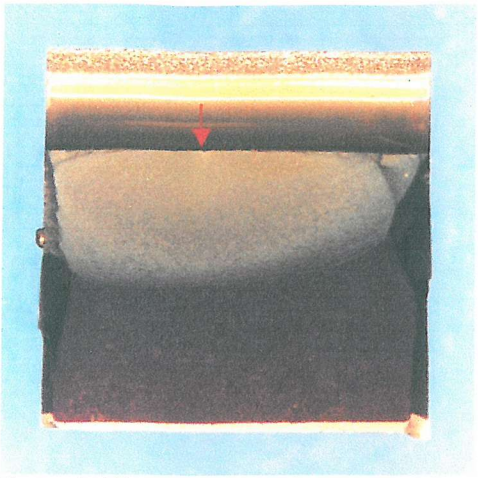

Figure 4-40b: U720Li 800MPa runout (Test 4HS); overall fracture surface.

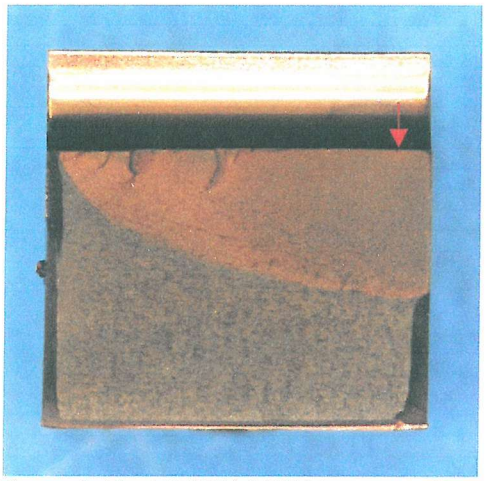

Figure 4-40c: U720Li 850MPa runout (Test 2HS); overall fracture surface.

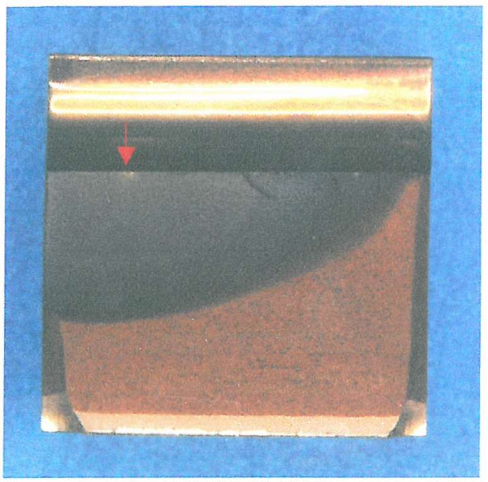

Figure 4-40d: U720Li 800MPa replica (Test 3HS); overall fracture surface.

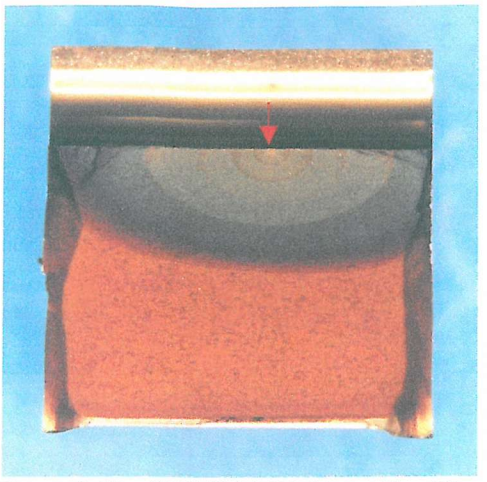

Figure 4-40e: U720Li 840MPa replica (Test 10HS); overall fracture surface.

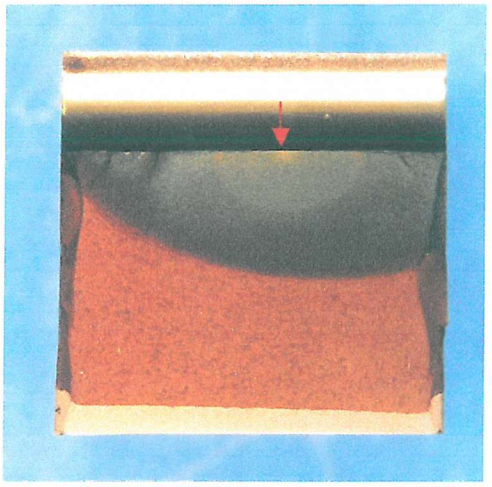

Figure 4-40f: U720Li 850MPa replica (Test 6HS); overall fracture surface.

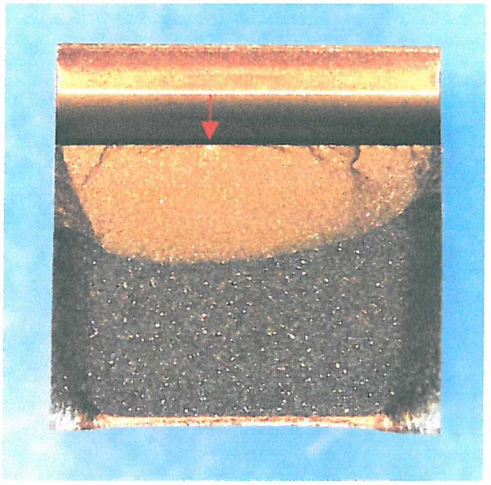

Figure 4-40g: U720Li-LG 840MPa replica (Test 8HS); overall fracture surface.

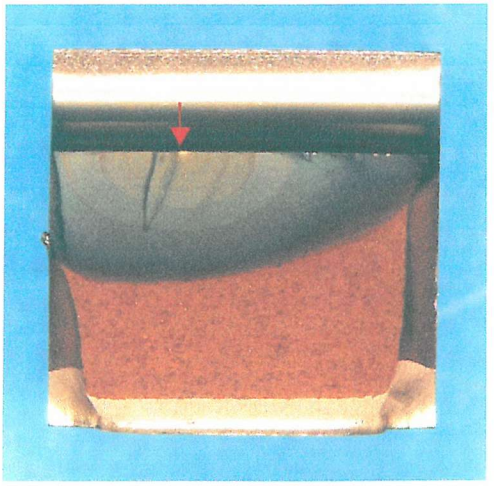

Figure 4-40h: U720Li-LP 840MPa replica (Test 9HS); overall fracture surface.

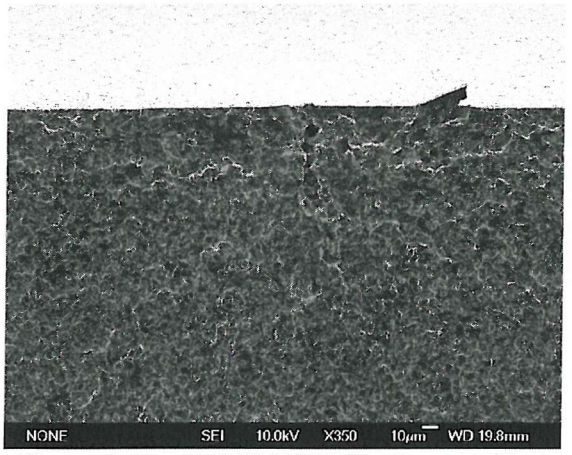

Figure 4-41a: U720Li 750MPa Runout (Test 1HS); primary crack initiation site 350x.

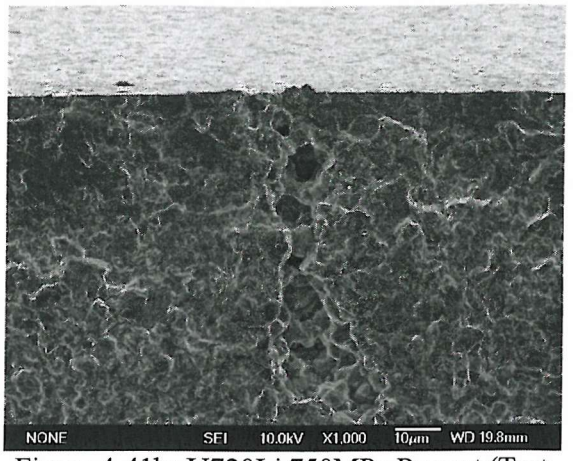

Figure 4-41b: U720Li 750MPa Runout (Test 1HS); primary crack initiation site 1000x.

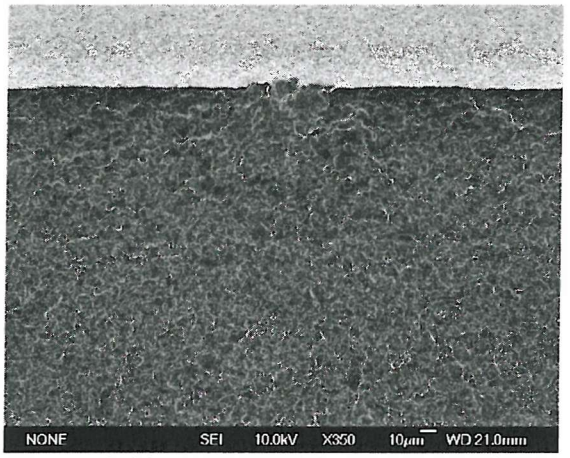

Figure 4-41c: U720Li 800MPa Runout (Test 4HS); primary crack initiation site 350x.

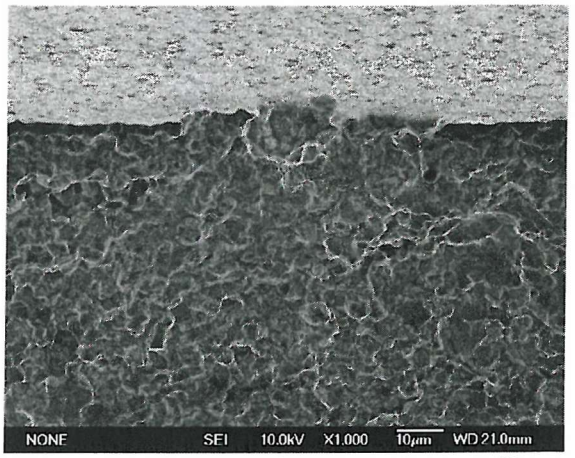

Figure 4-41d: U720Li 800MPa Runout (Test 4HS); primary crack initiation site 1000x.

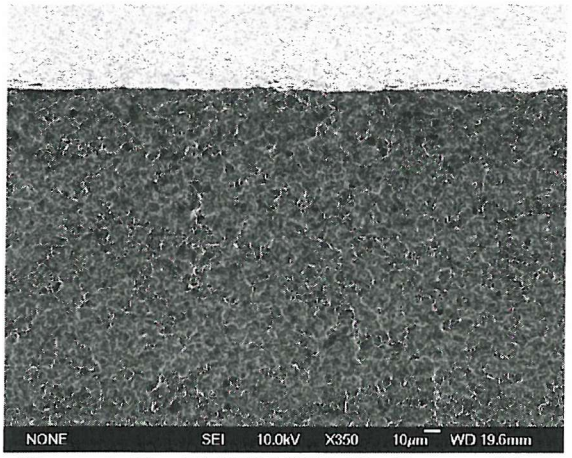

Figure 4-41e: U720Li 850MPa Runout (Test 2HS); primary crack initiation site 350x.

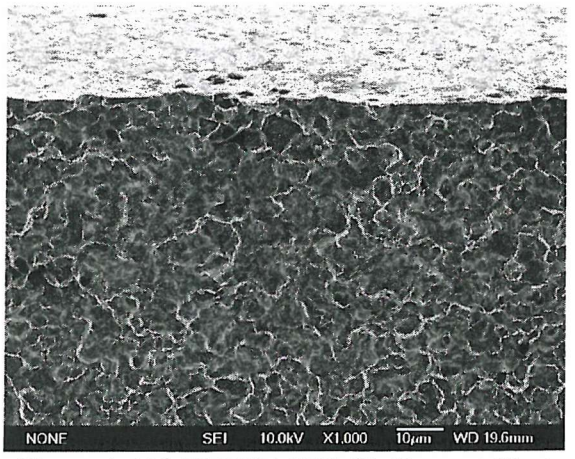

Figure 4-41f: U720Li 850MPa Runout (Test 2HS); primary crack initiation site 1000x.

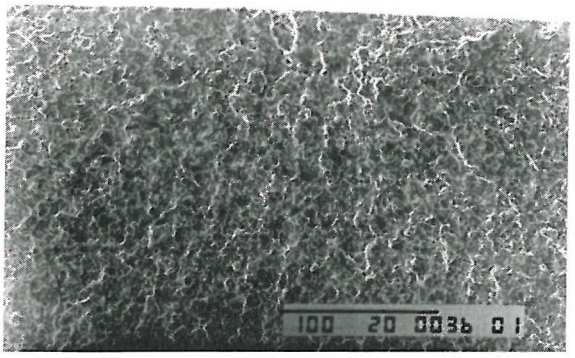

Figure 4-42a: U720Li 800MPa Replica (Test 3HS); primary crack initiation site 350x.

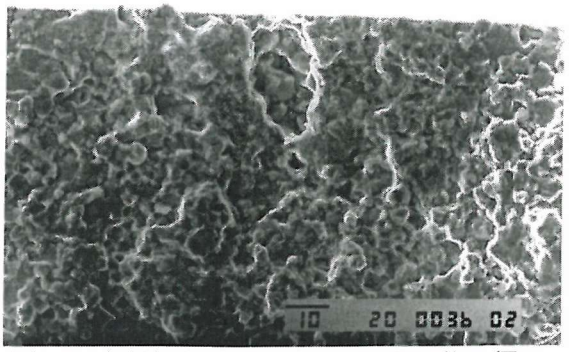

Figure 4-42b: U720Li 800MPa Replica (Test 3HS); primary crack initiation site 1000x.

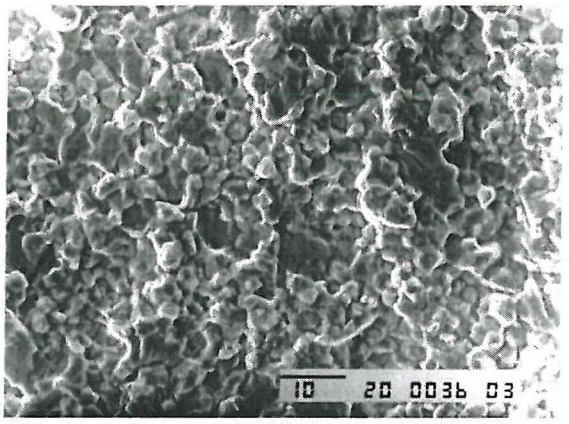

Figure 4-42c: U720Li 800MPa Replica (Test 3HS); crack growth 0.1mm below primary crack initiation site.

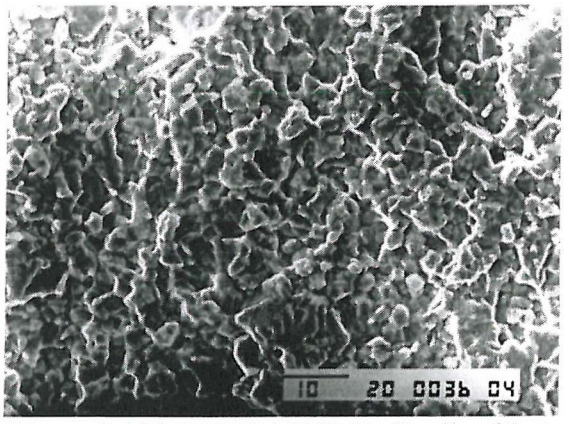

Figure 4-42d: U720Li 800MPa Replica (Test 3HS); crack growth 0.2mm below primary crack initiation site.

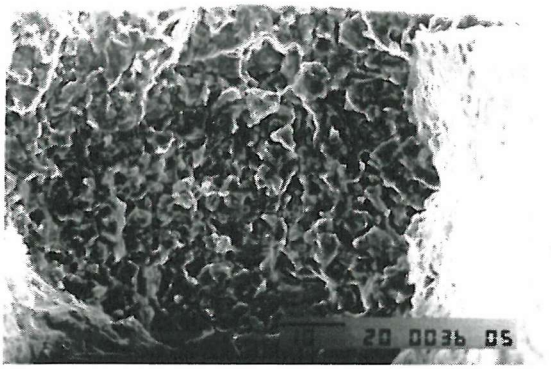

Figure 4-42e: U720Li 800MPa Replica (Test 3HS); secondary crack initiation from subsurface porosity.

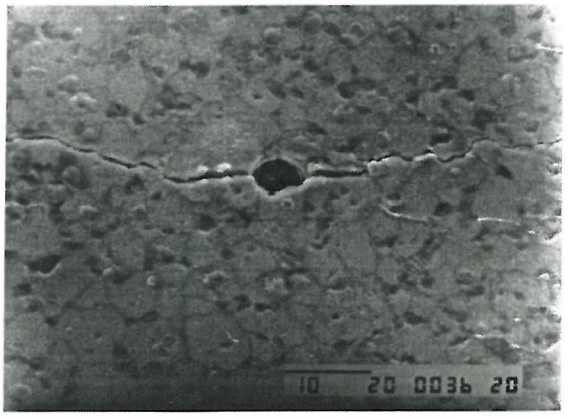

Figure 4-42f: U720Li 800MPa Replica (Test 3HS); secondary crack initiation from surface porosity.

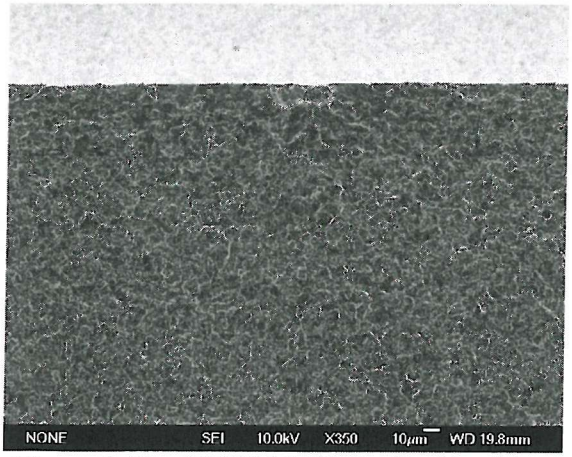

Figure 4-42g: U720Li 840MPa Replica (Test 10HS); primary crack initiation site 350x.

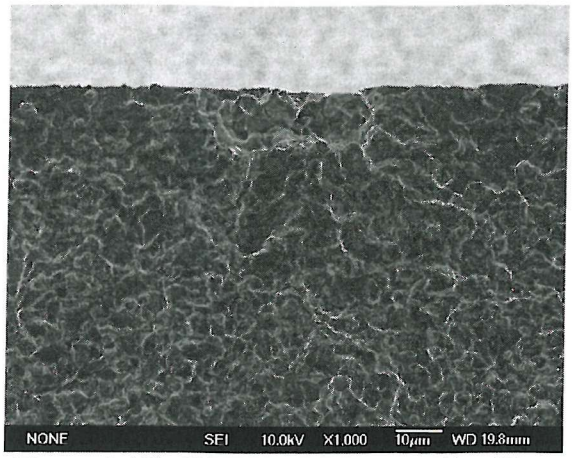

Figure 4-42h: U720Li 840MPa Replica (Test 10HS); primary crack initiation site 1000x.

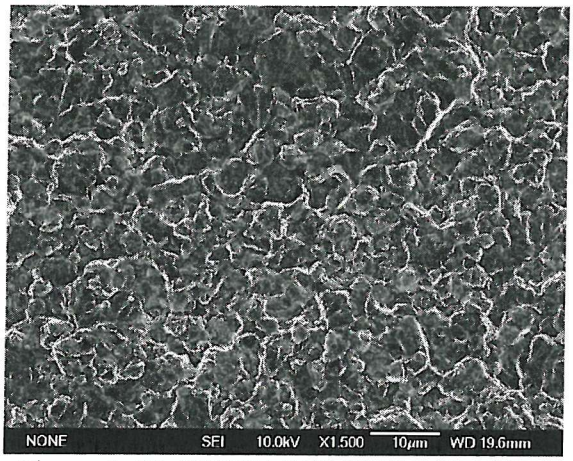

Figure 4-42i: U720Li 840MPa Replica (Test 10HS); crack growth 0.1mm below primary crack initiation site.

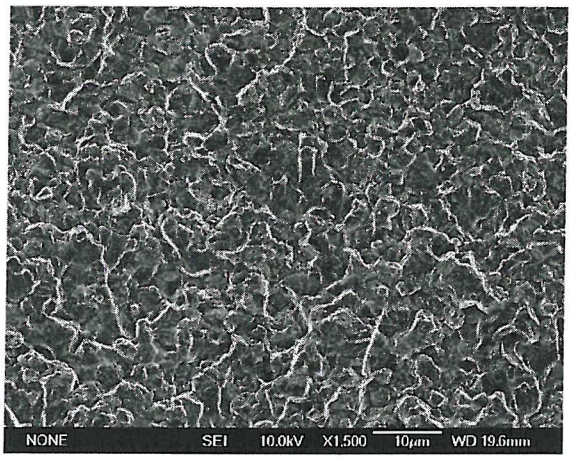

Figure 4-42j: U720Li 840MPa Replica (Test 10HS); crack growth 0.2mm below primary crack initiation site.

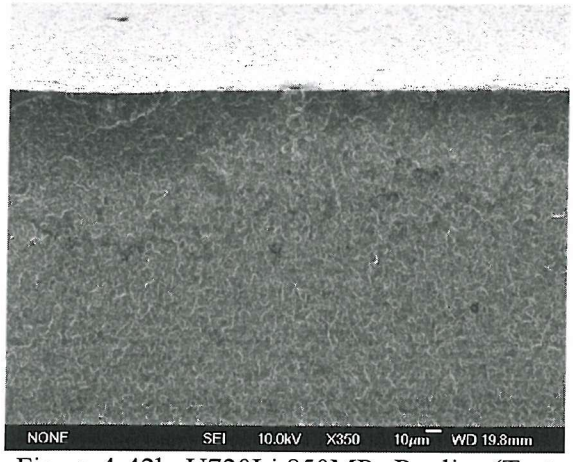

Figure 4-42k: U720Li 850MPa Replica (Test 6HS); primary crack initiation site 350x.

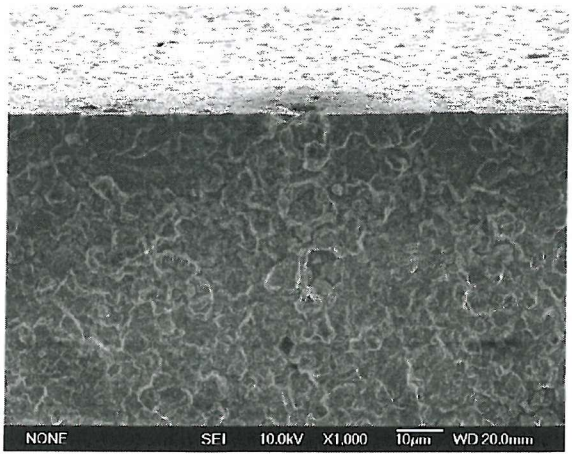

Figure 4-42l: U720Li 850MPa Replica (Test 6HS); primary crack initiation site 1000x.

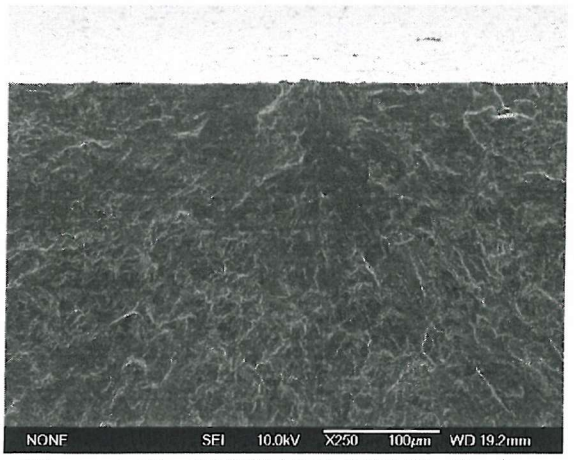

Figure 4-43a: U720Li-LG 840MPa Replica (Test 8HS); primary crack initiation site 250x.

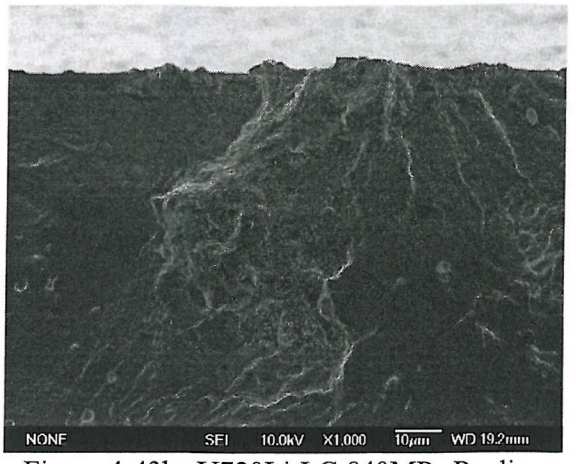

Figure 4-43b: U720Li-LG 840MPa Replica (Test 8HS); primary crack initiation site 1000x.

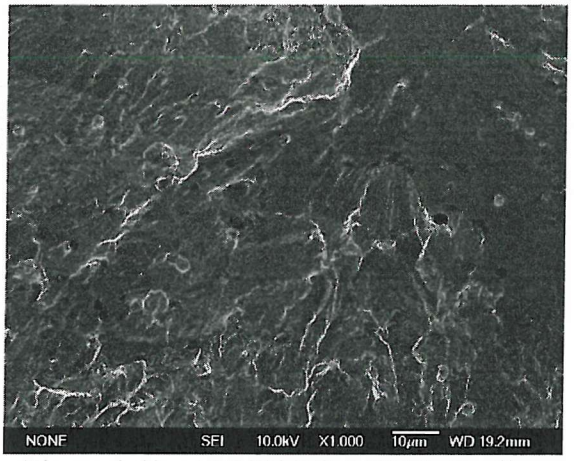

Figure 4-43c: U720Li-LG 840MPa Replica (Test 8HS); crack growth 0.1mm below primary crack initiation site.

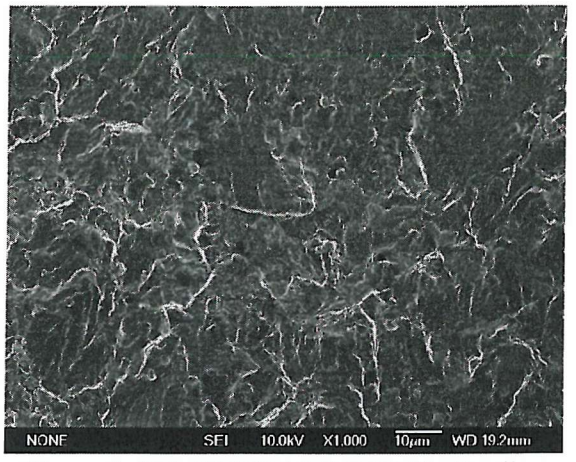

Figure 4-43d: U720Li-LG 840MPa Replica (Test 8HS); crack growth 0.2mm below primary crack initiation site.

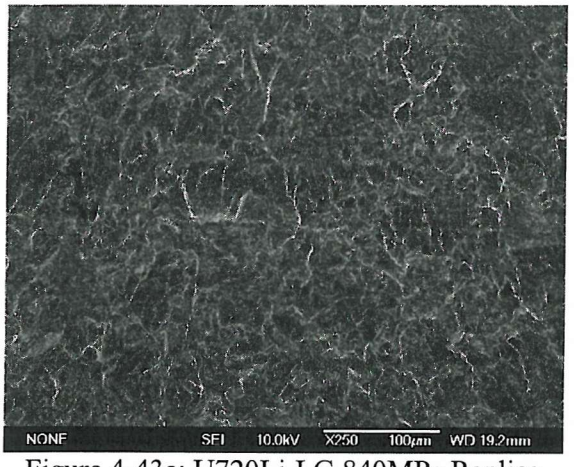

Figure 4-43e: U720Li-LG 840MPa Replica (Test 8HS); crack growth 0.5mm below primary crack initiation site.

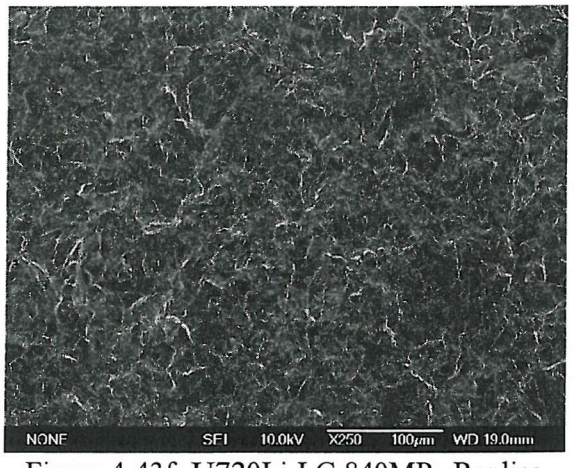

Figure 4-43f: U720Li-LG 840MPa Replica (Test 8HS); crack growth 1.0mm below primary crack initiation site.

Figure 4-43g: U720Li-LG 840MPa Replica (Test 8HS); top surface of example secondary crack #1.

Figure 4-43h: U720Li-LG 840MPa Replica (Test 8HS); top surface of example secondary crack #2.

Figure 4-43i: U720Li-LG 840MPa Replica (Test 8HS); top surface of primary crack initiation site 350x.

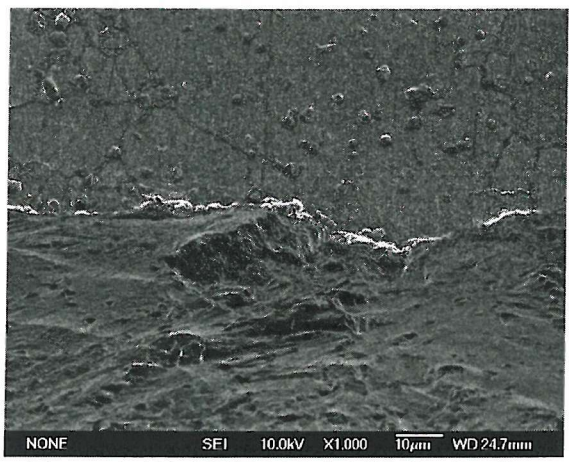

Figure 4-43j: U720Li-LG 840MPa Replica (Test 8HS); top surface of primary crack initiation site 1000x.

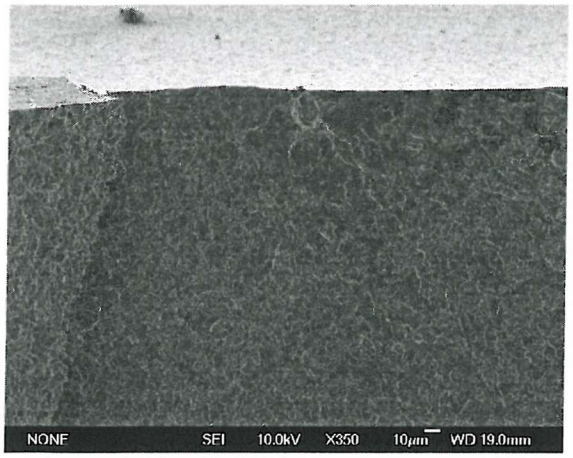

Figure 4-44a: U720Li-LP 840MPa Replica (Test 9HS); primary crack initiation site 350x.

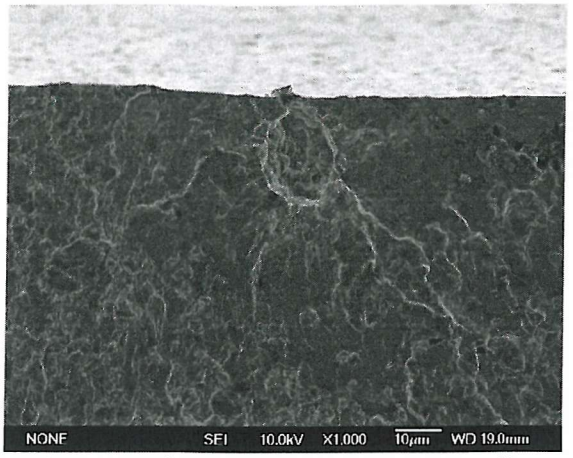

Figure 4-44b: U720Li-LP 840MPa Replica (Test 9HS); primary crack initiation site 1000x.

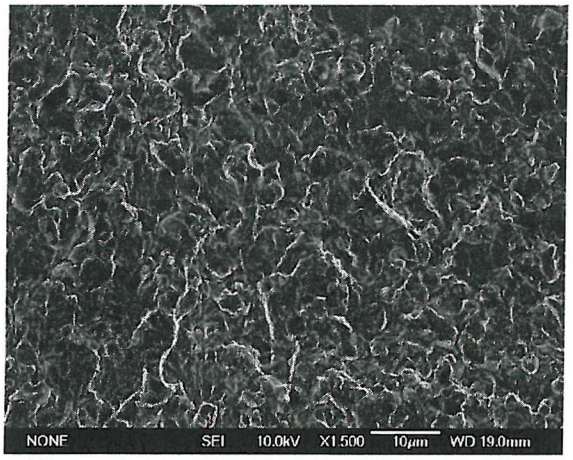

Figure 4-44c: U720Li-LP 840MPa Replica (Test 9HS); crack growth 0.1mm below primary crack initiation site.

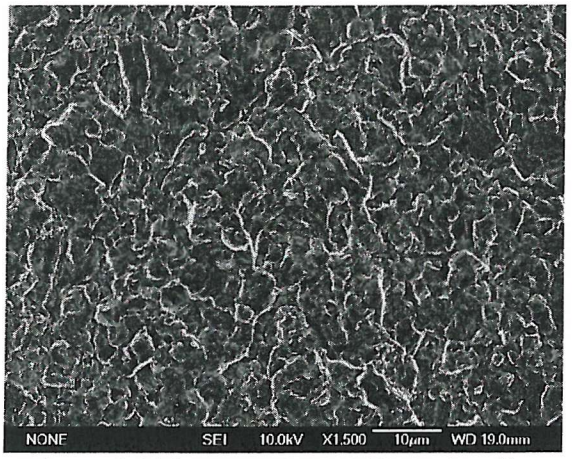

Figure 4-44d: U720Li-LP 840MPa Replica (Test 9HS); crack growth 0.2mm below primary crack initiation site.

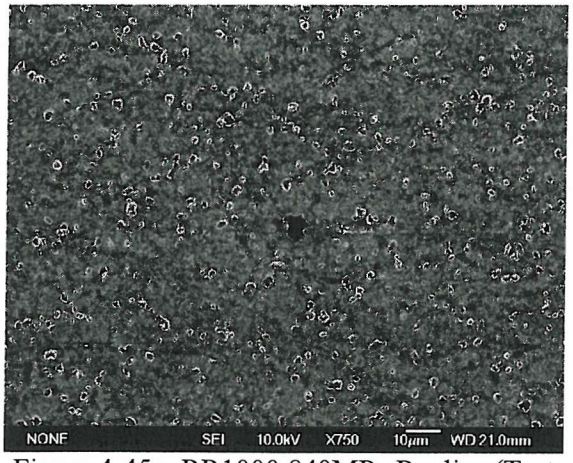

Figure 4-45a: RR1000 840MPa Replica (Test 7HS); top surface 750x.

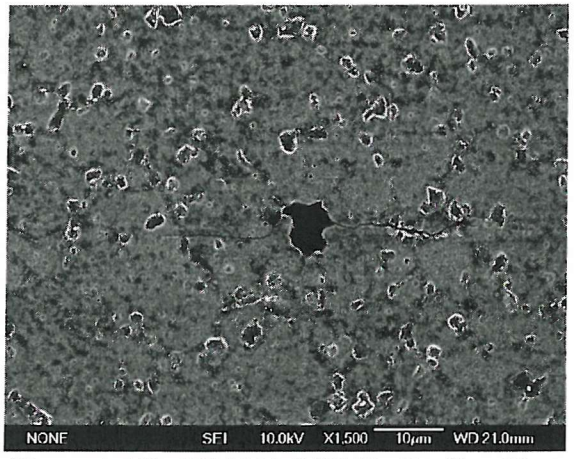

Figure 4-45b: RR1000 840MPa Replica (Test 7HS); top surface 1500x.

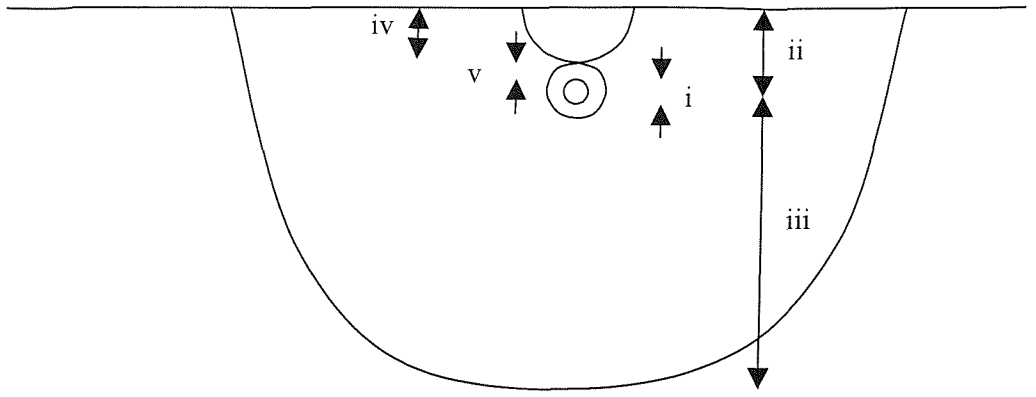

i - size of pore.

ii - distance from centre of pore to surface.

iii - distance from centre of pore to edge of flat area.

iv - crack depth when surface initiated crack coalesce with subsurface initiated crack.

v - crack length corresponding to crack growth in vacuum

Transgranular crack growth in vacuum, [v] = [ii] - [iv] - ½[i]

Transgranular crack growth in air = [iii] - [v] - ½ [i]

Figure 4-46: Crack initiation site feature of U720Li-LG.

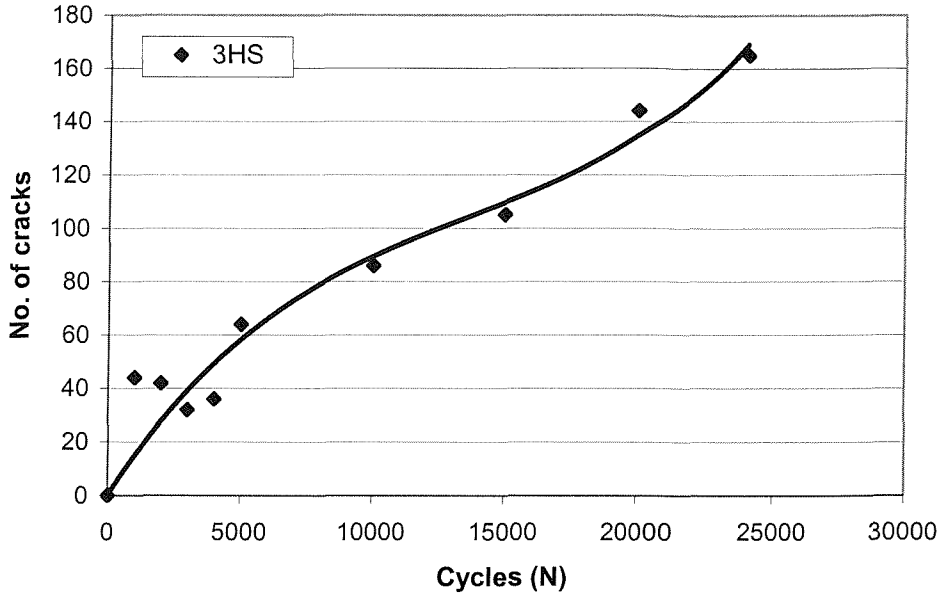

Figure 4-47a: Crack field characterisation; U720Li 800MPa (Test 3HS).

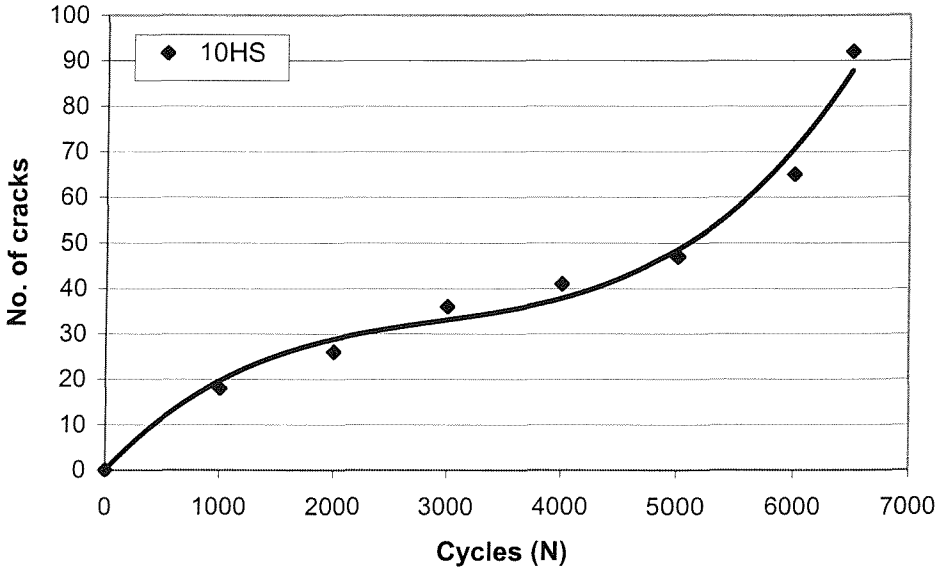

Figure 4-47b: Crack field characterisation; U720Li 840MPa (Test 10HS).

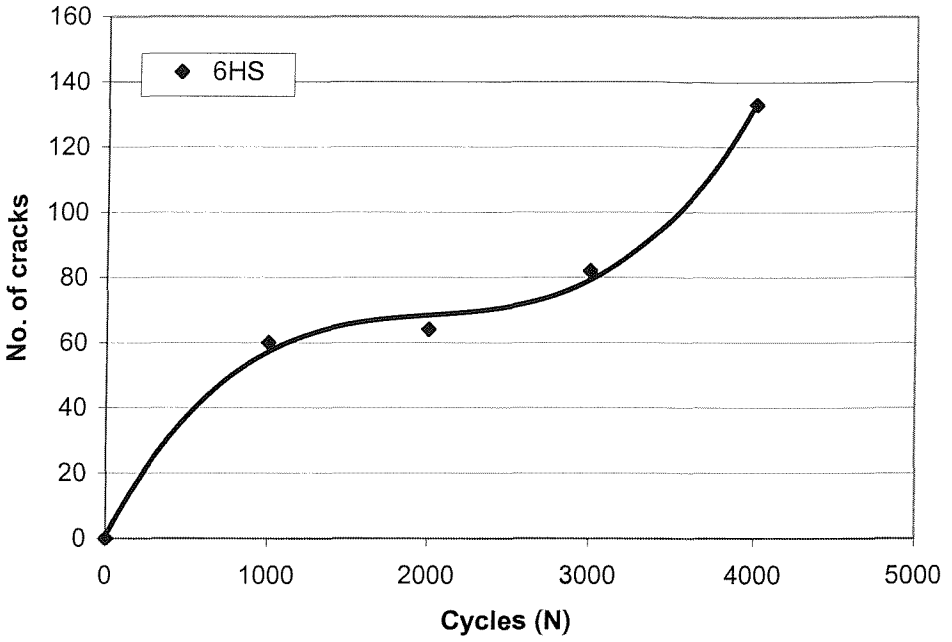

Figure 4-47c: Crack field characterisation; U720Li 850MPa (Test 6HS).

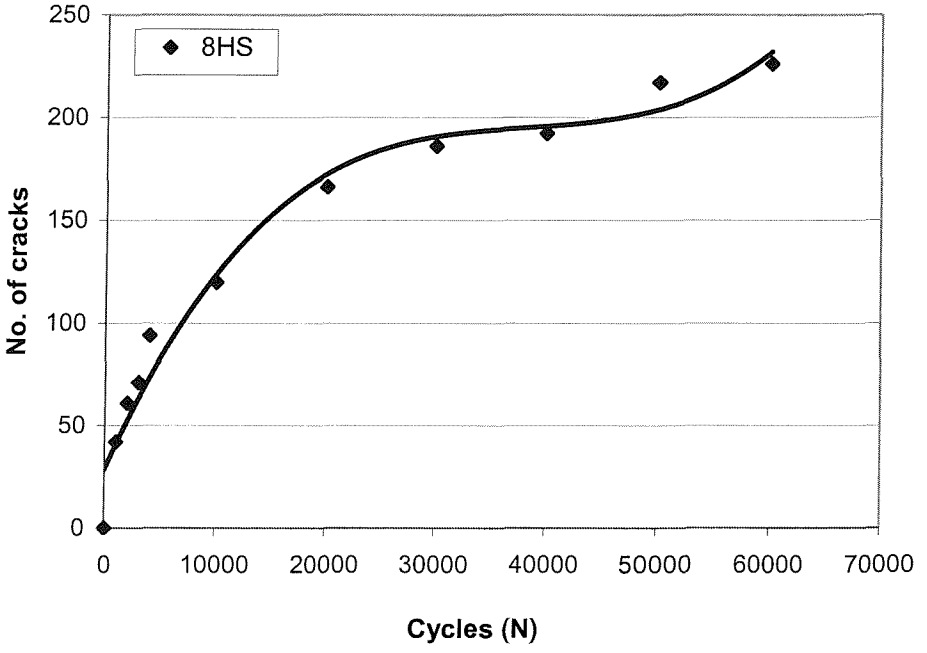

Figure 4-47d: Crack field characterisation; U720Li-LG 840MPa (Test 8HS).

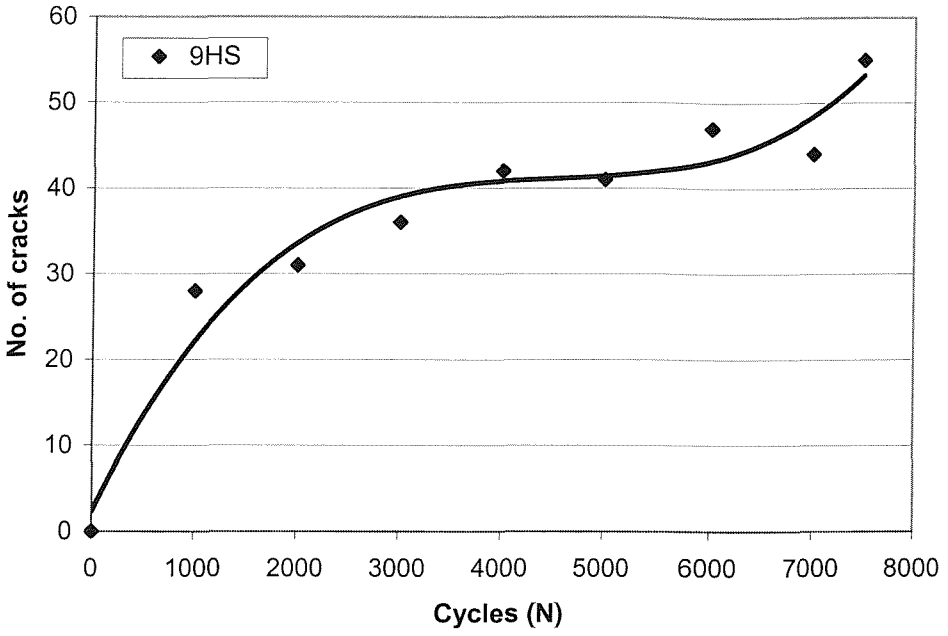

Figure 4-47e: Crack field characterisation; U720Li-LP 840MPa (Test 9HS).

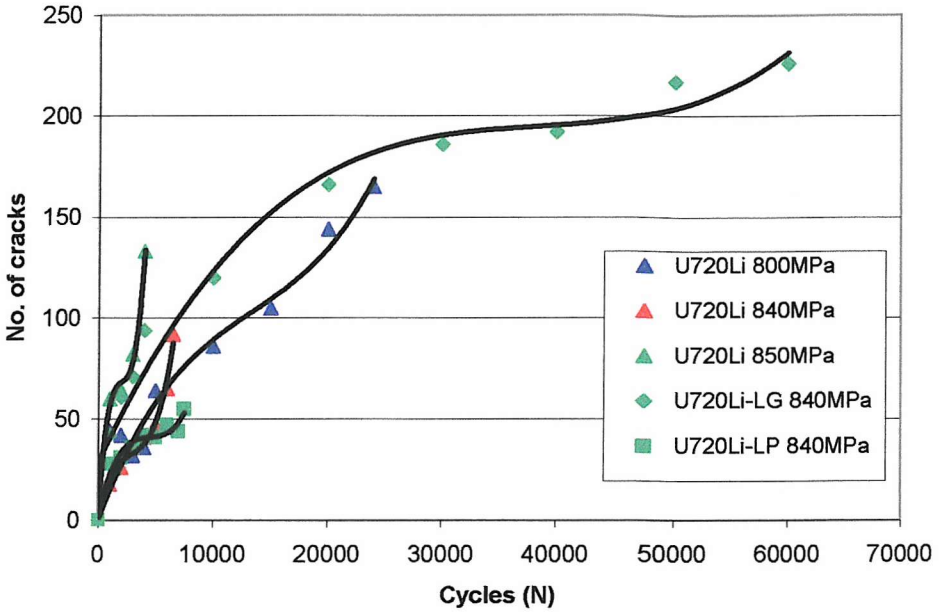

Figure 4-48a: Crack field characterisation; all tests.

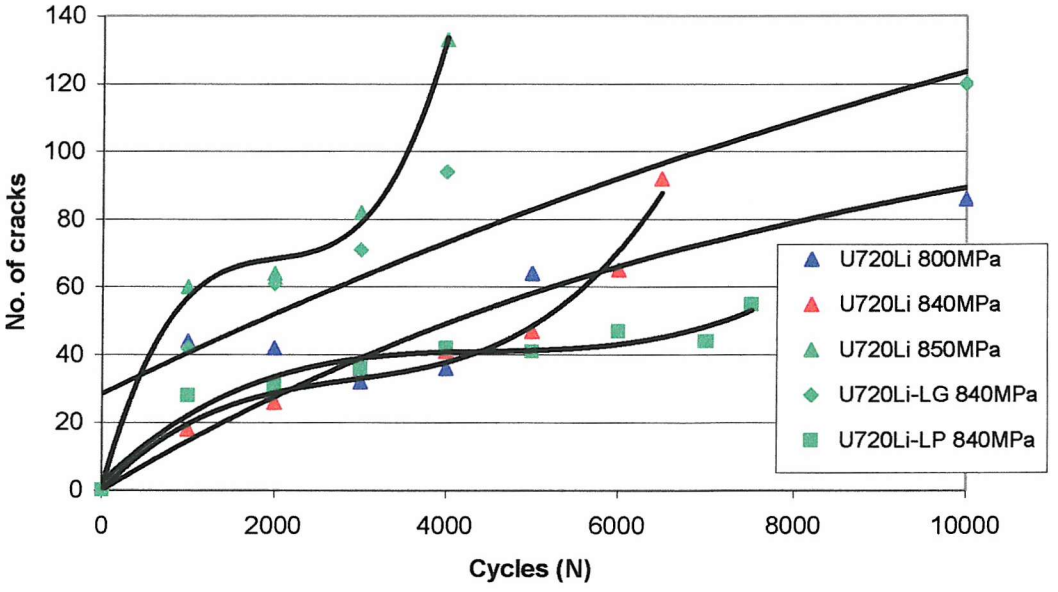

Figure 4-48b: Crack field characterisation; all tests higher detail.

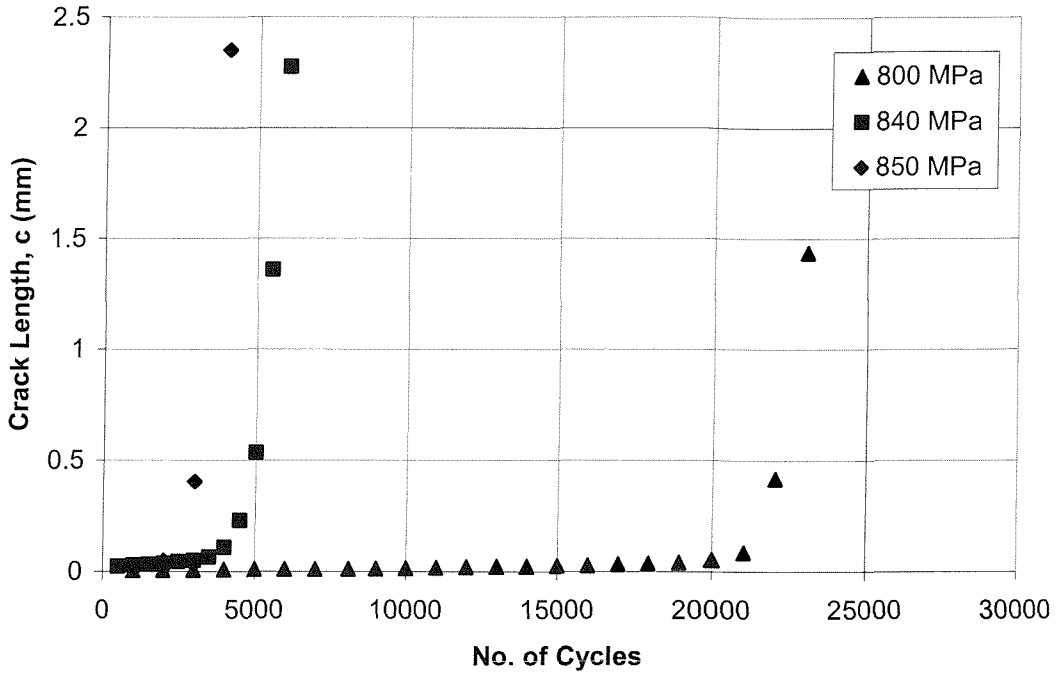

Figure 4-49a: Crack length vs. number of cycles (U720Li primary crack).

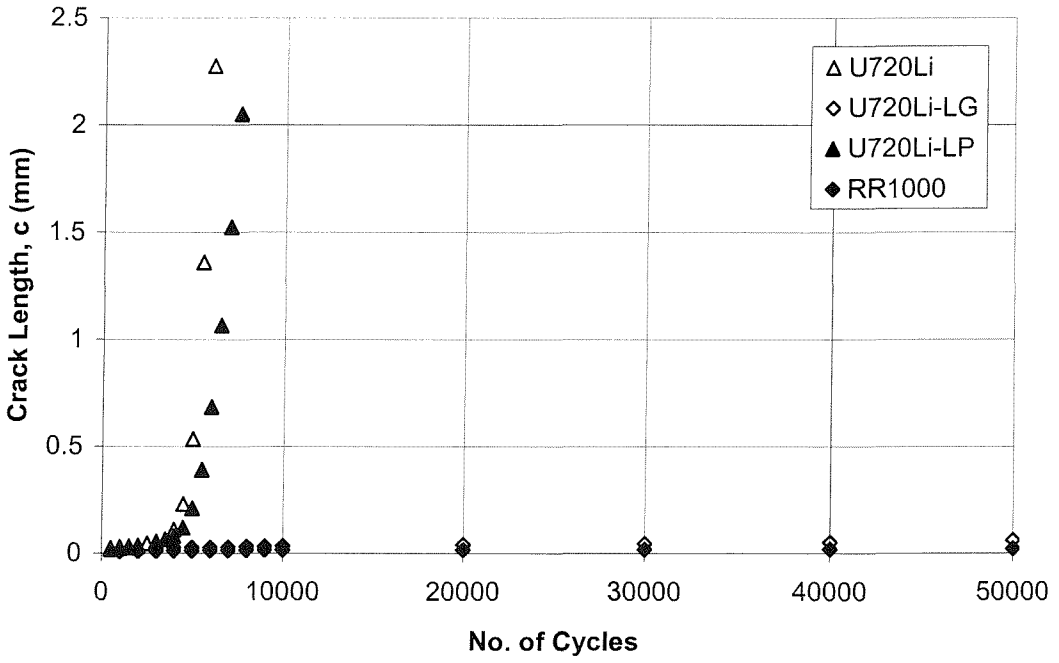

Figure 4-49b: Crack length vs. number of cycles (840MPa primary crack).

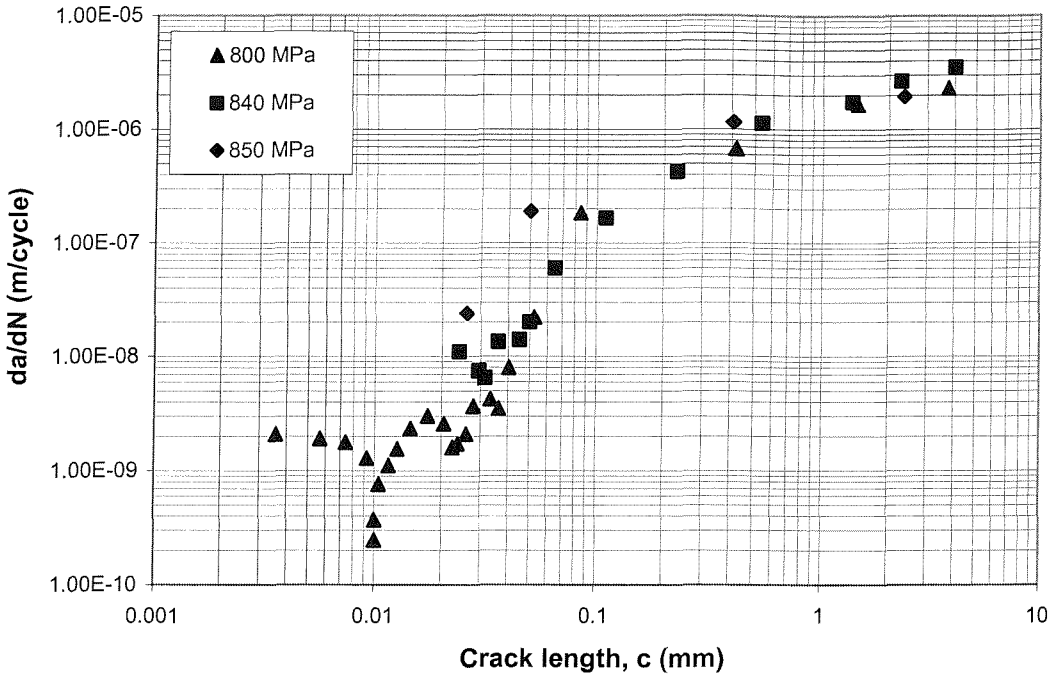

Figure 4-50a: Crack growth rates vs. crack length (U720Li primary crack).

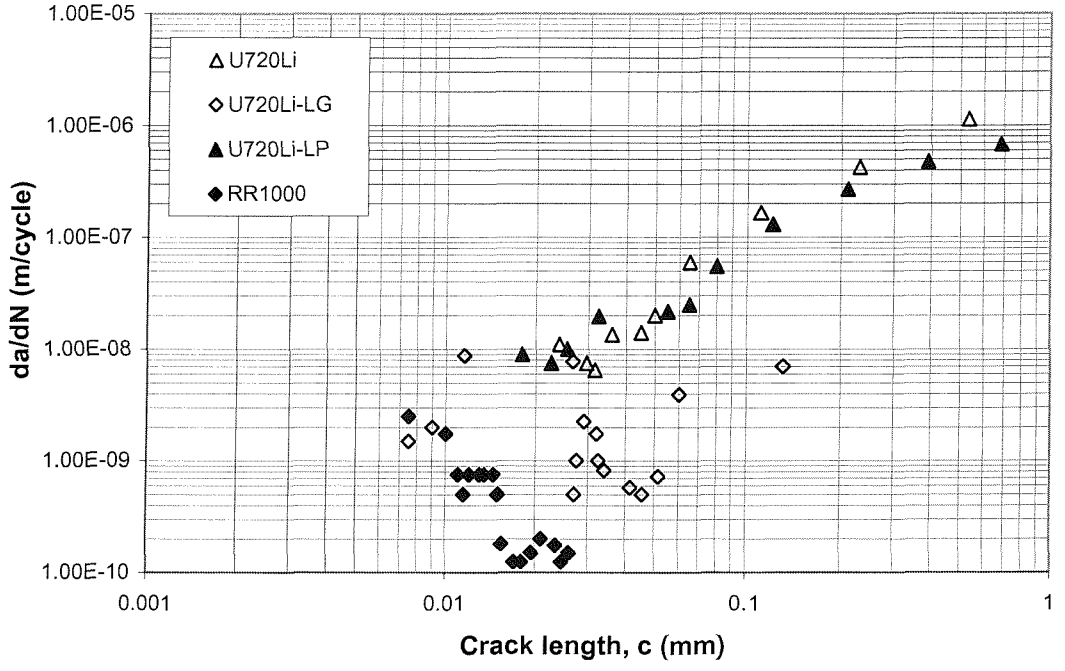

Figure 4-50b: Crack growth rates vs. crack length (840MPa primary crack).

First arrest point ~ 7000 cycles

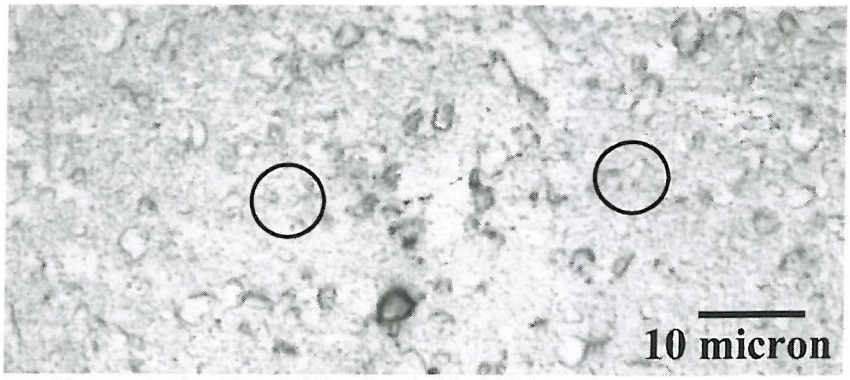

Figure 4-51a: Test 3HS - Crack 12, 1000 cycles 1000x

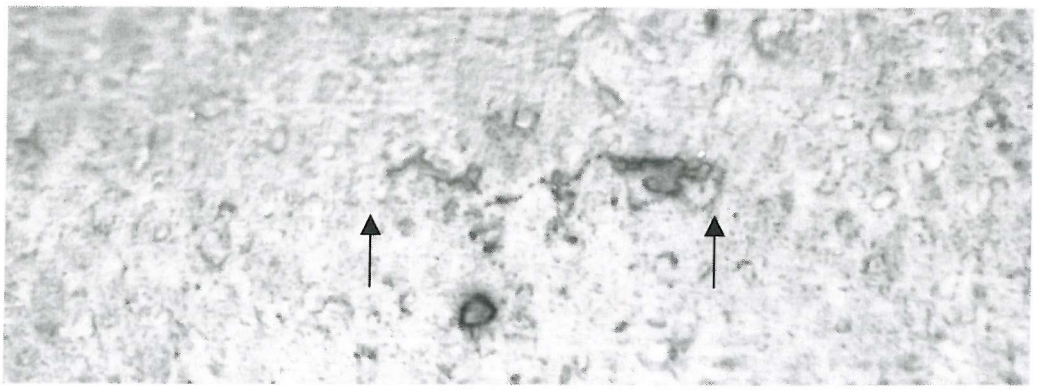

Figure 4-51b: Test 3HS - Crack 12, 5000 cycles 1000x

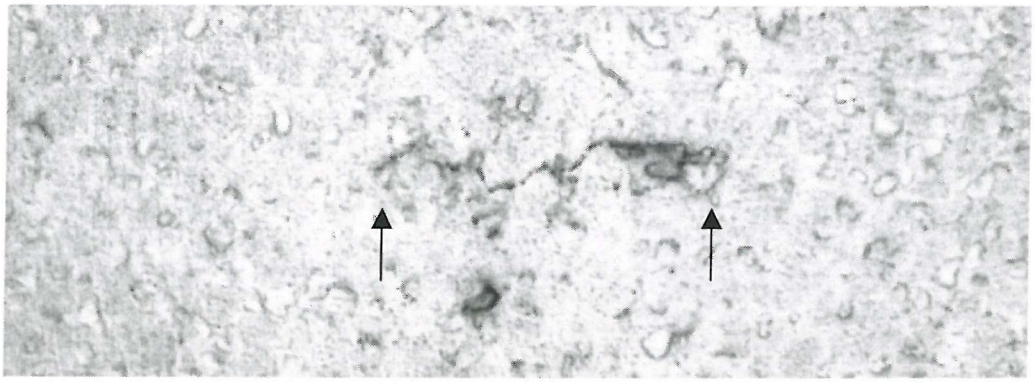

Figure 4-51c: Test 3HS - Crack 12, 6000 cycles 1000x

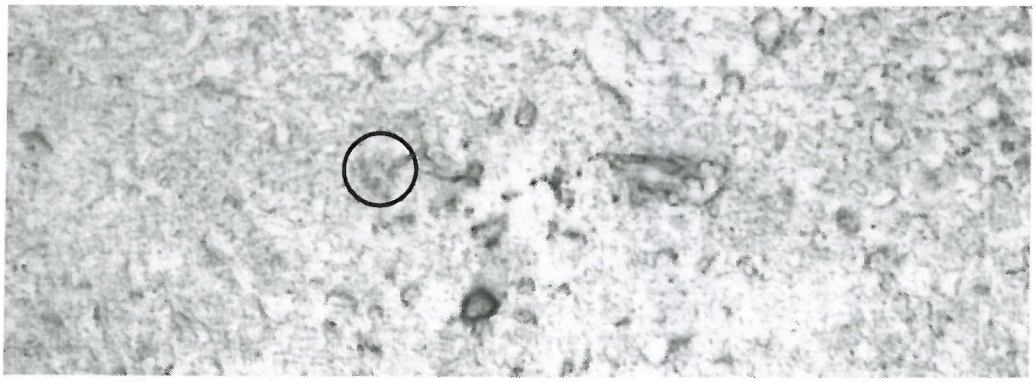

Figure 4-51d: Test 3HS - Crack 12, 7000 cycles 1000x

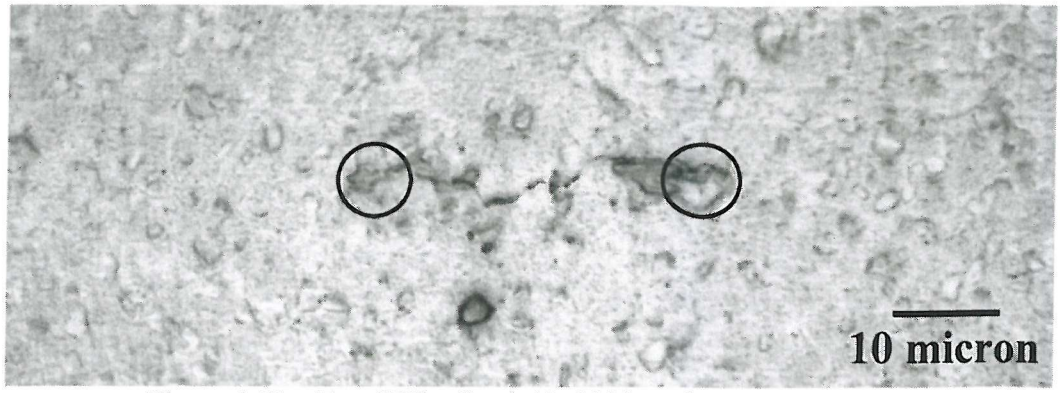

Figure 4-51e: Test 3HS - Crack 12, 8000 cycles 1000x

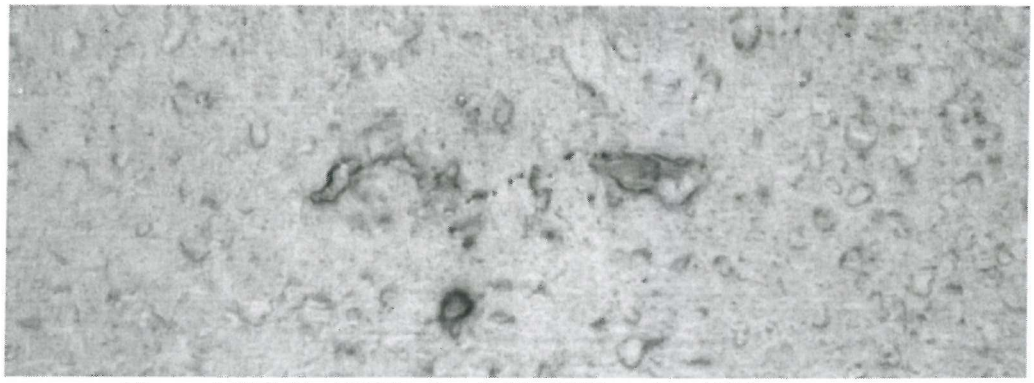
Figure 4-51f: Test 3HS - Crack 12, 9000 cycles 1000x

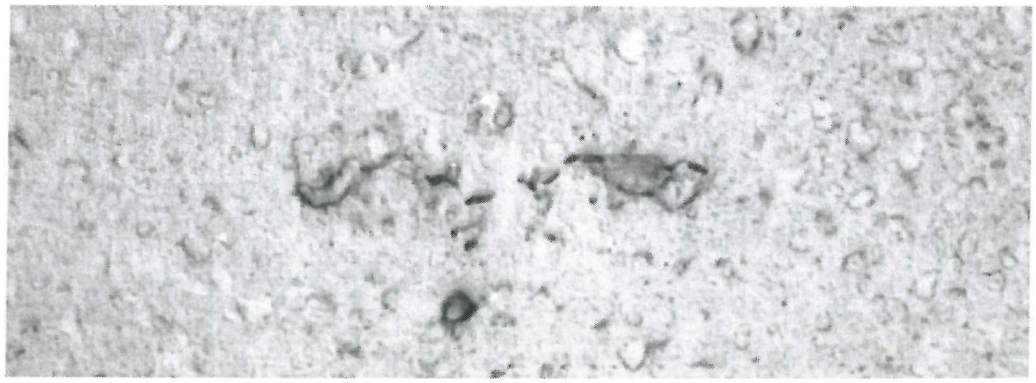
Figure 4-51g: Test 3HS - Crack 12, 10000 cycles 1000x

Second arrest point ~ 15000 cycles

Figure 4-52a: Test 3HS - Crack 12, 13000 cycles 1000x

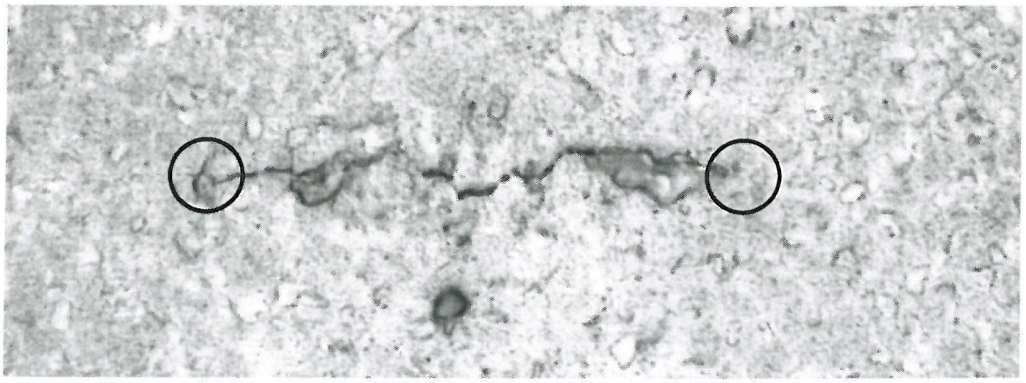

Figure 4-52b: Test 3HS - Crack 12, 14000 cycles 1000x

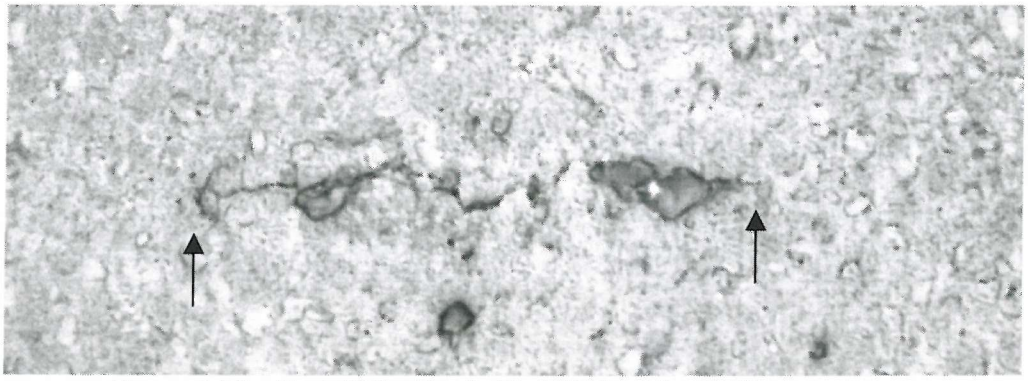

Figure 4-52c: Test 3HS - Crack 12, 15000 cycles 1000x

Figure 4-52d: Test 3HS - Crack 12, 16000 cycles 1000x

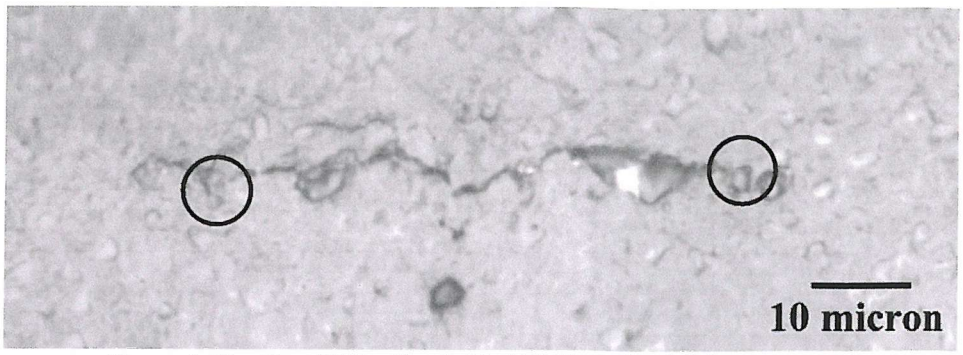

Figure 4-52e: Test 3HS - Crack 12, 17000 cycles 1000x

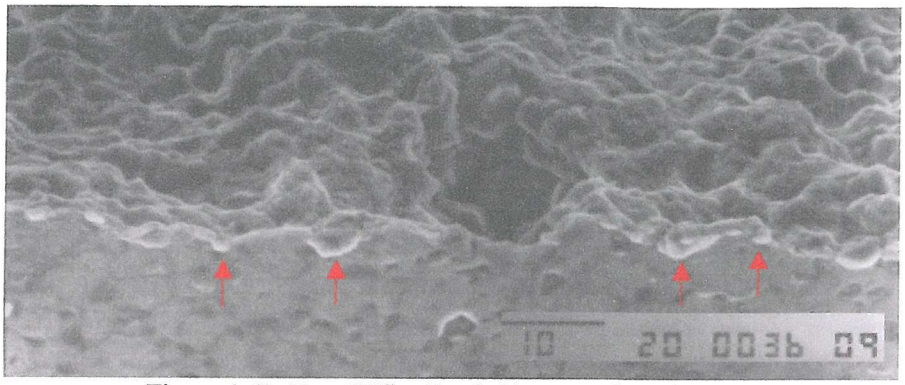

Figure 4-53: Test 3HS – Crack 12 top surface SEM.

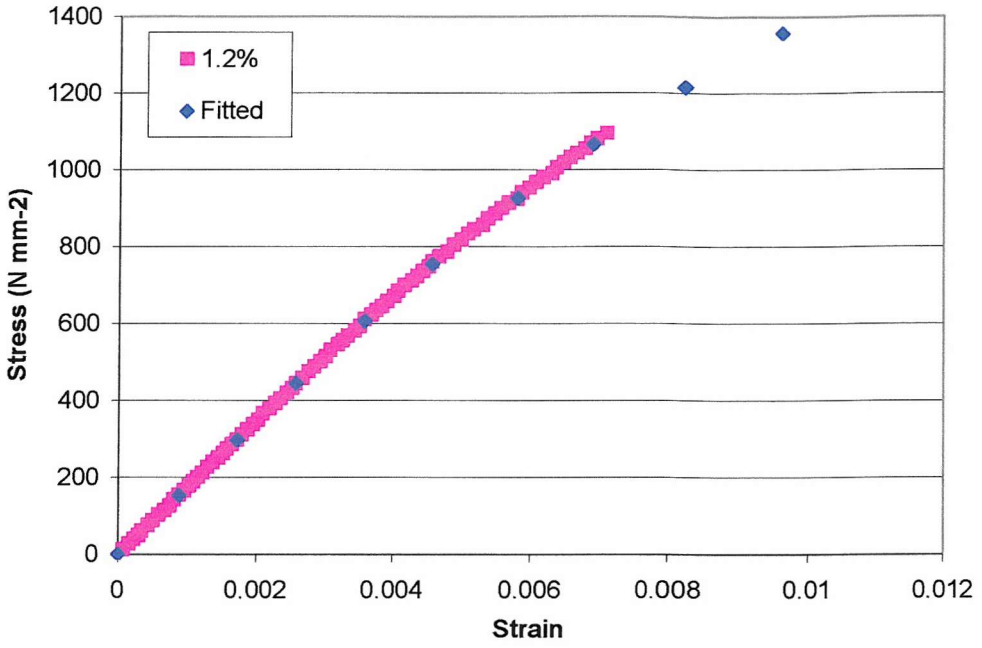

Figure 4-54: Stress-strain curve for FE analysis; U720Li.

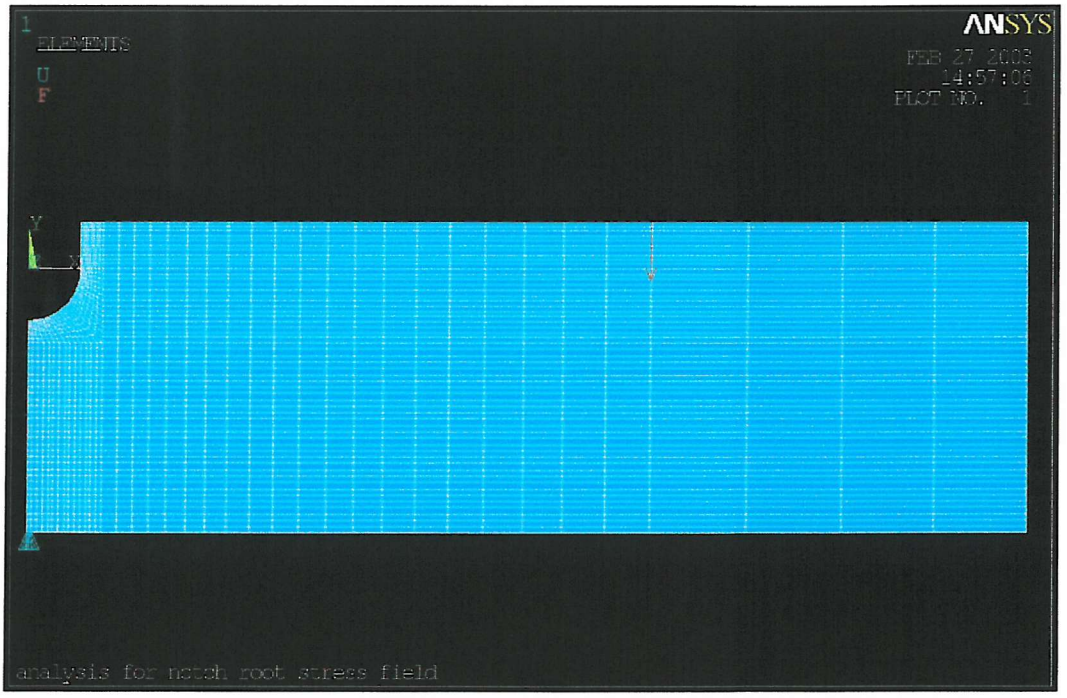

Figure 4-55: Finite element model geometry.

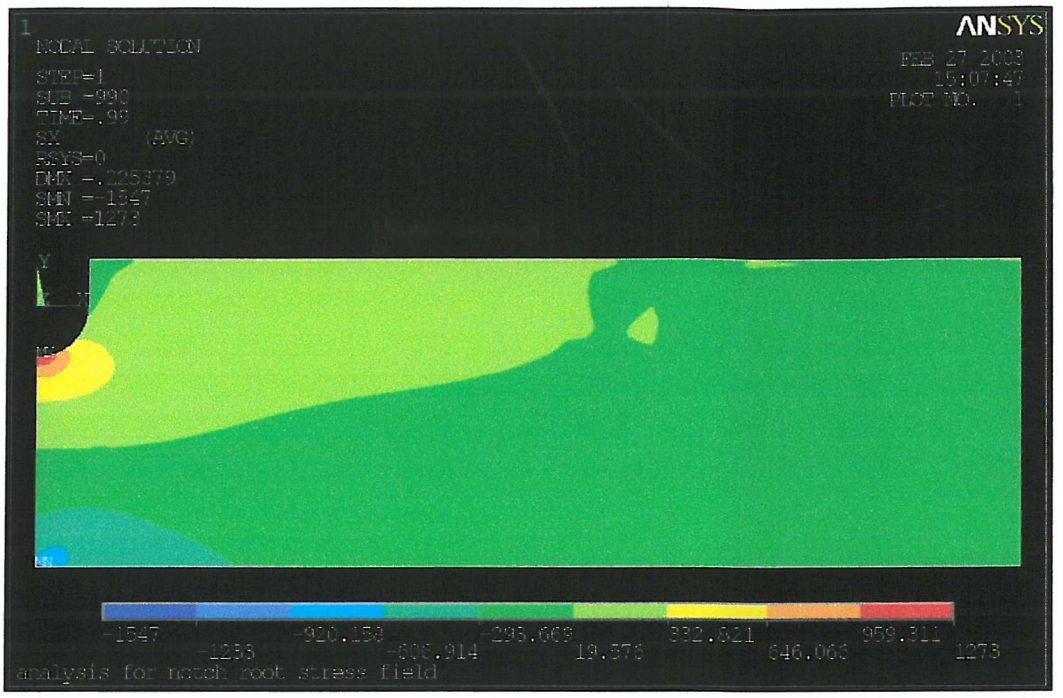

Figure 4-56a: Result of FE stress computation at maximum applied load of 9.9kN; U720Li 800MPa (Test 3HS).

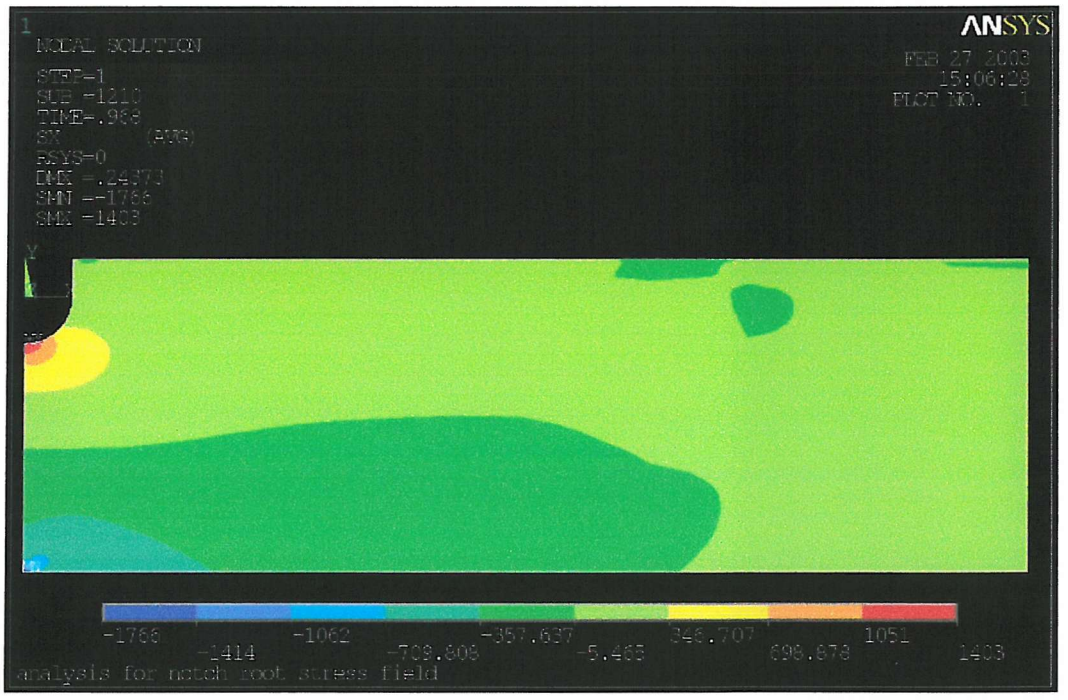

Figure 4-56b: Result of FE stress computation at maximum applied load of 12.1kN; U720Li 850MPa (Test 6HS).

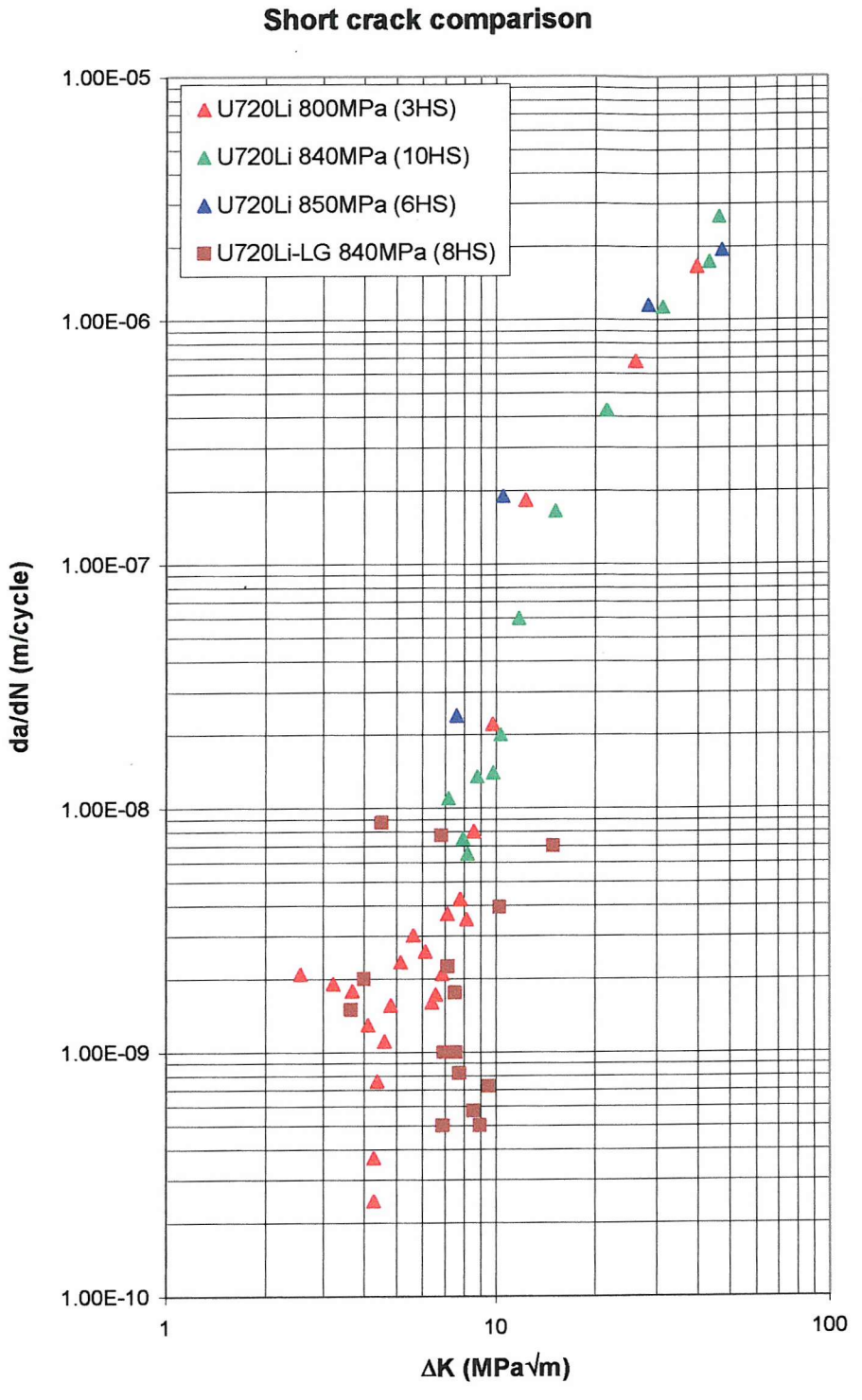

Figure 4-57: 650°C short crack growth rates vs. ΔK.

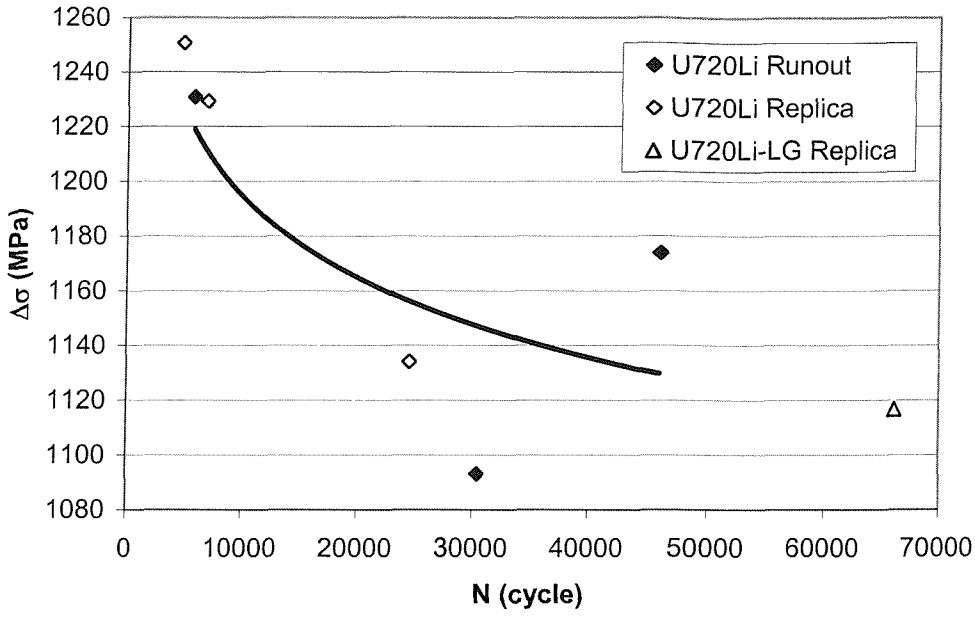

Figure 4-58a: Fatigue lifetime against stress-range in the notch root.

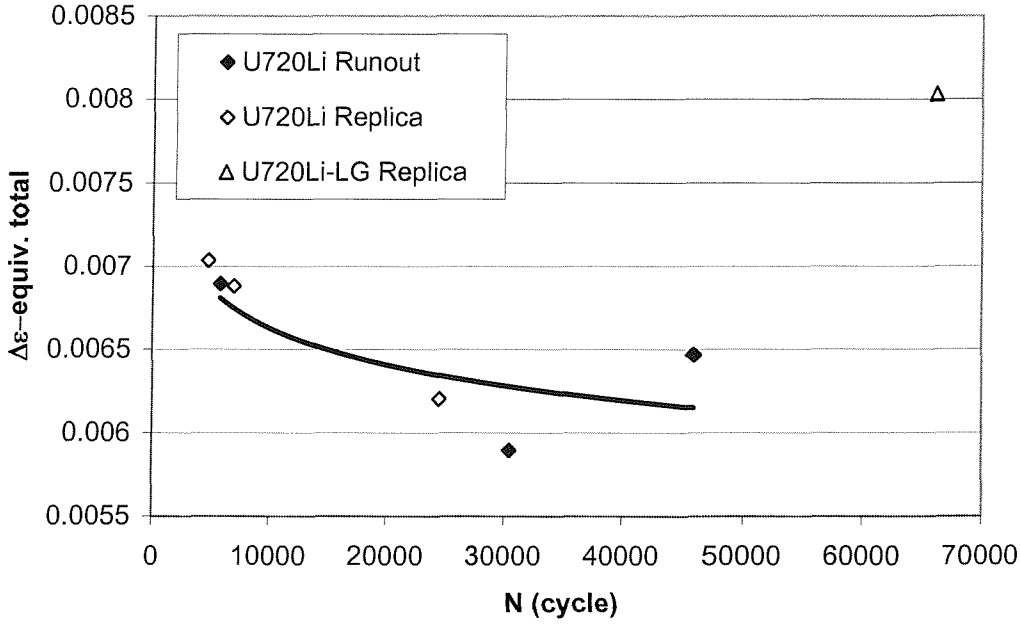

Figure 4-58b: Fatigue lifetime against total equivalent strain-range in the notch root.

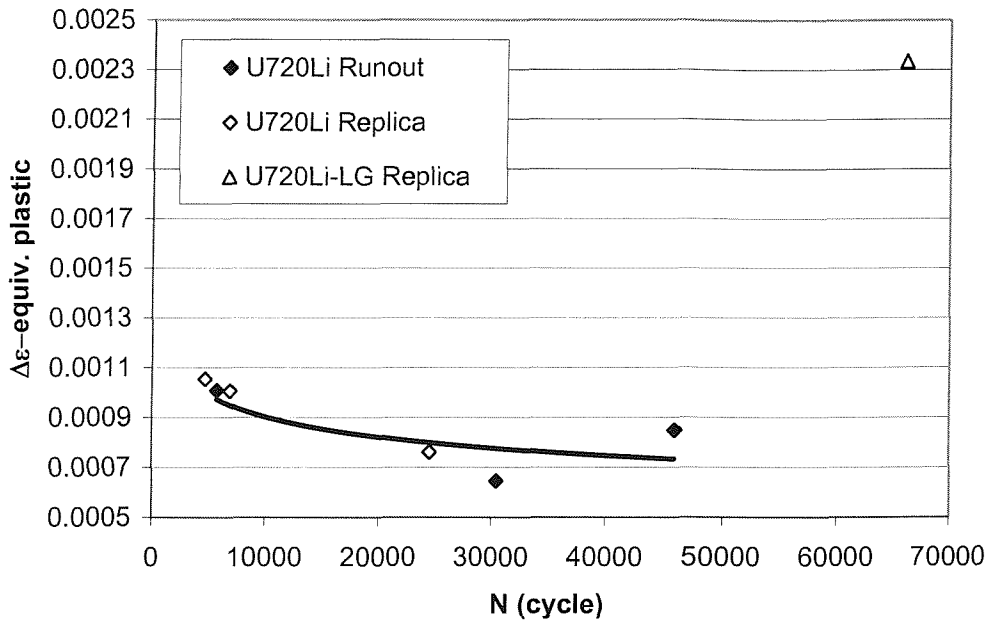

Figure 4-58c: Fatigue lifetime against equivalent plastic strain-range in the notch root.

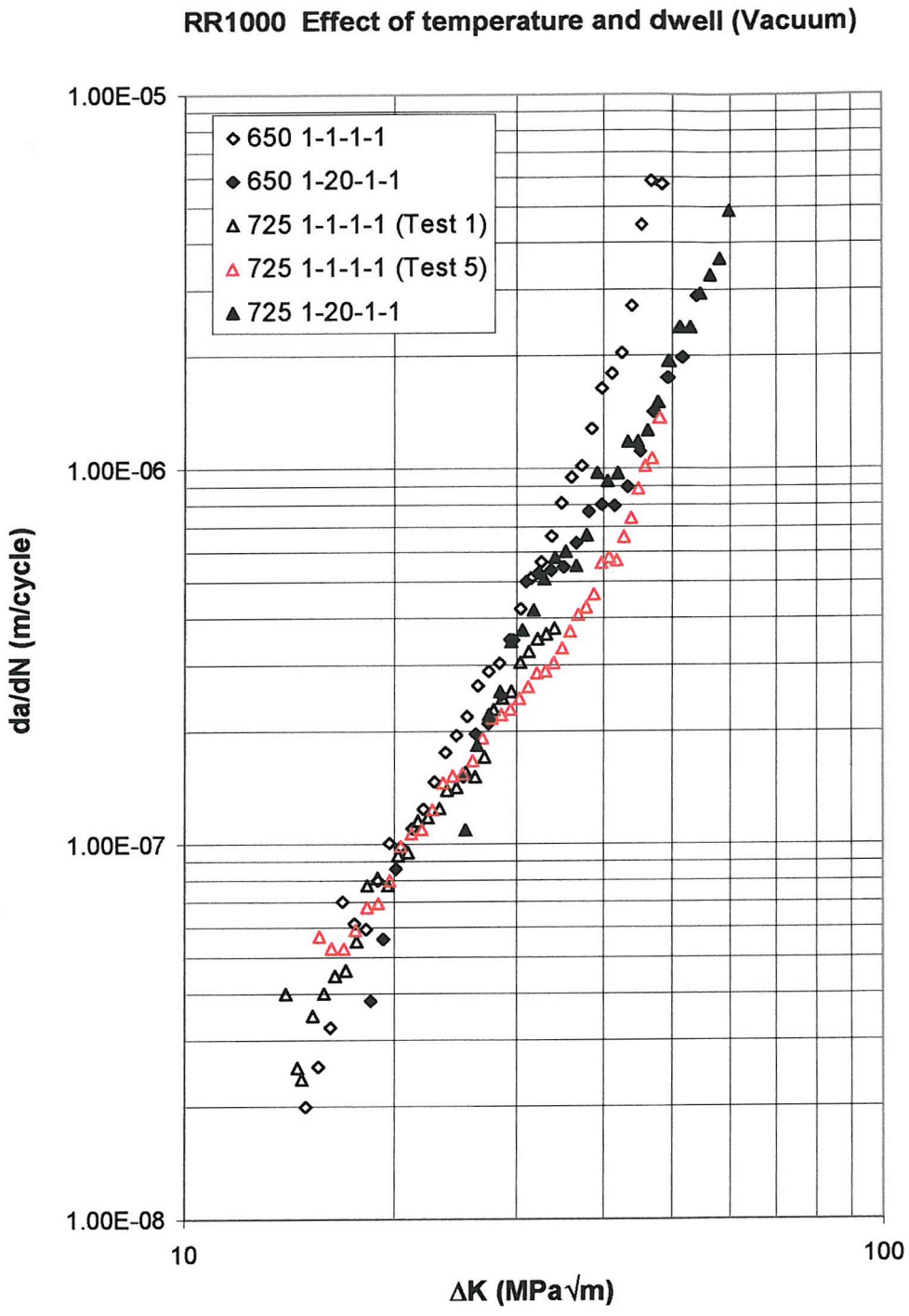

Figure 4-59: Vacuum growth out curves of RR1000 material.

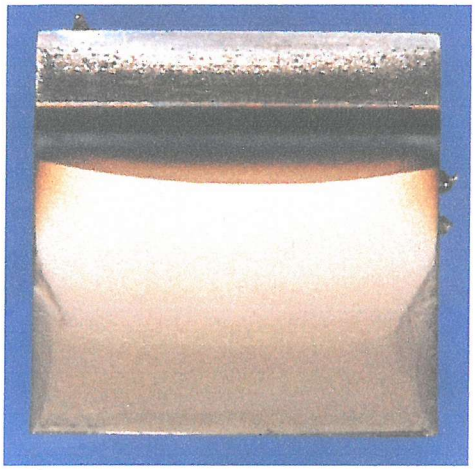

Figure 4-60a: RR1000; 650°C 1-1-1-1 vacuum; overall fracture surface.

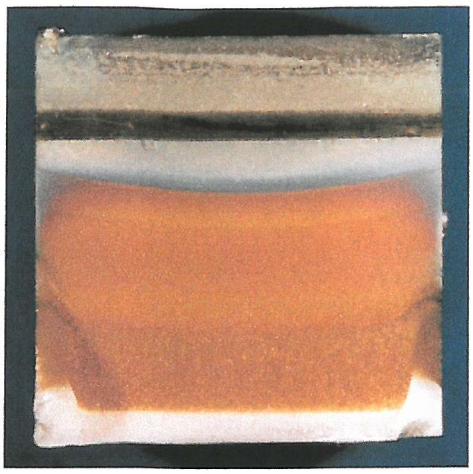

Figure 4-60b: RR1000; 650°C 1-20-1-1 vacuum; overall fracture surface.

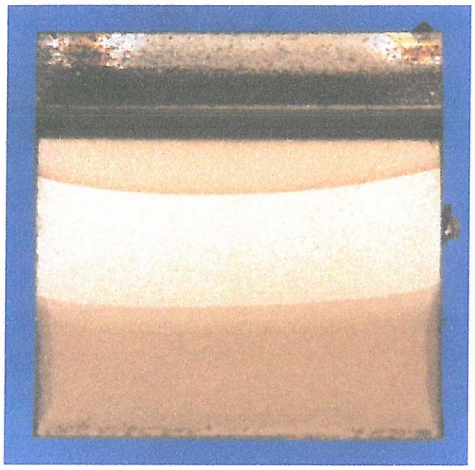

Figure 4-60c: RR1000; 725°C 1-1-1-1 vacuum (Test 1); overall fracture surface.

Figure 4-60d: RR1000; 725°C 1-1-1-1 vacuum (Test 5); overall fracture surface.

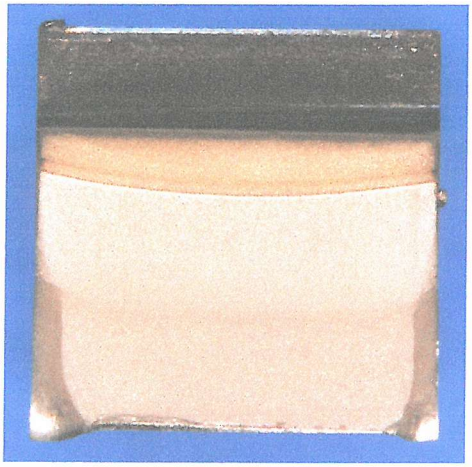

Figure 4-60e: RR1000; 725°C 1-20-1-1 vacuum; overall fracture surface.

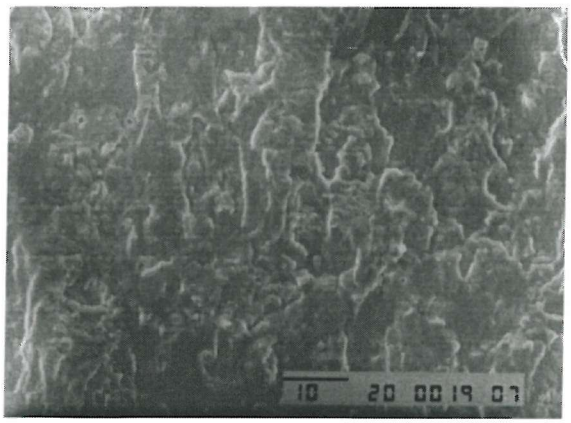

Figure 4-61a: RR1000; 650°C 1-1-1-1 vacuum ($\Delta K \approx 16$ MPa$\sqrt{m}$).

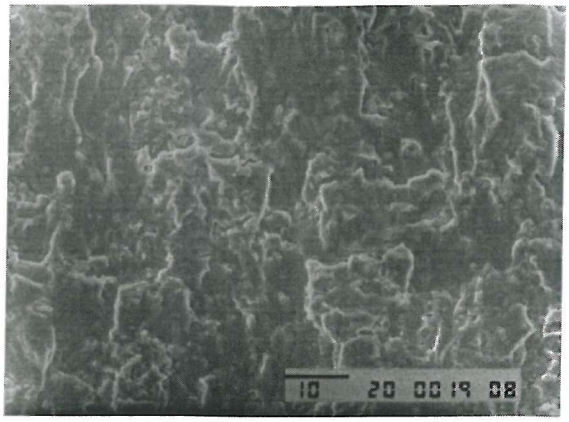

Figure 4-61b: RR1000; 650°C 1-1-1-1 vacuum ($\Delta K \approx 24.5$ MPa$\sqrt{m}$).

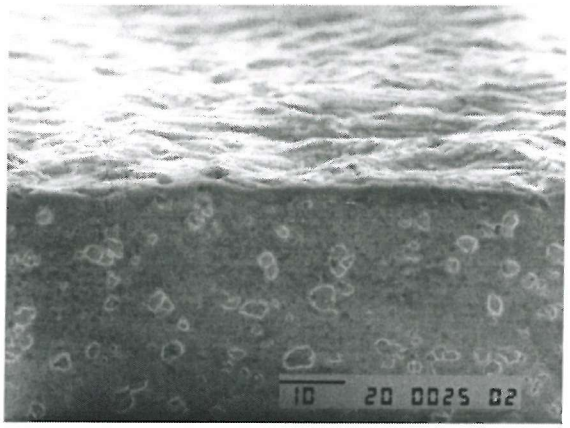

Figure 4-61c: RR1000; 650°C 1-1-1-1 vacuum ($\Delta K \approx 16$ MPa$\sqrt{m}$).

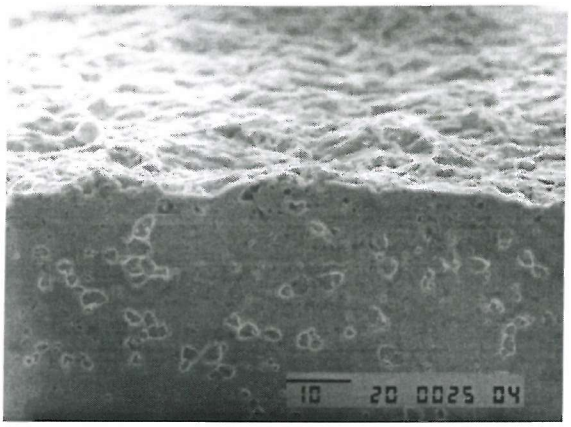

Figure 4-61d: RR1000; 650°C 1-1-1-1 vacuum ($\Delta K \approx 32.5$ MPa$\sqrt{m}$).

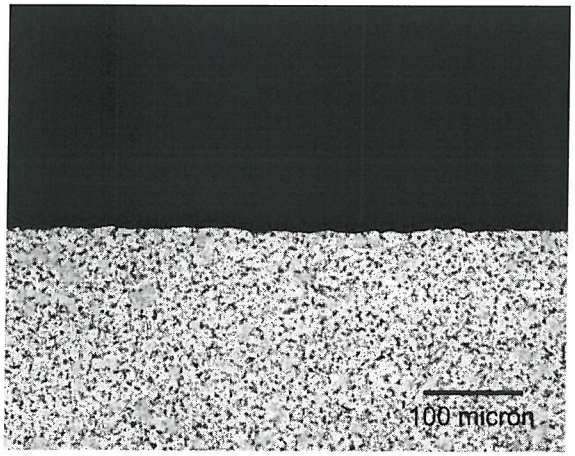

Figure 4-61e: RR1000; 650°C 1-1-1-1 vacuum ($\Delta K \approx 18$ MPa$\sqrt{m}$).

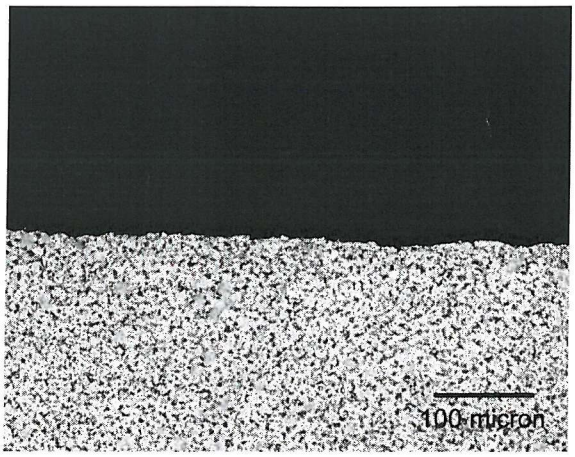

Figure 4-61f: RR1000; 650°C 1-1-1-1 vacuum ($\Delta K \approx 46$ MPa$\sqrt{m}$).

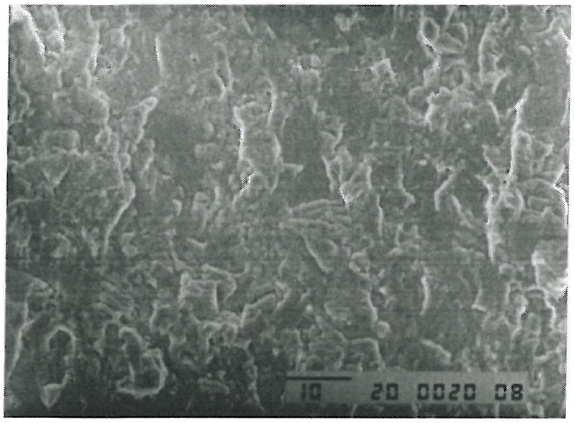

Figure 4-62a: RR1000; 650°C 1-20-1-1 vacuum ($\Delta K \approx 20$ MPa$\sqrt{m}$).

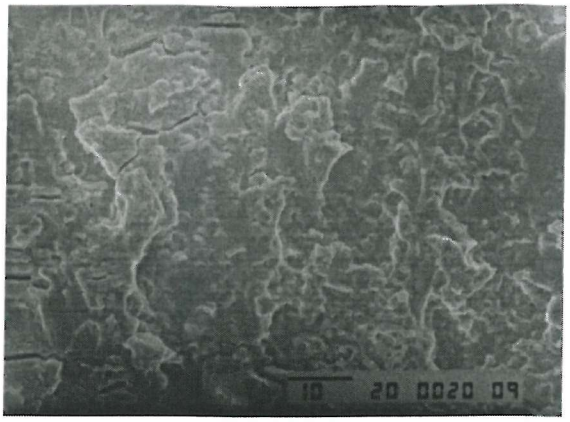

Figure 4-62b: RR1000; 650°C 1-20-1-1 vacuum ($\Delta K \approx 37$ MPa$\sqrt{m}$).

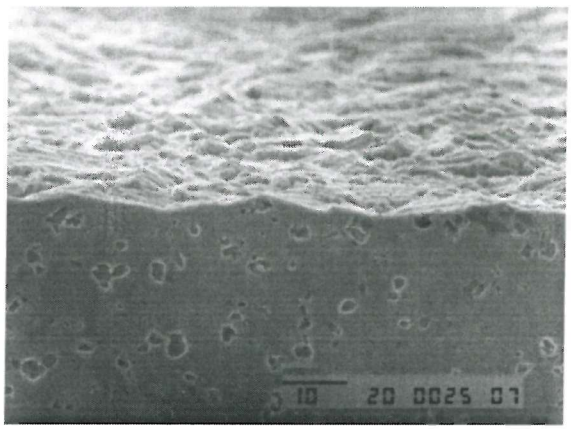

Figure 4-62c: RR1000; 650°C 1-20-1-1 vacuum ($\Delta K \approx 18.4$ MPa$\sqrt{m}$).

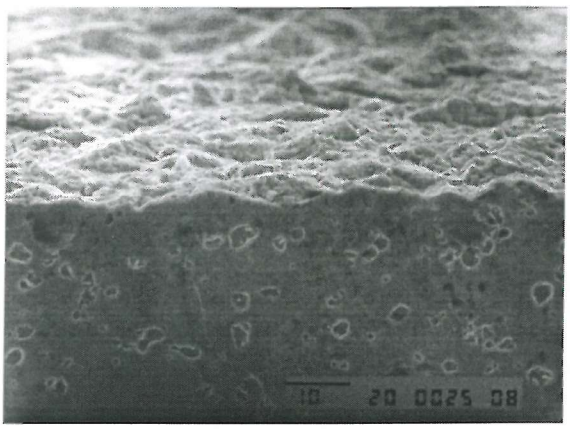

Figure 4-62d: RR1000; 650°C 1-20-1-1 vacuum ($\Delta K \approx 29.5$ MPa$\sqrt{m}$).

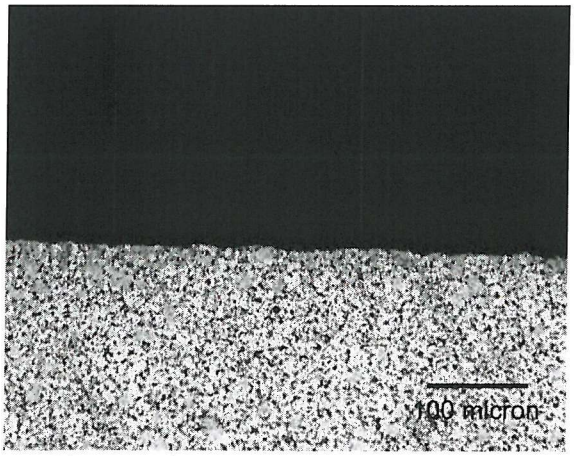

Figure 4-62e: RR1000; 650°C 1-20-1-1 vacuum ($\Delta K \approx 25.6$ MPa$\sqrt{m}$).

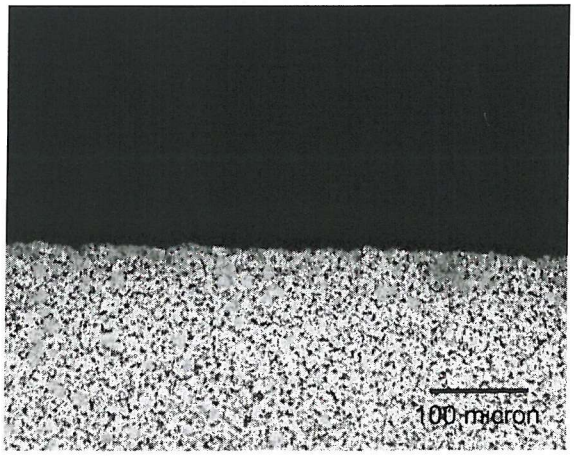

Figure 4-62f: RR1000; 650°C 1-20-1-1 vacuum ($\Delta K \approx 33.5$ MPa$\sqrt{m}$).

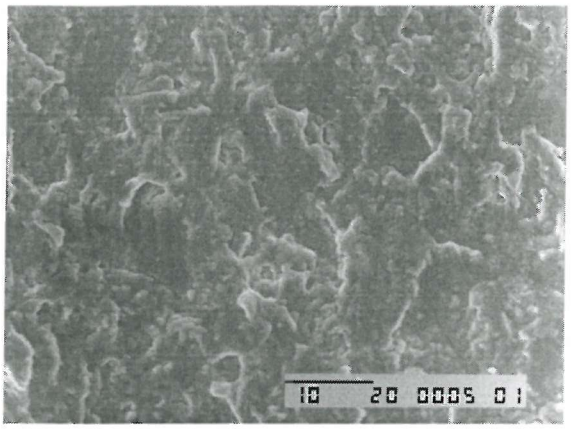

Figure 4-63a: RR1000; 725°C 1-1-1-1 vacuum ($\Delta K \approx 15$ MPa$\sqrt{m}$).

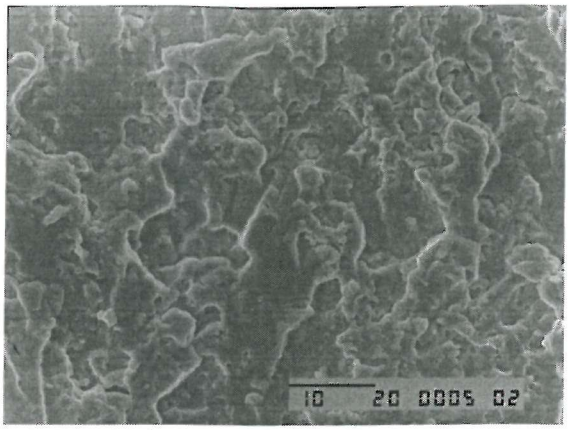

Figure 4-63b: RR1000; 725°C 1-1-1-1 vacuum ($\Delta K \approx 32$ MPa$\sqrt{m}$).

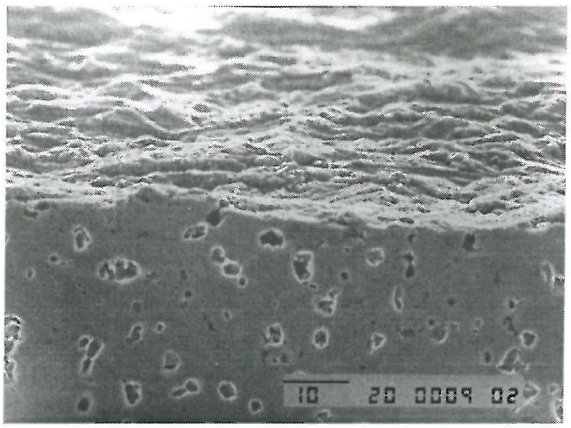

Figure 4-63c: RR1000; 725°C 1-1-1-1 vacuum ($\Delta K \approx 15$ MPa$\sqrt{m}$).

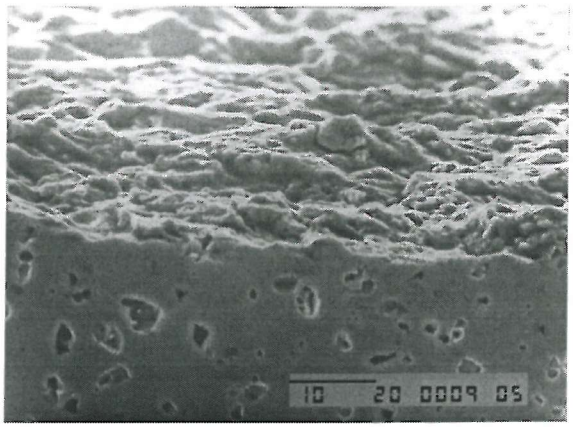

Figure 4-63d: RR1000; 725°C 1-1-1-1 vacuum ($\Delta K \approx 32$ MPa$\sqrt{m}$).

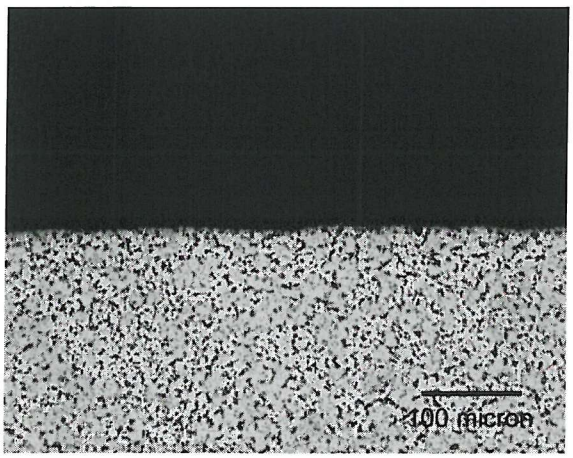

Figure 4-63e: RR1000; 725°C 1-1-1-1 vacuum ($\Delta K \approx 17$ MPa$\sqrt{m}$).

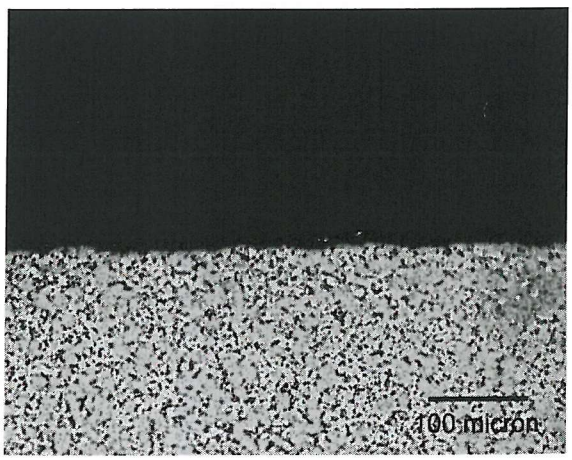

Figure 4-63f: RR1000; 725°C 1-1-1-1 vacuum ($\Delta K \approx 28.5$ MPa$\sqrt{m}$).

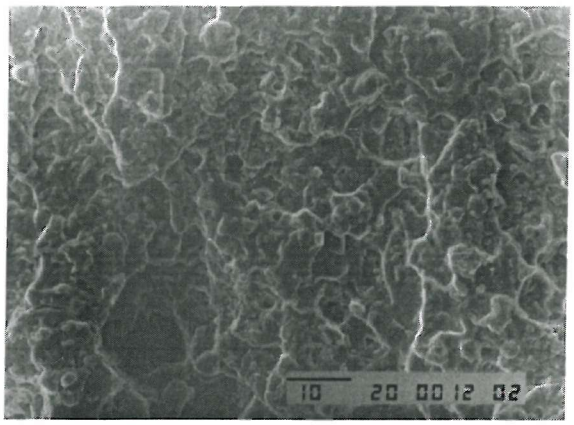

Figure 4-64a: RR1000; 725°C 1-20-1-1 vacuum ($\Delta K \approx 20$ MPa$\sqrt{m}$).

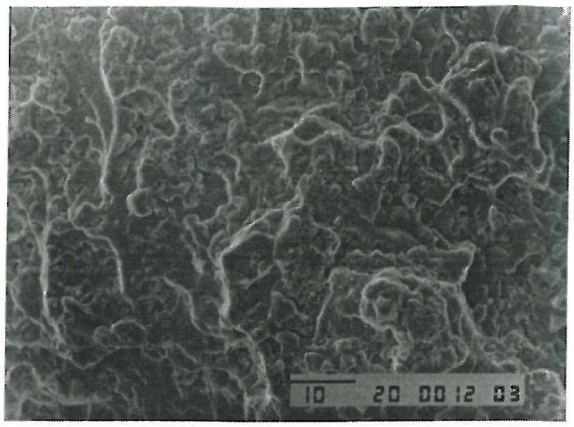

Figure 4-64b: RR1000; 725°C 1-20-1-1 vacuum ($\Delta K \approx 38$ MPa$\sqrt{m}$).

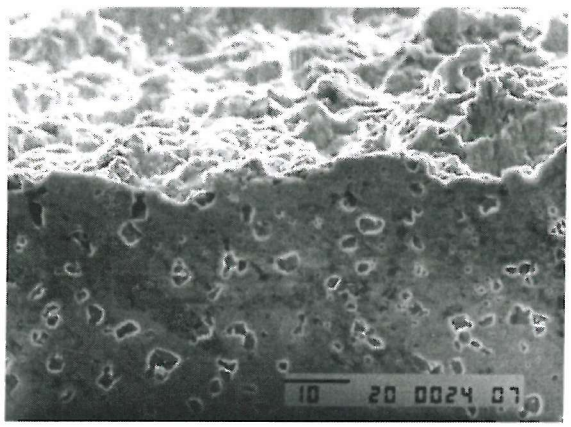

Figure 4-64c: RR1000; 725°C 1-20-1-1 vacuum ($\Delta K \approx 27.5$ MPa$\sqrt{m}$).

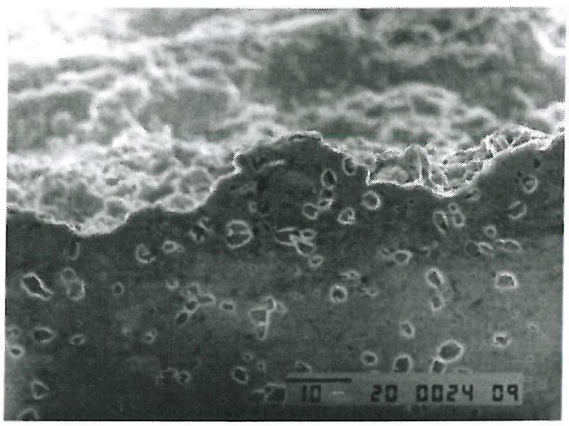

Figure 4-64d: RR1000; 725°C 1-20-1-1 vacuum ($\Delta K \approx 41$ MPa$\sqrt{m}$).

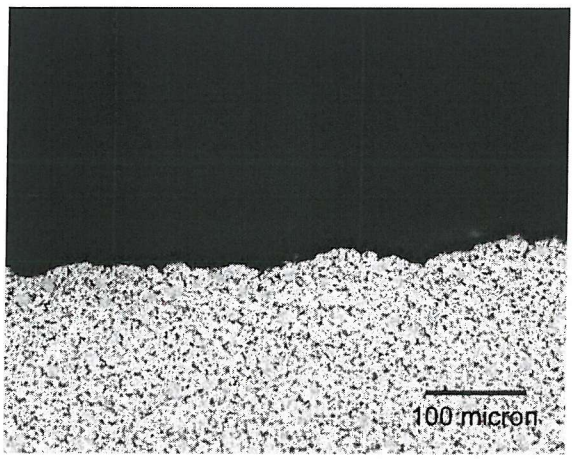

Figure 4-64e: RR1000; 725°C 1-20-1-1 vacuum ($\Delta K \approx 30.5$ MPa$\sqrt{m}$).

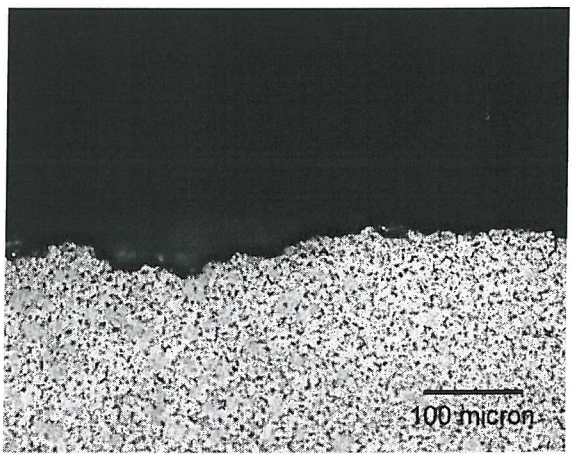

Figure 4-64f: RR1000; 725°C 1-20-1-1 vacuum ($\Delta K \approx 56$ MPa$\sqrt{m}$).

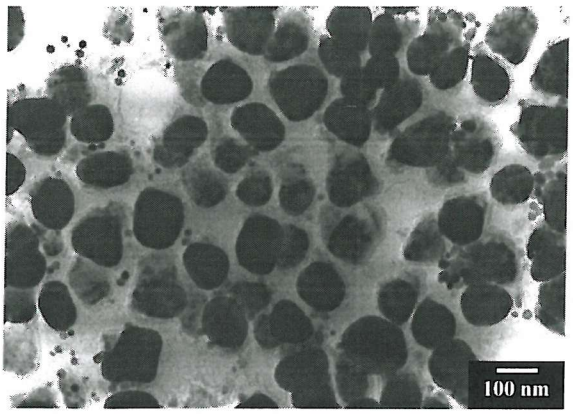

Figure 4-65a: RR1000 Test 2 725°C 1-20-1-1 (x50000).

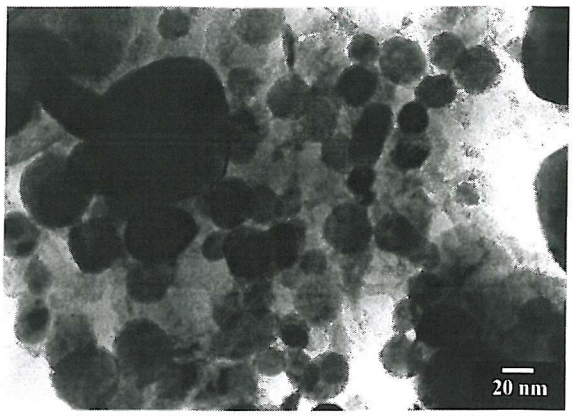

Figure 4-65b: RR1000 Test 2 725°C 1-20-1-1 (x200000).

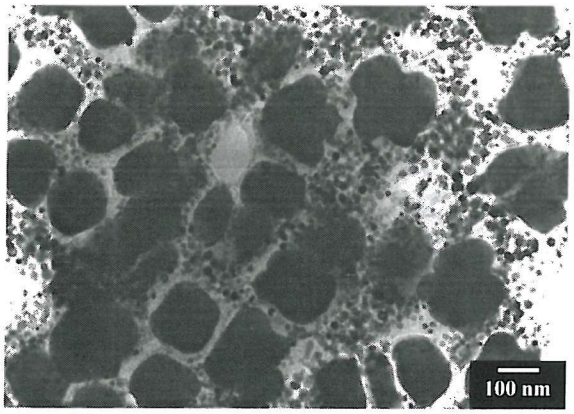

Figure 4-66a: RR1000 Test 4 650°C 1-20-1-1 (x50000).

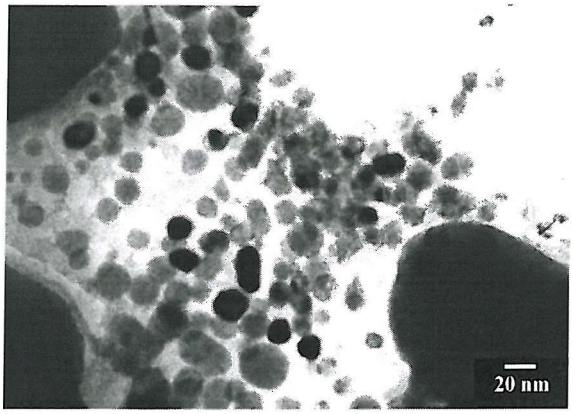

Figure 4-66b: RR1000 Test 4 650°C 1-20-1-1 (x200000).

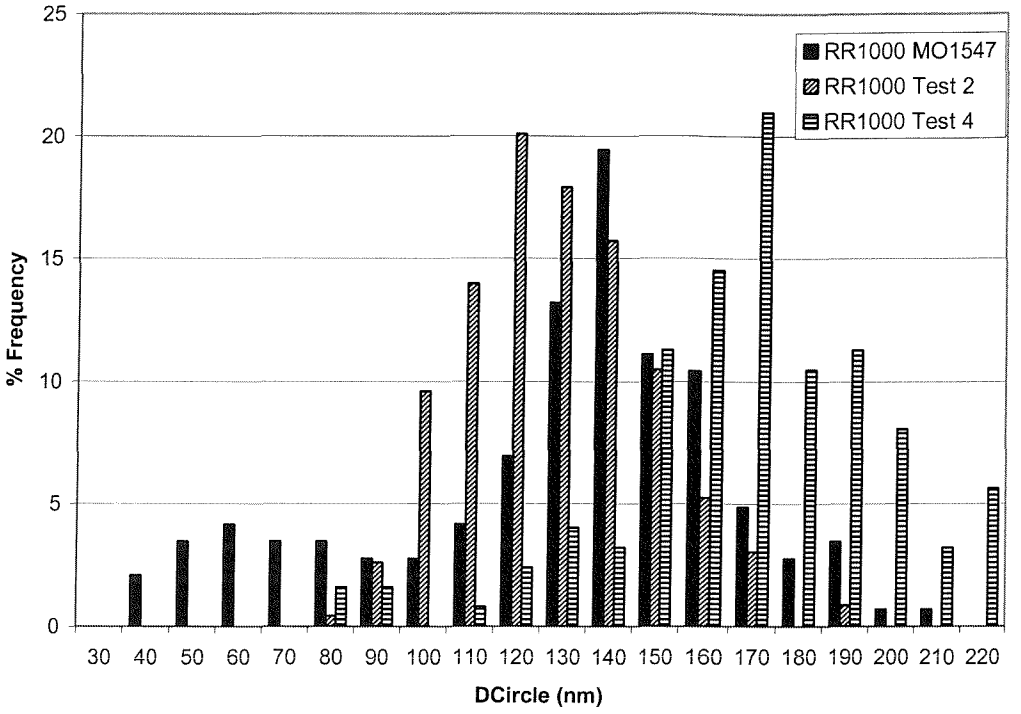

Figure 4-67a: Secondary γ' precipitate sizes in RR1000 specimens.

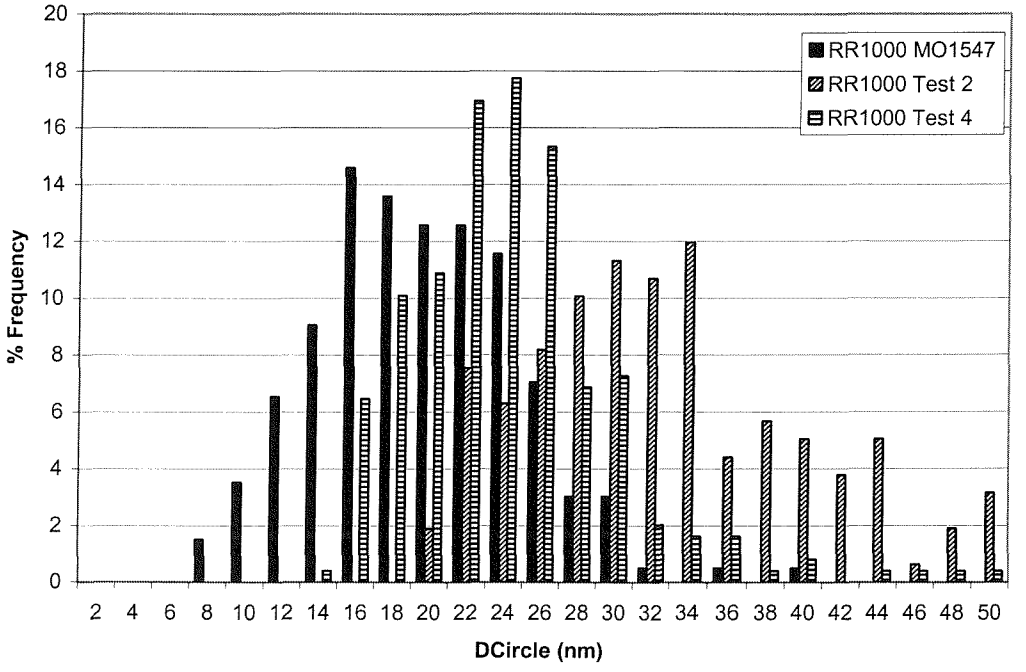

Figure 4-67b: Tertiary γ' precipitate sizes in RR1000 specimens.

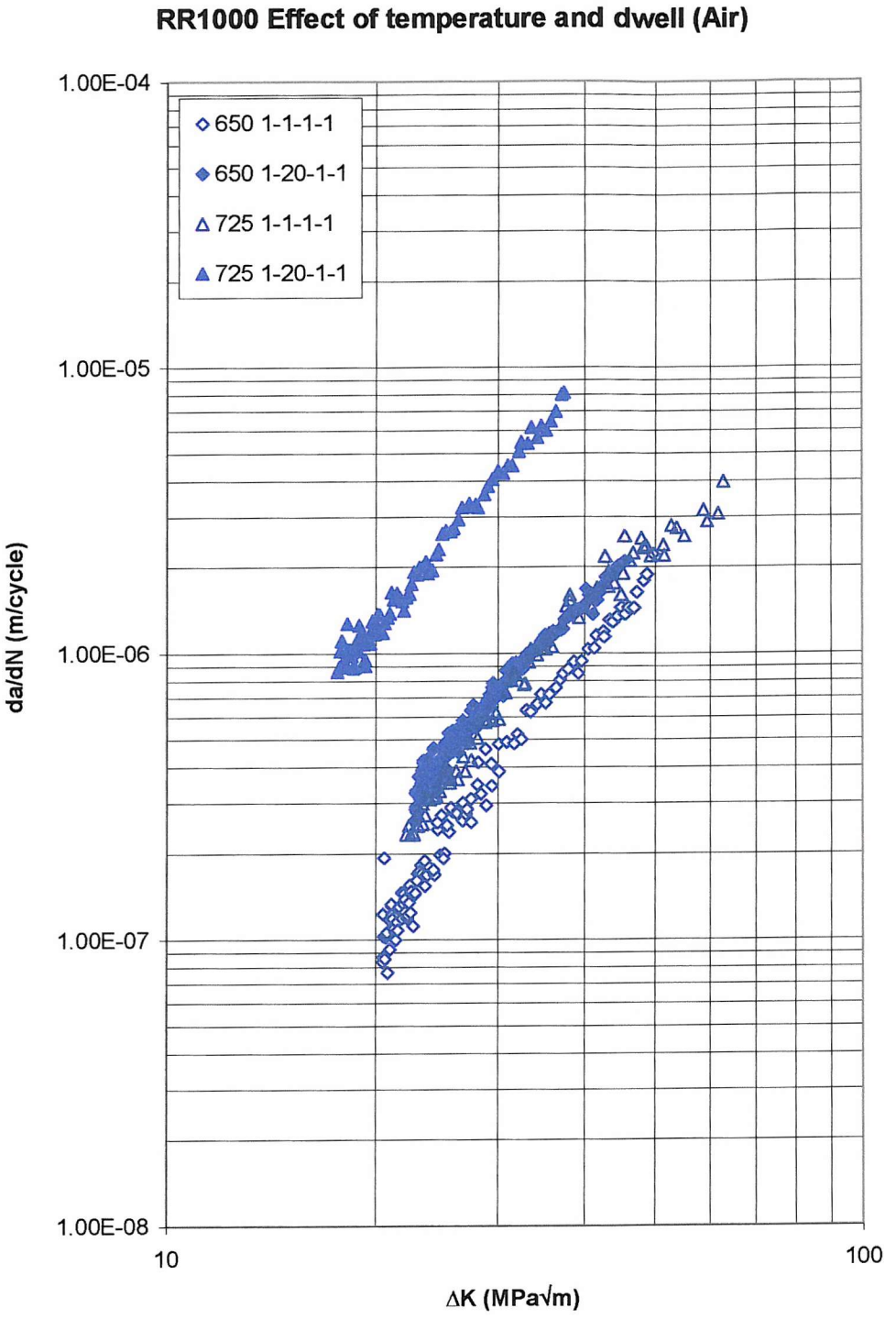

Figure 4-68: Air growth out curves of RR1000 material.

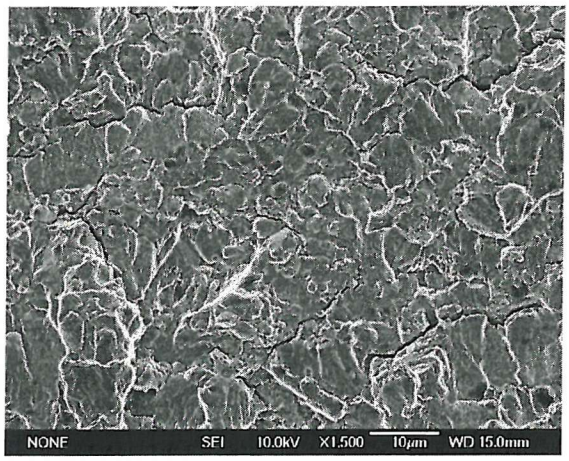

Figure 4-69a: RR1000; 650°C 1-1-1-1 Air ($\Delta K \approx 24.4$ MPa$\sqrt{m}$).

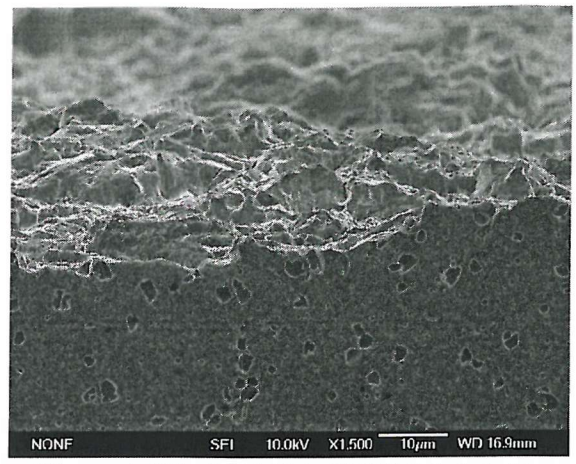

Figure 4-69b: RR1000; 650°C 1-1-1-1 Air ($\Delta K \approx 23.6$ MPa$\sqrt{m}$).

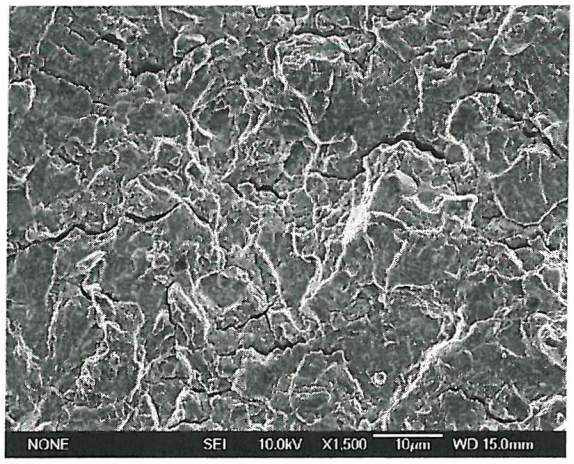

Figure 4-69c: RR1000; 650°C 1-1-1-1 Air ($\Delta K \approx 33.8$ MPa$\sqrt{m}$).

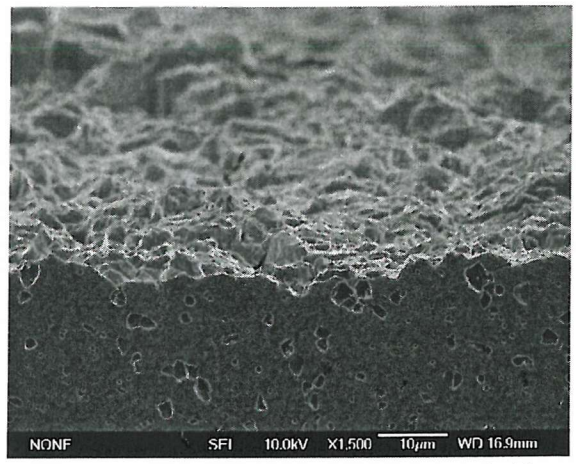

Figure 4-69d: RR1000; 650°C 1-1-1-1 Air ($\Delta K \approx 32.4$ MPa$\sqrt{m}$).

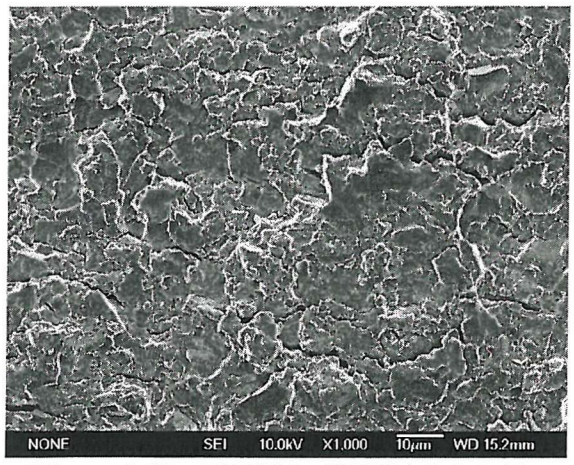

Figure 4-69e: RR1000; 650°C 1-1-1-1 Air ($\Delta K \approx 43.4$ MPa$\sqrt{m}$).

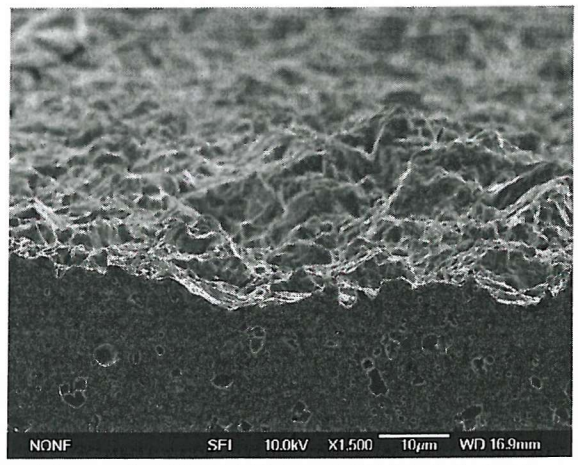

Figure 4-69f: RR1000; 650°C 1-1-1-1 Air ($\Delta K \approx 45.6$ MPa$\sqrt{m}$).

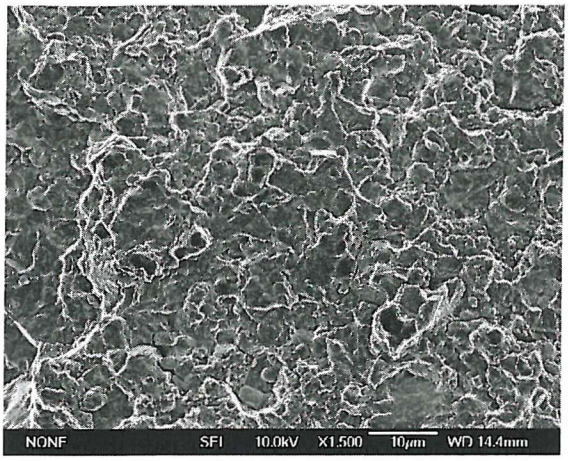

Figure 4-70a: RR1000; 650°C 1-20-1-1 Air ($\Delta K \approx 24.8$ MPa$\sqrt{m}$).

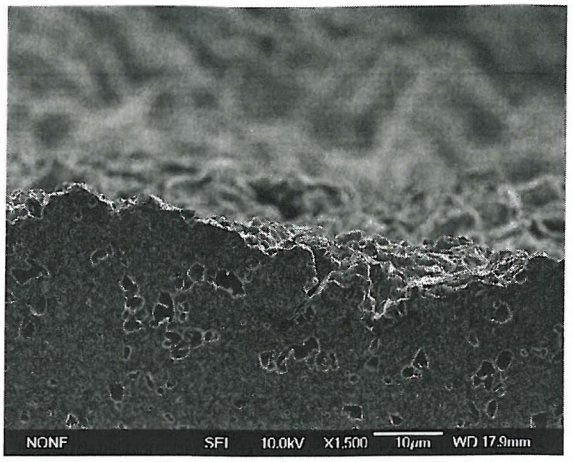

Figure 4-70b: RR1000; 650°C 1-20-1-1 Air ($\Delta K \approx 23.3$ MPa$\sqrt{m}$).

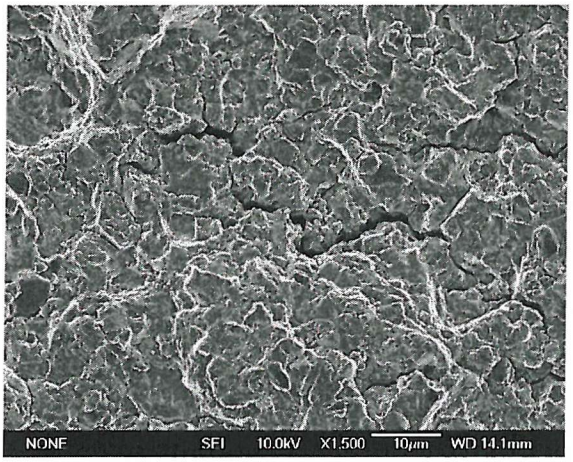

Figure 4-70c: RR1000; 650°C 1-20-1-1 Air ($\Delta K \approx 32.6$ MPa$\sqrt{m}$).

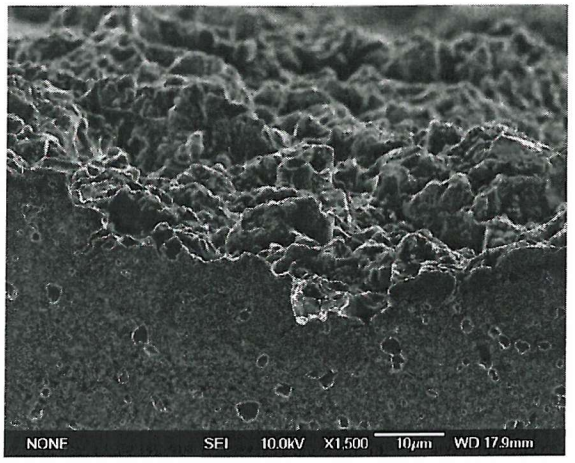

Figure 4-70d: RR1000; 650°C 1-20-1-1 Air ($\Delta K \approx 30.8$ MPa$\sqrt{m}$).

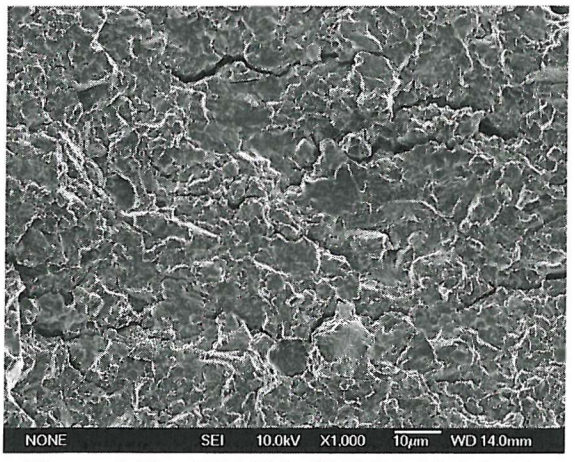

Figure 4-70e: RR1000; 650°C 1-20-1-1 Air ($\Delta K \approx 40.8$ MPa$\sqrt{m}$).

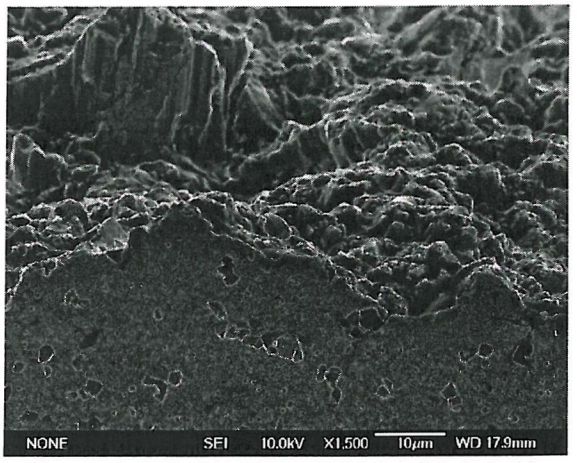

Figure 4-70f: RR1000; 650°C 1-20-1-1 Air ($\Delta K \approx 42.1$ MPa$\sqrt{m}$).

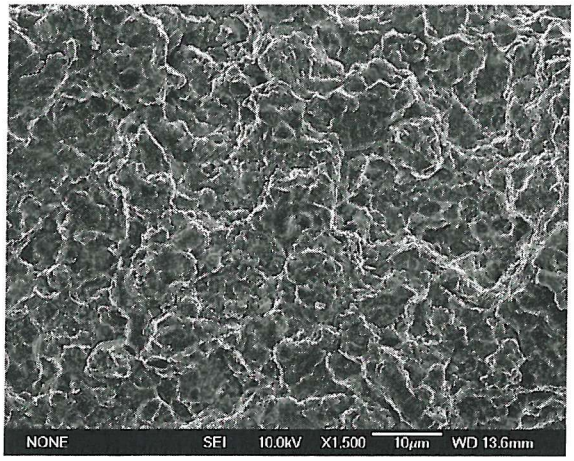

Figure 4-71a: RR1000; 725°C 1-1-1-1 Air ($\Delta K \approx 22.0$ MPa$\sqrt{m}$).

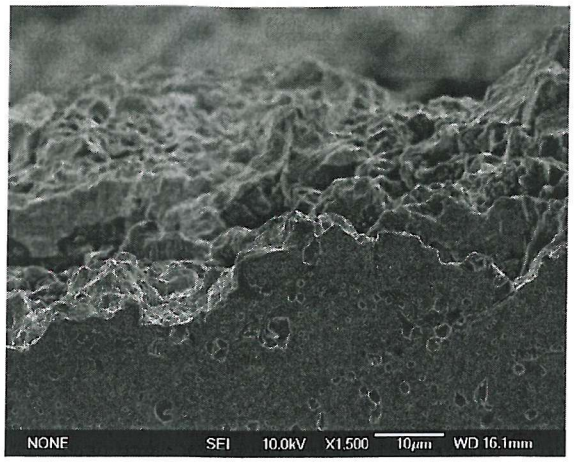

Figure 4-71b: RR1000; 725°C 1-1-1-1 Air ($\Delta K \approx 22.0$ MPa$\sqrt{m}$).

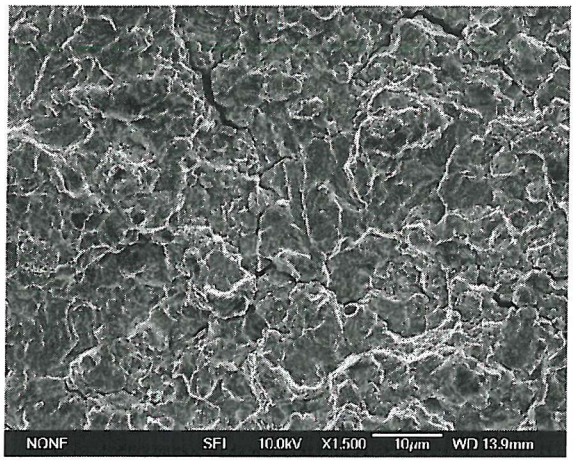

Figure 4-71c: RR1000; 725°C 1-1-1-1 Air ($\Delta K \approx 29.8$ MPa$\sqrt{m}$).

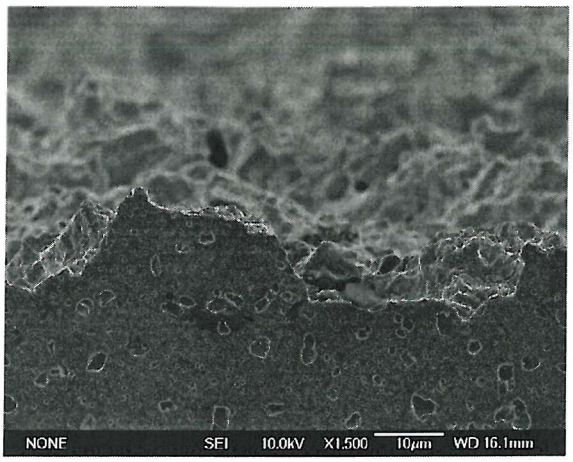

Figure 4-71d: RR1000; 725°C 1-1-1-1 Air ($\Delta K \approx 29.8$ MPa$\sqrt{m}$).

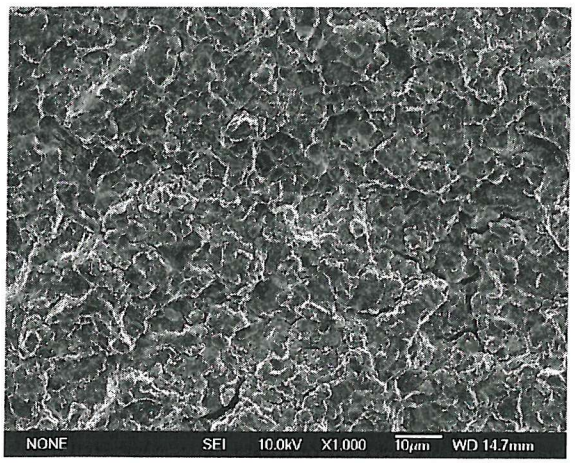

Figure 4-71e: RR1000; 725°C 1-1-1-1 Air ($\Delta K \approx 41.2$ MPa$\sqrt{m}$).

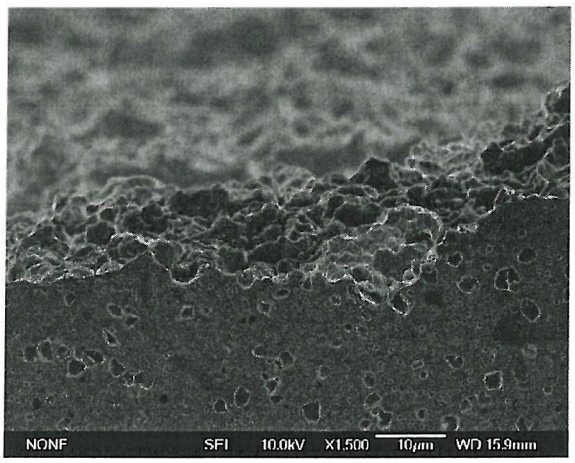

Figure 4-71f: RR1000; 725°C 1-1-1-1 Air ($\Delta K \approx 37.7$ MPa$\sqrt{m}$).

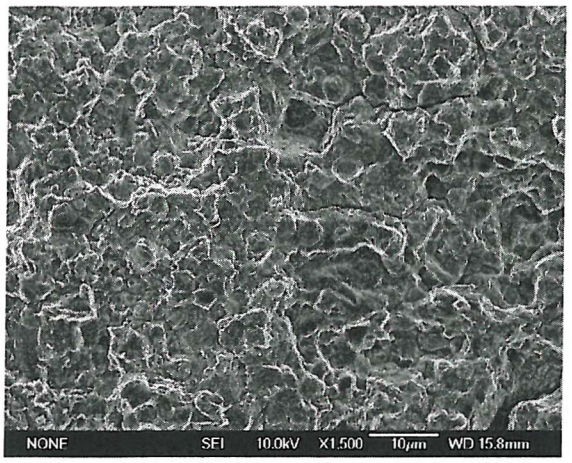

Figure 4-72a: RR1000; 725°C 1-20-1-1 Air ($\Delta K \approx 22.9$ MPa$\sqrt{m}$).

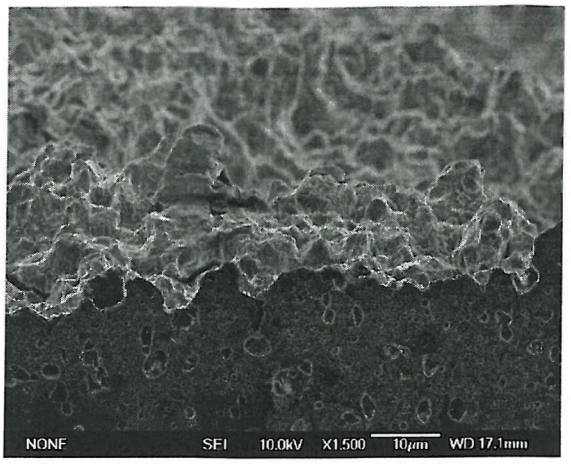

Figure 4-72b: RR1000; 725°C 1-20-1-1 Air ($\Delta K \approx 20.2$ MPa$\sqrt{m}$).

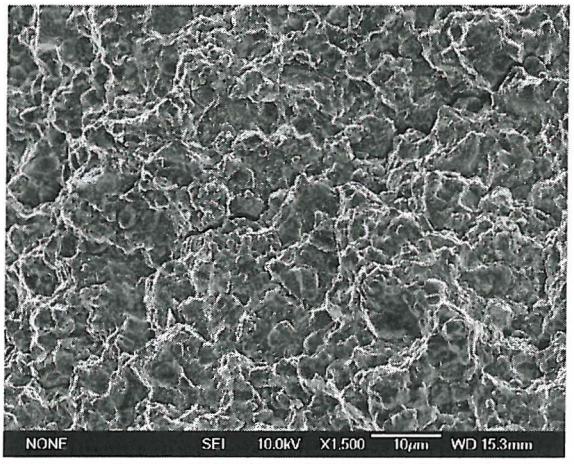

Figure 4-72c: RR1000; 725°C 1-20-1-1 Air ($\Delta K \approx 29.0$ MPa$\sqrt{m}$).

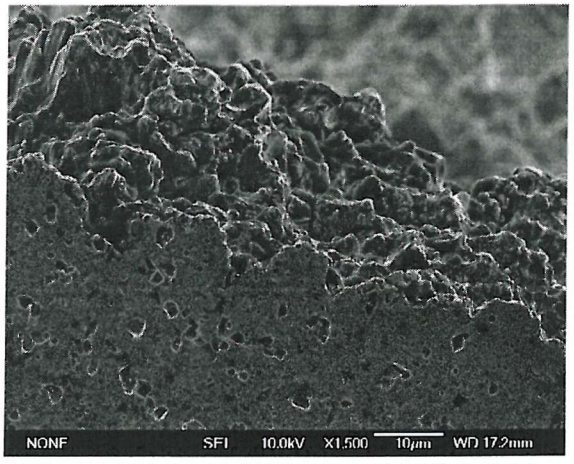

Figure 4-72d: RR1000; 725°C 1-20-1-1 Air ($\Delta K \approx 28.2$ MPa$\sqrt{m}$).

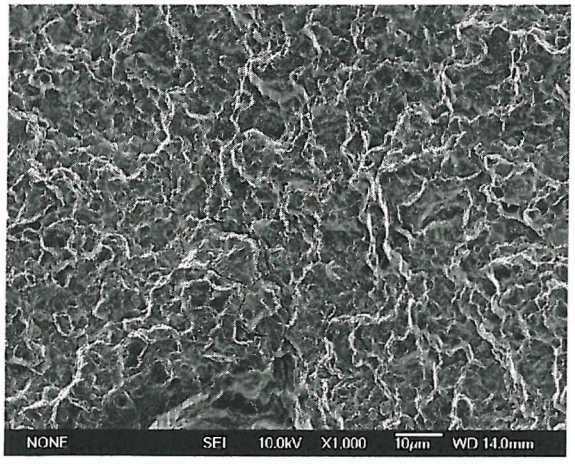

Figure 4-72e: RR1000; 725°C 1-20-1-1 Air ($\Delta K \approx 42.5$ MPa$\sqrt{m}$).

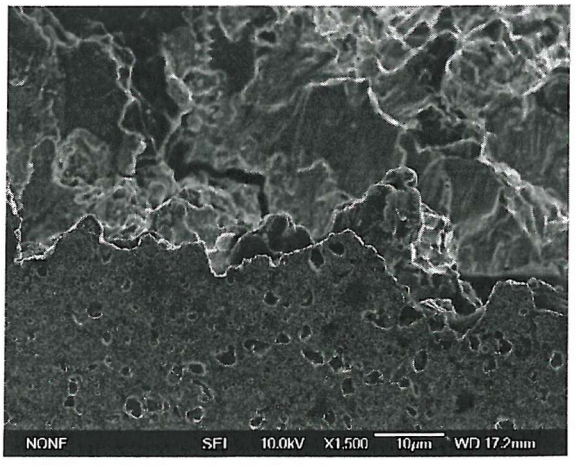

Figure 4-72f: RR1000; 725°C 1-20-1-1 Air ($\Delta K \approx 35.0$ MPa$\sqrt{m}$).

5. Discussion

In this discussion the microstructures of the test materials are first discussed. The differences in the microstructures of the materials are highlighted and rationalised with respect to the processing routes used during material processing. The fatigue crack initiation and growth mechanisms exhibited by the materials during room and elevated temperature short and long crack tests are then discussed. This is followed by a discussion of the effects of microstructure on fatigue crack initiation and growth mechanisms, and finally the optimal microstructural parameters giving rise to improved overall fatigue resistance are identified.

5.1. Microstructure

In the backscattered electron imaging mode on a SEM, heavier elements from the periodic table will appear brighter. This is because the backscattered electron coefficient η, i.e. the number of backscattered electrons emitted from the specimen for each incident electron, increases with increasing atomic number [153]. Bearing this in mind, the BEI observations on the materials can be discussed. The primary γ' precipitates in RR1000 are brighter than the γ matrix possibly due to the presence of tantalum in RR1000. Tantalum which is a heavier element is effectively insoluble in the γ matrix [154], hence almost all the tantalum in RR1000 will be dissolved in the γ' precipitates in addition to other elements such as titanium and aluminium. The presence of tantalum in the primary γ' precipitates may have caused these precipitates to appear brighter than the γ matrix in RR1000 in the BEI mode on the SEM. Tantalum and hafnium are not present in U720Li and its variants. The γ' precipitates in these materials will contain mainly titanium and aluminium, while the γ matrix is mainly made up of nickel and chromium. The primary γ' precipitates therefore appear darker than the γ matrix in these materials.

The bright spots observed in RR1000 are thought to possibly be carbides. The RR1000 has almost twice the carbon content compared to U720Li and its variants. The elements giving rise to the brighter spots are thought to be tantalum and hafnium. These elements tend to form MC carbides with carbon, giving regular spots throughout the RR1000 material. In U720Li and its variants, some of the darker spots may also be carbides instead of primary γ' precipitates. Due to the absence of heavier elements such as tantalum and hafnium in U720Li and its variants, carbon forms mainly $M_{23}C_6$ type carbides with chromium. The atomic number of chromium is very similar to that of titanium, which is part of the $Ni_3(Al:Ti)$ γ' precipitates. The carbides and primary γ' precipitates thus appear darker than the γ matrix in U720Li and its variants.

The similarities in the elements predicted from the EDX analysis for the γ and γ' phase in both U720Li and RR1000 were attributed to the sampling volume of the electron beam configuration used during the EDX analysis being larger than the average size of primary γ' precipitates. The

average sizes of the primary γ' precipitates in U720Li and RR1000 are approximately 1.5 to 2 μm while it was noted that the light-bulb shape of the sampling volume has a diameter of approximately 5-10 μm. Hence, while the results of the EDX analysis on the γ matrix is relatively accurate, the results of the EDX analysis on the primary γ' precipitates have been significantly masked by the elements in the γ matrix. However, slight differences in the relative amounts of elements in the γ and γ' phase in both U720Li and RR1000 were still noted, i.e. the γ matrix appears to have higher Cr and Co amounts compared to the γ' phase which is generally richer in Al and Ti. This is somewhat expected because chromium forms the γ phase with nickel while aluminium and titanium are γ'-forming elements, hence are more likely to be found in the γ' phase. The EDX analyses on RR1000 and U720Li were unable to pick up distinctive differences in the tantalum and hafnium contents in the γ' phase and possible carbides in the materials as deduced from BEI observations.

Higher solutionising temperatures for a given alloy chemistry would cause grains to grow at the expense of primary γ' precipitates, leading to larger grains and lower primary γ' volume fractions. The γ-γ' phase distributions in the alloys around the region of solution temperatures used (1105°C to 1135°C) are very similar as seen in Figure 4-15. Hence the grain size and primary γ' volume fraction would be expected to reflect the solution temperatures used during the heat treatment process.

U720Li and U720Li-LP were subjected to a solution temperature of 1105°C, which is lower than the solution temperature of 1120°C used for RR1000. U720Li-LG on the other hand was solution treated at 1135°C, i.e. at a higher temperature than the solution temperature of RR1000. U720Li and U720Li-LP should therefore be expected to have finer grain sizes and higher primary γ' volume fractions compared to RR1000, and vice versa for U720Li-LG which should be expected to have larger grain size and lower primary γ' volume fraction compared to RR1000.

The difference in the solution temperature used is reflected in the grain sizes of U720Li and U720Li-LG. U720Li-LP shows on average larger grains compared to RR1000 even though a lower solution temperature was used compared to RR1000. In terms of primary γ' volume fraction, all the materials appear to reflect the solution temperatures used during heat treatment. U720Li and U720Li-LP show higher primary γ' volume fractions compared to RR1000, and U720Li-LG shows lower primary γ' volume fraction compared to RR1000, consistent with the solution temperatures used during heat treatment.

When comparing the grain size of both batches of RR1000, it can also be seen that the batch with slightly finer grain size, i.e. the batch labelled MO1751, has a higher volume fraction of primary γ' precipitates. This reinforces the general statement that an increase in grain size in P/M superalloy

can only be achieved at the expense of the primary γ' volume fraction. The cause of the variation in grain size and primary γ' volume fraction is unknown due to the lack of detailed processing information, but may be due to a variation in the solution temperatures experienced across the disc forging or due to the closeness to which industrial processes are controlled if the specimens are from different discs.

Variations between the primary γ' volume fraction from micrographs and that predicted from Thermo-calc for RR1000 shown in Figure 4-15 can be explained in a similar manner to the differences observed for U720Li and its variants as discussed by Hide et al [30]. The variation between the primary γ' volume fraction from micrographs and that predicted from Thermo-calc can be explained in terms of the closeness to which the solution temperature is controlled in industry. A variation of ±10°C in the solution temperature would give a predicted primary γ' volume fraction between 10.0-15.7% for RR1000. The Thermo-calc predictions have also been carried out assuming equilibrium conditions, hence the difference observed might be due to possible non-equilibrium conditions attained during solution treatment in industrial processing. That is, all the non-equilibrium γ' present after HIPping may not have dissolved back into solution, if the material has not been heated for sufficient time.

In terms of the coherent γ' precipitates, nucleation of secondary and tertiary γ' occurs at different stages during cooling from solution temperature. Nucleation of secondary γ' precipitates occurs at temperatures very near the solution temperature due to changes in the equilibrium γ' fraction as temperature is lowered as shown in Figure 4-15, i.e. the matrix become supersaturated with γ'-forming elements when the disc forging is cooled from the solution temperature. Some growth of the nucleated secondary γ' precipitates is also expected to occur during cooling from the solution temperature. Tertiary γ' precipitates nucleate at lower temperatures during cooling when the diffusion rate of solutes slow and the secondary γ' precipitates are unable to grow fast enough to keep the supersaturation of the matrix low, and at a critical undercooling the driving force for nucleation is sufficient to allow nucleation of tertiary γ' to occur [23]. Growth of tertiary γ' precipitates is however expected to be limited as the temperature is likely to be too low to allow intensive solute diffusion when the tertiary γ' precipitates are nucleated [25]. The cooling rate during cooling from solution temperature has been indicated to be the controlling parameter governing the size of coherent γ' precipitates [25]. Higher cooling rates have been associated with finer size and lower volume fraction of secondary γ' precipitates, and vice versa for lower cooling rates. Higher cooling rates give greater γ' nucleation site frequency and in addition also limit the growth of secondary γ' precipitates as there is less time for diffusional processes necessary for the growth of precipitates, hence a finer size and lower volume fraction of secondary γ' precipitate is observed. Lower cooling rates are expected to give a more uniform nucleation of γ' precipitates throughout

the material and allow greater degree of precipitate growth during cooling from the solution temperature. The tertiary γ' size has been indicated to be relatively insensitive to the cooling rate used [23,25]. Further coarsening of the nucleated tertiary γ' precipitates (regardless of the cooling rates used after the solution treatment) occurs during the double ageing treatment stages. The secondary γ' size has been indicated to be unaffected during the ageing process, and the main microstructural change during ageing is growth of the tertiary γ' precipitates [23,25]. Coarsening of tertiary γ' precipitates occurs in an equilibrium manner and the driving force for the coarsening would be the deviation in the γ' volume fraction from equilibrium.

The secondary γ' sizes of the U720Li variants in this study were noted to reflect the cooling rates used. U720Li was oil quenched, while U720Li-LG was air cooled and U720Li-LP was insulated air cooled. The U720Li material which has experienced the highest cooling rate through oil quenching was noted to have the smallest secondary γ' size, while U720Li-LG which has been air cooled (i.e. lower cooling rate compared to U720Li) was noted to have larger secondary γ' precipitates compared to U720Li. U720Li-LP which has experienced the lowest cooling rate with an insulated air cool was noted to have the largest secondary γ' precipitates amongst the U720Li variants. RR1000 has been indicated to be fan air cooled from solution temperature, i.e. RR1000 experienced a cooling rate which is slower than oil quenching of U720Li but faster than air cooling of U720Li-LG. The secondary γ' sizes of both batches of RR1000 also reflect the cooling rate of the cooling method used, i.e. the secondary γ' precipitates in RR1000 are larger than the secondary γ' in U720Li but finer compared to the secondary γ' in U720Li-LG. However, the effect of cooling rate on the secondary γ' size in RR1000 may be slightly altered compared to the response of U720Li to different cooling rates due to difference in the alloy chemistries of RR1000 and U720Li.

Although the tertiary γ' precipitates have been indicated in the literature to be insensitive to the cooling rates used during cooling from the solution temperature [23], the microstructure of the materials in this study appear to suggest otherwise. After the ageing treatment, the material which experienced higher cooling rates during cooling from solution temperature was also noted to show finer tertiary γ' size. As all the materials were subjected to a similar two-stage ageing treatment, the degree of tertiary γ' precipitate growth in all the materials are expected to be relatively similar. This suggests that the size of tertiary γ' nuclei after cooling from solution temperature may be markedly different in the materials, and is likely to be smaller for materials which have undergone faster cooling, similar to the effect of cooling rate on secondary γ' precipitate size.

An attempt to calculate the volume fractions of secondary and tertiary γ' precipitates in the materials has also been carried out. The volume fraction of secondary γ' precipitates has been

indicated to be affected by the cooling rate. In a study by Mao et al [25], the volume fractions of secondary γ' expected in U720Li for cooling rates between 11°C/min and 170°C/min are presented in Table 5-1.

Cooling rate (°C/min)	Secondary γ' volume fraction (%)
171.6	33.3
110.2	37.5
56.5	42.5
27.6	45.8
11.0	44.1

Table 5-1: Cooling rate and secondary γ' volume fraction data for U720Li [25].

The volume fraction of secondary γ' was noted to decrease with increasing cooling rates as mentioned earlier. Note that supersolvus solution treatment has been employed in the study by Mao et al, i.e. all the γ' were dissolved during solution treatment and were precipitated as secondary and tertiary γ' precipitates on cooling from solution temperature. However in the study by Mao et al only the secondary γ' precipitates were resolved when observing the microstructures in the SEM, and the volume fraction of γ' measured was that of secondary γ' precipitates. In the current study, subsolvus solution treatment was employed for all the materials and a significant proportion of γ' remained unsolutioned and was retained as primary γ' precipitates at grain boundaries.

For the materials in the current study, the fastest cooling was oil quenching for U720Li, and the slowest cooling was insulated air cooling used for U720Li-LP. In between, U720Li-LG and RR1000 was air cooled and fan air cooled respectively. Oil quenching has been indicated to give cooling rates of approximately 130°C/min, while air cooling was indicated to have cooling rates of approximately 20°C/min [23]. For insulated air cooling, cooling rates are expected to be less than 20°C/min while for fanned air cooling, the cooling rate is between 20°C/min and 130°C/min. On inspecting Table 5-1, it was noted that for the range of cooling rates used for the materials in the current study, i.e. assuming insulated air cooling has a cooling rate of 11°C/min up to approximately 110°C/min for oil quenching, the variation in the volume fraction of secondary γ' was noted to be minimal with changes in the cooling rates.

In the same study by Mao et al on U720Li [25], the volume fraction of secondary γ' was also measured as a function of decreasing temperature during cooling from solution temperature. The investigation was carried out using a cooling rate of 55°C/min and the results are shown in Figure 5-9. The volume fraction of secondary γ' was noted to attain a relatively constant value at

approximately 900°C. This may also apply to the materials in the current study where the stable volume fraction of secondary γ' may be assumed to be formed at 900°C in the materials. Combining this assumption and the observation that the stable volume fraction of secondary γ' in the materials in the current study is relatively insensitive to the cooling rates used during cooling from solution temperature, and by assuming that the primary and secondary γ' volume fractions make up the equilibrium volume fraction of γ' expected at 900°C, the volume fraction of secondary γ' in the materials can be calculated by subtracting the volume fraction of primary γ' precipitates from the volume fraction of γ' expected at 900°C. Similarly, by assuming that the remaining γ' in the material forms tertiary γ' precipitates during ageing and on cooling from the ageing temperature, the volume fraction of tertiary γ' can be calculated by subtracting the volume fraction of γ' expected at 900°C from the volume fraction of γ' expected at 250°C (which is the temperature at which the maximum volume fraction of γ' is expected). In reality, the volume fraction of tertiary γ' in the materials will be slightly lower than the calculated value as the relatively low temperature especially during cooling from the final ageing temperature and possible rapid cooling may suppress diffusional growth of tertiary γ' precipitates to attain the equilibrium volume fraction of γ' expected at 250°C. The results of the calculations of secondary and tertiary γ' volume fraction for the materials in the current study are shown in Table 5-2. Note that the volume fractions of γ' expected at 900°C and 250°C were obtained from Thermo-calc predictions, the results of which are shown in Figure 4-15.

The line counting results appear to correspond to the primary γ' size and volume fraction in the materials. U720Li and U720Li-LP have the highest primary γ' volume fractions and approximately similar primary γ' sizes, hence approximately similar numbers of primary γ' precipitates were encountered in both materials. The number of primary γ' precipitates encountered in U720Li-LP is slightly lower than that in U720Li as the average size of the primary γ' precipitates in U720Li-LP is somewhat larger, i.e. the frequency of occurrence of primary γ' precipitates is lower in U720Li-LP. Both batches of RR1000 have relatively similar primary γ' sizes compared to U720Li, however the primary γ' volume fractions in RR1000 were much lower. The number of primary γ' precipitates encountered in RR1000 is therefore much lower than U720Li. Both batches of RR1000 have approximately similar precipitate sizes but the volume fraction of primary γ' in RR1000 MO1547 is lower than the primary γ' volume fraction in RR1000 MO1751, hence the number of primary γ' precipitates encountered in RR1000 MO1547 is lower than that for RR1000 MO1751. For U720Li-LG, it has the largest primary γ' size and lowest volume fraction of primary γ' compared to all other materials, hence the number of primary γ' precipitates encountered in U720Li-LG is the lowest amongst all the materials as expected.

Material	U720Li	U720Li-LG	U720Li-LP	RR1000 MO1547	RR1000 MO1751
Volume fraction of γ' at 900°C (%)	40.1	40.1	40.1	39.3	39.3
Volume fraction of γ' at 250°C (%)	48.1	48.1	48.1	49.2	49.2
Volume fraction of primary γ' (%)	18.9	8.6	18.3	8.7	11.8
Volume fraction of secondary γ' (%)	21.2	31.5	21.8	30.6	27.5
Volume fraction of tertiary γ' (%)	8.0	8.0	8.0	9.9	9.9

Table 5-2: Volume fractions of secondary and tertiary γ' precipitates in the test materials.

5.1.1. Summary

Microstructural characterisation work has revealed the microstructural characteristics of all the test materials. These include the grain size, primary γ' size and volume fraction, as well as the sizes of coherent secondary and tertiary γ' precipitates. The total volume fraction of coherent γ' as well as the volume fraction of secondary and tertiary γ' expected in each material has also been computed using Thermo-calc predictions and the volume fraction of primary γ' observed in each material. The BEI observations and EDX analyses on the materials are consistent with the alloying elements present. However some deductions of the elements present in the γ' phase and carbides from the BEI observations have yet to be confirmed. The grain size and the volume fraction of primary γ' precipitates of the materials are generally consistent with the solutionising temperature used. The secondary and tertiary γ' precipitate sizes are also consistent with the cooling rates used for the materials during cooling from solution temperature. To summarise, a consistent explanation can be put forward for the observed microstructural characteristics based on respective processing routes. Differences in the microstructures arise from the different parameters used during the heat treatment routes, in addition to the closeness to which these parameters are followed during the manufacturing process.

5.2. Fatigue crack initiation and growth behaviour

5.2.1. Room temperature fatigue crack initiation and growth behaviour

Crack initiation occurred due to intrinsic factors such as slip band cracking or due to defects and pores. Slip band crack initiation occurs due to the planar slip character of nickel-base superalloys. Intense impingement of slip bands occurs at grain boundaries due to build-up of dislocation density in the slip bands. Weakening of the slip band occurs due to repeated load cycling causing dislocations to move back and forth in the slip bands, and eventually the slip band material is weakened to the point where it is fractured (shear decohesion) and initiates a crack. The presence of defects and pores in the material can also cause crack initiation as the defects and pores may act as stress concentrators or discontinuities on the surface or within the material, favouring nucleation of fatigue cracks in these regions of locally raised stresses.

As mentioned in the literature review, Goto and Knowles [51] who investigated the initiation and propagation of microcracks in U720Li at room temperature found that at extremely early stages of cycling, cracking of TiN particles occurred. The cracked particles were responsible for the initiation of subsequent fatigue cracks. There is limited evidence to show that TiN particles are present in the alloys used in this study (Figure 4-1, Figure 4-2 and Figure 4-3). The microstructure of the U720Li material used by Goto and Knowles was noted to contain TiN particles having sizes similar to or larger than the primary γ' precipitates. It is possible that the large TiN particles in their study have cracked easily contributing to the initiation of fatigue cracks.

The crack field characterisation of the room temperature short crack tests indicated that although the number of cracks in individual tests are distinctly different, the rate of crack initiation in all the tests is relatively uniform throughout the life of the tests without any apparent acceleration or deceleration in the rate of crack initiation. Crack initiation occurs under the influence of local strains. At room temperature, these local strains at pores/cracked slip bands local stress concentrators seem to be developing/accumulating uniformly throughout the life as indicated by the steady rate of crack initiation.

Immediately after crack initiation, stage I type crack growth was observed in all the alloys at short crack lengths. Stage I crack growth also occurs in the near-threshold crack growth regime in the room temperature long crack tests. Stage I crack growth corresponds to crack growth where the zone of plastic deformation surrounding the crack tip is confined within a few grains, and crack growth occurs predominantly along slip bands in the slip system experiencing the maximum resolved shear. This gives rise to a zig-zag crack path and a highly facetted fracture surface as the crack path changes with slip systems going from grain to grain as observed in the early short crack growth region and near-threshold crack growth region. In the short crack tests, the plastic zone size associated with the small crack length immediately after crack initiation is much smaller than the

grain size, and crack propagation occurs along the slip system experiencing maximum shear within the grain. In the long crack tests, although the defect size is physically large, the low applied loads meant that the crack tip plastic zones are much smaller than the grain size, and multiple co-operative slip is not promoted and crack propagation occurs in a stage I manner. Stage I crack growth is generally considered to be highly sensitive to the local microstructure e.g. grain boundaries and other extrinsic factors which may be enhanced due to the crack growth mode (e.g. crack closure, crack tip shielding, etc). Differences in the crack growth resistance of the test materials was noted in the early crack growth and near-threshold crack growth region and this will be further discussed in section 5.3.4.2.

At longer crack lengths, the size of the plastically deformed zone ahead of the crack tip increases to encompass several grains and slip systems in several grains are activated. At this point, crack growth is able to occur through simultaneous or co-operative slip along these multiple slip systems, i.e. stage II crack growth. Stage II crack growth is characterised by a relatively flat and featureless fracture surface. Stage II crack growth is less sensitive to local microstructure compared to stage I crack growth and the crack samples the averaged microstructural characteristics of the materials during stage II crack growth. In the Paris regime, the materials in the current study all shared much more similar crack growth resistance compared to the near-threshold crack growth region and this is further discussed in section 5.3.4.2.

5.2.1.1. Room temperature short crack-long crack behaviour comparison

A general comparison of room temperature short crack and long crack growth behaviour is made by plotting the short crack growth curve and long crack growth curve on the same graph, as shown in Figure 5-10a to Figure 5-10d. In the short crack tests, initially random stage I short crack growth behaviour under the influence of local microstructure (e.g. grain boundaries and primary γ' precipitates giving rise to temporary crack arrests) is observed followed by a transition to stage II crack growth. For near-threshold crack growth, stage I long crack growth is less sensitive to the local microstructure but is heavily influenced by extrinsic factors such as crack closure at low and near-threshold ΔK followed by a transition to stage II crack growth at higher ΔK. Convergence of the two curves will therefore indicate the point of transition to structure-insensitive crack growth, i.e. a transition from stage I to stage II crack growth. In the current work, the short crack growth curves and long crack growth curves do not show a very distinct point of convergence, although the crack growth curves were noted to merge at higher ΔK. Although no truly distinct points of convergence were noted, an approximation can be made from the plots. The approximate ΔK values at the point of convergence between the short crack growth curves and the long crack growth curves, ΔK_{conv} are presented in Table 5-3. A comparison of the monotonic and cyclic

plastic zone size corresponding to ΔK_{conv} and the grain size of the material is made and shown in Table 5-3. The plastic zone size is estimated using Irwin's approximation [48].

Material	Approximate ΔK at convergence, ΔK_{conv} (MPa√m)	Approximate short crack length (c) at ΔK_{conv} (μm)	Corresponding plastic zone size at ΔK_{conv} (μm)		Average grain size (μm)
			Monotonic	Cyclic	
U720Li	25	325	55.3	11.2	6.4
U720Li-LG	20	240	37.5	7.6	15.4
U720Li-LP	20	230	40.7	8.2	10.1
RR1000	23	300	47.6	9.7	7.4

Table 5-3: Approximate ΔK at convergence and plastic zone size calculations.

Transition crack lengths (stage I to stage II type cracking) which were measured from short crack fractography, denoted c_{trans} herewith, is further analysed in Table 5-4. The ΔK corresponding to these transitional crack lengths c_{trans} are found using the empirical formula of Scott and Thorpe [89] and the corresponding plastic zone sizes are calculated again using Irwin's approximation [48].

Material	Approximate transition crack length, c_{trans} (μm)	Approximate ΔK at c_{trans}, ΔK_{trans} (MPa√m)	Corresponding plastic zone size at ΔK_{trans} (μm)		Average grain size (μm)
			Monotonic	Cyclic	
U720Li	110	14.7	19.1	3.9	6.4
U720Li-LG	100	12.8	15.4	3.1	15.4
U720Li-LP	90	12.6	16.7	3.3	10.1
RR1000	130	15.2	20.8	4.2	7.4

Table 5-4: Convergence data from fractography.

Stage I crack growth is thought to occur when plasticity is totally contained within the grains, i.e. when the monotonic plastic zone size is less than the grain size. For stage II crack growth, the definitive onset of this stage occurs when the cyclic plastic zone size exceeds the grain size, between these two stages a mixed stage I/stage II crack growth mode will be observed.

From these analyses, it was thought that the short crack fractography measurements revealed the end of pure stage I crack growth, but did not pick up the commencement of true stage II crack growth. This is indicated by the similarity in the monotonic plastic zone size and the grain size of the materials in Table 5-4. When the grain size is larger than the monotonic plastic zone size, all

the plasticity is contained within the grain and the crack grows in a stage I manner. As the crack length increases so does the associated plastic zone size. This plastic zone size will exceed some smaller grains due to the random nature of the grain size distribution. When this happens the crack grows in a stage II manner in these grains in addition to stage I crack growth in grains which are still containing the entire monotonic plastic zone. The point of convergence as indicated by the long crack-short crack comparison plot reveals the onset of true stage II crack growth, i.e. when the cyclic plastic zone exceeded the largest grains in the materials. When this happens every point at the crack front of the short crack and long crack are similar, i.e. both are growing in a pure stage II crack growth mode. It is unlikely that the short crack fractography carried out will pick up the point of the onset of true stage II crack growth as it would be difficult to distinguish mixed stage I/stage II crack growth from pure stage II crack growth.

From Table 5-3 which shows the crack length corresponding to the onset of pure stage II crack growth and Table 5-4 which shows the crack length at the end of the pure stage I crack growth, the proportion of life spent in the different regimes of crack growth, i.e. pure stage I, mixed stage I/stage II and pure stage II can be estimated for the materials. The number of cycles corresponding to the crack lengths at the point when the crack growth modes change are estimated from short crack length measurements and number of cycles information obtained from acetate replicas observations. The result of this estimation is shown in Table 5-5 together with all other relevant results and information from previous analysis. The number of cycles is estimated to the closest 5000/10000 cycles when a replica of the top surface is taken for analysis.

The results shown in Table 5-5 indicate that approximately 70% of the total life demonstrated in the room temperature short crack tests is spent in the crack initiation and pure stage I crack growth regimes in all the materials. Mixed stage I/stage II crack growth mode accounts for another 15% of the life after the end of pure stage I crack growth. The onset of pure stage II crack growth at approximately 85% of the life takes up the remainder of the fatigue life in the materials. The results in Table 5-5 give a clear indication that the life of the materials in the room temperature short crack tests are dominated by crack initiation and early crack growth through stage I crack growth mode. The short crack tests show convergence with the long crack behaviour (i.e. stage II crack growth) very late in the life. The results of this estimation are important in explaining the effects of microstructure on the different regimes of fatigue crack growth and are further discussed in section 5.3.4.

Material	U720Li (Test 10S)	U720Li-LG (Test 4S)	U720Li-LP (Test 6S)	RR1000 (Test 8S)
Lifetime (cycles)	128476	175867	248570	192077
Crack length at end of pure stage I growth (μm)	110	100	90	130
Number of cycles at end of pure stage I growth	90000	110000	195000	135000
% life spent up to the end of pure stage I crack growth	70.0	62.5	78.4	70.3
Crack length at beginning of pure stage II growth (μm)	325	240	230	300
Number of cycles at beginning of pure stage II growth	110000	145000	220000	170000
% life before onset of pure stage II crack growth at end of test	85.6	82.4	88.5	88.5

Table 5-5: Life spent in different crack growth regimes in room temperature short crack tests.

5.2.1.2. Summary

Crack initiation was noted from porosity/defects and slip band cracking at room temperature. After crack initiation, short crack propagation occurred in stage I mode at short crack lengths and stage II mode at larger crack lengths. Long crack growth at room temperature in air occurred in stage I mode at low and near-threshold ΔK and stage II mode at higher ΔK. Comparison of room temperature long crack and short crack behaviour revealed pure stage I crack growth in the short crack tests when the monotonic plastic zone is still contained within the grain. The point of convergence of the long crack and short crack growth out curves indicates the onset of true stage II crack growth in the short crack tests when the cyclic plastic zone exceeded the largest grains in the materials. In between, crack growth occurs through a mixed stage I/stage II mode. Lifetime proportion analysis on room temperature short crack tests indicates that approximately 70% of the total life is spent in the crack initiation and pure stage I crack growth regimes in all the materials. Mixed stage I/stage II crack growth mode accounts for approximately another 15% of the life after the end of pure stage I crack growth and the onset of pure stage II crack growth at approximately 85% of the life takes up the remainder of the fatigue life in the materials. Fatigue lives of the materials in the room temperature short crack tests are thus shown to be dominated by crack initiation and early crack growth in stage I crack growth mode.

5.2.2. Elevated temperature fatigue crack initiation and growth behaviour

5.2.2.1. Initiation and early crack growth

In the elevated temperature short crack tests, porosity was noted to be the dominant crack initiation mechanism with no evidence of slip band crack initiation observed. At elevated temperatures, dislocation cross-slip and climb processes will lead to wavy slip, where the build-up of stresses within slip bands to give slip band induced cracking is less likely to occur. Crack initiation from a pore will still be governed by features within a grain at a pore, e.g. protrusions at slip bands due to load cycling giving rise to micro-notch effects and stress concentrators. Early crack growth is via a stage II crack growth mechanism as evidenced from the flat transgranular fracture surface observed immediately after the crack initiation feature. The initiation at surface or near surface porosity is likely to be aided by the oxidation mechanisms which are at work. The stress concentration introduced by these pores together with any grain boundaries which may be present on or near the pores would cause accelerated oxidation-assisted cracking compared to grain boundaries on the surface not subjected to any stress concentrations. The oxidation rate could be stress-enhanced by lowering the apparent activation energy for oxygen diffusion through an expansion of the lattice and/or by oxide cracking which exposes fresh material for rapid oxidation [29]. This may also partially explain the early crack initiation observed in the replication tests as oxidation is effectively in action as soon as the specimen is exposed to the test temperature and it is further accelerated by the fatigue cycling and by possible stress concentrations due to the pores.

The crack field evolution in all the elevated temperature short crack tests shows distinct acceleration in the rate of crack initiation very early in the life, followed by a deceleration in the rate of crack initiation in the middle of the life and eventually acceleration in the rate of crack initiation is observed again towards the end of the life. The rate of crack initiation is related to local strain effects at stress concentration features in addition to any oxidation effects which may be present. The strains developed early in the life will be rapidly increasing due to cyclic softening which causes higher strains for a given applied stress. Cyclic softening at elevated temperatures is prevalent in these materials as evidenced from strain-controlled elevated temperature LCF tests on U720Li and U720Li-LG conducted at QinetiQ and should equally apply for U720Li-LP and RR1000. Eventually the cyclic softening stabilises or saturates and the strains developed for a given cyclic load will follow a stabilised stress-strain relationship. In the elevated temperature LCF tests at 650°C on U720Li and U720Li-LG conducted by QinetiQ, cyclic softening was noted to stabilise at approximately 20% to 50% of the life of the tests. The initial rapidly increasing strains are likely to give rise to a high rate of crack initiation. Eventually the strain softening stabilises leading to a slowdown in the rate of crack initiation towards the middle of the life.

Crack initiation is also highly related to grain boundary oxidation in U720Li-LG where oxide debris formation was frequently noted at grain boundaries. These oxidised grain boundaries eventually lead to initiation of a high number of small cracks and thus significantly higher numbers of cracks were noted in U720Li-LG compared to other materials. Crack initiation from oxidised grain boundaries has also been noted in other elevated temperature short crack study [29]. In other materials, oxidation is believed to have a less significant effect on crack initiation as cracks initiating from oxidised grain boundaries were noted less frequently in these materials compared to U720Li-LG. The oxidation in U720Li-LG is likely to be aided by the cyclic loading of the material, i.e. stress-assisted oxidation is occurring in the material [29]. On the surface of the material, grain boundaries constitute a discontinuity in the microstructure and higher stresses are experienced compared to regions within the grains. Grain boundaries are also less oxidation-resistant compared to other regions of the material and faster diffusion of oxygen occurs along these boundaries. Cyclic loading further weakens these boundaries and increases the degree of oxidation attack at these boundaries, and eventually initiates a fatigue crack. The initial high rate of crack initiation in U720Li-LG may be due to the rapidly increasing strains (due to cyclic softening) and oxidation of fresh material. Towards the middle of the life, the cyclic softening stabilises and the rate of oxidation is also expected to reach a steady-state level, leading to a slowdown in the rate of crack initiation.

The acceleration in the rate of crack initiation nearing the end of the life is thought to be due to the influence of the plastic zones of larger cracks in the notch root. Regions of the material in the plastic zones of larger cracks will experience higher strains, and hence a higher degree of driving force for fatigue crack initiation. The reduction in the yield stress of the material associated with the elevated test temperature of 650°C meant that the plastic zones of these cracks are much larger than expected for room temperature tests, i.e. larger regions of the material are experiencing the higher strains and hence increased fatigue crack initiation propensity. The higher strains experienced in the plastically deformed regions of the material may also cause accelerated degree of oxidation, additionally leading to an accelerated rate of crack initiation.

In the elevated temperature short crack tests, immediately after crack initiation a flat area characteristic of transgranular stage II crack growth was observed for the major cracks on all the fracture surfaces followed by an apparent shift to intergranular crack growth modes at longer crack lengths. Transgranular crack growth immediately after crack initiation has also been observed in other elevated temperature short crack or LCF studies [27,29,75,80]. The flat areas are thought to be due to the crack initiating from features within a grain as mentioned earlier and traversing the grains at short crack lengths, i.e. transgranular crack growth. The crack continues to grow by traversing grains until eventually at larger crack lengths the condition shifts to favour the crack following intergranular paths, and from that point onwards intergranular crack growth becomes predominant.

The possible factors favouring the shift to intergranular crack growth at larger crack lengths are likely to be due to a grain boundary sampling-related criterion and/or due to changes in stress intensities at the crack tip. The grain boundary sampling-related criterion may be more relevant as the results shown in Table 4-14 indicate that approximately 4-6 grains have to be traversed before intergranular crack growth modes are fully established, i.e. the transition to intergranular crack growth mode was noted after a certain number of traversed grains rather than at a given crack length, i.e. at a particular crack tip stress intensity. Nevertheless, changes in stress intensities at the crack tip at larger crack lengths may allow sufficient crack tip driving force to cause a transition to an oxidation-assisted intergranular crack growth mode. Grain boundary embrittlement due to oxygen diffusion along these boundaries will cause crack growth to follow these paths. Increased intergranular crack growth at longer crack lengths/higher ΔK levels is expected as similar crack growth modes were noted in corresponding elevated temperature long crack tests in air [30].

5.2.2.2. Long crack growth in vacuum

Elevated temperature long crack tests in vacuum on U720Li and its variants have been carried out during the post-doctoral project [30]. The crack growth rates of U720Li and its variants at 650°C in vacuum show little or no dwell time effects, i.e. crack growth is governed purely by fatigue damage processes which are cycle-dependent. The cycle-dependent nature of the crack growth at 650°C is also apparent from the flat transgranular stage II fracture surfaces. With an increase in temperature to 725°C, an increase in the crack growth rates was noted, and further increases in the crack growth rates were noted with imposition of dwell at 725°C. Crack propagation modes changed to a mixed transgranular/intergranular crack growth in the 725°C 1-1-1-1 condition, and predominantly intergranular crack growth was noted in the 725°C 1-20-1-1 condition. An increase in temperature to 725°C causes an increase in the time-dependent processes which contributes to crack growth such as creep deformation, and imposition of dwell leads to a greater extent of these time-dependent crack growth processes.

The RR1000 elevated temperature vacuum long crack results demonstrated a different trend to the U720Li variants [30] in that an increase in the dwell time from 1 second to 20 seconds at 650°C, and an increase in temperature from 650°C to 725°C in the 1-1-1-1 condition decreases crack growth rates. An increase in the dwell time from 1 second to 20 seconds at 725°C in vacuum gave higher crack growth rates in RR1000 as expected. However, the crack growth rates of the RR1000 650°C 1-1-1-1 vacuum test appear similar or higher than the crack growth rates of the RR1000 725°C 1-20-1-1 vacuum test. This is not expected as the fracture surface of the 650°C 1-1-1-1 test appears predominantly transgranular while the fracture surface of the 725°C 1-20-1-1 condition appears largely intergranular. The crack growth rates of U720Li and its variants in the 725°C 1-20-1-1 vacuum condition are generally noted to be significantly higher than the crack growth

rates in the 650°C 1-1-1-1 vacuum condition. To further investigate the trend in the observed fatigue crack growth rates of RR1000, reference is made to the stress-strain curves [2] of RR1000 at 650°C, 700°C and 750°C, shown in Figure 5-11. The plot demonstrates a similar or slightly lower yield stress of RR1000 on going from 650°C to 700°C, and at 750°C the yield stress was markedly lower and accompanied by a slight decrease in the Young's modulus of the material. This trend is normally observed in nickel-base superalloys, with the decrease in yield stress at higher temperature attributed to increased ease of dislocation cross-slip and climb. A decrease in yield stress with increasing temperature would generally imply an increase in crack growth rates with increasing temperature due to an increase in CTOD. However this is not observed in the current study.

The observed crack growth behaviour may be attributed to stress relaxation and/or crack tip blunting due to creep deformation ahead of the crack tip. When crack growth is predominantly transgranular, creep deformation at the crack tip is thought to be insufficient to cause crack advance but may contribute to stress relaxation and/or crack tip blunting. Stress relaxation and crack tip blunting reduces the crack growth driving force at the crack tip, giving lower crack growth rates. The fracture surfaces of RR1000 at 650°C with 1 and 20 seconds dwell as well as 725°C with 1 second dwell suggest a similar transgranular crack propagation mechanism. The increasing roughness of the fracture surface going from 650°C 1-1-1-1 to 650°C 1-20-1-1 to 725°C 1-1-1-1 suggests an increasing degree of (component of) intergranular crack growth and hence increasing creep deformation at the crack tip. This would imply greater extent of stress relaxation and/or crack tip blunting at longer dwell and/or higher temperatures, which may be reflected by the reduced crack growth rates. The lower σ_y at higher temperature (725°C) may also cause crack tip blunting to occur more easily. With imposition of dwell at 725°C, an increase in crack growth rates and a clearly more intergranular crack growth mode is observed. This may indicate that, in spite of stress relaxation/crack tip blunting due to creep deformation, increased creep damage processes at the crack tip (evidenced by the intergranular crack growth) are counterbalancing this effect, giving an increase in crack growth rates in the 725°C 1-20-1-1 test compared to the 725°C 1-1-1-1 condition.

5.2.2.3. RR1000 long crack growth in air

The elevated temperature fatigue growth out curves of RR1000 in air is shown in Figure 4-68. An increase in temperature and/or dwell leads to higher crack growth rates due to increased oxidation

---

[2] Stress-strain data produced at QinetiQ/DERA Farnborough

attack and creep deformation. The m-values of the tests are relatively similar, suggesting crack growth is dominated by the same crack growth mechanism, i.e. crack growth due to a combination of oxidation attack and creep deformation.

The effect of imposition of dwell was noted to be more marked at 725°C compared to at 650°C as the detrimental effects of oxidation and creep deformation are more severe with imposition of dwell at higher temperature. There is also a complex interaction between creep deformation and oxidation attack (e.g. increased oxidation attack due to creep deformation giving enhanced movement of oxidising species) which may cause significant increases in crack growth rates [99]. This may explain the marked increase in crack growth rates with imposition of dwell at 725°C compared to at 650°C.

Another point to note is that the crack growth rates of the 650°C 1-20-1-1 air test appear to be similar or slightly higher compared to the crack growth rates of the 725°C 1-1-1-1 air test. This similarity suggests that the increase in the extent of oxidation and creep deformation with an increase in temperature to 725°C or an imposition of a 20 second dwell at 650°C are similar compared to the 650°C 1-1-1-1 condition. However it is difficult to establish the individual contributions of oxidation and creep deformation to crack growth due to the synergistic effects of these two components of crack growth. At a constant temperature of 650°C the degree of oxidation would be approximately constant for a given amount of creep deformation. However with imposition of dwell the increase in creep deformation may cause increased diffusion of materials including oxidising species along the grain boundaries hence again giving increased creep damage and a more severe intergranular oxidation effect. With an increase in temperature to 725°C both the creep and oxidation contributions to crack growth are altered compared to 650°C 1-1-1-1 and 1-20-1-1 making it difficult to establish individual contributions to crack growth.

5.2.2.4. Comparison of elevated temperature long crack tests in air and vacuum

A comparison of the crack growth rates of long crack tests conducted at elevated temperatures in vacuum and air [3] is shown in Figure 5-12. Comparing the effect of environment, under similar temperature and dwell, tests conducted in air all show higher crack growth rates compared to tests conducted in vacuum due to increased oxidation in air which accelerates crack growth. When testing in air, intergranular oxidation crack growth mechanisms coupled with any creep deformation which may be present would be expected to dominate. Oxidation is likely to be the governing factor in the air tests as it progresses more rapidly compared to creep deformation which

is a much slower process. This is deduced from the crack growth rates of the vacuum tests which are primarily governed by creep deformation at higher temperatures and/or dwell and are generally much lower than the crack growth rates of the air tests. Any stress relaxation effects in RR1000 due to creep deformation giving rise to a lowered local stress concentration at the crack tip and hence improved crack growth resistance in the vacuum tests are also expected to be swamped by the rapid oxidation effects during the air tests.

For a given material, the m-values of the air tests were generally noted to be relatively similar under all temperature and dwell conditions but the m-values of the vacuum tests were generally noted to progressively increase with increasing temperature and/or dwell conditions. This may be an indication that the extent of creep damage in vacuum tests is much more sensitive to the ΔK level compared to the oxidation process during air tests [19]. The similarity in the m-values of the air tests of each material reiterates that crack growth in the air tests is dominated by oxidation attack as the progressively increasing m-values observed in the vacuum tests where creep deformation is likely to dominate at higher temperature and/or longer dwell were not observed in the air tests. The relatively constant increase in the crack growth rates of the air tests of each material at a given ΔK with increases in test temperature and/or dwell is due to a proportional increase in the oxidation attack at the higher temperature and/or dwell, leading to proportionally faster intergranular crack growth. In the vacuum tests where creep deformation are likely to dominate at higher temperature and/or longer dwell, the progressively increasing m-values is due to increasing degree of monotonic creep contribution to crack growth. The variation in the m-values of the RR1000 vacuum tests is due to creep deformation giving rise to stress relaxation and thus an altered crack growth behaviour compared to U720Li and its variants.

5.2.2.5. Elevated temperature short crack-long crack behaviour comparison

Comparison of long crack and short crack behaviour at 650°C in air is made for U720Li and U720Li-LG by plotting short crack and long crack growth curves on the same graph as shown in Figure 5-13. Comparison was made on a ΔK basis only for U720Li and U720Li-LG as notch root stress analyses required to calculate ΔK in the elevated temperature short crack tests was not possible for other materials. The short growth curve of U720Li was noted to collapse relatively close to corresponding long crack growth curve. For U720Li-LG, the short crack growth rates obtained were at relatively low ΔK which was below the lowest ΔK of the long crack growth curve, hence comparison of the two curves was not possible. However, the short and long crack

---

[3] All air data has been produced at DERA/QinetiQ Farnborough.

growth curves of U720Li-LG do appear to collocate when both curves are extrapolated to intermediate ΔK levels between the two curves.

In the short crack tests, the primary cracks propagate through a flat transgranular stage II crack growth mechanism almost immediately after crack initiation. Crack growth in the short crack tests changed to crack growth modes similar to long crack propagation modes after approximately 4-6 grains have been traversed by the crack in flat transgranular stage II mode. This transition occurs at approximately 40% and 90% of the lifetime of the short crack tests respectively for U720Li and U720Li-LG. Short crack growth in U720Li adopted a predominantly oxidation-assisted intergranular crack growth mode after the flat transgranular stage II crack growth, which is similar to the long crack growth mode of U720Li as shown in Figure 5-14a and Figure 5-14b, and likewise short crack growth in U720Li-LG adopted a mixed transgranular/ intergranular crack growth mode similar to the long crack growth mode of U720Li-LG as shown in Figure 5-14c and Figure 5-14d. Although the comparison of long and short crack growth behaviour was not made for U720Li-LP, the similar short crack growth mode and long crack growth mode (Figure 5-14e and Figure 5-14f) would suggest similar trends as observed for U720Li and U720Li-LG, i.e. the long crack and short crack growth out plots will collapse very close together on a ΔK basis.

Although crack growth in the short crack tests adopts the crack growth modes observed in corresponding long tests only after 40% and 90% of the lifetime of the short crack tests, the long crack and short crack growth plots may be suggesting limited differences in the crack growth behaviour in the long crack and short crack tests at 650°C in air. Flat transgranular crack growth may occur in the long crack tests if the tests are extended to sufficiently low ΔK levels. However at ΔK levels where flat transgranular crack growth occurs in the short crack tests, long cracks are likely to reach threshold. In the short crack tests, the crack is still able to propagate at these short crack lengths possibly due to the notched geometry of the short crack specimens giving a higher stress concentration and hence increased crack growth driving force.

The similarity in the long crack and short crack growth out curves also indicates some degree of applicability of the ΔK parameter as the correlating parameter in the current series of elevated temperature tests. At elevated temperatures the plastic zone size ahead of the crack tip will be significantly larger and creep processes will be more significant, both of which will most likely invalidate ΔK assumptions at smaller crack lengths.

5.2.2.6. Summary

In the elevated temperature short crack tests, crack initiation occurred primarily from porosity, and in U720Li-LG crack initiation from grain boundary oxidation was also frequently observed. In general, all the primary cracks in the tests were initiated from porosity on or just below the surface.

Growth of the primary cracks in the elevated temperature short crack tests was initially transgranular stage II crack growth in air followed by oxidation-assisted intergranular crack growth after 4-6 grains have been traversed by the crack.

At 650°C in vacuum, long crack growth appears to be cycle-dependent for U720Li and its variants. Increasing crack growth rates were noted for long crack tests of U720Li and its variants in vacuum with an increase in temperature to 725°C and imposition of dwell at 725°C due to increasing crack growth contribution from creep deformation which is a time-dependent process. For RR1000, elevated temperature long crack vacuum tests indicate trends that are different from U720Li and its variants in that an imposition of dwell at 650°C and an increase in temperature from 650°C to 725°C in the 1-1-1-1 condition gave progressively lower crack growth rates. Imposition of dwell at 725°C in vacuum gave higher crack growth rates compared to the 725°C 1-1-1-1 condition as expected. The behaviour of RR1000 in the long crack vacuum tests was attributed to stress relaxation giving reduced crack growth driving force.

The RR1000 long crack tests in air showed increasing crack growth rates with increase in temperature and/or dwell due to increased oxidation attack and creep deformation. The effect of imposition of dwell was noted to be more marked at 725°C compared to at 650°C as the detrimental effects of oxidation and creep deformation are more severe with imposition of dwell at higher temperature. The m-values of the air tests are relatively similar, suggesting crack growth is dominated by the same crack growth mechanism, i.e. crack growth due to a combination of oxidation attack and creep deformation.

Under similar temperature and dwell, long crack tests conducted in air all show higher crack growth rates compared to tests conducted in vacuum. The higher crack growth rates in air were attributed to increased contributions of oxidation and creep deformation to crack growth in air. The crack growth rates of the air and vacuum tests as well as the m-values of the air and vacuum growth out curves indicate that oxidation is the dominating factor in the crack growth mechanisms of the air tests.

Comparison of long crack and short crack behaviour at 650°C in air for U720Li and U720Li-LG indicates relatively similar crack growth behaviour of the long crack and short crack tests with the long crack and short crack growth curves collapsing relatively close to one another. The similar crack growth behaviour is expected due to similarities in the crack growth mechanisms in the short crack and long crack tests at elevated temperature in air.

5.2.3. Comparison of fatigue behaviour at room and elevated temperature

5.2.3.1. Fatigue crack initiation and early crack growth

At room temperature, fatigue cracks were noted to initiate from both porosity and slip bands. At 650°C, porosity was noted to be the dominant crack initiation mechanism with no slip band initiation observed. The absence of slip band cracking at 650°C is expected as dislocation cross-slip and climb processes at elevated temperatures will lead to wavy slip, and hence a reduction in the likelihood of slip band cracking.

In terms of short crack growth at room temperature, stage I type crack growth was observed in all the alloys at short crack lengths and stage II type crack growth was observed at longer crack lengths. At 650°C, the initial crack growth of the primary crack immediately after crack initiation was relatively smooth transgranular stage II type crack growth followed by an apparent shift to intergranular crack growth modes at longer crack lengths. Distinct stage I and stage II crack growth was noted at room temperature due to the highly planar slip character of the materials at room temperature. At 650°C, the initial flat transgranular region is due to the crack propagating by a stage II crack growth mechanism at short crack lengths and eventually shifting to intergranular crack growth modes at longer crack lengths due to the presence of the air environment and sufficient sampling of grain boundaries occurring to set up the intergranular crack growth mode.

Comparisons of room and elevated temperature short crack growth rates are shown in Figure 5-15 for U720Li and U720Li-LG. No comparison was made for U720Li-LP and RR1000 as the notch root stress analyses required to calculate ΔK in the elevated temperature short crack tests were not possible for these materials. Figure 5-15a shows that the short crack growth rates of U720Li at room temperature are approximately one decade lower compared to that at 650°C. U720Li was noted to show stage I and/or stage II crack growth at room temperature while at 650°C, approximately 60% of the fatigue life (Table 4-15) was spent in the oxidation-assisted intergranular crack growth regime. The difference in the short crack growth rates of U720Li at room temperature and at 650°C may therefore be attributed to the oxidising environment of the elevated temperature short crack tests which gives highly accelerated oxidation-assisted intergranular crack growth modes. The slip mechanisms in the materials are also expected to be altered at the elevated test temperature but this change is likely to have a less significant role in altering the crack growth rates when intergranular crack growth behaviour predominates. The short crack growth rates of U720Li-LG shown in Figure 5-15b appear to indicate that the room and elevated temperature short crack growth rates are relatively similar. At room temperature, U720Li-LG was noted to again show stage I and/or stage II crack growth, but at 650°C approximately 90% of the fatigue life (Table 4-15) was spent in the transgranular stage II crack growth regime. The similarity in the short crack growth rates of U720Li-LG at room temperature

and at 650°C may be reflecting the relatively similar crack growth modes observed in U720Li-LG at room temperature and at 650°C. The different crack growth modes observed in U720Li and U720Li-LG at 650°C is likely to be linked to the variation in oxidation resistance of the materials and this is further discussed in section 5.3.6.1.

5.2.3.2. Long crack growth

A comparison of room temperature long crack growth behaviour in air and elevated temperature long crack growth behaviour in vacuum for each material is shown in Figure 5-16a to Figure 5-16d. Note that the room temperature data used are from the constant load growth out (increasing ΔK) portion of the tests. The room temperature long crack growth rates are compared with the elevated temperature vacuum long crack growth rates due to the absence of significant oxidising effects in the vacuum long crack tests, hence the comparison will give a more simplified picture of the effect of temperature on long crack growth behaviour. The room temperature crack growth rates in all materials are significantly lower than elevated temperature crack growth rates.

The crack growth behaviour of U720Li and its variants at 650°C in vacuum is cycle-dependent due to the absence of any significant dwell time effects. A comparison between the room temperature growth rates in air, which are cycle-dependent and the growth rates at 650°C in vacuum would hence reveal the effects of temperature on cycle-dependent crack growth behaviour. The cycle-dependent crack growth nature at both temperatures (20°C and 650°C) is enforced by the similarity in the m-values of the room temperature and 650°C growth out curves, as well as by the similar transgranular stage II crack growth observed at both temperatures. Both observations would suggest a similar crack growth mechanism at both temperatures. The crack growth rates at 650°C in U720Li and variants are generally about one decade higher than the room temperature crack growth rates. This is due to the elevated temperature of 650°C giving rise to more dislocation cross-slip and climb, i.e. increased dislocation mobility and more wavy slip which may lead to possible acceleration of stage II crack growth processes. The associated increase in dislocation mobility at elevated temperatures would also lead to reduction in the yield stress (and also possibly Young's Modulus) of the materials. This is expected to further contribute to increased crack growth rates due to an increase in the crack tip opening for a given stress level. The difference in crack growth rates is unlikely to be linked to increased oxidation effects due to the effective absence of environment effects at 650°C in vacuum compared to room temperature in air, although the change in environment may have affected slip behaviour. Generally, vacuum environments are considered to promote slip reversibility and hence enhance heterogeneous slip processes.

In the case of RR1000, frequency-independent crack growth was not observed at 650°C. The crack growth rates in the 650°C 1-20-1-1 condition were lower than the crack growth rates in the 650°C 1-1-1-1 condition. However on comparing the 650°C growth out curves with the room temperature growth out curve, similar m-values of the room temperature and 650°C 1-1-1-1 growth out curves were noted. This would suggest cycle-dependent crack growth in the 650°C 1-1-1-1 condition, i.e. essentially a similar crack growth mechanism to room temperature crack growth. The crack growth rates at 650°C 1-1-1-1 are again higher than the room temperature crack growth rates due to changes in dislocation mobility associated with increases in temperature mentioned earlier.

In order to clarify the effects of temperature on crack growth rates due to changes in the crack tip opening displacement, the crack tip opening displacement experienced by U720Li at room and elevated temperatures was assessed. Similar changes in crack tip opening displacement may be expected in other tests materials due to similarity in the microstructure and alloy chemistry of the materials. The range of crack opening displacement $\Delta\delta$ per cycle is given by

$$\Delta\delta = Q\frac{\Delta K^2}{\sigma_{cy}E} \qquad \text{Equation 5-1}$$

where Q is a constant and σ_{cy} is the cyclic yield stress. The monotonic yield stress σ_y is often used in place of σ_{cy} as an approximation. As crack growth rates are directly related to the range of crack opening displacement $\Delta\delta$,

$$\frac{da}{dN} \propto \frac{\Delta K^2}{\sigma_y E} \qquad \text{Equation 5-2}$$

At a given ΔK,

$$\frac{\left(\frac{da}{dN}\right)_{650C}}{\left(\frac{da}{dN}\right)_{20C}} = \frac{(\sigma_y E)_{20C}}{(\sigma_y E)_{650C}} \qquad \text{Equation 5-3}$$

The Young's modulus and yield stress of U720Li at room temperature was not available as room temperature tensile data was not available. As the Young's modulus of nickel-base superalloys at room temperature is relatively insensitive to microstructure and alloy chemistry, the Young's modulus of U720Li at room temperature is taken as 207GPa which is the room temperature Young's modulus of nickel-base superalloys generally quoted in the literature. The room temperature yield stress of U720Li was estimated from the room temperature yield stress of U720 supplied by Loo-Morrey [40] and the relative hardness values of U720 and U720Li. The room

temperature yield stress of U720Li was estimated to be 1216MPa from the hardness values. Elevated temperature first cycle LCF data which is analogous to tensile data was used to estimate the Young's modulus and yield stress of U720Li at 650°C. The Young's modulus and yield stress of U720Li at 650°C are estimated to be 180GPa and 980MPa respectively. Using these values,

$$\frac{\left(\frac{da}{dN}\right)_{650C}}{\left(\frac{da}{dN}\right)_{20C}} = 1.43 \qquad \text{Equation 5-4}$$

The results appear to indicate that the crack growth rates of the elevated temperature tests will be 40% higher than the room temperature crack growth rates but this was not observed. The elevated temperature crack growth rates was generally observed to be approximately one order of magnitude higher than the room temperature crack growth rates, i.e. the elevated temperature crack growth rates is approximately 1000% higher than the room temperature crack growth rates.

In the literature, the range of crack tip opening displacement did not always account for the effects of temperature on crack growth rates [5]. Temperature effects are controlled by E and σ_y, and therefore by crack tip opening displacement, if the slip distribution and fracture path remain similar at both room and elevated temperatures. Changes in slip deformation behaviour and fracture path at elevated temperatures are expected to affect crack growth rates through changes in crack growth mechanisms which could not be accounted for by changes in E and σ_y alone.

5.2.3.3. Summary

Differences in the crack initiation and growth behaviour observed in the room and elevated temperature tests were attributed to changes in the slip mechanisms from planar slip at room temperature to wavy slip at elevated temperature. Planar slip at room temperature gives rise to initiation from slip band cracking in addition to crack initiation from porosity, while wavy slip at elevated temperature reduced the tendency of crack initiation from slip band cracking and only crack initiation from porosity was noted.

The differences in the crack growth rates observed in the room and elevated temperature short crack tests are attributed to the oxidising environment of the elevated temperature short crack tests and changes in the slip mechanisms of the materials at the elevated test temperature. Distinct stage I and stage II crack growth was noted at room temperature due to the highly planar slip character of the materials at room temperature. At 650°C, the initial flat transgranular region is due to the crack propagating by a stage II crack growth mechanism at short crack lengths and eventually shifting to intergranular crack growth modes at longer crack lengths due to the presence

of the air environment and sufficient sampling of grain boundaries occurring to set up the intergranular crack growth mode.

Transgranular stage II crack growth was noted in the room temperature long crack tests and long crack tests conducted in vacuum at 650°C. Differences in crack growth rates were primarily attributed to the effect of temperature on the slip mechanisms in the materials. The effect of temperature on crack growth rates could not be accounted for by changes in the crack tip opening displacement as the slip mechanisms were also altered at the elevated test temperatures.

5.3. Effect of microstructure

Microstructure controls fatigue partially through its effects on slip planarity. In order to quantify the planarity of slip in the materials, the microstructure of the materials in this study has to be physically represented based on the microstructural characteristics which have been measured and calculated in section 4.1 and section 5.1. As planar slip arises from the cutting of fine coherent precipitates, the precipitate cutting-to-looping transition diameter has to be assessed from the microstructural characteristics. The planarity of slip in the materials is then assessed based on methods already put forward in the literature [41,44].

The effects of microstructure on room temperature fatigue crack initiation and growth is discussed in light of the planarity of slip assessment and other microstructural effects which may be expected to be prevalent at room temperature. This is followed by a discussion of the effects of microstructure on elevated temperature fatigue crack initiation and growth resistance.

5.3.1. Physical representation

A physical representation of the microstructure of the materials based on the measured and calculated quantities of the microstructural characteristics was developed to clarify differences in the microstructures and also for use in further analyses such as the slip planarity assessment.

The grain and primary γ' precipitates were represented by a hexagonal-type array of equi-sized grains and primary γ' precipitates as illustrated in Figure 5-1 similar to the approach taken by Hide et al [30].

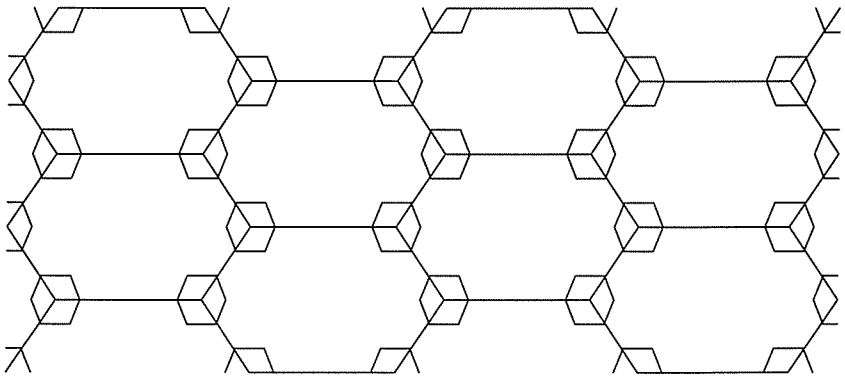

Figure 5-1: Representative hexagonal arrays of grains and primary γ' precipitates.

The elongated hexagon is treated as a unit cell with all internal angles taken as 120° and the height is taken as a ratio R of the length of the elongated side as illustrated in Figure 5-2. The dimensions of the elongated hexagon unit cell of the grain and primary γ' are chosen such that the area and circularity of the unit cell is equivalent to corresponding grain and primary γ' precipitate area and circularity obtained from microstructural characterisation of the materials.

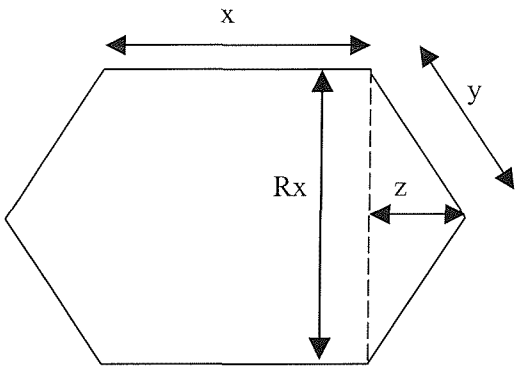

Figure 5-2: Elongated hexagon unit cell.

The quantities *y* and *z* can be related to x as follows:

$$y = \frac{Rx}{2\cos 30°} \qquad \text{Equation 5-5}$$

$$z = \frac{Rx\sin 30°}{2\cos 30°} \qquad \text{Equation 5-6}$$

The area of the unit cell can be calculated by treating the hexagon as two trapezium of height *Rx/2* and length of the two parallel sides as *x* and *(x+2z)*. Therefore

$$Area = 2\times\frac{1}{2}\times\left[x+\left(x+2z\right)\right]\times\frac{Rx}{2} \qquad \text{Equation 5-7}$$

Substituting Equation 5-6 into Equation 5-7 the yields

$$Area = \left[1+\frac{R}{2}\tan 30°\right]Rx^2 \qquad \text{Equation 5-8}$$

The perimeter of the unit cell is given by

$$Perimeter \;=\; 2x \;+\; 4y \qquad \text{Equation 5-9}$$

Substituting Equation 5-5 into the Equation 5-9 yields

$$Perimeter = 2x\left[1+\frac{R}{\cos 30°}\right] \qquad \text{Equation 5-10}$$

The circularity is given by Equation 3-1, substituting Equation 5-8 and Equation 5-10 into the equation yields

$$Circularity = \frac{\pi R\left[1+\frac{R}{2}\tan 30°\right]}{\left[1+\frac{R}{\cos 30°}\right]^2} \qquad \text{Equation 5-11}$$

The circularity of the grains in the materials were noted to be approximately 0.66 and to yield this circularity, R has to be chosen as 0.4. The circularity of the primary γ' on the other hand ranges from 0.67 to 0.72. The circularity of primary γ' in RR1000 MO1751 and U720Li-LP were noted to be 0.67 and R is again chosen to be 0.4. R is chosen as 0.45 for RR1000 MO1547 and U720Li as the circularity of the primary γ' in these materials were noted to be 0.70, while for U720Li-LG, R is chosen to be 0.5 to account for the primary γ' circularity of 0.72. Note that by choosing a value of R between 0.4-0.5 for the grains and primary γ' precipitates, the hexagonal unit cells will become highly elongated. Equation 5-5 indicates that y is approximately four times shorter than x for a value of R between 0.4-0.5.

Material	U720Li	U720Li-LG	U720Li-LP	RR1000 M1547	RR1000 MO1751
R_{grain}	0.4	0.4	0.4	0.4	0.4
$R_{primary\ \gamma'}$	0.45	0.5	0.4	0.45	0.4

Table 5-6: R values for grain and primary γ' in the materials.

The grain size and primary γ' size were taken as equivalent circle diameter of the grain and primary γ' precipitate during microstructural characterisation, therefore the grain and primary γ' precipitate area is given by

$$Area = \frac{\pi r^2}{4} \qquad \text{Equation 5-12}$$

where r is the grain size or primary γ' precipitate size. Substituting Equation 5-12 into Equation 5-8 yields

$$x = r\sqrt{\frac{\pi}{4R\left[1+\frac{R}{2}\tan 30°\right]}} \qquad \text{Equation 5-13}$$

The representation of the grains and primary γ' precipitates using a hexagon-type array also allows the volume fraction of primary γ' precipitates to be calculated according to the sizes of the elongated hexagon unit cells of the grains and primary γ' precipitates. It will be useful to compare the calculated volume fraction and actual volume fraction measured during microstructural characterisation to ascertain if the volume fraction of primary γ' precipitates is governed by the sizes of the grains and primary γ' precipitates.

For a given unit cell of the grain, primary γ' precipitates occupy the six corners of the hexagon and it was noted that each grain unit cell has two complete primary γ' unit cells as shown in Figure 5-3.

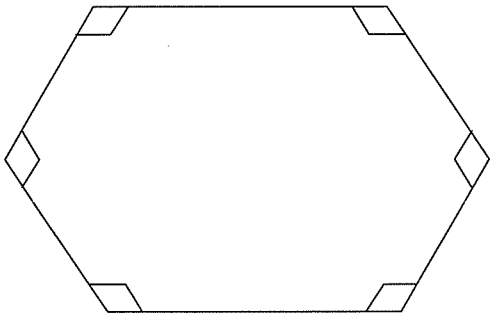

Figure 5-3: Primary γ' in a grain unit cell.

Therefore the volume fraction of primary γ' can be calculated according to the following equation

$$V_f \text{ primary } \gamma' = \frac{2\left(\left[1+\frac{R}{2}\tan 30°\right]Rx^2\right)_{primary\ \gamma'}}{\left(\left[1+\frac{R}{2}\tan 30°\right]Rx^2\right)_{grain}} \qquad \text{Equation 5-14}$$

The measured and calculated microstructural parameters of the grains and primary γ' precipitates are summarised in the table below.

Material	U720Li	U720Li-LG	U720Li-LP	RR1000 M1547	RR1000 MO1751
r_{grain} (μm)	6.4	15.4	10.1	7.4	7.1
$r_{primary\ \gamma'}$ (μm)	1.99	2.52	2.12	1.75	1.80
V_f primary γ' (measured) (%)	18.9	8.6	18.3	8.7	11.8
x_{grain} (μm)	8.5	20.4	13.4	9.8	9.4
$x_{primary\ \gamma'}$ (μm)	2.5	3.0	2.8	2.2	2.4
V_f primary γ' (calculated) (%)	19.3	5.3	8.8	11.2	12.8

Table 5-7: Summary of measured and calculated microstructural parameters of the grains and primary γ' precipitates.

The calculations indicate values of x which are proportional to the measured grain sizes and primary γ' sizes as the x values were calculated using the measured grain size and primary γ' size. In terms of the primary γ' volume fraction, other than for U720Li-LP, the calculated values are relatively similar to the measured values. This may indicate that the volume fraction of primary γ' precipitates in the material are reflected by the sizes of the grains and primary γ' precipitates. This is expected as grain growth occurs at the expense of primary γ' precipitates during the solution treatment stage.

The calculated volume fraction of primary γ' of U720Li-LP was noted to be much lower than the measured volume fraction. This may be due to the actual grain size in U720Li-LP being smaller than the measured grain size. Note that the measured grain size of U720Li-LP was taken from Hide et al [30] as etching of U720Li-LP did not give adequate grain boundary resolution for accurate grain size measurement in the current study. A rough estimate indicates that in order to give a calculated volume fraction of primary γ' which is much closer to the measured volume fraction, the grain size in U720Li-LP has to be relatively similar to the grain size of U720Li.

Another possible explanation for the difference in the calculated and measured volume fraction of primary γ' precipitates of U720Li-LP may be that the primary γ' precipitates in U720Li-LP are distributed differently compared to other materials. An example of an alternative distribution of primary γ' precipitates in U720Li-LP is shown in Figure 5-4 where in addition the primary γ' precipitates located at the six corners of the hexagonal grain unit cell, primary γ' precipitates were also present in the middle of each of the sides of the unit cell. In an individual grain unit cell with this alternative distribution of primary γ' precipitates, there are 5 complete primary γ' unit cells and the volume fraction of U720Li-LP is calculated to be 22.0 with this alternative precipitate

distribution which is closer to the measured value. The similarity in the calculated primary γ' volume fraction of U720Li-LP with the alternative distribution of primary γ' precipitates as shown in Figure 5-4 to the measured volume fraction appear to suggest that the primary γ' precipitates distribution in U720Li-LP will be more similar to the distribution shown in Figure 5-4 while the primary γ' precipitates distribution in other materials is likely to be resemble the distribution shown in Figure 5-3.

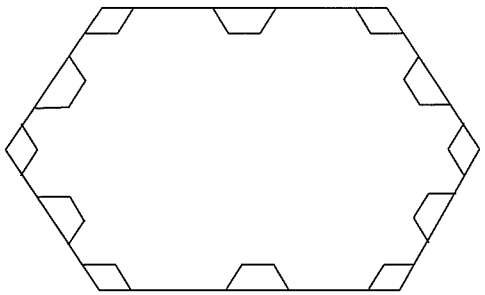

Figure 5-4: Alternative primary γ' precipitate distribution in U720Li-LP.

The elongated hexagon unit cells of the grains are further divided to represent the coherent γ' precipitates distribution in the materials. Calculations of microstructural parameters associated with the secondary and tertiary γ' precipitates are slightly complicated by the overlapping positions of the secondary and tertiary γ' precipitates over each other, and over primary γ' locations at the corners of the unit cells as will be highlighted later.

The secondary and tertiary γ' precipitates are represented by circles as these precipitates were noted to have average circularity values of approximately 0.9 during microstructural characterisation. The coherent γ' precipitates are placed in the model such that a single precipitate is surrounded by six other precipitates as shown in Figure 5-5 similar to the arrangement that would be expected from the arrangement of atoms in a close-packed plane.

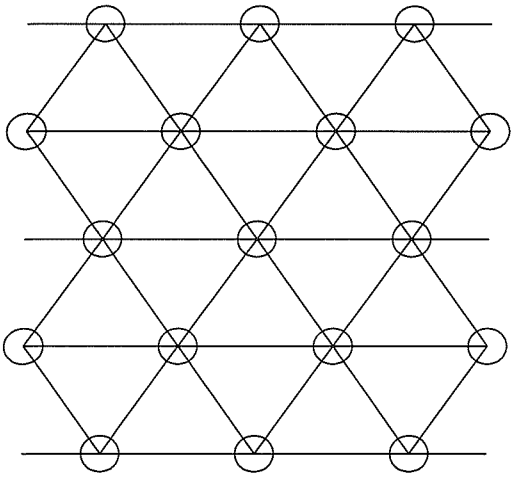

Figure 5-5: Assumed coherent γ' precipitates distribution in the materials

The unit cell of the coherent γ' precipitate arrangement is therefore an equi-axed triangle with 1/6 of a circular precipitate occupying the three corners as illustrated in Figure 5-6. The mean distance between the precipitates and the precipitate radius are denoted r and r_p respectively.

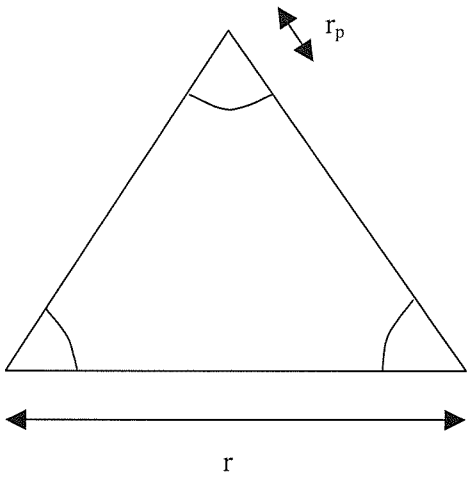

Figure 5-6: Unit cell of coherent γ' precipitates.

The area of the triangular unit cell, A and the area occupied by precipitates in the triangular unit cell, A_{ppt} are given by

$$A = \frac{1}{2} r^2 \sin 60° \qquad \text{Equation 5-15}$$

$$A_{ppt} = \frac{1}{2} \pi r_p^{\,2} \qquad \text{Equation 5-16}$$

The volume fraction of precipitates in the triangular unit cell V_f is therefore given by

$$V_f = \frac{\pi}{\sin 60°}\left(\frac{r_p}{r}\right)^2 \qquad \text{Equation 5-17}$$

Equation 5-17 can be applied almost directly to calculate the secondary γ' precipitates spacing in the materials. However, the volume fraction of secondary γ' precipitates in the triangular unit cell should not be assumed to be equal to the volume fraction of secondary γ' calculated in section 5.1 as the volume fraction of secondary γ' precipitates in the triangular unit cell, denoted (2° γ' V_f)', is given by

$$\left(2° \gamma' V_f\right)' = \frac{\left(2° \gamma' \mathrm{V_f}\right)}{1 - \left(1° \gamma' \mathrm{V_f}\right)} \qquad \text{Equation 5-18}$$

where 1° γ' V_f and 2° γ' V_f are the volume fractions of the primary γ' and secondary γ' precipitates respectively. As the secondary γ' precipitates can only occur at locations not occupied by primary γ' precipitates in the grains, the primary γ' volume fraction can be seen to be subtracted from the total area (100%) in Equation 5-18 to account for the area which has been taken up by the primary γ' precipitates in the grains. With the known secondary γ' precipitate size and the volume fractions of the primary γ' and secondary γ' precipitates, the secondary γ' precipitates spacing, denoted r_{II} can be calculated from Equation 5-17 and Equation 5-18.

With the known r_{II} values, the secondary γ' cell arrangement in the grain unit cell could be envisaged. Two new quantities are introduced, the number of secondary γ' cells along the maximum feret of the grain (i.e. along the $x+2z$ length), denoted n_{II}, and the number of secondary γ' cells in the grain unit cell, N_{II}. The number of secondary γ' cells along the maximum feret of the grain, n_{II}, is given by

$$n_{II} = \frac{\left(x + 2z\right)_{grain}}{r_{II}} \qquad \text{Equation 5-19}$$

where x and z are given by Equation 5-13 and Equation 5-6. The number of secondary γ' cells in the grain unit cell, N_{II}, is approximately given by

$$N_{II} = \frac{Area\ grain\ cell - 2(Area\ primary\ \gamma'\ cell)}{Area\ \mathrm{sec}\ ondary\ \gamma'\ cell} \qquad \text{Equation 5-20}$$

The area of the grain cell and primary γ' cell can be calculated using Equation 5-8, and the area of the secondary γ' cell is given by Equation 5-15. The value of N_{II} obtained from Equation 5-20 represents the theoretical N_{II}, i.e. Equation 5-20 considers only the area available for the placement of secondary γ' cells in the grain cell and ignores the constraints associated with the actual physical dimensions available for the placement of secondary γ' cells within the grain cell.

The measured and calculated microstructural parameters of secondary γ' precipitates are summarised in the table below.

Material	U720Li	U720Li-LG	U720Li-LP	RR1000 M1547	RR1000 MO1751
Volume fraction of secondary γ' (%)	21.2	31.5	21.8	30.6	27.5
Secondary γ' size (nm)	102	190	254	140	146
r_{II} (nm)	190	308	468	230	249
n_{II}	28.3	53.9	21.2	30.7	26.0
N_{II}	1660	4286	769	1663	1285

Table 5-8: Summary of measured and calculated microstructural parameters of secondary γ' precipitates.

The model is further extended to calculate the tertiary γ' precipitate spacing in the materials using Equation 5-17 and the volume fraction of tertiary γ' precipitates in the tertiary γ' cell, i.e. a modified form of Equation 5-18. By considering the remaining area not occupied by both the primary and secondary γ' precipitates in the model, the volume fraction of tertiary γ' precipitates in the tertiary γ' cell, denoted (3° γ' V_f)', is given by

$$\left(3^\circ \gamma' V_f\right)' = \frac{\left(3^\circ \gamma' \mathrm{V_f}\right)}{1-\left(1^\circ \gamma' \mathrm{V_f}\right)-\left(2^\circ \gamma' \mathrm{V_f}\right)} \qquad \text{Equation 5-21}$$

The tertiary γ' cell arrangement in the secondary γ' cell can be determined using similar methodologies behind Equation 5-19 and Equation 5-20. Similar to the calculations of secondary γ' cell arrangement in the grain cell, two new quantities are introduced, i.e. the number of tertiary γ' cells along the length not occupied by the secondary γ' precipitates at the sides of the secondary γ' cell, denoted n_{III}, and the number of tertiary γ' cells in the secondary γ' unit cell, N_{III}. The number of tertiary γ' cells along the length not occupied by the secondary γ' precipitates at the sides of the secondary γ' cell, n_{III} is given by

$$n_{III} = \frac{r_{II} - r_{2\circ}}{r_{III}}$$ Equation 5-22

where r_{II} and $r_{2\circ}$ are the secondary γ' precipitate spacing calculated earlier and the secondary γ' precipitate size respectively. The number of tertiary γ' cells in the secondary γ' unit cell, N_{III} is approximately given by

$$N_{III} = \frac{Area\ \sec ondary\ \gamma'\ cell - \frac{1}{2}(Area\ \sec ondary\ \gamma'\ precipitate)}{Area\ tertiary\ \gamma'\ cell}$$ Equation 5-23

The measured and calculated microstructural parameters of tertiary γ' precipitates are summarised in the table below.

Material	U720Li	U720Li-LG	U720Li-LP	RR1000 M1547	RR1000 MO1751
Volume fraction of tertiary γ' (%)	8.0	8.0	8.0	9.9	9.9
Tertiary γ' size (nm)	16	17	27	18	21
r_{III} (nm)	41.7	44.3	70.3	42.4	49.5
n_{III}	2.1	2.7	3.0	2.1	2.1
N_{III}	15	32	32	20	17

Table 5-9: Summary of measured and calculated microstructural parameters of tertiary γ' precipitates.

The area not occupied by the secondary γ' precipitates in the secondary γ' cell can be seen to be approximately six-sided and take the shape of a hexagon as illustrated in Figure 5-7, where the tertiary γ' cell packing with n_{III} equal to 1 is shown.

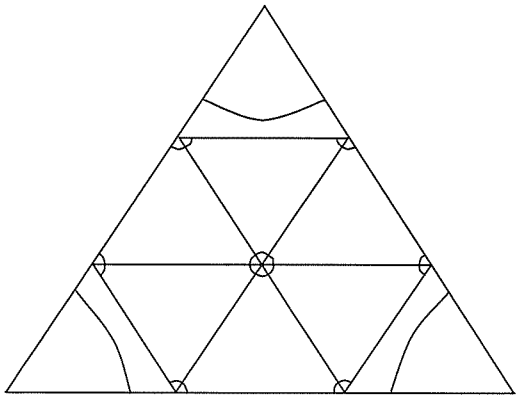

Figure 5-7: Tertiary γ' unit cell arrangement in secondary γ' unit cell.

Calculations of secondary and tertiary γ' precipitate spacing indicate larger precipitate spacing with larger precipitate size for a given volume fraction of precipitates. This was noted when comparing materials which have approximately similar volume fractions of precipitates, e.g. U720Li and U720Li-LP as well as both batches of RR1000 which have approximately similar volume fractions of secondary γ' precipitates, and U720Li and variants as well as both batches of RR1000 which have approximately similar volume fractions of tertiary γ' precipitates. The lowest secondary γ' spacing was noted in U720Li, while the largest secondary γ' spacing was noted in U720Li-LP. U720Li-LG and both batches of RR1000 have secondary γ' spacing distances between that of U720Li and U720Li-LP. In terms of the tertiary γ' precipitate spacing, U720Li, U720Li-LG and both batches of RR1000 were noted to have tertiary γ' spacing between 40-50nm, while in U720Li-LP the tertiary γ' spacing was approximately 70nm which is significantly larger compared to other materials. The calculations also indicate that approximately two tertiary γ' precipitates were present between the secondary γ' precipitates along the slip direction in U720Li and both batches of RR1000, while in U720Li-LG and U720Li-LP this figure is approximately three tertiary γ' precipitates.

5.3.1.1. Summary

The microstructure of the materials has been physically represented in a simple geometrical array based on the measured and calculated quantities of the microstructural characteristics. The grains and primary γ' precipitates were represented by elongated hexagons with primary γ' precipitates occupying the six corners of larger hexagons representing the grains. The secondary and tertiary γ' precipitates were represented as circular objects and were placed in the model such that one precipitate is surrounded by six other precipitates similar to the arrangement of atoms in a close-packed plane.

The calculated microstructural parameters of the grains and primary γ' precipitates in the geometrical array model are similar to the trends of the measured values of corresponding

microstructural parameters. The volume fraction of primary γ' precipitates which were calculated according to the sizes of the grains and primary γ' precipitates in the model and the assumed primary γ' precipitate arrangement in the model appear to be close to the measured value for all materials except U720Li-LP. The discrepancy between the calculated and measured value of the primary γ' precipitate volume fraction of U720Li-LP may indicate that the primary γ' precipitates in U720Li-LP are distributed differently along the grain boundaries compared to other materials. Calculations of secondary and tertiary γ' precipitate spacing have also been carried out. The coherent γ' precipitate spacing was noted to scale with the volume fraction and size of precipitates in the materials.

5.3.2. Effect of microstructure - slip deformation behaviour

5.3.2.1. Precipitate cutting to looping transition

Order hardening has been shown to be the dominant strengthening mechanism for γ' precipitates in nickel-base superalloys such as Astroloy and Waspaloy [155]. In these alloys the main strengthening arises from coherent γ' precipitates similar to the materials in the current study, hence order strengthening is also expected to be dominant in the materials in the current study. Order hardening arises from the creation of an antiphase boundary when a single matrix dislocation enters an ordered γ' precipitate.

The critical precipitate size for dislocation cutting to bowing transition can be estimated by examining the force F which a single precipitate is able to exert on a single dislocation. The force due to a single matrix dislocation is given by $G_m b^2$ where G_m is the matrix shear modulus and b is the Burgers vector of a matrix dislocation. If $F < G_m b^2$, then shearing occurs, and if $F = G_m b^2$ then bowing occurs.

For the case of order hardening and full coherency, F is given by

$$F = \gamma d \qquad \text{Equation 5-24}$$

where γ is the antiphase boundary energy and d is the precipitate diameter (or the precipitate cross-section on the slip plane). Equating this to $G_m b^2$ and solving for d yields the critical precipitate size at cutting to looping transition, d_c.

$$d_c = \frac{G_m b^2}{\gamma} \qquad \text{Equation 5-25}$$

The material information required to calculate d_c was not available for the materials in the current study. However as these values are expected to be relatively insensitive to alloy chemistry and microstructure, the material information of other nickel-base superalloys found from the literature

was used. For the majority of nickel-base superalloys, G_m was noted to be approximately 80GPa [23], while b and γ was generally estimated to be approximately 0.26 nm [23] and 0.17 Jm^{-2} [156,157] respectively. The antiphase boundary energy value of approximately 0.280 Jm^{-2} in reference [23] was not used in this analysis as it was deemed to be much higher than the antiphase boundary energy generally quoted in the literature. Using this general nickel-base superalloy information, d_c was found to be approximately 32 nm.

This estimate does not take into account the fact that dislocations travel in pairs, which would tend to increase d_c. This phenomenon occurs because as the first dislocation creates an antiphase boundary, the second dislocation restores order to the $L1_2$ crystal structure of γ', making it possible for larger precipitates to be cut by paired dislocations. There is some confidence in the calculated d_c value of 32 nm for the materials in the current study as the transition from precipitate cutting to looping diameter has been experimentally observed to be approximately 20nm-25nm in Waspaloy [22] and Nimonic 90 [35] which are quite similar alloy systems to the materials in the current study.

In Waspaloy, precipitate shearing was noted in the material with γ' size of 8 nm, while in the material with γ' size of 25 nm, precipitate shearing and bowing was observed, and for two other materials each containing γ' precipitates 50 nm and 90 nm in size, precipitate bowing was observed [22]. The critical precipitate size for transition from precipitate shearing to looping in Nimonic 90 was noted to be approximately 20 nm [35]. In the underaged condition, Nimonic 90 containing γ' precipitates with a size of 11 nm was noted to exhibit precipitate shearing, while in the peak-aged material containing γ' precipitates with a size of 27 nm, precipitate shearing and looping was observed, and in the overaged material containing γ' precipitates approximately 60 nm in size, dislocation loops was observed around almost all the precipitates [35]. Shearing of precipitates has also been observed at room temperature in U720Li with a bimodal γ' distribution approximately 20 nm and 80 nm in size [158].

The assessment suggests that the tertiary γ' precipitates in all the materials in the current study are being cut. However, the average tertiary γ' precipitate diameter of U720Li-LP is similar to the calculated critical precipitate diameter at cutting to looping transition. The significantly larger tertiary γ' spacing in U720Li-LP (section 5.3.1) compared to the absolute size of the tertiary γ' precipitates also mean that lower stresses are required for dislocations to loop the tertiary γ' precipitates. Both provide strong evidence that in U720Li-LP dislocations bypass tertiary γ' precipitates through a combination of precipitate cutting and bowing processes. Larger tertiary γ' precipitates are expected to be bowed rather than cut.

5.3.2.2. Planarity of slip in materials

Deformation behaviour giving rise to varying degrees of slip planarity is expected to have a significant effect on fatigue crack initiation and growth behaviour of the materials at room temperature. The planarity of slip in the materials is affected by differences in the microstructure of the materials. Larger grain materials are expected to show a higher degree of slip planarity due to increased slip length with larger grains while larger precipitate size (below the precipitate cutting to bowing transition size) and higher volume fraction of the precipitates have been associated with increased planarity of slip [44].

There are however some difficulties in quantifying the planarity of slip in the materials in the current study as systematic variation of microstructural parameters was not present in the materials in the current study. This is due to the lack of independent control of microstructural variables during fabrication as these variables are highly correlated to one another. For example, heat treatment routes which increase grain size generally reduce the volume fraction of primary γ' whilst increasing the volume fraction of coherent γ' precipitates.

Comparing U720Li and its variants, the planarity of slip in U720Li can be gauged to be the lowest in quite a straightforward manner. U720Li and its variants were noted to have similar tertiary γ' volume fractions but U720Li has finer grains and tertiary γ' precipitates compared to its variants. Both these factors are expected to give rise to a relatively lower degree of slip planarity in U720Li compared to its variants. U720Li-LG has larger grains but finer tertiary γ' precipitates compared to U720Li-LP, i.e. two aspects which have opposing effects on the planarity of slip in the materials, making quantification of the planarity of slip in these materials slightly complicated. Finally, there is also a need to quantify the planarity of slip in RR1000.

In a bid to quantify the slip planarity in the materials in a more consistent manner, the approach suggested by Duva et al [44] was used. In the approach put forward by Duva et al, slip intensity, i.e. planarity of slip is quantified by calculating the number of dislocations expected in the slip band. Note that this approach does not account for many subtle factors, including interactions between slip planes, the nature of dislocation sources present and the full variety of possible hardening and softening mechanisms [44]. The authors started by defining the strength τ of a particular slip plane. By considering the strengthening effects of both the precipitates and the dislocation pile-ups at grain boundaries, the strength of a particular slip plane can be written as

$$\tau = \tau_o + C_p V_f^{1/2} \left(r_p - Nb/2\right)^{1/2} + \frac{C_B Nb}{L} \qquad \text{Equation 5-26}$$

where τ_o is the Peierls stress, V_f the precipitate volume fraction, r_p the precipitate radius, N the number of dislocations gliding along the slip length and L the slip length. C_p is related to the precipitate hardening mechanisms and for order hardening, C_p is given by [41]:

$$C_p = \frac{\gamma^{3/2}}{2b}\left(\frac{3}{\pi G_m b^2}\right)^{1/2} \qquad \text{Equation 5-27}$$

C_B is related to the matrix shear modulus and is given by [41]:

$$C_B = \frac{G}{\pi(1-\upsilon)} \qquad \text{Equation 5-28}$$

The last term in Equation 5-26, C_BNb/L, can be regarded as the backstress at the centre of the grain due to a superdislocation (with Burgers vector Nb) at the grain boundary or as the backstress at the end of a pile-up of length L containing N dislocations, accounting for the inhibiting effect of dislocation pile-up on subsequent slip.

The slip intensity relationship was derived based on the assumption that if slip weakens a particular plane (by reduction in the cross-sections of strengthening precipitates), then slip will continue on that plane until it regains the strength (by work hardening) it had when softening commenced. The indicator of slip intensity is taken as the number of dislocation N that passes a typical slip plane from the time the deformation begins until local slip ends. Larger slip intensity as measured by N indicates coarser deformation, i.e. more planar slip will be expected. For the case of initial softening expected for the materials in the current study, $\delta\tau/\delta n \leq 0$ and slip will continue until τ reaches its initial value, thus:

$$N = V_f^{1/2} r_p^{1/2} L \frac{C_p}{C_B b} \qquad \text{Equation 5-29}$$

The approach predicts increasing slip intensity for increasing volume fraction and increasing precipitate diameters (below the cutting-bowing transition size) and larger slip lengths.

Using the material information as used in section 5.3.2.1 (i.e. G_m = 80 GPa, b = 0.26 nm, γ = 0.17 Jm^{-2}) and assuming a Poisson's ratio of 0.33, C_p/C_Bb were calculated to be 1.81x10^{11}. The volume fraction of tertiary γ' precipitates has been calculated in section 5.1. For the initial calculations of N for the materials, the slip length L is assumed to be equal to the grain size.

Material	U720Li	U720Li-LG	U720Li-LP	RR1000 MO1547	RR1000 MO1751
Volume fraction of tertiary γ' (%)	8.0	8.0	8.0	9.9	9.9
Tertiary γ' size (nm)	16	17	27	18	21
Grain size (μm)	6.4	15.4	10.1	7.4	7.1
N	29	73	60	40	41

Table 5-10: Initial assessment of N for the materials.

The initial calculations of N indicate relatively similar planarity of slip in U720Li-LG and U720Li-LP, while in U720Li and both batches of RR1000 the planarity of slip are relatively similar but much lower than U720Li-LG and U720Li-LP. Calculation of N for U720Li-LP is likely to be of less relevance as the tertiary γ' precipitates in U720Li-LP have been highlighted as being likely to be bypassed through a combination of precipitate cutting and looping processes.

However, assuming the slip length L to be equivalent to the grain size as done in the initial calculations of N is not strictly accurate due to the presence of larger secondary γ' precipitates in the material which are expected to affect the slip planarity. The large size of the secondary γ' precipitates is a more significant obstacle to dislocation motion compared to the tertiary γ' precipitates and may reduce the slip length to the spacing between secondary γ' precipitates instead of the grain size as the slip length.

Further assessment of the planarity of slip in the materials is made using Duva's approach with the microstructural quantities as calculated in section 5.3.1. The slip length L is taken as the spacing between secondary γ' precipitates, i.e. the mean free path assuming that the secondary γ' precipitates are not sheared by the pile-up of dislocations from cutting of tertiary γ' precipitate. Secondary γ' precipitate cutting/looping is to be examined in the following section.

Material	U720Li	U720Li-LG	U720Li-LP	RR1000 MO1547	RR1000 MO1751
Volume fraction of tertiary γ' (%)	8.0	8.0	8.0	9.9	9.9
Tertiary γ' size (nm)	16	17	27	18	21
Mean free path (nm)	88	118	214	90	103
N	0.40	0.56	1.28	0.49	0.60

Table 5-11: Calculations of N for the materials using spacing between secondary γ' precipitates as slip length L.

The N values in Table 5-11 are generally in fractions < 1 compared to corresponding N values calculated by Blankenship et al [41] for aluminium alloys which are generally equal to or larger than 1. The fraction < 1 of N essentially indicates that there is a fraction of a single dislocation in the slip band which is not sensible. The calculated N values in Table 5-11 are likely to be due to the material properties values chosen from the literature for this analysis which do not fully reflect the properties of the materials in the current study.

Nevertheless, a comparison of the N values in Table 5-11 will reveal the relative planarity of slip in the materials in the current study. The calculation of N for U720Li-LP is again to be regarded as somewhat dubious due to the combination of precipitate cutting and looping processes expected in the material. The calculations indicate relative similar planarity of slip in U720Li-LG and both batches of RR1000, while the planarity of slip in U720Li is slightly lower. U720Li-LG and both batches of RR1000 have longer slip lengths and slightly larger tertiary γ' compared to U720Li, giving rise to generally higher planarity of slip in U720Li-LG and both batches of RR1000 as expected.

5.3.2.3. Effect of secondary γ' on planarity of slip in materials

The interactions between secondary γ' precipitates and the pile-up of dislocations due to tertiary γ' precipitate cutting are assessed in this section. The secondary γ' precipitates of the materials in the current study are expected to be strengthened by ordered strengthening during cyclic deformation. Elastic mismatch between secondary γ' precipitates and the γ matrix is also likely to contribute to further strengthening. As a first approximation, only the forces due to order strengthening are considered, i.e. the lower bound of the strength expected. This will give the upper bound d_c value for the secondary γ'. The force due to order strengthening is given by Equation 5-24. Similar to the approach by Blankenship [41], the force which the precipitate would have to exert to avoid being

sheared by a pile-up of dislocations is given by $F = NG_m b^2$ where N is the number of dislocations in the pile-up. Equating the force expected from order strengthening and the condition for dislocation bowing and solving for d_c gives

$$d_c = NG_m b^2/\gamma \qquad \text{Equation 5-30}$$

i.e. the upper bound value of d_c. This critical precipitate cutting-to-looping size for secondary γ' precipitates again does not take into account dislocations travelling in pairs which would tend to increase d_c. Pairing of dislocations reduces the antiphase boundary region and larger precipitates may be cut.

The d_c for the secondary γ' is to be calculated by using the number of dislocations in the pile-up N calculated from Duva's approach using the mean free path between secondary γ' precipitates as the slip length as shown in Table 5-11. As indicated in the previous section, the N values are generally in fractions < 1 and application of these N values into Equation 5-30 will yield d_c values which are even smaller than the critical precipitate size for a single matrix dislocation.

Alternatively, the N values although in fractions < 1 are useful to illustrate the possible degree of dislocation pile-ups at the secondary γ' precipitates. This will give an idea of the relative ability of dislocation pile-up to cut secondary γ' precipitates in the materials. The N values in Table 5-11 indicate pile-up of dislocations being more pronounced, and hence the secondary γ' precipitates are more able to be cut by the pile-up of dislocations in U720Li-LG and both batches of RR1000 compared to U720Li. The N value of U720Li-LP is again set aside for reasons already stated in the previous sections.

5.3.2.4. Validation of planarity of slip assessment results

To validate the slip planarity assessment results, the predicted planarity of slip in the materials are compared to the observed planarity of slip in the materials during room temperature tests. As highlighted in section 5.3.2.2, it should be noted that the theoretical analyses carried out to predict the planarity of slip in the materials are unlikely to fully reflect the complex precipitate-dislocation interactions which may be expected in slip bands during fatigue cycling processes.

The fracture surfaces of room temperature tests appear to indicate that secondary γ' precipitates are indeed being cut by the pile-up of dislocations. This is evident as the facets are of the order of the grain size and the slip bands are able to extend across the entire grain diameter, indicating that secondary γ' precipitates are being cut by the pile-up of dislocations.

The predicted planarity of slip in the materials appears to be reflected on the fracture surfaces of the room temperature short crack tests. Highly facetted fracture surface indicative of planar slip

was noted on the fracture surfaces of U720Li-LG and RR1000. Lower degree of faceting was observed in U720Li and U720Li-LP where the facets although still observed were less distinct.

The faceting on the fracture surfaces of room temperature long crack tests does not appear to be reflecting the slip planarity assessment results. Facets in U720Li were most distinct, while in U720Li-LG and RR1000 microfacets and occasional large facets were noted. In U720Li-LP microfacets were observed in addition to occasion smaller facets. For U720Li-LP, although slip planarity assessment indicates slip to be due to a combination of precipitate cutting and bowing, higher degree of precipitate cutting is observed as noted from microfacetting on the fracture surface. Tertiary and secondary γ' precipitates may be cut locally depending on the local conditions, e.g. pairing of dislocations and relatively small local γ' precipitate sizes.

The planarity of slip observed in the room temperature long crack tests may be due to possible influence from the constraints of the long crack geometry, i.e. faceting is governed more by extrinsic factors rather than intrinsic factors which will be further discussed in section 5.3.4.2.

5.3.2.5. Summary

Precipitate cutting to looping assessment using general material information of nickel-base superalloys indicates a critical diameter for transition from precipitate cutting to looping to be 32nm. This indicates that the tertiary γ' precipitates in all the materials in the current study are being cut. However as this critical diameter is approximately similar to the average size of tertiary γ' precipitates in U720Li-LP, it is thought that larger tertiary γ' precipitates in U720Li-LP are likely to be bowed, i.e. in U720Li-LP dislocations bypass tertiary γ' precipitates through a combination of precipitate cutting and looping processes.

Planarity of slip assessment using Duva's approach assuming the slip length to be the mean free path between secondary γ' precipitates indicates relatively similar slip planarity in U720Li-LG and both batches of RR1000, while U720Li shows lower slip planarity. The planarity of slip assessment of U720Li-LP using Duva's approach is thought to be dubious as combination of precipitate cutting and looping processes has been highlighted to be prevalent in this material.

Correlation of the N values to the ability of the dislocation pile-up in cutting secondary γ' precipitates was used to assess the effect of secondary γ' on the planarity of slip in the materials. The N values indicate pile-up of dislocations being more pronounced, and hence the secondary γ' precipitates are more able to be cut by the pile-up of dislocations in U720Li-LG and both batches of RR1000 compared to U720Li.

The results of the planarity of slip assessment have also been validated with the observed planarity of slip in the materials during room temperature tests. The predicted planarity of slip in the

materials appears to be reflected on the fracture surfaces of room temperature short crack tests, but not on the fracture surfaces of room temperature long crack tests. The planarity of slip observed in the room temperature long crack tests may be due to possible influence from the constraints of the long crack geometry.

5.3.3. Effect of microstructure - room temperature hardness

Hardness of the material is directly related to the strength of the material, hence microstructural factors affecting the strength of the material are also expected to govern the hardness of the material.

The strength of the material is primarily governed by grain size and the size and volume fraction of coherent γ' precipitates in the material. The effect of grain size on strength can be approximated by the Hall-Petch relationship. Larger grain materials which have less grain boundaries as barrier/ discontinuity in the dislocation path enable dislocation movement over larger distances with less resistance compared to finer grain materials, hence lower strength is observed for larger grain materials. For a given volume fraction of coherent γ' precipitates, larger precipitate sizes imply a lower frequency of the precipitates in the material and larger mean distances between the precipitates. These factors may give rise to lower strengthening as the precipitate distribution in the material is a less effective barrier to dislocation motions, in addition to reducing the stresses required by dislocations for precipitate looping which is one of the precipitate bypass methods. A higher frequency of coherent γ' precipitates of finer sizes meant dislocation movements are blocked more effectively in the material.

The difference in the hardness of both batches of RR1000 is governed by the volume fraction of coherent γ' precipitates in the two materials as the grain size and coherent γ' precipitate size are very similar for both materials. Given the approximately similar coherent γ' precipitate sizes in both materials, the higher volume fraction of coherent γ' precipitates in RR1000 MO1547 implies a higher frequency of occurrence of coherent γ' precipitates in the material. This is expected to give more effective barriers to dislocation motion and higher hardness in RR1000 MO1547 as observed.

Comparing the hardness of U720Li and RR1000 MO1547, the slightly finer grains of U720Li are partially contributing to increases in hardness. U720Li also has lower coherent γ' volume fraction compared to RR1000 MO1547 which would imply a decrease in the hardness but the size of the secondary coherent γ' precipitates in U720Li is much finer, i.e. more uniformly distributed coherent γ' precipitates in the material to give increased strengthening. Similarity in hardness values of U720Li and RR1000 MO1547 reflects the balance in the grain size, and the sizes and volume fractions of coherent γ' precipitates in both materials.

Comparing U720Li-LG and U720Li, U720Li-LG has larger grains as well as higher volume fraction and larger sizes of coherent γ' precipitates compared to U720Li. The results in section 5.3.1 indicate that the larger sizes of coherent γ' precipitates in U720Li-LG compared to U720Li are accompanied by higher average distances between coherent γ' precipitates in U720Li-LG even though U720Li-LG has higher volume fraction of coherent γ' precipitates compared to U720Li. The lower hardness of U720Li-LG compared to U720Li is therefore due to the decrease in hardness associated with the larger grains and larger coherent γ' precipitates which was unable to be offset by an increase in strength contributed by higher volume fraction of coherent γ' precipitates.

Comparing the hardness of U720Li and U720Li-LP, the slightly larger grains of U720Li-LP are partially causing the decrease in hardness of the material. Similar volume fractions of coherent γ' precipitates were noted in U720Li and U720Li-LP, but significantly larger coherent γ' precipitate sizes in U720Li-LP meant that the coherent γ' precipitates in U720Li-LP are further spaced apart compared to U720Li. This is expected to give poorer resistance to dislocation motion, causing a further decrease in the hardness of U720Li-LP compared to U720Li. The onset of precipitate bowing in U720Li-LP as predicted in section 5.3.2.1 due to larger tertiary γ' precipitate sizes and higher average distances between the tertiary γ' precipitates is also likely to reduce the resistance to dislocation motions, hence a lower hardness is observed for U720Li-LP.

Similar trends in the strength of materials was noted in the microstructural variants of U720 used by Brooks and Rainforth in their study [158]. The microstructural characteristics and 0.2% proof strength at room temperature of the U720 microstructural variants used by Brooks and Rainforth are shown in Table 5-12. Lower strength was noted in materials with larger grain and larger coherent γ' precipitates compared to the as-received material, with the decrease in strength being more marked in the material with larger γ' precipitates. In the case of the material with larger grains, the material has been heat-treated such that the material does not have any primary γ' precipitates, i.e. all the γ' phase is coherent implying higher yield strength but the observed reduction in yield strength shows the dominant effect of grain size on yield strength [158].

Material	U720FG	U720CG	U720LGP
Key attributes	Fine grain	Coarse grain	Coarse coherent γ'
Mean grain size (μm)	10±5	48±29	12±7
Mean primary γ' size (μm)	3	none	2
Primary γ' volume fraction (%)	36	none	14
Coherent γ' size (nm)	20±7, 80±14	140±35, 410±94	480±110
0.2% PS at 20°C (MPa)	1229	965	804

Table 5-12: Microstructural characteristics and 0.2% proof strength at 20°C of U720 microstructural variants used by Brooks and Rainforth [158].

5.3.4. Effect of microstructure - room temperature fatigue behaviour

In the room temperature tests, fatigue crack initiation and growth resistance is strongly dependent on the planarity of slip in the materials, and hence also strongly influenced by the microstructure of the materials due to the effects of microstructure on planarity of slip in the materials. The effects of microstructure on other intrinsic and extrinsic factors are also expected to strongly affect the fatigue crack initiation and growth resistance of the materials.

5.3.4.1. Room temperature fatigue crack initiation

Crack initiation from slip band cracking is heavily dependent on the planarity of slip in the materials. Crack initiation from porosity is also likely to be influenced by slip behaviour of the materials. Crack initiation from porosity occurs along crystallographic slip planes close to the pore due to protrusions of slip bands at the pore and the deformation of the material is made easier by the stress concentration feature of the pore. Higher crack initiation resistance should be expected for the material showing the lowest degree of slip planarity. Less planar slip has been associated with strain accommodation within the slip band, thus reducing dislocation pile-up length within the slip band for slip band cracking [65] and also resulting in the material being more damage tolerant to cyclic deformation in the presence of stress concentrators such as pores. A higher amount of porosity on the surface of the material is expected to be detrimental to crack initiation resistance as there are more sites for crack initiation.

The slip planarity assessment results in section 5.3.2 indicated the lowest degree of slip planarity in U720Li-LP, slightly higher in U720Li while U720Li-LG and both batches of RR1000 have been highlighted to show the highest degree of slip planarity. The highest crack initiation resistance may therefore be expected in U720Li-LP, followed by slightly lower crack initiation resistance in U720Li while U720Li-LG and both batches of RR1000 are expected to show the lowest crack initiation resistance. This trend of crack initiation resistance was indeed observed for U720Li and its variants when comparing the number of cracks in the materials. Lower numbers of cracks were noted in the U720Li-LP tests compared to other materials. U720Li and U720Li-LG show relatively similar numbers of cracks in the tests, which may be related to the similar planar slip mechanism and the relatively similar degree of slip planarity in these materials. During the crack field characterisation analysis, more rapid crack initiation rates were also noted in U720Li and U720Li-LG compared to U720Li-LP. In both the RR1000 tests, only one crack was noted in each test, suggesting other factors e.g. alloy chemistry may also be playing a role in giving increased damage tolerant behaviour.

In terms of the first observed crack, the as-polished tests do not appear to indicate distinctive slip band crack initiation resistance between the materials. All the as-polished tests show a possible slip band crack after 10000 cycles, but it is reasonable to say that the crack has initiated much earlier in U720Li than in U720Li-LG and U720Li-LP. The largest slip band initiated crack at 10000 cycles in U720Li was noted to be about 65 μm in length, compared to the largest slip band initiated crack at 10000 cycles observed in U720Li-LG (14 μm) and U720Li-LP (20 μm). Hence, in the as-polished condition, the slip band crack initiation resistance of U720Li-LG and U720Li-LP appears very similar, with U720Li showing the poorest slip band crack initiation resistance. These results do not fully reflect the fractographic results and planarity of slip assessment results. It is possible that what appear to be slip band cracks in these surface observations are actually cracks that have initiated from porosity just beneath the surface. This may explain the random crack initiation periods and the unexpected crack initiation resistance observed. The pores are not visible from the acetate replica observations, and crack initiation due to the pore beneath the surface will give an impression of an intrinsically initiated crack. As mentioned earlier, it is difficult to carry out detailed analysis of the initiation mechanisms of all these cracks in the SEM as they rarely appear on the fracture surface.

In the etched condition, the first observed cracks indicate higher slip band crack initiation resistance in U720Li and U720Li-LP compared to U720Li-LG which is consistent with fractographic results and the planarity of slip assessment results. In the etched condition, U720Li exhibits a largest slip band crack of about 4 μm at 40000 cycles, while the first slip band initiated crack was noted in the etched U720Li-LP at 50000 cycles with an initial length also of about 4μm.

The etched U720Li-LG shows a slip band initiated crack at 10000 cycles with a length of about 9μm.

U720Li-LP also shows better resistance to crack initiation due to surface porosity compared to other materials which is likely to be linked to the more homogeneous slip behaviour of this material. In U720Li and U720Li-LG the first observed crack from surface porosity was noted generally after 10000 cycles; the crack initiation likely to be accelerated by the planar slip behaviour in these materials. The improved crack initiation resistance from surface porosity in RR1000 (similar to levels in U720Li-LP) even though planar slip was expected in RR1000 again reiterates the effects of other factors in RR1000 e.g. alloy chemistry in giving the improved damage tolerant behaviour. The different alloy chemistry of RR1000 may give rise to different oxidation behaviour, different γ/γ' misfit as well as altered APB and SFE values.

5.3.4.2. Room temperature fatigue crack growth

Crack growth in a stage I manner during early crack growth in the short crack tests and near-threshold crack growth in the long crack tests is heavily influenced by the planarity of slip of the materials. Stage I crack growth is also sensitive to local microstructure when the defect is small, i.e. during early crack growth in the short crack tests.

Planarity of slip has various effects on fatigue crack growth. Highly planar slip has been associated with more intense impingement of slip bands at grain boundaries due to greater pile-up of dislocations in the slip bands. Therefore dislocation sources are able to nucleate more easily in the adjacent grain and crack growth processes continue in the next grain. Under such circumstances, grain boundaries are less effective as crack growth barriers, resulting in poorer crack growth resistance. Planar slip has also been associated with increased reversibility of slip giving lower damage accumulation and increased intrinsic crack growth resistance. Intense planar slip confined to relatively few slip bands meant that dislocations move to and fro in these limited number of slip bands, giving higher reversibility of slip and increased intrinsic crack growth resistance. Finally, highly planar slip has also been associated with more tortuous crack path compared to homogeneous slip. Large crack path deflection with heterogeneous slip due to intense slip bands extending the diameter of the grain may give rise to crack tip shielding and possible roughness-induced crack closure, i.e. higher extrinsic crack growth resistance. The contribution to crack growth resistance from crack tip shielding may be expected during both long crack and short crack growth, however crack closure contribution to crack growth resistance is likely to be expected only during long crack growth as in the short crack test the limited crack wake behind the crack tip implies that there will be little closure contribution. The crack closure contribution is also likely to be influenced by the grain size which will be discussed later.

Local microstructural effects on crack growth resistance arise from the grains and primary γ' precipitates. Grain size reflects the number of grain boundaries acting as barriers to dislocation motion, which are in turn crack growth barriers. Materials with larger grains have less grain boundaries, giving a lower degree of discontinuity in the material and cracks are able to propagate more continuously resulting in poorer crack growth resistance. Grain size together with the planar slip behaviour of the material also influences extrinsic crack growth resistance. Larger grains have been associated with a more tortuous crack path, giving increased crack tip deflection and shielding in addition to increased crack closure during long crack growth, all of which will result in better crack growth resistance. The effect of grain size on the crack growth barrier effect and the extrinsic crack growth resistance contributions are two opposing effects on the crack growth resistance for a particular grain size. The primary γ' precipitates are also important during stage I crack growth in the room temperature short crack test which is highly sensitive to local microstructure. These precipitates were noted to give rise to multiple temporary crack arrest events by acting as effective crack growth obstacles. Higher frequency of these precipitates in the material is expected to give better crack growth resistance during early short crack growth.

The opposing effects of slip planarity on crack growth resistance make selecting microstructural parameters for good fatigue performance difficult. The same can be said of the opposing effects of grain size on crack growth resistance. In terms of the effect of primary γ' precipitates during early crack growth, the materials in this study all have approximately similar primary γ' size, hence higher early crack growth resistance may be expected from material with a high volume fraction of primary γ' precipitates.

In the room temperature short crack tests, transition from pure stage I crack growth to mixed stage I/stage II crack growth was noted to occur at approximately similar proportions of the fatigue lifetimes and at roughly similar crack lengths in all the materials, i.e. at approximately 70% of the fatigue lifetimes (Table 5-5) when the crack lengths are roughly 100 μm (Table 5-4). Hence it may be said that the material with the longest fatigue lifetime also has the highest stage I crack growth resistance as it spent the highest number of cycles in the pure stage I crack growth regime to attain a similar crack length compared to other materials. In order to attain a crack length of approximately 100 μm before the onset of mixed stage I/stage II crack growth in the materials during room temperature short crack tests, U720Li-LP was noted to spend the highest number of cycles in pure stage I crack growth regime, followed by RR1000 and U720Li-LG while U720Li spent the lowest number of cycles of its lifetime in stage I early crack growth. This may be indicating the highest stage I crack growth resistance in U720Li-LP, followed by lower stage I crack growth resistance in RR1000 and U720Li-LG with U720Li showing the lowest stage I crack growth resistance. This is also highlighted in Figure 4-20 where at crack lengths up to approximately 100 μm, crack growth of the primary crack was noted to be slowest in

U720Li-LP, followed by RR1000 and U720Li-LG with the most rapid growth of the primary crack in U720Li.

A combination of precipitate cutting and bowing mechanisms has been highlighted to be prevalent in U720Li-LP. Precipitate bowing mechanisms are likely to give rise to significant reduction in the impingement of slip bands at grain boundaries, i.e. crack growth processes are not so easily initiated in the adjacent grains. At the same time precipitate cutting gives rise to some degree of slip reversibility. Precipitate bowing by dislocations in U720Li-LP is however expected to give rise to a lower degree of possible crack tip shielding and lower degree of slip reversibility compared to other materials. In U720Li, U720Li-LG and RR1000 where planar slip has been predicted to occur, contribution to stage I crack growth is expected to be higher compared to U720Li-LP. Comparing the crack growth resistance of each material, the higher crack growth resistance of U720Li-LG and RR1000 may be in part due to the higher degree of slip reversibility and possible crack tip shielding associated with more planar slip in U720Li-LG and RR1000 compared to U720Li. Differences in the intensity of slip band impingement at grain boundaries may be small in these microstructures as planar slip in these materials are expected to give significant pile-up of dislocations at grain boundaries.

The grain sizes of U720Li and RR1000 are approximately similar, with slightly larger grains noted in U720Li-LP and the largest grains were noted in U720Li-LG. Abundant grain boundaries in U720Li and RR1000 provide effective crack growth barriers in these materials. Lower crack growth barrier effects are expected in U720Li-LP, and in U720Li-LG even poorer crack growth barrier effects are expected. Conversely the highest degree of crack tip shielding is expected in U720Li-LG, decreasing slightly in U720Li-LP and the lowest degrees of crack tip shielding are expected in U720Li and RR1000.

In the room temperature short crack tests where stage I crack growth is sensitive to local microstructures, it appears that in U720Li-LP the primary γ' precipitates are being picked out by the small cracks, i.e. the number of primary γ' precipitates encountered by small cracks in U720Li-LP is on average much higher than the number primary γ' precipitates encountered by small cracks in U720Li, giving additional crack growth resistance in U720Li-LP where primary γ' precipitates are acting as effective crack growth obstacle when the cracks are small. However U720Li-LP was noted to have the same volume fraction of primary γ' and approximately similar primary γ' size as U720Li, suggesting equal frequency of occurrence of primary γ' in U720Li-LP and U720Li as observed from the primary γ' line counting analysis. The higher number of primary γ' precipitates encountered by small cracks in U720Li-LP compared to U720Li may be due to more tortuous crack paths of the small cracks in U720Li-LP, or due to the different primary γ' precipitate distribution in the materials as suggested in section 5.3.1 where the primary γ'

precipitates in U720Li-LP may be distributed according to Figure 5-4 compared to the primary γ' precipitates distribution in U720Li as illustrated in Figure 5-3. The results from the primary γ' line counting analysis however do not appear to highlight the significant difference in the number of primary γ' precipitates encountered which may be expected with the different primary γ' precipitate distributions as shown in Figure 5-3 and Figure 5-4. The average number of primary γ' precipitates encountered by small cracks in U720Li, U720Li-LG and RR1000 are lower compared to U720Li-LP. Among U720Li, U720Li-LG and RR1000, the average number of primary γ' precipitates encountered by the small cracks in RR1000 is the highest, this will most likely contribute to higher crack growth resistance in stage I early crack growth. The number of primary γ' precipitates encountered in U720Li is lower than in RR1000, and in U720Li-LG the average number of primary γ' precipitates encountered is the lowest.

Overall, in U720Li-LP the combination of precipitate cutting and bowing mechanisms leading to reduced impingement of slip bands at grain boundaries and some degree of reversible slip in addition to crack growth barrier effects of grain boundaries and the effect of primary γ' precipitates giving temporary crack arrests are able to offset the decrease in stage I crack growth resistance associated with the lower degree of possible crack tip shielding and lower degree of slip reversibility in U720Li-LP, giving the highest stage I crack growth resistance in the room temperature short crack tests. Comparing U720Li and U720Li-LG, poorer crack growth barrier effects and lower number of primary γ' precipitates encountered in U720Li-LG compared to U720Li suggests lower crack growth resistance in U720Li-LG but this is overcome by the increase in crack growth resistance associated with increased reversibility of slip and the possible increase in crack tip shielding due to larger grain sizes in U720Li-LG. Intense impingement of slip bands at grain boundaries are expected to be relatively similar in both U720Li and U720Li-LG but much higher compared to U720Li-LP due to dislocation pile-ups associated with planar slip behaviour in both U720Li and U720Li-LG. In terms of the crack growth resistance of RR1000, planar slip in the material implies some degree of slip reversibility. In RR1000 there are also effective crack growth barriers due to relatively fine grains and higher number of primary γ' precipitates encountered by small cracks compared to U720Li and U720Li-LG, resulting in higher crack growth resistance. In addition there are also possible contributions from other factors in RR1000, e.g. alloy chemistry in giving rise to improved crack growth resistance analogous to the high crack initiation resistance of the material.

Crack tip shielding and reversibility of slip appear to have higher importance to crack growth resistance during stage I early crack growth compared to the crack growth barrier effect. This is observed when comparing U720Li and U720Li-LG. In U720Li-LG, higher crack growth resistance contribution from crack tip shielding and slip reversibility are able to overcome the decrease in crack growth resistance due to poorer crack growth barrier effect associated with larger

grains and lower number of primary γ' precipitates encountered by the crack to give significant improvement in crack growth resistance in U720Li-LG compared to U720Li.

As mentioned earlier, stage I near-threshold crack growth in the room temperature long crack tests is also heavily influenced by the planarity of slip of the materials. Due to the overall larger defect size, the effects of local microstructure on crack growth resistance are reduced, i.e. contribution to crack growth resistance from local grain boundaries and primary γ' precipitates as crack growth barriers/obstacles becomes less significant. Other intrinsic and extrinsic effects arising from the averaged microstructural features are expected to have greater influence on crack growth resistance. There are also possible constraints of neighbouring slip systems from adjacent grains along the crack front when the defect size is large. In addition, at larger defect size, plane strain conditions become prevalent at the crack front compared to the plane stress conditions expected in the short crack tests when the defect size is small. Slip is expected to resolve in a different manner along the slip systems with a change in the stress state at the crack tip.

In the stage I near-threshold crack growth region in the room temperature long crack tests where the crack is also propagating in stage I crack growth mode, U720Li-LP was noted to show the lowest crack growth resistance as evidenced from the lower ΔK_{th} compared to other materials. U720Li, U720Li-LG and RR1000 show approximately similar ΔK_{th}, suggesting similar stage I crack growth resistance in these materials.

Although the planarity of slip assessment results suggest higher planarity of slip in both U720Li-LG and RR1000 and lower in U720Li, the fracture surfaces of room temperature long crack tests appear to show a different trend. This may be related to the stress state and/or constraints of the long crack growth geometry. The constraints of neighbouring slip systems from adjacent grains along the crack front, i.e. the requirement to conform to slip systems in the grains of a multi-grained crack front implies that slip may not be able to extend across the entire grain diameter compared to the short crack situation where there are less grains at the crack front for the slip to conform to.

U720Li-LG has the largest grains and slip has been predicted to be most planar but the fracture surface only shows microfacetting and occasional large facets. This may be due to bowing at secondary γ' precipitates in addition to migration of slip from one slip plane/slip system to another to satisfy conformity of a multi-grained crack front or the maximum resolved shear stresses condition which favours slip in a particular direction. The finer grains of RR1000 compared to U720Li-LG meant that in most grains slip is more able to extend across the entire grain diameter, giving a more facetted appearance and occasional large facets when conditions are suitable and slip extends across the entire grain diameter. Among all the materials, U720Li has the smallest grain and secondary γ' precipitates, which are more favourable conditions to allow slip to extend

across the entire grain diameter resulting in a distinctly crystallographic fracture surface. Therefore, the effective reversibility of slip in U720Li-LG and RR1000 is thought to be not as high as in U720Li in the near-threshold crack growth regime. Microfacets and occasional large facets observed on the fracture surfaces of U720Li-LG and RR1000 in the near-threshold crack growth region meant that slip is not restricted to a single slip plane along the grain diameter and slip constantly migrates from one slip plane to another in U720Li-LG and RR1000 compared to in U720Li where slip is able to extend across the entire grain diameter and dislocation movement is more confined and hence more reversible within the slip bands, suggesting effective reversibility of slip is highest in U720Li, followed by RR1000 and lower in U720Li-LG. The differences in the alloy chemistry of RR1000 and U720Li may also give rise to different slip behaviour and hence different intrinsic crack growth resistance in RR1000 compared to U720Li. In U720Li-LP, combination of precipitate cutting and bowing mechanisms as noted from microfacetting and occasional small facets on the fracture surface are likely to result in reduced intense impingement of slip bands at grain boundaries and some degree of slip reversibility, both of which are expected to give some degree of intrinsic crack growth resistance. This effect is again of little relevance in U720Li, U720Li-LG and RR1000 due to pile-up of dislocations at grain boundaries associated with planar slip in these materials. For reasons that will become clear when discussing the stage II crack growth behaviour, the intrinsic crack growth resistance contribution due to precipitate cutting and bowing mechanisms in U720Li-LP is marginally lower than the intrinsic crack growth resistance contribution that can be expected from higher reversibility of slip in other materials.

Extrinsic crack growth resistance contributions are expected to arise from crack tip shielding and crack closure. Crack tip deflection leading to crack tip shielding which may be significant when the defect size is small, i.e. during short crack growth appears to have a less significant effect on crack growth driving force (ΔK_{eff}) at the crack tip in the long crack tests. This is shown in the assessment in section 4.3 where the crack tip deflections in the long crack tests were noted to give only marginal fluctuations in the local crack growth driving force at the crack tip. Local ΔK_{eff} at the crack tip on average remains at approximately 80% of global ΔK_{eff} for various deflection angles noted from the fracture surface sections of the test specimens, suggesting that any extrinsic contribution to crack growth resistance is likely to arise primarily from crack closure.

Crack closure measurements were not made during room temperature long crack tests, hence closure levels were only qualitatively estimated from the fretting damage associated with crack closure on the near-threshold crack growth fracture surfaces. Limited evidence of fretting damage was noted on the U720Li fracture surface, suggesting minimal crack closure in U720Li. In U720Li-LP, a higher degree of fretting damage was noted compared to U720Li and in RR1000 and U720Li-LG the degree of fretting damage is even higher, suggesting some degree of closure in U720Li-LP and a higher degree of closure in U720Li-LG and RR1000. The degree of fretting

damage in the materials appear to suggest that closure is not controlled so much by slip planarity/faceting but is governed more by the grain size of the materials. The fracture surface of U720Li in the near-threshold crack growth regime appears to be highly crystallographic, i.e. higher planarity of slip but the smaller facets due to relatively fine grain size of U720Li do not appear to give rise to much crack closure as little fretting damage was observed. The occasional large facets and somewhat rougher appearance of the RR1000 and U720Li-LG fracture surfaces due to their larger grain size compared to U720Li are giving rise to a higher degree of crack closure as evidenced from the fretting damage, and similarly some degree of crack closure (as evidenced from some degree of fretting damage) was also noted in U720Li-LP due to the larger grain size of U720Li-LP.

Overall, the fractographic observations and crack growth results indicate that the overall crack growth resistance during stage I long crack growth is governed by a combination of intrinsic and extrinsic crack growth resistance contributions. Intrinsic crack growth resistance contributions arise from reversibility of slip in U720Li, U720Li-LG and RR1000, and the combination of reduced intense impingement of slip bands at grain boundaries and some degree of reversible slip in U720Li-LP. Extrinsic crack growth resistance contributions arise from crack closure during the tests. U720Li, U720Li-LG and RR1000 show similar overall crack growth resistance due to varying balances between crack growth resistance contributions from crack closure and increased reversibility of slip in the materials. U720Li shows a high degree of slip reversibility giving improved intrinsic crack growth resistance but appears to have limited crack closure contributions to extrinsic crack growth resistance. RR1000 and U720Li-LG show a lower degree of slip reversibility but a higher degree of crack closure compared to U720Li, giving similar overall crack growth resistance to U720Li. Reversibility of slip and crack closure contributions to overall crack growth resistance appear to be marginally higher in U720Li-LG compared to RR1000 as evidenced from the slightly higher ΔK_{th} of U720Li-LG compared to RR1000; this may be due to the larger grain size in U720Li-LG compared to RR1000. U720Li-LP shows the lowest overall stage I crack growth resistance compared to other materials due to lower intrinsic crack growth resistance contribution in U720Li-LP compared to other materials which was not compensated for by the extrinsic crack growth resistance contribution from crack closure. The lower intrinsic crack growth resistance contribution in U720Li-LP is attributed to the combination of precipitate cutting and bowing mechanisms in the material.

During stage II crack growth, the influence of local microstructural effects and extrinsic effects on crack growth resistance diminishes with increasing ΔK, i.e. the effects of microstructure on stage II crack growth are expected to be more generally governed by the intrinsic crack growth resistance expected from reversibility of slip and reduction in the intense impingement of slip bands at grain boundaries. The crack growth rates of U720Li, U720Li-LG and RR1000 in this

regime indicates relatively similar intrinsic crack growth resistance due to reversibility of slip associated with planar slip in these materials. In U720Li-LP, the intrinsic crack growth resistance contribution due to a combination of reduced intense impingement of slip bands at grain boundaries associated with homogeneous slip and some degree of reversible slip due to precipitate cutting is only marginally lower than the intrinsic crack growth resistance contribution expected for increased reversibility of slip with planar slip in U720Li, U720Li-LG and RR1000.

Overall, the slip deformation behaviour of the material, whether homogeneous or heterogeneous appears to have only a marginal effect on the crack growth resistance, i.e. the size and volume fraction of coherent γ' precipitates appears to be of less influence compared to other factors in the room temperature tests. Both long crack and short crack tests show reduced intense impingement of slip bands at grain boundaries associated with homogenous slip or higher reversibility of slip associated with heterogeneous slip in the material to be beneficial. When planar slip is expected in the material, more heterogeneous slip contributes to higher intrinsic crack growth resistance. In the room temperature short crack tests, presence of primary γ' precipitates giving temporary crack arrest events proved beneficial, and in general larger grains are beneficial in giving crack tip shielding in the short crack tests and a higher degree of crack closure in the long crack tests, resulting in improved crack growth resistance. In the short crack tests larger grains giving rise to crack tip shielding appear to have a more significant influence on crack growth resistance than the number of grain boundaries acting as crack growth barriers.

5.3.4.3. Comparison of the effects of microstructure on short crack and long crack behaviour at room temperature

Comparing the crack growth resistance of the materials during long crack and short crack tests at room temperature, different trends in the crack growth resistance of the materials were observed. In the room temperature long crack tests, U720Li, U720Li-LG and RR1000 show very similar crack growth behaviour with U720Li-LP showing the lowest crack growth resistance while in the room temperature short crack tests, crack growth resistance is increasing in the order from U720Li, U720Li-LG to RR1000 with U720Li-LP showing the highest short crack growth resistance. Differences in the planarity of slip of the materials as evidenced by the faceting levels on the fracture surfaces were also noted for the long crack and short crack tests. In the room temperature long crack tests, the highest degree of crystallographic faceting was noted in U720Li, followed by RR1000 and U720Li-LG while U720Li-LP appears to show much lower degree of crystallographic faceting. During room temperature short crack tests, the most distinct crystallographic facets were noted in RR1000 and U720Li-LG, followed by smaller and/or less distinct facets in U720Li and U720Li-LP.

The difference in crack growth resistance is primarily due to the influence of local microstructure, i.e. crack growth barrier effects of grain boundaries and primary γ' precipitates in the short crack test and extrinsic factors, i.e. crack closure and constraints of long crack geometry in the long crack tests. The effects of local microstructure diminish at larger defect sizes, and vice versa for extrinsic factors at small defect sizes, i.e. both effects are almost mutually exclusive. In U720Li-LP, crack growth resistance contribution due to a combination of precipitate cutting and bowing mechanisms was present in both the short crack and long crack case. Crack growth barrier effects of grain boundaries and primary γ' precipitates giving rise to the highest crack growth resistance in U720Li-LP during room temperature short crack tests becomes less significant at larger defect size, and instead was replaced by a mild degree of crack closure contribution to extrinsic crack growth resistance in the room temperature long crack test. In the room temperature short crack tests, the short crack growth resistance of U720Li, U720Li-LG and RR1000 are governed by the combination of reversibility of slip, crack tip shielding and local microstructure effects. In the room temperature long crack tests, the crack growth resistance of these materials are governed by the intrinsic crack growth resistance contribution from reversibility of slip and the extrinsic crack growth resistance contribution from crack closure in the materials.

The difference in the planarity of slip of the materials in the long crack and short crack tests is attributed to the difference in the crack geometry. During crack growth, there is a need to maintain continuity from the slip system in one grain to the favourable slip systems in the adjacent grains at the crack front. In the short crack test, there are fewer grains at the crack front for the slip systems in the grains to conform to compared to a multi-grained crack front of the long crack test. Therefore in the short crack test, slip conditions are more favourable to allow slip to extend across the entire grain diameter and hence more able to demonstrate the intrinsic planarity of slip of the materials. The planarity of slip observed on the fracture surface is thus closer to the predicted planarity of slip of the materials.

In the long crack test, the crack front is more constrained and needs to conform to the slip systems in higher overall number of grains, i.e. conditions are less favourable for slip to extend the entire grain diameter especially in larger grain materials. Microfacetting as noted on the U720Li-LG and RR1000 fracture surfaces in the long crack tests is indicative of slip moving from one slip system to another alternately to satisfy the conformity of a multi-grained crack front or the maximum resolved shear stress condition which favours slip in a particular direction. In U720Li which has finer grains, conditions are more favourable for slip to extend across the entire grain diameter giving the distinctly crystallographic fracture surface. U720Li-LP consistently shows a relatively low degree of faceting which may be related to the combination of precipitate cutting and bowing mechanism giving rise to a more homogeneous slip compared to other materials, and there would

be less influence of the difficulties associated with conformity of slip systems in the grains at the crack front.

5.3.4.4. Summary

U720Li-LP and RR1000 were noted to have higher crack initiation resistance due to more homogenous slip in U720Li-LP and possible contributions from the alloy chemistry of RR1000 in giving highly damage tolerant behaviour. U720Li and U720Li-LG shows much lower crack initiation resistance due to the expected planar slip behaviour in these materials.

The effects of microstructure on crack growth resistance in the stage I crack growth regime appears to be sensitive to the defect size. During stage I crack growth, higher crack growth resistance was noted in U720Li-LP during early crack growth due to a combination of precipitate cutting and looping processes in addition to a crack growth resistance contribution from local microstructure effects. Lower crack growth resistance was noted in other materials in this regime due to planar slip behaviour in the materials and a lower crack growth resistance contribution from local microstructure effects. In the long crack tests, crack growth resistance was noted to be governed by a combination of intrinsic and extrinsic crack growth resistance contributions. In this regime higher crack growth resistance was noted in U720Li, U720Li-LG and RR1000 due to combinations of reversibility of slip and extrinsic crack growth resistance contributions giving higher overall crack resistance in these materials. U720Li-LP shows lower crack growth resistance in this regime due to lower intrinsic crack growth resistance compared to other materials which was not compensated for by the extrinsic crack growth resistance contribution from crack closure.

During stage II crack growth, the influence of local microstructure and extrinsic factors diminishes, and the effects of microstructure on crack growth in this regime are governed more solely by the intrinsic crack growth resistance of the materials. All the materials show relatively similar crack growth resistance except U720Li-LP which shows marginally lower crack growth resistance compared to other materials. The marginally lower intrinsic crack growth resistance in U720Li-LP may be related to the combination of precipitate cutting and looping processes in the material.

Different trends in the crack growth resistance and planarity of slip of the materials were noted when comparing the crack growth resistance of the materials in the long crack and short crack tests at room temperature. The difference in crack growth resistance trends is attributed to the different effects of microstructure on crack growth resistance in the different crack growth regimes, while the difference in the planarity of slip of the materials in the long crack and short crack tests is due to the difference in the crack geometry.

5.3.5. Effect of microstructure - elevated temperature fatigue behaviour

Elevated temperature fatigue crack initiation and growth is generally dominated by oxidation and creep deformation due to the relevance of elevated temperatures to these processes. The effects of microstructure on elevated temperature fatigue crack initiation and growth is therefore linked to the effects of microstructure on oxidation and creep deformation. Microstructural parameters giving rise to increased oxidation and creep resistance should be expected to give increased resistance to fatigue crack initiation and growth.

In a vacuum environment where oxidation effects are minimised, creep deformation becomes the dominant mechanism in accelerating fatigue crack initiation and growth. Larger grains and larger coherent γ' precipitates have been associated with improved creep resistance at elevated test temperatures [1]. Larger grains reduce the amount of grain boundaries in the material. During creep deformation, grain boundary sliding is a significant mechanism of failure, and the lower amount of grain boundaries associated with larger grains is expected to give improved creep resistance. In terms of the coherent γ' precipitate size, larger sizes and higher numbers of precipitates are expected to give rise to increased resistance to dislocation cross-slip and climb mechanisms operating at elevated temperatures. Creep at elevated temperatures is essentially driven by diffusion, i.e. movement of material which is enhanced by dislocation motions. The increased difficulty of dislocation motion with larger size and higher number coherent γ' precipitates is expected to give increased resistance to creep deformation [1].

In an oxidising environment, larger grains and larger coherent γ' precipitate sizes are also linked to improved fatigue crack initiation and growth resistance. The larger grains mean that there are less grain boundary areas for diffusion of oxygen in the material. This reduces the embrittlement of grain boundaries due to oxidation and the propensity for oxidation-assisted intergranular crack growth is lowered. At elevated temperatures, larger coherent γ' precipitates are expected to give rise to a more homogenous slip deformation in the grains in addition to increased difficulty of dislocation motions. Homogeneous slip is expected to give increased elevated temperature crack initiation and growth resistance as it may contribute to improved grain boundary oxidation resistance (section 2.11.1) and/or a reduced propensity for intergranular crack propagation due to lower localised stress concentrations at intersection of slip bands at grain boundaries.

In an oxidising environment at elevated temperatures, it is expected that there will be a complex interaction between oxidation and creep deformation during fatigue crack initiation and growth processes. Synergistic effects of oxidation and creep deformation may augment one another giving accelerated crack initiation and growth or oppose each other thereby retarding crack initiation and growth and sometimes even contributing to crack arrests.

In general, it is thought that only the secondary coherent γ' precipitates are of significance in the elevated temperature tests. The tertiary coherent γ' precipitates which have relatively small sizes are likely to be overcome easily by dislocation cross-slip and climb mechanisms expected at the elevated test temperatures.

5.3.5.1. Elevated temperature fatigue crack initiation and growth

In the 840MPa replication tests, U720Li and U720Li-LP appear to show approximately similar crack initiation rates, while U720Li-LG was noted to show much more rapid crack initiation rates. In these tests, crack initiation occurred from local stress concentrations such as pores and weakened grain boundaries under the influence of local strains. The observed rates of crack initiation in Figure 4-48 appear to be consistent with the strain ranges computed from finite element analysis for U720Li and U720Li-LG. For the same applied nominal stress across the uncracked ligament, the strain range experienced in U720Li-LG was noted to be much larger than the strain range experienced in U720Li (Figure 4-58). The first cycle LCF data of U720Li and U720Li-LG obtained at 650°C [4] which is analogous to stress-strain data of equivalent tensile tests are shown in Figure 5-17. The plot shows lower strength in U720Li-LG compared to U720Li as expected due to the larger grains of U720Li-LG. U720Li-LG will therefore show higher strains for a given applied stress compared to U720Li.

The rapid crack initiation rates in U720Li-LG were also thought to be in part due to grain boundary oxidation on the surface leading to the appearance of small cracks or crack-like features. The accelerated grain boundary oxidation observed on the surface of U720Li-LG leading to crack initiation should not be perceived to be due to the larger grains possessing poorer grain boundary oxidation resistance, rather the accelerated oxidation attack in the U720Li-LG replication test is somewhat expected as the local strains are much higher in the notch root of U720Li-LG compared to other materials. The improved oxidation resistance of U720Li-LG may be inferred from the reduced propensity of oxidation-assisted intergranular crack growth modes in U720Li-LG as well as the less severely oxidised fracture surface of U720Li-LG compared to U720Li and U720Li-LP (Figure 4-40).

When tested at 840MPa, the fatigue lifetime of U720Li-LP is only marginally greater than the fatigue lifetime of U720Li. The approximately similar fatigue life in both cases is as expected as both show relatively similar crack initiation and growth characteristics. Crack initiation in both cases occurred due to porosity near the surface, and relatively similar extents of transgranular

---

[4] Elevated temperature LCF tests conducted at QinetiQ Farnborough.

crack growth were noted before transition to intergranular crack growth modes. Both U720Li and U720Li-LP tested at 840MPa spent approximately 40% of their fatigue life in the flat transgranular crack growth regime before adopting an intergranular crack growth mode. After the transition to intergranular crack growth, the degree of intergranular crack growth, i.e. the intergranularity of the crack growth was noted to be very similar in both cases.

The extended life of U720Li-LG at 840MPa is attributed to a few factors. Primary crack initiation in the U720Li-LG test appears to be due to a combination of a surface initiated crack from grain boundary oxidation and a subsurface initiated crack from a sub-surface pore. The short crack growth rates against crack length plot (Figure 4-50b) appears to indicate that the interaction between the two cracks has caused crack growth deceleration of the surface initiated crack, which may be linked to the interactions between the plastic zones of the two cracks. Initiation from the sub-surface pore would also imply a certain degree of transgranular crack growth in vacuum until the sub-surface initiated crack coalesces with the surface initiated crack. Transgranular crack growth at 650°C in vacuum is much slower compared to corresponding crack growth in air. The subsequent transgranular region immediately after crack initiation is also significantly larger than that of U720Li and U720Li-LP. This is linked to the larger grain sizes of U720Li-LG, which imply extended transgranular crack growth which is much slower than intergranular crack growth. Beyond the transgranular crack growth region, the crack growth mode in U720Li-LG appears to be mixed transgranular/intergranular compared to predominantly intergranular crack growth beyond the transgranular region in U720Li and U720Li-LP. After the transition from the flat transgranular crack growth regime, U720Li-LG was noted to only spend approximately 10% of the fatigue life in mixed transgranular/intergranular crack growth regime before catastrophic failure occurred compared to approximately 60% of fatigue lifetime for U720Li and U720Li-LP (Table 4-15). This result should not be misinterpreted as to be due to the poor crack growth resistance of U720Li-LG, but again it is rather due to the higher local strains in the notch root of U720Li-LG giving the accelerated catastrophic failure. The increased fatigue crack growth resistance of U720Li-LG compared to U720Li has been highlighted when the elevated temperature short crack growth rates at 650°C in air of U720Li and U720Li-LG are compared on a ΔK basis in Figure 4-57. When compared on a ΔK basis, the crack growth rates of U720Li-LG are lower than the crack growth rates of U720Li for short crack tests carried out at 650°C in air.

The extended life of U720Li-LG tested at 840MPa compared to U720Li and U720Li-LP should be considered to be solely due to the improved fatigue resistance of the U720Li-LG microstructure. Although the primary crack initiation in U720Li-LG has been noted to be due to a complex combination of two cracks which implies some degree of deceleration in the crack growth and some degree of transgranular crack growth in vacuum for the crack initiated from the sub-surface pore, absence of other large cracks in U720Li-LG which could give catastrophic failure despite the

rapid crack initiation and high number of cracks in U720Li-LG compared to U720Li and U720Li-LP does indicate better fatigue resistance of the U720Li-LG microstructure. The higher fatigue resistance of U720Li-LG compared to U720Li is also highlighted in Figure 4-58 when the fatigue lifetimes are compared on a stress-range and strain-range basis. While U720Li-LG appear to fall on the same stress-range against lifetime curve as U720Li, the strain-range against lifetime plots indicates that U720Li-LG is showing much longer life for a given strain-range compared to U720Li. Similar trends were also observed when comparing the elevated temperature (650°C) LCF data of U720Li and U720Li-LG obtained at QinetiQ Farnborough as shown in Figure 5-18. The results were compared on a total equivalent strain-range basis and the results from this study were also included in the plot. At a given strain-range, U720Li-LG was generally noted to show longer life compared to U720Li in the elevated temperature LCF tests. In the LCF tests, the difference in lifetime between U720Li and U720Li-LG is relatively minor at high strain ranges. At the lowest strain range of 0.007, marked difference in the lifetime of U720Li and U720Li-LG was noted from the LCF test results similar to the results obtained from the elevated temperature short crack tests in this study.

In terms of the superior fatigue performance of RR1000 (MO1751), it is likely that stress relaxation has contributed to reduced stresses in the notch root and a reduction in the driving force for crack initiation and growth compared to other materials. This behaviour is supported by long crack test results of RR1000 conducted under similar conditions where stress relaxation is likely to have contributed in some part to lower crack growth rates.

Grain size increases from U720Li to U720Li-LP to U720Li-LG, which is also the trend observed for increasing fatigue lifetimes in the 840MPa replication tests. Larger coherent γ' precipitates are also found in U720Li-LG and U720Li-LP. However U720Li-LP which has twice as large coherent γ' precipitates compared to U720Li only shows a marginal improvement in fatigue performance. The elevated temperature short crack tests thus indicate larger grain size to be beneficial to crack growth resistance as it not only prolongs the initial slow transgranular crack growth after crack initiation but also improves high temperature oxidation-assisted intergranular fatigue crack growth resistance. In terms of the coherent γ' precipitate sizes, the improvement in fatigue resistance expected for larger precipitate sizes is not as marked. It is believed that the overall fatigue performance is governed more by grain size rather than the coherent γ' precipitate sizes in U720Li and its variants.

5.3.5.2. Elevated temperature long crack tests in vacuum

The da/dN vs. ΔK plots of fatigue tests of RR1000 (MO1547) and U720Li and its variants [30] in vacuum obtained for a given temperature and dwell condition are shown in Figure 5-19a to Figure 5-19d. At 650°C, U720Li-LG is consistently showing the lowest crack growth rates amongst the

test materials. The crack growth rates of U720Li and U720Li-LP at 650°C were approximately similar to each other but were slightly higher than the crack growth rates of U720Li-LG. Although relative differences were noted in the crack growth rates of U720Li and its variants at 650°C, the crack growth curves were confined very closely to each other and the difference in crack growth rates was minimal. RR1000 exhibits the highest crack growth rates amongst all the test materials at 650°C. The crack growth rates of RR1000 were markedly higher than the crack growth rates of U720Li and its variants in the 650°C 1-1-1-1 condition compared to the difference in the 650°C 1-20-1-1 condition. In the 650°C 1-20-1-1 condition, the crack growth rates of RR1000 were only marginally higher than the crack growth rates of U720Li and its variants.

At 725°C however, a different picture emerges in that U720Li-LP shows the highest crack growth rates amongst the test materials. The crack growth rates of U720Li and U720Li-LG are relatively similar, with U720Li-LG showing slightly lower crack growth rates in the 725°C 1-1-1-1 condition and slightly higher crack growth rates in the 725°C 1-20-1-1 condition compared to U720Li. The spread in crack growth rates of U720Li and its variants at 725°C is much larger compared to the spread in crack growth rates observed at 650°C. RR1000 generally shows the lowest crack growth rates at 725°C compared to U720Li and its variants. The difference in the crack growth rates of RR1000 compared to the crack growth rates of U720Li and its variants was more marked under the 725°C 1-20-1-1 condition.

The m-values of each material were compared for a given test condition to ascertain the crack growth characteristics for the particular test condition. The m-values are usually associated with the mechanisms of crack growth, with fatigue tests under the same conditions having the same m-value usually assumed to have similar mechanisms of crack growth. The m-values of the 650°C tests in both the 1-1-1-1 and 1-20-1-1 conditions appear to be very similar for all the materials, suggesting similar cycle-dependent crack growth mechanisms. In the 725°C 1-1-1-1 condition, the m-values for the crack growth curves of U720Li and its variants are approximately similar to each other while the m-value of the RR1000 crack growth curve appears to be slightly lower compared to other materials. As the m-value of RR1000 at 725°C 1-1-1-1 is as low as or lower than the m-values of the 650°C growth out curves, this would suggest that the RR1000 microstructure and/or alloy chemistry may have altered the crack growth mechanism to one which suppresses intergranular crack growth compared to other alloys, and transgranular crack growth has been maintained to higher temperatures in RR1000 as borne out by fractographic observations. In the 725°C 1-20-1-1 condition, similar m-values were demonstrated by RR1000 and other materials. This suggests that with the same mechanism of intergranular crack growth, RR1000 has demonstrated lower crack growth rates, i.e. improved intergranular crack growth resistance compared to other materials.

The fracture surfaces of U720Li, U720Li-LG and U720Li-LP from the 725°C 1-1-1-1 and 1-20-1-1 vacuum tests [30] are shown in Figure 5-20 and Figure 5-21 for comparison with corresponding RR1000 fracture surfaces in Figure 4-63 and Figure 4-64. At low ΔK in the 725°C 1-1-1-1 condition, RR1000, U720Li and U720Li-LG exhibits predominantly transgranular crack growth, while the fracture surface of U720Li-LP indicates a higher degree of intergranular crack growth compared to other materials. At higher ΔK, the 725°C 1-1-1-1 fracture surfaces generally indicate a predominantly intergranular crack growth mode; however the crack growth in RR1000 appears to be less intergranular compared to other materials. The relatively similar appearance of the fracture surfaces of RR1000, U720Li and U720Li-LG at low ΔK in the 725°C 1-1-1-1 condition are consistent with the relatively similar crack growth rates of these materials; and the higher degree of intergranular crack growth observed in U720Li-LP at low ΔK may have caused the higher crack growth rates in U720Li-LP compared to other materials. At higher ΔK in the 725°C 1-1-1-1 condition, the fracture surfaces become increasingly more intergranular, and this is reflected in the progressively increasing crack growth rates. The lower crack growth rates of RR1000 compared to other materials at high ΔK in the 725°C 1-1-1-1 condition may be reflecting the relatively lower degree of intergranular crack growth in the material.

In the 725°C 1-20-1-1 condition, the fracture surfaces of all the materials appear to be predominantly intergranular at both low and high ΔK. The crack growth curves in Figure 5-19d suggests increasing degree of intergranular crack growth modes should be noted in RR1000, followed by U720Li and U720Li-LG whilst the most intergranular crack growth should be expected in U720Li-LP. The degree of intergranular crack growth observed on the fracture surfaces appear to be consistent with the relative crack growth rates of the materials, with the lowest and highest degree of intergranular crack growth observed in RR1000 and U720Li-LP respectively. The degree of intergranular crack growth in U720Li and U720Li-LG appear to be relatively similar consistent with the relatively similar crack growth rates of the two materials.

Comparison of crack growth rates of U720Li and its variants indicates larger grains to be beneficial to crack growth resistance in a vacuum environment. The effect of precipitate sizes on the crack growth resistance was less clear although larger coherent γ' precipitate sizes are expected to give improved crack growth resistance due to the larger precipitate sizes giving increased difficulty of dislocation movement and hence improved creep resistance. As mentioned earlier, the tertiary coherent γ' precipitates are of less significance in the elevated temperature tests and the effects of coherent γ' precipitates on fatigue crack resistance is mainly due to the secondary coherent γ' precipitates.

U720Li-LG was noted to consistently show lower crack growth rates at 650°C and 725°C compared to U720Li and U720Li-LP. The improvement in the crack growth resistance of

U720Li-LG is attributed in part to the larger grains giving improved creep resistance, thereby reducing the contribution of creep deformation to creep-fatigue crack growth in the vacuum testing environment. The creep deformation in U720Li and its variants is thought to be detrimental to crack growth, i.e. rarely giving rise to stress relaxation and only contributing to crack growth through accumulation of damage, hence the increased creep resistance in U720Li-LG is thought to be giving the consistently lower crack growth rates. The secondary coherent γ' precipitates in U720Li-LG are also much larger compared to U720Li, and U720Li-LG also has higher volume fraction of secondary γ' precipitates compared toU720Li and U720Li-LP. This may give further increase in crack growth resistance in U720Li-LG compared to U720Li and U720Li-LP.

U720Li-LP generally shows similar or higher crack growth rates compared to U720Li at 650°C and 725°C. The larger coherent γ' precipitates in U720Li-LP also appear to be detrimental to the crack growth resistance at 725°C with U720Li-LP showing much higher crack growth rates compared to U720Li. As larger coherent γ' precipitates are expected to give improved crack growth resistance, the lower crack growth resistance observed for U720Li-LP compared to U720Li is believed to be due to differences in the precipitate size and mean distances between the precipitates in both materials. The larger secondary γ' precipitates in U720Li-LP have been shown to be spaced further apart compared to secondary γ' precipitates in U720Li (section 5.3.1). The higher mean distances between the secondary γ' precipitates give rise to increased dislocation mobility, and therefore lower creep resistance which is detrimental to crack growth resistance. The observed crack growth rates of U720Li and U720Li-LP may be elucidated by the balance in the crack growth resistance associated with differences in the coherent γ' precipitate size and spacing in both materials. The similar crack growth rates of U720Li and U720Li-LP observed at 650°C suggests that the increase in dislocation mobility associated with further spaced precipitates in U720Li-LP is approximately equalled by the increased difficulty of dislocation cross-slip and climb processes when the dislocations encounter larger coherent γ' precipitates, giving a crack growth resistance level similar to that of U720Li. At the higher temperature of 725°C, dislocation mobility in the γ matrix is further increased compared to at 650°C, and the larger coherent γ' precipitates which are spaced further apart in U720Li-LP will be less effective in restricting dislocation motion, i.e. in U720Li-LP the increase in crack growth resistance associated with larger precipitate sizes is unable to offset the increased detrimental effects of further spaced precipitates on crack growth resistance. This is reflected in the higher crack growth rates of U720Li-LP compared to U720Li at 725°C.

The crack growth behaviour demonstrated by RR1000 MO1547 is unusual in that it shows the highest crack growth amongst the materials at 650°C, but much lower crack growth rates compared to other materials at 725°C. Comparison of microstructural characteristics to explain the

trends of crack growth behaviour in RR1000 and U720Li and its variants appears to be applicable only at 650°C; at 725°C the comparison of microstructural characteristics to explain the crack growth behaviour in RR1000 and U720Li and its variants appears to break down. Comparing the crack growth behaviour of U720Li-LG and RR1000 at 650°C, U720Li-LG shows better crack growth resistance compared to RR1000 MO1547 as expected as U720Li-LG has approximately similar coherent γ' volume fraction but larger grains and larger coherent γ' precipitates compared to RR1000 MO1547. Comparison of the crack growth behaviour of RR1000, U720Li and U720Li-LP at 650°C on the basis of the microstructural characteristics of the materials is also generally as expected. The comparison of the crack growth behaviour of RR1000 and U720Li and its variants on the basis of microstructural characteristics however breaks down at 725°C as RR1000 consistently shows lower crack growth rates compared to other materials.

The crack growth behaviour of RR1000 is attributed to stress relaxation effects due to creep deformation as discussed in section 5.2.2.2 giving rise to increased crack growth resistance during vacuum tests. This may explain the lower crack growth rates of RR1000 at 725°C compared to other materials. The higher crack growth rates of RR1000 compared to other alloys at 650°C appear to contradict the stress relaxation argument. However, it is thought that the stresses involved in these tests are not sufficient to trigger extensive stress relaxation at the particular test temperature and dwell cycling. At higher temperature and/or longer dwell, the stresses required to trigger stress relaxation should be lower, i.e. increased extent of stress relaxation would be expected at a given ΔK at higher temperature and/or longer dwell. This may explain the behaviour of RR1000 compared to other alloys where it was noted to have the highest crack growth rates at 650°C 1-1-1-1 to having approximately similar or lower crack growth rates compared to other alloys at 650°C 1-20-1-1 and 725°C 1-1-1-1 and eventually significantly lower crack growth rates compared to other alloys at 725°C 1-20-1-1.

The stress relaxation effects may be due to the altered alloy chemistry and/or the differing grain boundary character in RR1000 compared to U720Li and its variants. Changes in the coherent γ' precipitate sizes with prolonged thermal exposure are also expected to have an effect on the creep characteristics and hence the stress relaxation in RR1000. As seen in Figure 4-15, the volume fraction of coherent γ' precipitates expected at 725°C is slightly lower that that expected at 650°C, and this may be reflected in the slightly reduced size of the secondary γ' precipitates and the dissolution of tertiary γ' precipitates for the specimen tested at 725°C compared to the secondary and tertiary γ' precipitates size and volume fraction observed for the specimen tested at 650°C. In another study of elevated temperature fatigue resistance of RR1000 after prolonged thermal exposure at 800°C [19], the secondary γ' precipitates were noted to be relatively stable towards

coarsening while the tertiary γ' precipitates were noted to dissolve after prolonged thermal exposure to give 2 wt% precipitation of the σ phase.

The stress relaxation effects will undoubtedly be affected by the changes in coherent γ' precipitate sizes. Stress relaxation effects arise from creep deformation at the crack tip due to higher temperature and/or imposition of dwell cycling. The creep deformation due to enhanced movement of dislocations enables accommodation of the strains from cyclic loadings, hence reducing the stresses at the crack tip, but the movement of these dislocations are affected by the changes in the coherent γ' precipitate morphology. The extent to which the stress relaxation effects are affected by the changes in coherent γ' precipitates morphology however remains unclear. The complicated effects of stress relaxation and crack growth resistance can be better illustrated by the following diagram:

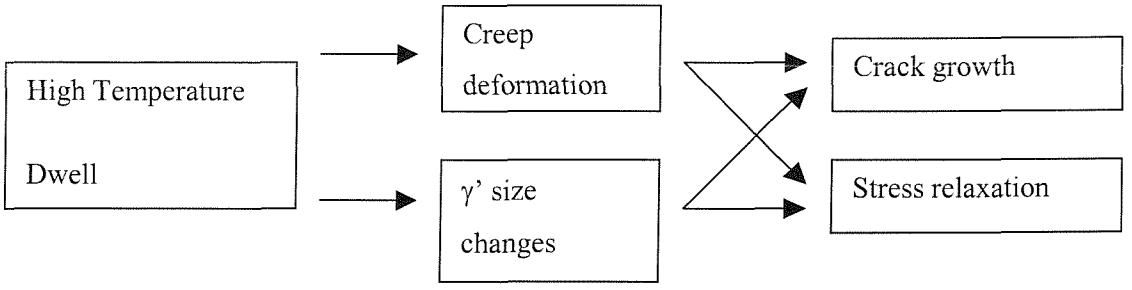

Figure 5-8: Possible effects of temperature and dwell.

The different test temperatures and dwells give rise to different extents of creep deformation and changes in coherent γ' morphology. Each of the creep or coherent γ' size changes can have opposing effects on crack growth resistance. Creep may slow down crack growth by stress relaxation, or contribute to crack growth by accumulated creep damage at the crack tip. For a given coherent γ' size, e.g. coarser precipitates, the cyclic crack growth resistance may be enhanced due more restricted dislocation movement (increased difficulty in precipitate cutting/looping) but at the same time this restriction gives rise to lower stress relaxation, i.e. higher resultant stresses at the crack tip and higher crack growth driving force. The observed crack growth rates are due to the additional effects of crack growth and possible stress relaxation, but it is difficult to work out the individual contributions of creep and coherent γ' size changes to crack growth and stress relaxation.

5.3.5.3. Elevated temperature long crack tests in air

The elevated temperature long crack data in air were obtained from tests conducted at QinetiQ Farnborough. These results are included in the discussion and also discussed together with other elevated temperature fatigue tests results to give a more comprehensive and complete picture of the effects of microstructure on fatigue crack growth resistance.

Material comparison plots for elevated temperature long crack tests in air are shown in Figure 5-22a to Figure 5-22d. RR1000 and U720Li-LG generally show lower crack growth rates compared to other test materials. RR1000 was noted to show lower crack growth rates compared to U720Li-LG in the 1-1-1-1 condition at both 650°C and 725°C. In the 1-20-1-1 condition at both 650°C and 725°C, the crack growth rates demonstrated by U720Li-LG in the low ΔK regime were lower compared to RR1000 before the crack growth rates of U720Li-LG becomes progressively higher than the crack growth rates of RR1000 beyond a ΔK of 30-40 MPa$\sqrt{m}$. The crack growth behaviour trends of U720Li-LG imply that the crack growth rates of U720Li-LG will be highest amongst all the test materials at ΔK beyond 30-40 MPa$\sqrt{m}$. U720Li and U720Li-LP generally show relatively higher crack growth rates compared to RR1000 and U720Li-LG. Other than in the 650°C 1-20-1-1 condition, the crack growth rates of U720Li-LP are much lower compared to U720Li under all other testing conditions. In the 650°C 1-20-1-1 condition, the crack growth rates of U720Li and U720Li-LP appear approximately similar to each other at low ΔK, and at higher ΔK the crack growth rates of U720Li-LP appear higher compared to U720Li.

Comparing the m-values, the m-values of U720Li and U720Li-LP were relatively similar under all testing conditions, suggesting similar crack growth mechanisms in both materials under various testing conditions. The m-values of the U720Li-LG curves were noted to be distinctly higher than the m-values of the U720Li and U720Li-LP curves under all conditions. This may be an indication that crack growth in U720Li-LG is more sensitive to monotonic creep effects. The m-values of the RR1000 curves appear similar to the m-values of the U720Li-LG curve in the 650°C 1-1-1-1 condition, but were similar to the m-values of the U720Li and U720Li-LP curves in the 650°C 1-20-1-1 and 725°C 1-1-1-1 conditions. In the 725°C 1-20-1-1 condition, the m-value of the RR1000 curve is in between that of the m-value of U720Li-LG and the m-values of U720Li/ U720Li-LP. The m-values of RR1000 indicate that similar crack growth mechanisms are operating in RR1000 and U720Li-LG in the 650°C 1-1-1-1 condition, while in the 650°C 1-20-1-1 and 725°C 1-1-1-1 conditions, crack growth mechanisms in RR1000 were similar to that operating in 720Li/U720Li-LP at the given testing conditions. In the 725°C 1-20-1-1 condition, crack growth in RR1000 is altered to an intermediate crack growth mechanism in between that of U720Li-LG and U720Li/U720Li-LP.

U720Li-LG is generally showing low crack growth rates and in the dwell tests U720Li-LG shows the lowest crack growth rates at low ΔK. The observed crack growth behaviour of U720Li-LG is attributed to the larger grains giving improved oxidation and creep resistance. The larger size and higher volume fraction of coherent γ' precipitates in U720Li-LG may also be contributing to the low crack growth rates. The progressively higher crack growth rates of U720Li-LG at high ΔK and the increased sensitivity of the crack growth in U720Li-LG to monotonic creep contributions may

be due to the poorer strength of the U720Li-LG compared to U720Li as shown in Figure 5-17. The larger plastic zone size and higher local strains at the crack tip due to the lower strength may give rise to accelerated crack growth processes at the elevated ΔK levels. Similar trends of accelerated crack growth in U720Li-LG were observed in the elevated temperature short crack tests.

Comparison of the crack growth behaviour of U720Li and U720Li-LP indicates generally better crack growth resistance in U720Li-LP which may be attributed to the slightly larger grains and larger coherent γ' precipitates in U720Li-LP. The larger size but further spaced apart secondary coherent γ' precipitates in U720Li-LP (section 5.3.1) were thought to be ineffective in giving enhanced crack growth resistance in the vacuum long crack tests conducted at 725°C where crack growth is likely to be dominated by creep processes. In the air tests however, creep processes are likely to be swamped by the significantly faster oxidation processes, and crack growth is dominated by oxidation-assisted crack growth mechanisms. The improved crack growth resistance of U720Li-LP compared to U720Li may be indicating that larger coherent γ' precipitates do improve crack growth resistance possibly due to the associated improvement in grain boundary oxidation resistance with larger γ' precipitates, and the crack growth resistance in air is less sensitive to the precipitate spacing in the material due to the reduced significance of creep processes. The larger precipitates although further spaced apart may be giving rise to increased difficulty of transportation of oxidising species via slip band impingement from within the grains to the grain boundaries, hence giving improved grain boundary oxidation resistance in U720Li-LP compared to U720Li.

The low crack growth rates of RR1000 may be due to stress relaxation effects which were noted from corresponding long crack tests in vacuum, or due to possible higher oxidation resistance of RR1000. However, the creep deformation processes leading to stress relaxation are expected to be overtaken by the significantly faster oxidation-assisted crack growth processes, hence improvement in crack growth resistance from stress relaxation effects is likely to be minimal. The more likely factor giving rise to improved crack growth resistance in RR1000 may be the higher oxidation resistance of the RR1000 material. RR1000 which has finer grains compared to U720Li-LG would be expected to be more susceptible to oxidation-assisted crack growth mechanisms, but RR1000 is showing generally lower crack growth rates compared to U720Li-LG which appear to point to RR1000 having increased oxidation-assisted crack growth resistance, i.e. increased oxidation resistance of the material. The higher oxidation resistance of RR1000 may also explain the lower crack growth rates of RR1000 compared to U720Li and U720Li-LP. In the dwell tests, the higher crack growth rates of RR1000 compared to U720Li-LG at low ΔK may be indicating that creep-fatigue crack growth mechanisms are predominant in this regime, and the enhanced creep and oxidation resistance of the U720Li-LG microstructure is able to offset the

lower oxidation resistance of the U720Li alloy chemistry, giving lower crack growth rates in U720Li-LG compared to RR1000.

5.3.5.4. Comparison of the effects of microstructure on long crack resistance at elevated temperature in vacuum and air

During elevated temperature long crack tests in vacuum, U720Li-LG was noted to consistently show higher crack growth resistance compared to U720Li and U720Li-LP while RR1000 was noted to show relatively poor crack growth resistance at 650°C but the highest crack growth resistance at 725°C. In the elevated temperature long crack tests in air, RR1000 and U720Li-LG generally show higher crack growth resistance compared to U720Li and U720Li-LP.

The effect of environment on elevated temperature long crack growth rates of the materials is shown in Figure 5-12. Comparing the effect of environment on crack growth of individual materials, the crack growth curves in air and vacuum were noted to be clustered closer together for U720Li-LG and RR1000 compared to the larger scatter of air and vacuum crack growth curves for U720Li and U720Li-LP. The m-values of the long crack tests in air and in vacuum were also noted to be only marginally different for U720Li-LG and RR1000 compared to the difference in the m-values of the air and vacuum tests of U720Li and U720Li-LP. The clustered crack growth curves and the similarity of the m-values of the air and vacuum tests of U720Li-LG and RR1000 might indicate that environmental factors have a smaller effect on the crack growth rates i.e. both these materials have higher oxidation resistance, or that less monotonic creep contributions are made to the overall crack growth rates in vacuum.

5.3.5.5. Comparison of the effects of microstructure on short crack and long crack resistance at elevated temperature

The results of the elevated temperature short crack and long crack tests indicate similar crack growth resistance trends in U720Li and its variants, i.e. increasing crack growth resistance from U720Li to U720Li-LP to U720Li-LG. This is noted when comparing the short crack growth curves shown in Figure 4-57 and the 650°C 1-1-1-1 air and vacuum long crack growth curves shown in Figure 5-19a and Figure 5-22a respectively. The similarity in the crack growth resistance trends is expected due to the similarity in the crack growth modes in the short crack and long crack tests. The vacuum long crack growth curves give a measure of the crack growth resistance in the flat transgranular regions at the initial stages of short crack growth (particularly sub-surface), while the air long crack growth curves are representative of the intergranular crack growth modes at larger crack lengths in the short crack tests. The larger grains in U720Li-LG compared to U720Li have been shown to be beneficial for mixed transgranular/intergranular crack growth modes in long crack vacuum tests and for intergranular crack growth modes during long crack air tests. The marginally improved crack growth resistance of U720Li-LP compared to U720Li in the

elevated temperature short crack test may be due to the larger coherent γ' precipitates in U720Li-LP. U720Li-LP was noted to have crack growth rates similar to U720Li in the 650°C 1-1-1-1 long crack vacuum tests, but in the 650°C 1-1-1-1 long crack air tests U720Li-LP is showing much lower crack growth rates compared to U720Li.

In terms of the fatigue resistance of RR1000, RR1000 was noted to show the highest fatigue resistance in both the elevated temperature short crack test and long crack air tests. The improved fatigue crack initiation and growth resistance of RR1000 in the short crack tests is attributed to stress relaxation in RR1000 which gives a reduction in the driving force for crack initiation and growth. This argument is supported by RR1000 vacuum long crack test results where lower crack growth rates were noted at higher temperature and/or longer dwell. In long crack tests under 650°C 1-1-1-1 vacuum condition, RR1000 was noted to give the highest crack growth rates amongst all the test materials, which appears to contradict the stress relaxation argument. As mentioned in section 5.3.5.2, this is thought to be due to the stresses involved in the long crack test at the particular temperature and dwell cycling being insufficient to provoke stress relaxation. In the elevated temperature short crack tests, the localised stresses at the notch root are expected to be significantly higher due to the stress concentration feature of the notch. As such stress relaxation is more likely to be operating in RR1000 in the elevated temperature short crack tests.

5.3.5.6. Summary

Elevated temperature crack initiation and growth resistance was generally noted to be higher in U720Li-LG and RR1000 compared to U720Li and U720Li-LP. The improved fatigue crack initiation and growth resistance of U720Li-LG was attributed to the larger grains giving rise to generally higher oxidation and creep resistance, while the improved fatigue crack initiation and growth resistance of RR1000 was attributed to stress relaxation in RR1000 which gives a reduction in the driving force for crack initiation and growth. The larger coherent γ' precipitates in U720Li-LP were generally noted to give rise to little or no improvement in elevated temperature crack growth resistance.

5.3.6. Comparison of effects of microstructure on fatigue resistance at room and elevated temperature

5.3.6.1. Fatigue crack initiation and early crack growth

Comparing the fatigue crack initiation and early crack growth behaviour at room temperature and at 650°C, there is an apparent difference in the trends of the crack growth resistance of the materials at both temperatures. At room temperature, lowest crack initiation and early crack growth resistance was noted in U720Li, increasing in U720Li-LG and RR1000 with the highest crack initiation and early crack growth resistance noted in U720Li-LP. At 650°C, RR1000 was

noted to show the highest crack initiation and early crack growth resistance, decreasing slightly in U720Li-LG and lowest in both U720Li and U720Li-LP.

At room temperature, the improved crack initiation resistance was attributed to lower planarity of slip in the materials. Improved crack growth resistance was attributed to slip deformation behaviour leading to homogeneous slip or higher reversibility of slip, and due to crack growth barrier effects and crack tip shielding due to local microstructure in the materials. At 650°C, the improved fatigue resistance in this regime was attributed to the larger grains in U720Li-LG and the possible stress relaxation effects in RR1000. Larger coherent γ' precipitates was also thought to be beneficial to improved fatigue resistance in the elevated temperature short crack tests. The difference in the factors giving rise to improved crack growth resistance at room temperature and at 650°C reflects the different crack growth modes in operation during the room temperature and elevated temperature tests, i.e. stage I and mixed stage I/stage II crack growth at room temperature and a transgranular followed by a transition to intergranular crack growth mode at 650°C.

When the short crack growth curves of U720Li and U720Li-LG at room temperature and at 650°C were compared as shown in Figure 5-15, it was noted that the short crack growth rates of U720Li at room temperature were approximately one decade lower compared to corresponding elevated temperature short crack growth rates, while the short crack growth rates of U720Li-LG at room temperature and at 650°C appear to be approximately similar. The relatively similar short crack growth rates of U720Li-LG at room temperature and at 650°C may be due to higher oxidation resistance of U720Li-LG, hence the increase in temperature to 650°C gives rise to only marginal increase in the degree of detrimental oxidation attack in the material, resulting in crack growth resistance levels similar to that expected at room temperature. In U720Li, poorer oxidation resistance may cause higher degree of detrimental oxidation attack in the material at 650°C, resulting in lower crack growth resistance. The larger grains in U720Li-LG compared to U720Li meant that there is less grain boundary area for diffusion of oxidising species in U720Li-LG compared to U720Li, and grain boundary embrittlement due to these species are minimised in U720Li-LG. The relative difference in the oxidation resistance of U720Li and U720Li-LG has been highlighted in section 5.3.5.4.

5.3.6.2. Long crack growth

In the room temperature long crack tests, U720Li, U720Li-LG and RR1000 appear to be showing approximately similar crack growth resistance while U720Li-LP was noted to show a lower degree of crack growth resistance. In the elevated temperature long crack tests in air and vacuum, RR1000 and U720Li-LG generally show better crack growth resistance compared to U720Li and U720Li-LP.

In the room temperature tests, long crack growth resistance appeared to be governed by a combination of intrinsic crack growth resistance contribution due to slip behaviour in the materials and extrinsic crack growth resistance contribution from crack closure during the tests. At elevated temperatures, improved crack growth resistance is expected for materials with larger grains due to improved creep and oxidation resistance in addition to alloy chemistry giving rise to stress relaxation effects. The difference in the factors giving rise to improved crack growth resistance at room temperature and at elevated temperatures is again reflecting the different crack growth modes which are in operation during the room temperature and elevated temperature tests, i.e. stage I and mixed stage I/stage II crack growth at room temperature and crack growth mechanisms involving transgranular or intergranular or a mixed transgranular/intergranular crack growth mode at elevated temperatures.

When comparing the long crack growth curves of the materials at room and elevated temperatures as shown in Figure 5-16, the difference in the crack growth rates at room temperature and in the 650°C 1-1-1-1 vacuum condition was noted to be lower for U720Li-LG and U720Li-LP compared to the corresponding difference in U720Li. This may be indicating lower detrimental effects of temperature on crack growth resistance in U720Li-LG and U720Li-LP compared to U720Li which appear to agree well with the difference in the room and elevated temperature short crack growth resistance of U720Li-LG and U720Li as discussed in the preceding section.

The 650°C 1-1-1-1 vacuum crack growth rates of RR1000 were noted to be higher by more than one decade compared to the room temperature crack growth rates. In U720Li and its variants this difference in growth rates was noted to be approximately less than one decade. The more marked difference in crack growth rates at room temperature and 650°C 1-1-1-1 vacuum condition in RR1000 may be an indication of an increased sensitivity of slip deformation behaviour to changes in temperature in RR1000. The increase in temperature may be causing a more significant loss in cycle-dependent crack growth resistance in RR1000 compared to U720Li and its variants, which is noted when comparing Figure 4-29, Figure 5-19a and Figure 5-19b.

5.3.6.3. Summary

Different trends of crack initiation and growth resistance of the materials were noted at room and elevated temperatures. The difference is attributed to the different crack initiation and growth mechanisms at the different temperatures, giving rise to different effects of microstructure on crack initiation and growth resistance.

5.4. Optimal microstructural characteristics for improved fatigue performance

At room temperature, microstructures giving rise to lower planarity of slip have been shown to give improved crack initiation resistance. Crack growth resistance in both the long crack and short crack tests was noted to be improved with larger grain size, but does not appear to be highly sensitive to the size and volume fraction of coherent γ' precipitate sizes. Higher frequency of primary γ' precipitates in the materials was also found to give improved crack growth resistance.

At elevated temperatures, larger grain size is again shown to be beneficial to crack growth resistance both in the long crack and short crack tests. This is due to larger grains giving improved crack growth resistance against oxidation-assisted intergranular crack growth in air and creep-fatigue intergranular crack growth in vacuum. The larger grains were also noted to prolong the slow transgranular crack growth mode in the initial stages of elevated temperature short crack growth. The larger coherent γ' precipitates in U720Li-LP appear to give poorer crack growth resistance in vacuum long crack tests compared to U720Li, but were noted to give generally higher crack growth resistance in short crack and long crack tests conducted in air compared to U720Li.

In summary, the optimal microstructural characteristics for improved fatigue performance of turbine discs are larger grains and larger size and higher volume fraction of coherent γ' precipitates. Large grains have been shown to be beneficial under most of the different test conditions conducted in the current study. In terms of the size and volume fraction of coherent γ' precipitates, generally higher crack growth resistance was noted for larger size and higher volume fraction of coherent γ' precipitates in the elevated temperature long crack tests conducted in air. Although turbine disc fatigue life has been known to be dominated by crack initiation and short crack growth at elevated temperatures, higher crack growth resistance in elevated temperature long crack tests in air will give increased confidence in the overall fatigue performance of the turbine disc alloy. Porosity control is also an important aspect as porosity was noted to be the predominant crack initiation mechanism at both room temperature and at 650°C.

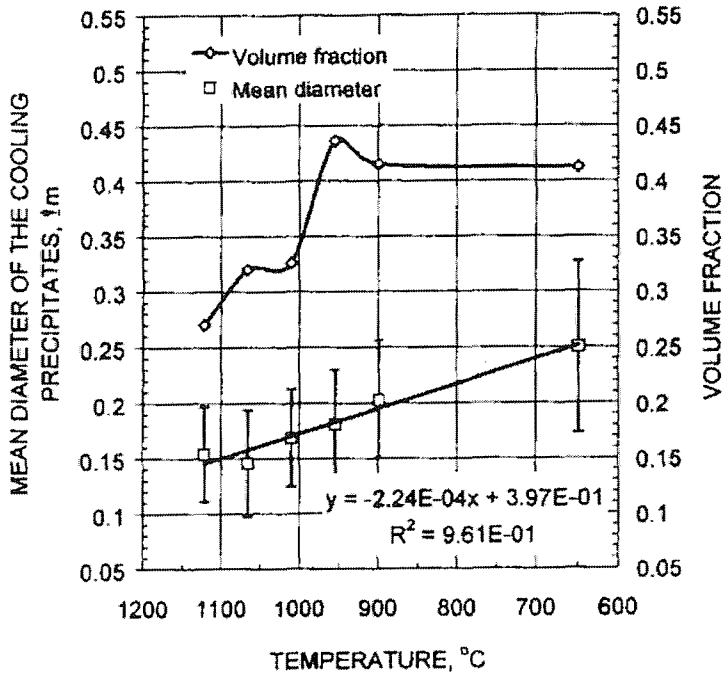

Figure 5-9: Volume fraction of secondary γ' as a function of decreasing temperature during cooling from solution temperature [25].

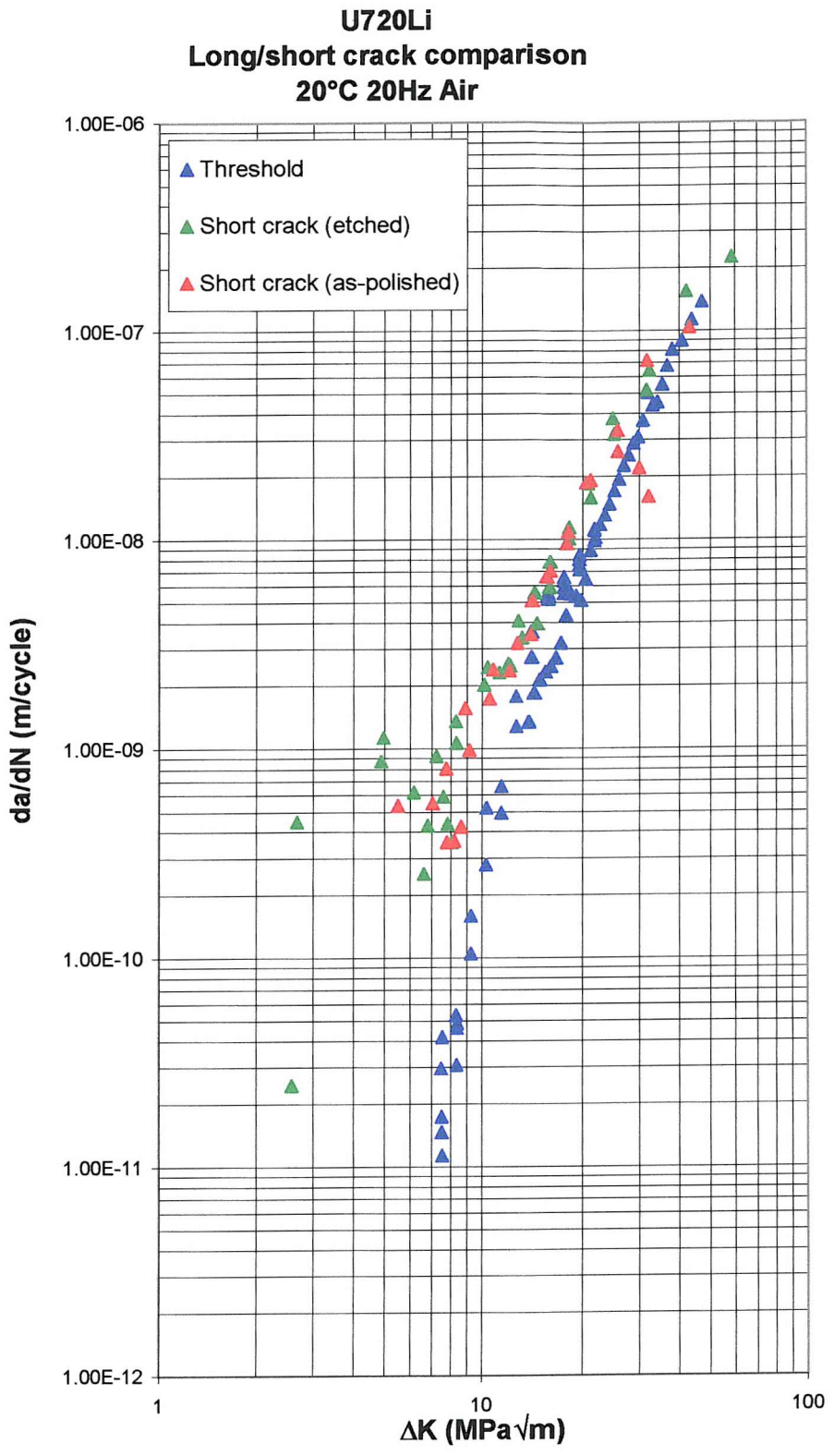

Figure 5-10a: U720Li room temperature long crack-short crack comparison.

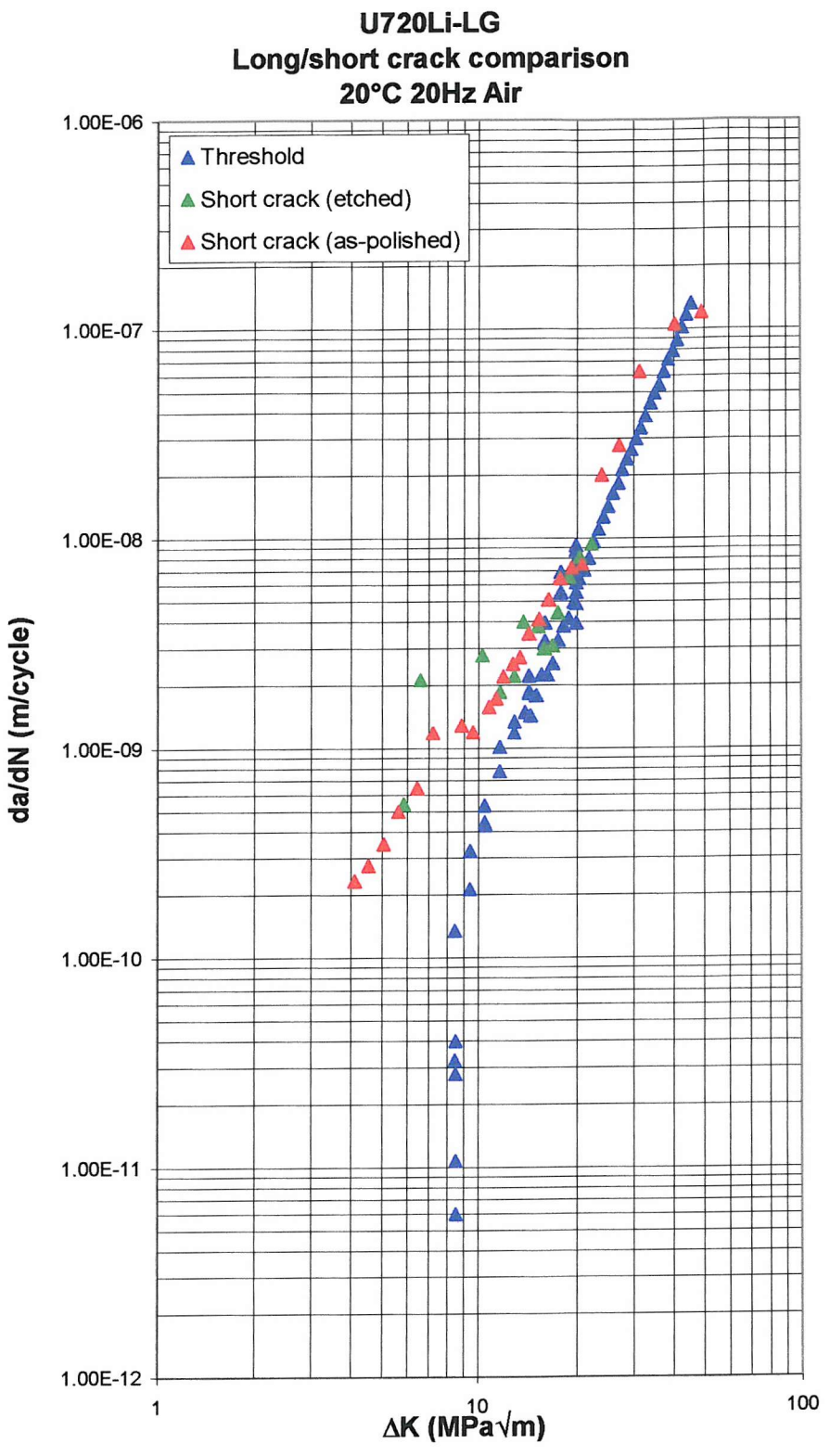

Figure 5-10b: U720Li-LG room temperature long crack-short crack comparison.

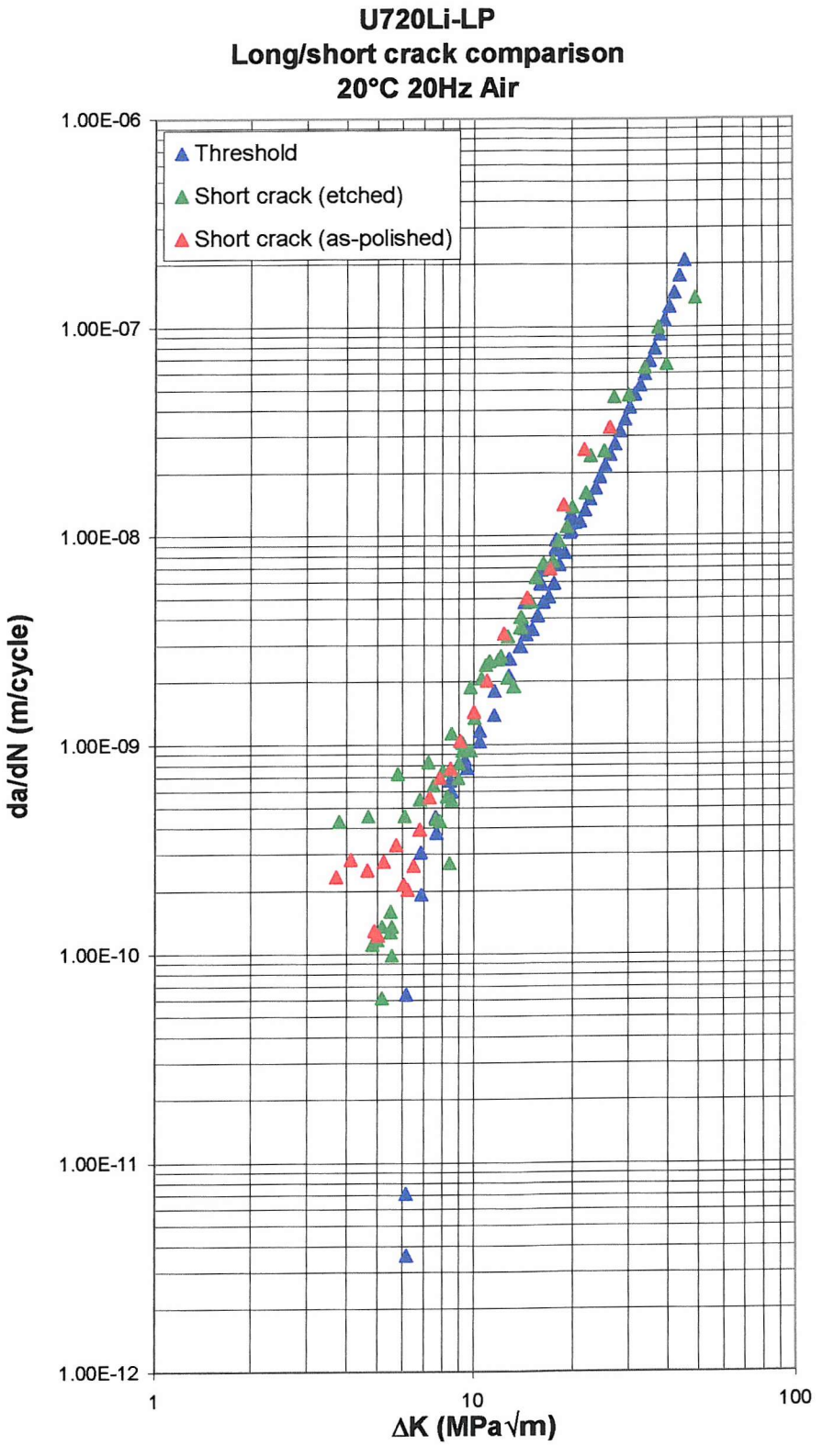

Figure 5-10c: U720Li-LP room temperature long crack-short crack comparison.

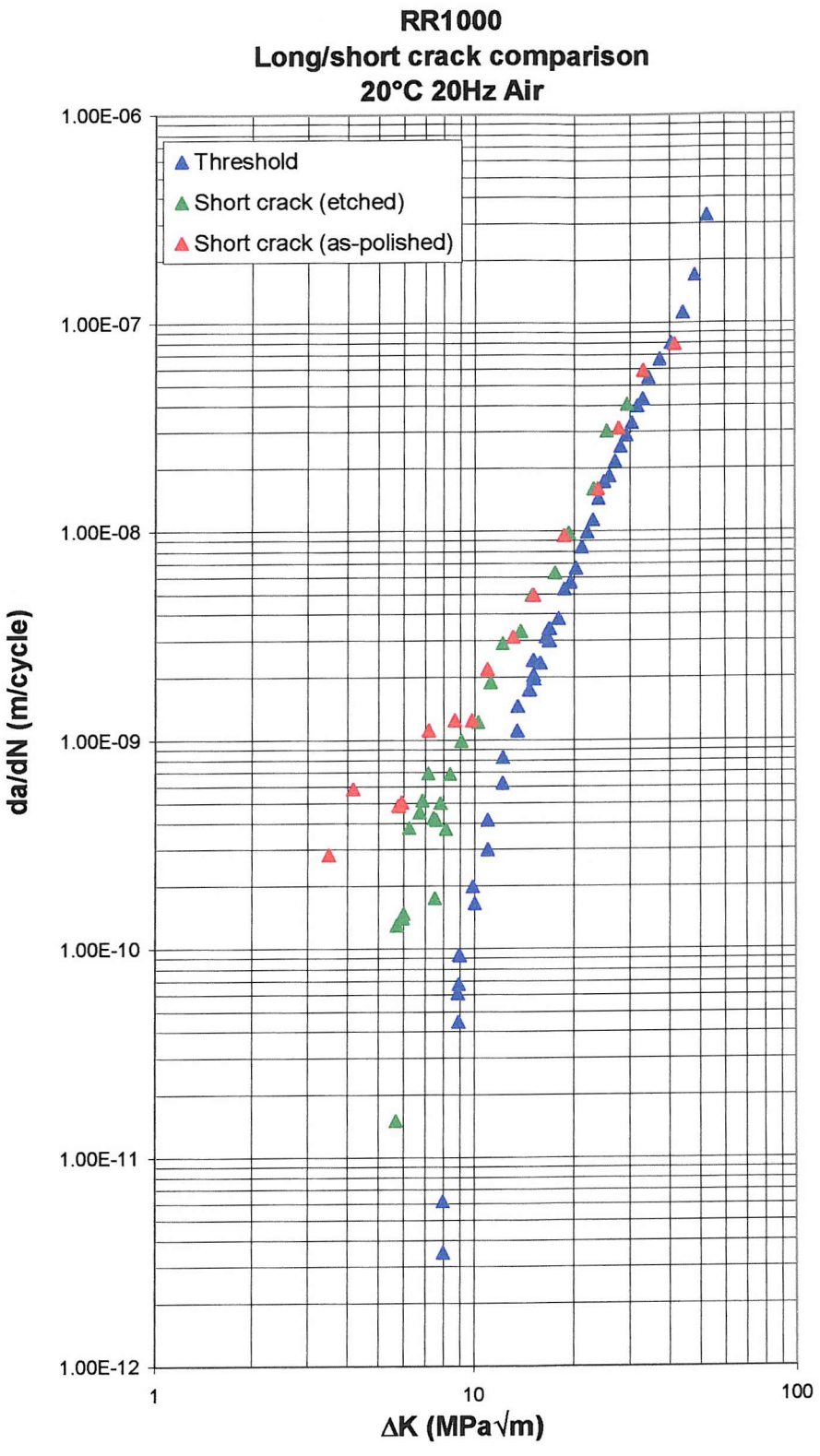

Figure 5-10d: RR1000 room temperature long crack-short crack comparison.

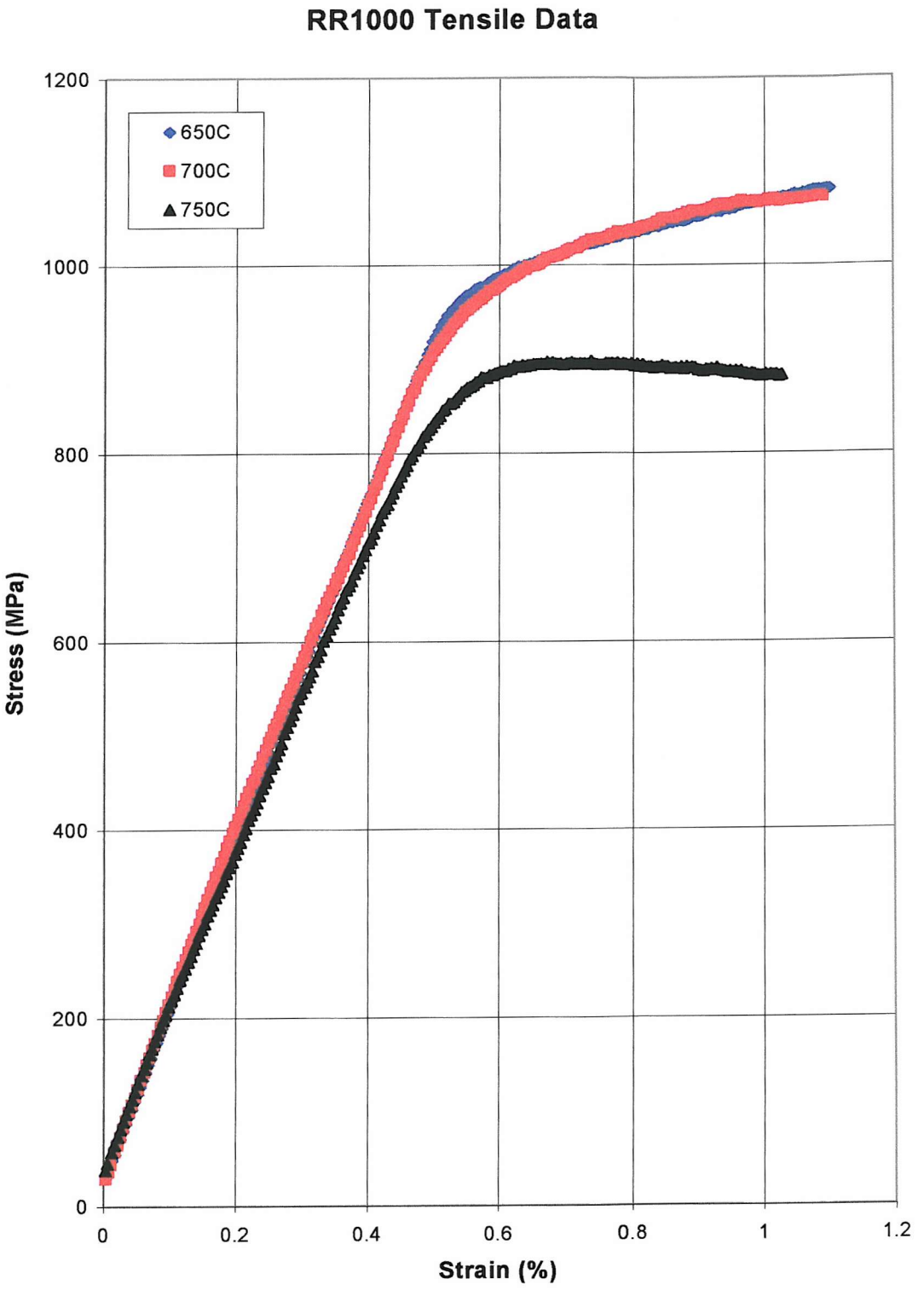

Figure 5-11: RR1000 tensile data.

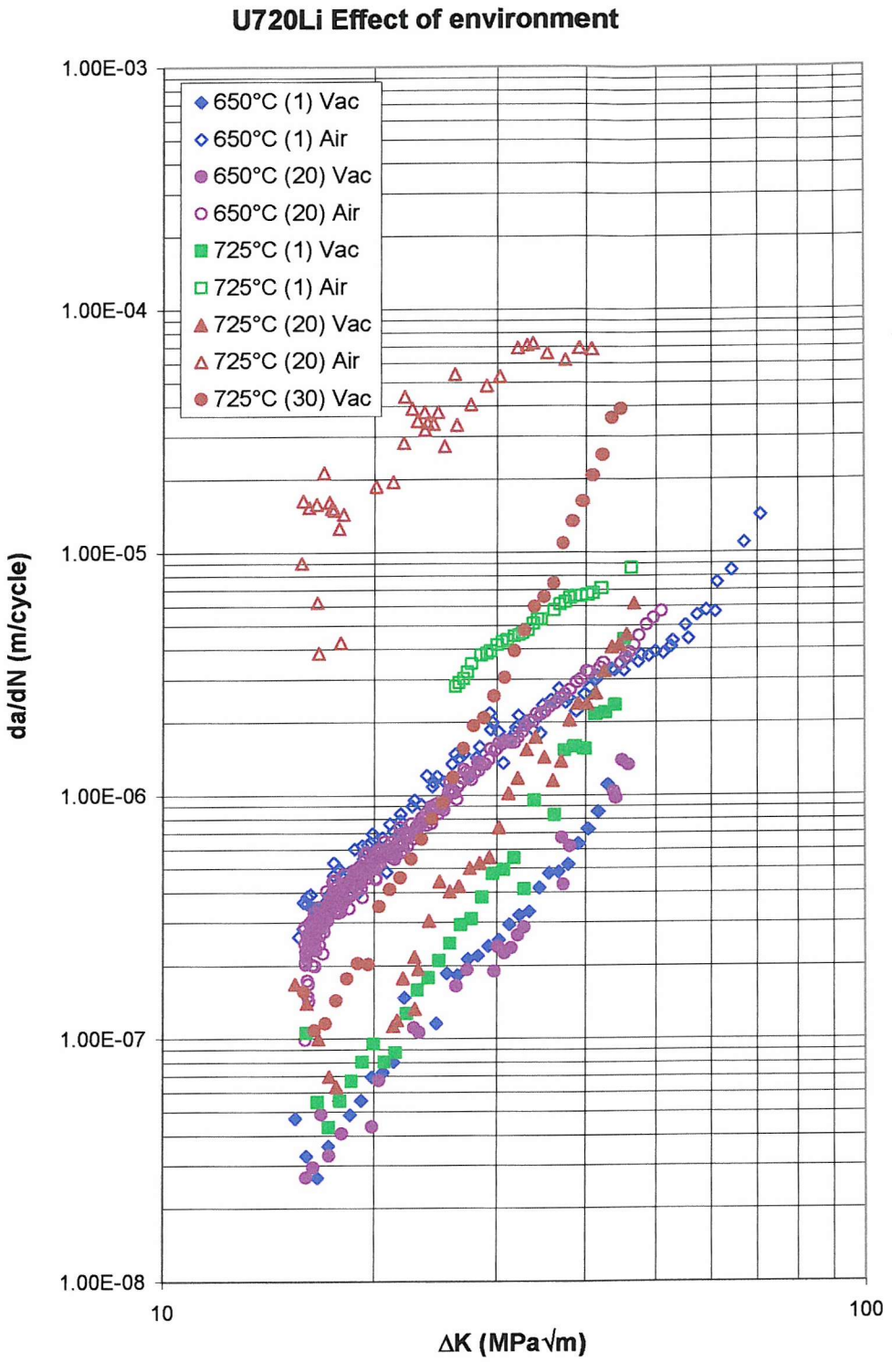

Figure 5-12a: U720Li effect of environment.

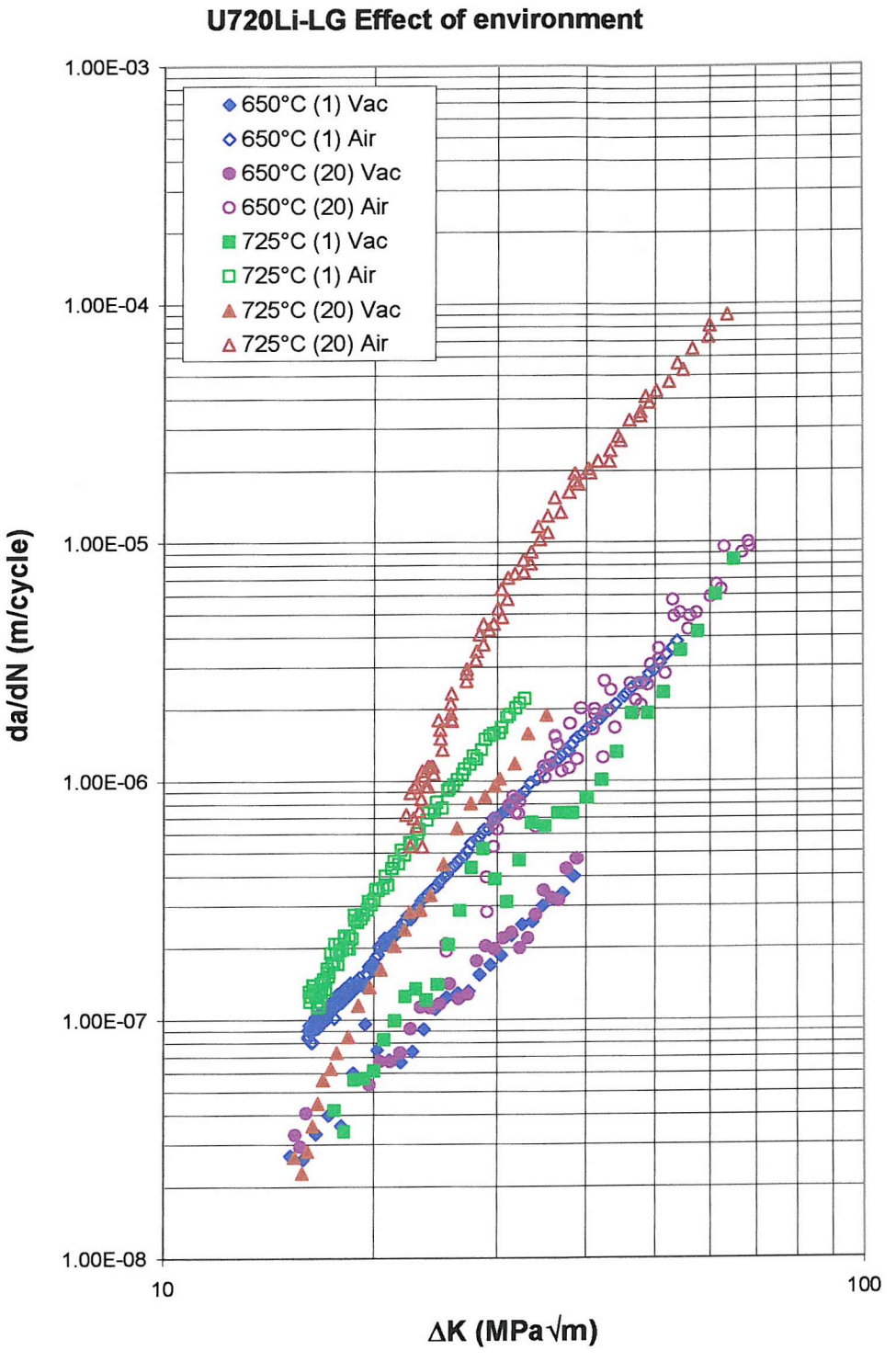

Figure 5-12b: U720Li-LG effect of environment.

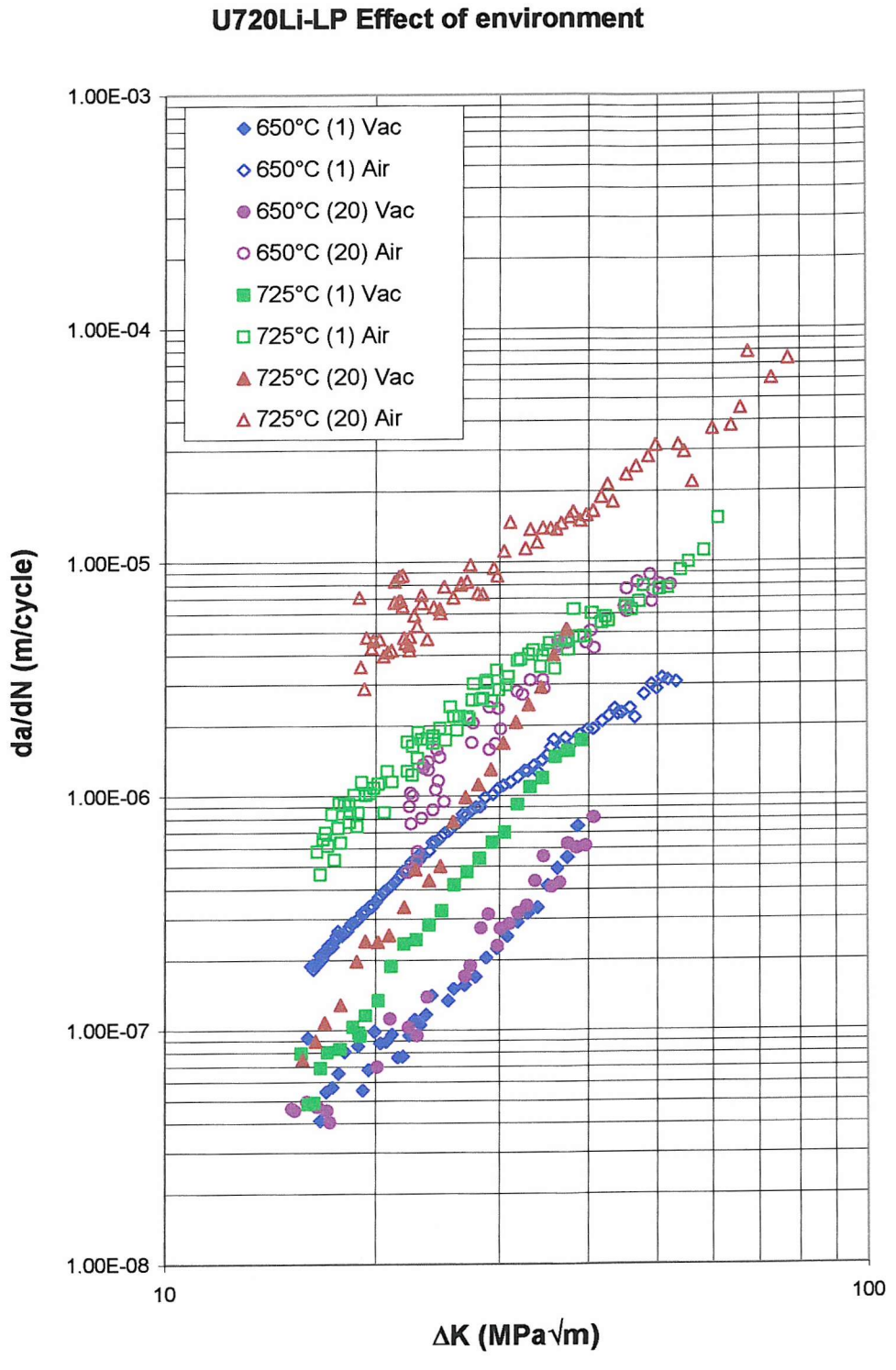

Figure 5-12c: U720Li-LP effect of environment.

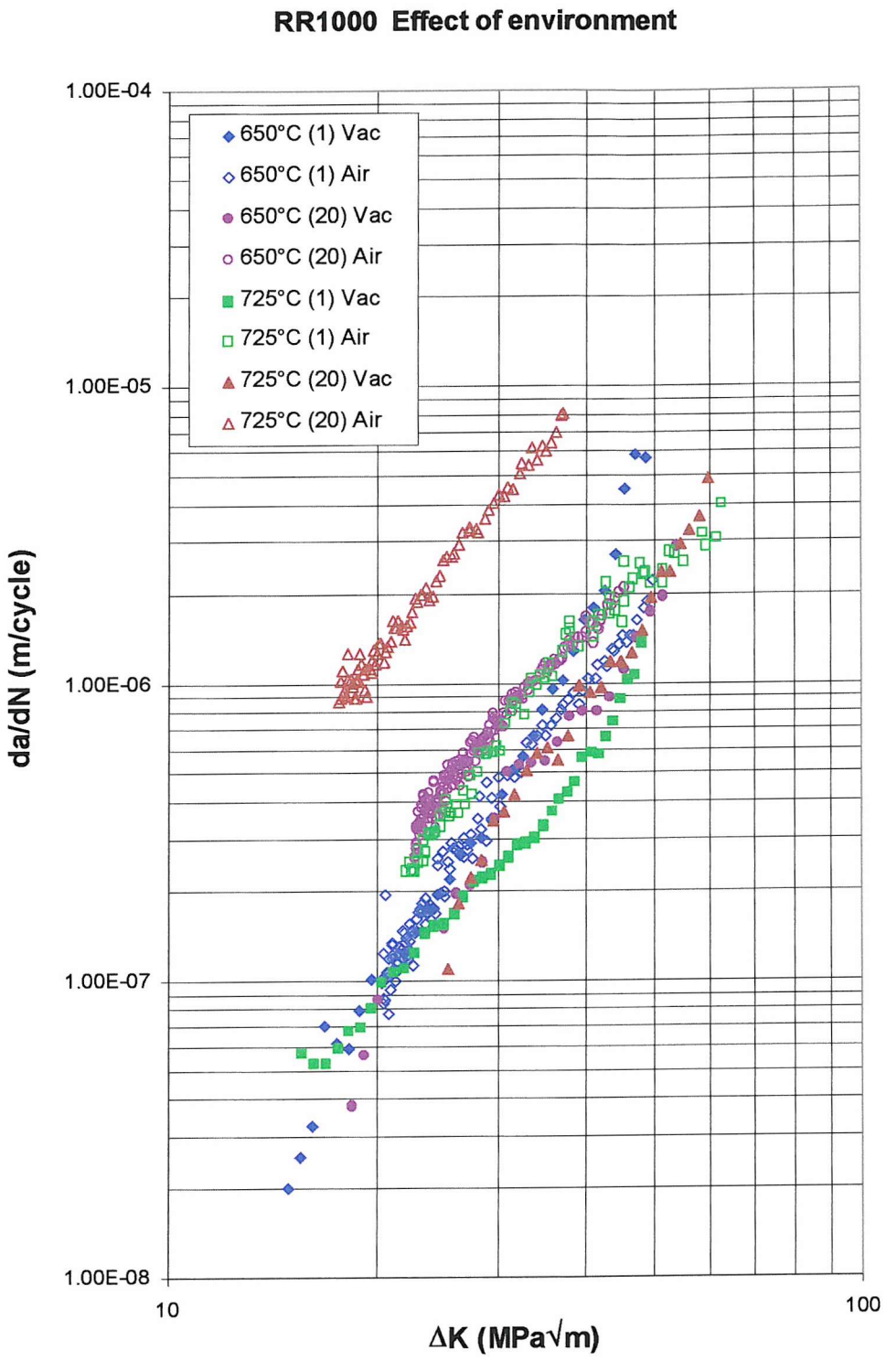

Figure 5-12d: RR1000 effect of environment.

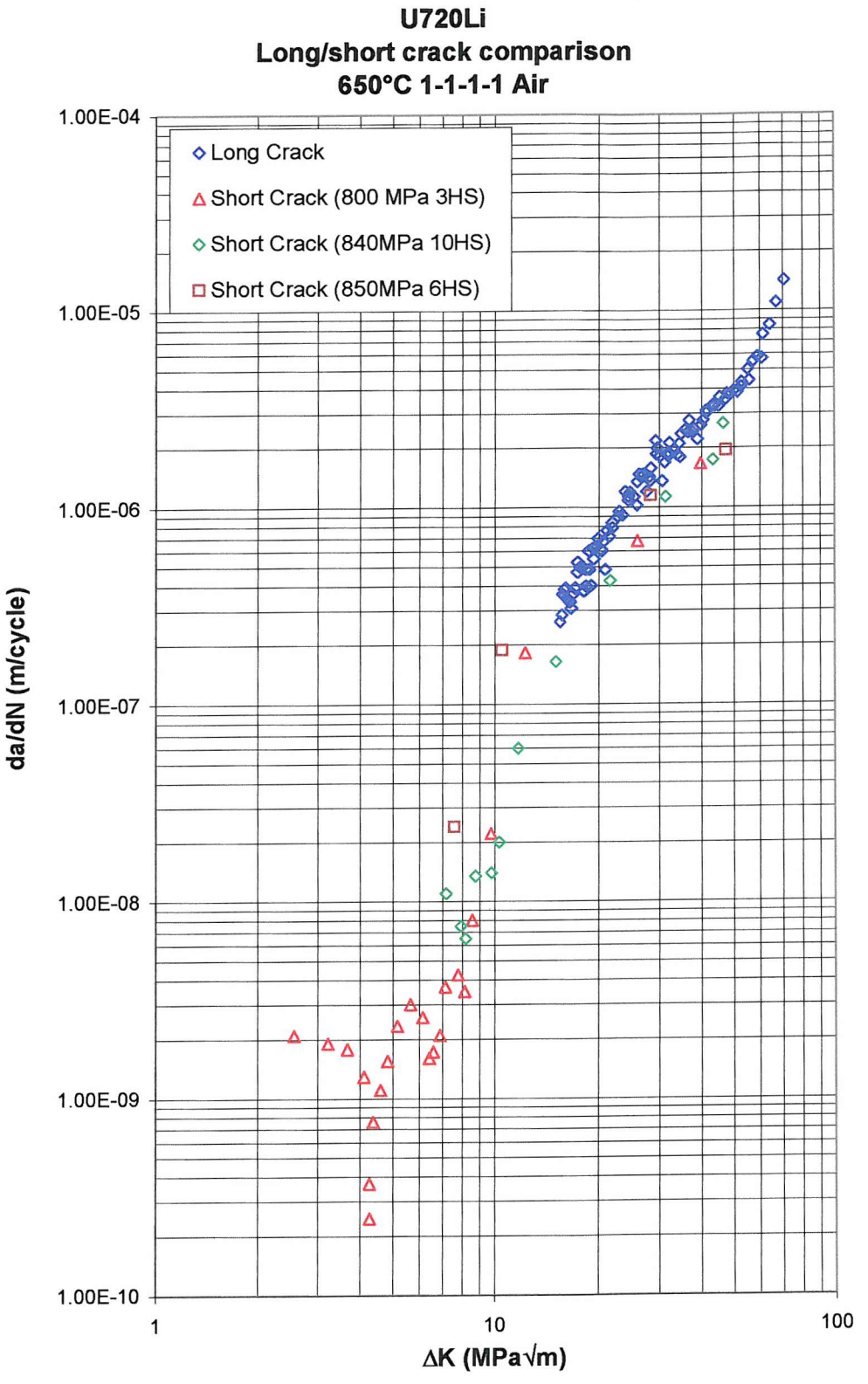

Figure 5-13a: U720Li 650°C long crack-short crack comparison.

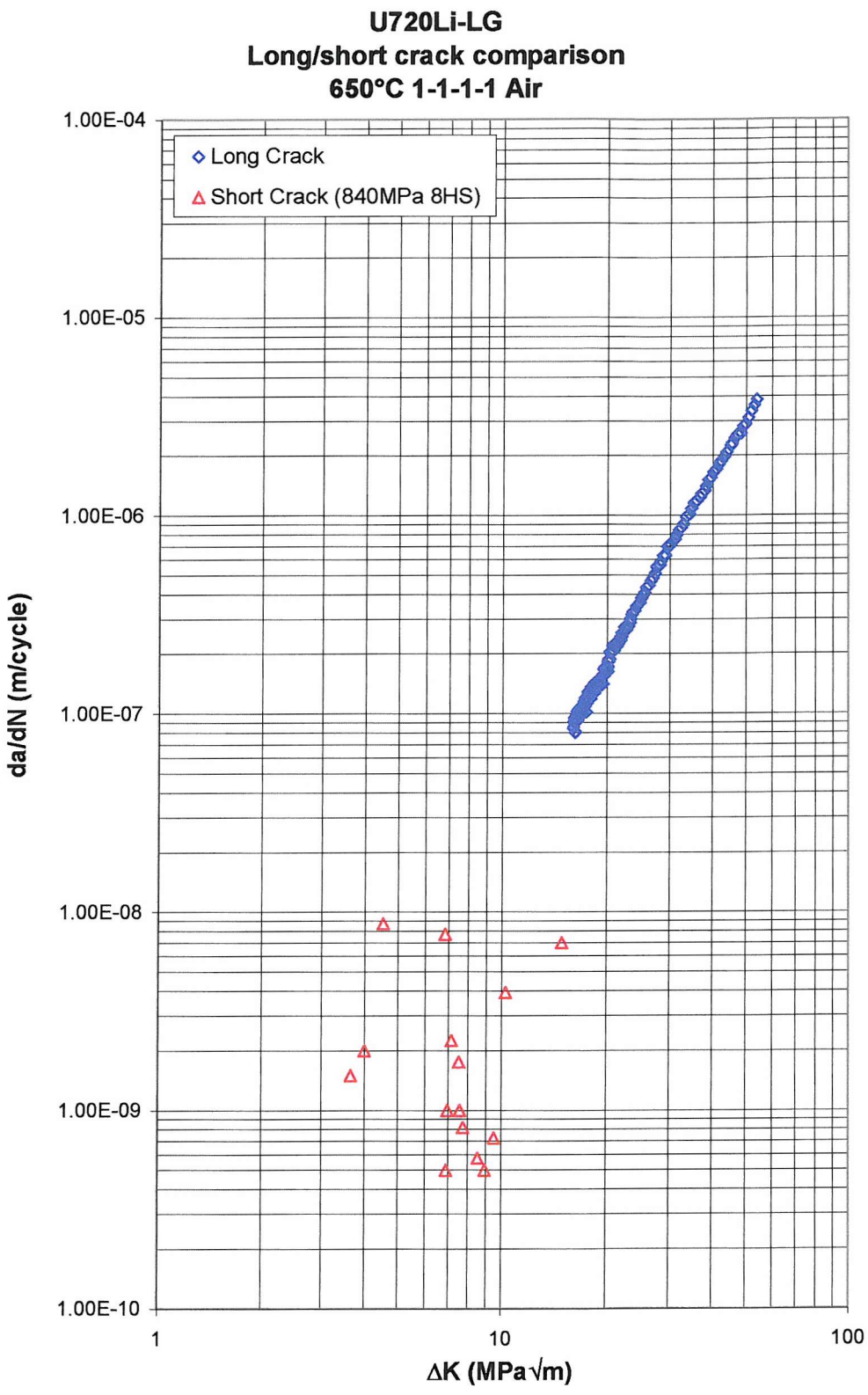

Figure 5-13b: U720Li-LG 650°C long crack-short crack comparison.

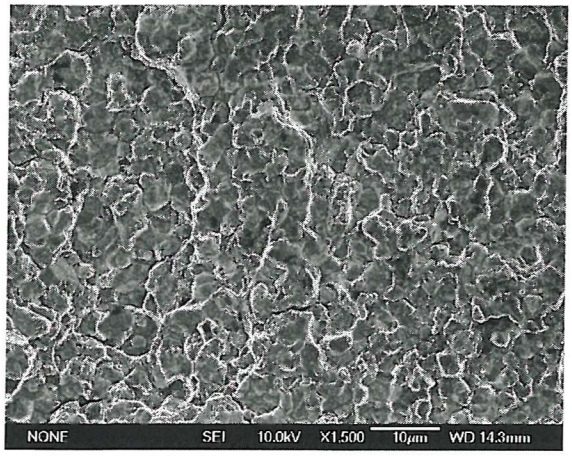

Figure 5-14a: U720Li; 650°C 1-1-1-1 Air ($\Delta K \approx 23.4$ MPa$\sqrt{m}$).

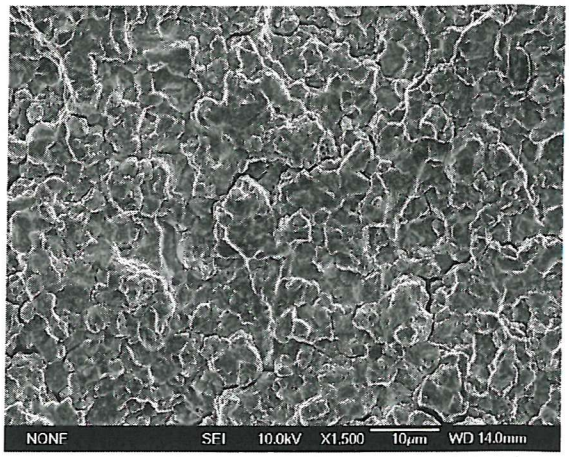

Figure 5-14b: U720Li; 650°C 1-1-1-1 Air ($\Delta K \approx 34.6$ MPa$\sqrt{m}$).

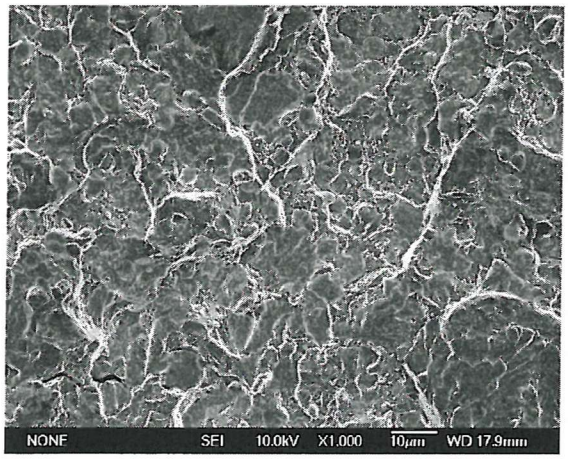

Figure 5-14c: U720Li-LG; 650°C 1-1-1-1 Air ($\Delta K \approx 24.4$ MPa$\sqrt{m}$).

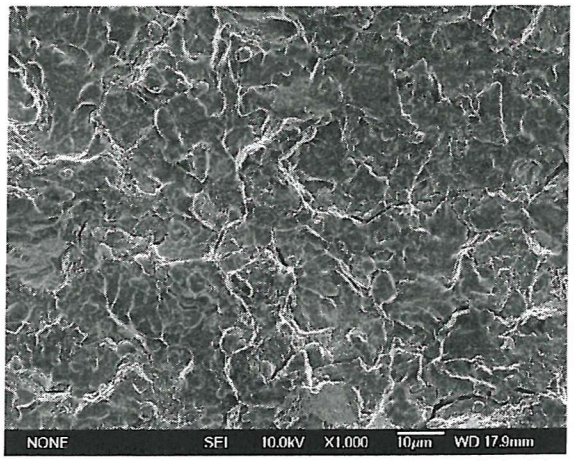

Figure 5-14d: U720Li-LG; 650°C 1-1-1-1 Air ($\Delta K \approx 34.2$ MPa$\sqrt{m}$).

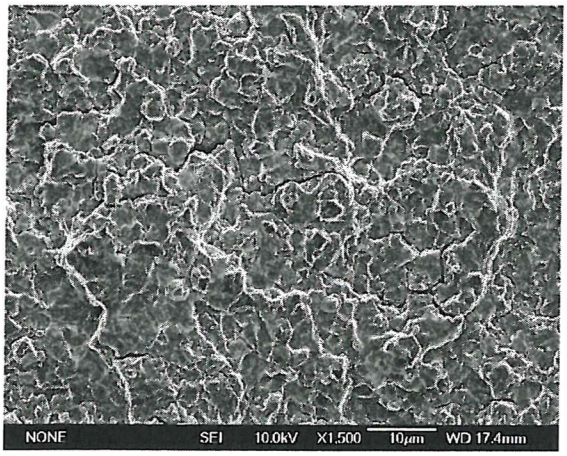

Figure 5-14e: U720Li-LP; 650°C 1-1-1-1 Air ($\Delta K \approx 24.3$ MPa$\sqrt{m}$).

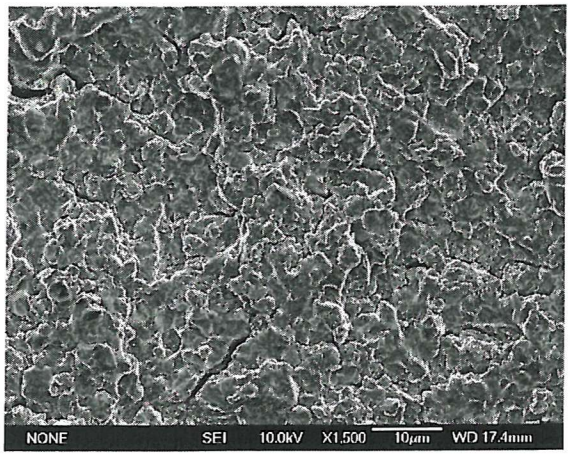

Figure 5-14f: U720Li-LP; 650°C 1-1-1-1 Air ($\Delta K \approx 33.8$ MPa$\sqrt{m}$).

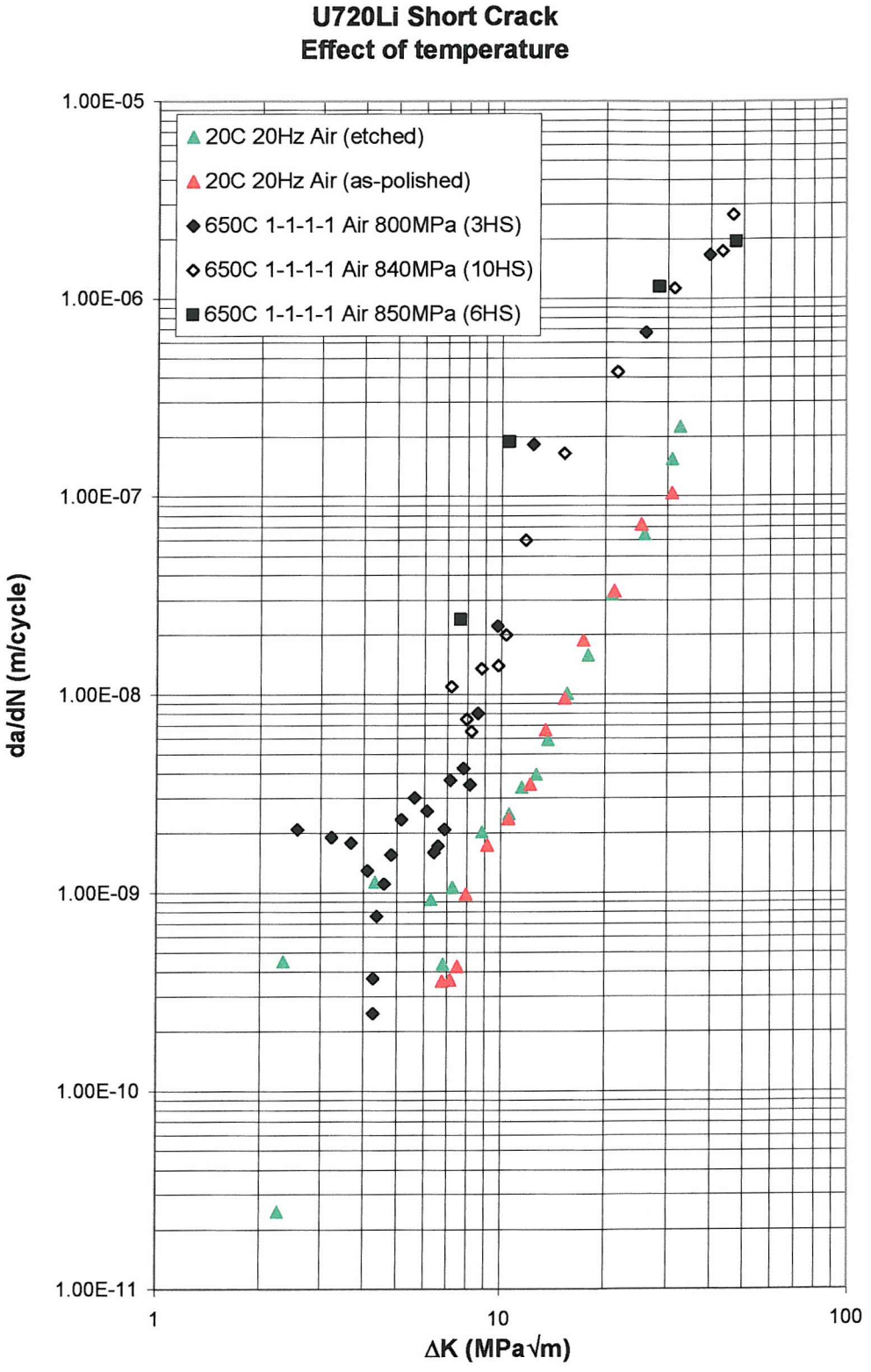

Figure 5-15a: U720Li room-elevated temperature short crack comparison.

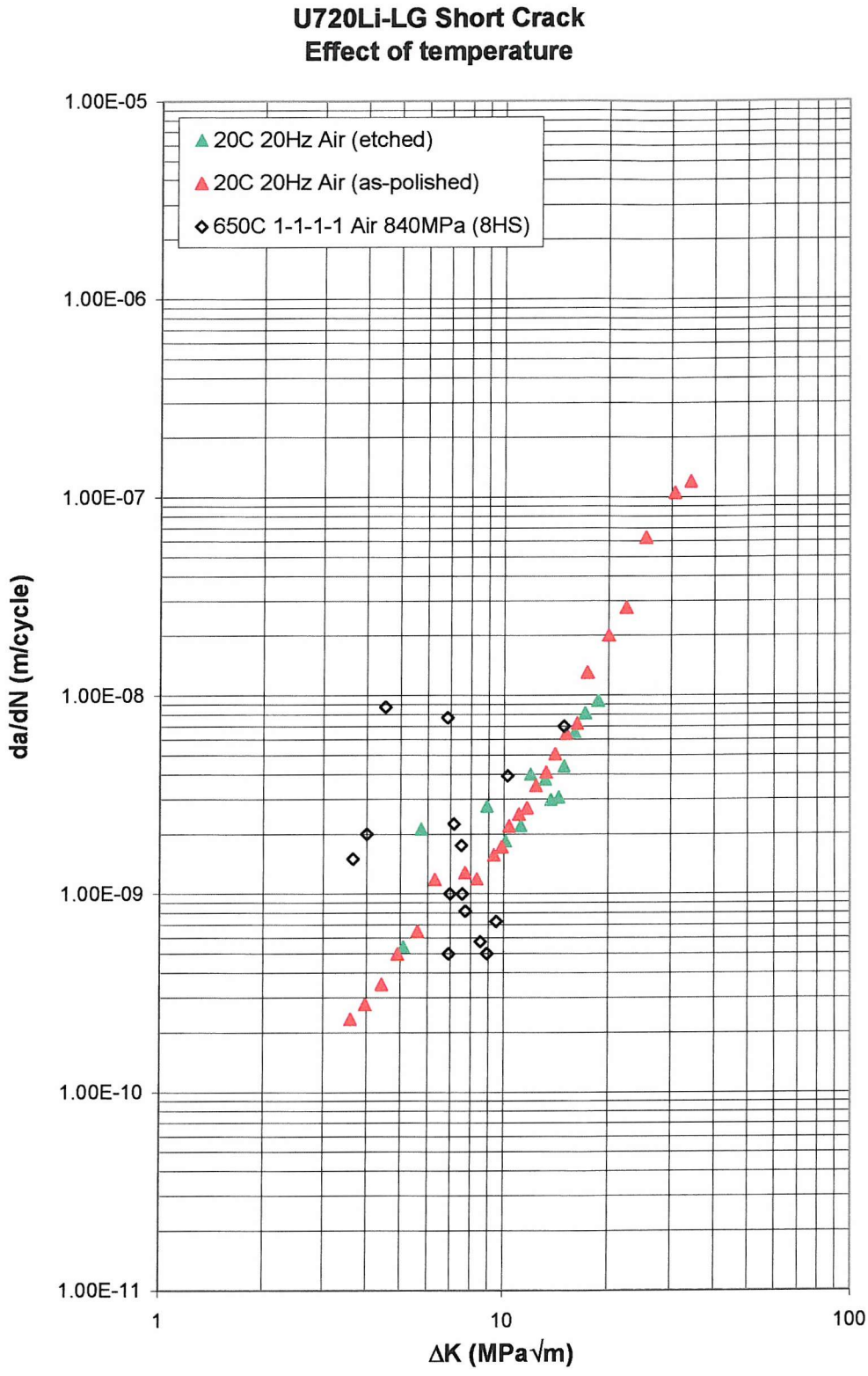

Figure 5-15b: U720Li-LG room-elevated temperature short crack comparison.

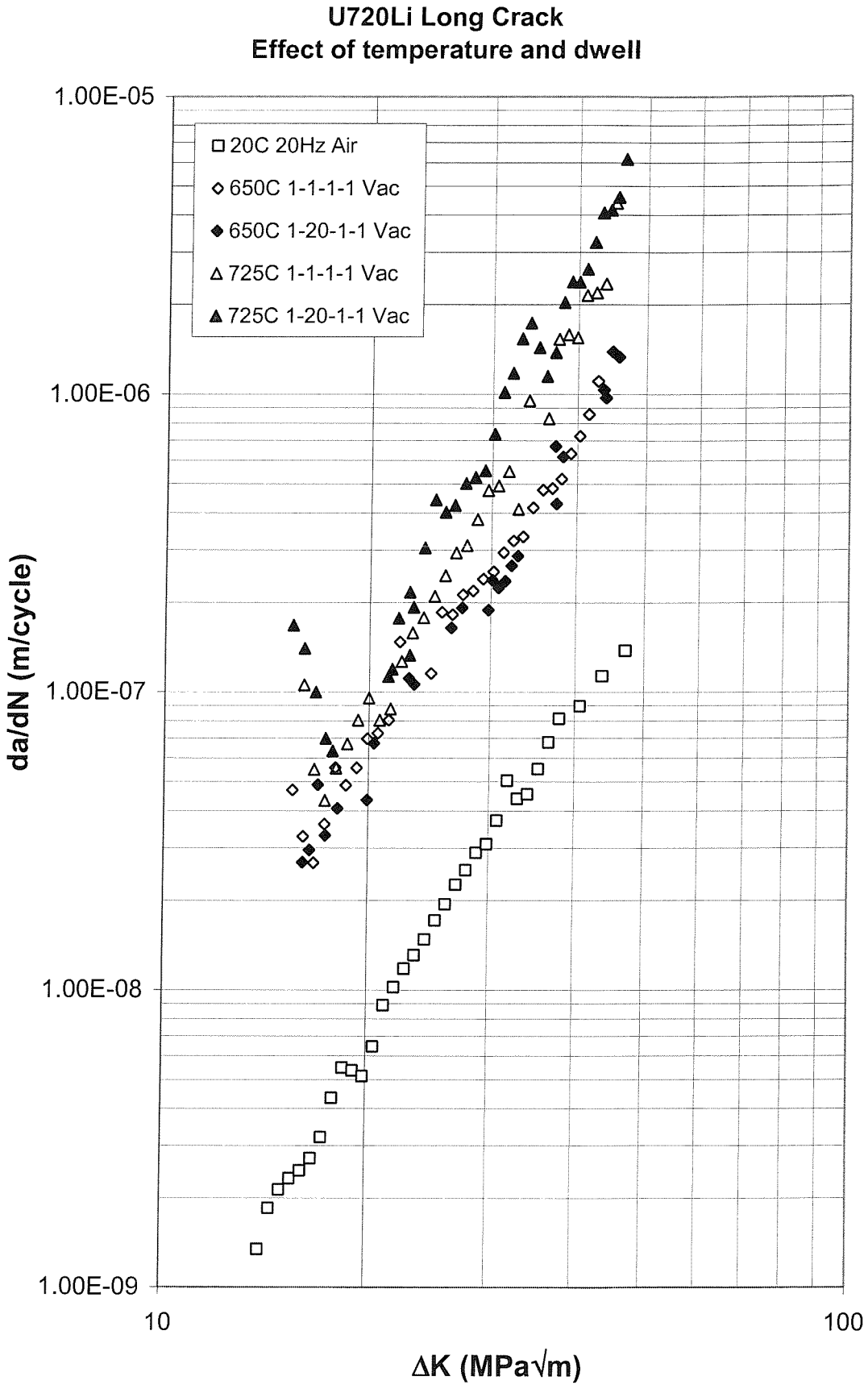

Figure 5-16a: U720Li room-elevated temperature long crack comparison.

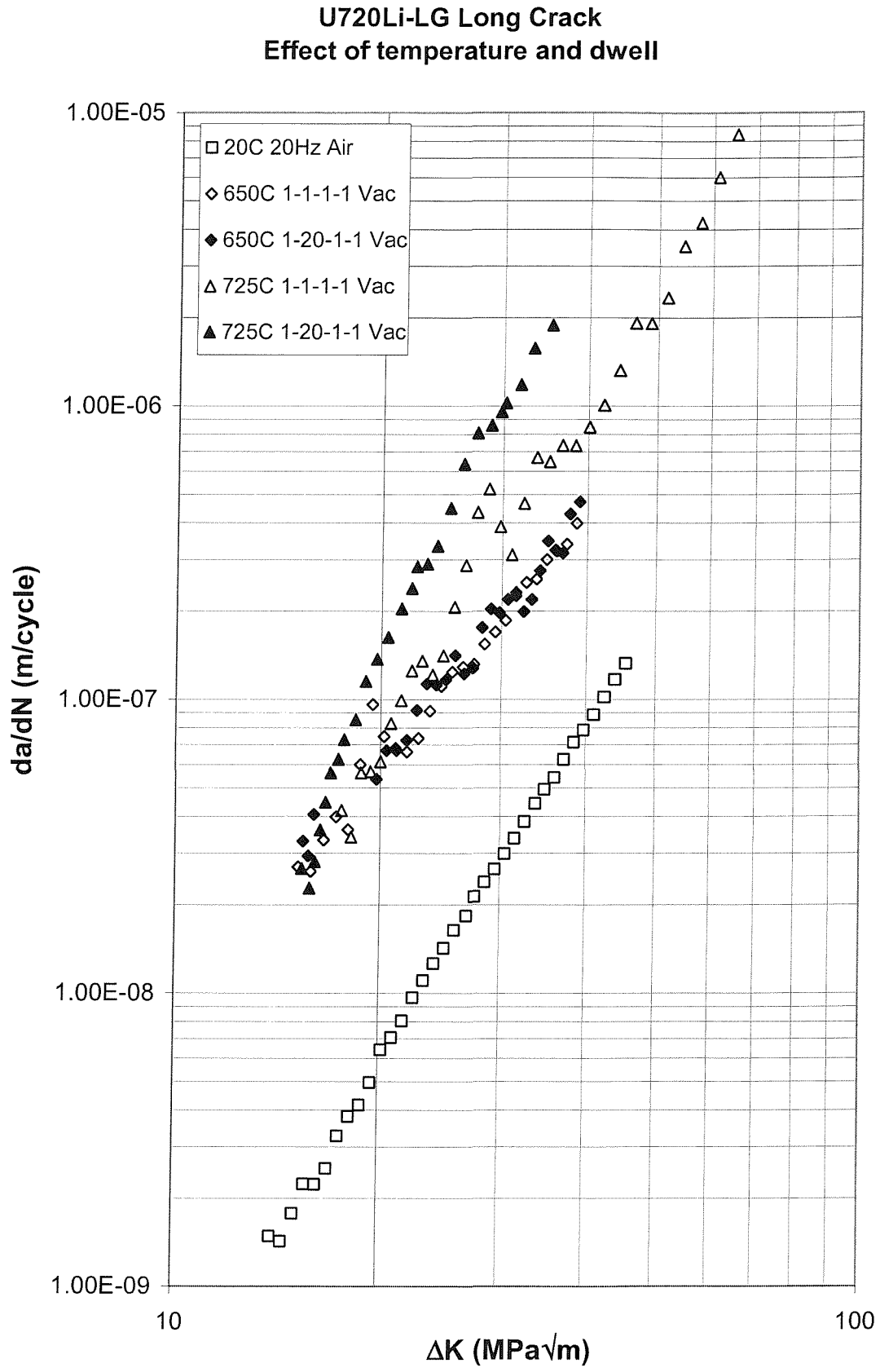

Figure 5-16b: U720Li-LG room-elevated temperature long crack comparison.

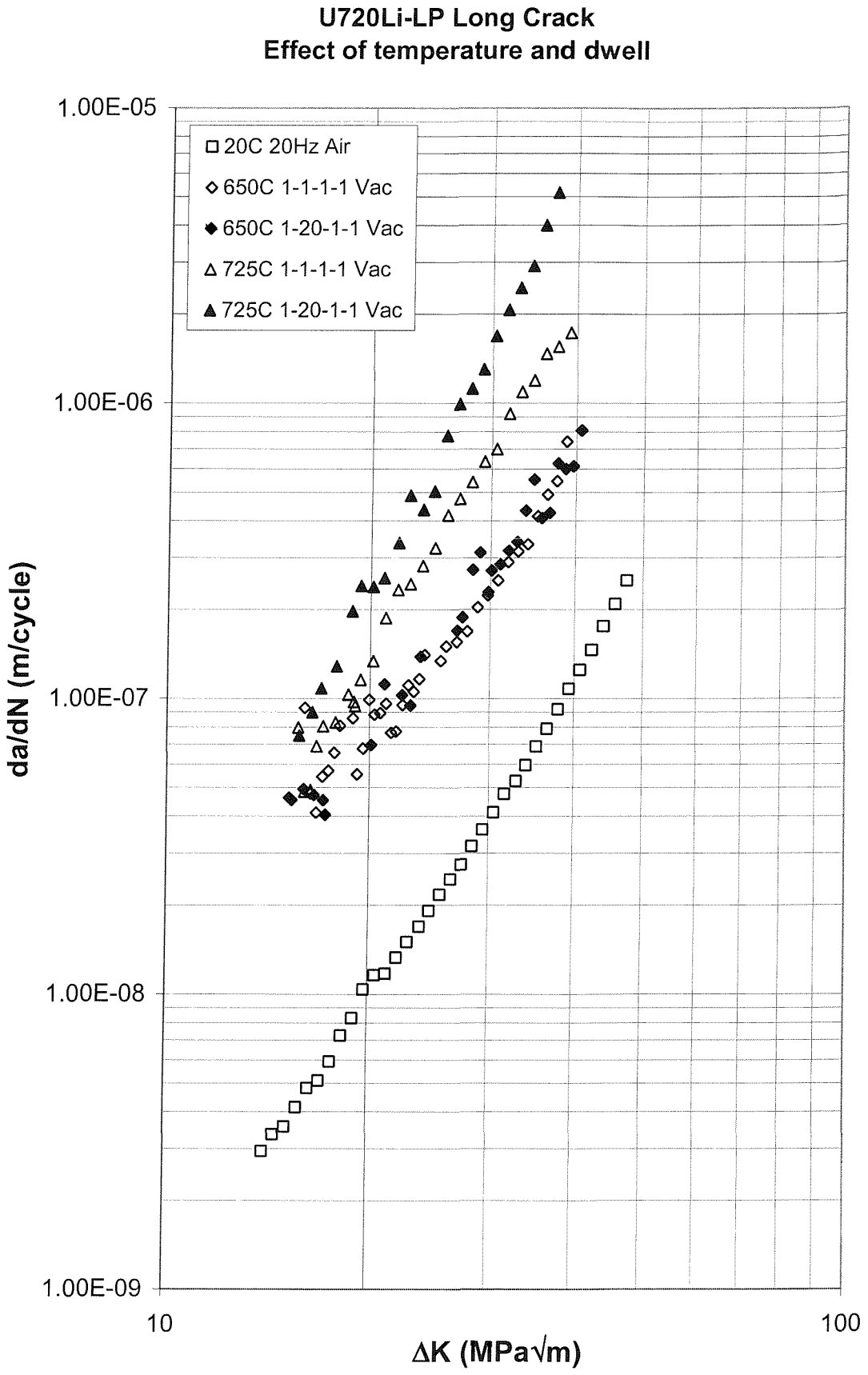

Figure 5-16c: U720Li-LP room-elevated temperature long crack comparison.

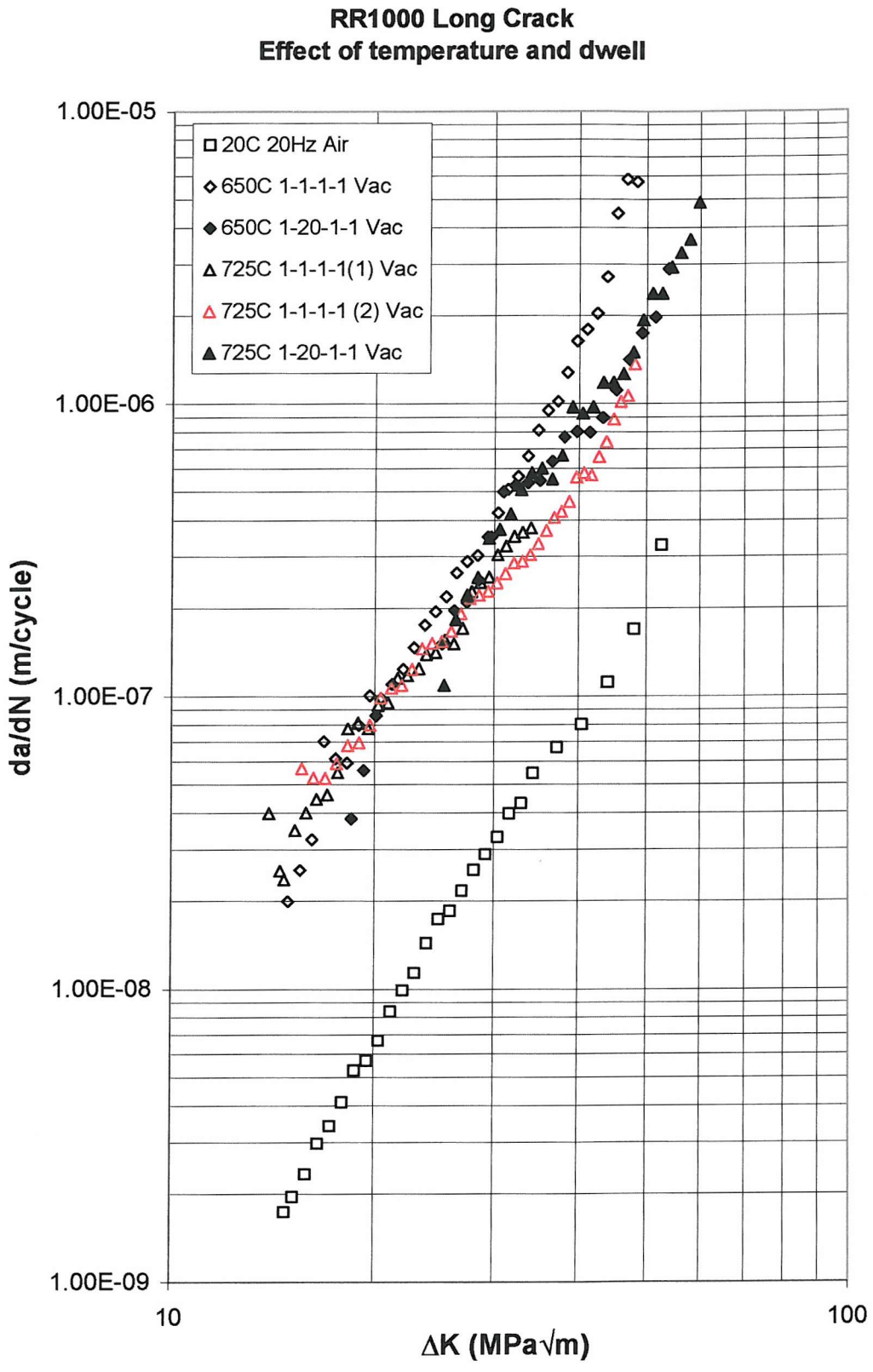

Figure 5-16d: RR1000 room-elevated temperature long crack comparison.

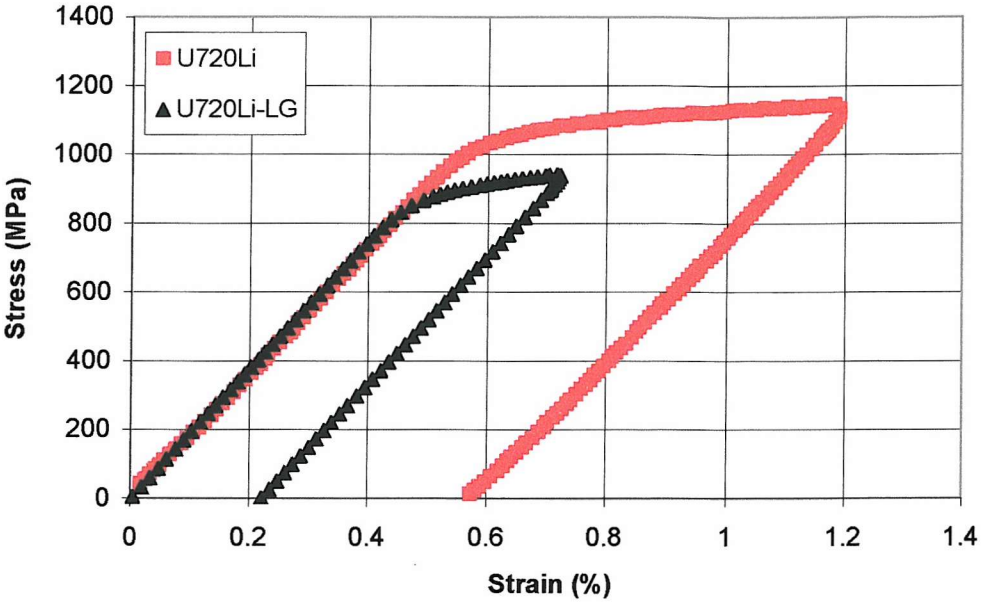

Figure 5-17: First cycle LCF data obtained at 650°C for the test materials.

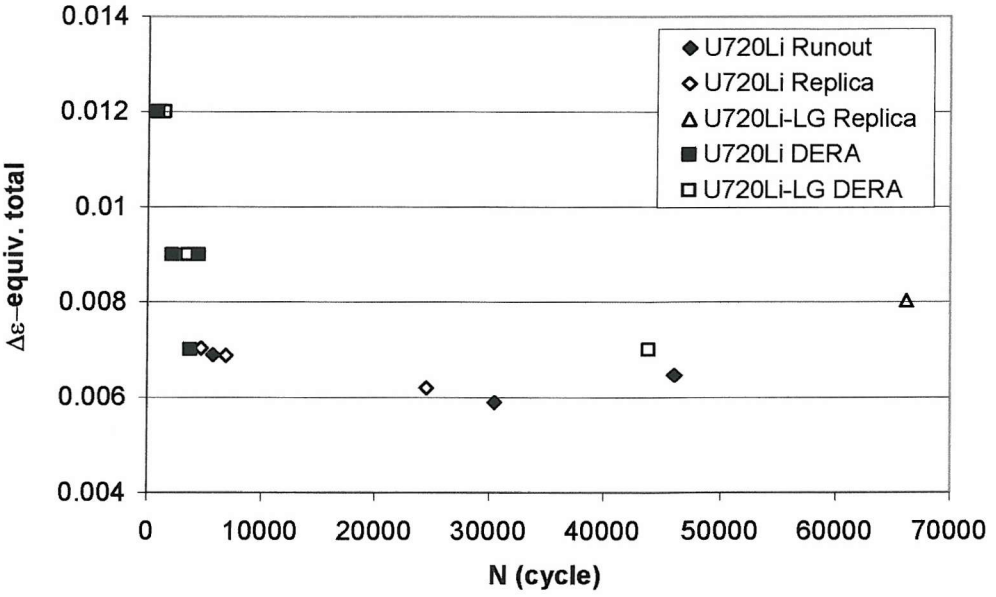

Figure 5-18: Fatigue lifetime against total equivalent strain-range in the notch root.

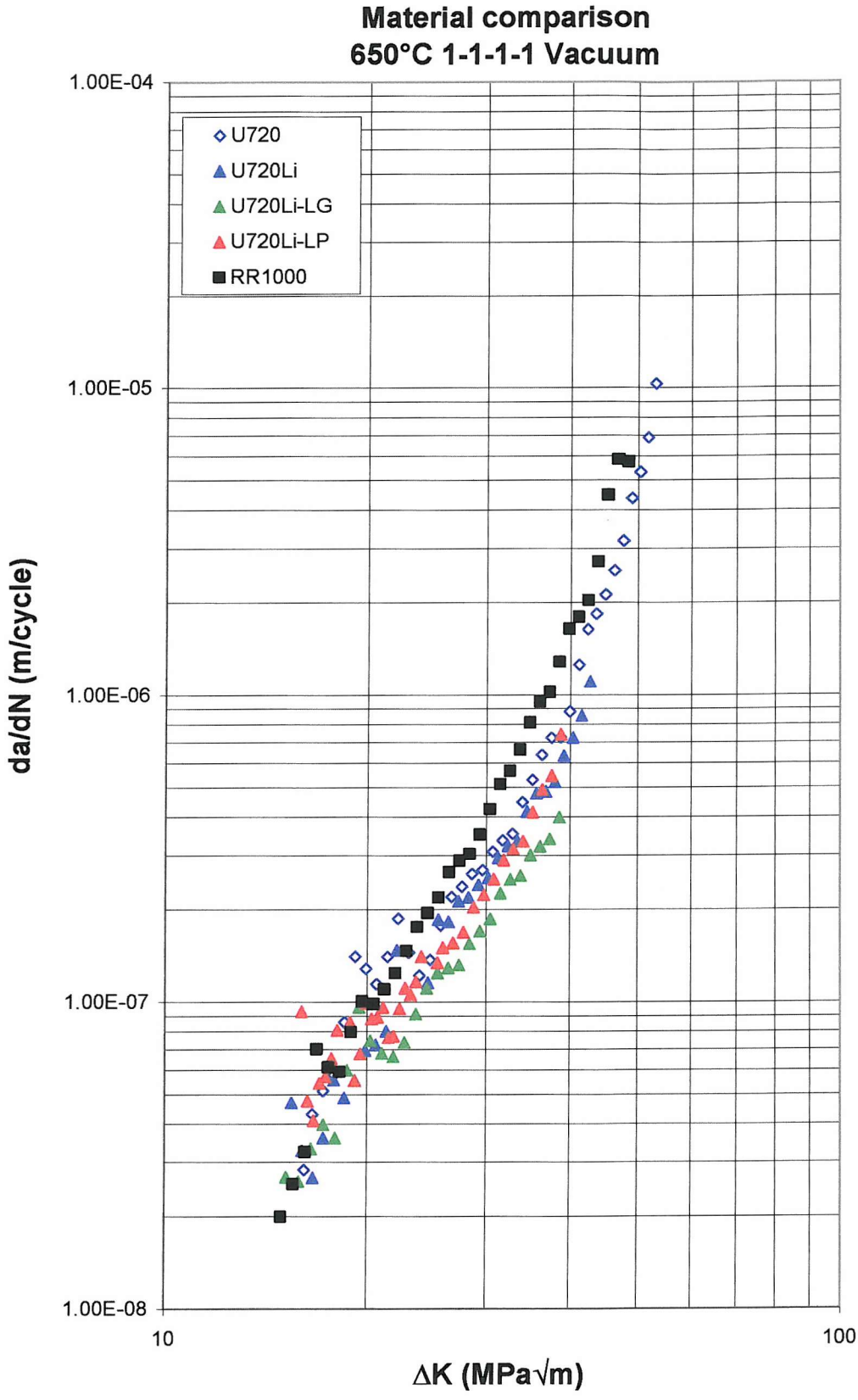

Figure 5-19a. Material comparison at 650°C 1-1-1-1 vacuum conditions.

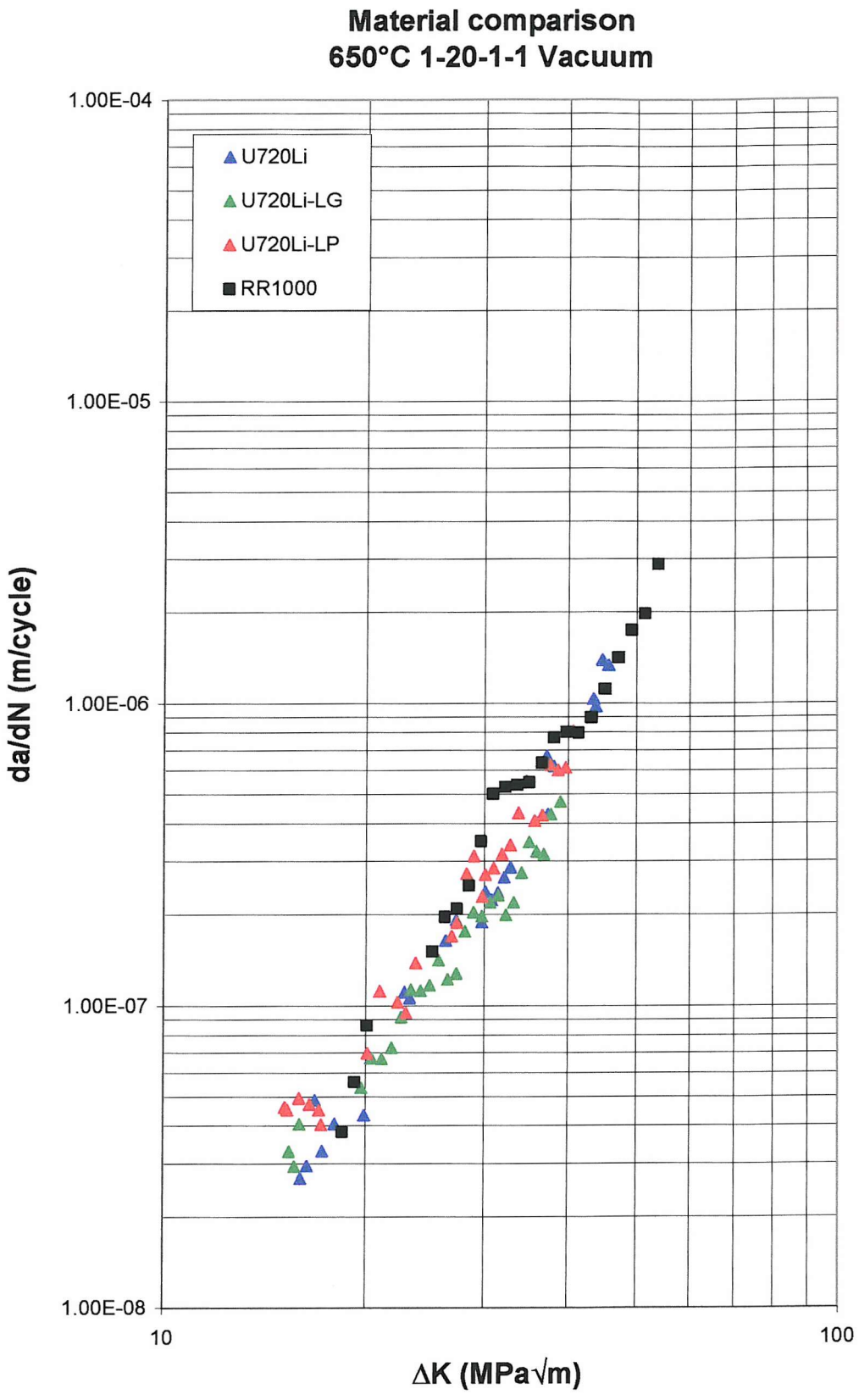

Figure 5-19b. Material comparison at 650°C 1-20-1-1 vacuum conditions.

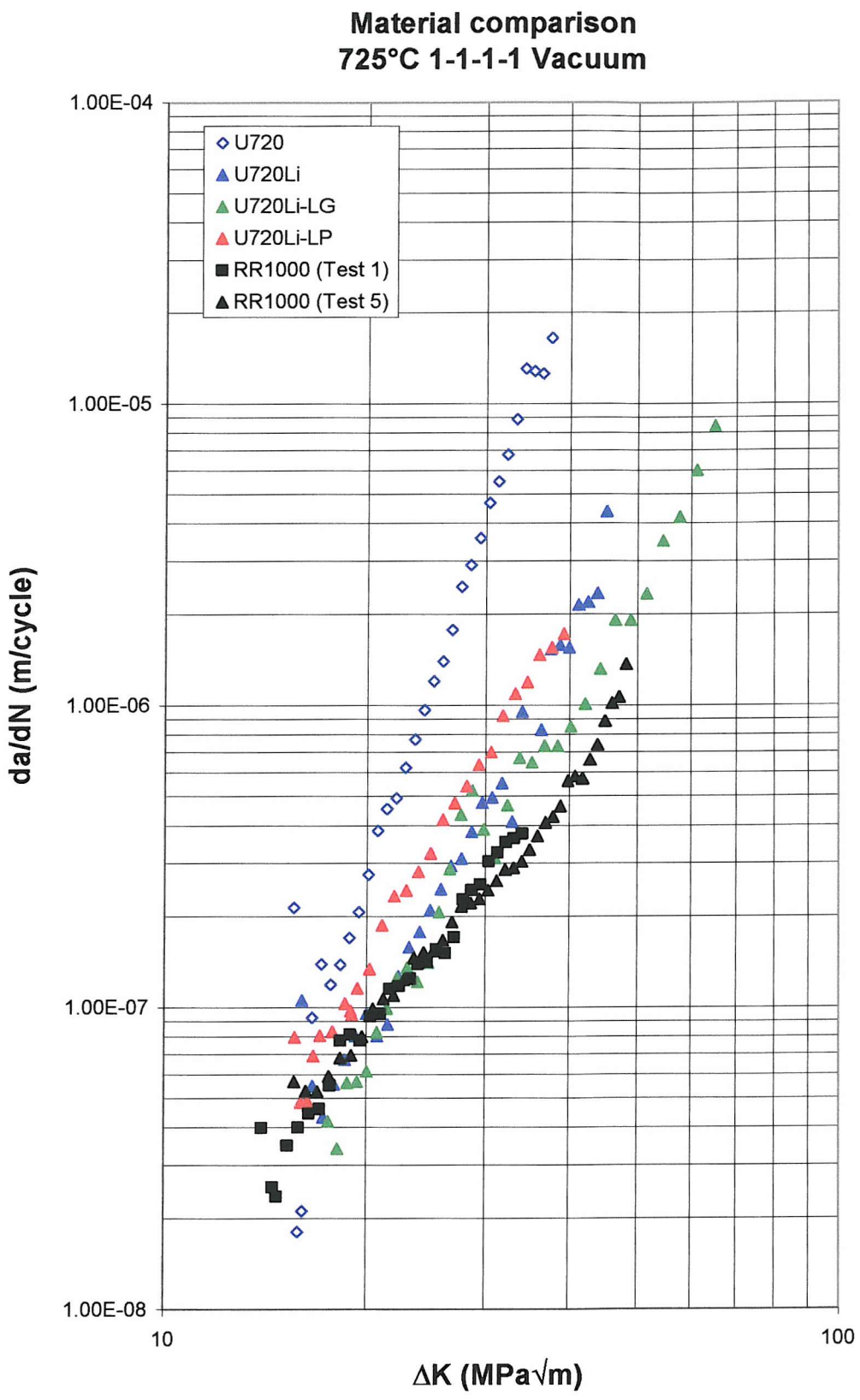

Figure 5-19c. Material comparison at 725°C 1-1-1-1 vacuum conditions.

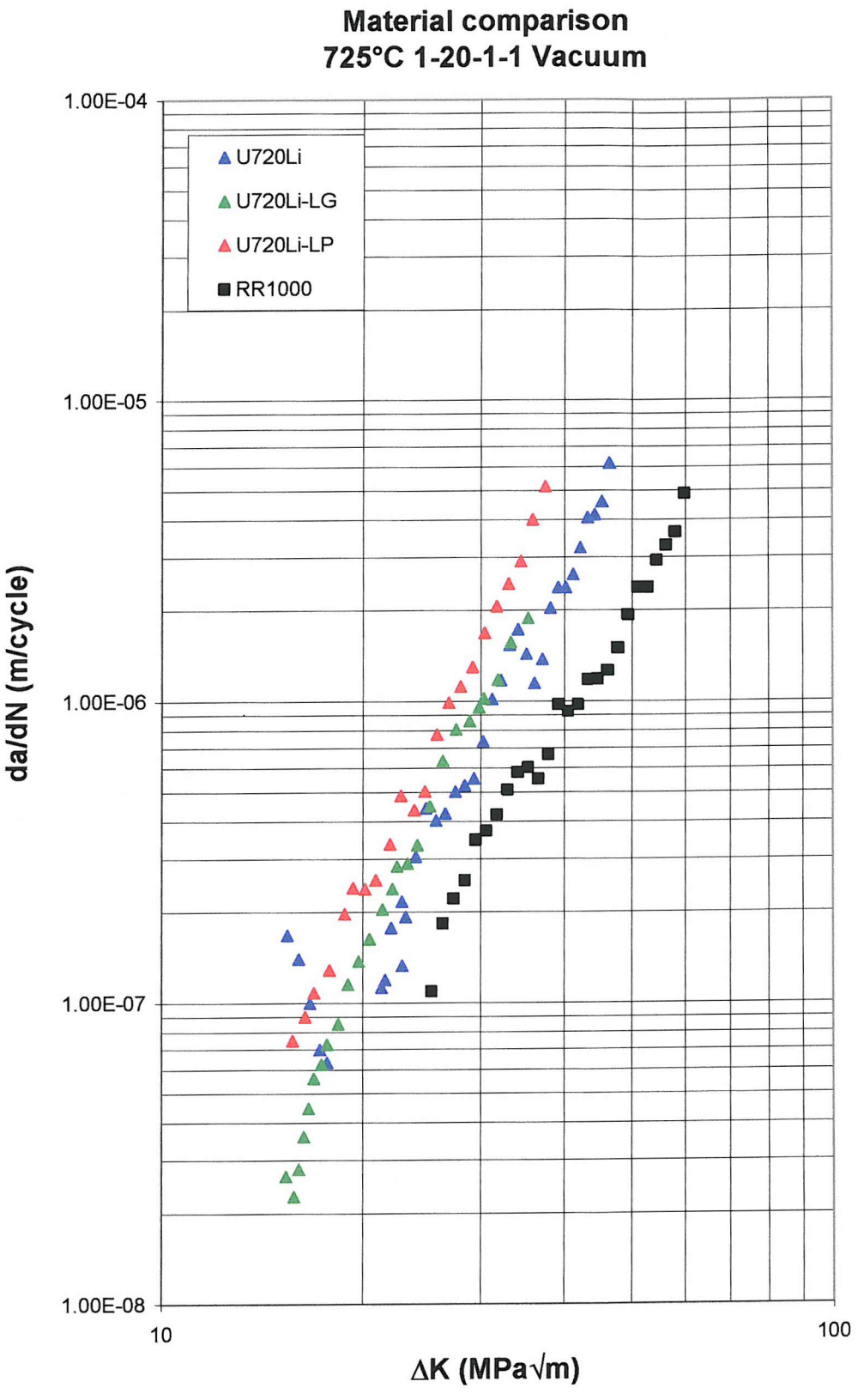

Figure 5-19d: Material comparison at 725°C 1-20-1-1 conditions.

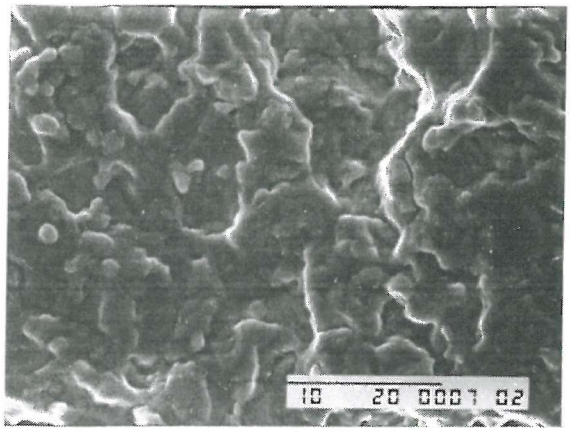

Figure 5-20a: U720Li 725°C 1-1-1-1 Vacuum; (ΔK≈17 MPa√m).

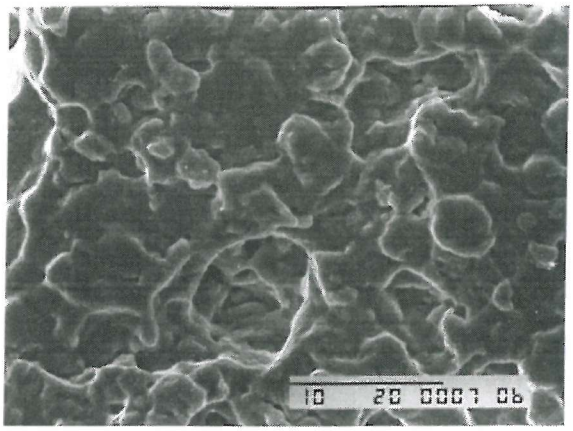

Figure 5-20b: U720Li 725°C 1-1-1-1 Vacuum; (ΔK≈35 MPa√m).

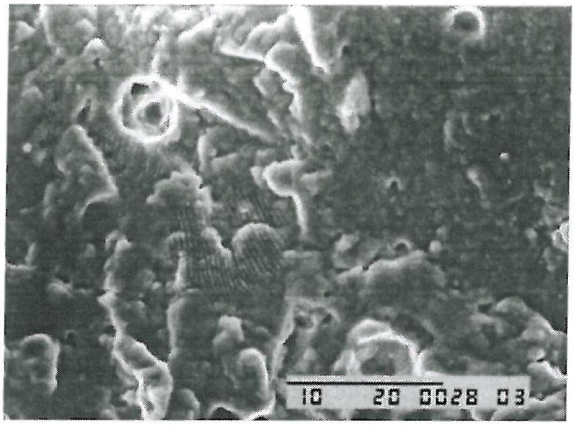

Figure 5-20c: U720Li-LG 725°C 1-1-1-1 Vacuum; (ΔK≈18 MPa√m).

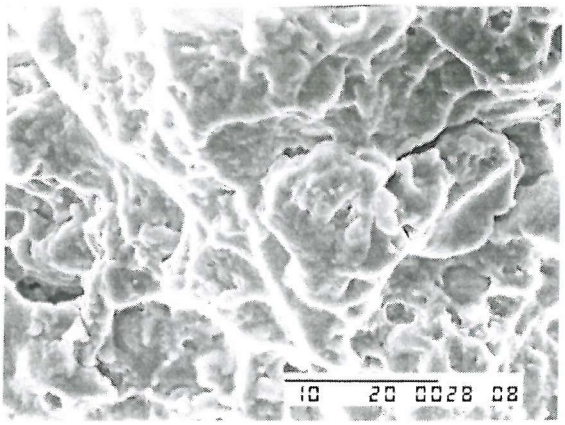

Figure 5-20d: U720Li-LG 725°C 1-1-1-1 Vacuum; (ΔK≈38 MPa√m).

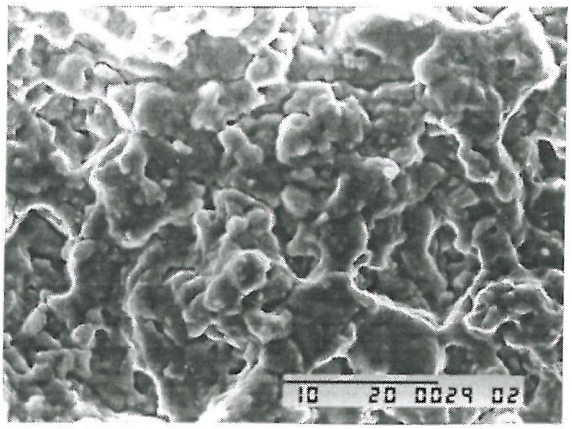

Figure 5-20e: U720Li-LP 725°C 1-1-1-1 Vacuum; (ΔK≈18 MPa√m).

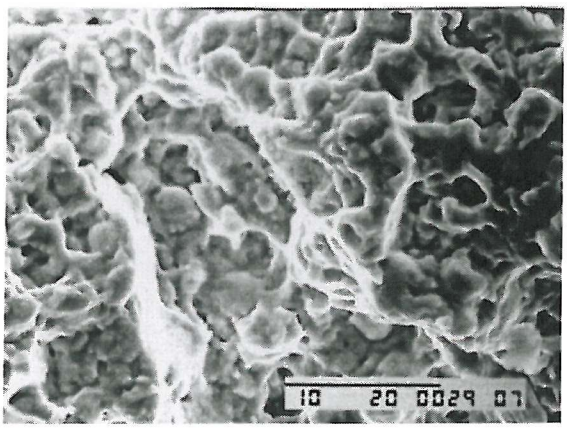

Figure 5-20f: U720Li-LP 725°C 1-1-1-1 Vacuum; (ΔK≈37 MPa√m).

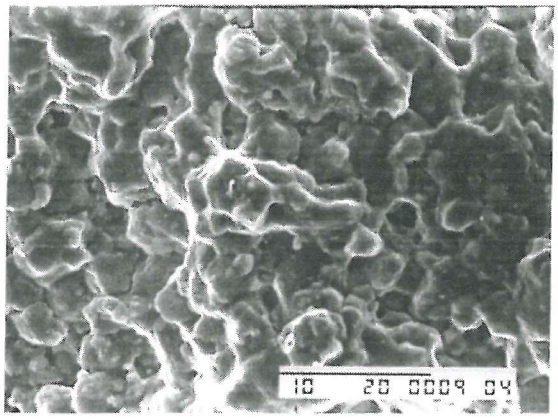

Figure 5-21a: U720Li 725°C 1-30-1-1 Vacuum; ($\Delta K \approx 17$ MPa$\sqrt{m}$).

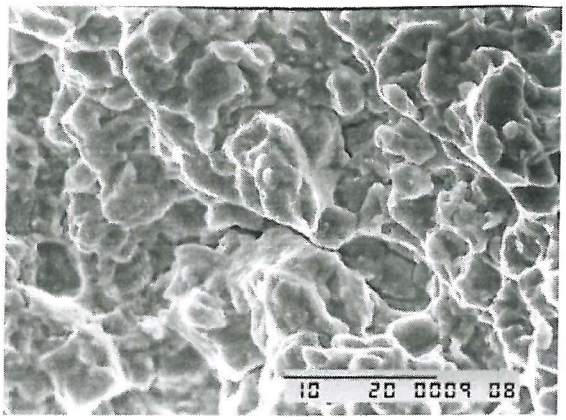

Figure 5-21b: U720Li 725°C 1-30-1-1 Vacuum; ($\Delta K \approx 35$ MPa$\sqrt{m}$).

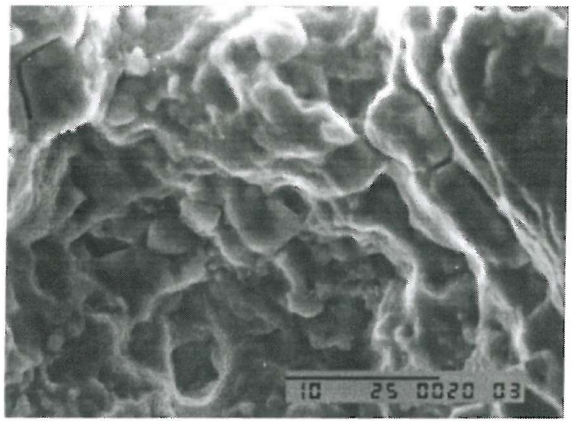

Figure 5-21c: U720Li-LG 725°C 1-20-1-1 Vacuum; ($\Delta K \approx 17$ MPa$\sqrt{m}$).

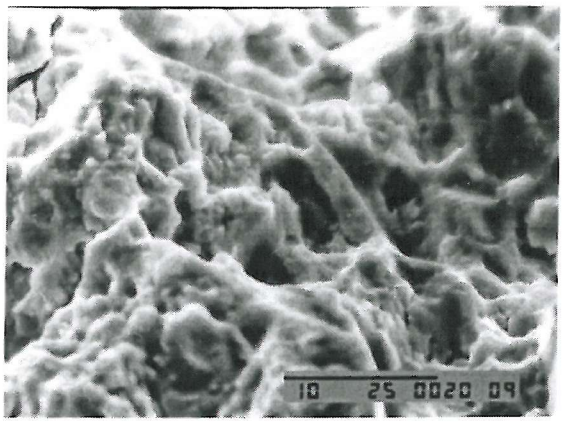

Figure 5-21d: U720Li-LG 725°C 1-20-1-1 Vacuum; ($\Delta K \approx 35$ MPa$\sqrt{m}$).

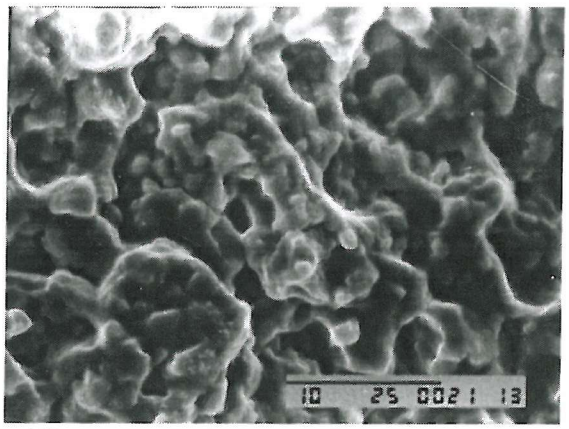

Figure 5-21e: U720Li-LP 725°C 1-20-1-1 Vacuum; ($\Delta K \approx 18$ MPa$\sqrt{m}$).

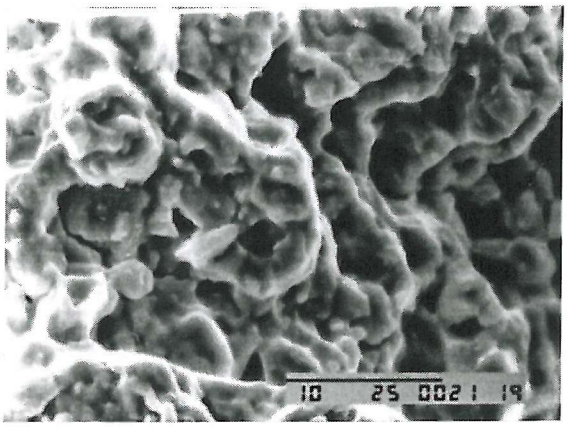

Figure 5-21f: U720Li-LP 725°C 1-20-1-1 Vacuum; ($\Delta K \approx 37$ MPa$\sqrt{m}$).

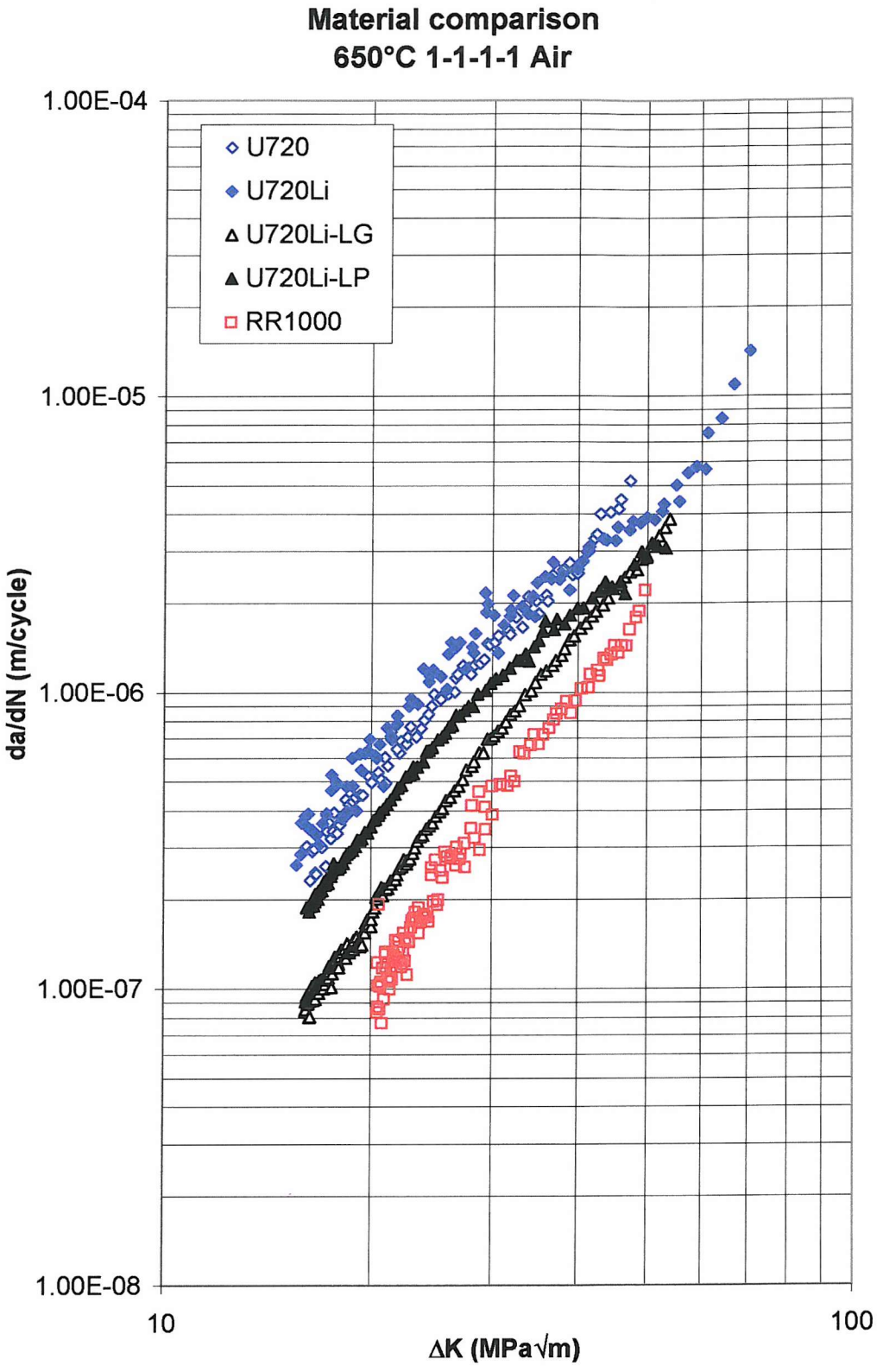

Figure 5-22a: Material comparison at 650°C 1-1-1-1 air condition.

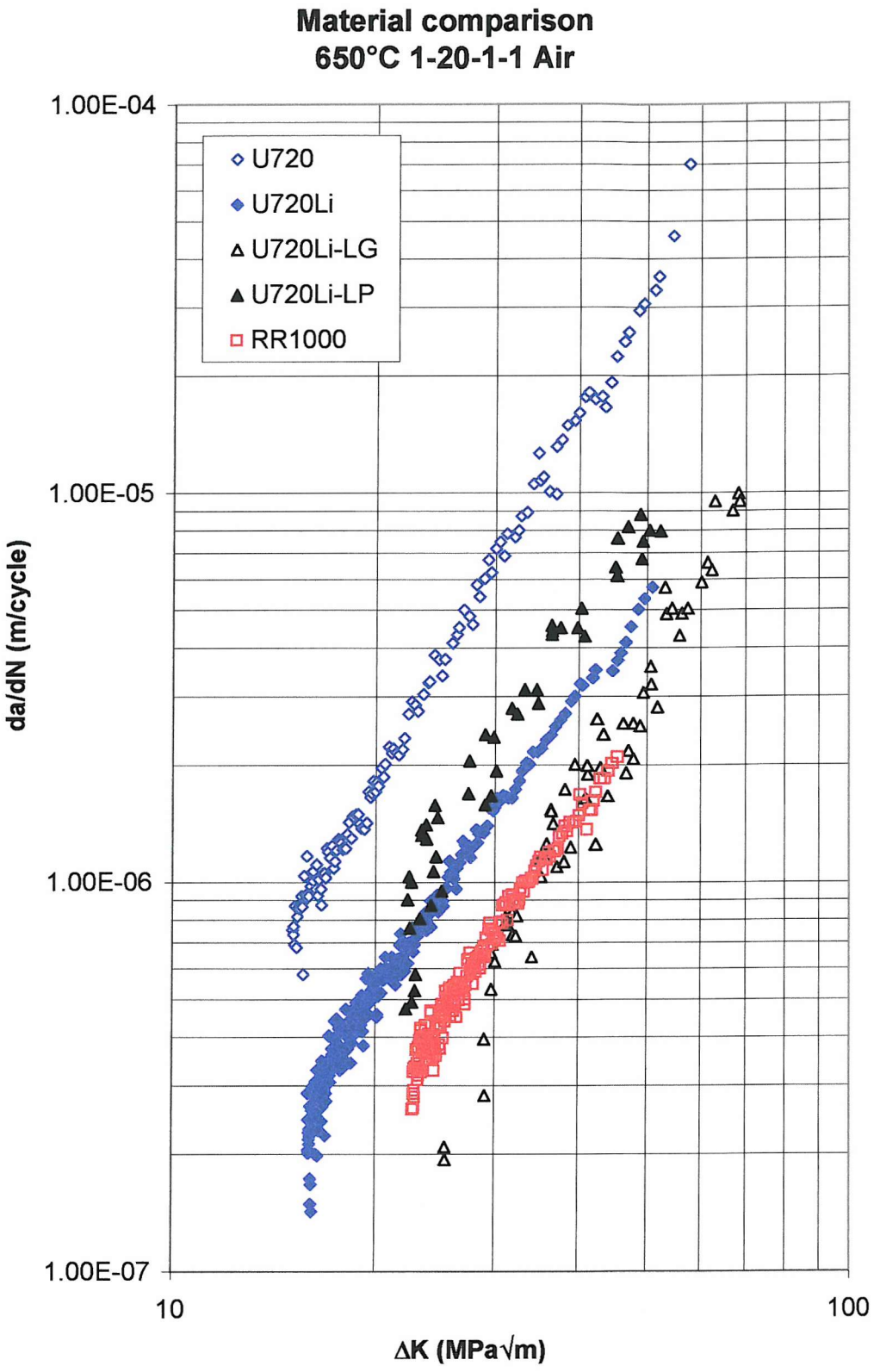

Figure 5-22b: Material comparison at 650°C 1-20-1-1 air condition.

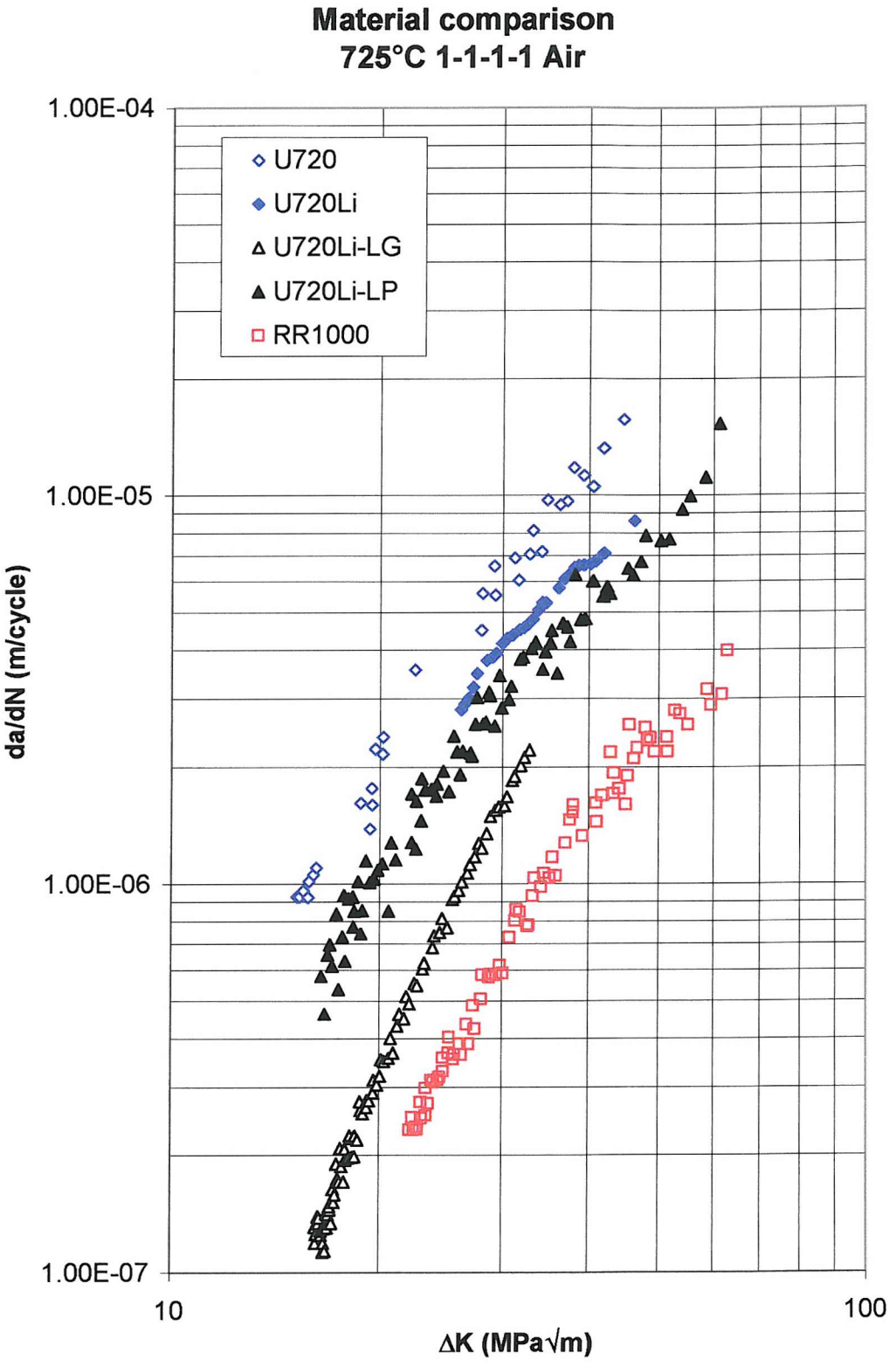

Figure 5-22c: Material comparison at 725°C 1-1-1-1 air condition.

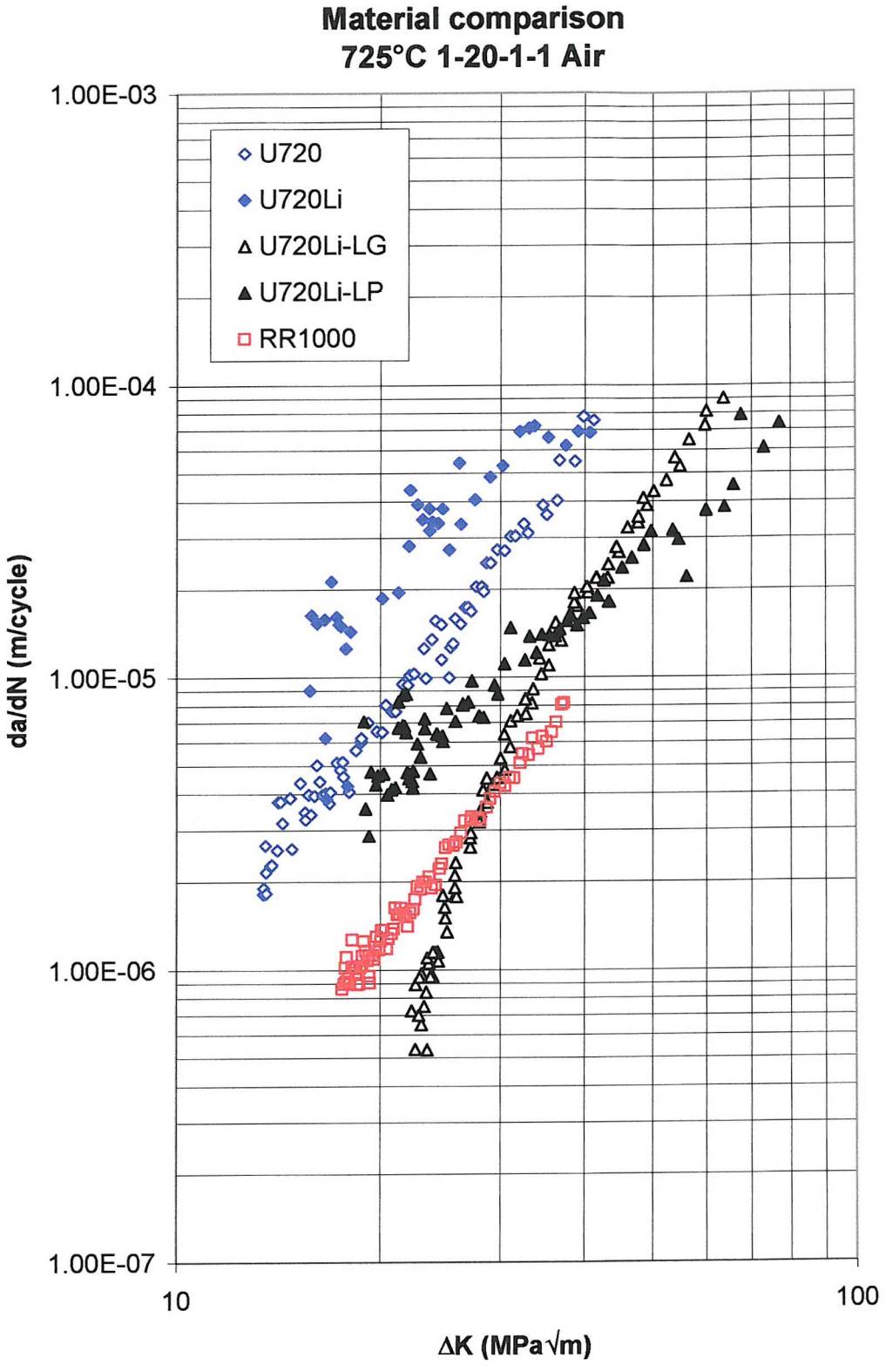

Figure 5-22d: Material comparison at 725°C 1-20-1-1 air condition.

6. Summary and Conclusion

6.1. Microstructure

Microstructural characterisation work has revealed the microstructural characteristics of all the test materials. These include the grain size, primary γ' size and volume fraction, as well as the sizes of coherent secondary and tertiary γ' precipitates. The total volume fraction of coherent γ' as well as the volume fractions of secondary and tertiary γ' expected in each material has also been computed using Thermo-calc predictions and the volume fraction of primary γ' observed in each material. The grain size and the volume fraction of primary γ' precipitates of the materials are generally consistent with the solutionising temperature used. The secondary and tertiary γ' precipitate sizes are also consistent with the cooling rates used for the materials during cooling from solution temperature. To summarise, a consistent explanation can be put forward for the observed microstructural characteristics based on respective processing routes. Differences in the microstructures arise from the different parameters used during the heat treatment routes, in addition to the closeness to which these parameters are followed during the manufacturing process.

The microstructure of the materials has been physically represented in a simple geometrical array based on the measured and calculated quantities of the microstructural characteristics. The grains and primary γ' precipitates were represented by elongated hexagons with primary γ' precipitates occupying the six corners of larger hexagons representing the grains. The secondary and tertiary γ' precipitates were represented as circular objects and were placed in the model such that one precipitate is surrounded by six other precipitates similar to the arrangement of atoms in a close-packed plane.

The calculated microstructural parameters of the grains and primary γ' precipitates in the geometrical array model are similar to the trends of the measured values of corresponding microstructural parameters. The volume fraction of primary γ' precipitates which were calculated according to the sizes of the grains and primary γ' precipitates in the model and the assumed primary γ' precipitate arrangement in the model appear to be close to the measured value for all materials except U720Li-LP. The discrepancy between the calculated and measured values of the primary γ' precipitate volume fraction of U720Li-LP may indicate that the primary γ' precipitates in U720Li-LP are distributed differently along the grain boundaries compared to other materials. Calculations of secondary and tertiary γ' precipitate spacing have also been carried out. The coherent γ' precipitate spacing was noted to scale with the volume fraction and size of coherent γ' precipitates in the materials.

6.2. Room temperature tests

In the room temperature short crack tests, U720Li-LP exhibits the longest overall fatigue lifetime, followed by RR1000, U720Li-LG and U720Li. The overall fatigue lifetime of the materials are reflected in the short crack growth rates vs. ΔK plots. Short crack growth rates of U720Li-LP and RR1000 appear similar or slightly lower compared to U720Li-LG, while the average short crack growth rates in U720Li are highest amongst the materials tested in the study. In the room temperature long crack tests, the lowest ΔK_{th} was observed in U720Li-LP (~6.2 MPa$\sqrt{m}$), while in RR1000, U720Li and U720Li-LG higher ΔK_{th} were observed, in the region of 7.5 MPa$\sqrt{m}$ to 8.5 MPa$\sqrt{m}$. In terms of crack growth rates, RR1000, U720Li and U720Li-LG exhibit approximately similar crack growth rates, while U720Li-LP shows higher crack growth rates especially in the near-threshold ΔK region.

Crack initiation was noted from porosity/defects and slip band cracking at room temperature. After crack initiation, short crack propagation occurred in stage I mode at short crack lengths and stage II mode at larger crack lengths. Long crack growth at room temperature in air occurred in stage I mode at low and near-threshold ΔK and stage II mode at higher ΔK. Comparison of room temperature long crack and short crack behaviour revealed pure stage I crack growth in the short crack tests when the monotonic plastic zone is still contained within the grain. The point of convergence of the long crack and short crack growth out curves indicates the onset of true stage II crack growth in the short crack tests when the cyclic plastic zone exceeded the largest grains in the materials. In between, crack growth occurs through a mixed stage I/stage II mode. Lifetime proportions analysis on room temperature short crack tests indicates that approximately 70% of the total life is spent in the crack initiation and pure stage I crack growth regimes in all the materials. Mixed stage I/stage II crack growth mode accounts for approximately another 15% of the life after the end of pure stage I crack growth and the onset of pure stage II crack growth at approximately 85% of the life takes up the remainder of the fatigue life in the materials. Life of the materials in the room temperature short crack tests are thus shown to be dominated by crack initiation and early crack growth through stage I crack growth mode.

U720Li-LP and RR1000 were noted to have higher crack initiation resistance due to more homogenous slip in U720Li-LP and possible contribution from the alloy chemistry of RR1000 in giving highly damage tolerant behaviour. U720Li and U720Li-LG shows much lower crack initiation resistance due to the expected planar slip behaviour in these materials.

The effects of microstructure on crack growth resistance in the stage I crack growth regime appears to be sensitive to the defect size. During stage I crack growth, higher crack growth resistance was noted in U720Li-LP during early crack growth due to a combination of precipitate cutting and looping processes in addition to crack growth resistance contribution from local

microstructure effects. Lower crack growth resistance was noted in other materials in this regime due to planar slip behaviour in the materials and lower crack growth resistance contribution from local microstructure effects. In the long crack tests, crack growth resistance was noted to be governed by a combination of intrinsic and extrinsic crack growth resistance contributions. In this regime higher crack growth resistance was noted in U720Li, U720Li-LG and RR1000 due to combinations of reversibility of slip and extrinsic crack growth resistance contributions giving higher overall crack growth resistance in these materials. U720Li-LP shows lower crack growth resistance in this regime due to lower intrinsic crack growth resistance compared to other materials which was not compensated for by the extrinsic crack growth resistance contribution from crack closure.

During stage II crack growth, the influence of local microstructure and extrinsic factors diminishes, and the effects of microstructure on crack growth in this regime are governed more solely by the intrinsic crack growth resistance of the materials. All the materials show relatively similar crack growth resistance except U720Li-LP which shows marginally lower crack growth resistance compared to other materials. The marginally lower intrinsic crack growth resistance in U720Li-LP may be related to the combination of precipitate cutting and looping processes in the material.

Different trends in the crack growth resistance and planarity of slip of the materials were noted when comparing the crack growth resistance of the materials in the long crack and short crack tests at room temperature. The difference in crack growth resistance trends is attributed to the different effects of microstructure on crack growth resistance in the different crack growth regimes, while the difference in the planarity of slip of the materials in the long crack and short crack tests is due to the difference in the crack geometry and constraints affecting the allowable slip systems being selected in the grains along the crack front.

6.3. Elevated temperature tests

High temperature short crack runout and replication tests using polished U-notch specimens have been carried out at 650°C in air using a 1-1-1-1 cycling waveform on the test materials. Stress levels between 750MPa and 850MPa (in the uncracked ligament) were applied in the tests. At 840MPa, U720Li and U720Li-LP show approximately similar fatigue lifetimes while U720Li-LG and RR1000 were noted to show significantly improved fatigue performance. Crack initiation occurred primarily from porosity, and in U720Li-LG crack initiation from grain boundary oxidation was also frequently observed. In general, all the primary cracks in the tests were initiated from porosity on or just below the surface. Growth of the primary cracks in the elevated temperature short crack tests was initially transgranular stage II crack growth in air followed by oxidation-assisted intergranular crack growth after 4-6 grains have been traversed by the crack.

The 4-6 grains represent the grain boundary sampling requirement necessary to set up oxidation-assisted crack growth mechanisms at the elevated test temperature.

At 650°C in vacuum, long crack growth appears to be cycle-dependent for U720Li and its variants. Increasing crack growth rates were noted for long crack tests of U720Li and its variants in vacuum with an increase in temperature to 725°C and imposition of dwell at 725°C due to increasing crack growth contribution from creep deformation which is a time-dependent process. For RR1000, elevated temperature long crack vacuum tests indicate trends that are different from U720Li and its variants in that an imposition of dwell at 650°C and an increase in temperature from 650°C to 725°C in the 1-1-1-1 condition gave progressively lower crack growth rates. Imposition of dwell at 725°C in vacuum gave higher crack growth rates compared to the 725°C 1-1-1-1 condition as expected. The behaviour of RR1000 in the long crack vacuum tests was attributed to stress relaxation giving reduced crack growth driving force.

The RR1000 long crack tests in air showed increasing crack growth rates with increase in temperature and/or dwell due to increased oxidation attack and creep deformation. The effect of imposition of dwell was noted to be more marked at 725°C compared to at 650°C as the detrimental effects of oxidation attack and creep deformation are more severe with imposition of dwell at higher temperature. The m-values of the air tests are relatively similar, suggesting crack growth is dominated by the same crack growth mechanism, i.e. crack growth due to a combination of oxidation attack and creep deformation.

Under similar temperature and dwell, long crack tests conducted in air all show higher crack growth rates compared to tests conducted in vacuum. The higher crack growth rates in air were attributed to increased contributions of oxidation to crack growth in air. The crack growth rates of the air and vacuum tests as well as the m-values of the air and vacuum growth out curves indicate that oxidation is the dominating factor in the crack growth mechanisms of the air tests.

The results of the elevated temperature short crack tests and the 650°C 1-1-1-1 long crack air data indicate similar fatigue resistance trends in RR1000 and U720Li and its variants, i.e. increasing fatigue resistance from U720Li to U720Li-LP to U720Li-LG and RR1000. Comparison of long crack and short crack behaviour at 650°C in air for U720Li and U720Li-LG indicates relatively similar crack growth behaviour of the long and short crack tests with the long and short crack growth curves collapsing relatively close to one another. The similar crack growth behaviour is expected due to similarities in the crack growth mechanisms in the short crack and long crack tests at elevated temperature in air.

In the elevated temperature long crack tests in vacuum, U720Li-LG is consistently showing the lowest crack growth rates amongst the test materials. The crack growth rates of U720Li and

U720Li-LP at 650°C were approximately similar to each other but were slightly higher than the crack growth rates of U720Li-LG, while RR1000 exhibits the highest crack growth rates amongst all the test materials at 650°C. At 725°C however, a different picture emerges in that U720Li-LP shows the highest crack growth rates amongst the test materials. The crack growth rates of U720Li and U720Li-LG are slightly lower but relatively similar, and RR1000 generally shows the lowest crack growth rates at 725°C compared to U720Li and its variants. In the elevated temperature long crack tests in air, RR1000 and U720Li-LG generally show lower crack growth rates compared to U720Li and U720Li-LP.

Elevated temperature crack initiation and growth resistance was generally noted to be higher in U720Li-LG and RR1000 compared to U720Li and U720Li-LP. The improved fatigue crack initiation and growth resistance of U720Li-LG was attributed to the larger grains giving rise to generally higher oxidation and creep resistance, while the improved fatigue crack initiation and growth resistance of RR1000 was attributed to stress relaxation in RR1000 which gives a reduction in the driving force for crack initiation and growth. The larger coherent γ' precipitates in U720Li-LP were generally noted to give rise to little or no improvement in elevated temperature crack growth resistance.

6.4. Optimal microstructural characteristics for improved fatigue performance

The optimal microstructural characteristics for improved fatigue performance of turbine discs are larger grains and larger size and higher volume fraction of coherent γ' precipitates. Large grains have been shown to be beneficial under most of the different test conditions conducted in the current study. In terms of the size and volume fraction of coherent γ' precipitates, generally higher crack growth resistance was noted for larger size and higher volume fraction of coherent γ' precipitates in the elevated temperature long crack tests conducted in air. Although turbine disc fatigue life has been known to be dominated by crack initiation and short crack growth at elevated temperatures, higher crack growth resistance in elevated temperature long crack tests in air will give increased confidence in the overall fatigue performance of the turbine disc alloy. Porosity control is also an important aspect as porosity was noted to be the predominant crack initiation mechanism at both room temperature and at 650°C.

7. Proposals for further work

The elevated temperature short crack tests carried out thus far represent an initial attempt to assess elevated temperature crack initiation and short crack growth behaviour. More tests are required to confirm the trends observed in the crack initiation and short crack growth behaviour in the materials as well as the relative crack initiation and growth resistance of the different microstructures. Repeat tests on U720Li-LG are necessary to confirm whether the extended life is a random occurrence or is indeed a characteristic of the U720Li-LG microstructure. Also, as none of the RR1000 specimens were failed during the elevated temperature short crack tests conducted thus far, it would be of interest in the future to conduct tests at higher loads to fail at least one RR1000 specimen in order to assess the elevated temperature crack initiation and growth behaviour in this material. Due to the random nature of fatigue, further runout tests are also necessary to establish the scatter band of fatigue lifetimes for each material. Elevated temperature short crack tests with dwell cycling or in vacuum environment may also be carried out to assess crack initiation and growth behaviour under such conditions and comparison can be made with corresponding elevated temperature long crack test results which have already been obtained.

Further work could also include EBSD analysis on room and elevated temperature test specimens to help quantify crack paths relative to microstructural features; this may help shed light on crack initiation and growth mechanisms under different test conditions. In addition, EBSD analysis is also useful to assess the crack path relative to the local grain orientations. Currently, QinetiQ Farnborough is conducting EBSD work on elevated temperature long crack test specimens to resolve the crack path relative to microstructural features and grain orientation.

In this study, an assessment of the planarity of slip in the test materials has been carried out by application of Duva's approach [44]. Hence another significant area of further work is the experimental observation of the planarity of slip of the materials to validate the results of the planarity of slip assessment. This may involve observations of the specimens fatigued at room temperature at high magnification in the SEM to assess the planarity of slip by quantifying the slip band spacing and width, as well as observations of the effect of secondary γ' precipitates on the planarity of slip of the materials. Further work may involve preparation of thin foil samples of the fatigued specimens for observation in TEM for a detailed study of the deformation behaviour of the materials, i.e. dislocation-precipitate interactions.

During elevated temperature long crack tests, it was noted that crack growth has varying degrees of transgranular and intergranular crack growth depending on testing conditions. It would be useful if the proportions of transgranular and intergranular crack growth could be quantitatively assessed. One suggestion is the use of Talysurf to assess the fracture surface roughness, and from

the fracture surface roughness profiles suitable parameters to describe the proportions of transgranular and intergranular crack growth may be derived.

8. References

[1] Betteridge W., Heslop J. "The Nimonic Alloys" Edward Arnold, U.K., ISBN 0-7131-3316-3.

[2] Chang K.M. "Metallurgical control of fatigue crack propagation in alloy 718" *Superalloys 718, 625 & Various Derivatives*, pp. 447-456, 1991.

[3] Hessell S.J., Voice W., James A.W., Blackham S.A., Small C.J., Winstone M.R. "United States Patent: Nickel Alloy for Turbine Engine Components" United States Patent 5897718, 1999.

[4] Tawancy H.M., Abbas N.M., Al-Mana A.I., Rhys-Jones T.N. "Thermal stability of advanced Ni-base superalloys" *Journal of Materials Science*, vol. 29, pp. 2445-2458, 1994.

[5] King J.E. "Fatigue crack propagation in nickel-base superalloys-effects of microstructure, load ratio, and temperature" *Materials Science and Technology*, vol. 3, pp. 750-764, 1987.

[6] Barrett C.A. "The effect of variations of cobalt content on the cyclic oxidation resistance of selected Ni-base superalloys" *Procs. Alternate Alloying for Environmental Resistance, New Orleans, Louisiana, USA, 2-6 Mar. 1986*, The Metallurgical Society/AIME, pp. 211-231, 1987.

[7] Chakravorty S., West D.R.F. "Ni_3Al-Ni_3Cr-Ni_3Ta section of Ni-Cr-Al-Ta system" *Materials Science and Technology*, vol. 1, pp. 978-985, 1985.

[8] Polvani R.S., Ruff A.W., Strutt P.R. "A mechanism for metalloid strengthening of Udimet-700" *Journal of Materials Science Letters*, vol. 3, pp. 287-290, 1983.

[9] Gayda J., Gabb T.P., Miner R.V. "Fatigue crack propagation of nickel-base superalloys at 650 C" *Low Cycle Fatigue, Bolton Landing, New York, USA, 30 Sept.-4 Oct. 1985*, ASTM STP 942, pp. 293-309, 1988.

[10] Xie X.S., Xu Z.C., Dong J.X. "High temperature crack propagation and fracture of superalloys" *Acta Metallurgica Sinica (English Letters)*, vol. 12, pp. 51-58, 1999.

[11] Xie X., Ni K., Xu Z., Ling G., Wang N. "Trace element and grain size effects on high temperature fatigue, creep and creep-fatigue interaction properties in nickel-base superalloys" *Proc. Mechanical Behaviour of Materials-VI. ICM6, Kyoto, Japan, 29 July-2 Aug. 1991*, Pergamon Press plc (UK), vol.4, pp. 613-618, 1992.

[12] Clement N., Coujou A., Jouniad M., Caron, P. Kirchner H.O., Khan T. "Local order and mechanical properties of the gamma matrix of nickel-base superalloys" *Superalloys 1996, Champion, Pennsyslvania, USA, 22-26 Sept. 1996*, Minerals, Metals and Materials Society/AIME (USA), pp. 239-248, 1996.

[13] Ricks R.A., Porter A.J., Ecob R.C. "The growth of γ' precipitates in nickel-base superalloys" *Acta Metallurgica*, vol. 31, pp. 43-53, 1983.

[14] Burke M.A., Greggi J. Jr., Whitlow G.A. "The effects of Boron and Carbon on the microstructural chemistries of two wrought nickel base superalloys" *Scripta Metallurgica*, vol. 18, pp 91-94, 1984.

[15] Andrieu E., Cozar R, Pineau A. "Effect of environment and microstructure on the high temperature behavior of Alloy 718" *Superalloy 718 - Metallurgy and Applications, Pittsburgh, Pennsylvania, USA, 12-14 June 1989*, TMS, pp. 241-256, 1989.

[16] Pieraggi B.,Uginet J.F. "Fatigue and creep properties in relation with Alloy 718 microstructure" *Superalloys 718, 625, 706 & Various Derivatives, Pittsburgh, Pennsylvania, United States, 26-29 June 1994*, The Minerals, Metals & Materials Society (United States), pp. 535-544, 1994.

[17] Connolley T. "Effect of dwell on high temperature initiation and early fatigue crack growth in turbine power generation materials" PhD. 6-month report, 1999.

[18] Antolovich S.D., Jayaraman N. "Effects of environment and structural stability on the low cycle fatigue behaviour of nickel-base superalloys" *High Temperature Technology*, vol. 2, pp. 3-13, 1984.

[19] Hunt D.W., Skelton D.K., Knowles D.M. "Microstructural stability and crack growth behaviour of a polycrystalline nickel-base superalloy" *Ninth International Symposium on Superalloys, Seven Springs, PA, USA, 17-21 Sept. 2000*, Minerals, Metals and Materials Society/AIME, *Superalloys 2000*, pp. 795-802, 2000.

[20] Sims C.T., Hagel W.C. "The Superalloys" John Wiley & Sons, ISBN 0-471-79207-1.

[21] Gayda J., Miner R.V. "The effect of microstructure on 650°C fatigue crack growth in P/M Astroloy" *Metallurgical Transactions A*, vol. 14A, pp. 2301-2308, 1983.

[22] Lerch B.A., Jayaraman N., Antolovich S.D. "A study of fatigue damage mechanism in Waspaloy from 25 to 800°C" *Material Science and Engineering*, vol. 66, pp.151-166, 1984.

[23] Jackson M.P., Reed R.C. "Heat treatment of UDIMET 720Li: the effect of microstructure on properties" *Materials Science and Engineering*, A259, pp. 85-97, 1999.

[24] Mao J., Chang K.M., Yang W., Furrer D.U., Ray K., Vase S.P. "Cooling precipitation and strengthening study in powder metallurgy superalloy Rene88DT" *Materials Science and Engineering*, A332, pp. 318-329, 2002.

[25] Mao J., Chang K.M., Yang W., Ray K., Vase S.P., Furrer D.U. "Cooling precipitation and strengthening study in powder metallurgy superalloy U720Li" *Metallurgical and Materials Transactions A*, vol. 32A, pp. 2441-2452, 2001.

[26] Sinharoy S., Virro-Nic P., Milligan W.W. "Deformation and strength behavior of two nickel-base turbine disc alloys at 650C" *Metallurgical and Materials Transactions A*, vol 32A, pp. 2021-2032, 2001.

[27] Albrecht J. "Comparing fatigue behaviour of titanium and nickel-based alloys" *Materials Science and Engineering*, A263, pp. 176-186, 1999.

[28] Antolovich S.D., Jayaraman N. "Metallurgical instabilities during the high temperature low cycle fatigue of nickel-base superalloys" *Material Science and Engineering*, vol. 57, L9-L12, 1982.

[29] Antolovich S.D., Rosa E., Pineau A. "Low cycle fatigue of Rene 77 at elevated temperatures" *Materials Science and Engineering*, vol. 47, pp. 47-57, 1981.

[30] Hide N.J., Reed P.A.S., Pang H.T. "A fundamental investigation of the effect of dwell time, grain size and environment on the high temperature fatigue and creep-fatigue resistance of turbine disc alloys" Final Report, 2000.

[31] Koul A.K., Wallace W. "Microstructural changes during long time service exposure of Udimet 500 and Nimonic 115" *Metallurgical Transactions A*, vol. 14A, pp. 183-189, 1983.

[32] Zheng, D. Ghonem H. "Influence of prolonged thermal exposure on intergranular fatigue crack growth behavior in alloy 718 at 650°C" *Metallurgical Transactions A*, vol. 23A, pp. 3169-3171, 1992.

[33] Cadek J., Pahutova M., Sustek V., Dlouhy A. "On the role of recovery in creep of precipitation-strengthened polycrystalline nickel-base alloys" *Materials Science and Engineering*, A238, pp. 391-398, 1997.

[34] Zamrik S.Y., Davis D.C. "Creep-fatigue damage mechanisms and life assessment of two materials: Type 316 Stainless Steel and Waspaloy" *Life Assessment & Repair: Technology for Combustion Turbine Hot Section Components, Phoenix, Arizona, USA, 17-19 Apr. 1990*, ASM International, pp. 77-85, 1990.

[35] Subramanya Sarma V., Sundararaman M., Padmanabhan K.A. "Effect of γ' size on room temperature low cycle fatigue behaviour of a nickel base superalloy" *Materials Science and Technology*, vol. 14, pp. 669-675, 1998.

[36] Valsan M., Sastry D.H., Bhanu Sankara Rao K, Mannan S.L. "Effect of strain rate on the high-temperature low-cycle fatigue properties of a Nimonic PE-16 superalloy" *Metallurgical and Materials Transactions A*, vol. 25A, pp. 159-171, 1994.

[37] Reed P.A.S., Gale W.F., King J.E. "Intrinsic threshold in polycrystalline Udimet 720" *Materials Science and Technology*, vol. 9, pp. 281-287, 1993.

[38] Grabowski L., King J.E. "Modelling short crack growth behaviour in nickel-base superalloys" *Fatigue and Fracture of Engineering Materials and Structures (UK)*, vol. 15, pp. 595-606, 1992.

[39] Sundararaman M., Chen W., Singh V., Wahi R.P. "TEM investigation of gamma-prime free bands in Nimonic PE16 under LCF loading at room temperature" *Acta Metallurgica et Materialia*, vol. 38, no. 10, pp. 1813-1822, 1990.

[40] Loo-Morrey M., Reed P.A.S. "Anomalous crack shape development (tear drop cracking) in turbine disc material Udimet 720" *Materials Science and Technology*, vol. 16, pp. 133-146, 2000.

[41] Blankenship C.P. Jr, Hornbogen E., Starke E.A. Jr. "Predicting slip behaviour in alloys containing shearable and strong particles" *Materials Science and Engineering*, A169, pp. 33-41, 1993.

[42] Blankenship C.P. Jr., Starke E.A. Jr. "Mechanical behavior of double-aged AA8090" *Metallurgical Transactions A*, vol. 24A, pp. 833-841, 1993.

[43] Jata K.V., Starke E.A. Jr. "Fatigue crack growth and fracture toughness behaviour of an Al-Li-Cu alloy" *Metallurgical Transactions A*, vol. 17A, pp. 1011-1026, 1986.

[44] Duva J.M., Daeubler M.A., Starke E.A. Jr., Luetjering G. "Large shearable particles lead to coarse slip in particle reinforced alloys" *Acta Metallurgica*, vol. 36, pp. 585-589, 1988.

[45] Antolovich S.D., Jayaraman N. "The effect of microstructure on the fatigue behaviour of Ni-base superalloys" *Procs. Fatigue: Environment and Temperature Effects, Bolton Landing, Lake George, NY, 14-18 July 1980*, Plenum, NY, pp. 119-144, 1980.

[46] Nilsson J.O. "Influence of dislocation-precipitate interaction on low cycle fatigue resistance of Alloy 800 at 600°C" *Metal Science*, vol. 18, pp. 351-355, 1984.

[47] Smith R.A., Liu Y., Grabowski L. "Short fatigue crack growth behaviour in Waspaloy at room and elevated temperatures" *Fatigue and Fracture of Engineering Materials and Structures (UK)*, vol.19, pp. 1505-1514, 1996.

[48] Suresh S. "Fatigue of Materials" Cambridge University Press ISBN 0-521-57847-7.

[49] Sadananda K., Shahinian P. "A fracture mechanics approach to high temperature fatigue crack growth in Udimet 700" *Engineering Fracture Mechanics*, vol. 11, pp. 73-86, 1979.

[50] Fournier, D. Pineau A. "Low cycle fatigue behavior of Inconel 718 at 298K and 823K" *Metallurgical Transactions A*, vol. 8A, pp. 1095-1105, 1977.

[51] Goto M., Knowles D.M. "Initiation and propagation behaviour of microcracks in Ni-base superalloy Udimet 720Li" *Engineering Fracture Mechanics*, vol. 60, pp. 1-18, 1998.

[52] Miller K.J. "The short crack problem" *Fatigue of Engineering Materials and Structures (UK)*, vol. 5, pp. 223-232, 1982.

[53] Wu Z., Sun X. "Multiple fatigue crack initiation, coalescence and growth in blunt notched specimens" *Engineering Fracture Mechanics*, vol. 59, pp. 353-359, 1998.

[54] Hicks M.A., Brown C.W. "A comparison of short crack growth behaviour in engineering alloys" Fatigue 1984.

[55] Stephens R., Grabowski L., Hoeppner D.W. "In-situ/SEM fatigue studies of short crack behaviour at ambient and elevated temperature in a nickel-base superalloy" *Short Fatigue Cracks,*

Sheffield, UK, Dec. 1990, Mechanical Engineering Publications Limited (UK), ISBN 0-85298-809-5, pp. 335-348, 1992.

[56] Yates J.R., Zhang W., Miller K.J. "The initiation and propagation behaviour of short cracks in Waspaloy subjected to bending" *Fatigue and Fracture of Engineering Materials and Structures (UK)*, vol. 16, pp. 351-362, 1993.

[57] Lankford J. "The influence of microstructure on the growth of small fatigue cracks" *Fatigue and Fracture of Engineering Materials and Structures (UK)*, vol. 8, pp. 161-175, 1985.

[58] Kendall J.M., King J.E. "Short fatigue crack growth behaviour : data analysis effects" *International Journal of Fatigue*, vol. 10, pp. 163-170, 1988.

[59] Mei Z., Krenn C.R., Morris J.W.Jr. "Initiation and growth of small fatigue cracks in a Ni-base superalloy" *Metallurgical and Materials Transactions A*, vol. 26A, pp. 2063-2073, 1995.

[60] Healy J.C., Grabowski L, Beevers C.J. "Short-fatigue crack growth behaviours of alloy 718" *International Journal of Fatigue*, vol.13, pp. 133-138, 1991.

[61] Davidson D.L., Hudak S.J. Jr. "The crack-tip mechanics and growth rates of small fatigue cracks in Astroloy" *Metallurgical and Materials Transactions A*, vol. 26A, pp. 2247-2257, 1995.

[62] Boyd-Lee A., King J.E. "Short fatigue crack path determinants in polycrystalline Ni-base superalloys" *Fatigue and Fracture of Engineering Materials and Structures (UK)*, vol. 17, pp. 1-14, 1994.

[63] Stephens R.R., Grabowski L., Hoeppner D.W. "The effect of temperature on the behaviour of short fatigue cracks in Waspaloy using an in situ SEM fatigue apparatus" *International Journal of Fatigue*, vol. 14, pp. 273-282, 1993.

[64] Merrick H.F. "The low cycle fatigue of three wrought nickel-base alloys" *Metallurgical Transactions*, vol. 5, pp. 891-897, 1974.

[65] Toh S.F., Rainforth W.M. "Fatigue of a nickel base superalloy with bimodal grain size" *Materials Science and Technology*, vol. 12, pp. 1007-1014, 1996.

[66] Sanders T.H. Jr., Starke E.A. Jr. "The effect of slip distribution on the monotonic and cyclic ductility of Al-Li alloys" *Acta Metallurgica*, vol. 30, pp. 927-939, 1982.

[67] Shiozawa K., Weertman J.R. "Observation of grain boundary microcracking in a nickel base superalloy after room temperature deformation" *Scripta Metallurgica*, vol. 15, pp. 1241-1244, 1981.

[68] Stahl D.R., Mirdamadi M., Zamrik S.Y., Antolovich S.D. "Effect of temperature, microstructure, and stress state on the low cycle fatigue behavior of Waspaloy" *Low Cycle Fatigue Bolton Landing, New York, USA, 30 Sept.-4 Oct. 1985*, ASTM STP 942, pp. 728-750, 1988.

[69] Gayda J. Miner R.V. "Fatigue crack initiation and propagation in several nickel-base superalloys at 650°C" *International Journal of Fatigue*, vol. 5, pp. 135-143, 1983.

[70] Reger M., Remy L. "High temperature, low cycle fatigue of IN100 superalloy I: influence of temperature on the low cycle fatigue behaviour" *Materials Science and Engineering A*, 101, pp. 47-54, 1988.

[71] De Bussac A. "Prediction of the competition between surface and internal crack initiation in PM alloys" *Fatigue and Fracture of Engineering Materials and Structures (UK)*, vol. 17, pp. 1319-1325, 1994.

[72] Plumtree A., O'Connor B.P.D. "Influence of microstructure on short fatigue crack growth" *Fatigue and Fracture of Engineering Materials and Structures (UK)*, vol.14, pp. 171-184, 1991.

[73] Choe S.J., Stoloff N.S., Duquette D.J. "Effects of temperature and hold times on low cycle fatigue of Astroloy" *Strength of Metals and Alloys (ICSMA 7). Vol. 2, Montreal, Canada, 12-16 Aug. 1985, Proc. of the 7th Int. Conf.*, Pergamon Press Ltd., pp. 1291-1298, 1986.

[74] Reed P.A.S., Hachette F., Thakar D., Connolley T., Starink M.J. "Creep-fatigue initiation and early crack growth in Inconel 718" *Progress in Mechanical Behaviour of Materials: Proceedings of the Eighth International Conference on the Mechanical Behaviour of Materials, ICM8, Victoria, British Columbia, Canada, 16-21 May 1999,* vol. 1, pp. 418-423, 1999.

[75] Liu Y., Smith R.A. "High temperature short fatigue crack and creep-fatigue crack propagation in a nickel-based superalloy" *Procs. 6th Int. Conf. on Creep and Fatigue: Design & Life Assessment at High Temperature, 15-17 Apr. 1996*, Mechanical Engineering Publications Ltd. (UK), pp. 261-270, 1996.

[76] Rosenberger A.H., Ghonem H. "High temperature elastic-plastic small crack growth behaviour in a nickel-base superalloy" *Fatigue and Fracture of Engineering Materials and Structures (UK)*, vol. 17, pp. 509-521, 1994.

[77] Zabett A., Plumtree A. "Microstructural effects on the small fatigue crack behaviour of an aluminium alloy plate" *Fatigue and Fracture of Engineering Materials and Structures (UK)*, vol.18, pp. 801-809, 1995.

[78] Isomoto T., Stoloff N.S. "Effect of microstructure and temperature on high cycle fatigue of powder metallurgy Astroloy" *Materials Science and Engineering*, A124, pp. 171-181, 1990.

[79] Arslan G., Doruk M "Cyclic crack growth behaviour of two nickel base turbine disc alloys" *Journal of Materials Science*, vol. 33, pp. 2653-2658, 1998.

[80] Connolley T., Reed P.A.S., Starink M.J. "Short crack initiation and growth at 600C in notched specimens of Inconel718" *Materials Science and Engineering*, A340, pp. 139-154, 2003.

[81] Davidson D.L., Chan K.S. "The crystallography of fatigue crack initiation in coarse grained Astroloy at 20°C" *Acta Metallurgica*, vol. 37, pp 1089-1097, 1989.

[82] Gerard D.A., Koss D.A. "Porosity and crack initiation during low cycle fatigue" *Materials Science and Engineering*, A129, pp. 77-85, 1990.

[83] Lindstedt U., Karlsson B., Masini R. "Influence of porosity on deformation and fatigue behaviour of P/M austenitic stainless steel" *International Journal of Powder Metallurgy*, vol. 33, pp. 49-61, 1997.

[84] Vecchio R.S., Hertzberg R.W. "A rationale for the 'apparent anomalous' growth behaviour of short fatigue cracks" *Engineering Fracture Mechanics*, vol. 22, pp. 1049-1060, 1985.

[85] Soniak F., Remy L. "Behaviour of long and short fatigue cracks in a powder metallurgy superalloy at room and at high temperature" *Fatigue '87 Proceedings of 3rd Int. Conf. on Fatigue and Fatigue Thresholds, Charlottesville, Virginia, USA, 28 June-3 July 1987*, Engineering Materials Advisory Services Ltd, pp. 351-360, 1987.

[86] Brown C.W., King J.E., Hicks M.A. "Effects of microstructure on long and short crack growth in nickel base superalloys" *Metal Science*, vol. 18, pp. 374-380, 1984.

[87] Zhang Y.H., Edwards L. "The development of plastic zones ahead of small fatigue cracks and their consequences for crack growth rate" *Aluminium alloys*, vol. 2, pp. 563-568, 1992.

[88] Reed P.A.S., King J.E. "Comparison of long and short crack growth in polycrystalline and single crystal forms of U720" *Short Fatigue Cracks, Sheffield, UK, Dec. 1990*, Mechanical Engineering Publications Limited (UK), ISBN 0-85298-809-5, pp. 153-168, 1992.

[89] Scott P.M., Thorpe T.W. "A critical review of crack tip stress intensity factors for semi-elliptic cracks" *Fatigue of Engineering Materials and Structures (UK)*, vol. 4, pp. 291-309, 1981.

[90] Zhang Y.H, Edwards L. "On the blocking effect of grain boundaries on small crystallographic fatigue crack growth" *Materials Science and Engineering*, A188, pp. 121-132, 1994.

[91] Zurek A.K., James M.R., Morris W.L. "The effect of grain size on fatigue growth of short cracks" *Metallurgical Transactions A*, vol. 14A, pp. 1697-1705, 1983.

[92] Zhai T., Wilkinson A.J., Martin J.W. "The effects of micro-texture and B' particle distribution on short fatigue crack in an Al-Li 8090 alloy" *Materials Science Forum*, Vols. 331-337, pp. 1549-1554, 2000.

[93] Hussey I.W., Bryne J., Locke W. "Fatigue crack growth of small corner defects from blunt notches in an aeroengine alloy" *Short Fatigue Cracks, Sheffield, UK, Dec. 1990*, Mechanical Engineering Publications Limited (UK), ISBN 0-85298-809-5, pp. 305-318, 1992.

[94] Sadananda K., Shahinian P. "Analysis of crystallographic high temperature fatigue crack growth in a nickel base alloy" *Metallurgical Transactions A*, vol. 12A, pp. 343-351, 1981.

[95] Gerard D.A., Koss D.A. "The influence of porosity on short fatigue crack growth at large strain amplitudes" *International Journal of Fatigue*, vol. 13, pp. 345-352, 1991.

[96] King J.E. "Effects of grain size and microstructure on threshold values and near threshold crack growth in powder-formed Ni-base superalloy" *Metal Science*, vol. 16, pp. 345-355, 1982.

[97] Yuen J.L., Schmidt C.G., Roy P. "Effects of air and inert environments on the near threshold fatigue crack growth behavior of alloy 718" *Fatigue and Fracture of Engineering Materials and Structures (UK)*, vol. 8, pp. 65-76, 1985.

[98] King J.E. "Surface damage and near-threshold fatigue crack growth in a Ni-base superalloy in vacuum" *Fatigue and Fracture of Engineering Materials and Structures (UK)*, vol. 5, pp. 177-188, 1982.

[99] Sadananda K., Shahinian P. "Effect of environment on high temperature crack growth behaviour of several nickel-base alloys" *Proc. Int. Conf. on Corrosion of Nickel-Base Alloys, Cincinnati, Ohio, USA, 23-25 Oct. 1984*, American Society for Metals, pp. 101-115, 1985.

[100] Nikbin K.M., Webster G.A. "Creep-fatigue crack growth in a nickel-base superalloy" *Proceedings 2nd International Conference on Creep and Fracture of Engineering Materials and Structures, Swansea, U.K., 1-6 Apr. 1984*, Pineridge Press Ltd., vol. 2, pp. 1091-1104, 1984.

[101] James L.A. "Fatigue crack propagation in alloy 718: A review" *Superalloy 718 - Metallurgy and Applications, Pittsburgh, Pennsylvania, USA, 12-14 June 1989*, TMS, pp. 499-515, 1989.

[102] Winstone M.R., Nikbin K.M., Webster G.A. "Modes of failure under creep/fatigue loading of a nickel-based superalloy" *Journal of Materials Science*, vol. 20, pp. 2471-2476, 1985.

[103] Sadananda K., Shahinian P. "Hold-time effects on high temperature fatigue crack growth in Udimet 700" *Journal of Materials Science*, vol. 13, pp. 2347-2357, 1978.

[104] Byrne J., Hall R., Grabowski L. "Elevated temperature fatigue crack growth under dwell conditions in Waspaloy" *International Journal of Fatigue*, vol. 19, pp. 359-367, 1997.

[105] Ghonem H., Nicholas T., Pineau A. "Elevated temperature fatigue crack growth in Alloy 718 I: effects of mechanical variables" *Fatigue and Fracture of Engineering Materials and Structures (UK)*, vol. 16, pp. 565-576, 1993.

[106] Shahinian P., Sadananda K. "Effects of stress ratio and hold-time on fatigue crack growth in alloy 718" *Trans. ASME, Journal of Engineering Materials and Technology*, vol. 101, pp. 224-230, 1979.

[107] Onofrio G., Lupinc V. "High temperature fatigue crack growth behaviour of the Udimet 720Li alloy" *ECF12 - Fracture From Defects, Sheffield, UK, 14-18 Sept. 1998*, Engineering Materials Advisory Services Ltd. (UK), vol. 1, pp. 387-392, 1998.

[108] Hyde T.H., Xia L., Becker A.A. "Fatigue, creep and creep/fatigue crack growth behaviour of a nickel base superalloy at 700°C" *Experimental Mechanics*, Allison, pp. 1079-1084, 1998.

[109] Hicks M.A., King J.E. "Temperature effects on fatigue thresholds and structure sensitive crack growth in a nickel-base superalloy" *International Journal of Fatigue*, vol. 5, pp. 67-74, 1983.

[110] King J.E. Venables R.A., Hicks M.A. "The effects of microstructure, temperature and R-ratio on fatigue crack propagation and threshold behaviour in two Ni-base alloys" *Advances in Fracture Research (Fracture '84), New Delhi, India, 4-10 Dec. 1984, Proceedings of the 6th Int. Conf. on Fracture (ICF6)*, Pergamon Press Ltd., pp. 2081-2089, 1984.

[111] Antunes F.V., Ferreira J.M., Branco C.M., Byrne J. "High temperature fatigue crack growth in Inconel 718" *Materials at High Temperatures*, vol. 17, pp. 439-448, 2000.

[112] Lynch S.P., Radtke T.C., Wicks B.J., Byrnes R.T "Fatigue crack growth in nickel-based superalloys at 500-700°C I: Waspaloy" *Fatigue and Fracture of Engineering Materials and Structures (UK)* vol. 17, pp. 297-311, 1994.

[113] Hide N.J., Henderson M.B. Reed P.A.S. "Effects of grain and precipitate size variation on creep-fatigue behaviour of Udimet 720 in both air and vacuum" *Ninth International Symposium on Superalloys, Seven Springs, PA, USA, 17-21 Sept. 2000*, Minerals, Metals and Materials Society/AIME, *Superalloys 2000*, pp.495-503, 2000.

[114] Clavel M. Pineau A. "Intergranular fracture mode associated with heterogeneous deformation during low cycle fatigue in a Ni-base superalloy" *Scripta Metallurgica*, vol. 16, pp. 361-364, 1982.

[115] Clavel M., Pineau A. "Fatigue behaviour of two nickel-base alloys I: experimental results on low cycle fatigue, fatigue crack propagation and substructures" *Materials Science and Engineering*, vol. 55, pp. 157-171, 1982.

[116] Golwalkar S., Stoloff, N.S. Duquette D.J. "The effects of frequency and hold times on fatigue crack propagation rates in a nickel base superalloy" *Strength of Metals and Alloys (ICSMA 6), Melbourne, Australia, 16-20 Aug. 1982, Proc. of the 6th Int. Conf.*, Pergamon Press, pp. 879-885, 1982.

[117] Lynch S.P., Radtke T.C., Wicks B.J. "Fatigue crack growth in a nickel-based superalloy at 500-700 C" *Mechanical Behaviour of Materials-VI., Kyoto, Japan, 29 July-2 Aug. 1991, Proc. ICM6*, Pergamon Press plc (UK), vol.4, pp. 355-360, 1992.

[118] Yuen J.L., Roy P., Nix W.D. "Effects of oxidation kinetics on the near threshold fatigue crack growth behaviour of a nickel base superalloy" *Metallurgical Transactions A*, vol. 15A, pp. 1769-1775, 1984.

[119] Affeldt E.E., Floge H., Konig G.W. "Influence of time and temperature on crack growth rate in the P/M Nickel base alloy Udimet 700 with three different microstructures" *Low Cycle Fatigue and Elasto-Plastic Behaviour of Materials 3, Berlin, Germany, 7-11 Sept. 1992*, Elsevier Science Publishers Ltd. (UK), pp. 166-171, 1992.

[120] Affeldt E.E., Konig G.W. "Effect of time and temperature on crack propagation in a nickel-base superalloy (Udimet 700)" *Advanced Materials and Processes--Proceedings of the First European Conference. EUROMAT '89, Aachen, FRG, 22-24 Nov. 1989*, DGM Informationsgesellschaft, vol. 1, pp. 523-528, 1990.

[121] Morley S.A., Martin J.W. "The effect of precipitate distribution on fatigue crack propagation in a powder-formed superalloy (AP1)" *Procs. Life Assessment of Dynamically Loaded Materials and Structures. Vol. II, Lisbon, Portugal, 17-21 Sept. 1984*, Engineering Materials Advisory Services Ltd., vol. 2, pp. 721-727, 1985.

[122] Wei R.P., Huang Z. "Influence of dwell time on fatigue crack growth in nickel-base superalloys" *Materials Science and Engineering*, vol. 336, pp. 209-214, 2002.

[123] Loyer-Danflou H., Marty M., Walder A., Mendez J., Violan P. "The effect of environment and structure on creep fatigue crack propagation in a P/M Astroloy" *Journal de Physique IV*, vol. 3, pp. 359-362, 1993.

[124] Mendez J., Violan P., Quintard M., Marcon G., Marty M., Thevenin P., Walder A. "Effect of environment of creep-fatigue crack propagation in turbine disc superalloys" *Corrosion-Deformation Interactions '92, Fontainebleau, France, 5-7 Oct. 1992*, Les Editions de Physique (France), pp. 531-541, 1993.

[125] Zheng D., Rosenberger A., Ghonem H. "Influence of prestraining on high temperature, low frequency fatigue crack growth in superalloys" *Materials Science and Engineering*, A161, pp. 13-21, 1993.

[126] Clavel M., Pineau A. "Frequency and wave-form effects on the fatigue crack growth behavior of alloy 718 at 298K and 823K" *Metallurgical Transactions A*, vol. 9A, pp. 471-480, 1978.

[127] Ghonem H., Zheng D. "Frequency interactions in high-temperature fatigue crack growth in superalloys" *Metallurgical Transactions A*, vol. 23A, pp. 3067-3072, 1992.

[128] Ghonem H., Nicholas T., Pineau A. "Elevated temperature fatigue crack growth in alloy 718 – part II: effects of environment and material variables" *Fatigue and Fracture of Engineering Materials and Structures (UK)* vol. 16, pp. 577-590, 1993.

[129] Tong J., Bryne J. "Effects of frequency on fatigue crack growth at elevated temperature" *Fatigue and Fracture of Engineering Materials and Structures (UK)*, vol. 22, pp.185-193, 1999

[130] Tong J., Bryne J. "Mechanism map of U720Li superalloy at 650°C" *ECF12 - Fracture From Defects, Sheffield, UK, 14-18 Sept. 1998*, Engineering Materials Advisory Services Ltd. (UK), vol. 1, pp. 327-332, 1998.

[131] Wicks B.J., Radtke T.C "Fatigue crack growth in two gas turbine engine disc alloys" *Australian Fracture Group 1990 Symposium, Sydney, Australia, 3-4 Dec. 1990*, Australian Fracture Group, pp. 81-88, 1990.

[132] Lynch S.P., Radtke T.C., Wicks B.J., Brynes R.T. "Fatigue crack growth in nickel-based superalloys at 500-700°C II: direct-aged Alloy 718" *Fatigue and Fracture of Engineering Materials and Structures (UK)*, vol. 17, pp. 313-325, 1994.

[133] Merrick H.F., Floreen S. "The effects of microstructure on elevated temperature crack growth in nickel-base alloys" *Metallurgical Transactions A*, vol. 9A, pp. 231-236, 1978.

[134] Reger M., Remy L. "High temperature, low cycle fatigue of IN100 superalloy II: influence of frequency and environment at high temperatures" *Materials Science and Engineering A*, 101, pp. 55-63, 1988.

[135] Carbou C., Mendez J., Violan P. "Factors influencing creep-fatigue crack propagation in P/M Astroloy at 650°C and 750°C" *Mechanisms and Mechanics of Damage and Failure, Proc. of 11th Biennial European Conf. on Fracture (ECF11), Poitiers-Futuroscope, France, 3-6 Sept. 1996*, vol. 2, pp. 1305-1310, 1996.

[136] Chateau E., Remy L. "Creep and creep-fatigue behaviour of Udimet 720 at 850°C" *ECF12 - Fracture From Defects, Sheffield, UK, 14-18 Sept. 1998*, Engineering Materials Advisory Services Ltd. (UK), vol. 1, pp. 339-344, 1998.

[137] Reger M., Remy L. "Fatigue oxidation interaction in IN100 superalloy" *Metallurgical Transactions A*, vol. 19A, pp 2259-2269, 1988.

[138] Andrieu E., Molins R, Ghonem H., Pineau A. "Intergranular crack tip oxidation mechanism in a nickel based superalloy" *Materials Science and Engineering*, A154, pp. 21-28, 1992.

[139] Andrieu E., Hochstetter G., Molins R., Pineau A. "Oxidation mechanism in relation to high temperature fatigue crack growth properties of Alloy 718" *Superalloys 718, 625, 706 and Various Derivatives, Pittsburgh, Pennsylvania, United States, 26-29 June 1994*, The Minerals, Metals & Materials Society (United States), pp. 619-631, 1994.

[140] Nazmy, M. Hoffelner W., Wuthrich C. "Elevated temperature creep-fatigue crack propagation in nickel-base alloys and 1Cr-Mo-V steel" *Metallurgical Transactions A*, vol. 19A, pp. 855-862, 1988.

[141] Bernede P., Remy L. "Fatigue crack growth of small defects in a superalloy at high temperature in air and in vacuum" *Short Fatigue Cracks, Sheffield, UK, Dec. 1990*, Mechanical Engineering Publications Limited (UK), ISBN 0-85298-809-5, pp. 251-262, 1992.

[142] Loo-Morrey M., PhD. Thesis, University of Southampton, 1997.

[143] Xie J.Z. "Low cycle fatigue and fatigue crack growth behaviours of alloy IN718" *Superalloys 718, 625 & Various Derivatives*, pp. 491-500, 1991.

[144] Hyde T.H., Xia L., Becker A.A., Sun W. "Fatigue, creep, and creep/fatigue behaviour of a nickel base superalloy at 700°C" *Fatigue and Fracture of Engineering Materials and Structures (UK)*, vol. 20, pp. 1295-1303, 1997.

[145] Cowles B.A., Sims D.L., Warren J.R., Miner, R.V. Jr. "Cyclic behaviour of turbine disk alloys at 650°C" *Journal of Engineering Materials Technology*, vol. 102, pp. 356-363, 1980.

[146] Gayda J.,. Miner R.V, Gabb T.P. "On the fatigue crack propagation behaviour of superalloys at intermediate temperature" *Superalloys 1984. Champion, PA., U.S.A., 7-11 Oct. 1984, Proc. of 5th Int. Symp. on Superalloys*, The Metallurgical Society/AIME, pp. 731-740, 1984.

[147] Krueger D.D., Antolovich S.D., Van Stone R.H. "Effects of grain size and precipitate size on the fatigue crack growth behaviour of Alloy 718 at 427 C" *Metallurgical Transactions A*, vol 18A, pp. 1431-1449, 1987.

[148] Terlinde G., Luetjering G. "Influence of grain size and age hardening on dislocation pile-ups and tensile fracture for a Ti-Al alloy" *Metallurgical Transactions A*, vol. 13A, pp. 1283-1292, 1982.

[149] Lewandowska M., Mizera J., Wyrzykowski J.W. "Cyclic behaviour of model Al-Li alloys: effect of the precipitate state" *Materials Characterisation*, vol. 45, pp. 195-202, 2000

[150] Miner R.V., Gayda J., Maier R.D. "Fatigue and creep-fatigue deformation of several nickel-base superalloys at 650°C" *Metallurgical Transactions A*, vol. 13A, pp. 1755-1765, 1982.

[151] Floreen S., Kane R.H. "Controlling intermediate temperature fatigue crack growth in nickel base superalloys by microstructural variations" *4th Int. Symp. on Superalloys (Superalloys 1980), Champion, PA., 21-25 Sept. 1980*, American Society for Metals, pp. 595-604, 1980.

[152] Connolley T., PhD. Thesis, University of Southampton, 2001.

[153] Goodhew P.J., Humphreys F.J. "Electron Microscopy and Analysis" Taylor & Francis, U.K., ISBN 0-85066-414-4.

[154] Starink M.J., Omar M.Z., Thomson R.C. "A method for analysis of EDX data containing contributions from several phases using SEM" Unpublished work.

[155] Charturvedi M.C., Han Y. "Strengthening mechanisms in Inconel 718 superalloy" *Metal Science*, vol. 17, pp. 145-149, 1984.

[156] Sundararaman M., Mukhopadhyay P., Banerjee S. "Deformation behaviour of γ" strengthened Inconel 718" *Acta metallurgica*, vol. 36, pp. 847-864, 1988.

[157] Ardell A.J., Huang J.C. "Antiphase boundary energies and the transition from shearing to looping in alloys strengthened by ordered precipitates" *Philosophical Magazine Letters*, vol. 58, pp. 189-197, 1988.

[158] Brooks R.R., Rainforth W.M. "The effect of microstructure on the morphology of fatigue cracks in UDIMET 720" *Fatigue and Fracture of Engineering Materials and Structures (UK)*, vol.23, pp. 725-736, 2000.